Towards Processable Metal-Organic Frameworks

Porous Glasses and Water-Processable Materials

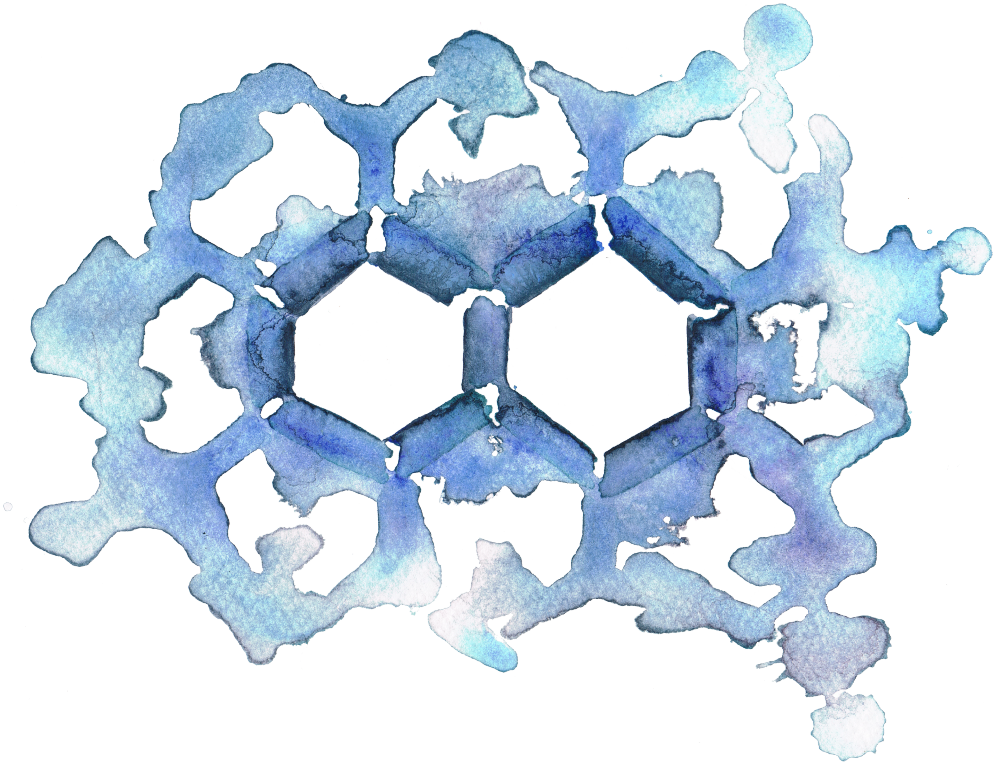

Dissertation

Louis Frentzel-Beyme

December 2021

Towards Processable Metal-Organic Frameworks

Porous Glasses and Water-Processable Materials

Faculty of Chemistry and Chemical Biology
Technische Universität Dortmund

Dissertation

Submitted by
Louis Frentzel-Beyme

December 2021

This work has been performed in the time between November 2017 and December 2021 in the Inorganic Chemistry Department of the Faculty of Chemistry and Chemical Biology – Technische Universität Dortmund.

1st referee: Prof. Dr. Sebastian Henke

2nd referee: Prof. Dr. Guido Clever

Date of submission : 22.12.2021

Date of examination: 09.03.2022

The difficulty lies not so much in developing new ideas as in escaping from old ones.

– John Maynard Keynes

I would like to express my deepest gratitude to my supervisor
Prof. Dr. Sebastian Henke
for giving me the opportunity to work on this exciting topic as well as excellent teaching, support and motivation throughout the course of this dissertation.

I also thank Prof. Dr. Guido Clever for accepting to be the 2nd referee of this dissertation.

Furthermore, I would like to thank the following people for their help with synchrotron experiments, without them it would not have been possible to realize major parts of this work:

- Dr. Phil Chater and Dr. Dean Keeble for data collection and processing as well as fruitful discussions of X-ray total scattering at Diamond Light Source (DLS, UK).
- Dr. Christian Sternemann and Dr. Michael Paulus for their tremendous help during numerous beamtimes at Dortmunder ELekTronenspeicherring-Anlage (DELTA, Germany).
- Dr. Michael Wharmby, Dr. Alba San Jose Mendez and Dr. Alexander Schökel for their help during beamtimes at Deutsches Elektronen-Synchrotron (DESY, Germany).

I also like to acknowledge Dr. Henning Moldenhauer and Dr. Jörg Debus for conducting Raman scattering experiments.

Further, Dr. Soma Salamon, Dr. Joachim Landers and Prof. Dr. Heiko Wende are acknowledged for collecting magnetic measurements as well as the discussion and interpretation of the data.

I would also like to thank trainees, as well as students who worked with me in the last years and whose results also partially contributed to parts of this thesis:
Carolin Jaworski, Anna Krupp, Rebecca Scheel, Andrijan Ohmann, Lena Ostermeier, Jelena Auch, Pascal Kolodzeiski, Sven Golenia, Julian Dyrda and Jannik Engel.

In particular, I thank Marvin Kloss and Pascal Kolodzeiski for their dedicated work on ZIF glasses during their Master studies which were essential for the success of this thesis.

I would also like to thank Helga Schulte, Peggy Sieg, Birgit Thormann as well as Dr. Gabriele Trötscher-Kaus for their help with everyday problems and administrative support.

I also thank all the present and past members of the group of Prof. Jurkschat, Prof. Clever and Prof. Strohmann, especially for welcoming me at TU Dortmund and making the beginning of this thesis much easier. Especially to acknowledge are: Dr. Robin Rudolf, Dr. Marcel Krick, Dr. Philip Punt, Dr. Lukas Zibula, Dr. Britta Glowacki, Moritz Achternbosch and in particular Rana Seymen, for her support during the last weeks of completing this thesis.

I want to thank Dr. Gregor Kieslich, Dr. Pia Vervoorts and Stefan Burger for entertaining meetings at conferences and workshops.

Warm thanks to the present and past members of *The Henke Group* for a pleasant working atmosphere as well as fun group events and conference trips:
Roman Pallach, Marvin Kloss, Stefan Koop, Julia Kuhnt, Pascal Kolodzeiski, Kai Terlinden, Jianbo Song, Jan-Benedikt Weiß, Dr. Athanasios Koutsianos, Dr. Collins Erinmwingbovo, Andrea Machallica, Xue Wenlong, Christian Nelle, Michael Strobl, Denise Zickler and Dr. Chinmoy Das.

I thank in particular, Roman Pallach for sharing the office and lab with me in the last years, for the numerous discussions about chemistry as well as extensive support in the last days of this thesis.

I thank Christopher for the wonderful study time at the RUB.
Further, I thank my best friend Sebastian for his support and constant balance by sharing many important moments with me throughout the years. Furthermore, together with Sina, both were especially important to overcome difficult Corona times.
Likewise, Winni and Silvi are acknowledged for providing a relaxing and calming spot in Monte Clérigo as well as other perspectives.
Of course, I thank my parents and my sister for their tremendous, unceasing spiritual support and motivation throughout my whole studies and life.
Finally, I thank Louise for standing by me in all situations; without you, the completion of this work would not have been possible.

Meiner Familie und Louise.

Abstract

In this work, porous metal-organic framework (MOF) materials were investigated towards processability. Processability of porous materials is an advantageous ability for industrial applications, where it is often mandatory to form materials into certain shapes, such as pellets or thin films. Materials can be formed if they are in a *liquid/melted* state and their films are accessible e.g. during *solution-processing* (i.e. 'liquid-casting').

Melting of MOFs was investigated for the formation of porous MOF glasses, which are currently an emerging field in MOF chemistry. Fundamentals of the melting behavior of MOFs were systematically investigated by deriving relations between the inorganic building units (metal ions) and organic building units (linkers) of melting MOFs, their structural features and their thermal properties (e.g. melting temperature and glass transition temperature). Most importantly, it was demonstrated that the melting point of a melting mixed-linker MOF system (i.e. MOFs containing two different types of linkers) can be systematically controlled by adjusting the linker ratio. These in-depth studies also allow to derive structural and compositional requirements for MOF melting, which set the stage for the targeted search and discovery of new meltable MOFs. Further, it was shown that porosity appears to be an intrinsic feature of MOF glasses based on imidazolate linkers, a feature, which was so far unknown. Adjusting their compositions allows even to vary the porosity features (i.e. pore sizes and volumes) and thus tune their gas sorption properties.

Solution-processability of MOFs was realized by the development of a new class of water-processable MOFs, termed amphiphile salt frameworks (ASFs). ASFs are based on systematically designed amphiphilic molecules linked by kinetically labile sodium ions, forming honeycomb-like structures. These well-defined framework materials reversibly assemble from an aqueous solution by evaporation of water and disassemble again by dissolution in water. Remarkably, ASFs are shown to be porous towards sorption of several gases (N_2, CO_2, propane, propylene, and *n*-butane) and also feature high thermal and mechanical stability.

In summary, the results of this thesis provide new insights towards processable MOFs adressed by two different approaches (i.e. melting and solution-processability). Overall, this aids for a better understanding of how the macrostructure of MOF materials can be influenced and adjusted in the future.

Kurzfassung

In dieser Arbeit wurden poröse metallorganische Gerüstmaterialien (metal-organic frameworks (MOFs)) auf ihre Prozessierbarkeit hin untersucht. Die Prozessierbarkeit poröser Materialien ist eine wichtige Eigenschaft für industrielle Anwendungen bei denen es oft erforderlich ist Materialien in bestimmte Formen zu bringen, wie Pellets oder dünne Filme. Materialien können geformt werden, wenn sie sich in einem flüssigen/geschmolzenen Zustand befinden und Filme sind z. B. durch die Prozessierung in Lösung zugänglich (z. B. Abscheidung aus Lösung).

Das *Schmelzen* von MOFs wurde für die Bildung von porösen MOF-Gläsern untersucht, die derzeit ein aufstrebendes Feld in der MOF-Chemie darstellen. Hierbei, wurden die Grundlagen des Schmelzverhaltens von MOFs systematisch analysiert, indem Beziehungen zwischen den anorganischen Baueinheiten (Metallionen) und organischen Baueinheiten (Linkern) schmelzender MOFs, ihren strukturellen Merkmalen und ihren thermischen Eigenschaften (z. B. Schmelztemperatur und Glasübergangstemperatur) abgeleitet wurden. Vor allem konnte gezeigt werden, dass der Schmelzpunkt eines schmelzenden MOF-Systems mit gemischten Linkern (d. h. MOFs, die zwei verschiedene Arten von Linkern enthalten) durch Anpassung des Linker-Verhältnisses systematisch gesteuert werden kann. Aus diesen eingehenden Untersuchungen lassen sich auch strukturelle und kompositorische Voraussetzungen für das Schmelzen von MOFs ableiten, die die Grundlage für die gezielte Suche und Entdeckung neuer schmelzbarer MOFs bilden. Darüber hinaus wurde gezeigt, dass Porosität ein intrinsisches Merkmal von MOF-Gläsern auf der Basis von Imidazolat-Linkern zu sein scheint, ein Merkmal, das bisher unbekannt war. Durch Anpassung der Zusammensetzung von MOF-Gläsern können sogar die Porositätsmerkmale (d. h. Porengröße und -volumen) variiert und somit ihre Gassorptionseigenschaften eingestellt werden.

Das *Prozessieren in Lösung* von MOFs wurde durch die Entwicklung einer neuen Klasse von in Wasser prozessierbaren MOFs realisiert, die als amphiphile Salzgerüste (amphiphile salt frameworks (ASFs)) bezeichnet werden. ASFs basieren auf systematisch entworfenen amphiphilen Molekülen, die durch kinetisch labile Natriumionen verbunden sind und Bienenwaben-artige Strukturen bilden. Diese wohldefinierten Gerüstmaterialien bauen sich aus einer wässrigen Lösung durch Verdampfen von Wasser reversibel auf und zerfallen wieder durch Auflösen in Wasser. Bemerkenswerterweise, sind ASFs direkt porös nach der Abscheidung aus Wasser, was durch die Sorption verschiedener Gase (N_2, CO_2, Propan, Propylen und *n*-Butan) gezeigt wurde. Zudem weisen sie eine hohe thermische und mechanische Stabilität auf.

Zusammengefasst, die Ergebnisse dieser Arbeit liefern neue Erkenntnisse über die Prozessierbarkeit von MOFs, die mit zwei verschiedenen Ansätzen (d.h. Schmelzen

und Prozessieren in Lösung) untersucht wurden. Insgesamt trägt dies zu einem besseren Verständnis dazu bei, wie die Makrostruktur von MOF-Materialien in Zukunft beeinflusst und angepasst werden kann.

Contents

List of Abbreviations

K	bulk modulus
S_{BET}	specific BET surface area
S_{IAST}	IAST selectivity
T_{g}	glass transition temperature
T_{m}	melting temperature
T_{am}	amorphization temperature
T_{rc}	recrystallization temperature
V_{pore}	pore volume
ΔH_m	melting enthalpy
ΔS_m	melting entropy
$n_{\mathrm{ads}}^{\mathrm{max}}$	maximum molar gas capacities
*.cif	crystallographic information file
ABB	amphiphilic building block
ASF	amphiphile salt framework
BET	Brunauer-Emmett-Teller
bim^-	benzimidazolate
COF	covalent organic framework
CSD	Cambridge Structural Database
DELTA	Dortmunder ELekTronenspeichering-Anlage
DESY	Deutsches Elektronen-Synchrotron
DLS	Diamond Light Source
DMF	*N,N*-dimethylformamide
DMSO	dimethyl sulfoxide
DSC	differential scanning calorimetry
eVF	experimental void fraction

FC	field-cooled
FSDP	first sharp diffraction peak
FTIR spectroscopy	Fourier-transform infrared spectroscopy
FWHM	full width at half maximum
GFA	glass forming ability
HK	Horvath-Kawazoe
HP-PXRD	high-pressure powder X-ray diffraction
IAST	ideal adsorbed solution theory
im^-	imidazolate
IUPAC	International Union of Pure and Applied Chemistry
$mbim^-$	5-methylbenzimidazolate
MOC	metal-organic cage
MOF	metal-organic framework
MRO	medium range order
NaCl	sodium chloride
NaOH	sodium hydroxide
NLDFT	nonlocal density functional theory
NMR spectroscopy	nuclear magnetic resonance spectroscopy
OD	outer diameter
PFM	porous framework material
PIMs	polymers with intrinsic microporosity
PMM	porous molecular material
POC	porous organic cage
PSD	pore size distributions
PXRD	powder X-ray diffraction
SBU	secondary building unit
SCXRD	single crystal X-ray diffraction
SEM	scanning electron microscopy
TGA/DSC	simultaneous thermogravimetric analysis/differential scanning calorimetry

tVF	theoretical void fraction
XPDF	X-ray pair distribution function
ZFC	zero-field-cooled
ZIF	zeolitic imidazolate framework

1 Motivation and Aims

An important class of porous materials are metal-organic frameworks (MOFs). MOFs are typically polycrystalline materials built from inorganic (nodes; e.g. metal ions or metal-oxo clusters) and organic building units (linkers; i.e. multidentate molecules). Their frameworks adopt zeolite-like structures. In the last decades, a huge variety of MOFs, interesting for many different application fields, has been synthesized. However, the developments in MOF chemistry were mainly focused on adjusting and optimizing materials on the molecular scale. Nevertheless, the macrostructure of the materials is also very important for industrial applications, where materials need to be formed into e.g. pellets, fibres or thin films. In this context, it is beneficial, when the materials feature the ability to be processed or shaped in the liquid/melted state into desired solid forms, as well as solution-processed (e.g. 'liquid-casted'). Investigations towards processable MOFs are addressed by two different approaches in this thesis and presented in two parts, respectively.

Part I – ZIF Glasses

A subfamily of MOFs are zeolitic imidazolate frameworks (ZIFs). ZIFs are constructed from divalent metal ions of tetrahedral coordination geometry (e.g. Zn^{2+} or Co^{2+}) and imidazolate-type linkers (e.g. imidazolate, im^- or benzimidazolate, bim^-). Strikingly, some representatives of ZIFs have been recently reported to melt and to form glasses upon cooling back to room temperature. Glass forming ZIFs overcome the intrinsic limitations of polycrystalline MOFs as they can be shaped in their liquid/melted state. So far, only a few examples of glass forming ZIFs are known (e.g. only ZIFs containing Zn^{2+} ions are known to form glasses), so that the requirements for ZIF melting and the parameters influencing the melting behavior are unknown thus far. Moreover, only very little information is documented about the porosity of ZIF glasses.

Thus, this part will contribute to gain a deeper understanding of (i) the porosity of ZIF glasses and (ii) the fundamentals of ZIF melting. Both aspects will be investigated in two sections each, answering the following questions.

(i) Porosity of ZIF glasses

(a) Do ZIF glasses feature intrinsic structural porosity and how does the porosity depend on their composition (e.g. the imidazolate-type linkers)? (Section 6)

(b) Are ZIF glasses potential candidates for applications in important gas separation processes, such as the separation of propylene and propane? (Section 9)

(ii) Fundamentals of ZIF melting

(a) Is it possible to obtain ZIF glasses with metal cations other than Zn^{2+} ions as the inorganic building unit? (Section 7)

(b) What are the fundamental structural and compositional requirements for ZIF melting and glass formation? (Section 8)

Part II – A New Class of Water-Processable MOFs

MOFs are typically not solution-processable, which is due to the strong bonding between their building units prohibiting a reversible assembly of the porous framework. However, the bonding situation in MOFs (and in generall porous framework materials) yields also materials with well-defined structures (i.e. defined pore sizes and volumes) and comparably high thermal and mechanical stability; essential requirements for real-life technological applications.

Thus, the following question arises:

Is it possible to systematically design MOF building units to achieve porous materials, which are solution-processable and form well-defined structural motifs, exhibiting high thermal and mechanical stability?

In this part, this question will be addressed in one section (Section 10), where a new class of water-processable MOFs is introduced by:

(i) Developing a systematic design concept for water-processable MOFs based on considerations regarding coordination chemistry and structure directing hydrophobic functionalities.

As *organic building unit*, amphiphilic molecules are chosen. Their hydrophobic part (i.e. alkyl chains) guides the assembly to a porous honeycomb-like structure motif. The hydrophilic part (i.e carboxylate groups) coordinates to the inorganic building units to form the connected framework.

As *inorganic building unit*, kinetically labile metal ions (i.e Na^+ ions) are chosen. They form strong coordinative bonds with the carboxylate groups

of the amphiphilic organic building units. This bonding situation provides thermal and mechanical stability by also aiding assembly/disassembly of the framework by hydrolysis.

(ii) Applications of this concept leading to the synthesis of a series of suitable amphiphilic building units and their utilization for the formation of a new family of water-processable MOFs.

Subsequently, the obtained materials will be investigated regarding:

(a) Their crystal structures.

(b) Their processing ability (e.g. reversible assembly from solution).

(c) Their porosity features (e.g. pore volume and pore size).

(d) Their stability towards temperature and mechanical pressure.

2 General Introduction

2.1 Metal-Organic Frameworks

2.1.1 A Broad Definition

Metal-organic framework (MOF) are a subclass of coordination networks which in turn are a subclass of coordination polymers. This hierarchical nomenclature was recommended from a task force of the International Union of Pure and Applied Chemistry (IUPAC) in 2013.[1] The three terms for itself are defined as shown in Table 2.1. According to the IUPAC definition, MOFs are potentially porous framework structures made by the linkage of inorganic and organic building units.

Table 2.1: Definitions of the materials classes for the hierarchical nomenclature for MOFs as given by the IUPAC.[1]

Term	Definition
Coordination Polymer	A coordination compound continuously extending in 1, 2 or 3 dimensions through coordination bonds
Coordination Network	A coordination compound extending, through coordination bonds, in 1 dimension, but with cross-links between two or more individual chains, loops or spiro-links, or a coordination compound extending through coordination bonds in 2 or 3 dimensions
Metal-Organic Framework	A metal-organic framework, abbreviated to MOF, is a coordination network with organic ligands containing potential voids.

The definition of a MOF is phrased very general and broad which is because at the point the definition was invented the term MOF was already used in the academic literature for about 15 years.[2,3] Without having a clear definition, a lot of different materials were termed MOF spanning across multidisciplinary research fields.[4] Therefore, it seems useful to approach the important features of MOFs by a historical approach.

2.1.2 A Historical Approach

Representatives of coordination polymers were already reported 60 years ago.[5,6] They are based on Werner-type coordination chemistry and are build from transition metals or lanthanides coordinated with multitopic organic ligands. The multitopic organic ligands (mostly charged neutral) feature Lewis basic sides. Their assembly is driven by self-assembly mechanisms, yielding one-, two- or three- dimensional regular polymeric compounds. Further, it was found that the structure of porous coordination polymers (i.e. coordination polymers with voids) could be controlled by the choice of different solvents and counter ions in the synthesis. As a result many different coordination polymers with various structures could be obtained.[7,8] Unfortunately, the mostly positively charged frameworks collapsed if the guests (e.g. solvent molecules or counter ions) were removed from the pores. Consequently, it remained difficult to test the porous materials for real world applications.

The first materials, which can be denoted as MOFs, were published in the late 1990s.[9,10] At that time, the advancement of the materials was a charge neutral framework. This was achieved by applying oppositely charged inorganic and organic building units. Due to the charge neutrality of the framework, the solvent molecules hosted in the pores of the MOFs could be removed without structural collapse. The MOFs' inorganic building units are metal ions or metal-(oxo)-clusters and the organic building units are multitopic organic molecules (e.g. multidentate carboxylates, see Figure 2.1). The inorganic building units are referred to as nodes whereas the organic

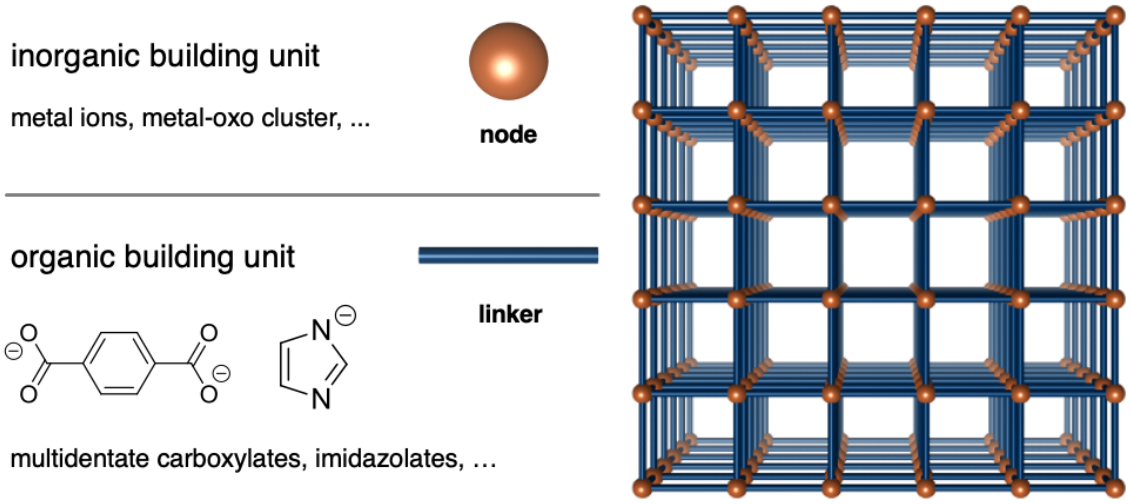

Figure 2.1: Schematic representation of a MOF with inorganic and organic building units (left) and an assembled framework (right).

building units are called linkers. These building units are assembled to a porous two- or three-dimensional network. The main characteristics of MOFs are huge internal surface areas (up to 9140 m^2 g^{-1})[11] and relatively high thermal stability (up to

600 °C)[12]. This opens the possibility for applications in gas storage, separation, catalysis, sensor technology and many more.[13]

2.1.3 The Concept of Reticular Synthesis

The discovery of new MOFs was further accelerated by the invention of a design concept – the so-called *reticular synthesis*[14,15]. This concept was pioneered by O. M. Yaghi, M. O'Keeffe and co-workers and allows to design the network topology of MOFs based on the choice of the respective node and linker.[16] Here, the building units are interpreted as geometric figures in terms of their coordinating sites. The interpretation of building units as geometric figures is schematically demonstrated in Figure 2.2. Building units carrying a topological information are called secondary building units (SBUs). For a particular set of SBUs it is possible to identify possible network topologies. In turn, a desired network topology is obtainable by selecting the right set of SBUs.

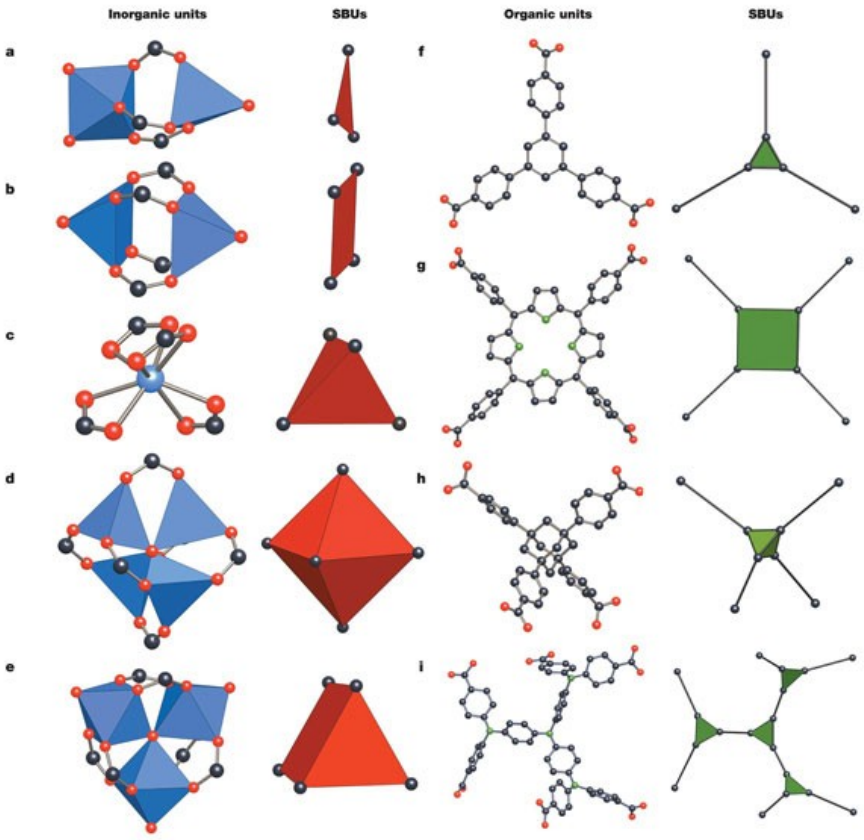

Figure 2.2: Representation of the interpretation of MOF building units as geometric figures. Reprinted by permission from Springer Nature Customer Service Centre GmbH: Springer Nature, Nature, Reticular synthesis and the design of new materials, Omar M. Yaghi et al, copyright 2003.

Despite controlling the building units connectivity, the linkers can be also function-

alized or elongated to generate isoreticular* materials.[17–20] This can be visualized with the prominent MOF-5 (see Figure 2.3).[10] Isoreticular MOF-5 materials are

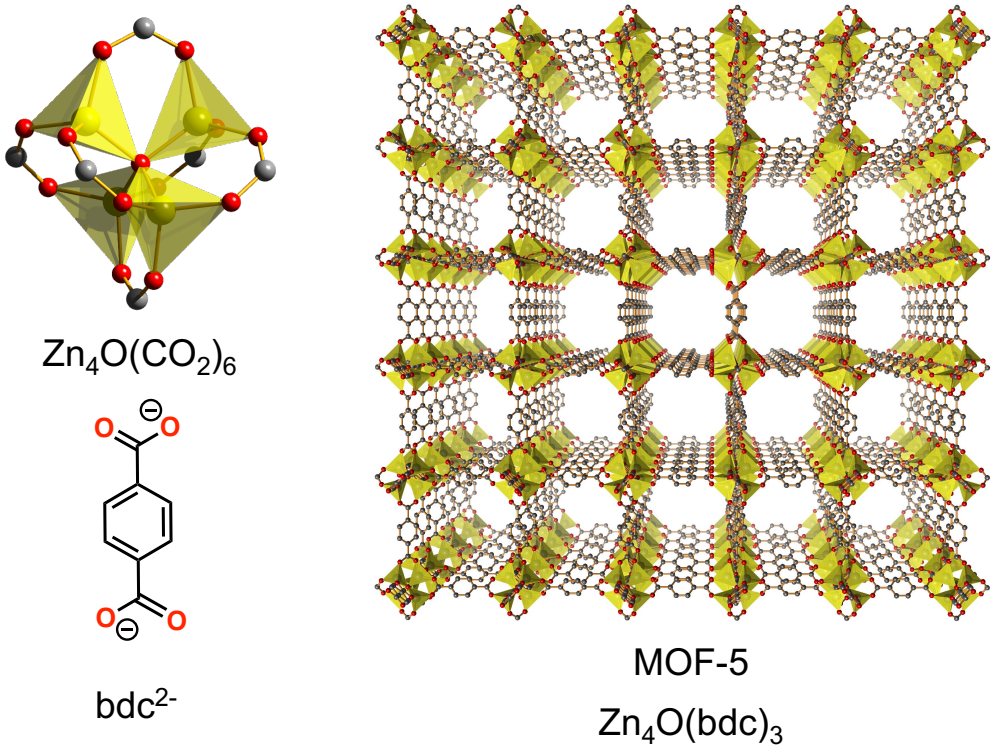

Figure 2.3: Representation the building units (left) and the extended crystal structure (right) of MOF-5. Crystal structure data to generate the image were taken from the Cambridge Structural Database (CSD)[21] (MOF-5 (CSD code MIBQAR)).

named IRMOF-X (X is a chronological number).[16] Two IRMOFs (IRMOF-2 and IRMOF-16) are displayed in Figure 2.4. The representations of the single cavity of each IRMOF (with two different linkers) shows that different pores (e.g. different metrics and functionalization of the pore surface) are generated. The underlying general concept consequently allows a precise adjustment of the porosity features, such as pore volume, diameter or the surface properties.[22,23] Here, MOFs as hybrid materials benefit especially from the variability of the organic building units, since a huge library of linkers is made available thanks to organic synthesis.

Based on this modular concept and the huge variety of possible building units, more than 6000 different MOF structures had been already reported back in 2003.[24] Over the past years, the number of newly reported MOFs is decreasing, while the number of new MOF papers is constantly increasing. This suggests that the trend has shifted from discovering new structures towards other aspects, such as studies on their functional properties as well as the macrostructure of the derived solids.[23] The macrostructure of the solids is especially important for industrial applications.

∗ Materials with feature the same framework topology.

This is because, the fabrication of thin film or pellets is often necessary for their usage in e.g. membrane techniques (i.e. gas or liquid processing)[25] or electronics[26] (e.g thin-film transistors)[27].

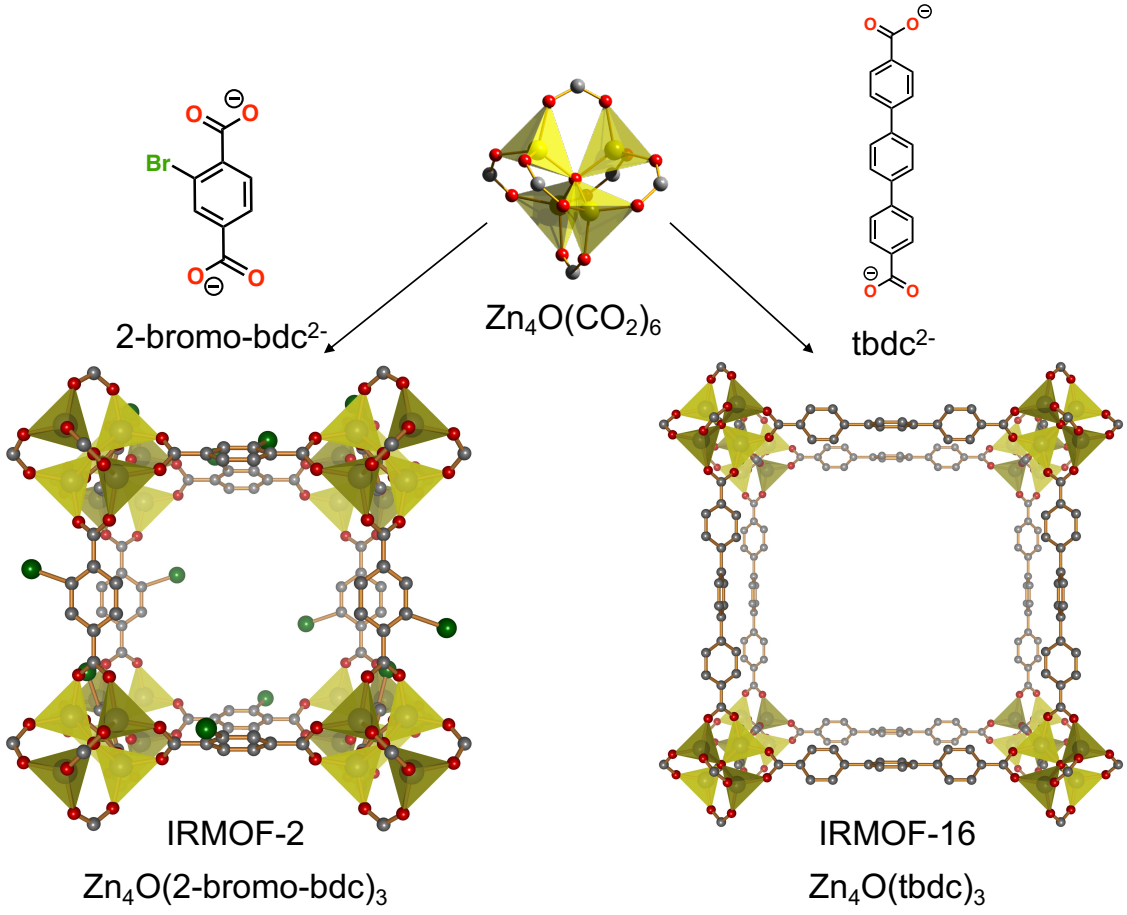

Figure 2.4: Representation of two cavities of two isoreticular structures of MOF-5 with two different linkers. Left: IRMOF-2. Right: IRMOF-16. Crystal structure data to generate the images were taken from the CSD[21] (IRMOF-2 (CSD code EDUSOL), IRMOF-16 (CSD code EDUWAB)).

2.2 Zeolitic Imidazolate Frameworks

A subclass of MOFs are zeolitic imidazolate frameworks (ZIFs). The name ZIF was established since the materials belonging to this subgroup feature structural similarities to zeolites, which results in MOF structures with zeolitic topologies. Zeolites are microporous materials based on a negatively charged aluminosilicate framework. The framework is build from TO_4 ($[SiO_4]^{4-}$ or $[AlO_4]^{5-}$) tetrahedra. The TO_4 units are cross-linked via corner-sharing by their oxygen atoms. In the pores of the framework, cations (Na^+, Ca^{2+}, Mg^{2+} etc.) are present, which balance the charge of the anionic framework.[28]

ZIF inorganic building units are mostly zinc(II) or cobalt(II) ions.[29] ZIF organic building units are imidazolate-type linkers. Similar to zeolites, the metal ions (M) are tetrahedrally coordinated by nitrogen donor atoms (N) of the imidazolate-type linkers, which results in MN_4 building units. The imidazolate-type linkers are bridging between neighboring metal ions to generate a three-dimensional framework structure. In such frameworks, the M−N−M angle of 144 ° as well as the N−M−N angle of approximate 109.5 °, are both very similar with the corresponding angles (O−Si−O and Si−O−Si) found for the Si−O coordination in zeolites (see Figure 2.5).[30]

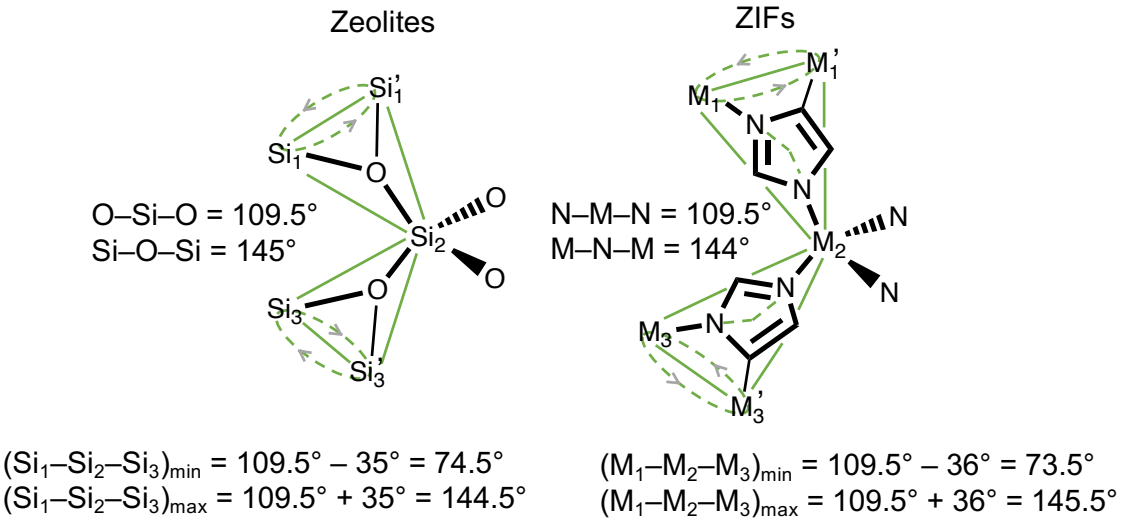

Figure 2.5: Schematic representation of structure directing angles in zeolites and ZIFs yielding similar structures. Adapted by permission from John Wiley and Sons: Chemistry - A European Journal, Design and Generation of Extended Zeolitic Metal–Organic Frameworks (ZMOFs): Synthesis and Crystal Structures of Zinc(II) Imidazolate Polymers with Zeolitic Topologies, Dong-Yuan Zhao, Lin-Hong Weng, Guang-Ning Zhang, et al, copyright 2007.

Since ZIFs are MOFs, their huge benefit is their structural diversity resulting from the variation of possible inorganic and organic building units (see Figure 2.6). On the contrary, for zeolites their purely inorganic nature limits their variability.[28,31] In ZIFs, the organic building unit is in the most simple case an imidazolate (im^-). Nevertheless, also various functionalized imidazolate linkers can be applied as well as mixing of different linkers yielding mixed-linker ZIFs. Further, ZIFs featuring iron(II), cadmium(II), manganese(II) or magnesium(II) metal ions and even ZIFs incorporating two different ions of different valence, such as lithium(I) and boron(III) ions, have been reported in the literature.[32–36]

After the appearance of the first ZIFs in 2006,[37] a huge number of new ZIFs have been synthesized and investigated − also for industrial applications, such as gas storage or separation as well as catalysis and membrane technologies.[29,30,38]

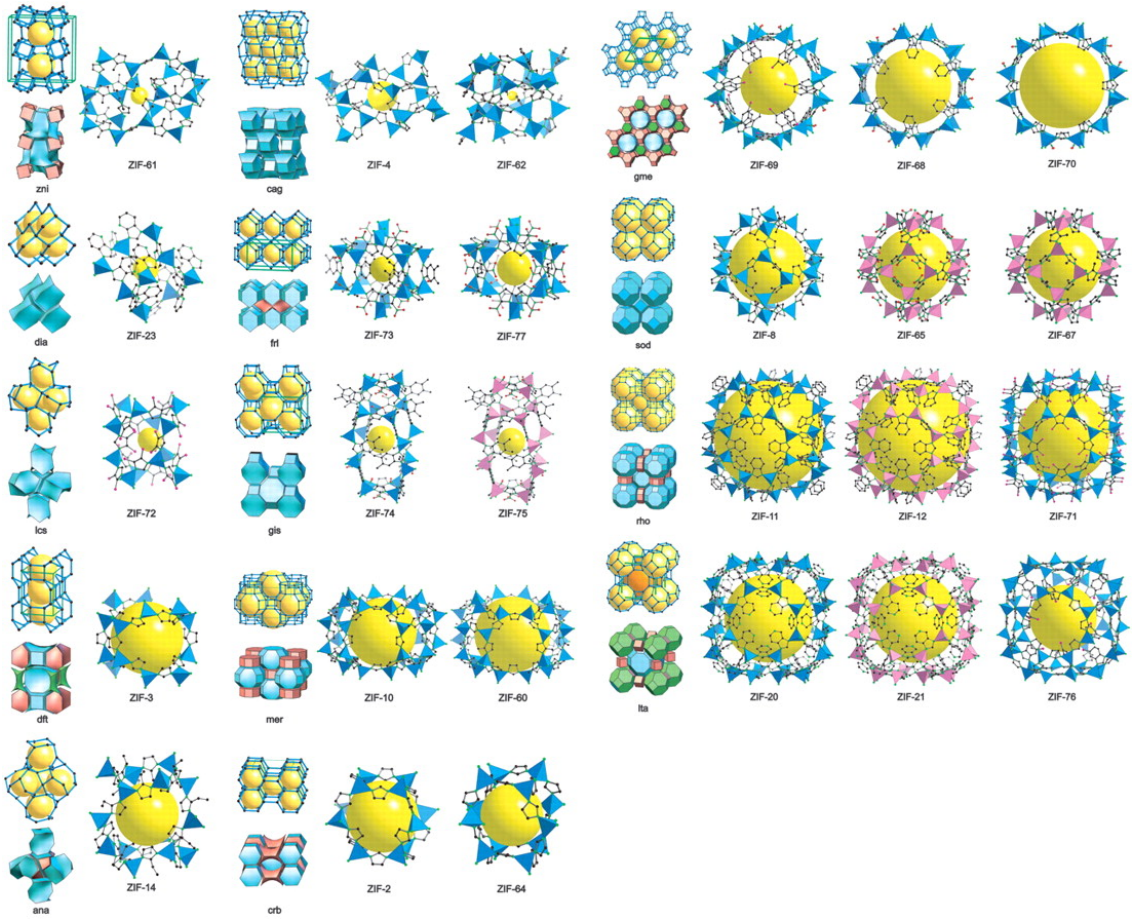

Figure 2.6: Representation of selected ZIFs reported in the literature. Each line shows the topology[a] (net and tile representation on top of each other), followed by the crystal structure of the ZIFs featuring this topology. The largest cavity of each ZIF is shown (ZnN_4 tetrahedra in blue and CoN_4 tetrahedra in pink). The yellow ball indicates the free space in the cavity. From Reference [29]. Reprinted with permission from AAAS.

a The topological codes (e.g. **zni**, **cag** etc.) are used to describe framework topologies. An overview of framework topologies and nets is given by the Reticular Chemistry Structure Resource (http://rcsr.anu.edu.au/). These codes are used to describe topologies throughout this thesis.

3 Characterization Methods

Over the course of this thesis porous solid state materials are synthesized and their materials properties are investigated. The later discussion of the results mainly focuses on how the structure and/or composition of the materials influences the properties to derive structure-property relationships. In the following, a selection of the most relevant characterization methods used in this thesis are shortly discussed. Insights are given into the theory behind selected techniques which are subsequently complemented by considerations regarding their feasibility and limitations.

The first section of this chapter (Section 3.1) focuses on X-ray diffraction techniques. Here, it will be answered how such methods can be used to uncover the periodic structures of crystalline materials. Additionally, it is explained how insights into the local structure of solids can be gained, which is especially interesting for disordered or amorphous materials. The second section (Section 3.2) will deal with gas sorption. Here, the general process of sorption of gases in porous materials is discussed and how this process can be used to gain insights into the pore architecture. Further, relevant data processing and interpretation approaches are outlined to analyze the pores and their potential for gas separation processes.

3.1 Uncovering the Invisible – X-ray Diffraction on Crystals

The invention of X-ray diffraction techniques was the starting point to uncover the structure of the crystalline solid state. All started with the discovery of X-rays by W. C. Röntgen[39] in 1896 and later the interpretation of their diffraction on crystals by M. Laue[40]. At the same time, father and son Bragg found an approach equivalent to Laue's which helped them to uncover the first crystal structures and consequently a so far invisible world.[41–43]

A crystal structure is an infinite, ordered arrangement of atoms where the smallest repeating unit is called unit cell. The basis of the approach made by Laue and the Braggs is the abstraction of a crystal structure as a periodic rigid arrangement of symmetry equivalent discrete points which gives the so-called crystal lattice. Importantly, the distance between atoms ($1 - 3\,\text{Å}$) within a crystal structure is in

the same order as the typical wavelength of X-rays ($\lambda = 0.5 - 3\,\text{Å}$).* Consequently, the crystal lattice acts as a three dimensional diffraction grid where X-rays are diffracted on the electron shell of the atoms. Whereas LAUE described the diffraction on single points of the crystal lattice, BRAGGS' theory is based on reflection on parallel lattice plains. Despite this different assumptions the derived descriptions are equivalent. After elastic scattering of X-rays on the crystal the phenomenon of interference occurs. The interference is then visualized in diffraction patterns.

A structure solution, which has become a standard technique today, is based on two main steps reverting the diffraction process by interpreting the information gained in diffraction patterns. First, the crystal symmetry and unit cell dimensions are determined from the positions of the reflections. Subsequently, the electron density distribution in the unit cell is calculated from the intensity of the reflections. This allows to define the positions of the atoms in the unit cell which finally gives the structure model.

3.1.1 Crystal Symmetry and Unit Cell

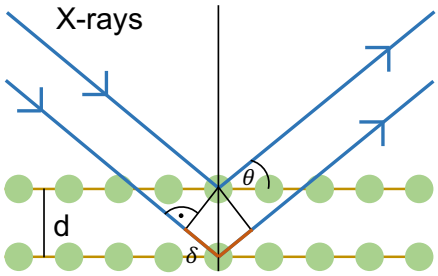

Fig. 3.1: Schematic representation of the reflection geometry of two X-ray beams on parallel lattice planes as a visualization of the Bragg equation.

In the following, we will only focus on BRAGGS' interpretation of the diffraction phenomenon. The BRAGGS found that a appropriate description of the complex diffraction phenomenon is given by simple reflection on parallel lattice planes. A schematic representation of the reflection geometry is shown in Figure 3.1. Two parallel coherent X-rays are reflected at parallel lattice planes. The derived Bragg equation is given as:

$$n\lambda = 2dsin(\theta) \tag{3.1}$$

The right-hand side of the equation 3.1 expresses the path difference (δ, marked orange in Figure 3.1) between two parallel X-rays reflected on two parallel lattice planes. The distance between the two planes is denoted by d. Constructive interference occurs if the path difference is an integer multiple of the wavelength ($n = 0, 1, 2, ...$; left-hand side equation 3.1). If this is fulfilled for an entire set of lattice planes, the reflected waves superimpose which yields a detectable reflection. Consequently, in a

* e.g. $CuK_\alpha = 1.5413$ Å or $MoK_\alpha = 0.7107$ Å.

X-ray scattering experiment where the angle (θ) and the wavelength (λ) are known, d can be calculated for each reflection. d corresponds to a set of parallel planes which can be further assigned to characteristic d-spacings (d_{hkl}; hkl = Miller indices*). For a crystal a set of characteristic d-spacings exist which allows to determine the symmetry (crystal system and space group) of the crystal and unit cell dimensions.[44]

3.1.2 Structure Factor and Atomic Positions

As mentioned above, the X-rays are diffracted on the electron shells of the atoms. Therefore, the intensities of the observed reflections (d_{hkl}) are directly correlated to the electron density distribution in the unit cell and thus the positions of the respective atoms. In principle, the scattering process can be understood as a Fourier transformation of the coherent X-ray wave into several single waves. To determine the electron density distribution in the unit cell this transformation has to be reversed. Therefore, it is necessary to know the wavelength, amplitude and phase of the scattered wave. The wavelength equals the incident beam wavelength since only elastic scattering is taken into account. The amplitude and phase are hidden in the observed reflection. The intensity of each reflection (I_{hkl}) is related to the structure factor F_{hkl}:[44]

$$F_{hkl} = \sum_n f_n e^{-i\phi_n} \tag{3.2}$$

F_{hkl} is the sum of each single scattering factors (f_n) of the atoms n on the lattice planes. f_n contains the atomic form factor (characteristic for each atom) and the thermal displacement of the single atom n. Additionally, a phase shift (ϕ_n) occurs since the X-rays are scattered not only on one kind of atom but several atoms shifted towards each other present in the same crystal lattice. ϕ_n is given by:[44]

$$\phi_n = 2\pi(hx_n + ky_n + lz_n) \tag{3.3}$$

Thus, the phase shift for a scattering wave originating from an atomic species n can be described with respect to the zero point of the unit cell $(h;k;l)$. From that the atomic coordinates $(x_n;y_n;z_n)$ of the atom n within the unit cell can be calculated given the atomic positions.[44]

In a X-ray scattering experiment, we only collected the absolute intensity of a reflection which is proportional to the square of the absolute value of the structure

* Miller indices are used to describe a set of lattice planes in a translation grid.

factor (see Equation 3.4).[44]

$$I \propto |F_{hkl}|^2 \tag{3.4}$$

Consequently, we only know the amplitude of the wave and the phase information is lost which is the so-called *phase problem* in crystallography. The phase problem can be solved by either *direct methods** or *indirect methods*†. Knowing the phase and amplitude of a reflection allows then to determine a three dimensional electron density map and subsequently the development of a structure model. The proposed structure model is refined against the observed intensities till a reasonable match is obtained.[44]

3.1.3 Single Crystal X-ray Diffraction

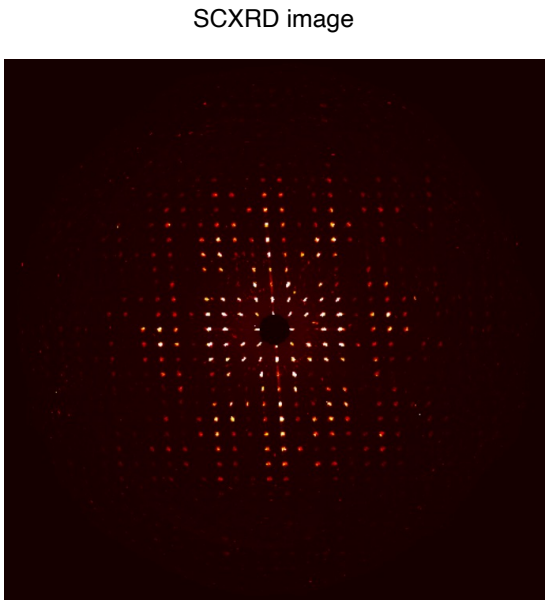

Fig. 3.2: Representative SCXRD images of a crystalline material.

Single crystal X-ray diffraction (SCXRD) experiments are mainly used for structure determination. Here, a single crystal is irradiated by a X-ray beam. Irradiation of the crystal yields a detector image with discrete reflections (see Figure 3.2). The crystal is rotated during the experiment which provides many single diffraction patterns in regard to the crystal orientation. Combination of the information (observed/absent reflections, intensity, ..) gained in many single diffraction patterns are used to solve the single crystal structure (see above). With state-of-the-art computers and software solutions with graphical interfaces, such as Olex2[48], this process has become straight forward and is used daily in chemical laboratories. Nevertheless, for SCXRD experiments always a single crystal of high quality and descend size (approximately $50 - 300\ \mu$m) is needed. This can

* Solving the phase problem following *direct methods* is based on correlations between the intensities within reflections groups (i.e. symmetry elements) and the phases.[44] Thus, they provide the structure 'directly' from the collected data and are especially useful for crystal structures containing small organic molecules.[45]

† *Indirect methods* (e.g. Patterson method) solve the phase problem based on a Fourier series. Following this approach, only interatomic vectors are obtained. Thus, the structure is only provided 'indirectly'. They are especially applicable if a crystal structure contains a few heavy and many light atoms.[46,47]

become challenging because materials are often only obtained as polycrystalline powders with much smaller crystallite sizes. To investigate such crystalline powders, it is then possible to perform powder X-ray diffraction (PXRD) experiments.

3.1.4 Powder X-ray Diffraction

PXRD experiments can be performed in transmission mode or reflection mode (Bragg-Brentano geometry[49]; see Figure 3.3). In reflection mode, the arrangement of X-ray source, sample stage and detector leads to a re-focusing of the diffracted beam on the detector (parafocusing). This practical advantage yields to the wide application of the reflection geometry in in-house PXRD machines. The sample is placed on a flat sample holder (e.g. a glass substrate). In this set-up, data collection is mainly performed with slit detectors.

In transmission mode, data collection is often performed with 2D detectors and the sample is filled into capillaries. Filling the sample into a closed capillary allows to perform measurements in defined environment such as inert atmosphere. In this context, *in-situ* techniques are developed where it is possible to conduct such experiments directly under precise conditions. External stimuli (e.g. variable temperature or mechanical pressure) can be applied in a closed system. This provides insights into the stability of the materials under the applied conditions but also uncover their potential structural response. Nowadays, such experiments are largely performed at synchrotron facilities.

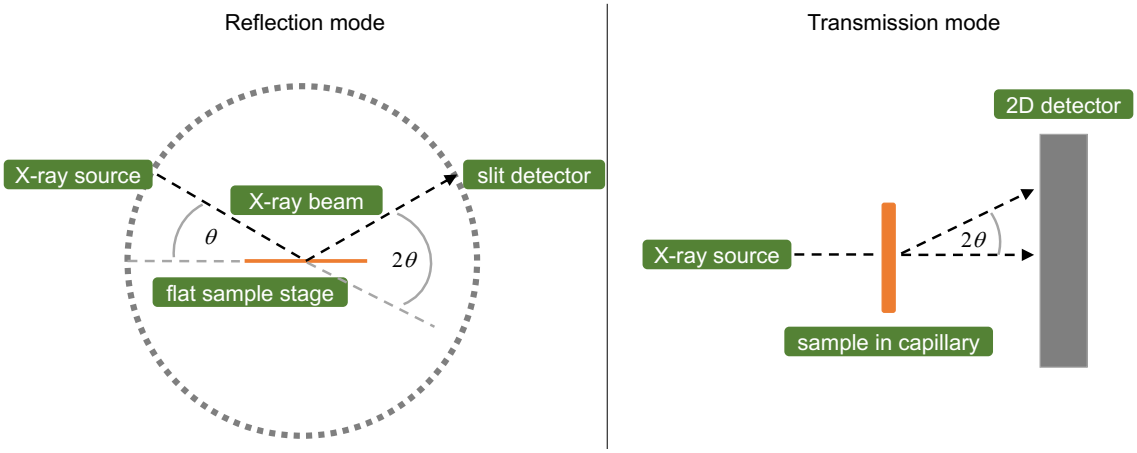

Figure 3.3: Schematic sketch of the reflection and transmission mode set-ups used for PXRD experiments.

In a PXRD experiment many small crystallites rather than a single crystal are irradiated by a X-ray beam. In an idealized case, all crystal orientations are already covered by the random orientation of the crystallites in the bulk. Consequently, the discrete reflections superimpose which yields diffraction rings (see Figure 3.4 (left)). Radial integration of the two-dimensional PXRD diffraction image (as collected in

the transmission mode set-up) yields the one-dimensional PXRD pattern, where the observed intensity is plotted against the 2θ angle (see Figure 3.4). In reflection mode, the slit detector scans across 2θ angels, thus the collected intensity can be directly plotted against the angle giving the one dimensional PXRD pattern. The peak positions can be ascribed to Bragg reflection positions (d_{hkl}) and contain information about the symmetry and unit cell dimensions (see Section 3.1.1). The peak intensities carry information about the electron density distribution in the unit cell and correspond to the atomic positions (see Section 3.1.2).

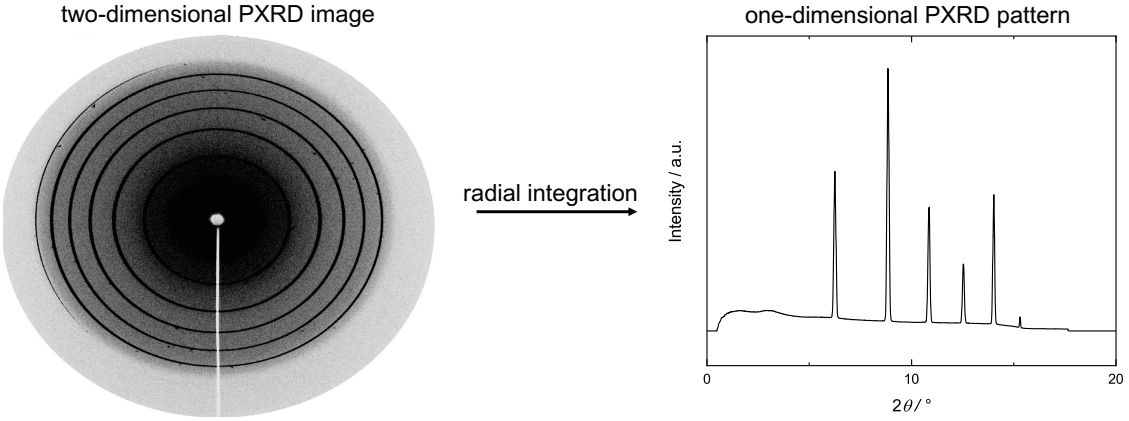

Figure 3.4: Representative two-dimensional PXRD image (as collected on transmission mode; left) and radially integrated one-dimensional PXRD pattern (right).

It is possible to refine crystal structures from PXRD data. For that purpose, the Rietveld method has been developed.[50]* Here, the peak positions and peak intensities are taken into account. Nevertheless, by probing many crystallites which are randomly orientated the geometric relation between the reflections is lost. Hence, less information about the crystal structure are provided as in a SCXRD experiment. Further, problems can occur if not all crystallites are perfectly randomly orientated (i.e. poor powder averaging) or preferred orientation of single crystallites (e.g. due to the morphology of the crystallites such as needles). This varies the observed relative peak intensities.[51] Consequently, the information about the atomic positions are sometimes poorly reliable.[52] These circumstances make the structure refinement following the Rietveld method challenging.

The main advantage of PXRD experiment is that they are practically easy to perform and also on a short time scale. Additionally, in such an experiment many different micro crystals are probed at the same time. Consequently, it is possible to derive information of the uniformity of a sample. This is especially important if properties (e.g. porosity, thermal or mechanical response) of a bulk sample are

∗ Notably, for Rietveld refinements an initial structural model is necessary, which is subsequently refined against the PXRD pattern.

intended to be probed. Thus, PXRD is mainly used for so-called phase identification since the powder diffraction pattern is like a fingerprint for a given crystal structure. For a known crystal structure it is possible to simulate the corresponding PXRD pattern. The simplest way of phase identification of a known phase is by a visual comparison between the collected diffraction pattern and a simulated diffraction pattern. Further, mathematical methods are developed for phase identification which are discussed in the next section.

3.1.5 Profile Fitting of PXRD Data

In this section, it will be focused on structureless profile fitting to derive refined unit cell parameters from PXRD data for known crystalline systems. This method is especially useful for phase identification and monitoring of structural changes during *in-situ* diffraction experiments which yield valuable insights into their structural response. There are two common methods for structureless profile fitting – the Pawley[53] and Le Bail[54] method. The former is used over the course of this theses.

In a structureless profile fit a theoretical diffraction pattern is calculated. Allowed Bragg reflection positions are determined based on provided unit cell parameters and a space group. The peak intensities are arbitrary and can be freely refined (this is where the name structureless profile fit comes from). During the refinement process the peak positions are adjustable by varying the unit cell parameters. The aim of the fitting process is to minimize the difference between the calculated and observed pattern.[55] Such fitting processes can be performed with software solutions such as the TOPAS software package.[56]

A representative plot of the result of a profile fit is shown in Figure 3.5 displaying the observed diffraction pattern (black crosses), the calculated diffraction (red line), the difference between those two (green line) and the position of the allowed Bragg reflection positions (blue tick marks). In a perfect fit, the difference line is consequently a horizontal line. Beside the obtained refined unit cell parameters, potential impurities become visible in variation in the difference line (e.g. presence of an another phase). Based on structureless profile fits even small impurities of additional phases can be uncovered.

3.1.6 X-ray Total Scattering

The X-ray diffraction techniques introduced in the previous section help to uncover the structures (and structural parameters) of crystalline materials. Nevertheless, in general X-ray scattering of materials can be also used to uncover structural information of amorphous materials (e.g. liquids or glasses). A commonly used

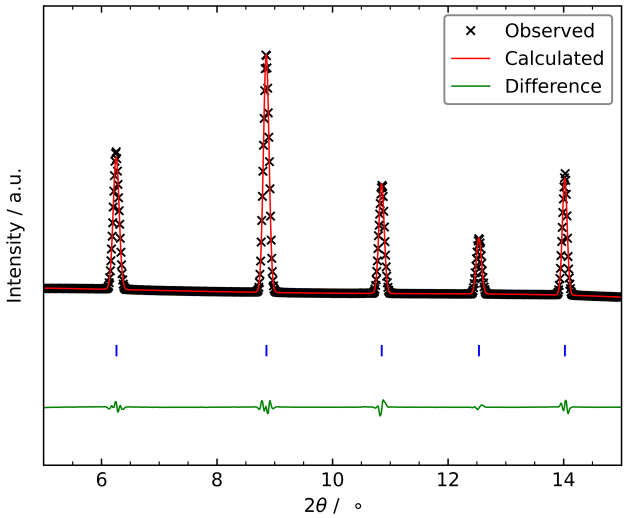

Figure 3.5: Plot of a representative PXRD pattern with corresponding structureless profile fit and difference line. The blue tick marks indicate the allowed Bragg reflection positions for the provided unit cell and space group.

technique to obtain information about the local structure (e.g. interatomic distances) of such materials is total scattering. From the obtained data it is possible to derive a X-ray pair distribution function (XPDF).

Before focusing on the physical and mathematical background, it seams useful to first simulate a hypothetical PDF (see Figure 3.6). As the theoretical material a two dimensional square grid of atoms is chosen. In a simple case of PDF as a radial distribution function ($R(r)$), single peaks are present at distances of neighboring atoms to the purple atom in the origin. The integral of the peaks relates to the number of neighbors at that distance. It is clear that the $R(r)$ contains valuable information about the arrangement of the atoms in the grid. Translating this to real materials, the XPDF is the sum of all interatomic distances present in the material. Thus, it is possible to get information on the local structure (e.g. environment of atoms, etc.) even of amorphous materials with this method.

X-ray total scattering data are collected on powdered samples or liquids. The data collection is similar to PXRD in transmission mode but data are collected to a much higher scattering angle which provides information about short distances in the material. For data processing, contribution of Bragg scattering – a sign for long range order (see above) – and also weak diffuse scattering (detected as broad features) are taken into account and are treated on an equal basis.[58]

> "In fact, the total scattering name comes from the fact that all the coherent scattering [...] is measured."[59]

Before data processing, the raw data need to be corrected regarding several extrinsic contributions to the background intensity. This includes incoherent scattering (i.e.

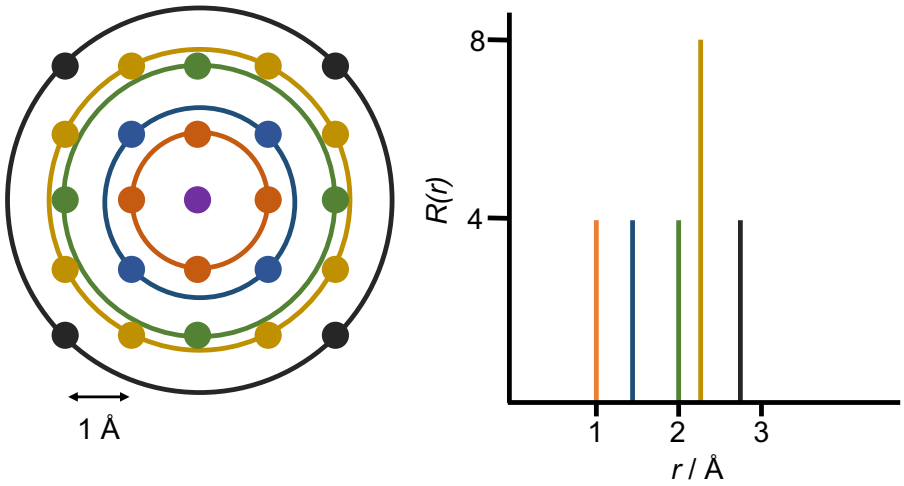

Figure 3.6: Schematic illustration of generating a hypothetical PDF ($R(r)$) from a two dimensional square grid of atoms. The colored rings indicate the distance of the neighbors to the atom in the origin (left). The integral of the peaks relates to the number of respective distances. The same colors are assigned to the corresponding peaks (right).[57]

Compton scattering), fluorescence and scattering of the sample holder. Finally, the data are normalized by the incident flux.[59] The obtained scattering intensity is termed $I(Q)$ and is expressed as a function of the scattering vector Q:

$$Q = \frac{4\pi sin(\theta)}{\lambda} \tag{3.5}$$

with the scattering angle θ and the experimental wavelength λ. $I(Q)$ is then further normalized to yield $S(Q)$ the 'total-scattering structure factor' given in absolute of scattering per atom. For this normalization $I(Q)$ is divided by the number of scatterers and their average scattering power per atom which is the square of the atomic form factor $f(Q)$. Since $f(Q)$ decreases for higher scattering angles, which equals higher Q, the normalization helps to amplify the data at high Q.[59] Thus, knowing the precise materials composition and packing fraction is crucible for the data processing.

> "It is worth remembering that $S(Q)$ is nothing other than the powder diffraction pattern that has been corrected for experimental artifacts and suitably normalized."[59]

For data interpretation $S(Q)$ is transformed into the real-space via Fourier transformation. Thus, a function $G(r)$ is obtained by:

$$G(r) = \frac{2}{\pi}\int_0^\infty Q[S(Q) - 1]sin(Qr)dQ \tag{3.6}$$

The function $G(r)$ describes the change in density as a function of interatomic

distances in the material what is called the XPDF.[60] It has to be noted that $G(r)$ makes the peaks at low r prominent. Therefore, $D(r)$ is often used in the literature:

$$D(r) = 4\pi r \rho_0 G(r) \tag{3.7}$$

with $\rho_0 = N/V$ the average number density of the material. Among other functions, the XPDF in the form $D(r)$ represents the best compromise of balancing the peak intensities in real-space especially for quantitative data interpretation.[61]

3.2 Gas Adsorption

In a gas adsorption process a gas is adsorbed in the pores or on the surface of a compound generally termed adsorbent or substrate. The gas in its gas phase is named adsorptive whereas the adsorbed gas is called adsorbate. The adsorption of gases in porous structures can happen following two mechanisms − physorption or chemisorption. The later includes a chemical reaction between the adsorptive and adsorbent. In the case of a physisorption process attractive dispersion interactions (e.g. London dispersion interactions) are observed between adsorptive and adsorbent.[62] In the investigated materials during the course of this thesis only physisorption processes are investigated.

Table 3.1: Classification of porous materials regarding their pore width as proposed by the IUPAC.[62]

Term	Pore width
Micropore	<2 nm
Mesopore	2 − 50 nm
Macropore	>50 nm

The IUPAC has classified porous materials based on their pore width back in 1985 (see Table 3.1).[62] Here, the three classes micro-, meso- and macroporous are distinguished. Porous materials can contain solely one type of these pores but can also feature mixed pore architectures.[63,64] Further, there are also other terms appearing in the literature to denote microporous materials with very small pores, such as materials with ultrasmall-pores or ultramicro-porous materials, which feature promising results towards the separation of small molecules, single atoms or even isotopes.[65,66]

3.2.1 Analysis of the Pores

The pore analysis is commonly performed with isothermal gas adsorption experiments. Here, the adsorbed amount of gas is measured − volumetric or gravimetric − as a function of the pressure at a constant temperature. In a standard measurement, data are collected while increasing and decreasing pressure. The obtained gas sorption isotherm features an adsorption and desorption brunch. Properties of the pores (e.g pore volume, specific surface areas, pore sizes or pore size distributions etc.) can be evaluated from the gas sorption isotherm. Already the shape of the sorption isotherm and the difference between the adsorption and desorption branches have been observed to be characteristic for specific types of materials. Six different types of isotherms have been defined by the IUPAC (see Figure 3.7).[62] The different shapes are characteristic for the following properties of a material:

- The reversible **Type I** isotherm is found for microporous materials. The steep slope at low pressures points towards strong attractive interactions between the adsorbate and adsorbent in the narrow pores.
- The shape of the reversible **Type II** isotherm characterizes either a non-porous or macroporous adsorbent. The rise of the isotherm at higher pressure is often a sign for unrestricted multilayer adsorption.
- **Type III** isotherms are generally very uncommon. The gradual curvature origins from weak adsorbate-adsorbent interactions and is found for non- or macroporous materials.
- For mesoporous systems often **Type IV** isotherms are found. The reversible part at low pressure is a sign for monolayer adsorption. At higher pressure multilayer adsorption and particle condensation occurs which becomes further visible in the discrepance between the adsorption and desorption brunch the so-called hysteresis.
- A mesoporous system can also feature a **Type V** form but here, the adsorbate-adsorbent interaction are weak − analogical with Type III isotherms.
- **Type VI** isotherms are very rare. The single steps representing single layer-by-layer adsorption which only occurs on very uniform surfaces.

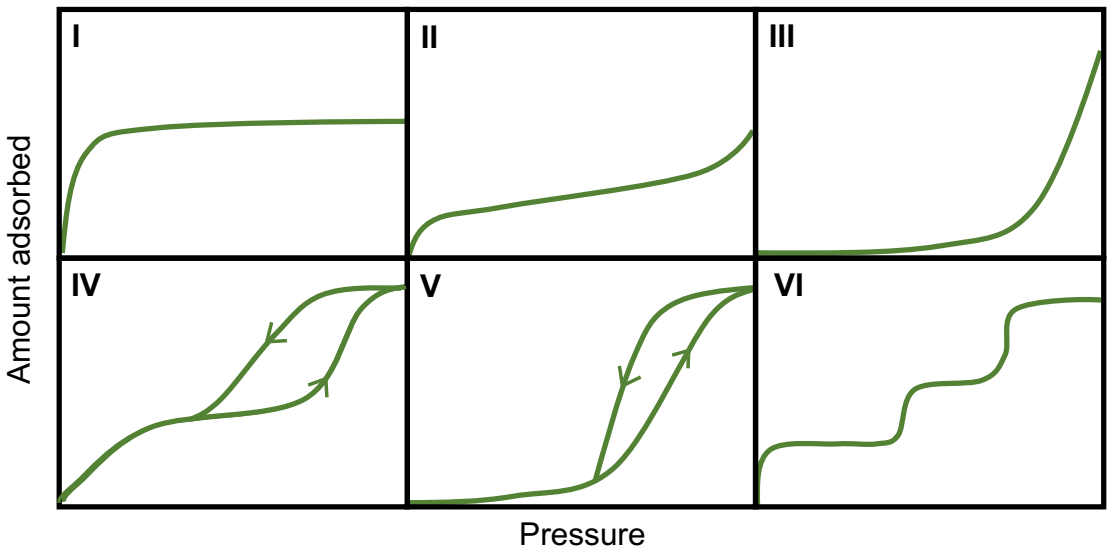

Figure 3.7: The six isotherm types defined by the IUPAC.[62] The respective **Type** (**I-VI**) is marked in the top left corner of each graph. Adopted from Reference [62]. Copyright 1985 IUPAC.

Importantly, appearing hystereses show that the thermodynamic equilibrium is not completely attainable (during the measurement).[67] Hence, hystereses are a sign for a kinetic effect involved in the sorption process. This can originate from several

circumstances such as narrow pores or phase transition happening during the sorption processes.[68]

Due to the increasing field of gas physisorption studies on porous materials, IUPAC has extended the classification guidelines in 2015.[69] This was especially necessary since many new experiments utilizing various gases at different temperatures have been published in recent years and also new procedures for data evaluation have been developed based on density functional theory and molecular simulation. The aim was to update the current guidelines regarding terminology but also practical considerations for performing a physisorption experiment are outlined. Additionally, advantages and limitations of the use of physisorption techniques for the pore characterization are discussed.[69] Some recommendations are highlighted in the following section. Here, it will be focused on microporous materials, since the materials investigated within this thesis belong to this class.

3.2.2 Total Pore Volume

The total pore volume for microporous materials can be determined from the plateau of the **Type I** shaped isotherm and is often simply the adsorption at the maximum pressure. Nevertheless, sometimes gas condensation independent of the porous structure (e.g. between surfaces) is observed. This is indicated by a sharp rise of the isotherm at the maximum investigated pressure region. Consequently, a more differentiated selection of an appropriate pressure point for the calculation of the pore volume becomes necessary.[70] This point should be close to the initiation of the sharp rise of the isotherm − otherwise an overestimation occurs. The pore volume (V_{pore}) is calculated after the following equation:

$$V_{pore} = \frac{n^{\mathrm{ads,sat}}}{\rho^{\mathrm{liq}}} \tag{3.8}$$

with $n^{\mathrm{ads,sat}}$ the specific amount of gas adsorbed at saturation and ρ^{liq} the liquid density of the gas. From this value it is then possible to determine the experimental void fraction (eVF) by multiplication with the materials density (ρ):

$$\mathrm{eVF} = V_{pore} * \rho \tag{3.9}$$

3.2.3 Pore Size Distributions

Pore sizes can be first of all estimated by the choice of the adsorbent. Bigger gas molecules are most likely not able to access narrow structures. Moreover, semi-empirical models, such as e.g. the Horvarth-Kawazoe (HK method)[71] have been

proposed to evaluate pore size distribution based on defined pore geometry, such as slits or cylinders. However, the underlying pore models are sometimes insufficient to describe the pore dimensions of especially microporous materials. In this context, theoretical methods based on density functional theory (DFT) and molecular dynamic simulations (e.g. Monte Carlo simulation) have been developed. Consequently, the adsorbate-adsorbent interactions are described on a molecular level yielding an accurate description of the pore structure.[72,73] One example is the non-local-density functional theory (NLDFT) approach.[74–76] Based on this method single isotherms for a particular adsorptive/adsorbent pair with varying pore widths of an underlining pore shape (e.g cylindrical- or slit-like) are calculated. The set of calculated isotherms is called kernel. Several kernels have been developed for different adsorbates (e.g. N_2, Ar or CO_2) at different temperatures and pore geometries.[77,78] The relation between the kernel of the theoretically calculated isotherms ($N(p/p_0, W)$) and experimental isotherm ($N(p/p_0)$) is given by the generalized adsorption isotherm (GAI) equation:

$$N(p/p_0) = \int_{W_{\min}}^{W_{\max}} N(p/p_0, W) f(W) dW \tag{3.10}$$

In principle, the equation describes that the experimental isotherm ($N(p/p_0)$) can be divided into single isotherms with varying pore widths (W) of the kernel of theoretical adsorption isotherms ($N(p/p_0, W)$). Thus, solving the equation for $f(W)$ which is the fraction of a theoretical isotherm with a particular pore width yields the pore size distribution. The pore volume and surface area (see below) can also be obtained from this approach. Such method of course strongly depends on how good the chosen kernel fits the investigated porous system.[69]

3.2.4 Specific Surface Area

The most widely used method to evaluate the specific surface area is the Brunauer-Emmett-Teller (BET) method. This method is named after their developers S. Brunauer, P. H. Emmett and E. Teller in 1938 and is a model which describes the multilayer physisorption on the surface of porous solids.[79] The method is a further development of the description of the monolayer adsorption process derived by I. Langmuir.[80] For the BET method, the following assumption are made:[81]

- adsorption takes place on a uniform surface
- the number of physisorbed gas layers is infinite
- all adsorbates in the monolayer cover the same area and are assumed to feature a hexagonal close-packing
- interactions between adjacent layers are not considered

- all adsorption sites have the same heat of adsorption
- the heat of adsorption for the first layer is greater than for the second layer
- from the second layer on, the heat of adsorption is equal to the heat of condensation

Based on these assumptions the BET equation can be derived which is given here in the linear form:[82]

$$\frac{p}{V_{\mathrm{ad}}(p_0 - p)} = \frac{1}{V_{\mathrm{mono}}C} + \frac{C-1}{V_{\mathrm{mono}}C}\frac{p}{p_0} \tag{3.11}$$

In a physisorption experiment, the volume of adsorbed gas V_{ad} is determined as a function of pressure (p). p_0 is the saturation pressure of the adsorbed gas at the chosen experimental temperature and V_{mono} the volume of a monolayer. C is an empirical constant sometimes also referred to as BET constant and represents the strength of interaction between adsorbate and adsorbent. Since p_0 is a constant, it is possible to plot $p/V_{\mathrm{ads}}(p_0 - p)$ against p/p_0. Following, V_{mono} and C can be calculated from the slope and the intercept of the plot. In a real experiment this plot is only linear in a small pressure region of p/p_0= 0.05-0.30. For microporous materials (e.g MOFs) this pressure range is even shifted to a lower region of p/p_0 $= 0.02 - 0.10$.[83] In general, the linear low pressure region of the linear BET plot should be used to determine the specific surface area.[84] It has to be noted that the pressure range in which the BET method is applied has a huge influence on the determined value of the specific surface area.

The monolayer volume (V_{mono}) can be converted to the molar amount of adsorbates (N_{mono}) with the molar gas volume. The specific BET surface area (S_{BET}) is calculated according to the following equation:[82]

$$S_{\mathrm{BET}} = N_{\mathrm{mono}} N_A \sigma \tag{3.12}$$

where N_A is the Avogadro constant and σ the molecular cross-sectional area which describes the area occupied by a single adsorbate.

Traditionally, nitrogen (N_2) isotherms collected at its boiling point of 77 K were used to determine S_{BET}. Nevertheless, it has to been noted that the derived absolute values have to be treated carefully, because the assumptions[85] made by the simplified BET model lead to an inaccurate description of the adsorption process, especially for heterogeneous pore surfaces. Consequently, the calculated value is highly dependent on absorbate-absorbent interactions and temperature. The collection of N_2 isotherms at cryogenic temperatures (77 K) brings kinetic restrictions for diffusion of the gas into mircoporous materials with very small pores. Here, CO_2 isotherms measured

at 273 K or 195 K have been shown to access the smaller pores and are today an accepted method to study very narrow micropores.[86,87] An another occurring issue originates from the precise determination of the molecular cross-sectional area especially for multi-atomic adsorbates. Therefore, also argon (Ar, at 87 K; spherical probe molecules, less polarizable) is utilized to face these issues and obtain more appropriate results for specific materials.[69]

3.2.5 Gas Separation

Porous materials are interesting for gas separation processes. Gas separation is necessary as often gas mixtures are present and only single components are useful for a certain process. Further, it is also possible that hazardous or unwanted gases need to be removed from a gas stream. Thus, studies of the adsorption of gas mixtures are found in the literature already for a long time.[88,89]

Gas separation processes can be divided into thermodynamic and kinetic separation processes. From the adsorbent side, the former is achieved by favored adsorption of a single component which is mostly dependent on the pore surface properties. Following, an adjustment of the surface properties (e.g. hydrophilic, hydrophobic, etc.) can help to tune the materials separation ability for a specific adsorbate. Kinetic separation processes are guided by favored diffusion of a single component through the material. Here, the pore architecture is most relevant by means of mainly pore size and shape. Nevertheless, a strict separation between these processes is difficult because pore surface as well as pore architecture play an important role for all interactions of gases with porous materials.

The potential of a material to act beneficially in a certain process can be evaluated practically by so-called gas breakthrough measurements. Here, a gas mixture is flown through a potential adsorbent and the gases which pass through the material are monitored. This provides information about how fast a gas diffuses through the adsorbent (kinetic) and indirectly how much of a particular gas is adsorbed (thermodynamic). Today, experimental set-ups are commercially available but their use remains limited since such measurements are still complicated and time consuming.[90,91] Already early publications outlined that a comparable characterization of materials for gas mixtures is challenging due to various influences of the experimental methods and data interpretation.[89] To come around this issues, gas adsorption data for single components can be interpreted to abstract separation abilities. Such approaches have become widely used because single component gas isotherms are readily available as they are standardly collected or also simulated during the characterization of porous materials.

Thermodynamic Gas Separation

The thermodynamic gas separation can qualitatively be estimated directly from single component gas isotherms. Therefore, simply the adsorption capacities of relevant gases at the same conditions can be compared. In this context, the ideal adsorbed solution theory (IAST) has been developed which allows a more detailed investigation of the thermodynamic gas separation ability of a porous material in regard to a gas mixture.[92]

Ideal Adsorb Solution Theory

IAST calculations allow to calculate the adsorption of a defined gas mixture on measured single component isotherms.

> "The essential idea of the calculation lies in the recognition that in an ideal solution the partial pressure of an adsorbed component is given by the product of its mole fraction in the adsorbed phase and the pressure which it would exert as a pure adsorbed component at the same temperature and spreading pressure* as those of the mixture."[92]

Due to the wide use of this method, a Python package (pyIAST) has been developed to perform IAST calculations in a convenient way. Following this procedure, the single component isotherms are fitted first with one of the several common analytical models (e.g. Freundlich or Langmuir)[94] or by interpolating the pure component isotherm by numerical quadrature to calculate the spreading pressure.[93]

Based on these fits, IAST calculations can be performed to estimate gas uptakes of a defined gas mixture at a given temperature and pressure. For a two component gas mixture (gas A and B) the IAST selectivity (S_{IAST}) can be calculated from these values which is defined as:

$$S_{\mathrm{IAST}} = \frac{x_i}{y_i} \tag{3.13}$$

here $x_i = x_{\mathrm{A}}/x_{\mathrm{B}}$ is the molar ratio of the adsorbed fluids and $y_i = y_{\mathrm{A}}/y_{\mathrm{B}}$ is the chosen molar ratio of the fluids in the gas phase. Naturally, these calculations can also be performed for mixtures containing more than two gases.

It has to be noted that even if IAST calculations often give reasonable predictions to experimentally found data, some deviations occur. This is due to the fact that IAST calculations are based on the following assumptions:[93]

∗ The spreading pressure is the analogy of pressure in two dimensions and can be calculated from the experimental sorption isotherms.[92,93]

- the adsorbates form an ideal mixture
- all adsorption places are accessible equally to all adsorbates
- the investigated adsorbent does not experience any thermodynamic change during the adsorption process (e.g. a structural transition) despite the adsorption process itself

Naturally, these assumptions have be taken into account while performing IAST calculations and interpreting the obtained selectivity factors. In this context, the IAST approach has been further developed to tackle this issues by e.g. heterogeneous IAST (HIAST)[95] for heterogenous adsorbent surfaces.

Kinetic Gas Separation

Kinetic gas separation is mostly performed by membranes.[96,97] Membranes are mainly composed of an active material attached to a support material. Especially in academia typically the gas separation properties of only the active material are investigated. Subsequently, only diffusion rates for measured gas isotherms are discussed for the active material. This helps to estimate the ability of a porous material to work beneficially in a gas separation process.

Insights into different diffusion rates by single gas component measurements are obtained by collecting kinetic sorption profiles.[98–100] In such an experiment, a certain amount of gas is dosed on a porous material and the amount of adsorption is determined over time till the equilibrium is reached. Following, time dependent adsorption data are obtained for a particular pressure point in a corresponding gas adsorption isotherm. Two representative kinetic sorption profiles are shown in Figure 3.8 for two gases with similar diffusion rates on the left hand side and strongly different diffusion rates on the right hand side. It is further possible to quantify the

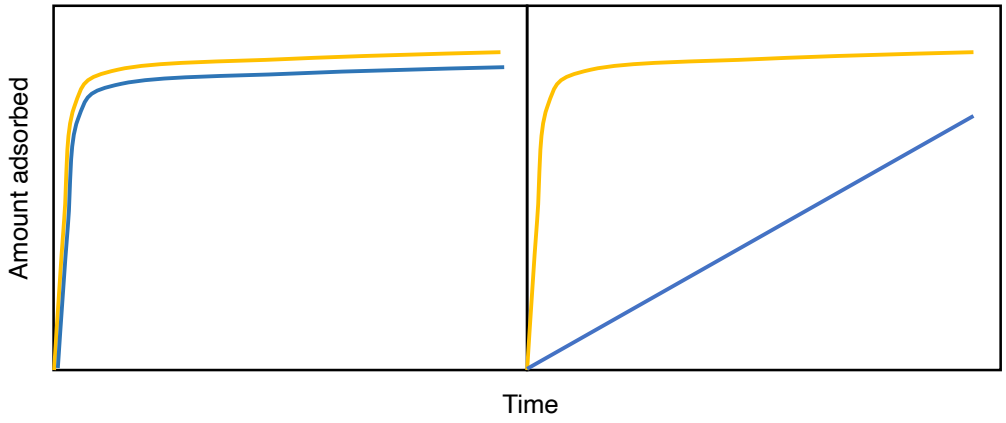

Figure 3.8: Generalized kinetic sorption profiles for two different gases shown in yellow and blue. The case of nearly no differences in diffusion (left), as well as strong differences (right) is shown.

separation ability by fitting of the time dependent data to a kinetic model (i.e. a pseudo-first order kinetic model, an Avrami kinetic model, a diffusional time constant based model).[100,101]

Part I
ZIF Glasses

The work presented in this part has been published in the following peer-reviewed research articles or is submitted for publication and a preprint is available online. These publications (text and figures) are subsequently reprinted or adapted with permission of the publisher. Author contributions are distinctly given under each publication.

Peer-reviewed Publications

1. L. Frentzel-Beyme, M. Kloß, R. Pallach, S. Salamon, H. Moldenhauer, J. Landers, H. Wende, J. Debus, S. Henke. Porous purple glass – a cobalt imidazolate glass with accessible porosity from a meltable cobalt imidazolate framework. *J. Mater. Chem. A* **2019**, *7*, 985-990. Reproduced or adapted by permission of The Royal Society of Chemistry.

   Author contributions:
   L.F.-B. and M.K. synthesized the materials and performed and analyzed in-house PXRD, solid state FTIR spectroscopy, solution ^{1}H NMR spectroscopy and thermal analysis experiments. X-ray total scattering data were collected during a service measurement (rapid access) by beamline scientists Phil Chater and Dean Keeble at Diamond Light Source (UK). L.F.-B. and M.K. analyzed X-ray total scattering data. L.F.-B. collected and analyzed gas physisorption data. H.M. and J.D. collected Raman scattering data. S.S., J.L. and H.W. performed magnetic measurements. All authors contributed to discussing the data. L.F.-B., M.K. and S.H. wrote the manuscript.
   Some of the results are obtained during the Master thesis of Marvin Kloß (TU Dortmund, 2018)

2. L. Frentzel-Beyme, M. Kloß, P. Kolodzeiski, R. Pallach, S. Henke. Meltable Mixed-Linker Zeolitic Imidazolate Frameworks and Their Microporous Glasses: From Melting Point Engineering to Selective Hydrocarbon Sorption. *J. Am. Chem. Soc.* **2019**, *141*, 12362-12371. Reproduced or adapted with permission. Copyright 2019 American Chemical Society.

   Author contributions:
   L.F.-B. and M.K. synthesized the materials and performed and analyzed PXRD, solid state FTIR spectroscopy, solution ^{1}H NMR spectroscopy and thermal analysis experiments. L.F.-B., M.K., R.P. and S.H. collected variable-temperature PXRD data and L.F.-B. and M.K. analyzed variable-temperature PXRD data. X-ray total scattering data were collected during a service measurement (rapid

access) by beamline scientists Phil Chater and Dean Keeble at Diamond Light Source (UK). L.F.-B. and M.K. analyzed X-ray total scattering data. L.F.-B. collected and analyzed gas physisorption data. All authors contributed to discussing the data. L.F.-B. and S.H. wrote the manuscript.
Some of the results are obtained during the Master thesis of Marvin Kloß (TU Dortmund, 2018)

Pre-prints

1. L. Frentzel-Beyme, P. Kolodzeiski, J.-B. Weiß, S. Henke. Quantification of gas-accesible microporosity in metal-organic framework glasses.
DOI:10.26434/chemrxiv-2021-lq308.

   Author contributions:
   L.F.-B., P.K. and J.-B.W. synthesized the materials and performed and analyzed in-house PXRD, solid state FTIR spectroscopy, solution ^{1}H NMR spectroscopy and thermal analysis experiments. L.F-B. and P.K collected and analyzed X-ray total scattering data. L.F.-B. collected and analyzed gas physisorption data. All authors contributed to discussing the data. L.F.-B. and S.H. wrote the manuscript.
   Some of the results are obtained during the Master thesis of Pascal Kolodzeiski (TU Dortmund, 2020).

4 Introduction

4.1 The Glass Age

Glasses are already known to mankind for more than 5000 years.[102] In the old days, natural glasses have been used as weapons or tools due to their hardness and also the sharpness of broken pieces. Here, obsidian was often used which is a naturally occurring glass formed during volcanic eruptions.[103] Later, it became possible to melt glasses where one of the first reports is from the ancient Egypt with first hints on synthetic glass manufacturing. In this times, being able to melt and consequently to process and shape such materials extended the use of glasses to build vases or vessels.[104,105]

Nevertheless, till the late 19th century, everything known about glasses was based on empirical findings. O. Schott was then one of the first who looked into the chemical and physical properties of glasses during his dissertation with the title "Beiträge zur Theorie und Praxis der Glasfabrikation".[106] Starting from these days, our understanding of glasses has grown immensely. Academic research on glassy materials yields a better understanding of glass formation and extended the scope of materials which are defined as glasses from purely inorganic also to organic glasses.[107] In parallel, interest grew also in industry and today glasses play an important role in our everyday life, where we have conventional applications as glass windows or drinking glasses, but are also found in more specialized applications, such as spectacles or glass fibers for fast data processing.[108]

Taking the number of publications per year as a measure of research interest, J. C. Mauro *et al.* found that whereas the publications related to glasses were solely about 5 a year in the late 19th century and early 20th century, this number has grown about more than three orders of magnitude in 100 years (1913 − 2013). Even more remarkable, the number of granted patents related to glasses has also increased rapidly since the 1940s, today even overcoming the total number of scientific papers on this topic ($\approx$ 370,000 *vs.* $\approx$ 200,000). This further underlines the importance and relevance of glasses for our todays world.[102]

4.2 What is a Glass?

Despite all development and progress in the glass field, it is quite surprising that a clear definition for the glassy state of matter, which satisfies all disciplines related to this topic, has not been found until today.[109] The typical glass formation is done by so-called melt-quenching. This process can be illustrated in an enthalpy versus temperature graph (see Figure 4.1). When a crystalline glass former (red) – defined as a solid which can form a glass – is heated, a point is reached where the solid turns into a liquid (blue). This occurring phase transition is called melting and is accompanied with a discontinuous change in enthalpy. The temperature at this point is defined as the melting temperature (T_m) of the glass former. Cooling down the liquid under certain conditions (e.g. fast quenching) leads to a metastable supercooled liquid state (black). By further cooling down, the material vitrifies at the glass transition. The glass transition is accompanied by a change in heat capacity ($c_p = dH/dT$) at the point of vitrification (yellow). Here, the glass transition temperature (T_g) is found which is a very important characteristic in glass science. In the glass state and also in the supercooled liquid state the material is metastable and can crystallize (form the crystalline phase).[109]

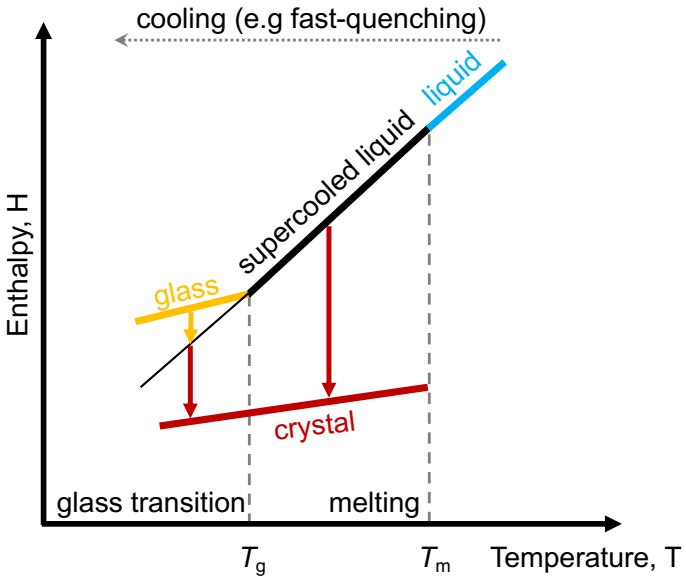

Fig. 4.1: Enthalpy versus temperature plot describing the glass forming process starting from a glass former in its crystalline state. Adapted from Reference [109]. Copyright 2017, with permission from Elsevier.

For the glass state many slightly different definitions are found in the literature.[110–112] Most of them are either describing the glass as similar to the liquid or solid sate. In 2007, E. D. Zanotto *et al.* came up with the idea to describe the glass as a unique state of matter featuring properties of a solid and liquid but also unique own properties.[109] Their definition is given by:

> "Glass is a non-equilibrium, non-crystalline state of matter that appears solid on a short time scale but continuously relaxes towards the liquid state."

In other words, from a structural point of view the glass appears non-crystalline/amorphous by means of lacking the well-ordered atomic arrangement of its crystalline precursor (see Figure 4.2). However, it has to be noted that the atomic arrangement is not completely random because the internuclear distances do not fall below a given minimum level.[113] Further, on the human time scale most glasses feature a plastic solid character and e.g. can break into shades. Nevertheless, on an infinite time scale a glass flows which is one of the prominent characteristic of a liquid. This property further distinguishes the glass state from a simple amorphous solid. If a glass is produced after the presented melt-quenching method, signs of flow are often also visible in the macroscopic appearance of the glass. Most importantly, unlike the liquid and solid state, the glass is a non-equilibrium, meta-stable state which can vary for a glass featuring the same composition at the same temperature and pressure. Here, different states can be reached by varying the ways of entering the glass state (e.g. different quenching rates).[109]

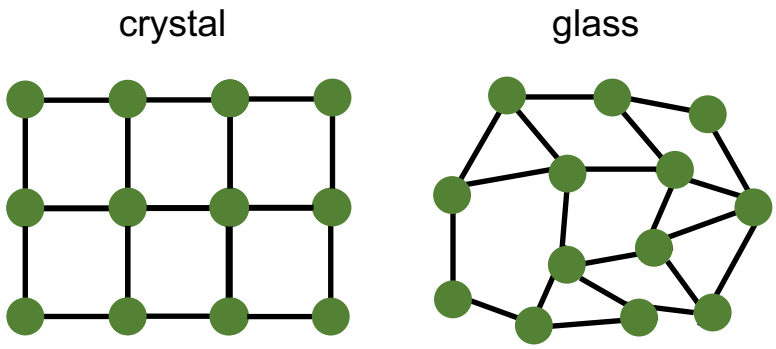

Figure 4.2: Cartoon of the structural arrangement on an atomic level for a crystal (left) and glass (right).

4.3 A New Class of Glasses

In this context, MOFs have recently gained much attention because some representatives have been shown to melt and form glasses after cooling back to room temperature. Remarkably, most melting MOFs are representatives of the subclass of MOFs called ZIFs (see Section 2.2).

The found liquid-to-solid transitions of ZIFs, yielding melt-quenched glasses upon cooling the liquid below T_g, are exciting, as they offer processing and shaping of the framework materials in their liquid state (i.e. above their T_m) and vitrification to a functional glass after cooling below T_g.[114–118] In this context, the manufacturing of large size bulk ZIF glasses has been already demonstrated in the literature (see Figure 4.3).[119,120] Here, the fabrication of even bubble-free monoliths, which appear transparent (see Figure 4.3 right), is important, as they allow to evaluate thermomechanical or optical properties of the glasses.[119]

Additionally, interesting physical properties are reported for MOF glasses, such as porosity, high glass forming ability*, luminescence or ionic conductivity.[122–129] Consequently, applications have been proposed in various fields ranging from solid electrolytes and membranes to non-linear optics and radioactive waste storage.[130–134] Due to their advantageous liquid state processibility, ZIF glasses are especially interesting for solid state ion conduction[135,136] and gas separation membranes[137,138] because of improved performance as a result of their monolithic structure and the potential absence of mass transport limiting grain boundaries.[117]

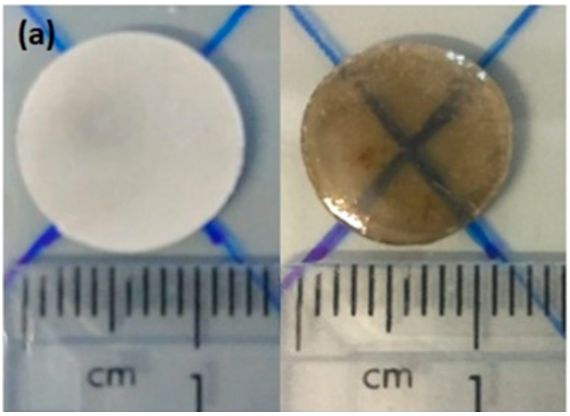

Fig. 4.3: Photographs of fabricated bulk ZIF glasses. Left: Melted ZIF glass. Right: Remelted ZIF glass which appears bubble-free. Adapted with permission from Reference [119]. Copyright 2019 American Chemical Society.

4.3.1 The Prototypical Melting and Glass Forming ZIF

ZIF-4 with the chemical composition $Zn(im)_2$ (im^- = imidazolate) was one of the first reported ZIF materials in the literature.[30,37] In the solid state structure, the zinc ions (Zn^{2+}) are tetrahedrally coordinated by the nitrogen atoms of the im^- linkers. One of these im^- linkers bridges between two Zn^{2+} ions generating a 3D framework with **cag** topology (see Figure 4.4 left). The phase behavior of ZIF-4 has been extensively studied towards external stimuli, such as mechanical and gas pressure as well as high and low temperature.[114,123,124,139–145] R. N. Widmer *et al.* even reported a phase diagram covering the region from ambient condition up to pressures of 8 GPa and temperatures of 600 °C.[145]

Focusing on the high temperature behavior under ambient pressure, several phase transitions are observed when heating ZIF-4 up to 750 °C under an inert atmosphere.[114] Phase identification and structural characterization has been achieved by combining thermal analysis data (e.g. simultaneous thermogravimetric analysis/differential scanning calorimetry (TGA/DSC)) with *in-situ* variable-temperature PXRD and XPDF data as well as simulations.[114,116,139,140,142] The phase behavior is

* The glass forming ability (GFA) is measured by the ratio T_g/T_m and is empirically found to be 0.66 for most molecular systems.[121]. A high GFA (>0.66) defines a liquid/melt with a low tendency to crystallize.[122]

best illustrated by looking at the TGA/DSC data (see Figure 4.5*).

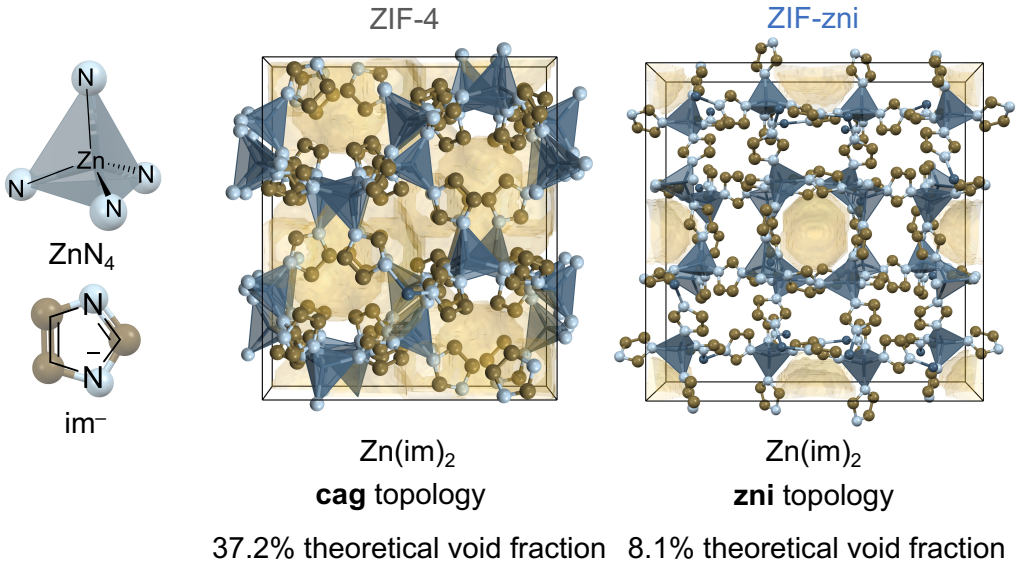

Figure 4.4: Representation of the crystal structures of ZIF-4 (middle) and ZIF-zni (right) viewed along the crystallographic c axis. The building units are displayed on the left. The theoretical void fraction (tVFs) is colored light yellow.[a]

a The tVFs values were calculated with the implemented routine in Olex2[48] applying a probe radius of 1.3 Å and grid spacing of 0.2 Å. The structures were taken from the CSD, missing hydrogen atoms have been added geometrically with Olex2 (ZIF-4 (CSD code IMIDZB11); ZIF-zni (CSD code IMIDZB)). Crystal structure images are generated from the stated CSD data.

The first exothermic signal at around 315 °C (T_{am}) can be ascribed to a collapse of the material generating a meta-stable amorphous phase. This amorphous phase recrystallizes to a polymorphic phase of **zni** topology at approximately 460 °C. The resulting material is termed ZIF-zni and features a denser crystal structure than ZIF-4 (see Figure 4.4 right). Hence, again an exothermic heat flow signal is observed in the DSC trace (T_{rc}). Finally, the material melts (T_m) at

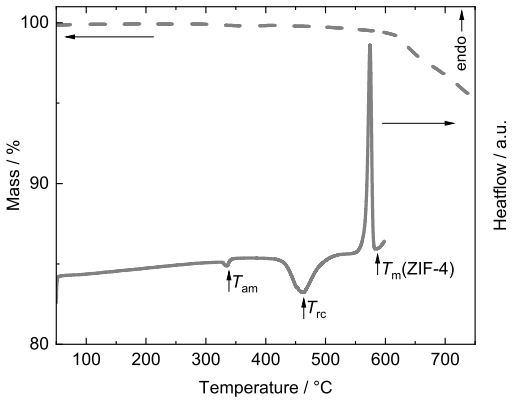

Fig. 4.5: TGA/DSC data of ZIF-4.

∗ During the course of this thesis ZIF-4 has been synthesized according to literature known protocols (see 12.9.1). Here, the TGA trace of a TGA/DSC experiment and the DSC trace, separately collected in a dedicated DSC apparatus, are displayed for ZIF-4. The combination of data from different machines was necessary due to the lower sensitivity of the DSC in the instrument for simultaneous TGA/DSC. The higher quality DSC data are only collected up to 600 °C to avoid decomposition.

around 580 °C accompanied by a strong endothermal signal in the DSC trace. Afterwards, the material decomposes indicated by a rapid mass loss in the TGA trace. A ZIF-4 glass (termed a_gZIF-4 for 'amorphous glass') is obtained by quenching the liquid ZIF back to room temperature before reaching the decomposition temperature.[114]

The melting mechanism was studied with density functional theory (DFT)-based molecular dynamics (MD) simulations combined with experimentally obtained X-ray and neutron scattering data. The postulated mechanism includes Zn−N bond breakage, leaving the Zn^{2+} shortly three-fold coordinated followed by approaching of another im^- yielding the porous ZIF liquid (see Figure 4.6).[116]

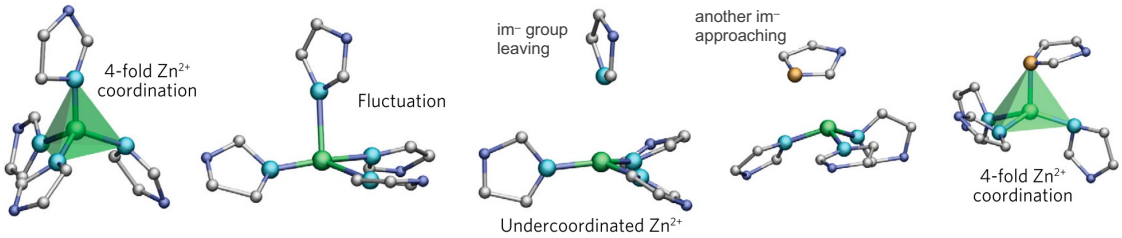

Figure 4.6: Visualization of the melting mechanism of ZIF-4(Zn). Color code: Zn (green), N (blue), N (initially coordinated to Zn^{2+}, light blue), N (coordinated after im^- exchange, yellow), C (grey). Adapted by permission from Springer Nature Customer Service Centre GmbH: Springer Nature, Nature Materials, Liquid metal–organic frameworks, Romain Gaillac et al, copyright 2017.

4.3.2 Known Melting ZIFs and Limitations

Hypothetically, every MOF should have a T_m were the solid state material converts to a liquid. Nevertheless, this hypothetical T_m is often above the decomposition temperature of the material and thus the liquid phase is not obtainable.[116]

As an example, we will first stay with the previously presented prototypical glass former ZIF-4. Its isoreticular Co^{2+}-based variant ZIF-4(Co) shows a similar high temperature phase behavior, but melting is directly accompanied by a simultaneous decomposition of the material.[146] Following, the melt-quenched ZIF-4(Co) glass is not obtainable. Interestingly, at the start of this thesis only ZIFs build from zinc ions were known to form melt-quenched glasses.

In general, even though more than 250 crystalline ZIFs featuring above 50 different topologies have been reported today,[147] just very few of these have been demonstrated to melt and form glasses via melt-quenching. ZIF glass formers reported today only include frameworks with **cag** (ZIF-4, ZIF-62, TIF-4, ZIF-UC-1 to ZIF-UC-5), **zni** (ZIF-zni) and **gis** (denoted $Zn(im)_2$ (GIS)) topologies.[123,148–150] Additionally, meltable ZIFs have further been shown to act as a flux for the melting of other ZIF structure types which are non-meltable on their own (i.e. ZIF-76, **lta** topology;

ZIF-8, **sod** topology).[127,151,152]

Interestingly, all of the meltable ZIFs are either featuring the small im^- linker ZIF-4, ZIF-zni and ZIF-gis or im^- and a second bulkier imidazolate-type linker. The secondary linkers are either benzimidazolate (bim^-) in ZIF-62 or functionalized benzimidazolate derivatives ($Xbim^-$; TIF-4, ZIF-UC-1 to ZIF-UC-4). This mixed-linker ZIFs feature the general chemical composition $Zn(im)_{2-x}(bim/Xbim)_x$. A library of the secondary bulky linkers is displayed in Figure 4.7. Remarkably, for such glass forming mixed-linker ZIFs melting is observed at lower temperatures (approximately $390 - 470\,°C$) and directly from the crystalline porous framework without any previous phase transition, as found for ZIF-4. T. D. Bennett *et al.* suggested that the lower melting point of ZIF-62 compared to ZIF-4/ZIF-zni may be caused by the higher electron donating properties and the larger steric hindrance of bim^-.[115] However, the physical origin of the very different melting temperatures of these ZIF materials remains poorly understood. Remarkably, already ZIF-8, which contains solely 2-methylimidazolate as the organic building unit does not melt. Here, the melting temperature has been calculated to be much higher than its decomposition temperature.[116]

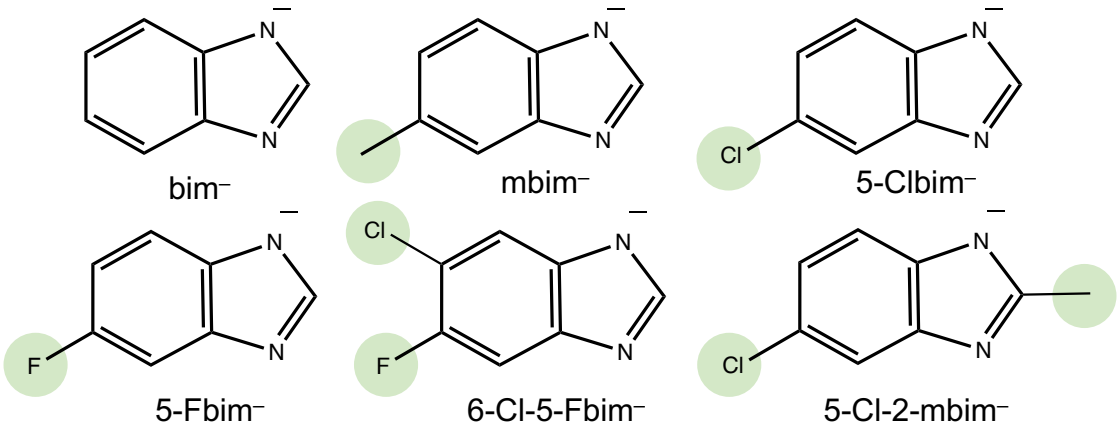

Figure 4.7: Library of secondary bulky linkers used for the synthesis of glass forming mixed-linker ZIFs. Functionalizations to the bim^- are marked green. Linker abbreviations: bim^- = benzimidazolate, 6-Cl-5-Fbim^- = 6-chloro-5-fluorobenzimidazolate, 5-Cl-2-$mbim^-$ = 5-chloro-2-methylbenzimidazolate, 5-Fbim^- = 5-fluorobenzimidazolate, 5-Clbim^- = 5-chlorobenzimidazolate, $mbim^-$ = 5-methylbenzimidazolate.

4.3.3 Porosity in ZIF glasses

At the starting point of this thesis in 2017, the porosity in ZIF glasses was poorly investigated. To the best of my knowledge only three publications covering porosity features of ZIF glasses had been published by then.[114,125,153] Nevertheless, given that the crystalline ZIF glass precursors are typically microporous solids with interesting

porosity features,[29,154–157] it is important to study the porosity of their melt-quenched glasses in detail.

Historically, a first study from 2016 revealed that a_gZIF-4 possesses residual microporosity by positron annihilation lifetime spectroscopy (PALS) measurements.[153] This finding was later supported by high-level molecular dynamics simulations.[116,158] Thereon, PALS has been employed to investigate the porosity of other MOF glasses.[122,137,150,151] However, PALS is unable to prove that the detected pores in the ZIF glasses are in fact accessible to gas molecules, i.e. that the glasses possess an open framework. Moreover, it is extremely difficult to quantify porosity (i.e. to determine the specific pore volume of the solid) via this method.[159]

The generally accepted analytical technique to quantify porosity and surface area of microporous materials is isothermal N_2 physisorption at cryogenic temperatures (i.e. 77 K). Unfortunately, at that temperature N_2 is not adsorbed in any ZIF glass investigated thus far (e.g. a_gZIF-4 and a_gZIF-UC-2 to a_gZIF-UC-5).[114,149] This has been proposed to originate from diffusion limitations of the N_2 molecule into the (presumably) narrow pores of the ZIF glasses at the low measurement temperature of 77 K.[149,160] Thereon, microporosity for some mixed-linker ZIF glasses was demonstrated with CO_2 physisorption measurements at 273 K or 298 K with a maximum CO_2 pressure of about 100 kPa (see Table 4.1). Such measurements

Table 4.1: Summary of maximum gas adsorption capacities of CO_2 at approximately 95 kPa at different temperatures of mixed-linker ZIF glasses reported in the literature. Capacities are given in mmol g^{-1}.

compound	chemical composition	@ 273 K	@ 298 K
a_gZIF-UC-1a	$Zn(im)_{1.74}(bim)_{0.17}(mbim)_{0.09}$	-	≈ 0.78[148] *a*
a_gZIF-UC-1e	$Zn(im)_{1.61}(bim)_{0.18}(mbim)_{0.21}$	-	≈ 0.72[148] *a*
a_gZIF-UC-2	$Zn(im)_{1.90}(6\text{-Cl-}5\text{-Fbim})_{0.10}$	≈ 0.48[149] *b*	
a_gZIF-UC-3	$Zn(im)_{1.75}(5\text{-Cl-}2\text{-mbim})_{0.25}$	≈ 0.86[149] *b*	
a_gZIF-UC-4	$Zn(im)_{1.63}(5\text{-Fbim})_{0.37}$	≈ 1.12[149] *b*	
a_gZIF-UC-5	$Zn(im)_{1.69}(5\text{-Clbim})_{0.31}$	≈ 0.95[149] *b*	
a_g(ZIF-62)	$Zn(im)_{1.76}(bim)_{0.24}$	0.90[161]	

a The molar capacities are approximated from figures in the literature. Therefore, the capacities in cm^3(STP) g^{-1} were read out from the figure in the paper and then divided by the molar gas volume (STP).

b The molar capacities are approximated from figures in the literature. Therefore, the capacities in cm^3(STP) cm^{-3} were read out from the figure in the paper, divided by the provided materials' pychnometric densities (g cm^{-3}, also read out from the corresponding figure) and then divided by the molar gas volume (STP).

provide an experimental proof for gas-accessible microporosity in these ZIF glasses. However, they do not allow quantification of the major parameter of porosity, such as the pore volume. This is because the gas sorption data are collected much too

far away from saturation (note, 100 kPa is equal to only about 0.03 p/p_0 at 273 K*). A quantification of the full gas-accessible pore volume of the ZIF glasses as well as a comprehensive comparison of the porosity of the glasses in relation to their crystalline precursors is absent in the literature.

* $p_0(CO_2, 273\ K) = 3485\ kPa$[162]

5 Nomenclature and Conventions

In the following chapters, various ZIF materials will be investigated. One important aspect will be their thermal phase transition behavior towards melting and glass formation. For clarity, various abbreviations are used to describe the ZIF materials as well as their thermally derived phases. Therefore, it seems useful to give an overview of the nomenclature used in the following part.

Additionally, temperatures and enthalpies of the transitions are evaluated from thermal analysis data. The conventions for determining these values are also given below.

Crystalline ZIFs

The literature known ZIF-4, ZIF-zni, TIF-4 and ZIF-62 are prepared and investigated. ZIF materials directly obtained after the synthesis are called as-synthesized and the prefix (as-) is added to the respective abbreviation (e.g. as-ZIF-4). The ZIF materials contain solvent molecules from the synthesis in their porous framework (except for ZIF-zni). The process of removing the solvent molecules from the framework is called activation which yields solvent-free materials. For activated materials the prefix (as-) is removed from the ZIF's abbreviation.

Various Metal Ions

All ZIFs are build solely from Zn^{2+} ions if not stated otherwise. During the course of this thesis some ZIF materials are synthesized which contain Co^{2+} ions as the inorganic building unit. If ZIFs containing Zn^{2+} or Co^{2+} ions are discussed comparably Zn or Co is added in brackets at the end of the respective ZIFs abbreviation (e.g. ZIF-4(Zn); ZIF-4(Co)).

Various Linker Ratios

The literature known ZIF-62(Zn) material features the approximate chemical composition ($Zn(im)_{1.75}(bim)_{0.25}$). During the course of this theses different ZIF-62(M) materials have been synthesized with varying im^- : bim^- ratios as well as metal ions (M

= Zn^{2+} or Co^{2+}). Materials with the general chemical composition $M(im)_{2-x}(bim)_x$ are obtained which are abbreviated with ZIF-62(M)-bim_x.

Phases Derived by Thermal Treatment

Phases derived by thermal treatment are obtained from crystalline ZIFs by heating the ZIF to a certain transition temperature and subsequently cooling back to room temperature. The abbreviation is constructed from the abbreviation of the parent crystalline ZIF with a prefix. For a material which was heated to its melting temperature and subsequently forms a melt quenched glass, the prefix a_g is used for amorphous glass (e.g. a_gZIF-4). Further, for ZIF-4 additional phases are investigated. These are the thermally amorphized phase a_TZIF-4 and the thermally to ZIF-zni recrystallized phase zni_TZIF-4.

Conventions for Evaluations via Thermal Analysis

All values were determined from signals observed in the DSC trace of thermal analysis data. The T_m is defined as the peak offset, the T_g as the peak onset, whereas all other derived temperatures − amorphization temperature (T_{am}) and recrystallization temperature (T_{rc}) − are defined as the peak temperature. Enthalpies are determined from the integral of the corresponding signal (e.g. melting enthalpy (ΔH_m)). The melting entropy (ΔS_m) is calculated as $\Delta H_m/T_m$.

6 Quantification of Intrinsic Microporosity in ZIF Glasses*

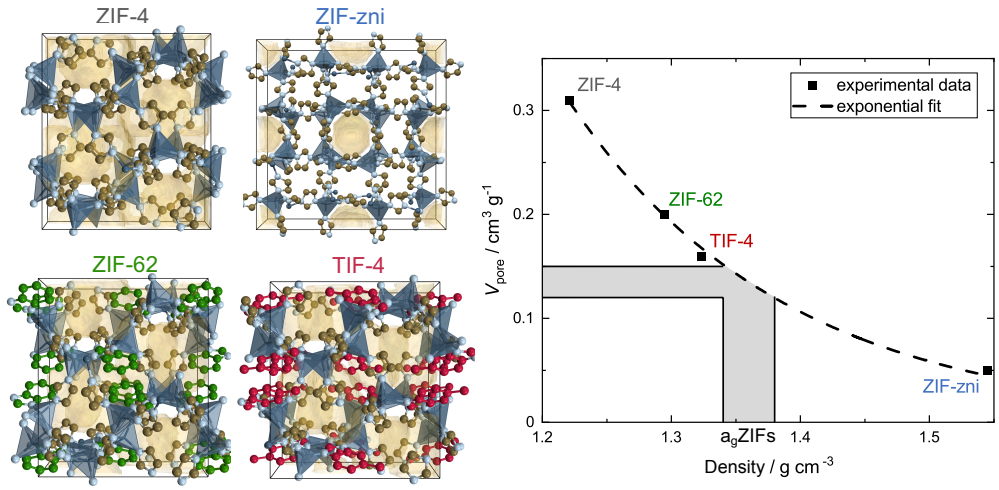

Abstract

So far, the intrinsic structural porosity of ZIF glasses is only poorly understood. Here, the porosity features of a series of literature known ZIF glass formers and their corresponding glasses are investigated comprehensively. CO_2 sorption at 195 K allows to follow the evolution of microporosity when transforming from the crystalline to the glassy state of these materials for the first time. On the basis of these data, the pore volume and the density of the ZIF glasses is quantified. Additional hydrocarbon sorption data (*n*-butane, propane and propylene) together with X-ray total scattering experiments prove that the porosity features (in particular the pore size) of the ZIF glasses are a function of the chemical composition (i.e. type of linkers) of the glass network.

* The content of this chapter is already submitted for publication and a preprint is available online: L. Frentzel-Beyme, P. Kolodzeiski, J.-B. Weiß, S. Henke. Quantification of gas-accesible microporosity in metal-organic framework glasses. DOI:10.26434/chemrxiv-2021-lq308.

6.1 A Versatile Series of Glass Forming ZIFs

In this chapter, a deeper understanding of the porosity in ZIF glasses will be gained. Therefore, four literature known glass forming ZIFs are investigated. The mixed-linker glass forming frameworks ZIF-62 (composition $Zn(im)_{1.65}(bim)_{0.35}$) and TIF-4 (composition $Zn(im)_{1.68}(mbim)_{0.32}$) are studied as well as the canonical glass formers ZIF-4 and ZIF-zni (composition $Zn(im)_2$ for both). The latter do not feature a secondary bulky imidazolate linker, but only the simple im^- linker (see Figure 6.1).

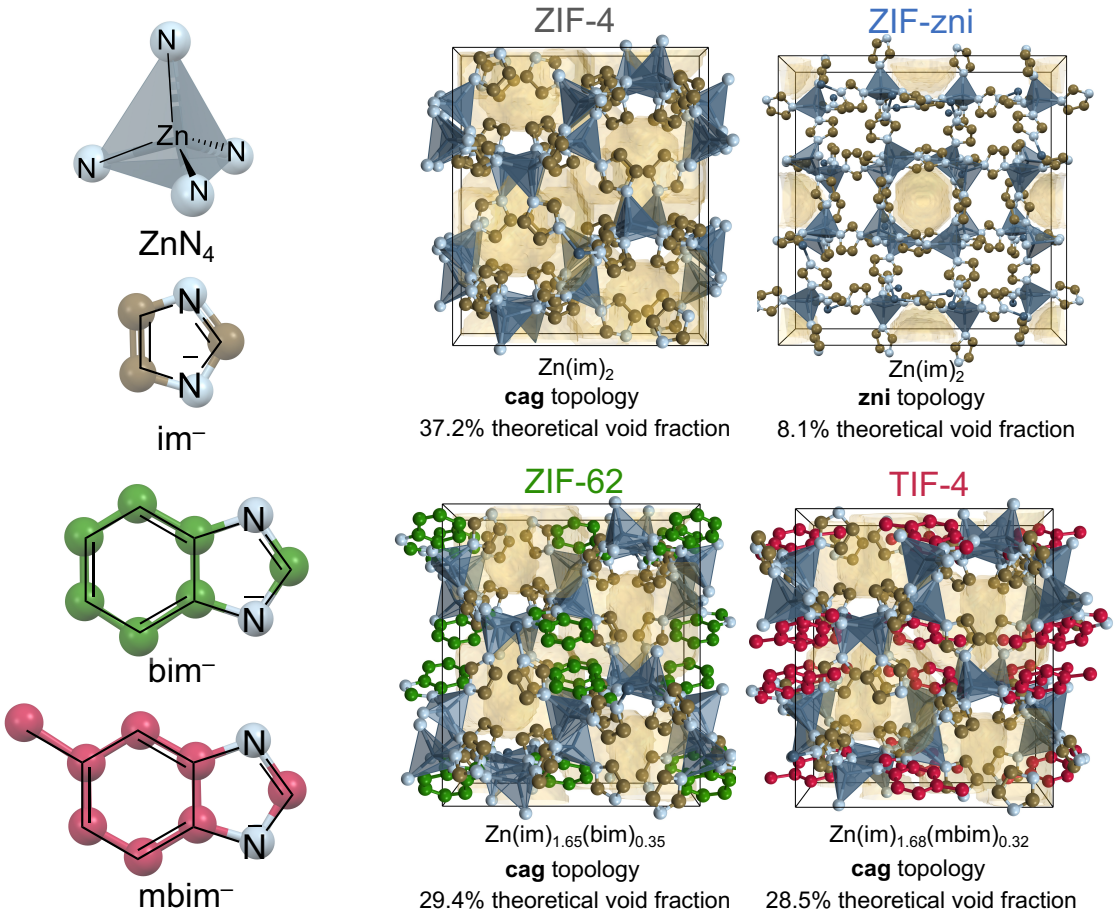

Figure 6.1: Left: Building units of the investigated ZIF glass formers. Right: Crystal structures of the ZIF glass formers. ZIF-4 (CSD code IMIDZB11), ZIF-62 (CSD code SIWJAM) and TIF-4 (CSD code QOSYAZ) viewed along the crystallographic *b* axis. ZIF-zni (CSD code IMIDZB) viewed along the crystallographic *c* axis. Hydrogen atoms are omitted for clarity. The respective theoretical void fraction (tVF) given below the structures are shown in pale yellow.[a] Crystal structure images are generated from the stated CSD data.

a The tVFs – based on the crystal structures of all four materials – were calculated with the implemented routine in Olex2[48] applying a probe radius of 1.3 Å and grid spacing of 0.2 Å. The structures were taken from the CSD database (CSD codes are given in the caption). For ZIF-4 and ZIF-zni, missing hydrogen atoms have been added geometrically with Olex2. For ZIF-62 and TIF-4 some disordered groups were resolved and solvent molecules were removed where present, before the calculations.

First, the literature known materials are chemically and structurally analyzed in detail. Subsequently, the porosity of this series of ZIF glasses as well as their crystalline or amorphous precursors is investigated with CO_2 physisorption measurements at 195 K (see Figure 6.2). ZIF-4 is particularly interesting, due to the series of reconstructive crystalline-to-amorphous-to-crystalline phase transitions (ZIF-4 to a_TZIF-4 to zni_TZIF-4) before melting at approximately 580 °C and forming the glass a_gZIF after melt-quenching.* It becomes clear that a_gZIF-4 is precisely formed from the recrystallized polymorph with **zni** topology. Therefore, it is also investigated whether the porosity features of the glass derived from solvothermally synthesized ZIF-zni (a_gZIF-zni) differ from a_gZIF-4.

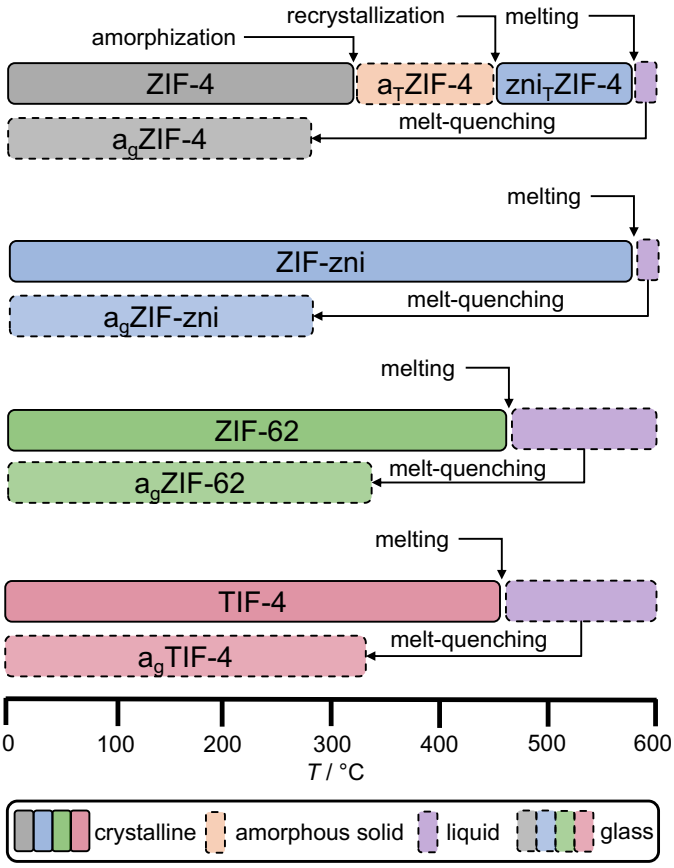

Fig. 6.2: Schematic representation of the high temperature phase behavior of the ZIF glass formers investigated in this chapter.

The low temperature CO_2 sorption data allow to quantitatively analyze the specific pore volume of the ZIF glasses and their precursors. Based on the derived specific pore volumes, the changes in the gas-accessible void fraction when progressing from the crystalline to the glassy state are further evaluated. Importantly, the void fraction is directly connected to the material's real density (i.e. the density including the intrinsic microporosity, sometimes also referred to as apparent density[163]). The real density is a fundamental physical parameter which is so far unknown for ZIF glasses, since previous studies utilized He pycnometry to determine their density[115,127,149] which only provides information on the skeletal density (that is the density excluding the intrinsic microporosity). Knowledge of the real density of the glasses, however, permits further insights into the thermodynamics of melting and glass formation of this family of glass formers. Combining the low temperature CO_2 sorption data with additional hydrocarbon sorption experiments (*n*-butane, propane and propylene) and

* A more detailed discussion of the high temperature behavior of ZIF-4 is given in Section 4.3.1.

structural insights derived from X-ray total scattering experiments, allows deducing important correlations of the chemical composition (i.e. linker functionality) of the ZIF glass former with the pore volume and the pore size of the derived ZIF glass.

6.1.1 Synthesis and Characterization of Crystalline ZIF Glass Formers

ZIF-4 (**cag** topology), ZIF-zni (**zni** topology), ZIF-62 (**cag** topology) and TIF-4 (**cag** topology) were synthesized reproducing or adapting established procedures (see 12.9.1). Solvent molecules were removed from the porous structure at 200 °C under dynamic vacuum yielding the activated (solvent-free) compounds. Phase purity of the activated crystalline ZIFs was verified by structureless profile fits (Pawley method) of PXRD patterns using reference data from the literature (see Section 4.3.1).*[29,164–166] The complete removal of solvents from the pores is demonstrated by Fourier-transform infrared spectroscopy (FTIR spectroscopy) data with the absence of a vibrational band at 1675 cm^{-1} which is ascribed to the carbonyl stretching vibration of *N,N*-dimethylformamide (DMF) (see Figure 6.3). DMF is found in the as-synthesized materials as the template for the porous channels (except for ZIF-zni).

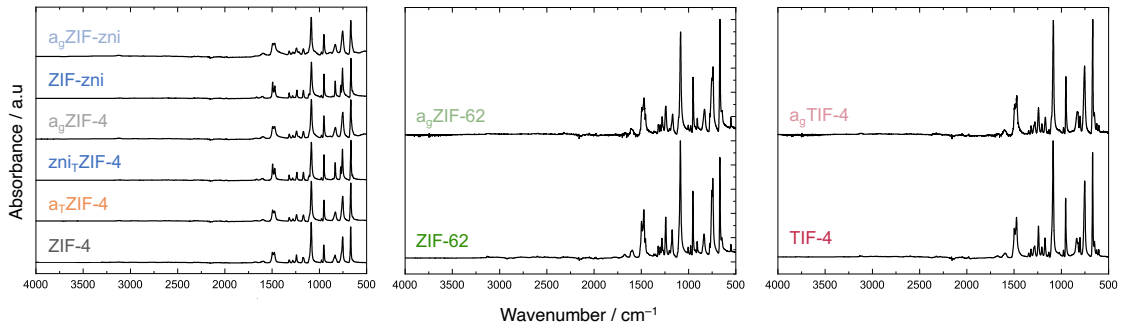

Figure 6.3: FTIR spectroscopy data of all investigated materials in this chapter.

The activation of all materials is further verified by the absence of signals ascribed to DMF in solution ^{1}H nuclear magnetic resonance spectroscopy (NMR spectroscopy) data on digested samples (see Section A.1.3). Solution ^{1}H NMR spectroscopy was further used to determine the linker ratio of the ZIF-62 and TIF-4 samples, leading to the chemical compositions given above. Therefore, the ratio between the implemented linkers has been determined by the integral corresponding to the proton attached to the carbon atom between the two nitrogen atoms in the imidazolate-type linkers. The corresponding signals are integrated and assigned in the spectra displayed in Figure 6.4. The sum of the integrals are set to 2, matching two protons. Consequently,

∗ Details about the phase identification by structureless profile fits can be found in Section 3.1.5.

the chemical compositions are determined to be $Zn(im)_{0.35}(bim)_{1.65}$ for ZIF-62 and $Zn(im)_{0.32}(bim)_{1.68}$ for TIF-4.

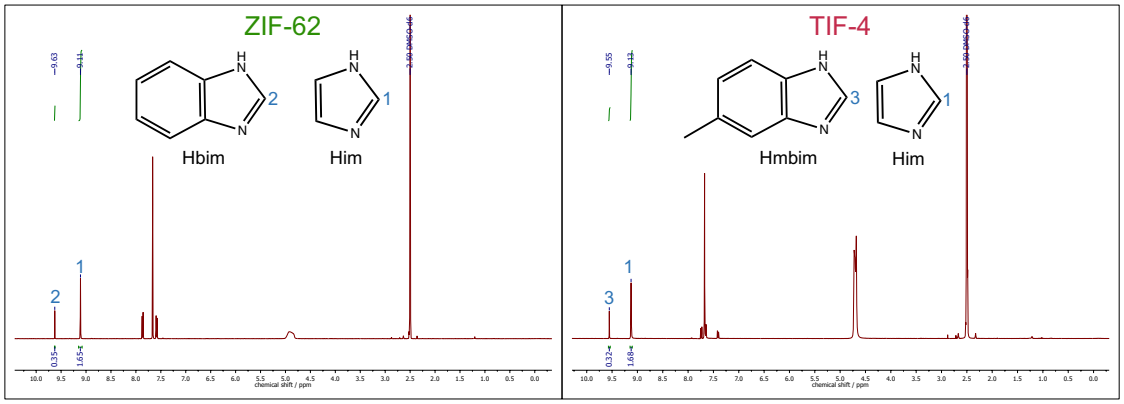

Figure 6.4: Solution ^{1}H NMR spectroscopy data of ZIF-62 and TIF-4. The signals used to determine the linker ratio are integrated and assigned to the marked protons.

6.1.2 Preparation and Characterization of Thermally Derived Phases

Based on the four crystalline reference materials, the corresponding thermally derived phases (a_TZIF-4, zni_TZIF-4, a_gZIF-4, a_gZIF-zni, a_gZIF-62 and a_gTIF-4) were obtained via thermal treatment under inert atmosphere in a TGA/DSC apparatus. Differential scanning calorimetry (DSC) data were used as a guide to pick the right temperature protocol to obtain the glasses, as well as the intermediate compounds a_TZIF-4 and zni_TZIF-4 in the case of ZIF-4 (Figure 6.5, determined temperatures values are summarized in Section A.1.5). Heating and cooling rates have been $+10\,°C\ min^{-1}$ and $-10\,°C\ min^{-1}$, respectively. The temperature profiles are summarized in the Table 6.1. The corresponding TGA/DSC data collected while preparing the respective products are plotted in Section A.1.4 showing the expected phase behavior. It has to be noted, that for the preparation of a_gZIF-4 and a_gZIF-zni an isothermal segment (10 min) at a maximum temperature of 578 °C was required to obtain amorphous glasses without crystalline residues of ZIF-zni (see Section A.1.1).

All products were characterized with PXRD and X-ray total scattering, solution ^{1}H NMR spectroscopy and solid state FTIR spectroscopy, as well as DSC, and the obtained data are in agreement with the literature.[114,115,122,140,150,166] PXRD data of the amorphous materials show only diffuse scattering and no sharp Bragg peaks (Figure 6.5). A profile fit to the PXRD pattern of zni_TZIF-4 testifies the recrystallisation of a_TZIF-4 to the $Zn(im)_2$ phase with **zni** topology (see Section A.1.1).

It has to be noted that the DSC curve for ZIF-zni shows a weak endothermic signal at 357 °C ($T_{\text{coi-zni}}$, see Figure 6.5). This signal is ascribed to the phase transition

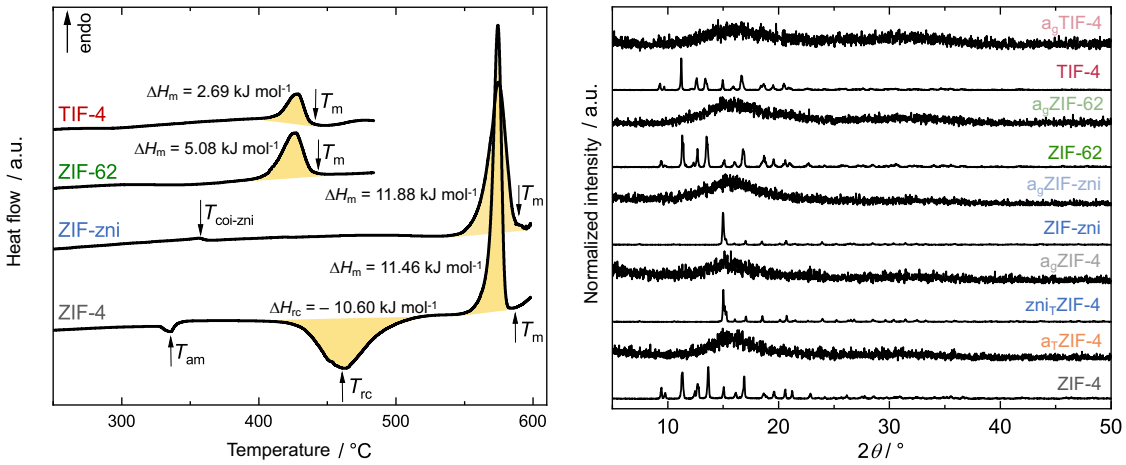

Figure 6.5: Left: DSC data for ZIF glass formers. Right: Stack plot of PXRD patterns of ZIF glass formers as well as thermally derived products.

of a minor impurity of another $Zn(im)_2$ polymorph with **coi** topology (ZIF-coi) to ZIF-zni. This transition has been already reported while heating of phase pure ZIF-coi whereas the enthalpy was found to be $\Delta H_{\text{coi-zni}} = 2.9$ kJ mol^{-1} for the complete conversion of ZIF-coi to ZIF-zni.[167] Here, an enthalpy of only $\Delta H_{\text{coi-zni}} = 0.08$ kJ mol^{-1} is determined for this signal which equals approximately 3% (m/m) of ZIF-coi in the solvothermally synthesized ZIF-zni sample. It has to be noted that this impurity is not visible in the profile fit of the PXRD pattern of ZIF-zni, which is due to the structural similarity of both compounds and the very small amount of ZIF-coi contained within the sample (see Section A.1.1 for the profile fit of ZIF-zni). Melting of the material is observed at 585 °C, where the whole material is considered to consist of ZIF-zni only.

The glasses a_gZIF-4, a_gZIF-zni, a_gZIF-62 and a_gTIF-4 further possess a fused monolithic structure characteristic for melt-quenched glasses (see Figure 6.6). It is noteworthy that solution ^{1}H NMR spectroscopy data of digested ZIF samples

Table 6.1: Summary of temperature profiles which were applied to obtain the products after thermal treatment in a TGA/DSC apparatus.

Product	Temperature program
a_TZIF-4	RT (+10 °C min^{-1}) → 379 °C (–10 °C min^{-1}) → RT
zni$_T$ZIF-4	RT (+10 °C min^{-1}) → 546 °C (–10 °C min^{-1}) → RT
a_gZIF-4	RT (+10 °C min^{-1}) → 578 °C –10 min → 578 °C (–10 °C min^{-1}) → 50 °C →RT
a_gZIF-zni	RT (+10 °C min^{-1}) → 578 °C –10 min → 578 °C (–10 °C min^{-1}) → 50 °C →RT
a_gZIF-62	RT (+10 °C min^{-1}) → 485 °C (–10 °C min^{-1}) → RT
a_gTIF-4	RT (+10 °C min^{-1}) → 485 °C (–10 °C min^{-1}) → RT

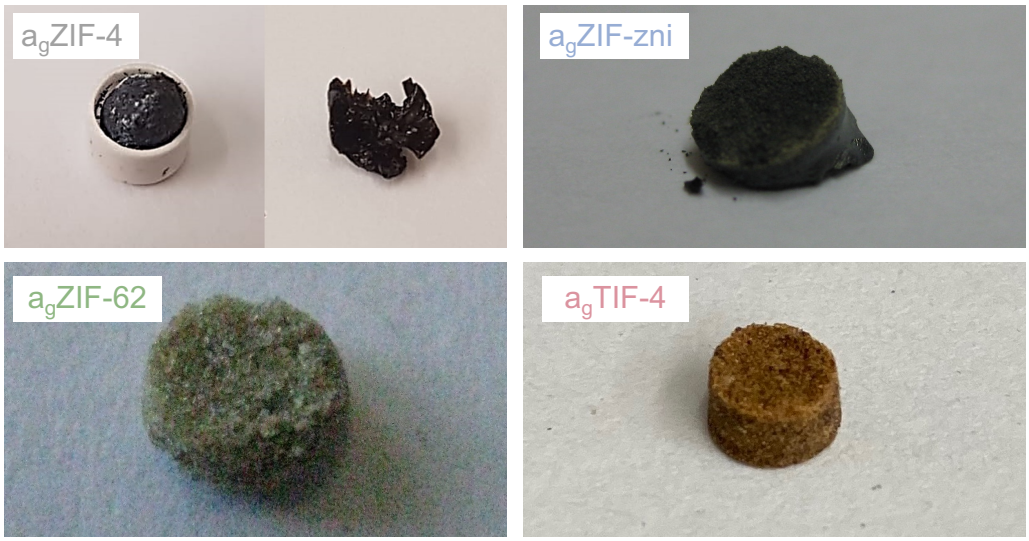

Figure 6.6: Photographs of the ZIF glass products obtained after the preparation in the TGA/DSC apparatus. It becomes evident that the materials show signs of macroscopic flow and are molten to a monolith.

demonstrate the full integrity of the organic linkers after thermal treatment, except for a_gZIF-4 and a_gZIF-zni (see Figure 6.7 and Section A.1.3 for the whole spectra). Weak signals for impurities are visible in the solution ^{1}H NMR spectra of the latter two ZIF glasses. These impurities are ascribed to the presence of some decomposition products which are a consequence of the much higher maximum processing temperature (578 °C) of these two glass materials compared to a_gZIF-62 and a_gTIF-4 (maximum processing temperature is 475 °C for these glasses).

Partial decomposition is further indicated by weak scattering signals in the X-ray total scattering function $S(Q)$ of a_gZIF-4 and a_gZIF-zni (Figure 6.8 and Section A.1.2 for the full datasets). The small but sharp peaks (marked red in Figure 6.8 left) found in a_gZIF-4 and a_gZIF-zni (but non of the other thermally derived phases) can be ascribed to zinc oxide (ZnO). This was uncovered by comparing a simulated PXRD pattern of ZnO to the collected $S(Q)$ data of a_gZIF-4 and a_gZIF-zni which are in a good agreement (see Figure 6.8 right). The formation of ZnO might arise from Zn metal which is formed during the partial decomposition of the organic linkers

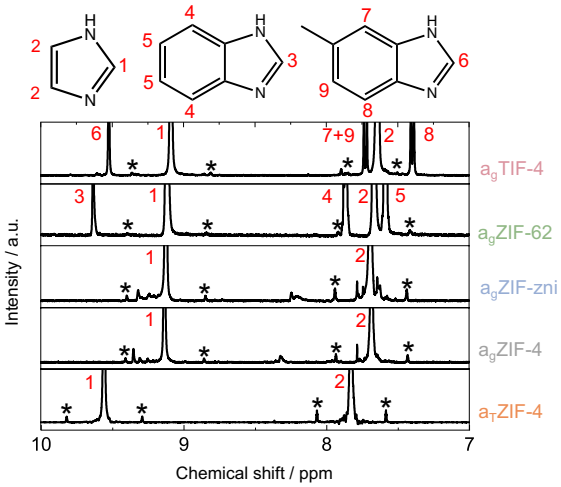

Fig. 6.7: Stack plot of solution ^{1}H NMR spectra of digested samples of the investigated amorphous materials. A zoom in the aromatic region is shown. The ^{13}C satellite signals are marked with asterisks (∗). Weak signals not marked with asterisks belong to decomposition products.

during melting. Zn metal is subsequently oxidized to ZnO when the material is exposed to air.

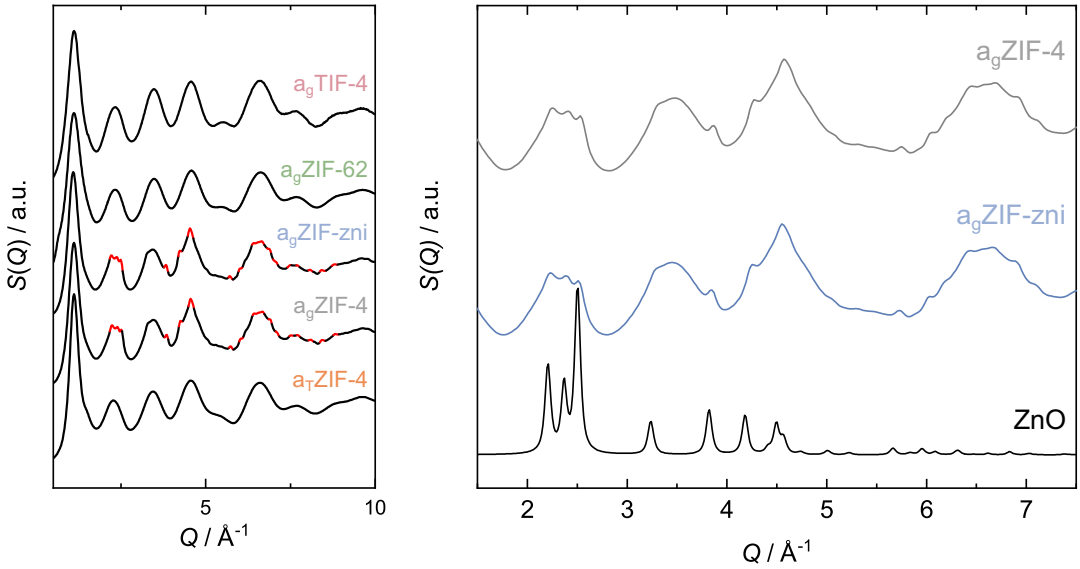

Figure 6.8: Left: X-ray total scattering data in the form $S(Q)$ of the amorphous phases. For a_gZIF-4 and a_gZIF-zni sharp scattering features ascribed to ZnO impurities are highlighted in red. Right: Zoom into the $S(Q)$ data of a_gZIF-4 and a_gZIF-zni compared to a simulated PXRD pattern of ZnO (crystallographic data taken from Reference [168]). It becomes evident that the small but sharp peaks found for a_gZIF-4 and a_gZIF-zni can be ascribed to ZnO.

The partial decomposition becomes further evident by significant mass losses (about 6%) during glass preparation in the TGA/DSC experiment (see Section A.1.4) as well as the very dark colour of a_gZIF-4 and a_gZIF-zni (see Figure 6.6). The other three amorphous materials (a_TZIF-4, a_gZIF-62 and a_gTIF-4) show neither signs of decomposition of the organic linkers nor formation of crystalline by-products.

XPDFs in the form of $D(r)$ derived via Fourier-transformation of the total scattering functions $S(Q)$[61] of all crystalline ZIFs and their thermal products demonstrate that the short-range structure of the crystalline phases (that is Zn^{2+} ions surrounded by four imidazolate-type linkers) is preserved in all amorphous phases (Figure 6.9 and Section A.1.2 for whole collected datasets).* The last sharp peak in the XPDFs of the amorphous materials is visible at about 5.9 Å and corresponds to the distance of two neighboring Zn^{2+} ions in the networks (see Figure 6.9). The XPDFs of a_TZIF-4, a_gZIF-62 and a_gTIF-4 show some weaker correlations for $r > 5.9$ Å, which are indicative of some mid-range order. At $r > 15$ Å, $D(r)$ of those materials converges

* In such data – visualized in the form $D(r)$[61] – every peak corresponds to an interatomic distance within the investigated material and thus provides information about its local structure. An introduction to X-ray total scattering and the derived XPDF function is given in Section 3.1.6.

towards zero. In contrast, the XPDFs of a_gZIF-4 and a_gZIF-zni show additional weak but significant pair correlations extending well beyond $r = 20$ Å. These correlations are ascribed to the crystalline ZnO impurities present in these ZIF glasses (see Figure 6.8).

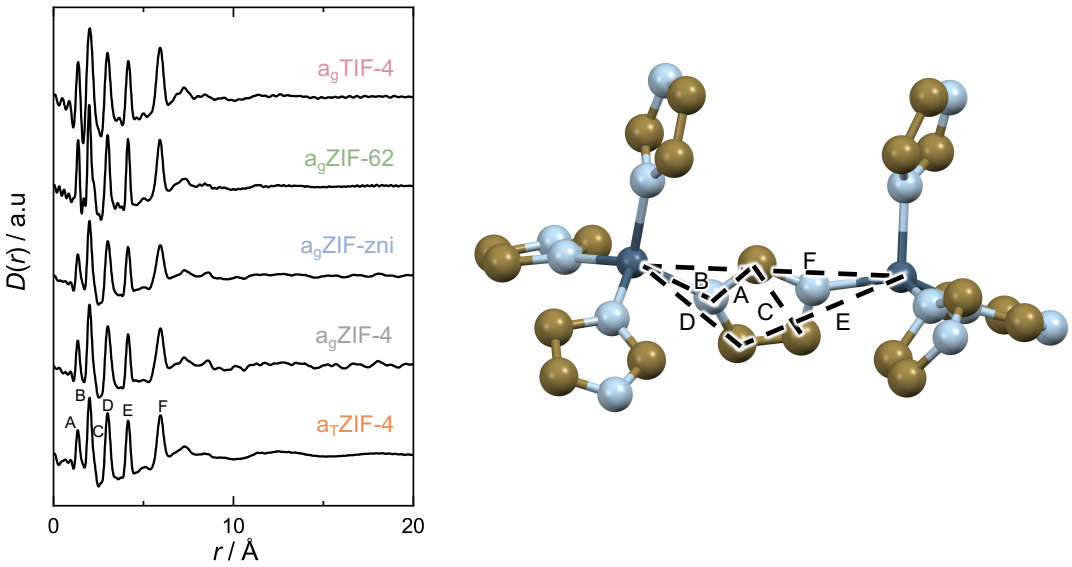

Figure 6.9: Left: Stack plot of XPDFs in the form $D(r)$ for all amorphous phases. Right: Representation of the coordination environment of two neighboring Zn^{2+} ions in the ZIF materials. Short range correlations which are found in the XPDFs of the amorphous phases (left) are highlighted and assigned to the XPDF of a_TZIF-4. The similarity of all XPDFs up to $r \approx 5.9$Å is clearly evident and demonstrates similar short range correlations for all materials. Atom label: Zn (dark blue), C (brown), N (light blue). Hydrogen atoms are omitted for clarity.

With the aim to get more insights into the structure of the amorphous ZIF derivatives, a closer look was taken at the first sharp diffraction peak (FSDP) of their scattering functions $S(Q)$ (see Figure 6.10). The FSDP contains valuable information about the medium range order (MRO) of amorphous network solids.[169–171] For the ZIF glasses this means some degrees of order extending beyond the first Zn−Zn neighbor distance. The position of the FSDP (Q_{FSDP}) has been associated with a real space correlation length between the strongest scattering centers (i.e. Zn^{2+} cations here), which are surrounded by interstitial voids.[172,173] As such, Q_{FSDP} can also be regarded as a reciprocal space signature of the glass networks' porosity and density. The full width at half maximum (FWHM) of the FSDP (ΔQ_{FSDP}) is inversely proportional to the real space coherence length over which the MRO (i.e. the correlation) exists.[172,173]

For quantification, the FSDP of the five amorphous materials under study here is fitted to a pseudo-Voigt function to derive Q_{FSDP} and ΔQ_{FSDP} (see Table 6.2).*

* The calculations have been performed with the Fityk software package.[174]

Q_{FSDP} is identical for all solids and found at about 1.11 Å^{-1}, suggesting the densities of a_TZIF-4 and the four glasses are very similar. Remarkably, ΔQ_{FSDP} is with 0.35 Å^{-1} significantly larger for a_gZIF-62 and a_gTIF-4 than for the amorphous ZIF-4/ZIF-zni derivatives ($\Delta Q_{\mathrm{FSDP}} = 0.24 - 0.29$ Å^{-1}). This translates to a shorter coherence length for the MRO in the mixed-linker ZIF glasses. Hence, a_gZIF-62 and a_gTIF-4 are more disordered than the single-linker materials, which can be explained by their more complex chemical composition involving two different but homogeneously distributed imidazolate-type linkers with largely different molecular size.

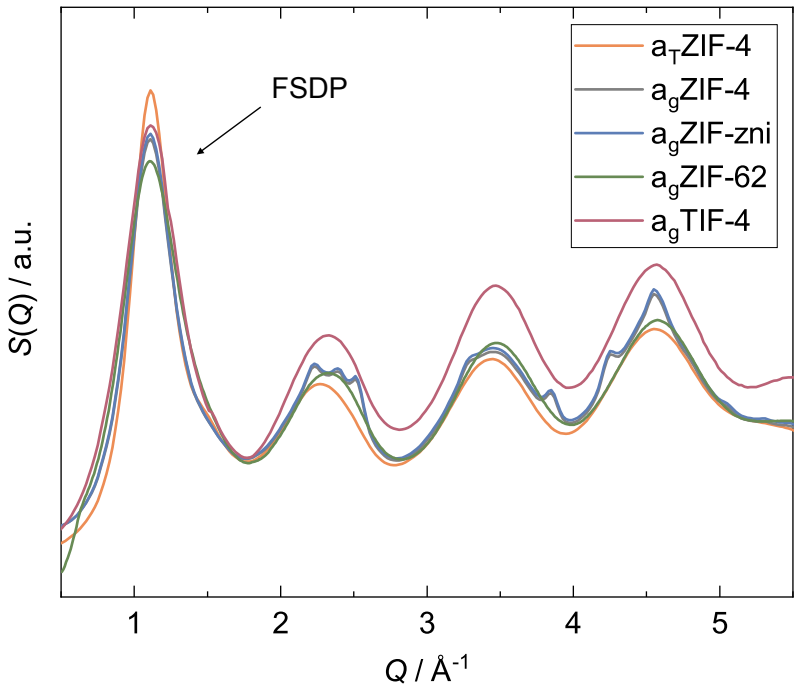

Figure 6.10: Overlay of X-ray total scattering data in the form $S(Q)$ for all investigated amorphous materials. A zoom into the region from 0.5 – 5.5 Å^{-1} is shown.

Table 6.2: Summary of the parameters obtained after fitting of the FSDP of the total scattering data for all amorphous phases.

materials	Q_{FSDP} / Å^{-1}	ΔQ_{FSDP} / Å^{-1}
a_TZIF-4	1.108	0.244
a_gZIF-4	1.097	0.286
a_gZIF-zni	1.105	0.287
a_gZIF-62	1.098	0.350
a_gTIF-4	1.109	0.348

6.2 Physisorption Studies

6.2.1 N_2 Physisorption Studies

N_2 sorption isotherms at 77 K were collected for all materials (see Figure 6.11). ZIF-4 shows a previously reported complex phase transition behavior during N_2 adsorption at 77 K[143,175,176] and adsorbs 8.57 mmol N_2 g^{-1} at saturation. ZIF-62 and TIF-4 adsorb significantly smaller amounts of N_2 at saturation (0.49 mmol g^{-1} for ZIF-62 to 0.54 mmol g^{-1} for TIF-4) and their isotherms show a strong hysteresis upon desorption. This is ascribed to diffusion limitations in the narrow pores of these two crystalline frameworks caused by the secondary bulky imidazolate linkers (bim^- and $mbim^-$). All other isotherms show linear shapes and very small total gas uptakes ($0.18 - 0.91$ mmol g^{-1}, see Figure 6.11 and Section A.1.6 for precise values). These observations are in accordance with available N_2 sorption data of ZIF glasses in the literature and point towards predominant gas adsorption on the materials' external surfaces.[114,142] Since the diffusion of N_2 in the materials is restricted by the small pore sizes and the low measurement temperature, the pore volume of the ZIF glasses and their precursors cannot be probed by N_2 sorption.

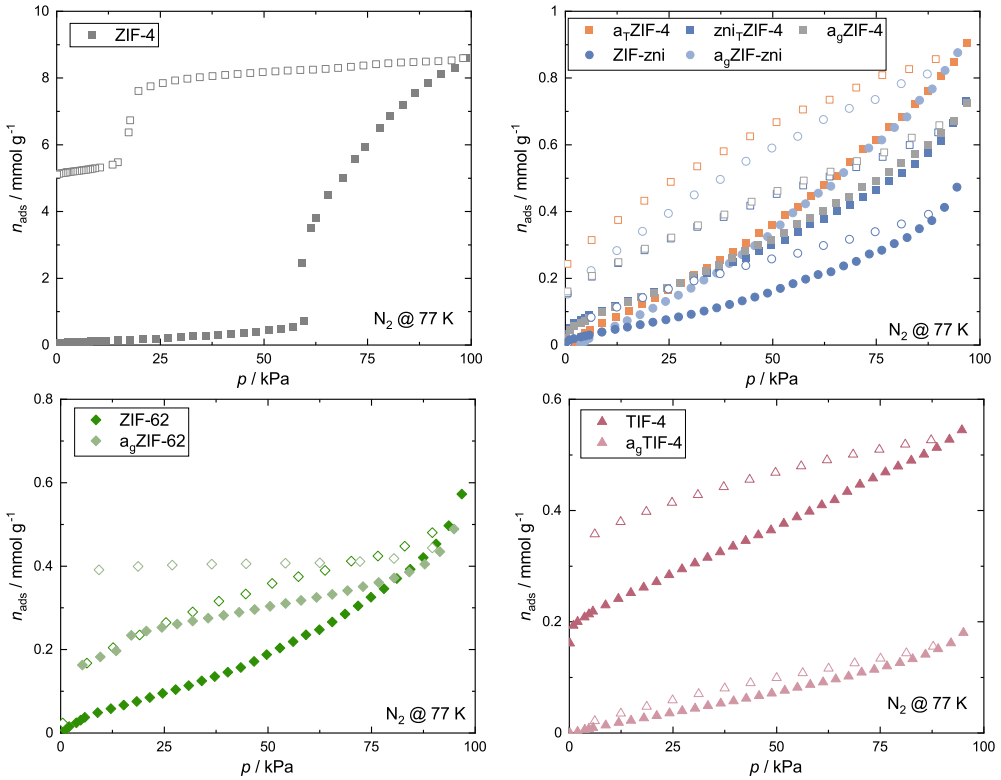

Figure 6.11: Plot of N_2 physisorption isotherms. Adsorption and desorption branches are shown as open and closed symbols, respectively.

6.2.2 CO_2 Physisorption Studies and Pore Volume Determination

In order to circumvent the gas diffusion limitations, the porosity features of all materials were probed by CO_2 physisorption at 195 K (see Figure 6.12). The smaller kinetic diameter of the CO_2 molecule (3.3 Å)[177] compared to N_2 (3.6 Å)[177] together with the higher temperature (195 K *vs.* 77 K) facilitates the diffusion of the gas into very small micropores (< 5 Å).[178,179] Compared to the CO_2 sorption studies performed at 273 K or 298 K in the literature*, running the experiment at 195 K allows reaching saturation (i.e. $p/p_0 \rightarrow 1$) at ambient pressure.

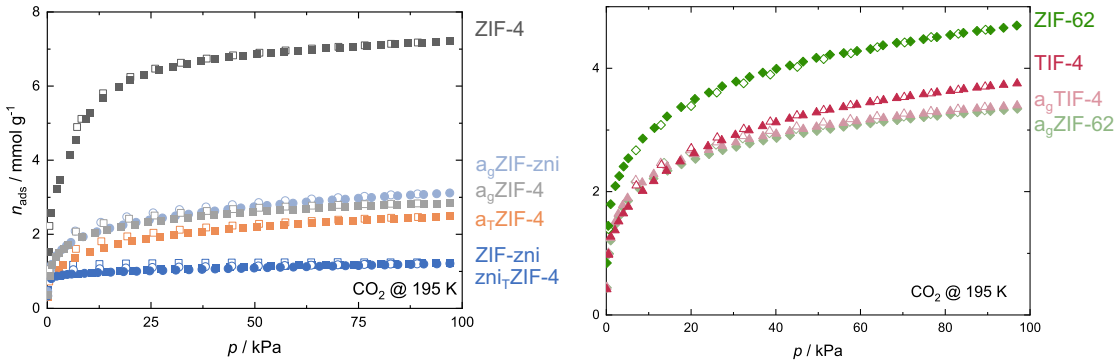

Figure 6.12: Left: CO_2 sorption isotherms collected at 195 K of ZIF-4 and ZIF-zni and their corresponding thermal products. ZIF-4 derivatives are shown as squares. ZIF-zni derivatives are shown as circles. Right: CO_2 isotherms collected at 195 K of ZIF-62 and TIF-4 and their corresponding glasses. ZIF-62 derivatives are shown as rhombs. TIF-4 derivatives are shown as triangles. In both panels adsorption and desorption branches are shown as closed and open symbols, respectively.

Consequently, the determined maximum molar gas capacities ($n_{\text{ads}}^{\text{max}}$) at the maximum collected pressure point ($p \approx 95$ kPa, $p/p_0 \approx 0.95$) allow to determine the specific pore volume (V_{pore}) of the investigated materials by making the established assumption that the adsorbate fills the entire pore space at this pressure[70] (Table 6.3 and Figure 6.13). Moreover, Brunauer-Emmett-Teller (BET) surface areas[180] have been determined from these data (see Table 6.3).† Even though application of the BET model is very common in research on porous materials, it has to be noted that this model is strictly not applicable for the microporous materials studied here.[160] Thus, these data are only provided for reference. A general discussion on the assumption and applicability of the BET model is given in Section 3.2.4.

First, it will be focused on the gas sorption data for ZIF-4, ZIF-zni and their corresponding amorphous and crystalline high temperature phases. Remarkably, all these phases adsorb CO_2 as evident from the Type I (or Langmuir) shaped

∗ A discussion on the state-of-the-art of ZIF glass porosity is given in Section 4.3.3.
† More methodical details about the calculation of the pore volume and BET surface areas can be found in Section 3.2.

Table 6.3: Summary of maximum gas capacities (n_{ads}^{max}), specific pore volumes (V_{pore}) and BET surface areas (S_{BET}) obtained from the CO_2 physisorption isotherms collected at 195 K.

compound	n_{ads}^{max} [mmol g^{-1}]	V_{pore} [cm^3 g^{-1}]	S_{BET} [m^2 g^{-1}]	ρ [g cm^{-3}]
ZIF-4	7.22	0.31	473	1.22[a]
a_TZIF-4	2.49	0.11	140	1.39[b]
zniTZIF-4	1.23	0.05	89	1.56[a]
a_gZIF-4	2.84	0.12	186	1.38[b]
ZIF-zni	1.21	0.05	92	1.56[a]
a_gZIF-zni	3.12	0.13	183	1.37[b]
ZIF-62	4.70	0.20	257	1.29[a]
a_gZIF-62	3.34	0.14	194	1.35[b]
TIF-4	3.76	0.16	180	1.32[a]
a_gTIF-4	3.40	0.15	199	1.34[b]

a crystallographic density.
b experimental density calculated from CO_2 adsorption data.

isotherms (Figure 6.12). As expected, the crystalline ZIF-4 exhibits the highest V_{pore} of 0.31 cm^3 g^{-1} (Table 6.3). Going along the other ZIF-4 phases consecutively formed via thermal treatment, a drastic decrease in V_{pore} is found for a_TZIF-4 to 0.11 cm^3 g^{-1} (−65% compared to ZIF-4), demonstrating a collapse and densification of framework, but preservation of about 35% of the pore space of the crystalline phase. V_{pore} drops further for the recrystallized zni$_T$ZIF-4 (V_{pore} = 0.05 cm^3 g^{-1}) to only about 16% of the porosity of crystalline ZIF-4. Strikingly, the solvothermally synthesized ZIF-zni features the same pore volume (V_{pore} = 0.05 cm^3 g^{-1}) as zni$_T$ZIF-4, suggesting that a_TZIF-4 completely recrystallizes to zni$_T$ZIF-4 during thermal treatment. This is in line with the very similar melting enthalpies for zni$_T$ZIF-4 (11.46 kJ mol^{-1}) and ZIF-zni (11.88 kJ mol^{-1}) determined via DSC (Figure 6.5). Since ZIF-zni, which is the densest and most stable Zn(im)$_2$ phase (at least at temperatures >360 °C[167]), is already microporous, it is not surprising that a_gZIF-4 and a_gZIF-zni also adsorb CO_2. Both glasses show very similar isotherms with calculated pore volumes of 0.12 cm^3 g^{-1} and 0.13 cm^3 g^{-1}, respectively.

Remarkably, the pore volumes of the mixed-linker glasses a_gZIF-62 (V_{pore} = 0.14 cm^3 g^{-1}) and a_gTIF-4 (V_{pore} = 0.15 cm^3 g^{-1}) are higher than for a_gZIF-4 and a_gZIF-zni (Figure 6.13). This is counterintuitive by comparing the pore volumes of the respective parent crystalline materials. The three crystalline precursors ZIF-4, ZIF-62 and TIF-4 feature the same **cag** topology. Their pore volumes decrease from 0.31 cm^3 g^{-1} (ZIF-4) to 0.20 cm^3 g^{-1} (ZIF-62) and 0.16 cm^3 g^{-1} (TIF-4). This correlates with the implementation of the secondary bulky imidazolate linkers (bim$^-$

and mbim$^-$) in ZIF-62 and TIF-4, reducing the void space of the crystalline framework (see theoretical void fractions calculated on the basis of the crystal structures shown in Figure 6.1). It has to be noted that the concentration of both secondary bulky linkers in the mixed-linker ZIFs is rather similar (ZIF-62: $Zn(im)_{1.65}(bim)_{0.35}$; TIF-4: $Zn(im)_{1.68}(mbim)_{0.32}$), while the steric bulk of mbim$^-$ containing an additional methyl group in TIF-4 is higher than for bim$^-$ in ZIF-62. This further decreases the free void space in crystalline TIF-4 and explains the higher V_{pore} of ZIF-62 over TIF-4 (Figure 6.13). The highest reduction in V_{pore} (approximately -61%) from the crystalline to the glass material is found for ZIF-4, while a reduction of just 30% and 6% is found for the glasses of ZIF-62 and TIF-4 compared to their crystalline parent compounds.

It must be noted that the presence of small amounts of decomposition products (ZnO and decomposed organic linkers, see above) in a_gZIF-4 and a_gZIF-zni could potentially reduce the mass weighted gas capacities and thus calculated pore volumes (see Figure 6.7 and Figure 6.8). Nevertheless, the thermally amorphized phase a_TZIF-4, which does not contain any decomposition products, features an even lower pore volume ($V_{\mathrm{pore}} = 0.11$ cm^3 g^{-1}) than a_gZIF-4 and a_gZIF-zni. This suggests that the partial decomposition has only a minor influence on the determined pore volume. Moreover, the finding that the pore volumes of a_TZIF-4, a_gZIF-4 and a_gZIF-zni are similar, is in line with the analysis of the FSDP of the scattering function.

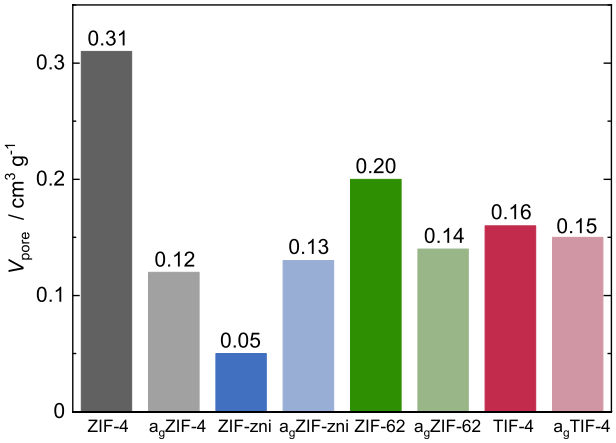

Fig. 6.13: Bar plot of specific pore volumes (V_{pore}) for all crystalline ZIFs and their corresponding glasses derived from the CO_2 isotherms at 195 K.

CO_2 sorption isotherms were also collected at 273 K for all materials (Figure 6.14). Here, the highest capacity is again found for ZIF-4 (2.64 mmol g^{-1}) followed by ZIF-62 (1.87 mmol g^{-1}) and TIF-4 (1.43 mmol g^{-1}), whereas the amorphous materials (a_TZIF-4, a_gZIF-4, a_gZIF-zni, a_gZIF-62, a_gTIF-4) as well as the materials adopting the **zni** topology (zni_TZIF-4, ZIF-zni) show similar and lower uptakes in the range from $0.81 - 1.21$ mmol g^{-1} (see Section A.1.6 for all values). Importantly, the trend in gas sorption capacity observed at 273 K and 95 kPa drastically varies from the trend observed at 195 K and 95 kPa. Thus, it is concluded that CO_2 isotherms collected at 273 K are insufficient to detect the inherent differences in porosity (particularly the pore volume) of these materials.

In order to get deeper insights into the porosity features of the glasses and their

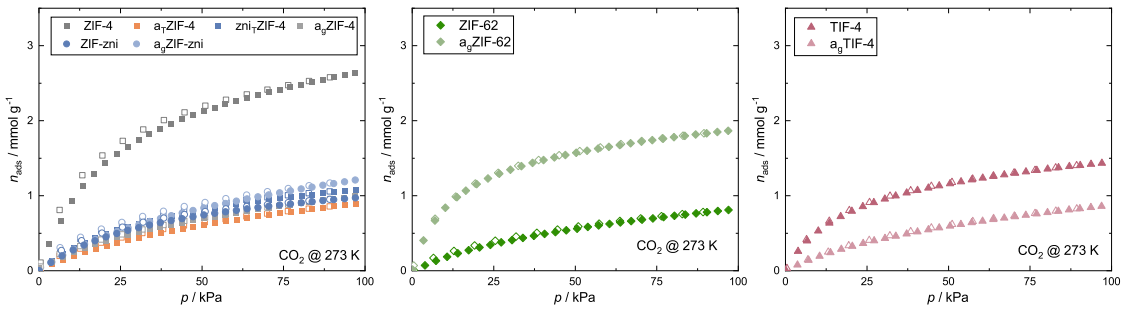

Figure 6.14: CO_2 gas isotherm data collected at 273 K. Adsorption and desorption branches are shown as close and open symbols, respectively.

crystalline precursors, pore size distributionss (PSDs) were calculated based on the CO_2 sorption data by utilizing the Horvath-Kawazoe (HK) method[71] (isotherms recorded at 195 K, slit pore model, Figure 6.15 left) or by nonlocal density functional theory (NLDFT)[74] models (isotherms recorded at 273 K, slit pore model, Figure 6.15 right).* Importantly, the PSDs of the crystalline ZIF-4 and ZIF-zni derived via both methods are in strong disagreement to the theoretical PSDs calculated from the corresponding crystal structures. These calculations were performed with the implemented routine for pore size distributions in the Zeo++ software package.†. The HK and NLDFT models both produce a much broader pore size distribution and significantly overestimate or underestimate the maximum pore diameter in comparison to the results expected from the simulations. Since neither the HK nor the NLDFT method are able to reproduce the theoretical PSDs of the crystalline ZIFs, it is concluded that these models are also inadequate to examine the pore size distributions of the non-crystalline materials under study here. Hopefully, future statistical models for CO_2 gas sorption will be able to safely reproduce the porous features of crystalline ZIFs, so that these models could also be applied to shed light on the pore size distribution of ZIF glasses.[183]

6.2.3 Density Determination

The CO_2 sorption data recorded at 195 K allow also to determine the real density of the glasses from the quantified specific pore volumes (V_{pore}). As stated above, the real density of porous ZIF glasses is unknown so far, since He pycnometry (the established method for density determination of small volume powder samples) only allows to determine the skeletal density, because He penetrates into the pores

* Details about the applied methods to determine the PSDs and a discussion about their feasibility and limitations can be found in Section 3.2.3.

† Theoretical pore size distributions were calculated with Zeo++[181] software package using the default CSD radii (-ha 'high accuracy' flag[182]) The probe size was set to 0.1 Å and 5000 Monte Carlo samples per unit cell were averaged.

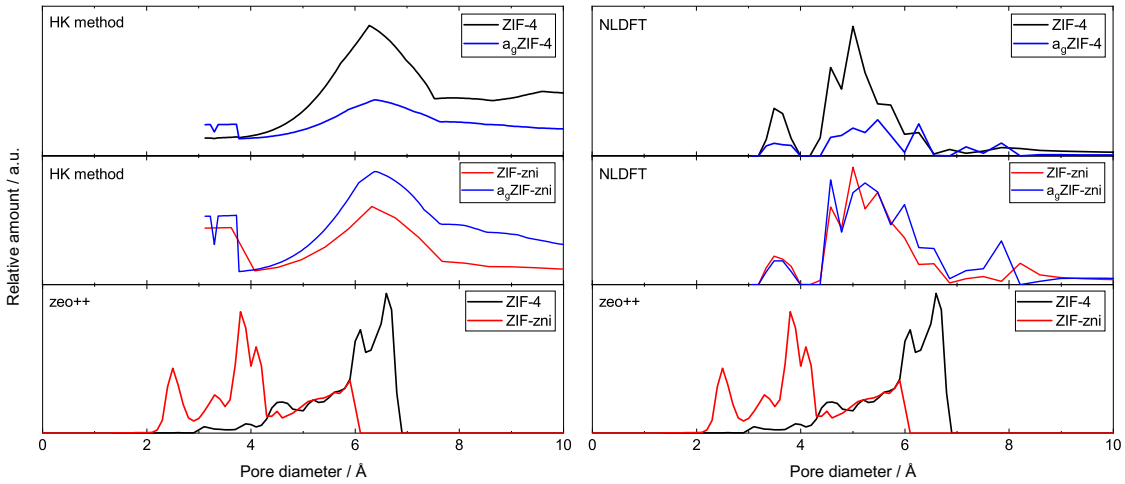

Figure 6.15: Theoretical pore size distribution calculated with Zeo++ for crystalline ZIF-4 and ZIF-zni in comparison to experimental pore size distributions for the crystalline and glassy phases of these materials. Left: Pore size distributions calculated from the CO_2 sorption isotherms recorded at 195 K using the HK method. Right: Pore size distributions calculated from the CO_2 isotherms recorded at 273 K using the NLDFT method.

of the materials (including the micropores).[184] Nevertheless, the real density by also considering the intrinsic micropores of the material is one of the key materials properties not only for technological applications, but also as a boundary condition for computational model development of such amorphous materials.

Here, the real densities of the ZIF glasses are determined according to the following steps. At first, the theoretical void fraction (tVF) is calculated for crystalline ZIF-4 and ZIF-zni based on their crystal structures (tVF(ZIF-4) = 37.2%, tVF(ZIF-zni) = 8.1%;* see Figure 6.1) and compared these values to the experimental void fraction (eVF = $V_{\mathrm{pore}} \cdot \rho_{\mathrm{cryst}}$) calculated from V_{pore} and the crystallographic densities (ρ_{cryst}†)‡. For both crystalline ZIFs a very good agreement was found between theory and experiment (eVF(ZIF-4) = 37.5%, eVF(ZIF-zni) = 7.7%). It has to be noted that a similar comparison of the tVFs to the eVFs for crystalline ZIF-62 and TIF-4 is

* The theoretical void fractions (tVFs) – based on the crystal structures for both materials – were calculated with the implemented routine in Olex2[48] applying a probe radius of 1.3 Å and grid spacing of 0.2 Å. The structures were taken from the CSD database(ZIF-4 (CSD code IMIDZB11); ZIF-zni (CSD code IMIDZB)). In both structures, missing hydrogen atoms have been added geometrically utilizing the Olex2 software package.

† The crystallographic densities ρ_{cryst} have been calculated from the mass of atoms in one unit cell and the unit cell volume determined via profile fits of room temperature PXRD data. The calculated densities are 1.22 g cm^{-3} (ZIF-4) and 1.56 g cm^{-3} (ZIF-zni)

‡ Further information about deriving the total pore volume and void fraction can be found in Section 3.2.2

challenging due to disorder of the secondary bulky linkers in their crystal structures.*

Subsequently, the specific pore volumes (V_{pore}) of the crystalline ZIF-4, ZIF-zni, ZIF-62 and TIF-4 were plotted against the densities (ρ_{cryst}) of these materials (Figure 6.16). The data could be very well fitted with an exponential function ($R^2 = 0.998$, see Figure 6.16 and Equation 6.1), which then allows to calculate the real densities of the glasses from their experimental pore volumes (see Table 6.3). In correspondence to their similar pore volumes, similar real densities are found for all glasses which are in the range from 1.34 − 1.39 cm^3 g^{-1}. Importantly, these real densities are up to 20% lower than the skeletal densities (those not including the intrinsic microporosity) for ZIF glasses previously determined by He pycnometry.[115] Based on the pore volumes and derived real densities, an eVF between 17% and 20% is estimated for the ZIF glasses.

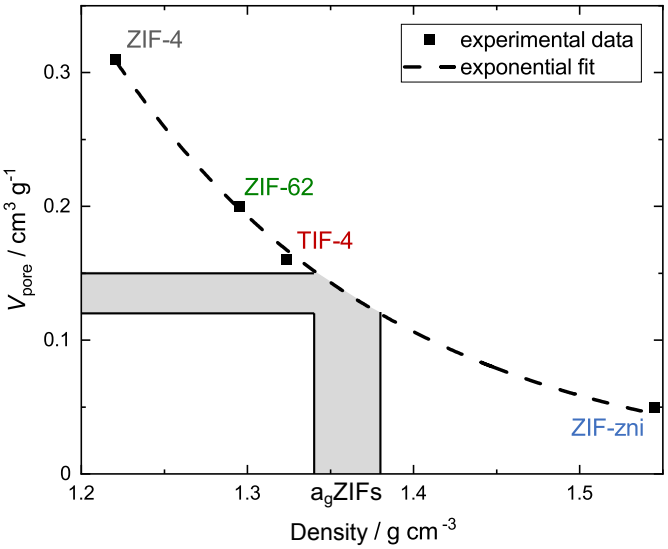

Fig. 6.16: Plot of density against V_{pore} of all crystalline ZIFs with exponential fit. The ZIF glass bulk densities can be estimated based on their experimental obtained V_{pore} (see light grey area).

$$V_{\text{pore}}(\rho) = a \cdot e^{-\frac{\rho}{b}} \tag{6.1}$$

with $a = 440.7 \pm 138.5$ cm^3 g^{-1} and $b = 0.168 \pm 0.007$ g cm^{-3}.

6.2.4 Hydrocarbons Physisorption Studies

Since the PSDs derived from the CO_2 sorption isotherms recorded at 195 K (HK method) as well as 273 K (NLDFT method) for all crystalline and amorphous materials are not representative for the real pore structure of the materials, it was intended to get deeper insights into the pore sizes of the ZIF glasses via hydrocarbon sorption. Isotherms were collected using *n*-butane as the probe molecule at 273 K as

* Nonetheless, the same calculation has also been performed for ZIF-62 (CSD code SIWJAM) and TIF-4 (CSD code QOSYAZ). Before the calculation, some disordered groups were resolved and solvent molecules were removed where present. tVF values are given in Figure 6.1. However, a comparison of these values to the corresponding eVFs is not applicable, because of some unresolvable remaining disorder leading to partially occupied secondary linkers (bim$^-$ or mbim$^-$).

well as propane and propylene sorption at 293 K (see Figure 6.18). A comparable adsorption of *n*-butane is found for a_gZIF-62 and a_gTIF-4. The isotherms are of Type I shape (Langmuir), typical for adsorption in microporous solids, and feature a strong hysteresis, signifying diffusion limitations of *n*-butane in the narrow pores of the ZIF glasses.

Calculation of the void volume occupied by *n*-butane close to saturation ($p \approx 95$ kPa) and comparison with the void volume determined via CO_2 sorption signifies that *n*-butane is only able to penetrate into about one third of the void space available in a_gZIF-62 and a_gTIF-4 (see Table 6.4). Surprisingly, a_gZIF-4 and a_gZIF-zni do not adsorb any *n*-butane in their pores but only on the external surface, resulting in linearly shaped isotherms. The contrasting gas sorption properties of a_gZIF-4 and a_gZIF-zni compared to a_gZIF-62 and a_gTIF-4 indicate important differences in the porosity features and hence the open network structure of these glasses. The larger kinetic diameter of *n*-butane (4.3 Å[177]) compared to CO_2 (3.3 Å[177]) signifies that the pore openings of a_gZIF-4 and a_gZIF-zni are smaller than the ones of the glasses featuring a secondary bulky imidazolate linker (a_gZIF-62 and a_gTIF-4). It appears that this difference is not originating from the higher processing temperatures and the slight decomposition of a_gZIF-4 and a_gZIF-zni, since a_TZIF-4 (thermally amorphized at 379 °C, no decomposition) does also only adsorb *n*-butane on its external surface (see Section A.1.6). Thus, the presence of a secondary bulky

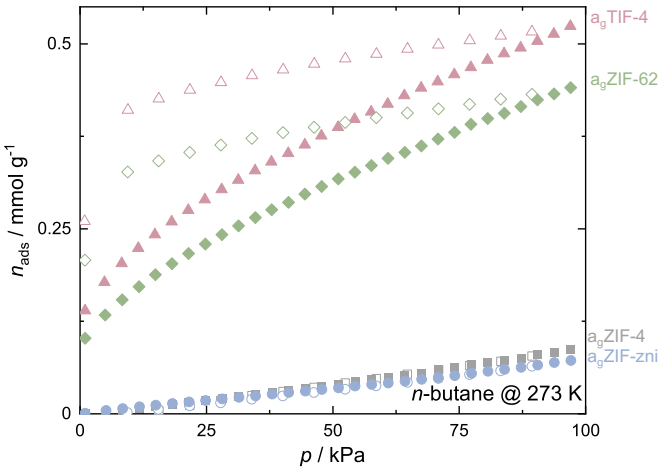

Fig. 6.17: *n*-butane sorption isotherms collected at 273 K of all ZIF glasses investigated in this study.

Table 6.4: Comparison of the specific pore volumes (V_{pore}) of a_gZIF-62 and a_gTIF-4 obtained from gas isotherms of *n*-butane (@ 273 K) and CO_2 (@ 195 K).

	V_{pore} (*n*-butane)[a]	V_{pore} (CO_2)[b]	ratio
a_gZIF-62	0.04 cm^3 g^{-1}	0.14 cm^3 g^{-1}	29%
a_gTIF-4	0.05 cm^3 g^{-1}	0.15 cm^3 g^{-1}	33%

a $p/p_0 \approx 0.95$, applied value for the density of pure liquid adsorbate ρ_{liq}(*n*-butane @273K) = 0.601 g cm^{-3}.[185]

b $p/p_0 \approx 0.95$, applied value for the density of pure liquid adsorbate ρ_{liq}(CO_2 @253K) = 1.032 g cm^{-3}.[87]

imidazolate linker appears to be a key parameter for the pore size and pore opening diameter of the ZIF glasses.

On the contrary, propane and propylene isotherms at 293 K feature a Langmuir-shape (typical for adsorption in micropores) and show comparable uptakes for the investigated ZIF glasses (Figure 6.18). The fact that a_gZIF-4 adsorbs propane and propylene, but not *n*-butane is surprising at first sight, since all three gases have almost identical kinetic diameters (*d*)[177] (*d*(propane) = 4.3 Å, *d*(propylene) = 4.5 Å, *d*(*n*-butane) = 4.3 Å). Thus, it is suspected that the exclusion of *n*-butane from the pores of a_TZIF-4, a_gZIF-4 and a_gZIF-zni is not a consequence of gas sorption kinetics, but of the significantly larger molecular size of the *n*-butane molecule ($V_{mol} \approx 161$ Å^3) compared to propane ($V_{mol} \approx 126$ Å^3) and propylene ($V_{mol} \approx 115$ Å^3).* Hence, these data suggest that the amorphous networks of the composition $Zn(im)_2$ (i.e. a_TZIF-4, a_gZIF-4 and a_gZIF-zni) exhibit narrower pore openings than the network glasses containing a secondary bulky imidazolate linker (i.e. a_gZIF-62 and a_gTIF-4).

Additionally, much higher gas adsorption affinity is found for propylene over propane (see Figure 6.18). This trend is already present in the crystalline parent materials ZIF-62 and TIF-4 (see Section A.1.6). A more detailed discussion on this phenomenon is given in Section 9.1.

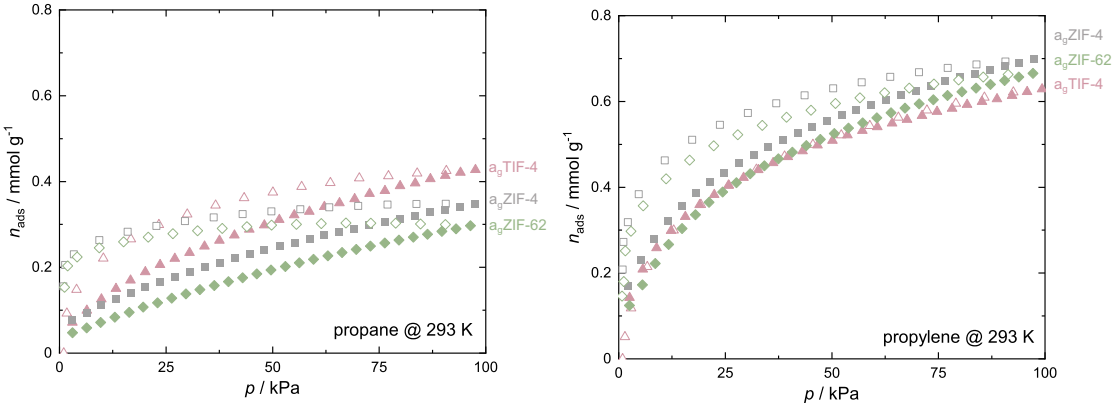

Figure 6.18: Left: Propane sorption isotherms of ZIF glasses collected at 293 K. Right: Propylene sorption isotherms of ZIF glasses collected at 293 K. In both panels, adsorption and desorption branches are shown as closed and open symbols, respectively.

6.3 Conclusion

The porosity of a series of ZIF glasses, their pore volumes were determined and compared to their crystalline framework precursors. This series includes crystalline ZIF glass formers and their corresponding glasses, some containing only the small

* V_{mol} is defined as the molecular volume of the hydrocarbons considering their densities at the boiling point[185–187].

im^- linker (ZIF-4 and ZIF-zni) and others featuring a secondary bulky imidazolate linker (bim^- or $mbim^-$) next to im^- (ZIF-62 and TIF-4). Most importantly, all glasses are found to own gas accessible microporosity by CO_2 sorption and specific pore volumes in the range from 0.12 to 0.16 $cm^3\ g^{-1}$. This also includes a_gZIF-4 and a_gZIF-zni whose open pore space was so far understood as being inaccessible for gases.[114,153] Thus, it is concluded that microporosity is an intrinsic feature of the class of ZIF glasses, which is a huge benefit compared to conventional inorganic glasses, whose microporosity needs to be generated via elaborate post treatment methods (e.g. leaching procedures).[188]

The specific pore volumes, derived from the CO_2 sorption isotherms recorded at 195 K, allow to uncover the real densities of these ZIF glasses. The densities are much lower than the previously reported skeletal densities of ZIF glasses and lie in between the density of the most porous glass former ZIF-4 and its most dense (but still microporous) crystalline polymorph ZIF-zni. This result is in accordance with the negative Clapeyron slope* behavior reported for ZIF-62[161] and suggest a similar behavior for TIF-4 (i.e. melting point lowering with increasing pressure). In turn, the higher density of ZIF-zni compared to the corresponding glass suggest a positive slope of the melting curve and thus ‚conventional' melting behavior (i.e. an increasing melting point with increasing pressure). Moreover, ZIF-4 transforms completely to its denser polymorph with zni topology (zni_TZIF-4) before melting occurs and thus is also not expected to show a negative Clapeyron slope behavior.

Slightly lower specific pore volumes and slightly higher real densities are found for a_gZIF-4 and a_gZIF-zni compared to the ZIF glasses containing a secondary bulky imidazolate-type linker. This proves the importance of the bulky linker during ZIF glass formation for a less dense packing of the molecular building units in the glass state[127,149,189] and is also in line with systematic differences in the peak width of the FSDP of the total scattering functions of the glasses, suggesting lower medium range order in the glasses containing two different imidazolate-type linkers.

The important structural differences of the glasses with and without the secondary bulky linkers are further corroborated by hydrocarbon sorption experiments, showing that a_gZIF-62 and a_gTIF-4 are able to adsorb *n*-butane, while a_gZIF-4 and a_gZIF-zni do not. This is in stark contrast with the porosity features of the corresponding crystalline ZIF phases, where more bulky linkers result in a significant reduction of pore volume and increased steric hindrance for the diffusion of larger molecules.

These findings suggest that conventional porosity design principles established

* R. N. Widmer *et al.* reported a *p*-*T* phase diagramm for ZIF-62. The melting curve in the region from ambient pressure to 2 GPa shows a negativ slope which suggest the formation of a solid with lower density then the liquid phase.[161]

for crystalline MOFs (and crystalline framework materials in general)[23] cannot be applied for the glassy state. Rather new design concepts for tuning and adjusting porosity and gas sorption selectivity of MOF glasses need to be developed. It is further suggested that principles which have already been established for other amorphous porous materials should be adaptable for MOF glasses. An example are porous polymers, such as polymers with intrinsic microporosity (PIMs), where molecular building blocks which facilitate inefficient packing of the polymer chains result in enhanced porosity.[190–193] Following this route, it is proposed that the porosity of MOF glasses can be tuned far beyond the current state of the art, thus opening the door for the development of much more porous MOF glasses with tailored porosity.

7 A Cobalt-based ZIF Glass*

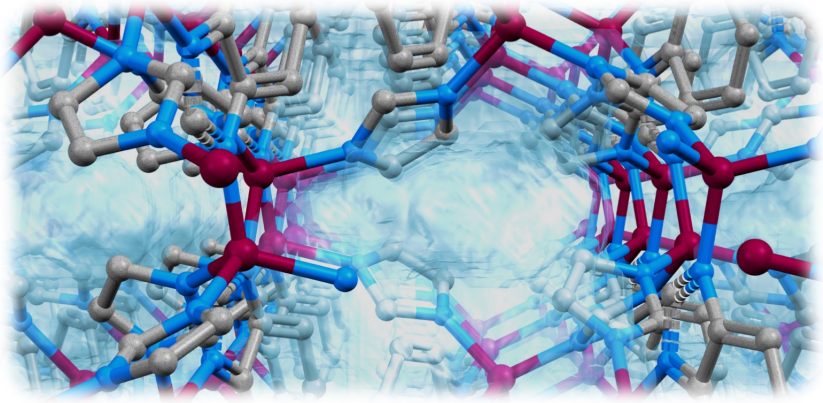

Abstract

Melting for ZIFs is so far only reported for materials based on Zn^{2+} ions as the inorganic building unit. For ZIF-4(Zn) it is found that replacing all Zn^{2+} ions with Co^{2+} ions a reduction of the decomposition temperature occurs which makes the ZIF glass unobtainable. The chapter uncovers that crystalline ZIF-62(Co) isomorphous to ZIF-62(Zn) but constructed from Co^{2+} cations, imidazolate and benzimidazolate (chemical composition $Co(im)_{1.70}(bim)_{0.30}$) also melts and converts into a glass upon cooling to room temperature. This material is the first example of a cobalt-based ZIF glass. X-ray total scattering and Raman spectroscopy reveal that the local structure of the glass and the crystalline parent material are very similar. Interestingly, magnetic measurements and X-ray diffraction uncover that ZIF-62(Co) partially decomposes upon melting and glass formation resulting in the reduction of about 3% of the Co^{2+} ions to metallic cobalt.

* The content of this chapter is already published in the following publication: L. Frentzel-Beyme, M. Kloß, R. Pallach, S. Salamon, H. Moldenhauer, J. Landers, H. Wende, J. Debus, S. Henke, *J. Mater. Chem. A* **2019**, *7*, 985-990. Reproduced or adapted by permission of The Royal Society of Chemistry.

7.1 Selection of the Cobalt Glass Precursor

As presented before, melting and glass formation is found ZIF-62(Zn) (chemical composition $Zn(im)_{1.65}(bim)_{0.35}$, isoreticular to the prototypical glass former ZIF-4(Zn) (chemical composition $Zn(im)_2$).[115] The cobalt derivative of ZIF-4(Co) melts but simultaneously decomposes and the melt quenched glass is not obtainable (see Section 4.3.2). Importantly, only zinc-based ZIFs have been reported to melt, so far. Since it is known that the mixed-linker material ZIF-62(Zn) melts at lower temperature than ZIF-4(Zn), a cobalt glass was prepared from ZIF-62(Co) (isoreticular to ZIF-62(Zn)) to overcome the issue of decompositon of the melt. Cooling the liquid ZIF-62(Co) to room temperature forms a glass.

Subsequently, the ZIF-62(Co) glass (a_gZIF-62(Co)) will be further analyzed regarding its local structure by X-ray total scattering experiments as well as Raman scattering. The paramagnetic nature of the Co^{2+} ions incorporated in the material gave the motivation to look deeper into its magnetic properties. Lastly, the porosity is investigated by CO_2 gas sorption.

7.2 Synthesis and Characterization of ZIF-62(Co)

ZIF-62(Co) grows as large ($0.2 - 1.0$ mm) deep purple single crystals with a truncated octahedral morphology via solvothermal reaction of $Co(NO_3)_2 \cdot 6H_2O$, Him and Hbim in DMF at 130 °C (see Section 12.9.1 for further details). A molar im^- : bim^- ratio of 7 : 1 was applied in the synthesis mixture, targeting the idealized composition $Co(im)_{1.75}(bim)_{0.25}$, analogous to the literature known ZIF-62(Zn) derivative. However, a molar ratio of 5.7 : 1 was determined by solution ^{1}H NMR spectroscopy of a solid sample of ZIF-62(Co) dissolved in DCl/D_2O/DMSO-d_6 (see Section A.2.4), denoting a chemical composition of $Co(im)_{1.70}(bim)_{0.30}$.

Single crystal X-ray diffraction at 100 K reveals that ZIF-62(Co) is indeed isostructural with ZIF-62(Zn) and crystallizes in the orthorhombic space group *Pbca*. The Co^{2+} cations are tetrahedrally coordinated by N-donor atoms of four different im^- or bim^- linkers, forming a 3D microporous framework of **cag** topology (see Figure 7.1). Two Co^{2+} ions, four imidazolate linkers and about one DMF solvent molecule are present in the asymmetric units. The bim^- linker could be localized at only one out of the four possible linker positions, causing this position to be occupied 50% with bim^- and 50% with im^- (see Section 8.1.2 for a deeper discussion on this topic). The theoretical void fraction (tVF) was estimated for ZIF-62(Co)* which amounts

* Calculated with a probe radius of 1.3 Å equally to the calculation on the tVFs performed in Section 6.1.

to about 28.7% (see Figure 7.1c).

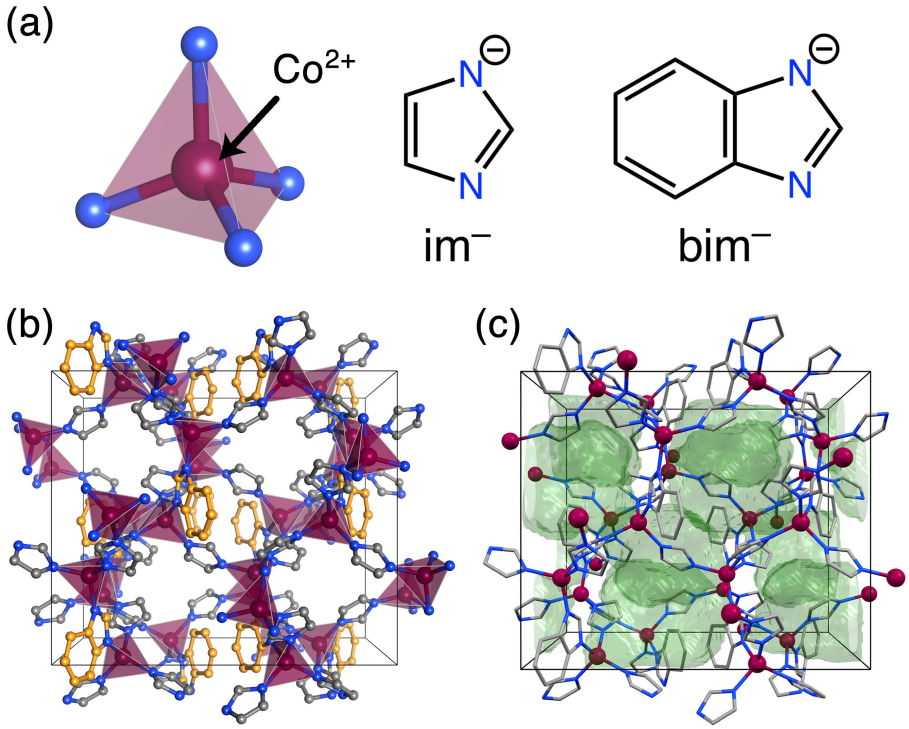

Figure 7.1: (a) Schematic illustration of the inorganic and organic building units of ZIF-62(Co). (b) Representation of the crystal structure of ZIF-62(Co) viewed parallel to the crystallographic *b* axis. The positions of the bim^- linkers are highlighted in orange. These positions are half-occupied by bim^- and half-occupied by im^-. (c) Illustration of the theoretical void fraction (tVF, green surface) of a unit cell of ZIF-62(Co). Unit cells are shown with black lines. Crystal structure data which were used to generate the images are availabe at the CSD (CSD code SIWJEQ).

The DMF-containing as-synthesized samples were filtered off, washed thoroughly with fresh DMF and then dried at approx. 200 °C under a dynamic vacuum ($\approx 10^{-4}$ kPa) for >16 h. As in the previous chapter, solid state FTIR and solution ^{1}H NMR spectroscopy (see Section A.2.3 and Section A.2.4) were performed to verify that the framework is DMF-free after this activation process. The phase purity of the as-synthesized and activated ZIF-62(Co) was further established by structureless profile fitting of PXRD data (see Figure 7.2).*

* Details about the phase identification method can be found in Section 3.1.5

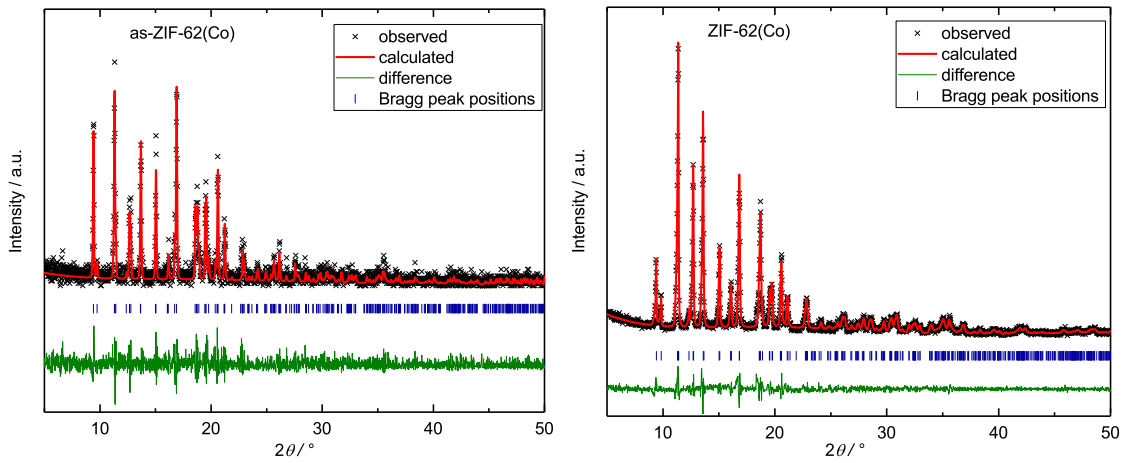

Figure 7.2: PXRD pattern with structureless profile fit (Pawley method) of as-ZIF-62(Co) (left) and ZIF-62(Co) (right).

Table 7.1: Unit cell parameters a, b, c and V (orthorhombic space group *Pbca*) determined by structureless profile refinements (Pawley method) of the PXRD data with corresponding R_{wp}, R_{exp} and χ values.

Compound	as-ZIF-62(Co)	ZIF-62(Co)
a / Å	15.477(4)	15.517(3)
b / Å	15.551(3)	15.640(2)
c / Å	18.152(5)	17.967(3)
V / Å^3	4369.0(19)	4360.4(13)
R_{wp}	42.96	11.2
R_{exp}	38.83	7.2
χ	1.11	1.56

7.3 Melting and Glass Formation of ZIF-62(Co)

During this section, the melting behavior of ZIF-62(Co) will be discussed comparative to the corresponding Zn derivative ZIF-62(Zn).* Thermal characterization of solvent-free ZIF-62(Zn) and ZIF-62(Co) was performed by TGA/DSC analysis under inert atmosphere (Ar). First, both materials were heated from room temperature up to 750 °C with a scan rate of 10 °C min^{-1}. In accordance with the literature, ZIF-62(Zn) shows an endothermal signal at 441 °C ascribed to melting of the material (see Figure 7.3 left). The compound decomposes from the liquid phase at ≈ 600 °C indicated by the beginning of the mass loss. ZIF-62(Co) also displays an endothermal signal in the same region (432 °C) which indicates melting of the material (see Figure 7.3 right). The liquid phase starts decomposing at ≈ 550 °C. This temperature is significant

* Details about the synthesis and structural characterization for ZIF-62(Zn) have already been discussed in Section 6.1.1.

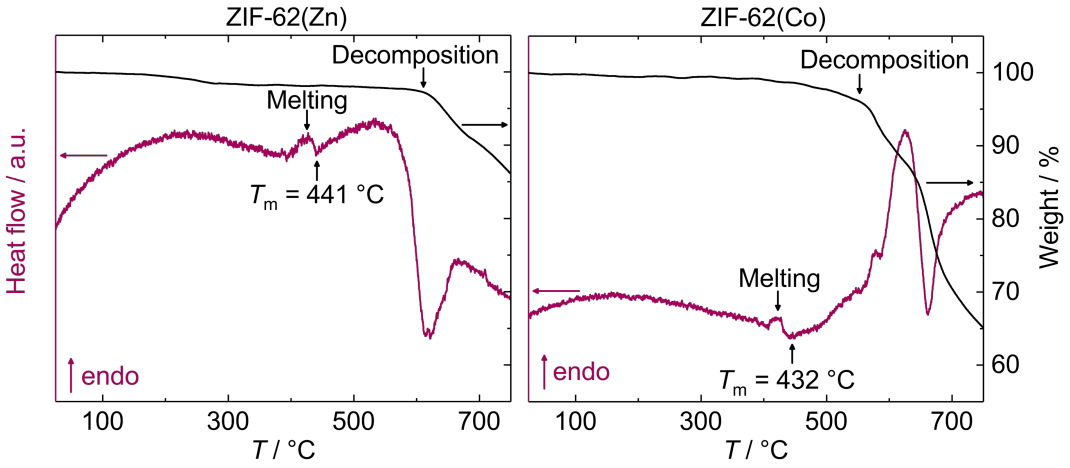

Figure 7.3: TGA/DSC data for ZIF-62(Zn) (left) and ZIF-62(Co) (right).

lower then for its Zn derivative (≈ 600 °C) and meets the observation found for ZIF-4(M) (see Section 4.3.1). Consequently, it can be concluded that the metal ion (Zn^{2+} *vs.* Co^{2+}) has an major influence on the decomposition temperature of the material whereas the T_m remains nearly unaffected.

Based on this results, a ZIF-62(Co) glass was prepared. Therefore, a powdered sample of ZIF-62(Co) was heated to 475 °C with a scan rate of 10 °C min^{-1} in a TGA/DSC experiment under inert atmosphere (Ar) and subsequently cooled down to ambient temperature with the same scan rate. At 475 °C the material is expected to be completely molten without starting to decompose. The obtained a_gZIF-62(Co) shows evidence of macroscopic flow resulting in fusion of the microcrystals into a compact monolithic glass lump, very similar to a_gZIF-62(Zn), which was derived from ZIF-62(Zn) via the same process (see Figure 7.4). The material was crushed and ground for further analysis. Here, the materials break into shards which additionally show signs of macroscopic flow, another proof for the material being a liquid before. Representative photographs of such shards can be found in Figure 7.5. Finely ground powders of a_gZIF-62(Zn) and a_gZIF-62(Co) were used for PXRD analysis. The resulting patterns display no Bragg peaks (as found for their crystalline precursors) and only diffuse scattering as expected for non-crystalline/amorphous material (see Figure 7.5).

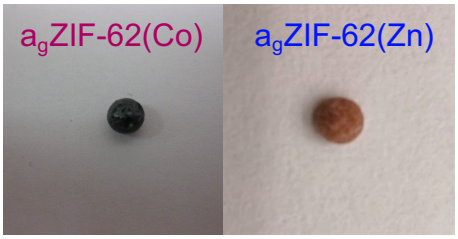

Fig. 7.4: Photographs of the vitreous products obtained after glass preparation. Fusion of the finely ground ZIF microparticles into a ZIF glass monolith as a consequence of melting is clearly evident.

The glass formation was further proven in cyclic TGA/DSC experiments. Therefore, a crystalline sample of ZIF-62(M) was heated to 475 °C and cooled down to 30 °C

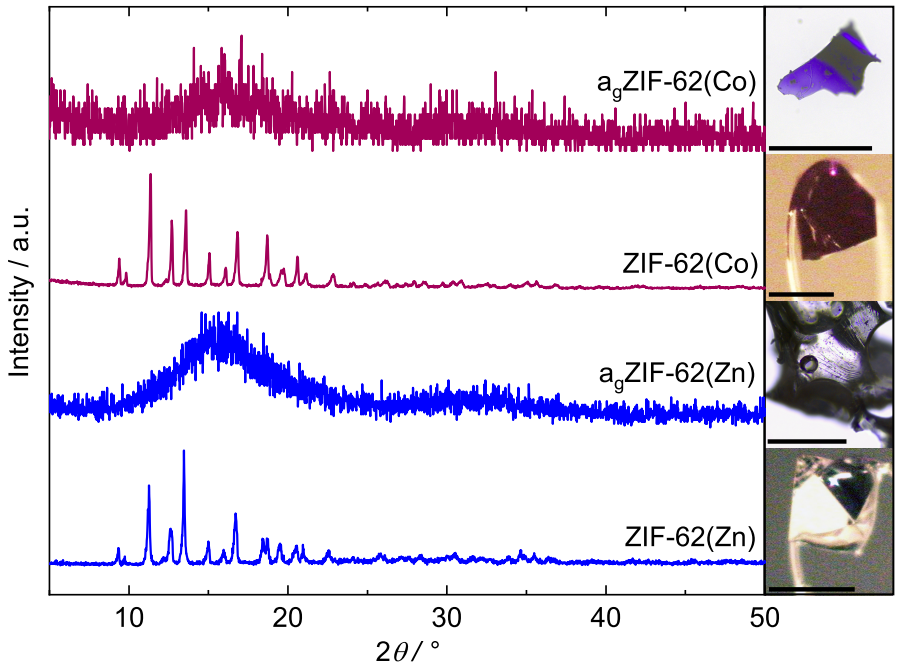

Figure 7.5: PXRD patterns of ZIF-62(M) and a$_g$ZIF-62(M) materials recorded at room temperature. Inlets of ZIF-62(M) single crystals and a$_g$ZIF-62(M) glass pieces are shown next to the diffraction patterns. The crystals are mounted on a nylon loop. The glass pieces were obtained by crushing a ≈ 5 mm large glass monolith. The size of the black bar in each panel is ≈ 300 µm.

which yields a$_g$ZIF-62(M). The DSC trace for the first upscan shows an endothermal signal ascribed to melting as expected. Subsequently, the temperature was increased a second time (second upscan) to 475 °C and again an endothermal signal was detected but now at lower temperature 320 °C for ZIF-62(Zn) and 290 °C for ZIF-62(Co). The signal is ascribed to the glass transition proving the glassy nature of a$_g$ZIF-62(M). Interestingly, the T_g is $\approx$ 30 °C lower for the Co derivative. The origin of this phenomenon is still not understood and requires further studies. As expected, a third upscan shows again only the glass transition for both materials at the same temperature.

Moreover, solid state FTIR spectroscopy and solution ^{1}H NMR spectroscopy of digested samples of a$_g$ZIF-62(M) prove the preservation of the organic linkers (see Section A.2.4 and Section A.2.3).

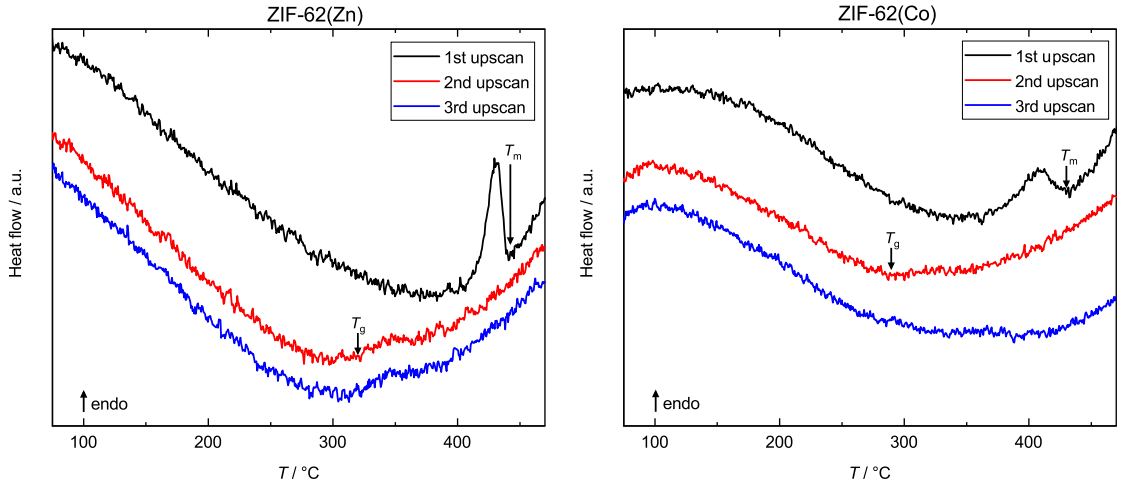

Figure 7.6: DSC traces of cyclic TGA/DSC experiments for ZIF-62(Zn) (left) and ZIF-62(Co) (right).

7.4 Structure and Properties the ZIF-62(Co) Glass

7.4.1 X-ray Total Scattering

Due to the X-ray amorphous nature of glasses, a_gZIF-62(Co) was studied with X-ray total scattering and the collected data were processed to yield the corresponding XPDF.* Data were collected for ZIF-62 and a_gZIF-62(Co) in order to get insights into their structural differences and similarities. Both data sets showing similar dominant peaks in the region up to about 6 Å. Assigning those peaks to interatomic distances within the ZIF-62(Co) material it becomes clear that correlations till about 6 Å representing all interatomic distances up to two neighboring Co^{2+} ions (see Figure 7.7 for peak assignment). This proves that the short range order is nearly identically for ZIF-62(Co) and a_gZIF-62(Co). Hence, the tetrahedral coordination of N atoms of imidazolate-type linkers around Co^{2+} of the crystalline state is preserved in a_gZIF-62(Co) (see Figure 7.7). At higher distances (6 − 40 Å) significant correlations are only found for ZIF-62(Co), proving its crystallinity and following the long range order in the material. The $D(r)$ for a_gZIF-62(Co) converges to zero for $r > 6$ Å verifying the absence of long range order and its glassy nature.

* In such data − visualized in the form $D(r)$[61] − every peak corresponds to an interatomic distance within the investigated material and thus provides information about its local structure. An introduction to X-ray total scattering and the derived XPDF function is given in Section 3.1.6.

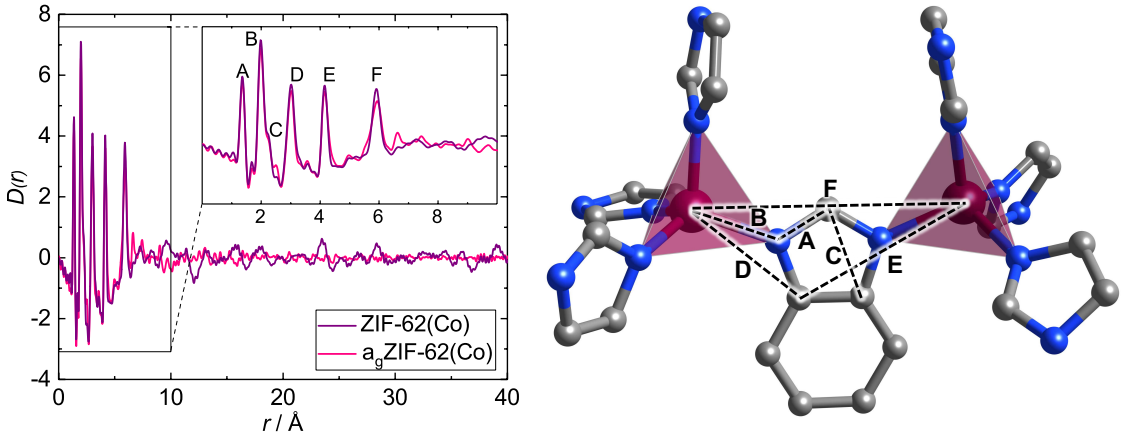

Figure 7.7: Left: XPDF data in the form $D(r)$ for ZIF-62(Co) and a_gZIF-62(Co). Inlet shows a zoom into the short range correlation region. Right: Representation of the coordination environment of two neighboring Co^{2+} ions. Short range correlations which are found in the corresponding XPDF are highlighted. Color Code: Co (purple), C (grey), N (blue). The tetrahedral coordination environment of Co^{2+} is represented by purple polyhedra. Hydrogen atoms are omitted for clarity.

7.4.2 Raman Spectroscopy

Further investigations of the local structure have been done via Raman scattering experiments. Data have been collected for ZIF-62(M) (M = Zn^{2+}; Co^{2+}) and their corresponding glasses a_gZIF-62(M) (M = Zn^{2+}; Co^{2+}). Similar spectra for the crystalline ZIF-62(M) and glassy a_gZIF-62(M) materials are obtained which proves again that the organic linkers stay intact during the melting process and the local coordination is preserved (see Figure 7.8). A closer look on the characteristic C−N stretching mode[122] located at $1150 - 1200\,\mathrm{cm^{-1}}$ for all materials uncovers that the band is found at slightly lower frequency for both cobalt containing materials. Consequently, the C−N bonds of the imidazolate-type linkers are a bit weaker in that case. This is presumably caused by a bit stronger Co−N bonds compared to the Zn−N bonds in the zinc containing materials. Different bond strengths are explainable by taking into account the higher electronegativity[194] (EN) of Co (EN = 1.88) compared to Zn (EN = 1.65) and the potential contribution of ligand-to-metal π-bonding for cobalt*.

Further hints for the stronger ligand-to-metal bonds for ZIF-62(Co) are found in the already discussed TGA/DSC data (see Figure 7.3). Therefore, the ΔH_m) was determined for ZIF-62(Zn) and ZIF-62(Co). ΔH_m is a bit higher for ZIF-62(Co) ($\Delta H_\mathrm{m} = 2.64\,\mathrm{kJ\ mol^{-1}}$) then for ZIF-62(Zn) ($\Delta H_\mathrm{m} = 2.46\,\mathrm{kJ\ mol^{-1}}$).

Lastly, inspection of the C−N stretching modes of both ZIF-62(M) materials

* Electron valence configuration $3d^7$ (Co^{2+}) *vs.* $3d^{10}$ (Zn^{2+}).

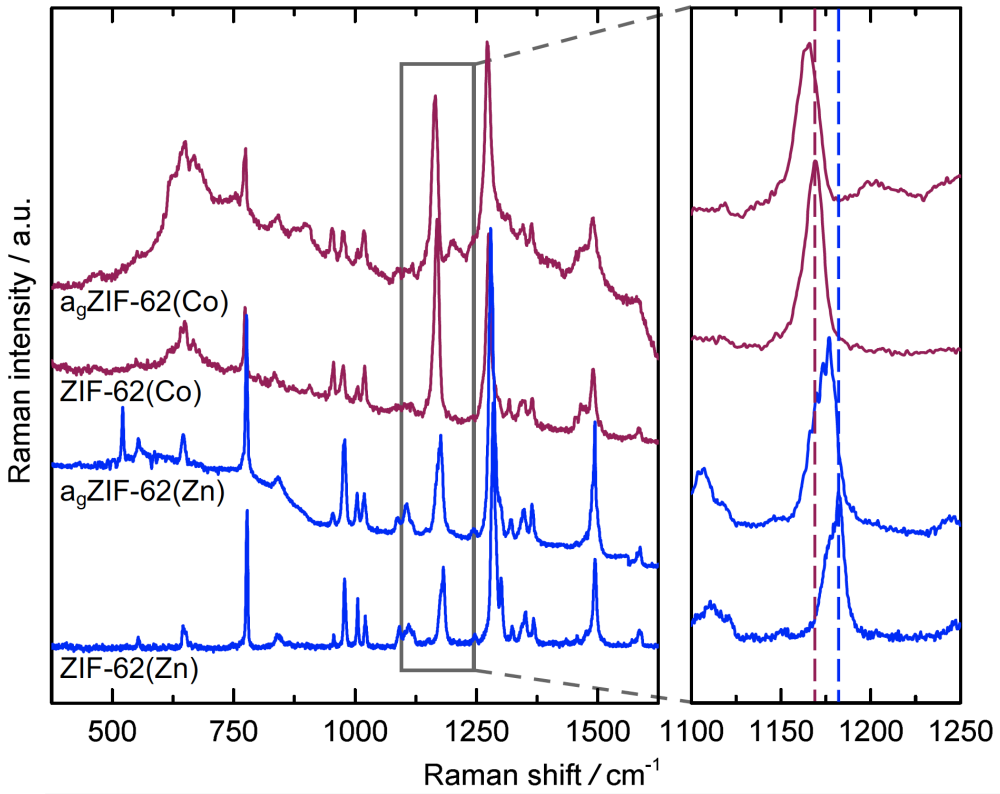

Figure 7.8: Raman spectra for ZIF-62(M) (M = Zn^{2+}; Co^{2+}) and their corresponding glasses a_gZIF-62(M) (M = Zn^{2+}; Co^{2+}) (left). Additionally, a zoom into the region from 1100 − 1250 cm^{-1} is displayed showing the C−N stretching band (right).

in comparison to their corresponding glasses unveils a shifting to slightly lower frequencies for a_gZIF-62(M). Consequently, the a_gZIF-62(M) materials generally possess slightly stronger metal−N bonds compared to their crystalline precursors. Here, the previously discussed absence of a long range ordered framework in the glass state leads presumably to less strained tetrahedral coordination environment for all metal ions and thus a stronger average metal−N bonding.

7.4.3 Magnetic Measurements

The paramagnetism of Co^{2+} ions − present in ZIF-62(Co) and the corresponding glass a_gZIF-62(Co) − motivates to investigate the magnetic properties of the materials. Temperature dependent magnetic measurements (field-cooled (FC) and zero-field-cooled (ZFC))* were performed for both materials between 5 K and 300 K (see Figure 7.9). In accordance with investigations on other Co^{2+}-based ZIFs,[195,196]

* In the field-cooled (FC) measurement, the magnetization is measured while decreasing the temperature with an applied magnetic field of 10 mT. In the zero-field-cooled (ZFC) measurement, the material is cooled to low temperature (here 5 K) in absence of a magnetic field and the magnetization is measured under application of an magnetic field of 10 mT while increasing the temperature.

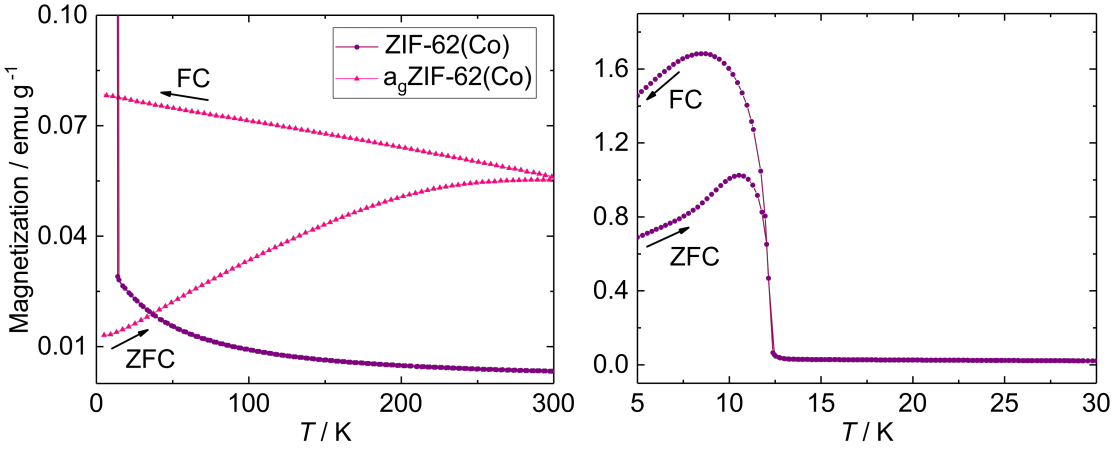

Figure 7.9: Curves to the temperature dependent magnetization measurements for ZIF-62(Co) (purple cycles) and a_gZIF-62(Co) (pink triangles). Data were collected between 5 K and 300 K with a heating/cooling rate of 2 K min^{-1} (left) or 0.25 K min^{-1} (right). Field-cooled (FC) and Zero-field-cooled (ZFC) curves are displayed. The lines are just a guide to the eye.

ZIF-62(Co) shows a paramagnetic behavior between 300 K and temperatures higher than 12 K. By heating across 12 K, a magnetic phase transition, presumably from the antiferromagnetic to the paramagnetic state, is observable by a fast decrease of magnetization for the crystalline sample, showing a splitting between the FC and ZFC magnetization curve. These results match well with those of other crystalline Co-based ZIFs.[195,196]

In contrast, a_gZIF-62(Co) does not show any magnetic phase transition as well as no typically paramagnetic $1/T$ behavior (see Figure 7.9). However, a splitting for the FC and ZFC curves are found over the whole investigated temperature window indicating a small residual magnetization. A closer inspection of the prior discussed XPDF in the form $D(r)$ revealed weak but sharp correlations in the range $r > 6$ Å (see Figure 7.7). The corresponding PXRD pattern* shows broad diffuse scattering originating from the ZIF glass but also weak but sharp Bragg peaks. A visual comparison to simulated patterns of metallic cobalt uncovers the presence of metallic cobalt (ccp (cubic closes packing) phase) in a_gZIF-62(Co) (see Figure 7.10).

The amount of metallic cobalt was determined by additional field dependent magnetization measurements (see Figure 7.11). ZIF-62 shows a purely paramagnetic behavior. The glass sample shows a small spontaneous magnetization, determined from the linear extrapolation of the high field region (1 − 9 T) to about 1.32 emu g^{-1}. Assigning the magnetic phase to metallic cobalt with a saturation magnetization of 161 emu g^{-1} at room temperature,[197] the amount of metallic cobalt in the a_gZIF-

* The PXRD pattern corresponds in this case to the uncorrected total scattering data which were collected to determine the XPDF.

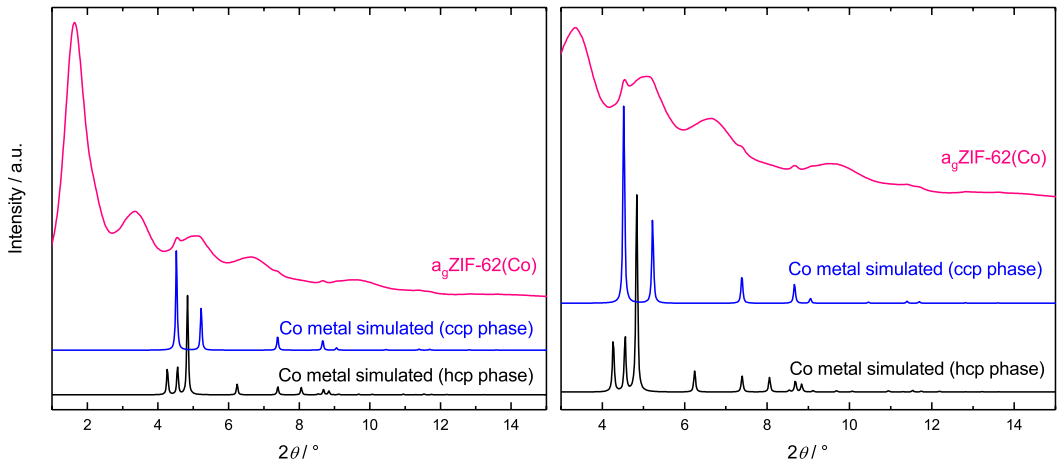

Figure 7.10: X-ray total scattering data for a_gZIF-62(Co) (pink) in comparison to simulated XRPD patterns of metallic cobalt (ccp phase, blue; hcp (hexagonal closest packing) phase, black). Left: survey pattern. Right: Zoom into the region of the pattern (left) where Bragg peaks are found. The small sharp peaks can be clearly identified as metallic cobalt (ccp phase) by visual comparison.

62(Co) sample corresponds to 0.82 wt%. This means that about 2.8% of all Co^{2+} ions in the parent crystalline structure are reduced to metallic cobalt during the melting process. Indeed, the solution ^{1}H NMR spectroscopy of digested a_gZIF-62(Co) materials showed a lower amount of im^- as found for crystalline ZIF-62(Co) (chemical composition: $Co(im)_{1.70}(bim)_{0.30}$ *vs.* $Co(im)_{1.69}(bim)_{0.31}$, see Section A.2.4). It is assumed, that a few im^- linkers decompose during the melting process and the decomposition products initiate the reduction of some Co^{2+} ions to metallic cobalt.

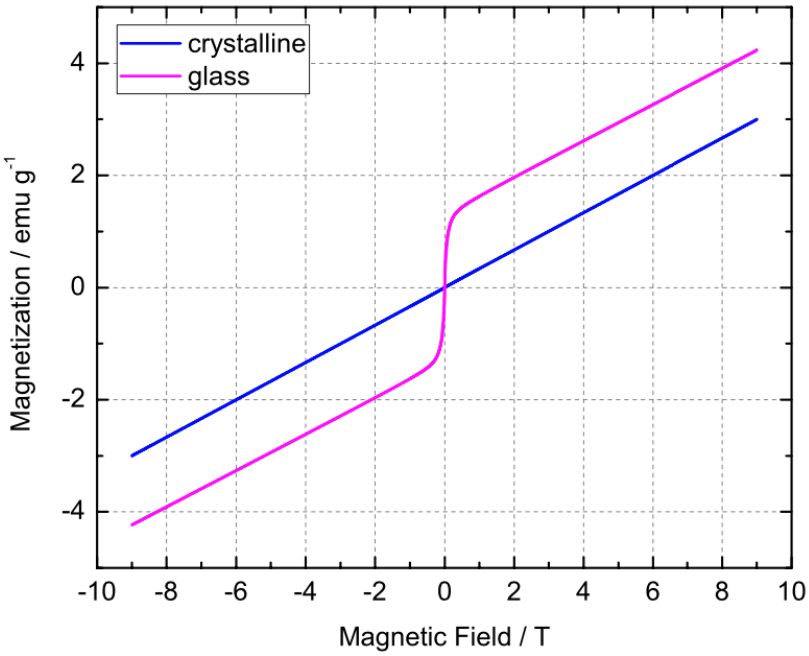

Figure 7.11: Magnetic field dependent measurements on both crystalline and glass samples of ZIF-62(Co), recorded at 300 K between +/−9 T.

7.4.4 CO_2 Physisorption Studies

Moving on from this, crystalline ZIF-62(Co) and the corresponding glass a_gZIF-62(Co) were investigated by CO_2 gas sorption at 273 K (see Figure 7.12). As stated

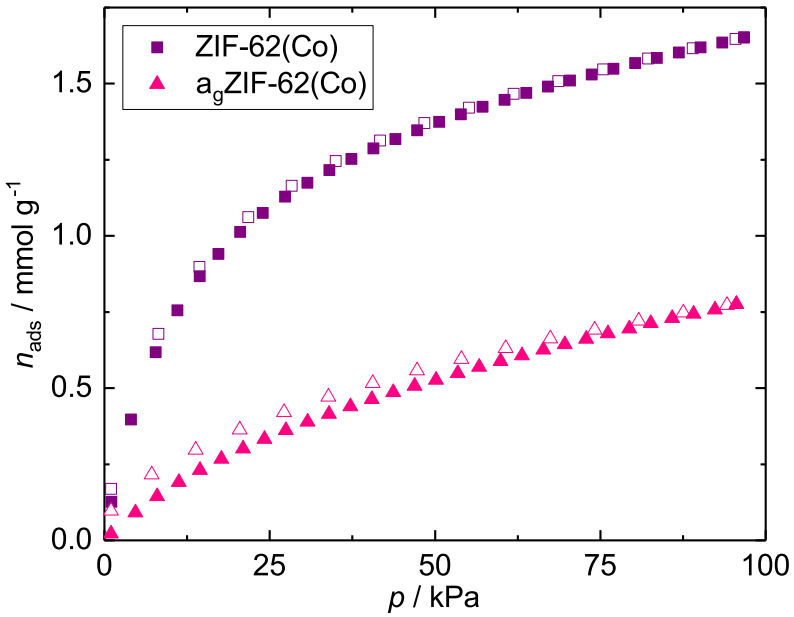

Figure 7.12: CO_2 gas sorption isotherms of ZIF-62(Co) and a_gZIF-62(Co) recorded at 273 K. Adsorption and desorption are shown as closed and open symbols, respectively.

in Section 6, such data are insufficient to detect the whole pore volume of ZIF glasses. Nevertheless, it is possible to investigate if the ZIF glass is microporous. ZIF-62(Co) features a type I isotherm characteristic for microporous MOFs and adsorbs about 1.65 mmol g^{-1} CO_2 at approx. 95 kPa. In accordance with the previous results presented in Section 6, the conversion of ZIF-62(Co) into a_gZIF-62(Co) via framework melting does not lead to a total collapse of the porous framework into a dense network. a_gZIF-62(Co) is still porous and the Langmuir-type shape of the isotherm of a_gZIF-62(Co) clearly suggests that the porosity of the glass originates from small micropores. These micropores must be intrinsic to the glass and cannot be formed by incomplete fusion of ZIF-62(Co) microcrystals. Remarkably, the desorption branch of the CO_2 sorption isotherm of a_gZIF-62(Co) only shows a small hysteresis, which indicates that mass transport experiences only minor diffusion limitations in the microporous glass, suggesting the presence of a well-connected, continuous network of micropores.

7.5 Conclusion

It is demonstrated that exchanging the Zn^{2+} ions by Co^{2+} ions in the meltable ZIF-62(Zn) yields a ZIF-62(Co) materials which is meltable as well. Cooling down the melted material (T_m = 432 °C) to room temperature yields a ZIF glass (a_gZIF-62(Co)). ZIF-62(Co) is the first reported meltable and glass forming cobalt-based

MOF. A paramagnetic MOF glass is obtained which local structure is found to be very similar to the parent crystalline ZIF-62(Co). This proof of concept demonstrates that MOF glasses with additional metal-centered functionality (e.g. magnetism, catalytic activity, optical properties, etc.) are accessible by suitable design of the corresponding crystalline ZIF containing the desired metal ion.

Magnetic measurements reveal the presence of a small amount of a ferromagnetic phase in the glass. In combination with X-ray total scattering experiments, this impurity could be identified as metallic cobalt which is formed during the melting process due to reductive processes caused by a partial decomposition of the organic linkers in ZIF-62(Co). Cobalt particles embedded into the ZIF glass matrix open the possibility for applications of this glass in e.g. cobalt catalyzed reactions. Lastly, in accordance with the isoreticular ZIF-62(Zn) glass, a_gZIF-62(Co) also remains microporous as demonstrated by CO_2 adsorption experiments.

8 Melting Point Engineering by Mixed-Linker ZIFs*

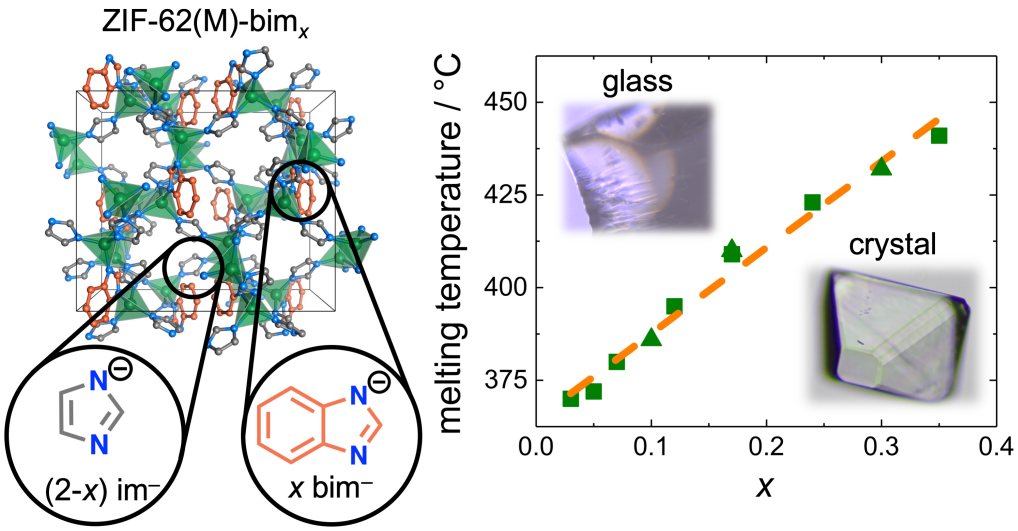

Abstract

Just a few ZIFs have been reported to melt and only very little is known about the structural and compositional requirements needed for ZIF melting and glass formation. This chapter shows how the melting point of a series of ZIF-62(M)-bim$_x$ materials (composition M(im)$_{2-x}$(bim)$_x$; with M^{2+} = Co^{2+}, Zn^{2+}) can be controlled systematically by adjusting the molar ratio of the two imidazolate-type linkers im$^-$ and bim$^-$. The obtained insights into the ZIFs thermal behavior allow to postulate compositional requirements for ZIF melting and glass formation, which may guide the search for other meltable ZIFs.

* The content of this chapter is reprinted or adapted from the following publication: L. Frentzel-Beyme, M. Kloß, P. Kolodzeiski, R. Pallach, S. Henke, *J. Am. Chem. Soc.* **2019**, *141*, 12362-12371. Reproduced or adapted with permission. Copyright 2019 American Chemical Society.

8.1 A Series of Isomorphous ZIF-62 Materials

The conventional ZIF-62(Zn) material was first reported in 2006 with the idealized chemical composition $Zn(im)_{1.75}(bim)_{0.25}$.[29] The material is isoreticular to ZIF-4 (**cag** topology) but about one-eighth of the im^- linkers is substituted by the bulkier bim^- linker (see Figure 8.1). ZIF-62(Zn) was reported to feature a drastically lower T_m than ZIF-4 and thus features a much larger thermal stability window of the liquid phase ($T_m \approx 435\,°C$; $T_{dec} \approx 600\,°C$).[115] Interestingly, A. Qiao *et al.* reported that ZIF-62(Zn) derivatives with larger concentrations of bim^- can be prepared.[122] When increasing the molar amount of bim^- per formula unit (x; formula unit $Zn(im)_{2-x}(bim)_x$) from $x = 0.25$ to 0.36 the melting point of the material increases slightly from 435 °C ($x = 0.25$) to 448 °C ($x = 0.36$).[122]

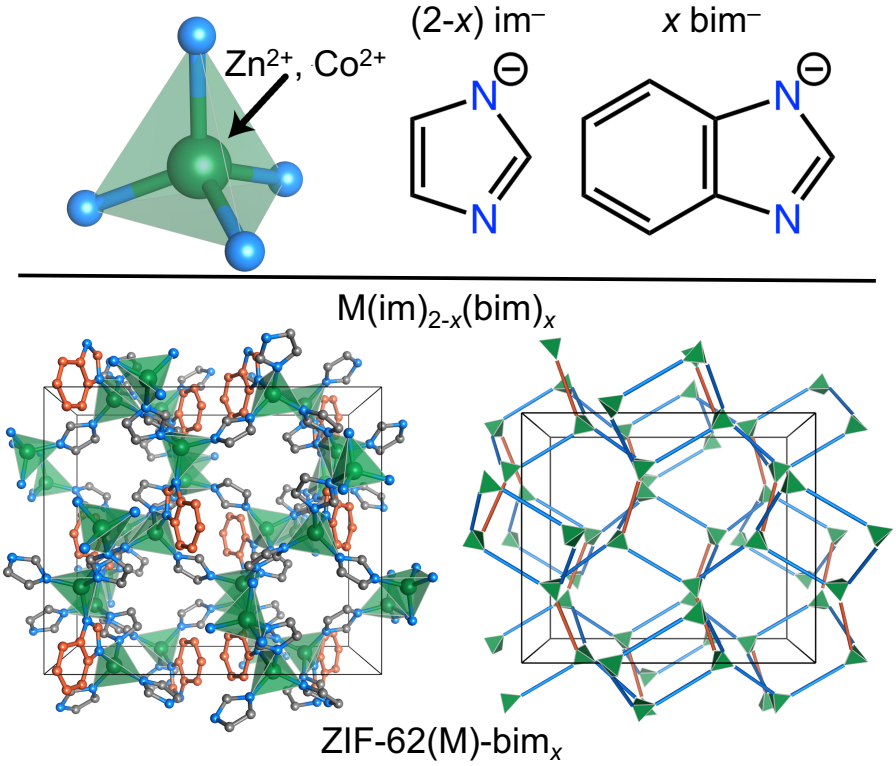

Figure 8.1: Top: Representation of the single building units of the synthesized ZIF-62(M)-bim_x materials. Bottom: Representative crystal structural of ZIF-62(M)-bim_x materials (left) and the underlying **cag** topology (right). The positions of the bim^- linkers are highlighted in dark orange and are half occupied by bim^- for $x = 0.25$. Color code: C (grey or dark orange); N (light blue); Zn^{2+} or Co^{2+} (green). Hydrogen atoms are omitted for clarity. Crystal structure data which were used to generate the images are availabe at the CSD (CSD code SIWJEQ).

Motivated from this findings, a series of ZIF-62 materials was synthesized with varying im^- : bim^- ratios as well as Zn^{2+} or Co^{2+} ions. Thus, materials having the general chemical composition of $M(im)_{2-x}(bim)_x$ ($M = Zn^{2+}$ or Co^{2+}) are obtained which are denoted as ZIF-62(M)-bim_x. Subsequently, this ZIF-62 series is

thoroughly analyzed with (variable-temperature) SCXRD, (variable-temperature) PXRD, X-ray total scattering (pair distribution function analysis), solid state FTIR and solution ^{1}H NMR spectroscopy as well as TGA/DSC. By covering the entire range from regular ZIF-4 ($x = 0$) over the zone with low bim$^-$ concentration ($0.02 < x < 0.24$) to conventional ZIF-62 ($x \geq 0.25$), a subtle transition is unveiled from derivatives showing sequential amorphization/ recrystallization ($x < 0.05$) to derivatives exhibiting coherent low temperature melting ($x \geq 0.05$). Via adjusting x, the melting point of ZIF-62 can be lowered to only about 370 °C.

On the basis of this variety of experimental data two main criteria are extracted for ZIF melting and glass formation which may paves the way for the discovery of many new melting ZIFs in the future.

8.1.1 Synthesis of ZIF-62(M)-bim$_x$ Materials

ZIF-62(M)-bim$_x$ (M = Zn^{2+} or Co^{2+}; $x = 0.02 - 0.35$)* were prepared after modified solvothermal synthesis routes adopted from procedures reported in the literature.[29,143,144,198,199] In short, $M(NO_3)_2 \cdot 6H_2O$ (M = Zn^{2+} or Co^{2+}) and varying molar ratios of imidazole (Him) and benzimidazole (Hbim) were dissolved in DMF (total molar amount 13.2 mmol, see Table 8.1 for applied molar ratios and Section 12.9.1 for exact molar amounts). From this solution, colorless (Zn-materials) or deep purple (Co-materials) large single crystals (morphology: truncated octahedron, size: 0.2 − 1.0 mm) grow at 100 °C (Zn-materials) or 130 °C (Co-materials) in a closed vessel (see Section 12.9.1 for further details). The as-ZIF-62(M)-bim$_x$ materials have been further filtered off the reaction solution and treated at 200 °C in dynamic vacuum ($p \approx 10^{-4}$ kPa) yielding the activated ZIF-62(M)-bim$_x$ materials.

The precise im$^-$: bim$^-$ concentrations of the ZIF-62(M)-bim$_x$ materials were determined as previously by solution ^{1}H NMR spectroscopy of digested crystals in DCl/D_2O/DMSO-d_6 (see Section A.3.6 for whole spectra). Figure 8.2 relates applied and found im$^-$: bim$^-$ concentrations.† Here, it becomes clear that bim$^-$ is preferentially incorporated into the materials. This observation can be attributed to the higher acidic strength of Hbim (pK_a = 12.78) compared to Him (pK_a = 14.52).[200] In order to verify if the amount of bim$^-$ varies between different crystals from the same reaction batch, solution ^{1}H NMR spectroscopy spectra were also recorded on several individual crystals of one batch. No variation of the im$^-$: bim$^-$ ratio was observed. Thus, it is concluded that bim$^-$ is homogeneously distributed

* It has to be noted that ZIF-62(Zn)-bim$_{0.35}$ and ZIF-62(Co)-bim$_{0.30}$ are equal to the prior discussed ZIF-62(Zn) and ZIF-62(Co), respectively. In this chapter, the corresponding data are partially reproduced to aid a comparative discussion.

† The corresponding values to generate this plot are given in Table 8.1

Table 8.1: Comparison of the molar im^- : bim^- ratios and the corresponding x values applied in the synthesis mixture and x values found by solution ^{1}H NMR spectroscopy from digested materials (see Section A.3.6.

Material	im^- : bim^- (applied)	$x_{applied}$ [a]	im^- : bim^- (found)	x_{found} [a]
ZIF-62(Zn)-$bim_{0.02}$	210:1	0.009	99:1	0.02
ZIF-62(Zn)-$bim_{0.03}$	168:1	0.012	66:1	0.03
ZIF-62(Zn)-$bim_{0.05}$	126:1	0.016	39:1	0.05
ZIF-62(Zn)-$bim_{0.07}$	84:1	0.024	28:1	0.07
ZIF-62(Zn)-$bim_{0.12}$	42:1	0.047	16:1	0.12
ZIF-62(Zn)-$bim_{0.17}$	28:1	0.069	11:1	0.17
ZIF-62(Zn)-$bim_{0.24}$	14:1	0.13	7.3:1	0.24
ZIF-62(Zn)-$bim_{0.35}$	7:1	0.25	4.7:1	0.35
ZIF-62(Co)-$bim_{0.10}$	42:1	0.047	19:1	0.10
ZIF-62(Co)-$bim_{0.17}$	28:1	0.0069	11:1	0.17
ZIF-62(Co)-$bim_{0.30}$	7:1	0.25	5.7:1	0.30

a $x = 2 \cdot c(bim^-)/(c(im^-) + c(bim^-))$; c = molar concentration.

throughout the samples.

For the later thermal analysis only activated materials were investigated. As previously described, the complete removal of DMF molecules from the materials was analyzed and confirmed by solution ^{1}H NMR spectroscopy (see Section A.3.6) and additionally with solid state FTIR spectroscopy (see Section A.3.5).

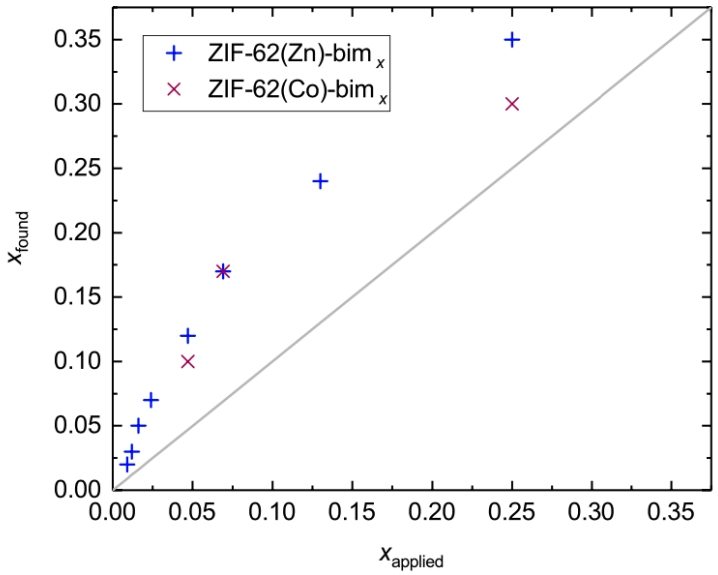

Figure 8.2: Plot of the values of $x_{applied}$ against x_{found} in the crystalline ZIF-62(M)-bim_x materials.

8.1.2 Structural Analysis of ZIF-62(M)-bim$_x$ Materials

SCXRD data have been collected for all as-ZIF-62(M)-bim$_x$ materials at 100 K. All materials are isomorphous (orthorombic space group (*Pbca*)) and composed of M^{2+} cations, which are tetrahedrally coordinated by N-donor atoms of four different im^- or bim^- linkers, assembling to a 3D microporous framework of **cag** topology (see Figure 8.1). The asymmetric unit contains two M^{2+} ions, four imidazolate-type linkers – either im^- or bim^- – and about one DMF molecule.

DMF occupancy

In the overall structure, the DMF molecules were located within in the pores of the framework templating the porous structure. The DMF guest molecules were found severely disordered for ZIF-62(Zn)-bim$_x$ with $x = 0.35$, 0.24, 0.17 and 0.12 as well as for ZIF-62(Co)-bim$_{0.30}$.* Here, the electron density corresponding to these guests was subtracted from the experimental data by a solvent mask as implemented in the Olex2 software package.[48] The number of subtracted electrons corresponds to about 0.5 DMF molecules (i.e. 20 electrons) per formula unit (see Table 8.2 for precise values). For all other as-synthesized compounds the only partially disordered guest molecules could be resolved and application of a solvent mask was not necessary.

Table 8.2: Determined void volume (V_{void}) and number of electrons (n_{e^-}) per void, utilising the implemented solvent mask routine in Olex2.[48]. Based on this values the number of DMF molecules per void and formula unit have been calculated.

compound	V_{void} / Å^3	number of voids	% of unit cell	n_{e} per void	n_{DMF} per void	n_{DMF} per formula unit
as-ZIF-62(Zn)-bim$_{0.35}$	305.6	4	27.9	74.3	1.85	0.46
as-ZIF-62(Zn)-bim$_{0.24}$	310.3	4	28.3	76.7	1.92	0.48
as-ZIF-62(Zn)-bim$_{0.17}$	304.6	4	28.1	71.9	1.80	0.45
as-ZIF-62(Zn)-bim$_{0.12}$	302.8	4	28.2	74.7	1.87	0.47
as-ZIF-62(Co)-bim$_{0.30}$	162.7	8	29.8	35.2	0.88	0.44

The presence of DMF molecules was further found in solution ^{1}H NMR spectroscopy data of digested as-ZIF-62(Zn)-bim$_x$ materials verifying the amount of ≈ 0.5 DMF molecules per formular unit (see Table 8.3 and Section A.3.6 for spectra).

∗ A number of different constraints and restraints were applied to the disordered DMF molecules. Details can be found in the crystallographic information files.

Table 8.3: Summary of the number of DMF molecules per formula unit for the as-ZIF-62(M)-bim$_x$ materials, determined by solution ^{1}H NMR spectroscopy.

Compound	DMF per formula unit
as-ZIF-62(Zn)-bim$_{0.35}$	0.41
as-ZIF-62(Zn)-bim$_{0.24}$	0.48
as-ZIF-62(Zn)-bim$_{0.17}$	0.48
as-ZIF-62(Zn)-bim$_{0.12}$	0.33
as-ZIF-62(Zn)-bim$_{0.07}$	0.49
as-ZIF-62(Zn)-bim$_{0.05}$	0.38
as-ZIF-62(Zn)-bim$_{0.03}$	0.45
as-ZIF-62(Zn)-bim$_{0.02}$	0.44
as-ZIF-62(Co)-bim$_{0.30}$	0.36
as-ZIF-62(Co)-bim$_{0.10}$	0.41

Bim$^-$ occupancy

In the asymmetric unit of all as-synthesized ZIF-62(M)-bim$_x$ materials, the bulky bim$^-$ linker could only by resolved on one of the four possible linker position which is occupied by $2x$ with bim$^-$ and $1-2x$ with im$^-$. The bim$^-$ linker occupancy was set to match the im$^-$: bim$^-$ ratio determined via solution ^{1}H NMR spectroscopy.

Interestingly, by collecting SCXRD data of selected activated ZIF-62(Co)-bim$_x$ ($x = 0.10$ or 0.30) it was found that a second position is also occupied by the bim$^-$ linker (20% or 10%). This position could not be resolved in the datasets collected for the corresponding as-synthesized materials, as it overlaps with the DMF molecules located at a similar position. The absence of DMF in the activated samples allows resolving the additional bim$^-$ position and the free refinement of its occupancy.*

Phase Purity Analysis

Experimental PXRD data of all materials were visually compared to a simulated pattern of ZIF-62(Zn)-bim$_{0.35}$ (see Figure 8.3). Comparing the data proves the phase purity of all ZIF-62(M)-bim$_x$. The phase purity was additionally verified by structureless profile fits (Pawley method) for ZIF-62(M)-bim$_x$ and as-ZIF-62(M)-bim$_x$ materials (see Section A.3.2).†

* A number of different constraints and restraints were applied to the disordered bim$^-$ and im$^-$ linkers. Details can be found in the crystallographic information files (*.cifs).

† Profile fits were performed to the PXRD data starting with the crystallographic parameters derived from SCXRD analysis. Details about the phase identification method can be found in Section 3.1.5.

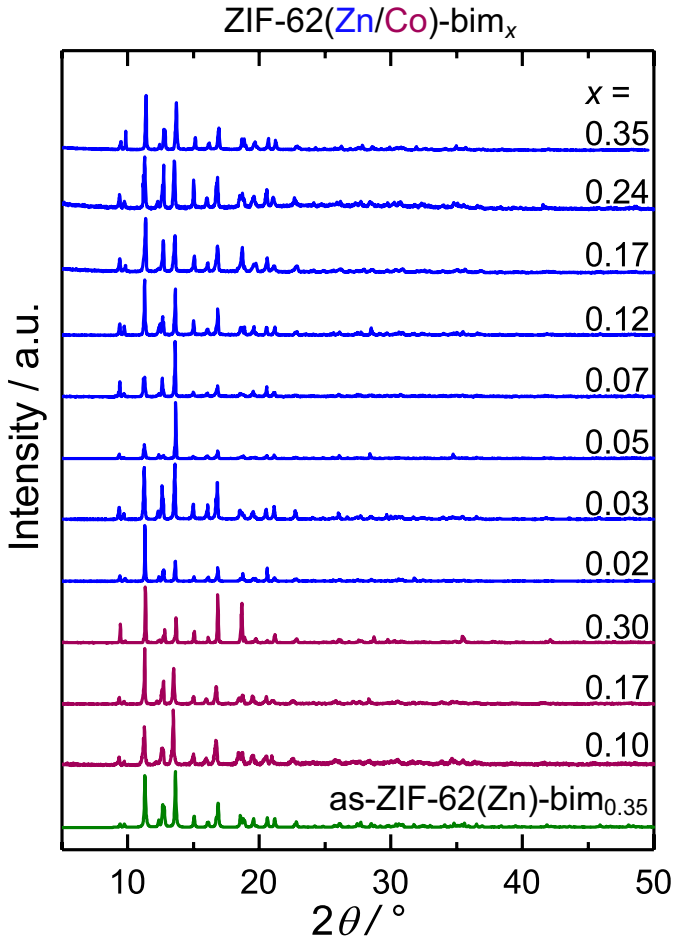

Figure 8.3: Stack plot of PXRD pattern of ZIF-62(M)-bim$_x$ materials. A simulated PXRD pattern based on structural data derived from a SCXRD experiment of as-ZIF-62(Zn)-bim$_{0.35}$ is displayed in green. A visual comparison of the patterns confirmed the formation of isostructural materials.[a]

a The varying peak intensities are a consequence of poor powder averaging due to preferred orientation.

8.2 Influencing the Melting Temperature

8.2.1 The Melting Behavior

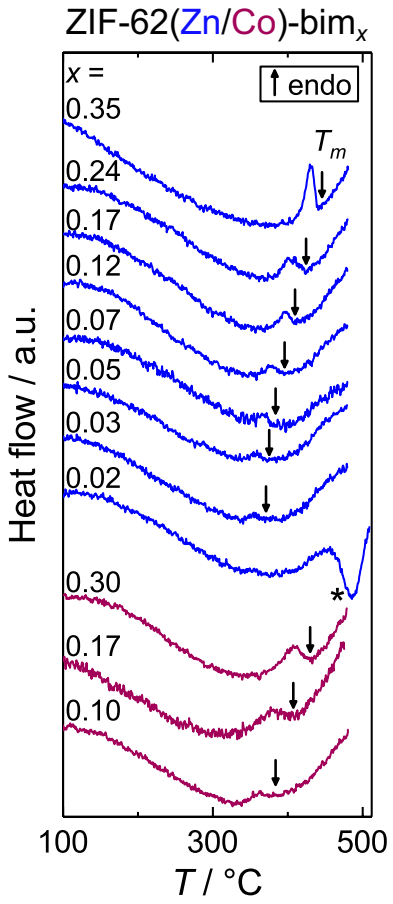

Fig. 8.4: DSC trace from TGA/DSC experiments for all investigated ZIF-62(M)-bim$_x$ materials. The black arrows indicate the position on which the T_m was determined. The asterisk (*) indicates the exothermal signal for ZIF-62(M)-bim$_{0.02}$ which is ascribed to the recrystallization to the ZIF-zni(Zn) phase.

TGA/DSC experiments were carried out from ambient temperature to 750 °C for all ZIF-62(M)-bim$_x$ materials under inert atmosphere (Ar). For materials with $x = 0.35 - 0.03$ the DSC trace clearly shows an endothermal signal between 370 °C to 440 °C which is ascribed to melting of the materials (see Figure 8.4 and Section A.3.7 for whole datasets). The T_m decreases by about 70 °C from 440 °C for $x = 0.35$ to only 370 °C for $x = 0.03$ (see Figure 8.5). Additionally, it becomes clear that T_m is largely independent of the utilized metal ion (Co^{2+} *vs.* Zn^{2+}) but a direct function of x. The calorimetric signal for ZIF melting gets weaker and broader with decreasing x, signifying a slightly broader melting regime for the frameworks with lower values of x. Nevertheless, down to $x = 0.03$ the melting points of the ZIF-62(M)-bim$_x$ materials clearly show a linear dependence on x.

The amorphization which comes along with melting of the materials was also monitored by variable-temperature dependent PXRD measurements of selected ZIF-62(M)-bim$_x$ materials (see Section A.3.3). Two representative datasets for ZIF-62(Zn)-bim$_{0.35}$ and ZIF-62(Co)-bim$_{0.30}$ are displayed in Figure 8.6. The collected data clearly show sharp Bragg peaks corresponding to the ZIF-62 phase at room temperature. A complete amorphization is found for ZIF-62(Zn)$_{0.35}$ at ~360 °C and ZIF-62(Co)$_{0.30}$ at ~350 °C shown by the disappearance of all Bragg peaks*. In both cases, the observed amorphization is ~80 °C lower than the prior determined T_m. Similar discrepancies are found for all datasets.

Such differences are ascribed to dissimilar temperature/time profiles of the temperature dependent PXRD and TGA/DSC experiments. In the TGA/DSC experiments a continuous heating ramp was applied (± 10 °C min^{-1}) whereas a discontinuous

* The still apparent broad peaks after 7° are assigned to the dome used during the experiment (see Section A.3.3 for further details).

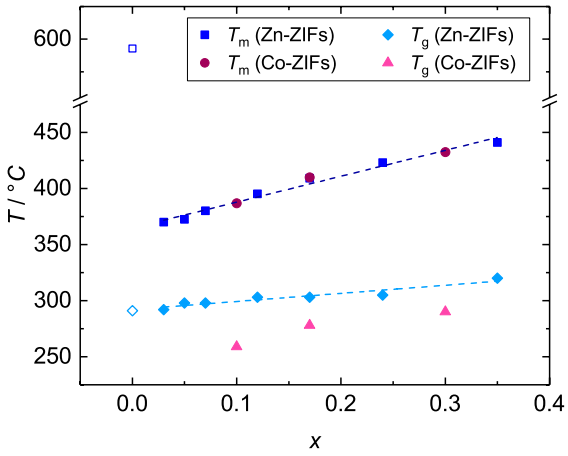

Figure 8.5: Graph representing the evaluation of T_m and T_g with varying im^- : bim^- concentration (x). The dotted lines display a linear fit to the T_m and T_g data for ZIF-62(Zn)-bim$_x$. Literature values for ZIF-4(Zn) are given with open symbols for comparison.[114]

heating ramp was used in the variable-temperature PXRD experiments which feature additional isothermal segments during data collection (see Section 12.1.3). Consequently, in the variable-temperature PXRD experiments the samples are at a particular temperature over a longer time frame. Hence, the variation in melting temperatures between TGA/DSC and temperature dependent PXRD are ascribed to kinetic effects. Similar observations have been already reported for temperature dependent wide angle X-ray scattering (WAXS) experiments.[127,151,201] Theoretically, it is also possible that the materials amorphize prior to melting due to dissociative bond rearrangement. The amorphous phase could be very similar in enthalpy to the prior crystalline phase, since no endothermal event is detected in the TGA/DSC experiments at that temperature.

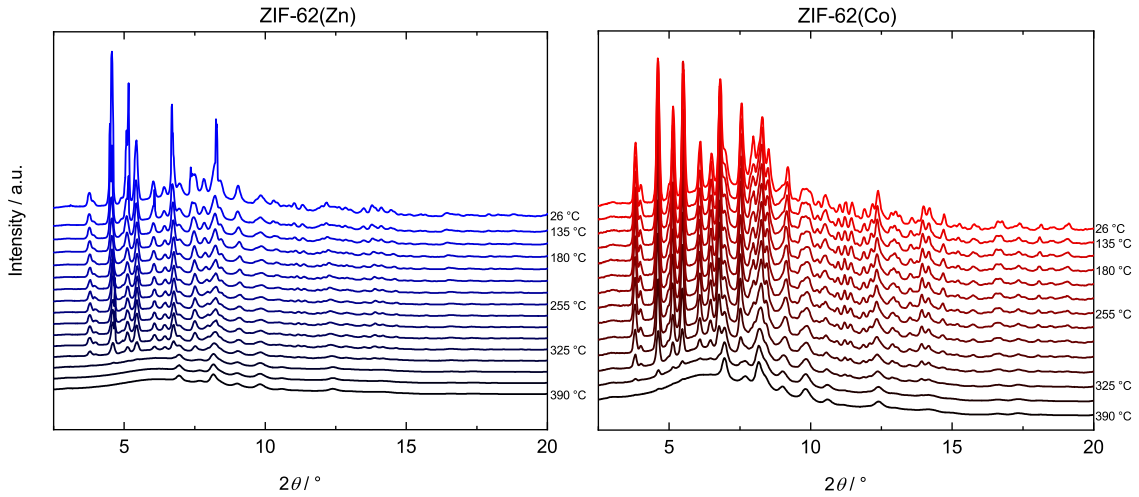

Figure 8.6: Diffraction patterns of temperature dependent PXRD experiments for ZIF-62(Zn)-bim$_{0.35}$ (left) and ZIF-62(Co)-bim$_{0.30}$ (right).

8.2.2 The Glass Formation

The glass preparation was performed in a TGA/DSC apparatus. Cooling the ZIF-62(M)-bim$_x$ liquids from 475 °C – above their T_m – to room temperature (cooling rate −10 °C min^{-1}) yields their corresponding ZIF glasses.

Optical Appearance

The obtained materials from the TGA/DSC apparatus are all fused together to a monolith (see Section A.3.8). These monoliths further break into shards showing clear evidence of microscopic flow. Representative photographs are presented in Figure 8.7.

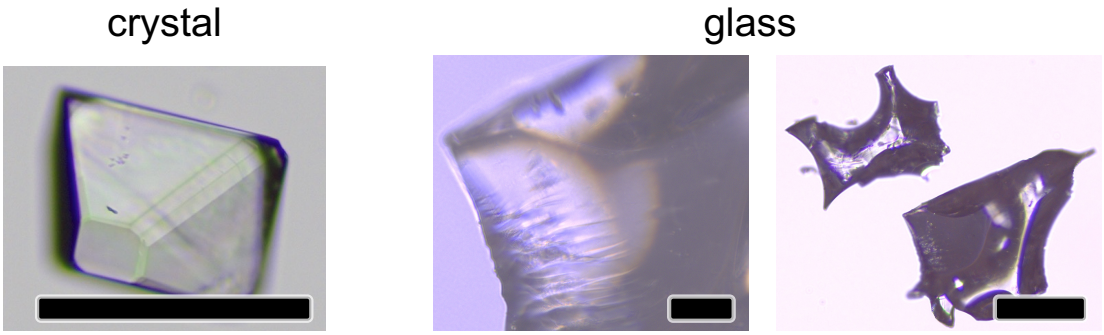

Figure 8.7: Representative photographs of a ZIF-62(M)-bim$_x$ single crystal (left) and of a$_g$ZIF-62(M)-bim$_x$ glass shards (right). The black scale bars indicate a length of ≈ 200 µm.

Structural Analysis

The obtained monoliths were ground into fine powders for further analysis. PXRD experiments revealed that all products with $x = 0.05 - 0.35$ are X-ray amorphous glasses (see Figure 8.8). Supplementary XPDFs were derived from X-ray total scattering data for selected materials ($x = 0.35 - 0.05$; see Figure 8.9 and Section A.3.4 for $S(Q)$ data)).* As previously found for ZIF glasses, the local structure of the crystalline materials was preserved in the corresponding amorphous glasses.

PXRD analysis of the vitreous products a$_g$ZIF-62(Zn)-bim$_{0.02}$ and a$_g$ZIF-62(Zn)-bim$_{0.03}$ (with low bim$^-$ concentration) shows Bragg peaks corresponding to the ZIF-zni(Zn) phase (see Figure 8.8). This recrystallization is also observed for ZIF-4(M) (M = Zn^{2+} or Co^{2+}, $x = 0$; see Section 4.3.1).

* In such data – visualized in the form $D(r)$[61] – every peak corresponds to an interatomic distance within the investigated material and thus provides information about its local structure. An introduction to X-ray total scattering and the derived XPDF function is given in Section 3.1.6.

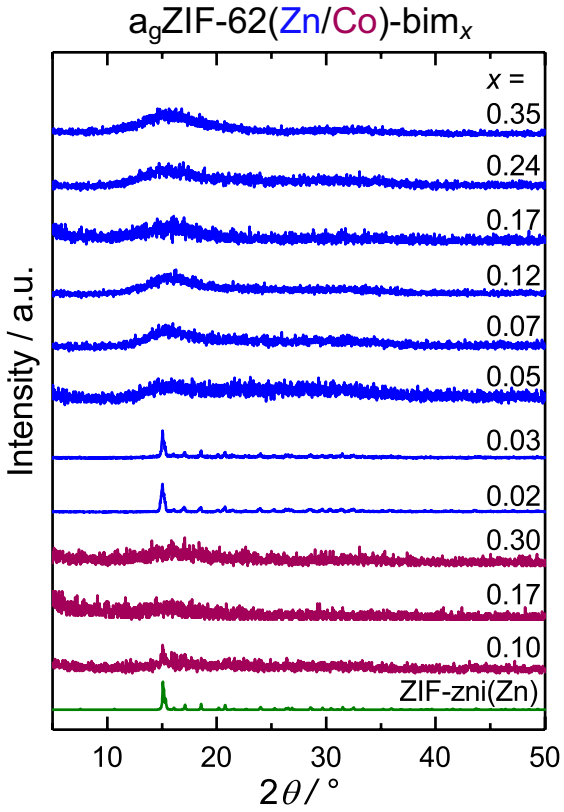

Figure 8.8: PXRD pattern of the ZIF-62(M)-bim$_x$ materials after they have been heated above their melting temperature (see Figure 8.4) and cooled down to room temperature. A simulated PXRD pattern of ZIF-zni(Zn) based on structural data derived from SCXRD data[166] is shown for comparison.

Thermal Analysis

Glass Transition. The thermal behavior of ZIF-62(Zn)-bim$_{0.02}$ is indeed very similar to conventional ZIF-4(Zn). No endothermic melting signal is observable in the DSC trace, but an exothermic peak for the recrystallization to ZIF-zni(Zn) at $\approx 500\,°C$ is evident (see Figure 8.4). For ZIF-62(Zn)-bim$_{0.03}$ an endothermal melting signal is still present in the collected DSC data. Consequently, the limit for homogeneous melting for the ZIF-62(M)-bim$_x$ system by preventing a recrystallization to ZIF-zni(M) lies in the region $0.03 \geq x < 0.05$.

The glassy nature of all ZIF glasses with $x \geq 0.03$ was further investigated by cyclic TGA/DSC experiments. Therefore, the materials were again heated above their T_m (scan rate $10\,°C\ min^{-1}$). All collected datasets show an endothermal event at lower temperature than their T_m which is ascribed to the glass transition verifying again their prior glass formation. The determined T_g values for Zn-compounds are in the range from 290 °C to 320 °C, whereas Co-compounds feature lower values between 260 °C and 300 °C (see Figure 8.5 and Section A.3.7 for full datasets). T_g is also a function of x and increases slightly with increasing bim$^-$.

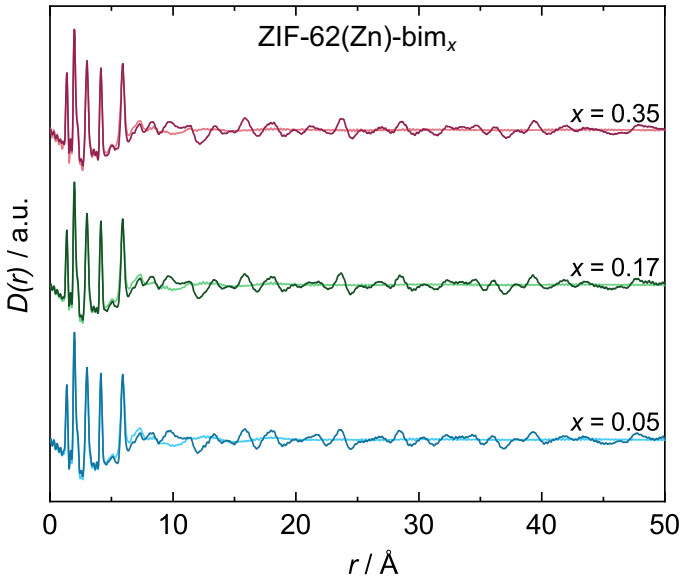

Figure 8.9: Stack plot of XPDF data in the form $D(r)$ for selected ZIF-62(Zn)-bim$_x$ materials and their corresponding glasses. An overlay of the crystalline and glass phases is shown, demonstrating that the local structure for both phases are essentially identical.

Glass Forming Ability. From T_g and T_m values, the glass forming ability (GFA, T_g/T_m)* of the materials can be calculated, which is an important criterion in glass science (see Section 4.3). A material with high glass forming ability resists recrystallization on laboratory time scales. The determined GFA values are in the range from 0.80 to 0.81 for all cobalt materials and are sligthly higher for the zinc materials (0.83 − 0.88) which underlines the ultrahigh GFA found for similar materials already reported in the literature (see Section A.3.7 for precise values).[122]

Enthalpy and Entropy of Melting. The molar enthalpies (ΔH_m) for the melting process were determined from the DSC curves (first upscan) of the TGA/DSC experiments by integration of the signal ascribed to melting. From the molar melting enthalpies the molar melting entropies have been calculated. It becomes clear that ΔH_m drops from 2.5 kJ mol^{-1} to only 0.4 kJ mol^{-1} from the ZIF-62(Zn)-bim$_x$ material with the highest ($x = 0.35$) to the lowest ($x = 0.03$) im$^-$: bim$^-$ concentration (see Figure 8.10 and Section A.3.7 for precises values). A similar trend is observed for ΔS_m. Cobalt materials show slightly higher values for ΔH_m and ΔS_m which may be related to the slightly higher density of these materials resulting from the smaller ionic radius of Co^{2+} compared to Zn^{2+}.[202]†

It is evident that the entropic difference between the crystalline and glass state for

∗ Calculations are performed with temperatures in Kelvin.
† Ionic radii according to Shannon (coordination number IV): 1.58 Å (Co^{2+}) *vs.* 1.60 Å (Zn^{2+})

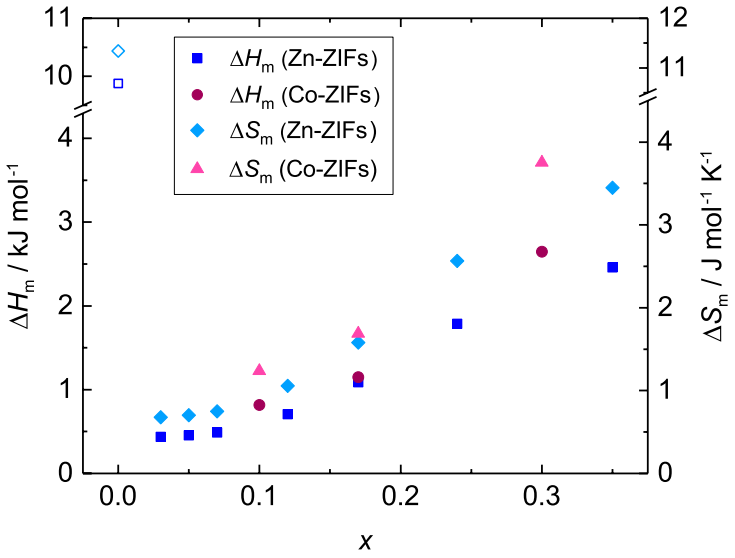

Figure 8.10: Graph compiling the ΔH_m and ΔS_m for melting ZIF-62(M)-bim$_x$ materials determined from the DSC curves of the TGA/DSC experiments. Literature values for ZIF-4(Zn) are given with open symbols for comparison.[114]

all materials becomes less with decreasing x. Consequently, the vibrational entropy of the porous crystalline phase gets almost comparable to the configurational entropy of the liquid phase. It has to be noted that ΔH_m and ΔS_m are an order of magnitude higher for ZIF-4(Zn) (see Figure 8.10). This is caused by the fact that ZIF-4(Zn) melts from its much denser polymorph ZIF-zni(Zn), whereas the ZIF-62(M)-bim$_x$ ($x \geq 0.03$) materials melt from the porous phase with **cag** topology.

8.2.3 Sequential Amorphization/Recrystallization *vs.* Coherent Melting

Melting and thermal amorphization are reconstructive phase transitions involving breakage and reformation of chemical bonds. The reported mechanism for ZIF melting also involves a bond dissociation between Zn^{2+} and the coordinating N of an imidazolate linker (see Section 4.3.1).[116] According to Lindemann's law bond dissociation is expected when the vibrational amplitudes of neighboring atoms reach a critical fraction of their bond distances.[203,204] In order to investigate this, a closer look was taken on the evolution of dynamical atomic displacements of the molecular building units (imidazolate linkers) with temperature in melting ZIFs.

SCXRD data were collected of evacuated, guest-free crystals of selected ZIFs at various temperatures. For this purpose, ZIF-62(Co)-bim$_{0.10}$ and ZIF-62(Co)-bim$_{0.30}$ as well as the isoreticular bim$^-$-free material ZIF-4(Co) and the denser polymorph

ZIF-zni(Co) were chosen.* SCXRD datasets were collected at −173, −73, +27 and +127 °C (100, 200, 300 and 400 K) for all materials (see Section A.3.1).

First, it becomes obvious that the anisotropic displacement parameters (ADPs) are 25 − 35% larger for all atoms in ZIF-62(Co)-bim$_x$ materials compared to ZIF-4(Co) at −173 °C (see Figure 8.11). In the ZIF-62(Co)-bim$_x$ materials, the bulky bim$^-$ linker is statistically distributed through the crystal and placed on positions also partially occupied by im$^-$, which causes small distortions on a local scale. From that circumstance already a *static* atomic displacement arises. Nevertheless, the atomic displacement parameters collected at variable-temperatures give valuable insights into the evolution of the *dynamic* atomic displacements over the investigated temperature range and will provide insights into the melting/ amorphization behavior of these compounds.

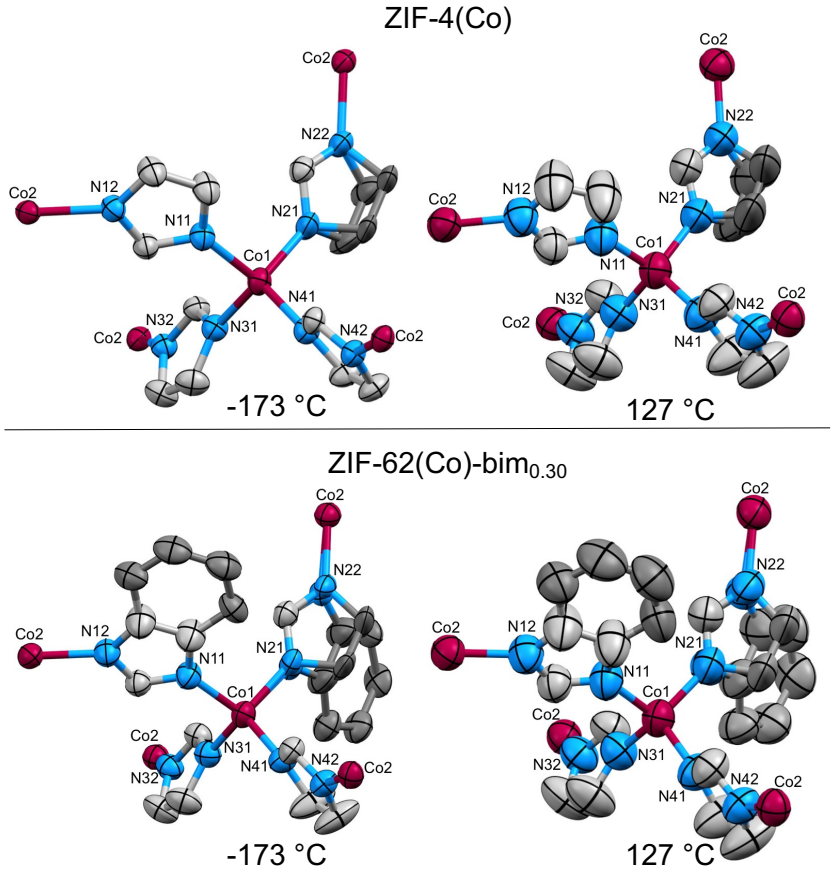

Figure 8.11: Representation of extended asymmetric units of the crystal structures of DMF free ZIF-4(Co) (top) and ZIF-62(Co)-bim$_{0.30}$ (bottom) obtained from SCXRD experiments at −173 and 123 °C. The ellipsoids are drawn at the 50% probability level. Co, N and C atoms are shown in purple, blue and gray, respectively. The dark gray atoms are only partially occupied. H atoms are omitted for clarity.

For the following discussion, it will be focused only on the mean equivalent

* ZIF-4(Co) and ZIF-zni(Co) have been synthesized after literature known protocols (see Section 12.9.1).

isotropic displacement parameters of the N atoms ($U_{eq}{}^{N}$)* in the ZIF structures. The vibrational amplitude of these atoms is most important for the metal-linker bond dissociation which triggers the melting/ amorphization process.[116] Upon heating from −173 to 127 °C, the $U_{eq}{}^{N}$ increases by a factor of 2.4 for ZIF-4(Co) whereas a lower increase for ZIF-62(Co)-bim$_x$ materials is observed (1.9 for $x = 0.10$; 1.8 for $x = 0.30$, see Figure 8.12). Thus, the metal−ligand bond dissociation which is triggered by the vibrational amplitude is expected to happen at lower temperature for ZIF-4(Co) than for ZIF-62(Co)-bim$_x$ materials. An even weaker increase of the $U_{eq}{}^{N}$ is observed for the denser ZIF-zni(Co) which suggests that an even higher temperature is needed for the Co−N bond breaking.

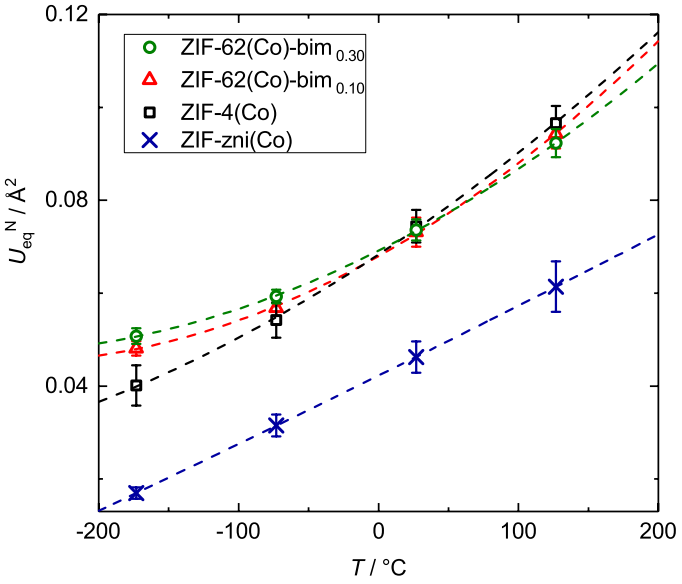

Figure 8.12: Graph representing the evolution of the mean equivalent atomic displacement parameters ($U_{eq}{}^{N}$) of two representative ZIF-62(Co)-bim$_x$ materials, ZIF-4(Co) and ZIF-zni(Co) against temperature. The data are derived from the temperature dependent SCXRD data. Error bars display the weighted standard deviations based on eight to ten crystallographically independent N atoms. The dashed lines represent quadratic fits to the data points in the same color.

Remarkably, these observations are in accordance with the high temperature behavior of these compounds. ZIF-4(Co) amorphize at lower temperatures (about 320 °C)[146] than the ZIF-62(Co)-bim$_x$ materials ($x \geq 0.03$) melt (370 − 440 °C). The amorphous phase of ZIF-4(Co) recrystallizes to the denser ZIF-zni(Co) phase upon further heating which finally melts and simultaneously decomposes at even higher temperatures (550 °C).

In combination with the discussed DSC data, a bond dissociation − either arising

* U_{eq} values for single N atoms can be read out from the crystallographic information file. $U_{eq}{}^{N}$ is calculated for eight (ZIF-4(Co)/ ZIF-zni(Co)) or ten (ZIF-62(Co)-bim$_x$) crystallographic independent N atoms.

from amorphization or melting − is expected at higher temperature for ZIF-62(M)-bim$_x$ materials than for ZIF-4(M). It is shown that recrystallization to the denser ZIF-zni(M) phase is suppressed by incorporating the bulky bim$^-$ linker ($x \geq 0.05$) and following the material melts at lower temperature, while the decomposition temperature is nearly unaffected by the linker concentration (510 − 600 °C). Consequently, ZIF-62(M)-bim$_x$ materials feature a much larger window of thermally stable liquid, which can be further adjusted by fine-tuning the linker ratio in the material. Remarkably, already a very low amount of the bulky bim$^-$ linker (1 bim$^-$ on 39 im$^-$ for $x = 0.05$) in the framework − far away from the amount found in the conventional ZIF-62(M) (1 bim$^-$ on 7 im$^-$ for $x = 0.25$) − efficiently suppresses the recrystallization and generates a ZIF liquid, which is thermally stable over a temperature window of approximately 230 °C. For comparison, the prototypical ZIF-4(Zn) forms a liquid which is stable over less than 10 °C, whereas the ZIF-4(Co) melt is unstable and simultaneously melts and decomposes.

8.3 Which MOFs Could Melt?

It is remarkable that all of the so far reported melting ZIFs contain the small im$^-$ linker (see Section 4.3.2). Nevertheless, the well-studied ZIF-7, including only the bulky bim$^-$ linker (chemical composition Zn(bim)$_2$) does not melt.[205] The same is true for ZIF-8 (Zn(mim)$_2$, mim$^-$ = 2-methylimidazolate) whose mim$^-$ linkers are only slightly larger than im$^-$.[114] Hence, the incorporation of im$^-$, seems mandatory to achieve meltable ZIFs. Larger imidazolate-type linkers result in larger tetrahedral units enhancing steric hindrance and hampering melting. However, ZIFs featuring only the small im$^-$ (such as ZIF-4), do not form stable ZIF liquids at lower temperature. ZIF-4(Zn) as well as its polymorphs (e.g., ZIF-zeg, ZIF-nog) amorphize at 320-330 °C and subsequently recrystallize to ZIF-zni(Zn).[150] As outlined, ZIF-zni(M) (M = Zn^{2+} or Co^{2+}) is highly stable and does not melt before approximate 590 °C.

Nevertheless, on the basis of the experimental data presented it can be hypothesized that a great number of other ZIFs may melt at lower temperatures (i.e., much below 590 °C), form stable liquid phases (i.e., do not recrystallize to a denser phase) and transform into porous glasses upon cooling from the melt, as long as the following two requirements are fulfilled:

(i) The ZIF must contain im$^-$ linkers and at least one other imidazolate-type linker that is bulky enough to prevent recrystallization to the ZIF-zni phase (as in the current case of ZIF-62(M), the concentration of the bulky imidazolate linker may be remarkably low, however).

(ii) Naturally, the bulky imidazolate-type linker must feature a decomposition

temperature higher than the framework's melting temperature in order to allow melting before decomposition.

The fact that amorphization (i.e., bond breaking and framework collapse) of ZIF-4(M) (M = Zn^{2+} or Co^{2+}) occurs at 320 − 330 °C further suggests that the lowest melting point that is achievable for crystalline ZIFs forming melt quenched glasses at atmospheric pressure lies around this region. As shown above, incorporation of just small amounts of the bulky bim^- linker results in a melting point of about 370 °C, about 40 − 50 °C higher than the temperature of amorphization of ZIF-4(M) (M = Zn^{2+} or Co^{2+}). Incorporation of functionalized imidazolate linkers that are smaller than bim^- might however lead to the discovery of ZIFs with melting points approaching 320 − 330 °C. Importantly, the two requirements outlined above are met by all known ZIF glass formers yielding melt quenched ZIF glasses (see Section 4.3.2).

Many other mixed-linker ZIFs satisfying at least the first requirement are known (see Table 8.4).[29,206] Future studies will show if these compounds indeed melt at elevated temperature. In analogy to what is presented here for the prototypical ZIF-62 system, it is very likely that T_m of all of the mixed-linker ZIFs mentioned above can also be tuned systematically by adjusting the molar ratio of their two linkers.

Table 8.4: Examples of literature-known mixed-linker ZIFs fulfilling the first requirement for ZIF melting.[29,206] Linker abbreviations: im^- = imidazolate; mim^- = 2-methylimidazolate; nim^- = 2-nitroimidazolate; $cbim^-$ = 5-chlorobenzimidazolate; bim^- = benzimidazolate; $nbim^-$ = 5-nitrobenzimidazolate; $bbim^-$ = 5-bromobenzimidazolate

Name	Chemical composition	Topology
ZIF-60	$Zn(im)_{1.5}(mim)_{0.5}$	**mer**
ZIF-70	$Zn(im)_{1.13}(nim)_{0.87}$	**gme**
ZIF-303	$Zn(cbim)_{0.70}(nim)_{0.30}(im)_{1.00}$	**cha**
ZIF-360	$Zn(bim)_{1.00}(nim)_{0.70}(im)_{0.30}$	**kfi**
ZIF-365	$Zn(cbim)_{0.95}(nim)_{0.60}(im)_{0.45}$	**kfi**
ZIF-376	$Zn(nbim)_{0.25}(mim)_{0.25}(im)_{1.50}$	**lta**
ZIF-386	$Zn(nbim)_{0.85}(nim)_{0.70}(im)_{0.45}$	**afx**
ZIF-486	$Zn(nbim)_{0.20}(mim)_{0.65}(im)_{1.15}$	**gme**
ZIF-412	$Zn(bim)_{1.13}(nim)_{0.62}(im)_{0.25}$	**ucb**
ZIF-413	$Zn(mbim)_{1.03}(nim)_{0.64}(im)_{0.33}$	**ucb**
ZIF-414	$Zn(nbim)_{0.91}(mim)_{0.62}(im)_{0.47}$	**ucb**
ZIF-725	$Zn(bbim)_{1.35}(nim)_{0.40}(im)_{0.25}$	**bam**

8.4 Conclusion

A series of 11 different ZIF-62(M)-bim$_x$ materials composed of different metal ions ($M^{2+} = Co^{2+}$ or Zn^{2+}) and varying ratios of two different imidazolate-type linkers (the small im$^-$ and the bulkier bim$^-$) are investigated toward their thermal behavior. It was revealed that these mixed-linker ZIF materials of the general chemical composition M(im)$_{2-x}$(bim)$_x$ melt at elevated temperatures and form ZIF glasses by cooling the liquid ZIFs down to ambient temperature. It was found that the metal ion (Co^{2+} *vs.* Zn^{2+}) has a major impact on the decomposition temperature ($\approx 510 - 550$ °C for the Co-ZIFs, $\approx 550 - 600$ °C for the Zn-ZIFs) but only minor on the frameworks' melting point. The melting point of the ZIF compounds, however, can be engineered over a wide range between 440 °C to 370 °C by simply adjusting the molar ratio of im$^-$ to bim$^-$ in the solid state. Remarkably, the melting point of the ZIFs is linearly dependent on the concentration of bim$^-$ in the material, resulting in a melting point of only 370 °C for $x = 0.03$. ZIFs containing low concentrations of bim$^-$ ($x < 0.05$) form a metastable liquid phase that partially recrystallizes to the denser ZIF-zni at about 500 °C. On the contrary, ZIFs containing higher concentrations of bim$^-$ ($x \leq 0.05$) form thermodynamically stable liquids which do not recrystallize to the ZIF-zni phase. Even though only a few ZIFs containing the small im$^-$ linker have been shown to melt so far, these data clearly demonstrate the impact of the bulkier bim$^-$ linker on the frameworks' melting point as well as on the formation of thermodynamically stable ZIF liquids. It is hypothesized that a large number of literature-known crystalline ZIFs also melt as far as they are composed of im$^-$ linkers and at least one other bulkier imidazolate-type linker. This sets the stage for the development of a large number of new functional and chemically diverse ZIF glasses. Moreover, the low melting point of the ZIFs with $x \approx 0.05 - 0.10$ further opens the door for the lower temperature preparation of MOF glass composites[119,126,201] incorporating temperature sensitive compounds (e.g., metal-organic or organometallic complexes, organic fluorophores, etc.).

9 Hydrocarbon Separation by ZIF Glasses*

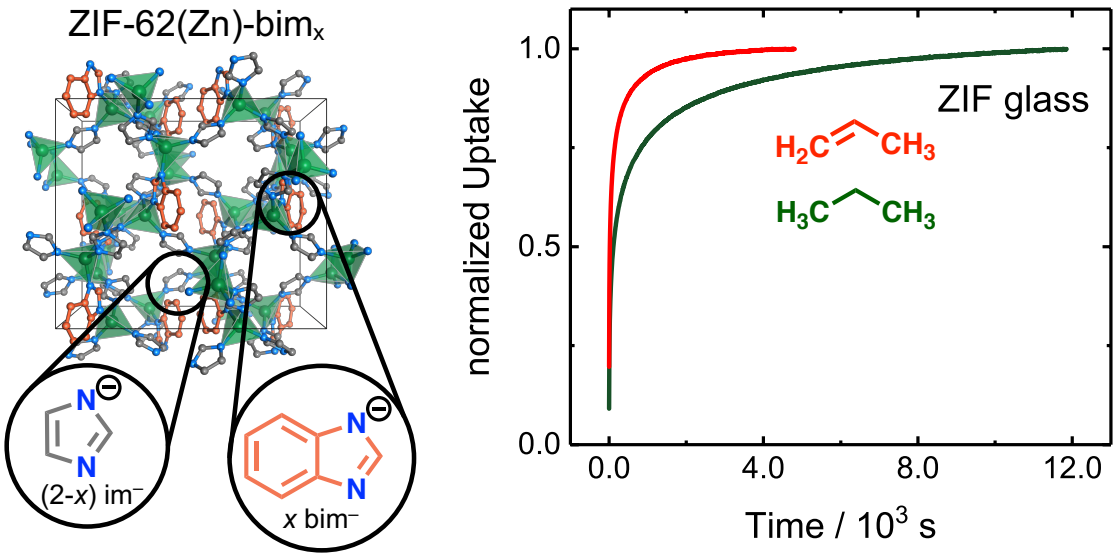

Abstract

In the previous chapter, it was demonstrated that ZIF glasses of the ZIF-62(M)-bim$_x$ family can be obtained by incorporating various amounts of bim$^-$ (x). Subsequently, three selected ZIF-62(Zn)-bim$_x$ (x = 0.35, 0.17, 0.05) glasses are investigated regarding their selective gas physisorption potential. Therefore, gas physisorption studies of the technologically relevant C_3 hydrocarbons propane and propylene were conducted. Importantly, it was found that the gas adsorption kinetics are much faster for propylene compared to propane and are also dependent on the im$^-$: bim$^-$ ratio, thus demonstrating the potential of these ZIF glasses for applications in gas separation.

∗ The content of this chapter is reprinted or adapted from the following publication: L. Frentzel-Beyme, M. Kloß, P. Kolodzeiski, R. Pallach, S. Henke, *J. Am. Chem. Soc.* **2019**, *141*, 12362-12371. Reproduced or adapted with permission. Copyright 2019 American Chemical Society.

9.1 Selective Hydrocarbon Adsorption

The separation of propane and propylene is an industrially relevant separation process which is very challenging since both gases feature very similar physical properties (see Table 9.1). Today, their separation is achieved via energy consuming cryogenic distillation on an industrial scale. Having in mind, that propylene is one of the most important feedstock chemicals produced in 100 million tonnes per year (2016), the research for materials which optimize this process is still highly relevant.[97]

In order to access the potential of ZIF glasses for the gas sorption and separation of technologically relevant hydrocarbons, the sorption behavior towards propylene and propane was investigated for three a_gZIF-62(Zn)-bim$_x$ materials (x = 0.05, 0.17, 0.35). Single component isotherms were collected at 273 K as well as at the more industrially relevant temperature of 293 K. At both temperatures, all glasses showed a preference for the adsorption of propylene over propane (see Figure 9.1). This observation is in accordance with the findings for the investigated ZIF glasses in Section 6.2.4.*

In a next step, the separation ability of the three different a_gZIF-62(Zn)-bim$_x$ (x = 0.05, 0.17, 0.35) materials should be quantified. Here, it will be distinguished between the separation potential derived from thermodynamic or kinetic processes.

9.1.1 Thermodynamic Gas Separation

To quantify the thermodynamic separation ability of the selected ZIF glasses ideal adsorption solution theory calculations after A. L. Myers and J. M. Prausnitz[92] were performed based on the single component propane and propylene isotherms (see Table 9.2).† The calculations were conducted using the Python package –

Table 9.1: Summary of selected physical properties of propane and propylene.[97] d_{kin} = kinetic diameter; α = polarizability; M = moleculare weight; T_b = boiling point.

	d_{kin} [Å]	α [10^{25} cm^3]	M [g mol^{-1}]	T_b [°C]
propane	4.3	62.9 – 63.7	44.10	−47.6
propylene	4.5	62.6	42.08	−42.1

∗ It has to be noted that the maximum gas capacities found for both gases for the investigated ZIF-62(Zn)-bim$_{0.35}$ material is slightly higher than for the same ZIF-62 material investigated in Section 6. This is ascribed to a kinetic effect arising from smaller particles of the material (new batch) investigated during the gas sorption studies present in this section. The appearance of nearly no hysteresis in the isotherms in comparison to the data shown in Section 6 suggest that the thermodynamic equilibrium is now reached during the timescale of the experiment. This yields higher maximum gas capacities, than in Section 6.

† A deeper discussion on this method can be found in Section 3.2.5.

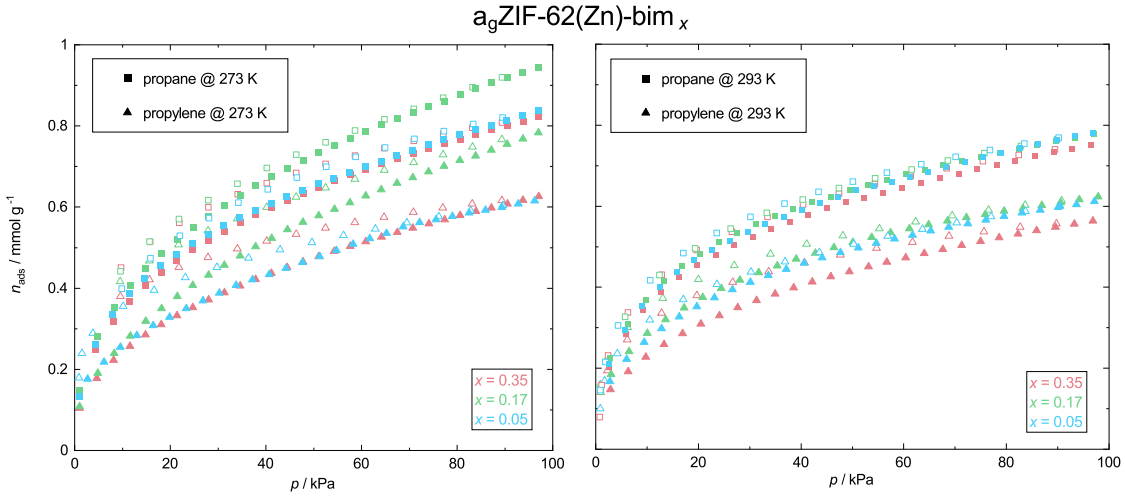

Figure 9.1: Propane and propylene isotherms of selected a_gZIF-62(Zn)-bim$_x$ materials collected at 273 K (left) and 293 K (right). Adsorption and desorption branches are shown with closed and open symbols, respectively.

pyIAST.[93] First, the implemented routine in pyIAST has been used to interpolate the pure component gas adsorption isotherms of propane and propylene at 273 K and 293 K of a_gZIF-62(Zn)-bim$_x$ (x = 0.35, 0.17, 0.05). In a second step, IAST calculations were performed to estimate the respective gas uptakes from a defined gas mixture at a given temperature and pressure. Based on these values, the gas adsorption selectivity was calculated according to:

$$S_{\mathrm{IAST}} = \frac{x_i}{y_i} \tag{9.1}$$

with $x_i = x_{\mathrm{propylene}}/x_{\mathrm{propane}}$ as the molar ratio of fluids adsorbed and $y_i = y_{\mathrm{propylene}}/y_{\mathrm{propane}}$ as the molar ratio of the fluids in the gas phase.

Three different molar propylene/propane ratios in the gas phase (10:90; 50:50; 90:10) were utilized. The calculated values propose a propylene/propane selectivity (S_{IAST}) between 1.8 and 2.5 (for a 50:50 mixture) for the ZIF glasses (see Table 9.2). The found separation factors are in the same range for all combinations of investigated materials, gas mixtures and temperatures. These results demonstrate for the first time that a (thermodynamic) propylene/propane separation is potentially possible by ZIF glasses.

Table 9.2: IAST selectivity factors (S_{IAST}) for selected a_gZIF-62(Zn)-bim$_x$ materials applying three different propylene/propane mixtures (molar ratio 10:90; 50:50; 90:10) at 100 kPa and 273 K or 293 K.

molar ratio (propylene/propane)	10:90		50:50		90:10	
T / K	273	293	273	293	273	293
a_gZIF-62(Zn)-bim$_{0.05}$	2.25	1.90	2.39	1.97	2.60	2.07
a_gZIF-62(Zn)-bim$_{0.17}$	1.97	1.70	1.96	1.83	1.96	2.00
a_gZIF-62(Zn)-bim$_{0.35}$	2.06	2.36	2.14	2.49	2.11	2.69

9.1.2 Kinetic Gas Separation

In a next step, further insight should be gained into the kinetic C_3 hydrocarbon gas separation properties of the ZIF glasses. Therefore, time-dependent gas sorption profiles for propane and propylene at 293 K were recorded after applying a desired gas pressure (see Figure 9.2). The kinetic adsorption data have been collected using the implemented VectorDose routine from the Quantachrome sorption machine. For a kinetic profile a gas dose ($\approx$ 55 kPa) has been applied and the pressure drop has been measured over time by collecting a data point every six seconds. From the uptake-time profiles it is clearly evident that the diffusion of propylene into the glasses is much faster than the diffusion of propane.

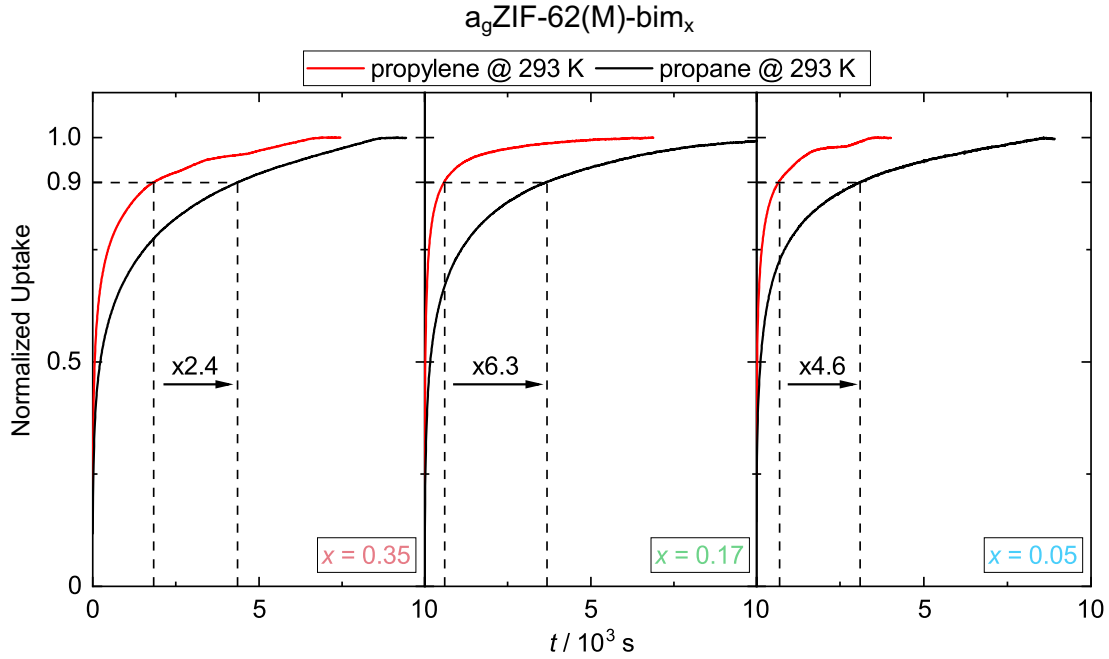

Figure 9.2: Kinetic gas sorption profiles of selected a$_g$ZIF-62(Zn)-bim$_x$ materials recorded for propane and propylene at 293 K and $\approx$ 55 kPa.

The differences in diffusion rates between propane and propylene were quantified by calculating the ratio of the times to reach a certain fraction of the equilibrium adsorption amount. Therefore, the times (t_f(gas); gas = propane or propylene) required to reach a certain fraction (f) of the equilibrium adsorption amount has been read out from the kinetic gas sorption data. These values have been determined for four different fractions – t_f(gas) (f = 80%, 90%, 95% and 99%; see Table 9.3).

Afterwards, the ratio k_f for each of the three ZIF glasses has been calculated based on the t_f(gas) values for propane and propylene to the equation:

$$k_f = \frac{t_f(\text{propane})}{t_f(\text{propylene})}. \tag{9.2}$$

For the following discussion, it will be focused on the values calculated to reach 90% of the equilibrium uptake (see Figure 9.2). In the case of a_gZIF-62(Zn)-bim$_{0.05}$ it takes almost five times longer for propane than for propylene to reach the 90% threshold and for a_gZIF-62(Zn)-bim$_{0.17}$ even more than six times longer. The difference is much less pronounced for a_gZIF-62(Zn)-bim$_{0.35}$. Furthermore, it is apparent that the diffusion rates of both single C_3 hydrocarbons is strongly dependent on x. Due to the larger concentration of bulky bim$^-$ linkers and hence narrower pores, a_gZIF-62(Zn)-bim$_{0.35}$ exhibits a much slower kinetic gas sorption profile compared to the glasses with lower bim$^-$ concentrations. Propylene takes about three times longer to reach 90% of its equilibrium uptake if $x = 0.35$ compared to $x = 0.17$ or 0.05. For propane the differences in diffusion rates are much less pronounced across the series of ZIF glasses. This observation implies that the diffusion rates and thus the kinetic gas sorption selectivity of particular gases of interest (e.g. other hydrocarbons) could be optimized by adjusting the linker ratios in these nanoporous ZIF glasses.

Table 9.3: Data for the qualitative evaluation of the kinetic gas adsorption profiles for reaching an equilibrium adsorption amount of 80%, 90%, 95% and 99%.

compound	gas @ 293 K	$t_{80\%}$ / s	k_f	$t_{90\%}$ / s	k_f
a_gZIF-62(Zn)-bim$_{0.35}$	propylene	720	3.03	1836	2.38
	propane	2185		4363	
a_gZIF-62(Zn)-bim$_{0.17}$	propylene	200	8.06	584	6.27
	propane	1611		3662	
a_gZIF-62(Zn)-bim$_{0.05}$	propylene	246	5.16	662	4.60
	propane	1269		3048	
compound	gas @ 293 K	$t_{95\%}$ / s	k_f	$t_{99\%}$ / s	k_f
a_gZIF-62(Zn)-bim$_{0.35}$	propylene	3434	1.83	6144	1.33
	propane	6277		8169	
a_gZIF-62(Zn)-bim$_{0.17}$	propylene	1314	4.46	4111	2.33
	propane	5862		9575	
a_gZIF-62(Zn)-bim$_{0.05}$	propylene	1291	3.99	3081	2.30
	propane	5152		7888	

9.2 Conclusion

Three different glasses of the ZIF-62(Zn)-bim$_x$ family were investigated towards gas sorption of propane and propylene. These two C_3 hydrocarbons are important feedstock chemicals whose separation remains challenging in industrial processes. Gas adsorption isotherms as well as time-dependent gas sorption profiles indicate that the ZIF glasses are an interesting new class of materials for the separation of

propylene from propane. It was uncovered that these materials are promising for gas selectivity based on thermodynamic and kinetic effects. Based on the results, it can be suggested that the diffusion rate can be also tuned by the chemical composition (e.g. linker ratio) in the ZIF materials.

Even though current crystalline benchmark MOFs feature much higher propylene/propane selectivities (S_{IAST} up to ≈ 60)[207–212] than the ZIF glasses investigated here, these first hydrocarbon sorption data for ZIF glasses are very encouraging for future studies. Together with the advantages of ZIF glasses in terms of processability and shaping[119,126] as well as their very high thermal decomposition temperatures, these findings pave the way for applications of ZIF glasses in composite membranes or even as free-standing glass membranes for technologically important separation processes.

Part II
A New Class of Water-Processable MOFs

10 Amphiphile Salt Frameworks*

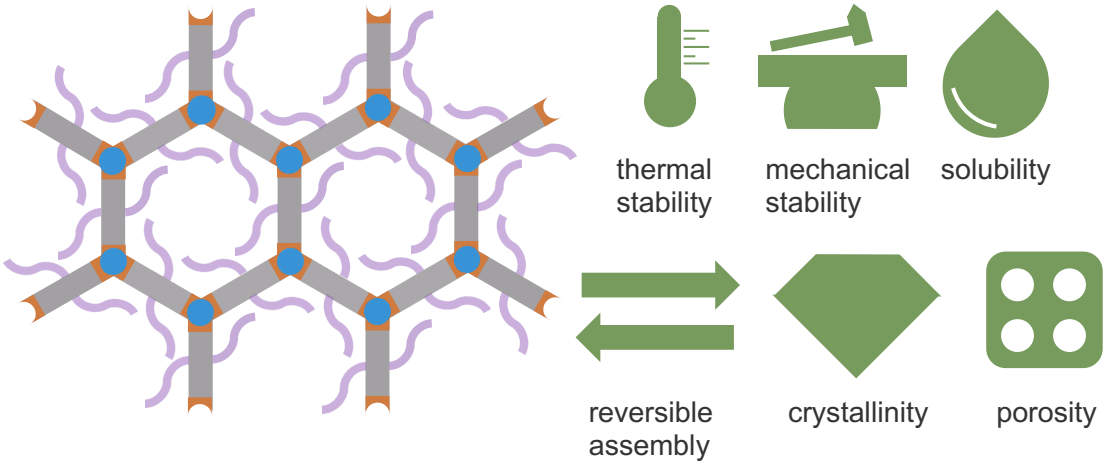

Abstract

Porous framework materials are of major importance for a wide range of technologies. Nevertheless, these compounds lack processibility as they are typically synthesized under rather harsh conditions and obtained as microcrystalline powders that cannot be coated or deposited from solution. Here, a new approach to water-processable MOF materials is presented. The design concept for such materials is based on amphiphilic organic building units, which reversibly self-assemble to a porous framework structure via interconnection with kinetically labile but strong bonding to alkali metal ions. The obtained materials are termed amphiphile salt framework (ASFs). ASFs are thermally and mechanically stable as well as porous against several gases. Importantly, the presented design concept outlines requirements on the building units which are potentially transferable to expanded as well symmetrically different amphiphilic building units. Hence, the presented ASFs represent the starting point for the initiation of a new class of solution-processable porous framework materials.

* The content of this chapter is partly comprised in the following publication: Microporous, Crystalline and Water-Processable Framework Materials of Organic Amphiphile Salts. L. Frentzel-Beyme, S. Henke. *Manuscript under preparation.* Preliminary work yielding to the results presented in this chapter was already performed during my Bachelor (2015) and Master (2017) thesis at Ruhr-University Bochum.

10.1 Introduction

10.1.1 The Search for New Porous Materials

Porous solid-state materials are essential for many technological processes in today's industrial society. Their most prominent application fields are in gas storage, separation, purification and catalysis.[213–215] On an industrial scale, conventional inorganic porous materials, such as zeolites and activated carbons, are predominantly used as they have two big advantages: low toxicity and very low cost.[31,216] Aside these conventional application fields, porous materials are also proposed to act beneficially in several emerging technologies specialized in the energy or health sector.[24,65,217–220] The requirements for this wide range of applications, however, cannot be fully covered by the state-of-the-art of porous materials.[221,222] Therefore, fundamental research on the development of new porous materials with tailored properties continues to be of high relevance.[217,223] For the precise control of the materials properties, utilization of organic building units in porous materials turned out to be particularly valuable, as the whole tableau of organic synthetic modifications can be used to implement numerous functions in the materials.[191,218,224,225]

10.1.2 PFMs vs. PMMs

In this context, academic research on porous materials containing organic building units has largely concentrated on porous framework materials (PFMs). PFMs feature robust crystalline structures with well-defined pore architectures (see Figure 10.1).[22,226] A prominent class of PFMs are MOFs.[2,227] As outlined in Section 2.1, MOFs are build from inorganic and organic building units which interact by coordination bonding forming two- or three-dimensional network structures. Further, purely organic framework compounds, such as covalent organic frameworks (COFs), are counted as PFMs.[228–230] In COFs the organic building units are linked together via strong covalent bonds (e.g. boronic esters or imines) forming porous framework structures.[228] Via the established designability concepts of reticular synthesis (see Section 2.1.3), structure and function of these materials can be tuned and tailored largely at will.[23,231]

Nevertheless, porous molecular materials (PMMs), such as polymers with intrinsic microporosity (PIMs)[190,232] but also porous organic cages (POCs)[233,234] or metal-organic cages (MOCs)[235,236] – also named coordination cages – have more recently emerged as a viable alternative for PFMs (see Figure 10.2).[217,237–239] PIMs are assemblies of 'inefficiently' backed molecules interacting by electrostatic interactions (e.g. dispersion interactions or hydrogen bonding) in the solid state, which yields cavities and thus potential void space. In POCs or MOCs, the porosity arises from

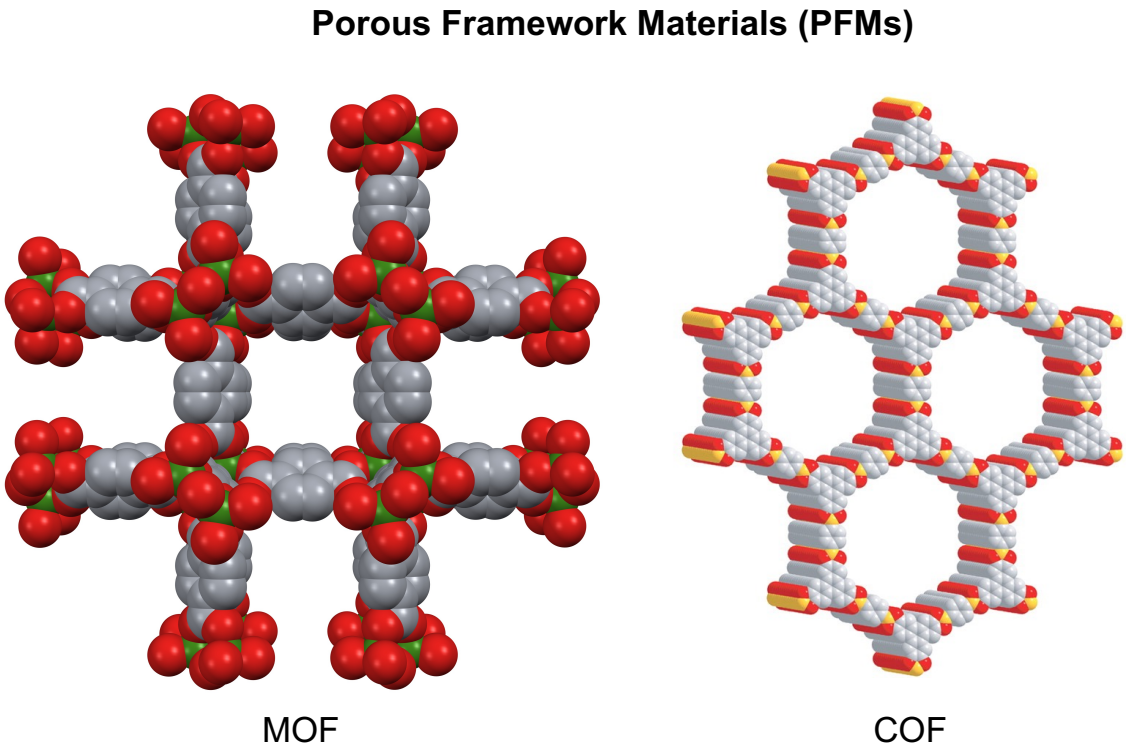

Figure 10.1: Representation of a representative materials of porous framework materials (PFMs). Left: Metal-organic framework (MOF), example MOF-5 (chemical composition $Zn_4O(bdc)_3$; bdc^{2-} = benzenedicarboxylate). Crystal structure data to generate the image were taken from the CSD[21] (MOF-5 (CSD code MIBQAR)). Right: Covalent organic framework (COF), example COF-5. (chemical composition $C_9H_4BO_4$). The image is taken from Reference [228]. Reprinted with permission from AAAS. Color code: C (gray), O (red), Zn (green), B (orange).

free void space within the discrete molecules/cages or between them. The cages can be formed from purely organics linked by covalent bonding (e.g. POCs) or inorganic and organic units interacting by coordination bonds (e.g. MOCs). In the solid state the discrete cages are interconnected mostly by electrostatic interactions.

An important conceptual advantage of PMMs is their solubility and straightforward processability from solution.[238] The weak intramolecular interactions between the porous molecules facilitate solubility and solution processability. This allows not only for simple solution casting of thin films and mixed matrix membranes, but also for increased structural and functional complexity via cocrystal formation as well as straight forward materials recycling by repeated dissolution and precipitation (idealy crystallization).[240] However, PMMs often feature only limited thermal and mechanical stability.[217] Moreover, the non-directionality of the mostly dispersive intermolecular interactions between PMMs results in a loose packing of the porous molecules in the solid-state[240] frequently causing partial loss of crystallinity or even full amorphization upon removal of solvent molecules from the pores.[217,236,238]

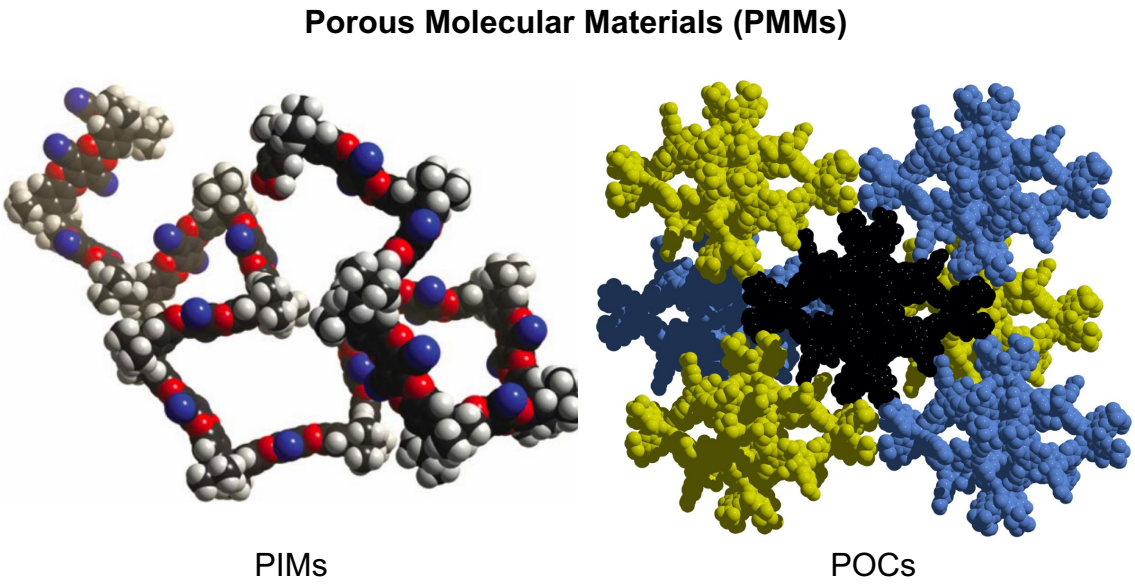

Figure 10.2: Illustration of a representative examples of porous molecular materials (PMMs). Left: Polymers of intrinsic microporosity (PIMs). Republished with permission of Royal Society of Chemistry, from Reference [190]; permission conveyed through Copyright Clearance Center, Inc. Right: Porous organic cages (POCs). Reprinted with permission from Reference [236]. Copyright 2020 American Chemical Society.

Nevertheless, highly regular materials with well-defined pore structures are especially important as porosity features (i.e. pore size, pore volume, pore aperture size and specific surface area) must be controllable for applications in gas storage/separation or molecular sieving.[13,222] Such control is achieved in PFMs which feature directive and comparably strong coordinative or even covalent intermolecular bonding.[24,229] This helps to obtain well-defined framework structures with precise pore sizes and high regularity[24,226] as well as high thermal[12] and mechanical[241] stability.

Unfortunately, for the synthesis of such framework materials energy consuming solvothermal reaction routes are commonly needed.[221] Solvent molecules – which are often required to template the porous structure[221] – are interacting strongly with the framework resulting in energy intensive activation processes (e.g. consecutive solvent exchange procedures followed by solvent removal at high temperature). Furthermore, repetitive materials recycling via disassembly and reassembly of the frameworks becomes unattractive and complex since framework dissolution is only achieved by strong changes in the pH milieu and/or high temperatures. Consequently, full reconstruction of the porous framework from solution requires repeated solvothermal synthesis, the presence of molecular templates as well as toxic, and/or corrosive solvents.

10.2 The Design Concept of ASFs

In the following, a unique class of permanently porous and water-processable MOF materials, termed amphiphile salt frameworks (ASFs), is presented. The ASFs are obtained from specifically designed amphiphilic organic building units (amphiphilic building blocks (ABBs), linkers) which assemble with alkali metal ions as inorganic building units (here Na^+ ions, nodes; see Figure 10.3) to form honeycomb-like framework structures.

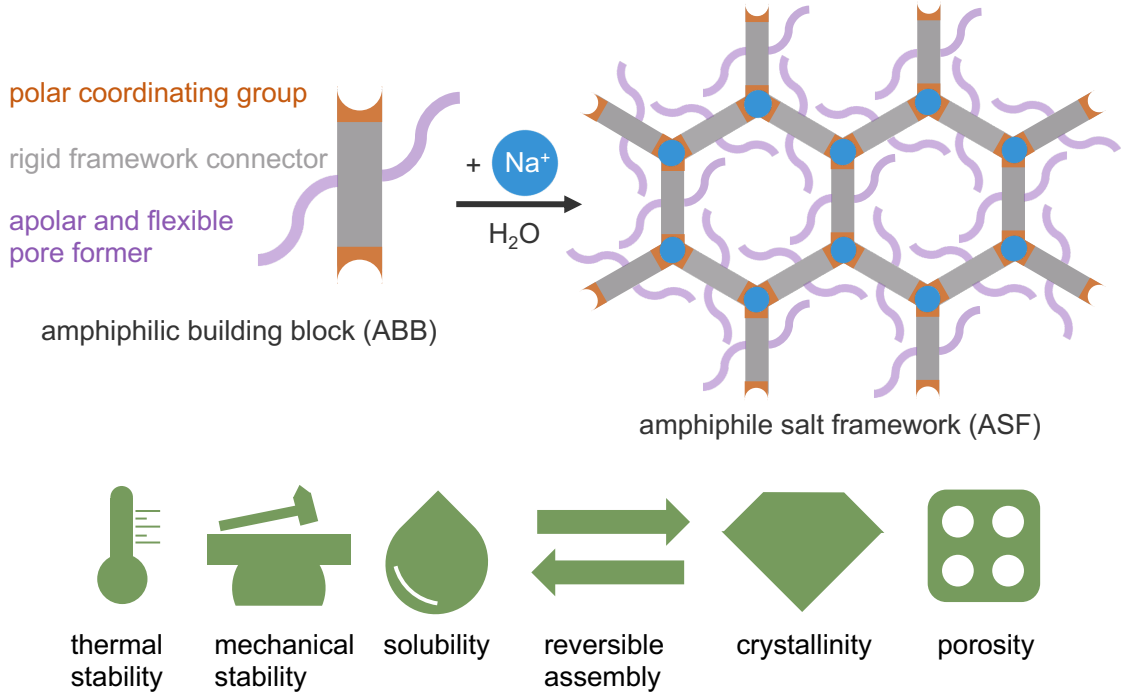

Figure 10.3: Top: Representation of the design principle for amphiphile salt frameworks (ASFs). Bottom: Pictographs of the beneficial properties of ASFs combined from PFMs and PMMs.

The ASFs can be reversibly disassembled and reassembled by dissolution in water followed by crystallization during water evaporation. Together with stability measurements regarding high temperature and high mechanical pressure as well as elaborate gas sorption measurements, it is demonstrated that ASFs combine the advantageous aspects of PFMs (rigidity, crystallinity, and thermal/mechanical stability) with those of PMMs (solubility and reversible assembly/disassembly) in a new class of framework solids (see Figure 10.3).

The design approach for reversible framework formation demands specific requirements for the coordination chemistry of the framework as well as its structure directing functionalities.
Specifically, the ABBs possess three important features (see Figure 10.3):

(i) A rigid framework connector which provides the framework with rigidity and determines the metrics of the framework assembly.

(ii) Two polar coordination groups, the hydrophilic part of the ABBs, arranged in a divergent manner to facilitate formation of an extended framework by coordination to the nodes (i.e. ions).

(iii) Two apolar and flexible pore formers, the hydrophobic part of the ABBs, which drive the assembly of the ABBs in water according to the hydrophobic effect.

The polar coordination groups of the ABBs shall coordinate to inorganic nodes to generate the framework structure. The nodes must feature the following properties:

(i) Formation of sufficiently strong coordination bonds with the coordinating group of the ABBs to support a robust framework structure.

(ii) Kinetic lability, facilitating fast ligand exchange kinetics and thus aiding a rapid assembly/disassembly of the framework.

As ABBs 2,5-dialkoxy-1,4-benzenedicarboxylic acid derivatives (H_2ABB-CX, see Figure 10.4) were chosen. In this molecules, the rigid framework connector is a benzene ring, two polar coordination groups are provided by negatively charged carboxylate groups and the two apolar and flexible pore former are alkoxy side chains. As described in the following sections, these ABBs assemble to a honeycomb-like

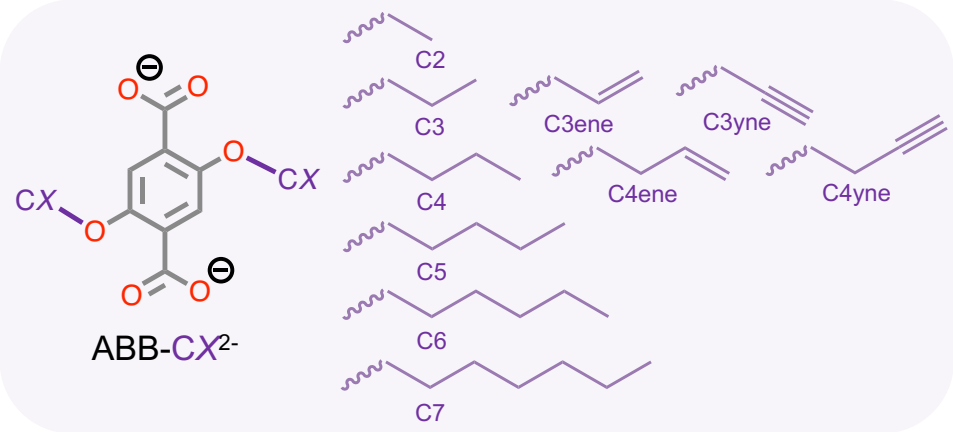

Figure 10.4: Generalized representation of the molecular structure of an amphiphilic building block (ABB-CX^{2-}) and library of utilized pore formers.

structure motif featuring porous channels when reacting with Na^+ ions (as inorganic nodes) in aqueous solution (see Figure 10.3).

10.3 Synthesis

Amphiphilic Building Blocks

Ten ABBs as 2,5-dialkoxy-1,4-benzenedicarboxylic acid derivatives (H_2ABB-CX) were synthesized following modified literature protocols (see Section 12.9.2 for the detailed synthesis protocols).[242] In the first reaction step, 2,5-dihydroxy-1,4-benzenedicarboxylic acid was converted to the corresponding dimethyl ester to protect the acidic carboxylate groups (see Figure 10.5; yellow box). Subsequently, the obtained dimethyl 2,5-dihydroxy-1,4-benzenedicarboxylate was used as the starting material to conduct either a Williamson[243] (Figure 10.5; green box) or Mitsunobu[244] etherification (Figure 10.5; blue box). In this step, the pore formers were added to the molecule either utilizing the corresponding alkyl halide (Williamson etherification) or alkyl alcohol (Mitsunobu etherification). Cleavage of the esters groups under basic condition and subsequent acidification yields the different H_2ABB-CX acid derivatives.

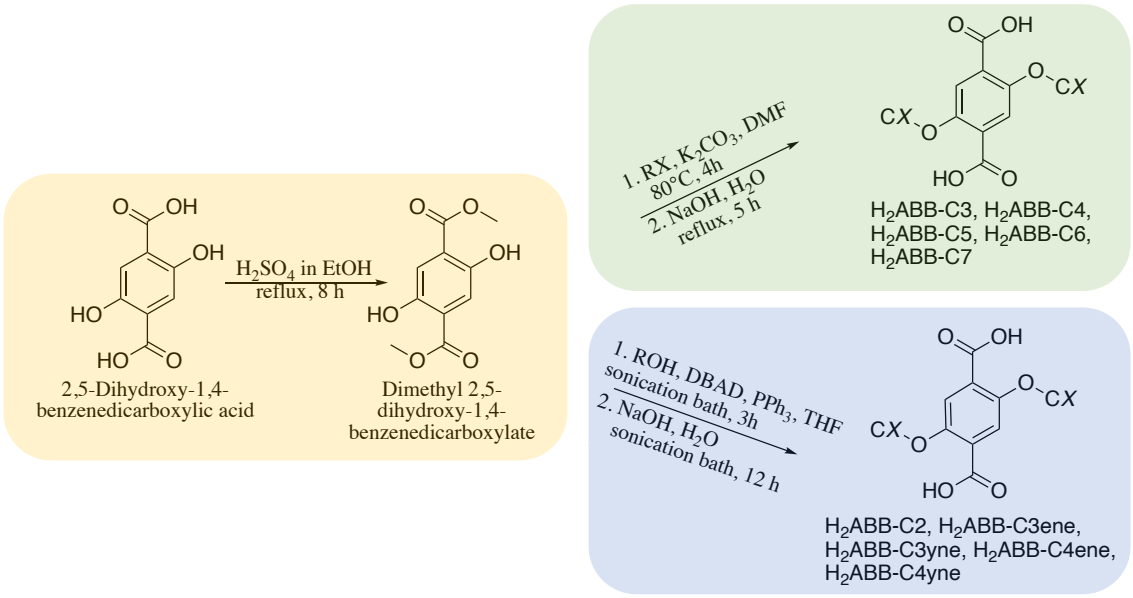

Figure 10.5: Reaction scheme for the synthesis of ABBs. Yellow box: Esterification. Green box: Williamson etherification. Blue box: Mitsunobu etherification. Abbreviations: RX = alkyl halide; ROH = alkyl alcohol; DBAD = diisobutyl azodicarboxylate; PPh_3 = triphenylphospine.

These H_2ABB-CX derivatives differ in the number of carbon atoms (CX = C2 − C7) of the pore forming alkoxy chains (see Figure 10.4). Additionally, for C3 and C4 variants with terminal double (denoted C3ene and C4ene) or triple bonds (denoted C3yne and C4yne) are included.

The purity of all H_2ABB-CX derivatives was verified by ^{1}H and ^{13}C NMR spectroscopy (see Section 12.9.2).

Amphiphile Salt Frameworks

The ASFs of the typical chemical formula Na_2(ABB-CX) were prepared using several different procedures (see Section 12.9.2 for detailed synthesis protocols). The two procedures most important for the upcoming discussion are shortly summarized below.

Solvothermal Synthesis

Slow solvothermal crystallization of the ABBs with sodium acetate was performed in a mixture of water, ethanol and DMF at 120 °C to obtain large single crystals (sizes up to 100 μm or more) suitable for structure determination via SCXRD.

Evaporation Synthesis

Microcrystalline powders were obtained by dissolution of the ABBs in aqueous sodium hydroxide (NaOH) solution followed by evaporation of the water under reduced pressure at 80 °C using a rotary evaporator (method evap-a) or from an open vessel at 50 °C in an oven (method evap-b).

10.4 Structural Characterization

10.4.1 Two Porous ASF Structure Types – ASF-1 and ASF-2

The ASFs with CX = C3, C3ene, C3yne, C4, C4ene, C4yne, C5 and C6 are crystallizing in 3D honeycomb-like microporous frameworks with trigonal space groups ($R\bar{3}$; $R\bar{3}c$, $P3_1$). The frameworks exhibit the general chemical composition Na_2(ABB-CX), except for ABB-C6^{2-} which yields a material of the composition Na_2(ABB-C6)$(H_2O)_{0.5}$ (see Table 10.2 – 10.4 for crystallographic data). Depending on the length and flexibility of the respective pore former two different honeycomb-like structure types were found denoted ASF-1(CX) (for CX = C3, C3ene, C3yne, C4, C4ene, C4yne) and ASF-2(CX) (for CX = C4, C5, C6) (see Figure 10.6).*

The framework formation is driven by a micellar aggregation of the amphiphilic building blocks controlled by their hydrophobic alkyl chains (pore formers) which are lining the porous channels of the honeycomb-like structure motifs.

In the ASF-1 structure type off-center parallel stacking of adjacent ABBs is found pointing towards attractive π-π-interactions between the benzene rings stabilizing this structure motif with shorter pore formers (see Figure 10.6 bottom).[245,246] On the

* Notably, both structure types are obtained with ABB-C4^{2-}. A deeper discussion on this topic is given in Section 10.4.2.

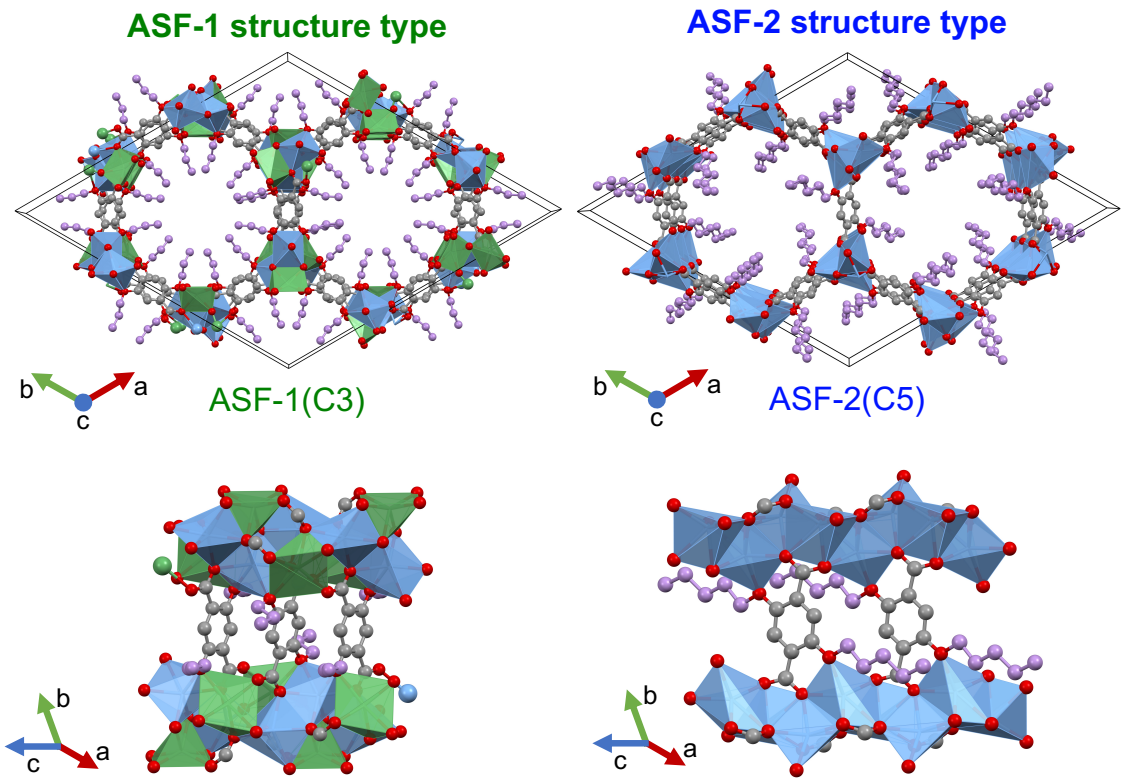

Figure 10.6: Representation of the ASF-1 structure type exemplary for ASF-1(C3) and the ASF-2 structure type exemplary for ASF-2(C5). Top: View along the crystallographic *c* axis visualizing the honeycomb-like structure motif. Bottom: View parallel to the crystallographic *c* axis representing the packing of the ABBs between adjacent Na^+ helices. Color code: Na (blue/green), C (gray/purple), O (red). Hydrogen atoms are omitted for clarity. Coordination environments of Na^+ are shown as blue or green polyhedra.

contrary, in the ASF-2 structure type a total offset of adjacent ABBs (benzene rings) is found resulting from the more sterically demanding pore formers (ABB-C5^{2-} and ABB-C6^{2-}) preventing such favorable stacking. Consequently, shorter alkyl groups (ASF-1 structure type) allow for a much denser packing of the amphiphilic building units (ASF-1 approximate 2.58 ABBs nm^{-3}; ASF-2 approximate 1.85 ABBs nm^{-3}) which overall results in a higher density of ASF-1 materials ($\rho \approx 1.28 - 1.48$ g cm^{-3}) compared to the ASF-2 materials ($\rho \approx 1.17 - 1.28$ g cm^{-3}).

The rigid part of the ABBs (framework connector) forms the edges of the honeycomb (see Figure 10.6). Based on this arrangement the carboxylate groups are clustering around the vertices of the honeycomb where they are coordinating to Na^+ ions. The Na^+ ions are six-fold coordinated by O atoms from the ABBs forming helical chains of [NaO_6] coordination polyhedra running parallel to the crystallographic *c* axes. As a result of the denser packing of the ABBs in ASF-1, the [NaO_6] helix is decorated by surrounding Na^+ ions (highlighted with green polyhedra in Figure 10.6).

The precise coordination environment of the Na^+ ions is best visualized by looking at the asymmetric units of both structure types (see Figure 10.7). The asymmetric unit of the ASF-1 structure type consists of two independent Na^+ ions (Na1 and Na2) and one-half of a deprotonated ABB. In the extended asymmetric unit, both sodium atoms are six-fold coordinated by oxygen atoms of the ABBs. Na1 is coordinated by five carboxylate oxygen atoms and one ether oxygen atom of the ABBs. Na2 is coordinated by four carboxylate oxygen atoms and two ether oxygen atoms.

The asymmetric unit of the ASF-2 structure type consists of only one Na^+ ion (Na1) but also one-half of a deprotonated ABB. Na1 is also six-fold coordinated, whereas coordination occurs via five carboxylate oxygen atoms and one ether oxygen atom.

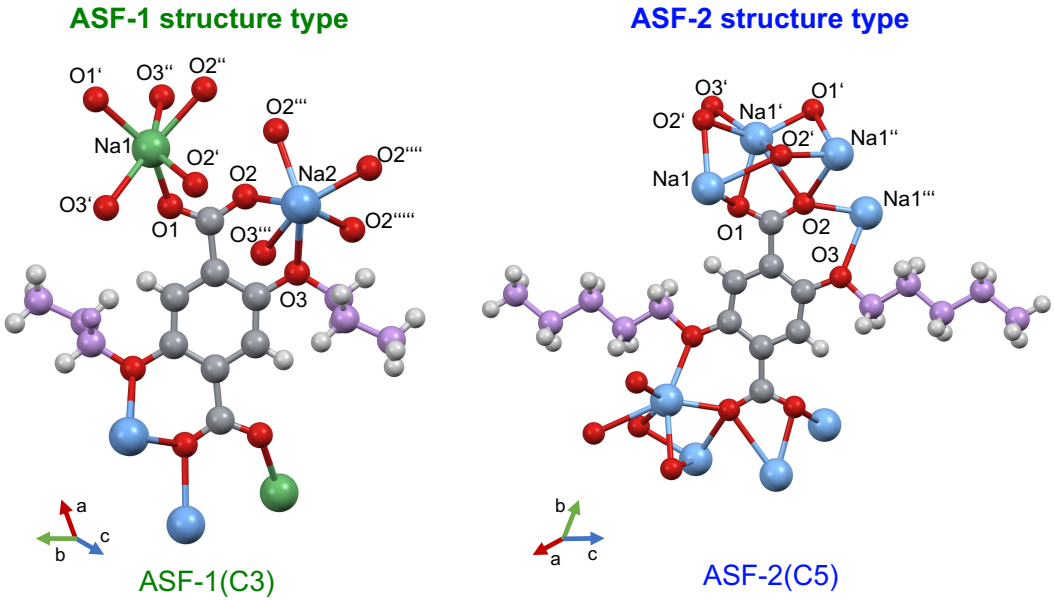

Figure 10.7: Representation of the extended asymmetric units of the ASF-1 structure type (exemplary for ASF-1(C3); left) and the ASF-2 structure type (exemplary for ASF-2(C5), right). Symmetry equivalent atoms are marked with primes (’). Color code: Na (blue/green), C (gray/purple), O (red), H (white). Partial disorder of carbon and hydrogen atoms in the pore former of ASF-2(C5) was removed for clarity.[a]

a H7BC, H7BD, C8B, H8BA, H8BB, C9B, H9BA, H9B and H9BC removed (see *.cif for atom label assignments).

In the honeycomb-like structure motifs, the hydrophobic alkyl chains point inside the one-dimensional channels driving the assembly of the structure. Thus, depending on the length of the alkyl chains the pore size and void fraction of the ASFs drastically varies (see Figure 10.8). The crystallographic void fractions amount to only 2.5% for ASF-2(C6) but increases to 20.5% for ASF-1(C3ene).

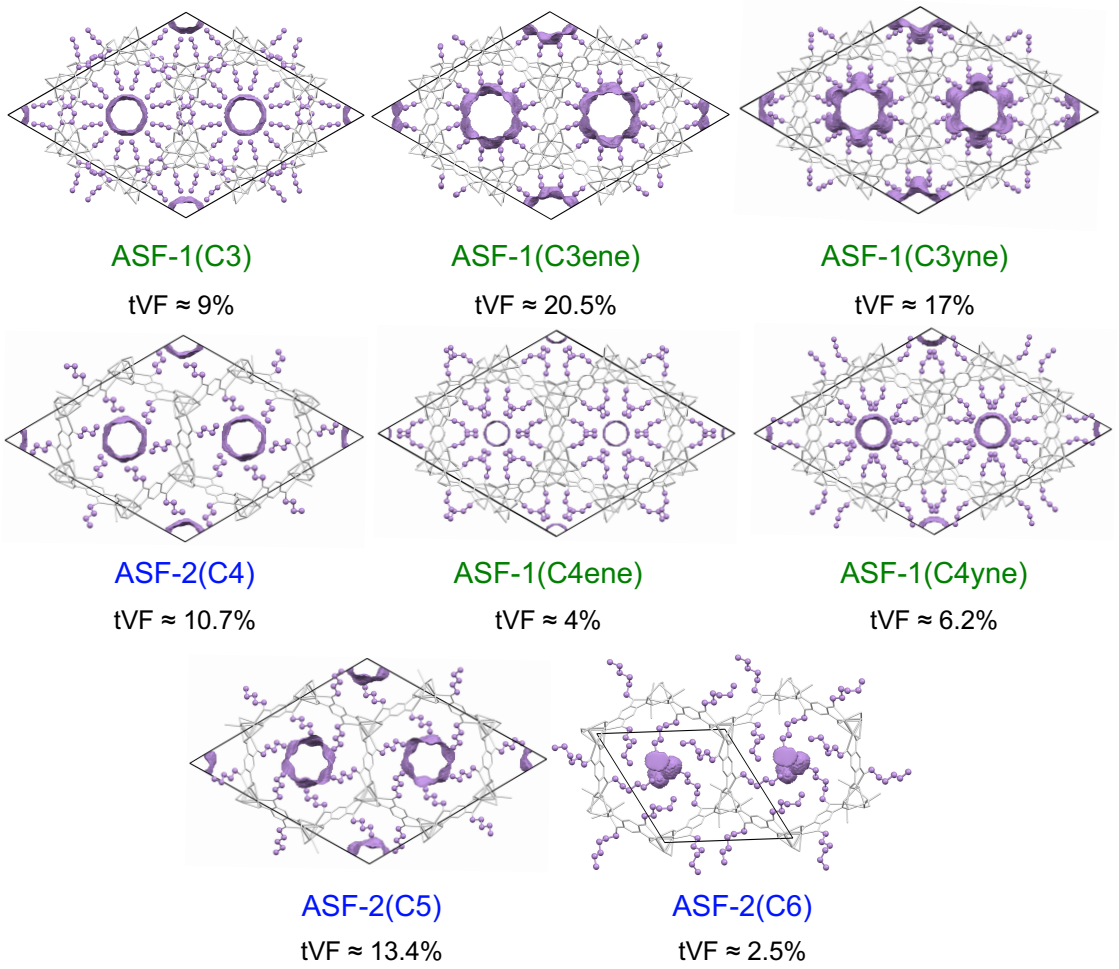

Figure 10.8: Graphical representations of the crystal structures with theoretical void fractions (tVFs[a]; purple) of ASFs. Crystal structures are viewed along the crystallographic *c* axis. All atoms are colored gray (style: wireframe) except for the pore formers highlighted in purple color (style: ball and stick). For ASF-1(C3ene)[b], ASF-1(C4ene)[c], ASF-1(C4yne)[d], ASF-2(C5)[e] and ASF-2(6)[f], various atoms of the pore formers are found disordered. Only two pore formers per ABB were considered for the calculations, the other partially occupied atoms were removed from the structural models. The removed atoms are specified in the footnotes (see *.cif for atom label assignments).

a The tVFs were calculated with the implemented routine in Olex2[48] applying a probe radius of 1.3 Å and grid spacing of 0.2 Å.
b C7B, H7BA, H7BB and H6B removed.
c H6AA, H6AB, H6CE, H6CF, C7B, H7B, C7C, H7C, C8B, H8BA, H8BB, C8C, H8CA and H8CB removed.
d C7B, C8B, H8B, H6BA and H6BB removed.
e H7BC, H7BD, C8B, H8BA, H8BB, C9B, H9BA, H9B and H9BC removed.
f H7BC, H7BD, C8B, H8BA, H8BB, H9BC, H9BD, C10A, H10A, H10B, H10C, H15C, H15D, C16B, H16C, H16D, C17B, H17C, H17D, C18B, H18C, H18D, C19B, H19C, H19D, C20B, H20D, H20E and H20F removed.

The unsaturated terminal bonds (double or triple) of some pore formers influence their flexibility and conformation, resulting in different pore shapes. In addition, the

triple and double bonds are located on the pore surface where they may affect the surface properties (e.g. towards adsorption of gases).

For the SCXRD measurements, the ASF single crystals were directly picked from the mother liquor. For most PFMs, such as MOFs or zeolites, residual electron density is often found in their pores. Such density is ascribed to solvent molecules or ions from the synthesis necessary to template the porous framework or even direct the structure formation. Remarkably, according to SCXRD data only for four ASFs (ASF-1(CX) (CX = 3, 4yne) and ASF-2(CX) (CX = 4, 5)) residual electron density is found in their hydrophobic pores (electrons per void $\approx 31 - 47$, equals about $0.14 - 0.40$ DMF molecules per formular unit; see Table 10.1). This rather small amount, which is only found for these four ASFs, suggests that a templating by solvent molecules is not necessary to achieve the porous framework structure of ASFs. However, for ASF-2(C5) (n_{DMF} per formula unit ≈ 0.40) a structural directing effect cannot be entirely excluded.

Table 10.1: Determined void volume (V_{void}) and number of electrons ($n_{\mathrm{e^-}}$) per void, utilizing the squeezing routine[247] while data refinement (see Section B.1.1 for further details). Based on this values the number of DMF molecules (n_{DMF}) per void and formula unit have been calculated.

Compound	V_{void} / Å^3	Number of voids	n_{e} per void	n_{DMF} per void	n_{DMF} per formula unit
ASF-1(C3)	222.2	3	34.0	0.85	0.14
ASF-2(C4)	153.0	3	31.3	0.78	0.26
ASF-1(C4yne)	121.1	3	32.2	0.81	0.14
ASF-2(C5)	203.5	3	47.4	1.19	0.40

Table 10.2: Crystallographic data for ASF-1(C3), ASF-1(C3ene) and ASF-1(C3yne) obtained from SCXRD.

Compound	ASF-1(C3)	ASF-1(C3ene)	ASF-1(C3yne)
Empirical formula	$C_{14}H_{16}Na_2O_6$	$C_{14}H_{12}Na_2O_6$	$C_{14}H_8Na_2O_6$
Formula weight / g mol^{-1}	326.25	322.22	318.18
Temperature / K	100.0	120.00(10)	100.0
Crystal system	trigonal	trigonal	trigonal
Space group	$R\bar{3}c$	$R\bar{3}c$	$R\bar{3}c$
a / Å	31.559(3)	31.6035(9)	31.6582(16)
b / Å	31.559(3)	31.6035(9)	31.6582(16)
c / Å	8.1020(15)	8.1711(2)	8.0420(4)
α / Å	90	90	90
β / Å	90	90	90
γ / Å	120	120	120
V / Å^3	6988.4(18)	7067.7(4)	6980.2(8)
Z	18	18	18
ρ_{calc} / g cm^{-3}	1.395	1.363	1.362
μ / mm^{-1}	0.154	1.368	1.384
F(000)	3060.0	2988.0	2916.0
Crystal size / mm^3	0.367 × 0.054 × 0.044	0.1307 × 0.0819 × 0.0264	1.363 × 0.109 × 0.054
Radiation	MoK_α (λ = 0.71073)	CuK_α (λ = 1.54178)	CuK_α (λ = 1.54178)
2Θ range for data collection / °	4.47 to 65.406	9.694 to 152.45	13.938 to 155.948
Index ranges	-12 ≤ h ≤ 47, -46 ≤ k ≤ 17, -11 ≤ l ≤ 9	-39 ≤ h ≤ 35, -38 ≤ k ≤ 39, -10 ≤ l ≤ 8	-29 ≤ h ≤ 33, -37 ≤ k ≤ 34, -10 ≤ l ≤ 10
Reflections collected	8043	11091	11076
Independent reflections	2639 [R_{int} = 0.0697, R_{sigma} = 0.0950]	1644 [R_{int} = 0.0531, R_{sigma} = 0.0246]	1656 [R_{int} = 0.0318, R_{sigma} = 0.0205]
Data/restraints/parameters	2639/0/102	1644/1/110	1656/0/101
Goodness-of-fit on F^2	1.021	1.121	1.077
Final R indexes [$I \geq 2\sigma$ (I)]	R_1 = 0.0616, wR_2 = 0.1191	R_1 = 0.0468, wR_2 = 0.1009	R_1 = 0.0357, wR_2 = 0.1113
Final R indexes [all data]	R_1 = 0.1151, wR_2 = 0.1381	R_1 = 0.0520, wR_2 = 0.1037	R_1 = 0.0375, wR_2 = 0.1136
Largest diff. peak/hole / e Å^{-3}	0.43/-0.35	0.27/-0.30	0.30/-0.27

Table 10.3: Crystallographic data for ASF-2(C4), ASF-1(C4ene) and ASF-1(C4yne) obtained from SCXRD.

Compound	ASF-2(C4)	ASF-1(C4ene)	ASF-1(C4yne)
Empirical formula	$C_{16}H_{20}Na_2O_6$	$C_{16}H_{16}Na_2O_6$	$C_{16}H_{12}Na_2O_6$
Formula weight / g mol^{-1}	354.30	350.27	346.24
Temperature / K	100(2)	100(2)	100.0
Crystal system	trigonal	trigonal	trigonal
Space group	$R\bar{3}$	$R\bar{3}c$	$R\bar{3}c$
a / Å	28.871(3)	31.6044(13)	31.668(4)
b / Å	28.871(3)	31.6044(13)	31.668(4)
c / Å	5.7230(7)	8.1966(5)	8.1049(7)
α / Å	90	90	90
β / Å	90	90	90
γ / Å	120	120	120
V / Å^3	4131.2(9)	7090.2(7)	7039.2(17)
Z	9	18	18
ρ_{calc} / g cm^{-3}	1.282	1.477	1.470
μ / mm^{-1}	0.136	0.158	0.158
F(000)	1674.0	3276.0	3204.0
Crystal size / mm^3	0.997 × 0.078 × 0.049	0.531 × 0.142 × 0.099	0.83 × 0.071 × 0.049
Radiation	MoK$_\alpha$ (λ = 0.71073)	MoK$_\alpha$ (λ = 0.71073)	MoK$_\alpha$ (λ = 0.71073)
2Θ range for data collection / °	7.304 to 58.994	4.464 to 61.138	4.456 to 59.484
Index ranges	-24 ≤ h ≤ 36, -39 ≤ k ≤ 34, -6 ≤ l ≤ 7	-44 ≤ h ≤ 44, -44 ≤ k ≤ 42, -11 ≤ l ≤ 11	-34 ≤ h ≤ 42, -41 ≤ k ≤ 40, -10 ≤ l ≤ 11
Reflections collected	4789	30709	15414
Independent reflections	2257 [R_{int} = 0.0315, R_{sigma} = 0.0482]	2360 [R_{int} = 0.0806, R_{sigma} = 0.0365]	2069 [R_{int} = 0.0457, R_{sigma} = 0.0270]
Data/restraints/parameters	2257/0/110	2360/24/134	2069/36/137
Goodness-of-fit on F^2	1.018	1.154	1.080
Final R indexes [$I \geq 2\sigma$ (I)]	R_1 = 0.0388, wR_2 = 0.0845	R_1 = 0.0550, wR_2 = 0.1311	R_1 = 0.0662, wR_2 = 0.1635
Final R indexes [all data]	R_1 = 0.0603, wR_2 = 0.0921	R_1 = 0.0749, wR_2 = 0.1400	R_1 = 0.0790, wR_2 = 0.1704
Largest diff. peak/hole / e Å^{-3}	0.37/-0.25	0.40/-0.34	0.58/-0.47

Table 10.4: Crystallographic data for ASF-2(C5) and ASF-2(C6) obtained from SCXRD.

Compound	ASF-2(C5)	ASF-2(C6)
Empirical formula	$C_{18}H_{24}Na_2O_6$	$C_{20}H_{29}Na_2O_{6.5}$
Formula weight / g mol^{-1}	382.35	419.41
Temperature / K	100.0	100.0
Crystal system	trigonal	trigonal
Space group	$R\bar{3}$	$P3_1$
a / Å	30.449(3)	17.4718(17)
b / Å	30.449(3)	17.4718(17)
c / Å	6.0563(6)	6.2180(6)
α / Å	90	90
β / Å	90	90
γ / Å	120	120
V / Å^3	4862.7(11)	1643.8(4)
Z	9	3
ρ_{calc} / g cm^{-3}	1.175	1.271
μ / mm^{-1}	1.062	1.108
F(000)	1818.0	669.0
Crystal size / mm^3	0.133 × 0.06 × 0.052	0.696 × 0.061 × 0.054
Radiation	CuK$_\alpha$ (λ = 1.54178)	CuK$_\alpha$ (λ = 1.54178)
2Θ range for data collection / °	5.804 to 138.018	5.84 to 145.138
Index ranges	-36 ≤ h ≤ 33, -36 ≤ k ≤ 36, 0 ≤ l ≤ 7	-21 ≤ h ≤ 21, -21 ≤ k ≤ 21, -7 ≤ l ≤ 7
Reflections collected	1893	4167
Independent reflections	1893 [R_{int} = –, R_{sigma} = 0.1369]	4167 [R_{int} = –, R_{sigma} = 0.1009]
Data/restraints/parameters	1893/6/139	4167/143/319
Goodness-of-fit on F^2	1.115	1.030
Final R indexes [$I \geq 2\sigma$ (I)]	R_1 = 0.0965, wR_2 = 0.1690	R_1 = 0.0592, wR_2 = 0.1297
Final R indexes [all data]	R_1 = 0.1765, wR_2 = 0.2155	R_1 = 0.0756, wR_2 = 0.1382
Largest diff. peak/hole / e Å^{-3}	0.45/-0.58	0.31/-0.35
Flack parameter	–	0.30(8)

10.4.2 Activation and Phase Analysis

For further characterization, all as-synthesized ASFs have been treated at elevated temperature (100 °C) and pressure yielding the activated/solvent-free compounds (see Section 12.9.2 for the detailed experimental protocol). Activation of the materials was verified by the absence of vibrational bands ascribed to solvent molecules from the synthesis (e.g. on the surface or pore) in FTIR spectroscopy data (see Figure 10.9). None of the datasets shows a broad band at $3200 - 3500\,\mathrm{cm^{-1}}$ which could be ascribed to the O−H stretching mode of water or ethanol, or a vibrational band at $1675\,\mathrm{cm^{-1}}$, characteristic for the carbonyl stretching vibration of DMF.

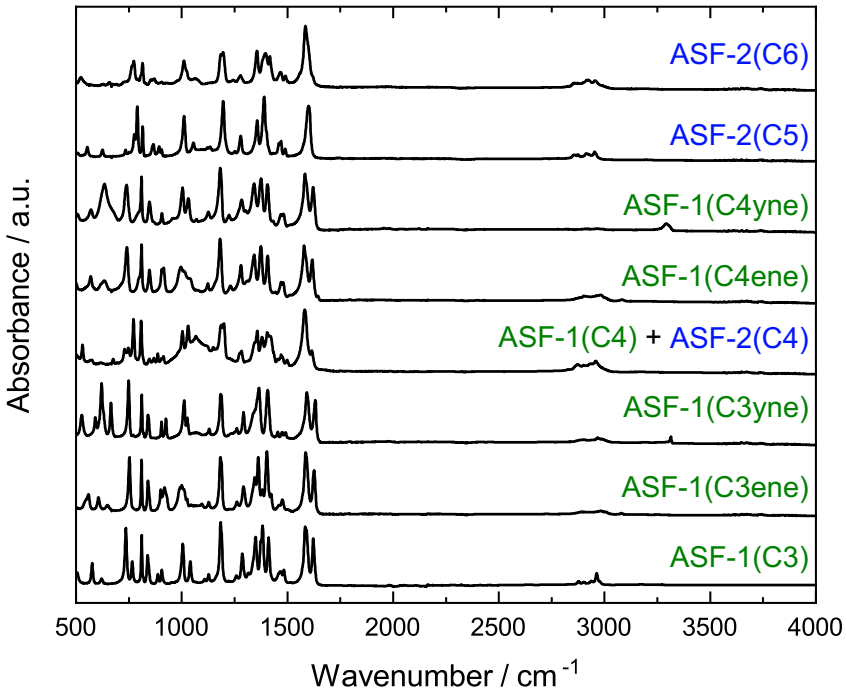

Figure 10.9: Stack plot of FTIR spectroscopy data for ASFs derived via solvothermal synthesis after activation. The spectra are normalized and vertically offset for clarity.

The activated materials have been further structurally analyzed by structureless profile fits (Pawley method)* to PXRD data starting with appropriate parameters obtained from SCXRD analyses (see Section B.1.2). The formation of phase pure ASFs is proven for the materials obtained after the solvothermal synthesis route except for H_2ABB-C4. Here, a phase mixture of the ASF-1 and ASF-2 structure type is found, verified by a dual-phase profile fit of the PXRD pattern (see Figure 10.10).

∗ Details about the phase identification by structureless profile fits can be found in Section 3.1.5.

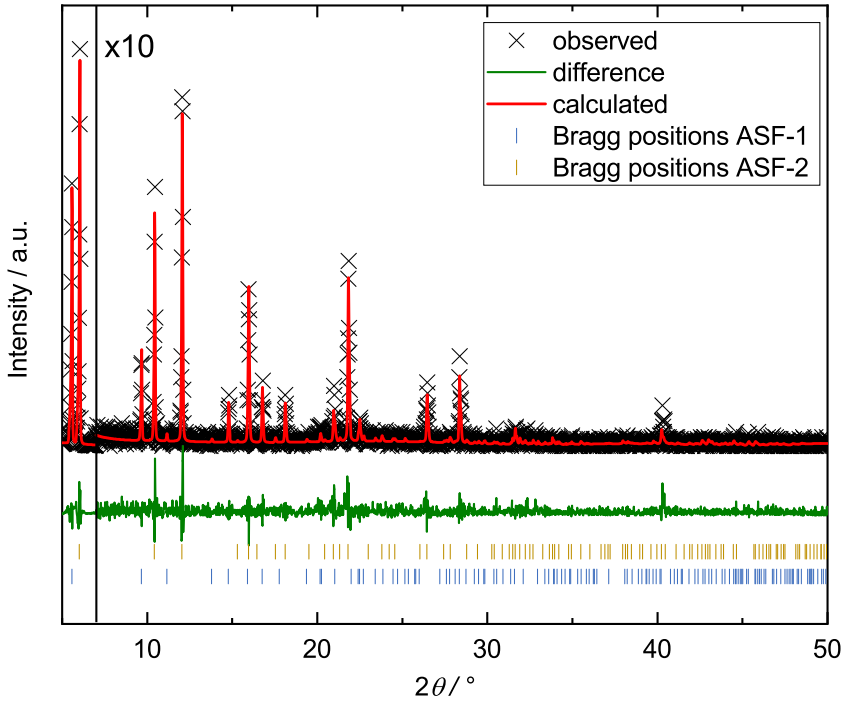

Figure 10.10: Plot of dual-phase profile fit to the PXRD data of the material obtained after conducting the solvothermal synthesis route with H_2ABB-C4. The formation of the ASF-1 and ASF-2 structure type is verified.

Table 10.5: Unit cell parameters determined by the above displayed structureless profile fits (Pawley method) of the obtained PXRD patterns and corresponding R_{wp}, R_{exp} and χ values.

Pawley fit	Figure 10.10	
Compound	ASF-1(C4)	ASF-2(C4)
crystal system	trigonal	trigonal
space group	$R\bar{3}c$	$R\bar{3}$
a / Å	31.721(5)	29.371(3)
b / Å	31.721(5)	29.371(3)
c / Å	8.1633(19)	5.943(2)
α / °	90	90
β / °	90	90
γ / °	120	120
V / Å^3	7114(3)	4440.2(17)
R_{wp} / %	32.96	
R_{exp} / %	26.59	
χ	1.24	

Unfortunately, by selecting several single crystals from the reaction mixture only crystals of the ASF-2 structure type were found for SCXRD experiments. Strikingly,

the reduced cell volume (V_{red})* of ASF-2(C4) (V_{red}(ASF-2(C4)) = 459 Å^3) is smaller than those of the other ASF-2 materials (V_{red}(ASF-2(C5) = 540.3 Å^3 and V(ASF-2(C6) = 547.9 Å^3). Thus, the length of the pore former also influences the metric of the porous channels within an ASF structure type.

Remarkably, utilizing H_2ABB-4ene and H_2ABB-4yne in the solvothermal synthesis yielded phase pure materials of the ASF-1 structure type. Here, the impact of the length and flexibility of pore former on the obtained structure type becomes evident. The steric demand and flexibility of the C4 side chain of ABB-C4^{2-} appears to define the border for the formation of either the ASF-1 or ASF-2 structure type.

10.4.3 Densely Packed ASFs

A short chain of only two carbon atoms as the pore former (H_2ABB-C2) generates an ASF material named ASF-3(C2). ASF-3(C2) crystallizes in a triclinic lattice (space group $P\bar{1}$) featuring a three-dimensionally connected densely packed crystal structure (see Figure 10.11 and Table 10.6 for crystallographic data). The chemical

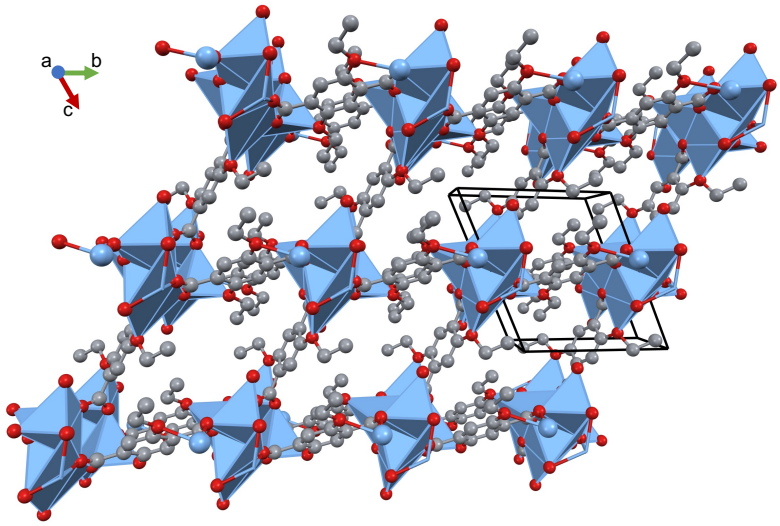

Figure 10.11: Representation of the extended crystal structure of ASF-3(C2). Viewed along the crystallographic a axis. The crystallographic unit cell is shown as black lines. Color code: Na (blue); O (red); C (gray). Hydrogen atoms are omitted for clarity. Coordination environments of Na$^+$ are displayed as blue polyhedra.

composition of the compound is Na_2ABB-C2. In the crystal structure, all O atoms of the ABB coordinate to Na$^+$ ions. Overall, all Na$^+$ ions are six-fold coordinated by O atoms of ABB-C2^{2-} forming [NaO_6] coordination polyhedra. The [NaO_6] coordination polyhedra form chains running along the crystallographic a axis. These chains are linked in the $b-c$ plane by the ABBs in a rhombic arrangement, leaving

* The reduced cell volume is defined as V/Z. Unit cell volume devided by formular unit. The values are taken from the SCXRD experiments.

the material non-porous. Strikingly, a similar change from a hexagonal to a rhombic arrangement of building units by shortening the length of the structure directing side chains has also been observed for amphiphilic liquid crystals in the literature.[248]

Table 10.6: Crystallographic data for ASF-3(C2) obtained from SCXRD.

Compound	ASF-3(C2)
Empirical formula	$C_{12}H_{12}Na_2O_6$
Formula weight / g mol^{-1}	298.20
Temperature / K	100(2)
Crystal system	triclinic
Space group	$P\bar{1}$
a / Å	6.4726(5)
b / Å	9.9134(11)
c / Å	11.1033(12)
a / Å	63.781(11)
β / Å	77.534(8)
γ / Å	76.668(8)
V / Å^3	616.60(12)
Z	2
ρ_{calc} / g cm^{-3}	1.606
μ / mm^{-1}	0.186
F(000)	308.0
Crystal size / mm^3	0.284 × 0.086 × 0.072
Radiation	MoK$_\alpha$ (λ = 0.71073)
2Θ range for data collection / °	4.636 to 65.084
Index ranges	-9 ≤ h ≤ 9, -14 ≤ k ≤ 14, -16 ≤ l ≤ 15
Reflections collected	8507
Independent reflections	4041 [R_{int} = 0.0543, R_{sigma} = 0.0907]
Data/restraints/parameters	4041/0/183
Goodness-of-fit on F^2	1.109
Final R indexes [$I \geq 2\sigma$ (I)]	R_1 = 0.0738, wR_2 = 0.1687
Final R indexes [all data]	R_1 = 0.1227, wR_2 = 0.1972
Largest diff. peak/hole / e Å^{-3}	0.75/-0.42

An increase of the chain lengths to seven carbon atoms (H_2ABB-C7) leads to a microcrystalline powder with a diffraction pattern that does neither match the ASF-1 nor the ASF-2 structure type (see Figure 10.12). Given that the pore space available in the ASF-2(C6) is already very small (tVF = 2.5%), the bulk of the C7 chain is too large to support the formation of a honeycomb-like ASF structure. Unfortunately, the growth of single crystals of Na_2(ABB-C7) large enough for SCXRD was unsuccessful, so that the structure of this material could not be resolved.

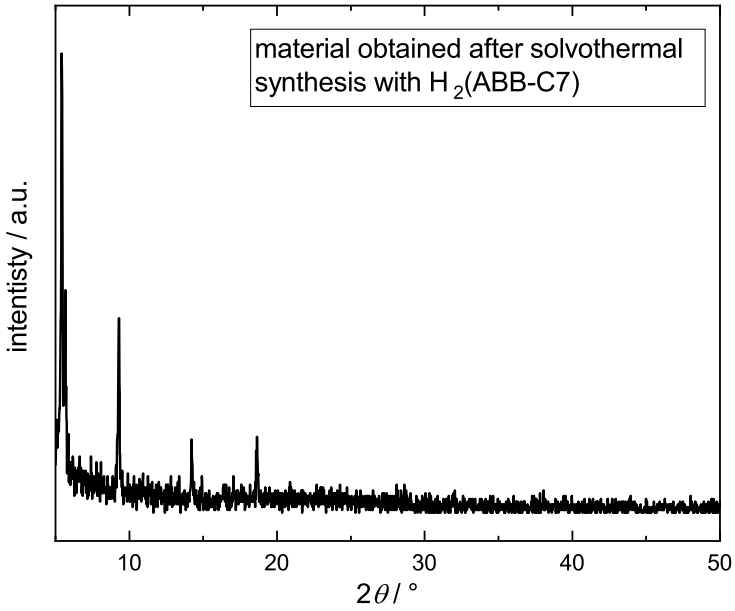

Figure 10.12: PXRD pattern obtained after the solvothermal synthesis with H_2(ABB-C7).

10.5 Rapid Formation and Processing of ASFs

10.5.1 ASF Formation from Water

As postulated by the design strategy, ASFs can be also crystallized from an aqueous solution of a chosen H_2ABB-CX derivative and NaOH. Polycrystalline powders were obtained by evaporating the water to dryness on a rotary evaporator at 80 °C (evap-a). PXRD data of the derived microcrystalline powders demonstrates the formation of the respective ASFs structure type (see Figure 10.13).

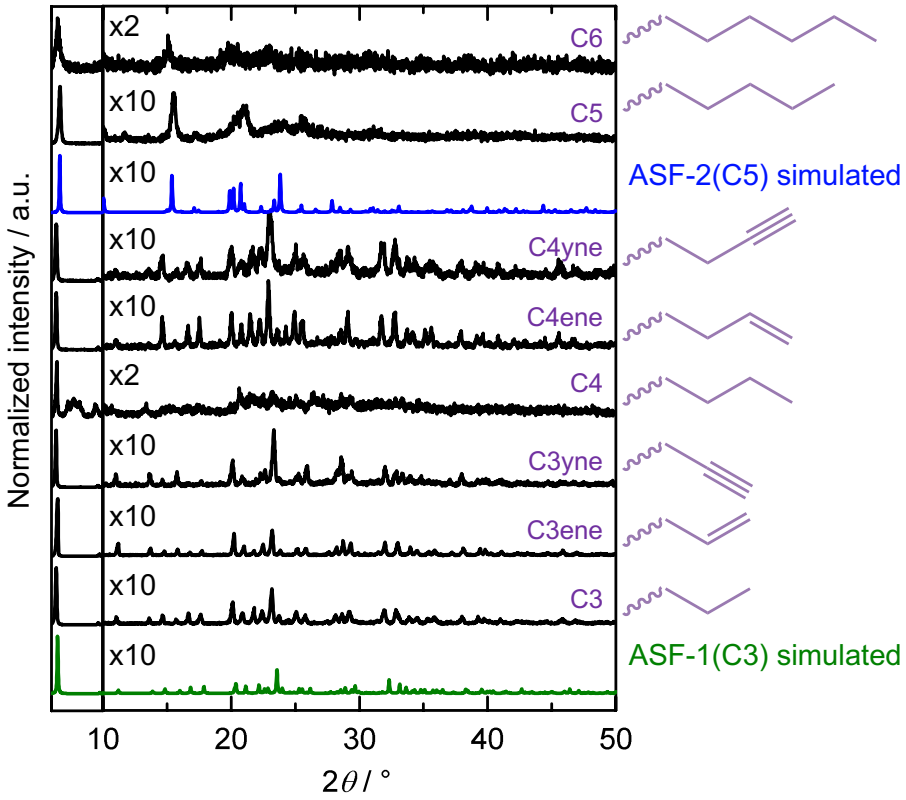

Figure 10.13: Stack plot of PXRD patterns obtained after the evaporation synthesis route (evap-a). The pore former (CX) attached to the ABB applied in the synthesis is shown on the right. Simulated PXRD patterns for ASF-1(C3) and ASF-2(C5) are displayed for comparison. The patterns are normalized and vertically offset for clarity.

Additionally, structureless profile fits (Pawley method) to the PXRD data confirm the formation of mostly phase pure ASFs via this route (see Section B.1.2 for profile fits). The only exception is found by conducting the evap-a synthesis protocol with H_2ABB-C4. Conducting the solvothermal synthesis route with this linker yielded a phase mixture of the ASF-1 and ASF-2 structure type (see Figure 10.10). The structureless profile fits to the PXRD data (evap-a) starting either with parameters of the ASF-1 or ASF-2 structure type were unsuccessful. Indeed, by comparing the PXRD pattern visually to simulated pattern for either the ASF-1 or ASF-2 structure type, it becomes obvious that a slightly different pattern is obtained (see Figure

10.14). Nevertheless, the visual comparison suggests that a slightly different but ASF-1- or ASF-2-like structure is formed, at least in parts. It is again demonstrated that the pore fomers have a major influence on the structure formation.

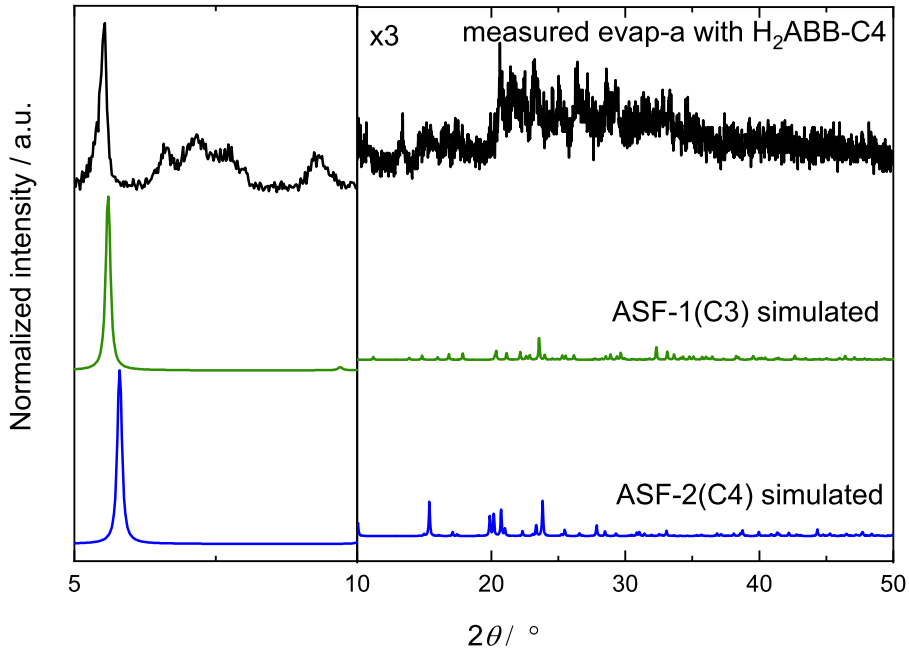

Figure 10.14: Stack plot of PXRD data obtained after the evaporation synthesis (evap-a) with H_2ABB-C4 in comparison to simulated pattern of the ASF-1 and ASF-2 structure type. The patterns are normalized and vertically offset for clarity.

All ASFs synthesized after the evaporation synthesis are already guest- and solvent-free as confirmed by FTIR spectroscopy showing no bands for residual water molecules (see Section B.1.4 for datasets). It is concluded that the hydrophobic nature of the pores expels the water which yields to readily porous materials supported by the applied reaction condition (80 °C, reduced pressure).

Further, scanning electron microscopy (SEM) images were collected from ASFs obtained after the solvothermal or evaporation synthesis approach (see Figure 10.15). Most of the crystallites obtained via solvothermal synthesis appear as needle shaped crystals about 10 μm in length. This morphology is expected from the trigonal space groups of their crystal structures. In comparison, ASFs generated via evaporation of water features particles of versatile morphologies and a significantly smaller size. This observation is ascribed to the much faster crystallization process (evap-a $\approx$ 10 $-$ 20 min vs. solvothermal $\approx$ 24 h).

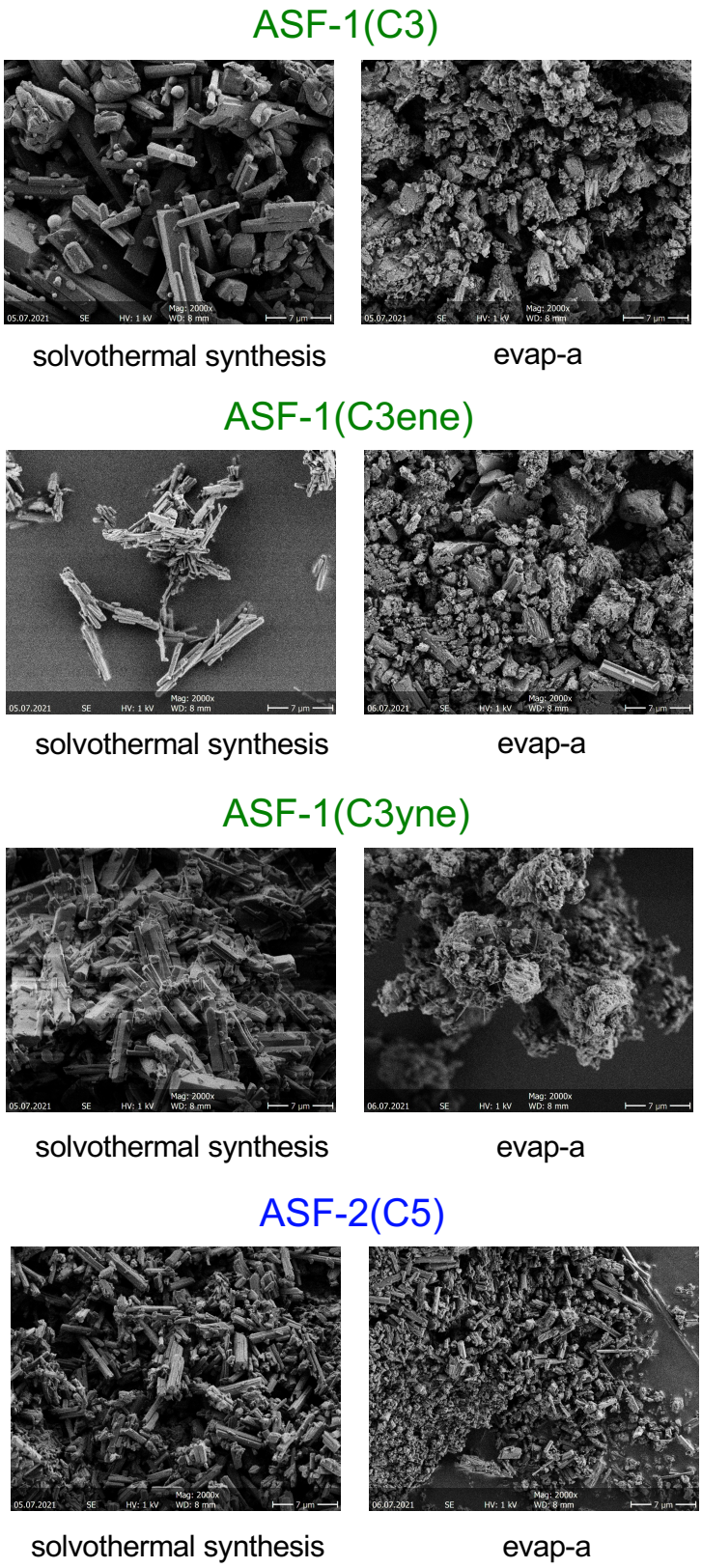

Figure 10.15: SEM images of ASFs material obtained after the different synthesis routes as indicated below the respective image.

10.5.2 Reversible Assembly

Based on the kinetically labile mainly electrostatic sodium oxygen interactions it is possible to repeat the synthesis of ASFs from water several times. An ASF powder can be dissolved in water and the porous framework is formed again after evaporation of the water. As a proof of concept, ASF-1(C3ene) was 10 times dissolved and precipitated again by evaporating the water (method evap-a, 10 times). PXRD patterns collected after each cycle demonstrate the formation of ASF-1(C3ene) (see Figure 10.16). A profile fit to the PXRD data obtained after the tenth cycle proves the repeated formation of phase pure ASF-1(3ene) (see Figure 10.17). This process consequently allows repeated or cyclic processing of ASFs in aqueous solution.

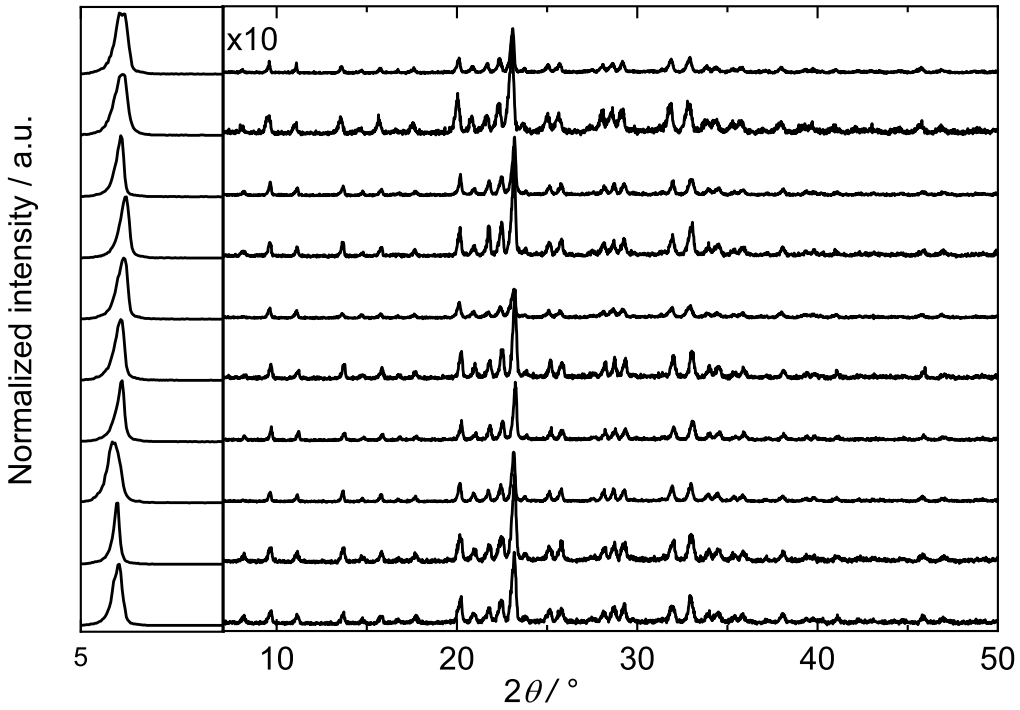

Figure 10.16: Stack plot of PXRD pattern collected of ASF-1(C3ene) after each cycle of precipitating from water and dissolving in water, again. The first pattern is presented on the bottom, the tenth pattern at the top. The varying peak intensities are a consequence of poor powder averaging due to preferred orientation. Small variations of peak positions and partial splitting of reflections is ascribed to an inhomogeneous sample surface on the substrate. The patterns are normalized and vertically offset for clarity.

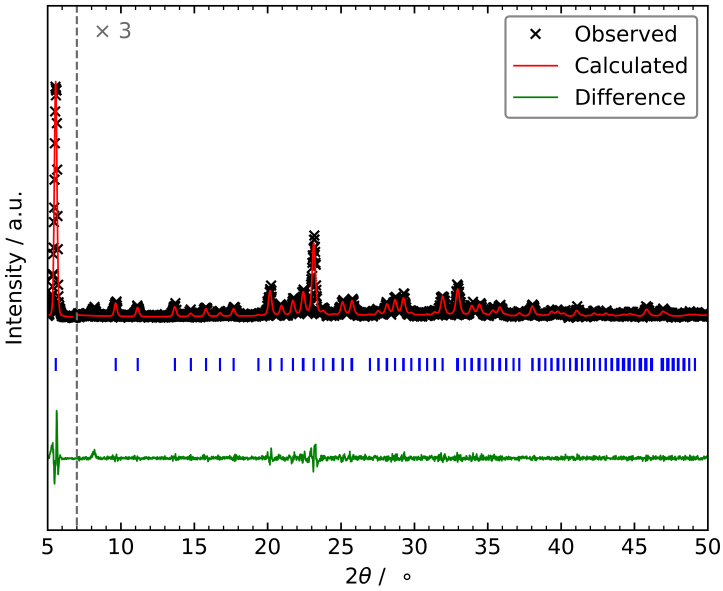

Figure 10.17: Plot of profile fit (Pawley method) to PXRD data of a material of ASF-1(C3ene) which was ten times dissolved and precipitated from water (evap-a, 10 times). Allowed Bragg reflection positions are displayed with blue thick marks. The Pawley fit verifies the formation of ASF-1(C3ene).

Table 10.7: Unit cell parameters determined by the above displayed structureless profile fit (Pawley method) of the obtained PXRD pattern and corresponding R_{wp}, R_{exp} and χ values.

Pawley fit Compound	Figure 10.17 ASF-1(C3ene)
crystal system	trigonal
space group	$R\bar{3}c$
a / Å	31.716(13)
b / Å	31.716(13)
c / Å	8.265(4)
α / °	90
β / °	90
γ / °	120
V / Å^3	7200(7)
R_{wp} / %	24.00
R_{exp} / %	16.52
χ	1.45

10.5.3 Drop Casting of Films

The evaporation synthesis approach allows also to drop cast ASFs on a surface yielding an ASF film after evaporation of the water. To demonstrate this, a drop of an aqueous solution of H_2ABB-CX (CX = 3, 3ene, 3yne, or 5) and NaOH was placed on a preheated glass plate. Subsequently, the glass plate was stored in an oven at 100 °C yielding to a solid film within 10 − 30 min (see Section 12.9.2 for the detailed protocol). The formation of the respective ASF was verified by PXRD data collected from materials directly on the glass plate (see Figure 10.18).

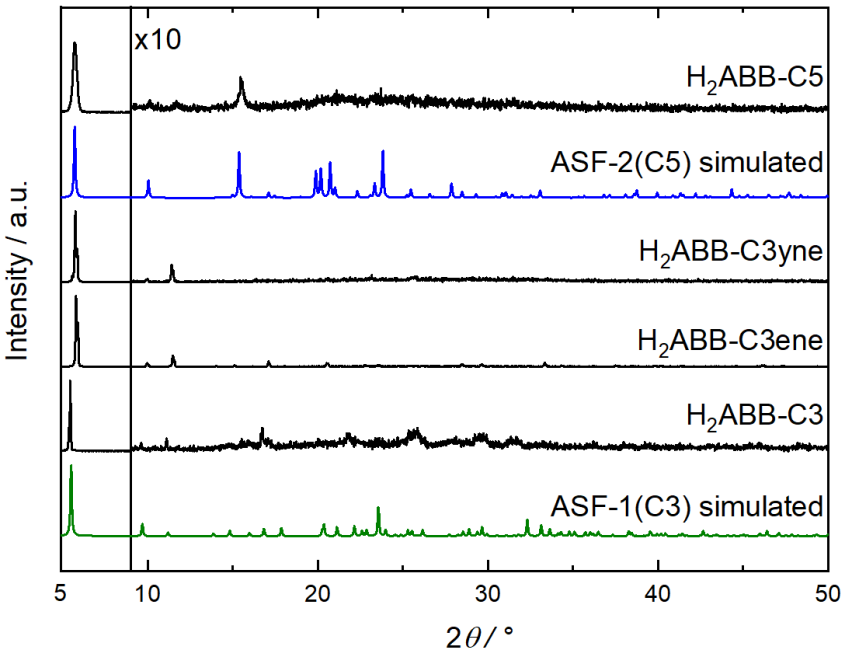

Figure 10.18: Stack plot of PXRD pattern of ASFs materials deposited on a glass plate. The respective ABB which was utilized in the synthesis is given in the figure. For comparison, simulated PXRD patterns of representative materials of the ASF-1 (ASF-1(C3)) and ASF-2 (ASF-2(C5)) are shown. The patterns are normalized and vertically offset for clarity.

From the PXRD data, the formation of ASF films on the glass substrate is clearly evident. It has to be noted that small shifts and partial splitting of reflections of patterns − directly collected from the deposited film on a glass substrate − are observed in comparison to the simulated patterns. This is ascribed to the inhomogeneous surface of the ASF films on the sample holder. Unfortunately, such circumstances also restrict a more detailed phase analysis via profile fitting. However, these data represent the conceptual proof that ASFs can be 'liquid-casted'.

10.5.4 Mechanochemical Synthesis

The self-templating of the porous ASFs also allows their formation in a solvent-free mechanochemical synthesis. Manual grinding of H_2ABB-C5 and NaOH in a laboratory mortar leads to the phase pure formation of ASF-2(C5), even though broad Bragg reflections point towards a very small particle size and rather poor crystallinity (see Figure 10.19 and Section 12.9.2 for the detailed synthesis protocol).

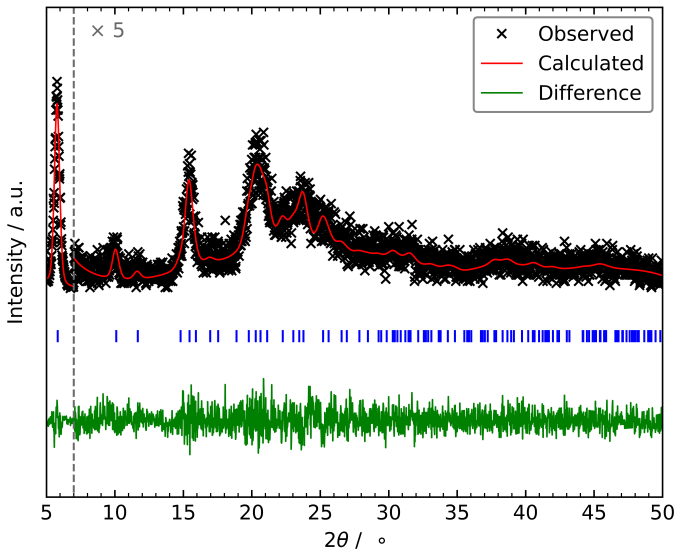

Figure 10.19: Structureless profile fit (Pawley method) to the PXRD data of the material obtained after manual grinding H_2ABB-C5 with two equivalents NaOH. Blue thick marks indicate the allowed Bragg reflection positions for the ASF-2(C5) phase.

Table 10.8: Unit cell parameters determined by the above displayed structureless profile fits (Pawley method) of the obtained PXRD patterns and corresponding R_{wp}, R_{exp} and χ values.

Pawley fit Compound	Figure 10.19 ASF-2(C5)
crystal system	trigonal
space group	$R\bar{3}$
a / Å	30.3(2)
b / Å	30.3(2)
c / Å	6.141(4)
α / °	90
β / °	90
γ / °	120
V / Å^3	4883(79)
R_{wp} / %	21.54
R_{exp} / %	19.00
χ	1.13

Performing this manual grinding attempt lead also to the formation of the ASF-1 structure type when grinding either H_2ABB-C3, H_2ABB-C3ene, or H_2ABB-C3yne with stoichiometric amounts of NaOH (see Figure 10.20). The formation of the ASF-1 structure type is clearly evident for all three materials, however, small residual peaks, which could not be ascribed to the ASF-1(CX) structure, are present in the PXRD patterns. These peaks have been identified in the difference curve of profile fits. Unfortunately, attempts to identify these peaks as unreacted starting materials (NaOH or H_2ABB-CX) were unsuccessful. It is possible that so far unknown intermediate phases (including hydrates) are formed during the grinding process.

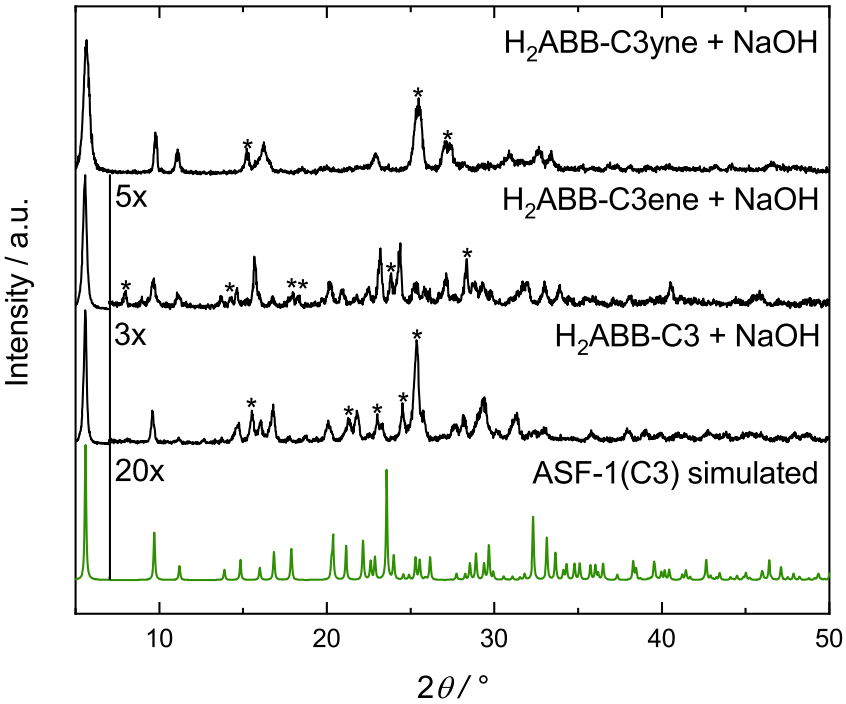

Figure 10.20: Comparison of the experimentally PXRD patterns from materials obtained after manual grinding of either H_2ABB-C3, H_2ABB-C3ene, or H_2ABB-C3yne with stoichiometric amounts of NaOH to a simulated pattern of ASF-1(C3). Peaks which could not ascribed to one of the respective ASF-1(CX) phases are marked with asterisk (*). The patterns are normalized and vertically offset for clarity.

On the basis of these data it is demonstrated that the ASFs can be synthesized via mechanochemical synthesis. In principle, it should be possible to obtain phase pure ASFs by optimizing the reaction conditions (e.g. longer grinding times or more intense grinding with an automatic ball mill) or to remove the impurities by washing procedures. Remarkably, no additional templating solvent is necessary for the formation of ASFs as mostly found for the synthesis of other porous materials (i.e MOFs) via mechanochemistry.[249]

10.6 Gas Physisorption Studies

ASF-1(CX) (CX = C3, C3ene, C3yne) and ASF-2(C5) were chosen for gas physisorption experiments. These four ASFS are the most porous regarding their tVF (see Figure 10.8 and Figure 10.21).

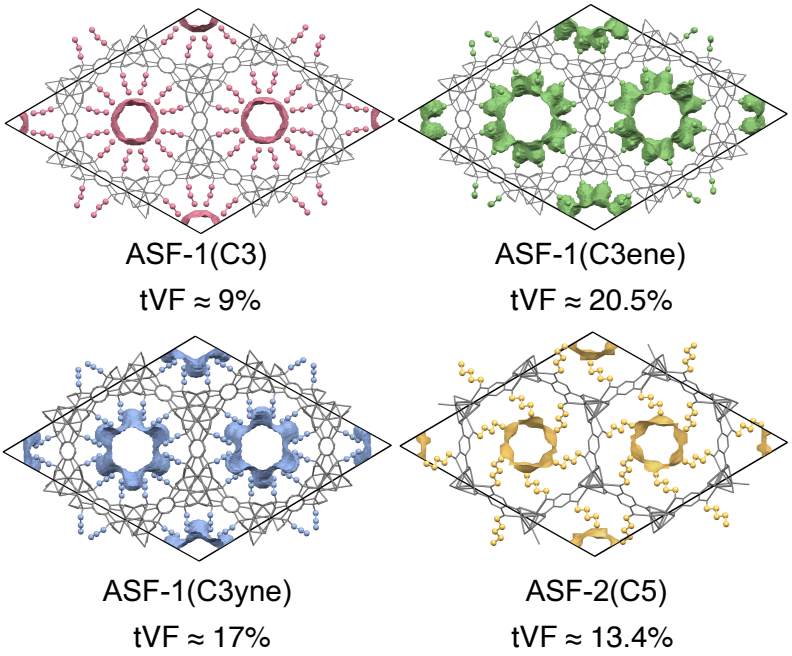

Figure 10.21: Representation of the crystal structures of the selected ASFs which are investigated via gas physisorption experiments. All atoms are colored gray (style: wireframe) except for the pore formers highlighted in different colors (style: ball and stick). The void fractions are displayed in the same color as the respective pore formers. The tVFs are calculated as previously described (see Figure 10.8).

10.6.1 N_2 and CO_2 Physisorption Studies

ASFs from Solvothermal Synthesis

First, the highly crystalline solvothermally synthesized materials were investigated towards their gas adsorption behavior. Increasing maximum gas adsorption capacities are found for ASF-1(C3) < ASF-2(C5) < ASF-1(C3ene) for N_2 at 77 K and CO_2 at 195 K, which is in the same order as expected from the calculated tVFs (see Figure 10.21 and Figure 10.22).* Remarkably, ASF-1(C3yne) shows by far the lowest uptake for N_2 and highest for CO_2 of all investigated ASFs. The rather low N_2 uptake of ASF-1(C3yne) is ascribed to reduced conformational flexibility of the terminal alkyne groups pointing into the cylindrical pores of the material. The diffusion of N_2 into the framework is restricted at 77 K. However, CO_2 can access the framework at

* Precise values of maximum gas adsorption capacities are summarized in Section B.1.5.

higher temperature (195 K). The CO_2 adsorption is presumably further supported by attractive interactions between CO_2 and the terminal polarizable C−C triple bonds pointing inside the pores which results in the highest CO_2 uptake among this series.

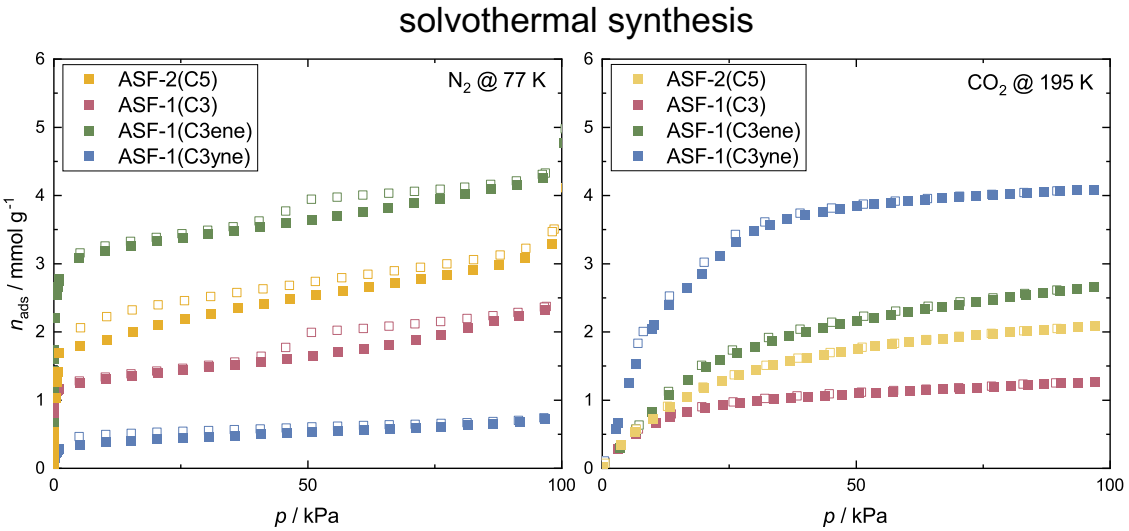

Figure 10.22: Physisorption isotherms for the selected ASFs shown in Figure 10.21 obtained after the solvothermal synthesis route for N_2 at 77 K and CO_2 at 195 K. Adsorption and desorption branches are shown as closed and open symbols, respectively.

From the N_2 and CO_2 gas isotherms the specific pore volumes (V_{pore}) of the ASFs have been determined (see Table 10.9).* The values are spanning a broad region reflecting the trends discussed above utilizing the maximum gas capacities.

Additionally, BET surface area calculated from these gas isotherms (S_{BET}; see Table 10.9 for values and Section B.1.5 for additional parameters to the calculations).† The S_{BET} for ASF-1(C3yne) determined from N_2 and CO_2 gas isotherms giving highly different values with 34 $m^2\ g^{-1}$ and 309 $m^2\ g^{-1}$, respectively. This corroborates that, even though the application of the BET model is very common for MOFs, this model is not applicable for the microporous materials studied here and the obtained values highly depend on the utilized probe molecule.[160] Hence, these data are only given for reference.

ASFs from Evaporation Synthesis

Gas physisorption isotherms (CO_2 at 195 K) were also collected of the ASFs derived by the evaporation synthesis route (see Figure 10.23).‡ Here, decreased maximum capacities are found compared to the solvothermally synthesized materials apart from ASF-1(C3), which is the densest ASF investigated here (ρ_{calc} = 1.395 g cm^{-3}).

* More details about the calculation of the V_{pore} can be found in Section 3.2.
† More methodical details about the calculation of the BET surface areas as well as a discussion on the assumption and feasibility of applying the BET model is given in Section 3.2.4.
‡ Precise values of maximum gas adsorption capacities are summarized in Section B.1.5.

Table 10.9: Summary of total pore volumes (V_{pore}) and BET surface areas (S_{BET}) determined from N_2 at 77 K and CO_2 at 195 K gas isotherms for ASF materials.[a]

Compound	CO_2 @ 195 K		N_2 @ 77 K	
	V_{pore} [$cm^3\ g^{-1}$]	S_{BET} [$m^2\ g^{-1}$]	V_{pore} [$cm^3\ g^{-1}$]	S_{BET} [$m^2\ g^{-1}$]
ASF-1(C3)	0.06	85	0.08	115
ASF-1(C3ene)	0.13	193	0.15	294
ASF-1(C3yne)	0.20	309	0.03	34
ASF-2(C5)	0.10	142	0.11	209

a Applied value for the density of pure liquid adsorbate for V_{pore} determinations: $\rho(CO_2$ @ 253 K) = 1.032 g cm^{-3} and $\rho(N_2$ @ 77 K) = 0.808 g cm^{-3}.[87]

For the other ASFs, the lower gas capacities are assigned to structural defects in the rapidly precipitated materials as a consequence of the fast crystallization process. Defects may lead to partial pore blocking and thus to a lower gas accessible volume within the materials.

It was attempted to reduce such defects and increase the gas adsorption capacity by slowing down the crystallization process from aqueous solution via decreasing the reaction temperature to 50 °C and performing the reaction without reduced pressure (method evap-b; see Section 12.9.2 for the detailed synthesis protocol). Indeed, an increase of CO_2 adsorption capacity is found for as such synthesized ASF-1(C3ene) (+8%) and ASF-2(C5) (+23%) materials compared to the faster crystallization conducting method evap-a (see Figure 10.23 and Section B.1.5 for precise values).

Unfortunately, by conducting the evap-b method with H_2ABB-C3yne a phase mixture of ASF-1(C3yne) and a non-porous hydrate phase of the composition Na_2(ABB-C3yne)$(H_2O)_6$ was obtained. The crystal structure of the hydrate phase could by resolved from large grown crystals picked from the reaction mixture before the whole water was evaporated (see Section B.1.1 for a structural description). The occurrence of the phase mixture was further verified by a dual-phase profile fit to PXRD data (see Section B.1.2). Hence, the resulting materials' mixture was not further investigated by gas adsorption studies.

Overall, the highest decrease in CO_2 gas capacity (−47%; solvothermal synthesis vs. evap-a) is found for ASF-2(C5). The profile fits to PXRD data of ASF-2(C5) synthesized via solvothermal synthesis and via the evap-a route reveal a decrease in unit cell volume of about −7% (see Section B.1.2). It is assumed that a closer

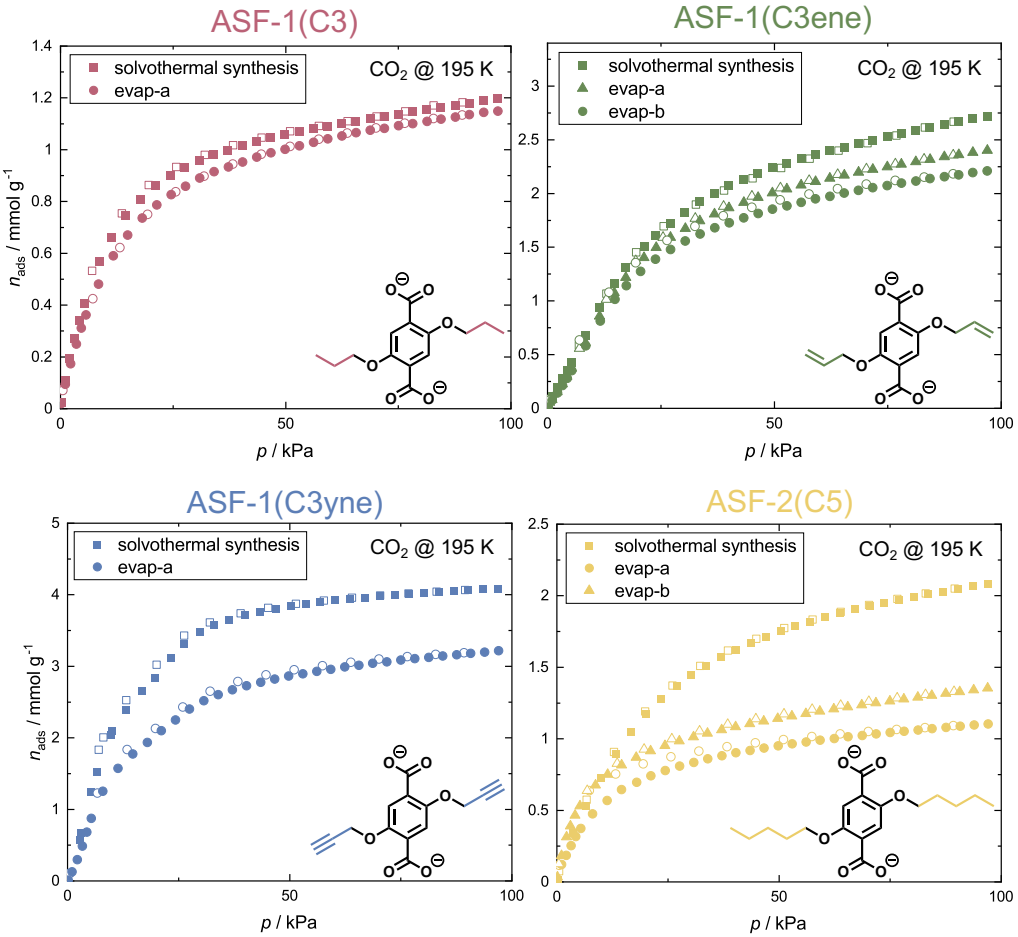

Figure 10.23: Physisorption gas isotherms for CO_2 collected at 195 K compared regarding different synthesis routes. The respective ABB present in the ASF is displayed on the bottom left of each graph. Adsorption and desorption branches are shown as closed and open symbols, respectively.

packing of the less dense ASF-2(C5) material (ρ_{calc} = 1.175 g cm^{-3}) is observed probably due to contraction of the single [NaO_6] helices in the ASF-2 structure type (see Section 10.4.1). This is supported by FTIR spectroscopy data for ASF-2(C5) materials obtained after the evaporation synthesis methods which uncover the occurrence of additional bands at approximate 1300 − 1400 cm^{-1} and shifting of the band at about 1600 cm^{-1} to lower wavenumbers. These bands are assigned to the asymmetric and symmetric carboxylate stretching mode, respectively (see Figure 10.24). Consequently, different coordination modes of carboxylates to Na^+ ions are present in the evaporated materials.[250] This points towards a difference in local coordination environments (e.g. due to distortion of the helices). Further, such differences in the coordination of carboxylates could also originate from defects (e.g. 'wrongly' coordinating linkers) in the materials, partially blocking pores which would then be inaccessible for gas molecules.

Similar defects might also be the reason for the smaller decreases in gas capacities

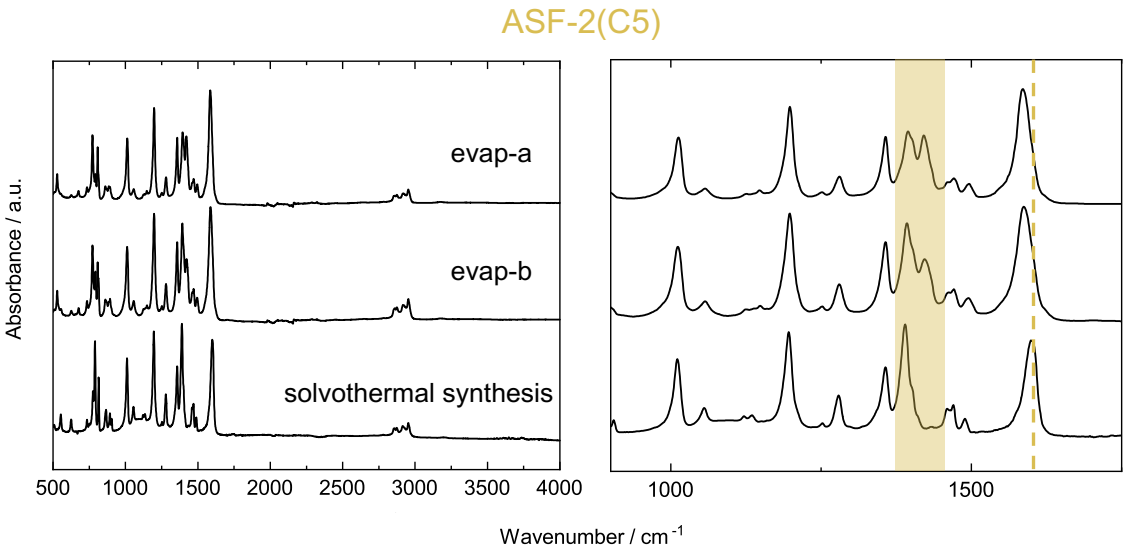

Figure 10.24: Stack plot of FTIR spectroscopy data of ASF-1(C5) obtained after three different synthesis routes. Left: Full spectra. Right: Zoom into the region from $900 - 1750$ cm^{-1}.

for the rapidly precipitated ASF-1(C3ene) and ASF-1(C3yne) derivatives (see Figure 10.23). However, a significant decrease in unit cell volume (derived from profile fits) is not observed for any of the ASF-1 materials (see Section B.1.2). A reason for that could be, that adjacent ABBs in the ASF-1 structure type feature additional $\pi-\pi$-interactions which may help to direct the formation of this frameworks (see Section 10.4.1). Hence, less defects arise even if the materials are crystallized on a short time scale.

Additionally, the [NaO_6] helices of the ASF-1 materials are here decorated with additional Na^+ ions yielding a higher connectivity of the rod-shaped inorganic building unit, which is consequently less contractible. Further, no changes in FTIR spectroscopy data are found for ASF-1 materials obtained via the different synthesis routes (see Section B.1.4). Here, it has to be noted that the ASF-1 structure type features already a more complex pattern of carboxylate stretching bands resulting from the different coordination modes already present in the inorganic building unit.

10.6.2 Hydrocarbon Physisorption Studies

All CO_2 isotherms feature a flat rise of the Typ I isotherm at low pressure – less pronounced for ASF-1(C3yne) – as a sign for the apolar (hydrophobic) nature of the pores' surfaces. Hence, it is not surprising that further gas adsorption studies with apolar hydrocarbons – namely *n*-butane, propane and propylene at 273 K, show hydrocarbons sorption for all ASFs (see Figure 10.25).* Gas physisorption isotherms

* Precise values of maximum gas adsorption capacities are summarized in Section B.1.5.

were again collected for materials obtained after the solvothermal synthesis route and evaporation synthesis routes (evap-a and evap-b).

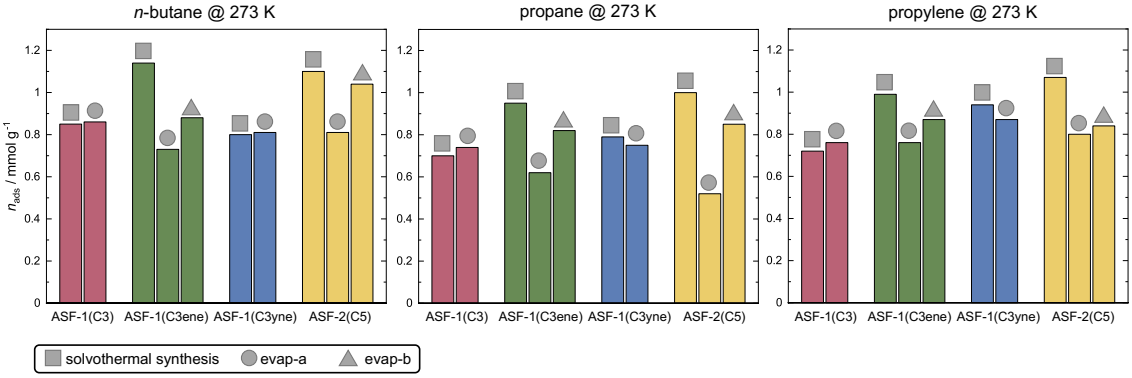

Figure 10.25: Graphs comparing the maximum gas adsorption capacities of several hydrocarbon gases for selected ASFs obtained after the solvothermal and evaporation synthesis routes.

Importantly, for all hydrocarbon gases, the differences between the maximum gas adsorption capacities of the materials derived via the solvothermal or evaporation synthesis routes are much less pronounced (see Figure 10.25 and Section B.1.5 for precise values). This is ascribed to attractive interactions between the hydrophobic probe molecules and hydrophobic pore surfaces, whereas CO_2 is expelled and its diffusion in the channels is limited at the lower temperature (195 K vs. 273 K). Importantly, for ASF-1(C3) and ASF-1(C3yne) nearly the same gas capacities are found independent on the crystallization process for all three hydrocarbons (see Figure 10.25).

Additionally, almost all *n*-butane isotherms of evaporated ASFs show a steep rise close to the maximum investigated pressure ($\approx$ 95 kPa $\widehat{=}$ 0.95 p/p_0, see Figure 10.26). This points towards condensation between particles (on the surface) further verifying a much smaller particle size than for the solvothermally synthesized materials, as already shown by SEM imaging (see Section 10.5.1). Furthermore, the *n*-butane isotherms collected from ASFs obtained after slower crystallization (method evap-b) not only display increased capacities but also the disappearance of priory existing hystereses, thus pointing towards better accessibility of the pore space (see Figure 10.26). This trend is also found for the corresponding propane and propylene isotherms supporting this assumption (see Section B.1.5).

10.6.3 Selective Gas Adsorption

Comparing the propane and propylene isotherms for ASF-1(CX) (CX = C3, C3ene) and ASF-2(C5), a steeper slope is visible for propane gas isotherms at pressures below 20 kPa (see Figure 10.27). With increasing pressure, a crossing of the isotherms is observed, yielding to a slightly higher propylene uptake at the maximum pressure of

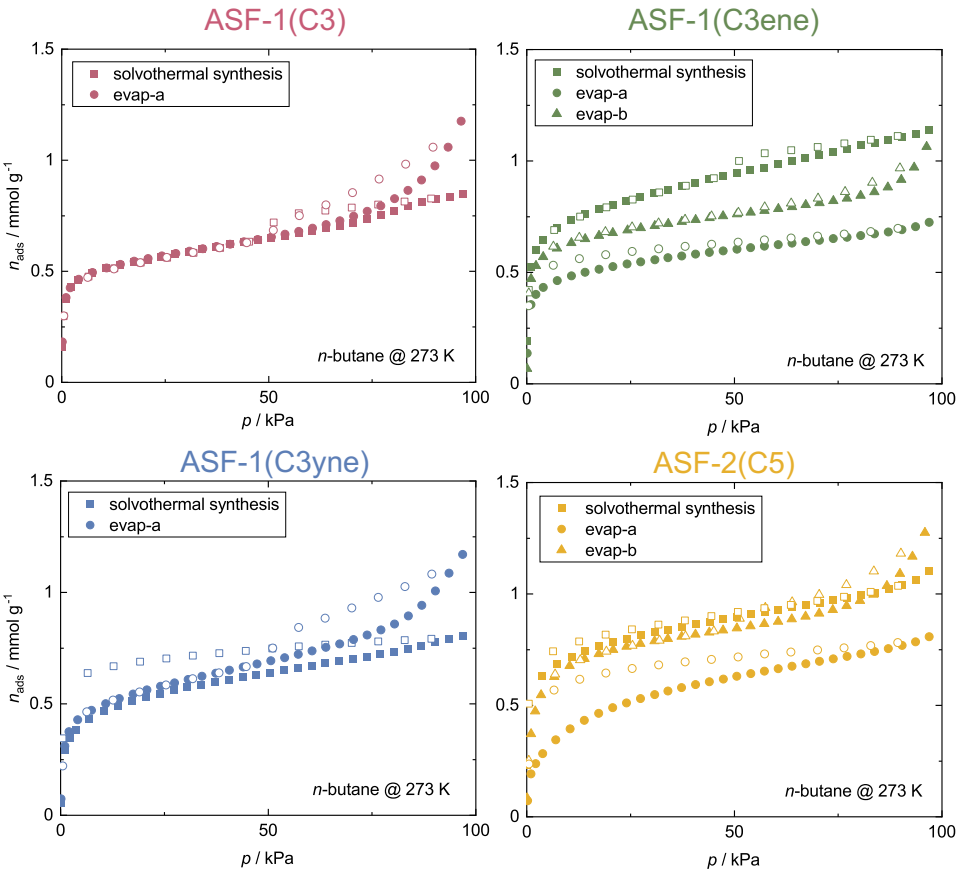

Figure 10.26: Physisorption gas isotherms for *n*-butane collected at 273 K compared regarding different synthesis routes. Adsorption and desorption branches are shown as closed and open symbols, respectively.

about 95 kPa. This observation suggests different gas affinity and thus gas adsorption selectivity change depending on the operating pressure window. It can be speculated that the flexible pore formers are changing their conformation with increasing gas pressure. This is supported by the overall lower uptake for propane over the whole pressure range for ASF-1(C3yne) featuring the most rigid pore former. Here, a higher uptake for propylene over propane is found which is much likely due to attractive interactions between the unsaturated pore former and the unsaturated gas molecule. Similar approaches, taking advantage of designable pore shapes with saturated and unsaturated bonds rather than only single functional groups on the pore surfaces, have recently been reported for MOFs and are interesting for gas separation processes.[251]

Ideal adsorbed solution theory (IAST) propylene/propane selectivity factor (S_{IAST}) were calculated from the above presented isotherms utilizing the Python package pyIAST.* The pure component gas adsorption isotherms of propane and propylene at 273 K of the respective ASF material were interpolated with the implemented routine

* A deeper discussion on this method can be found in Section 3.2.5.

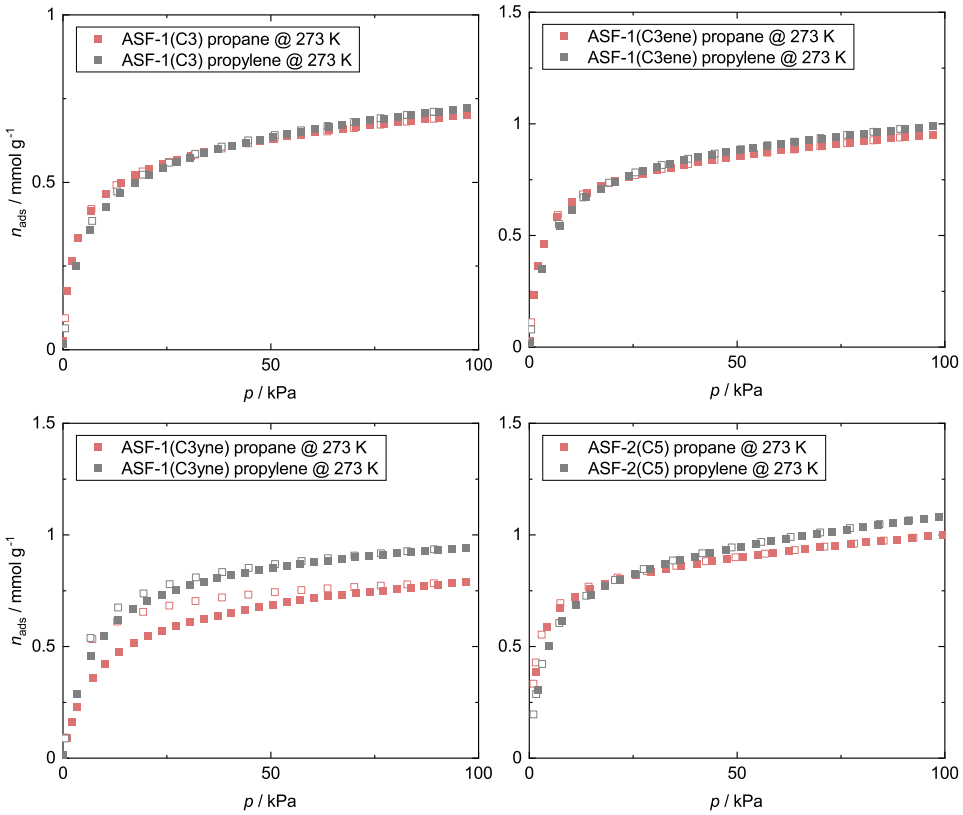

Figure 10.27: Comparison of propane and propylene physisorption isotherms collected at 273 K for ASFs obtained after the solvothermal synthesis route. Adsorption and desorption branches are shown as closed and open symbols, respectively.

in the pyIAST software package. Subsequently, IAST calculations were performed for three different molar ratios of propylene:propane (10:90; 50:50; 90:10) at 100 kPa (see Table 10.10).

The obtained S_{IAST} values uncover a selective gas adsorption of propane over propylene ($S_{\mathrm{IAST}} = 0.63 - 0.76$; for 50:50 mixtures) for all ASFs apart from ASF-1(C3yne) where the selectivity switches ($S_{\mathrm{IAST}} = 1.82$; for 50:50 mixtures). This finding proves the potential of ASFs for applications in gas separation processes. Especially the higher affinity of ASF-1(C3), ASF-1(C3ene) and ASF-2(C5) for propane is here promising for further investigations regarding membrane applications

Table 10.10: IAST selecticity factors (S_{IAST}) for ASFs applying three different propylene/propane mixtures at 100 kPa and 273 K.

molar ratio (propylene/propane)	10:90	50:50	90:10
ASF-1(C3)	0.69	0.63	0.68
ASF-1(C3ene)	0.75	0.75	0.74
ASF-1(C3yne)	1.76	1.82	1.89
ASF-2(C5)	0.77	0.76	0.75

since the valuable product (propylene) is interacting less strongly with the material.[97]

10.7 Stability of the ASFs Against Temperature and Pressure

Selected activated ASFs, obtained phase pure via solvothermal synthesis, were analyzed regarding their stability against high temperature and high mechanical pressure.

10.7.1 Thermal Stability

TGA/DSC data were collected under a constant argon flow from ambient temperature to 700 °C with a heating rate of 10 °C min^{-1}. The TGA/DSC experiments were conducted with the phase pure ASF materials obtained after the solvothermal synthesis route.

A significant mass loss in the TGA data is found for all ASFs, which is ascribed to the decomposition of the materials (see Figure 10.28). Most likely, (partially) decarboxylation processes as well as cleavage of the alkoxy groups (pore formers) initiate the materials decomposition. All ASFs carrying an aliphatic alkyl chain as the pore former are thermally stable up to approximately 375 − 425 °C. Earlier decomposition temperatures (≈ 250 − 300 °C) are found for the ASFs with unsaturated pore formers (terminal bond).

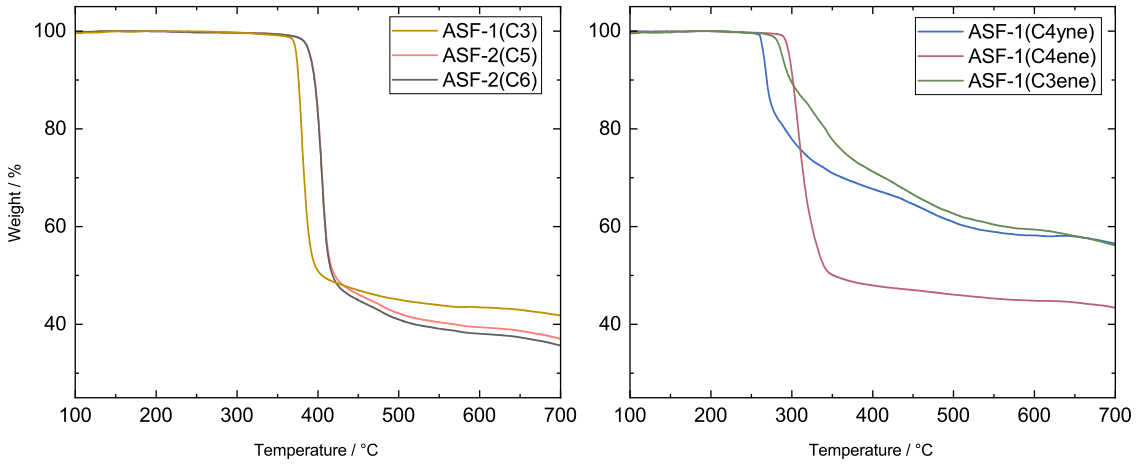

Figure 10.28: TGA data for ASFs with pore formers carrying saturated alkyl chains (left) and unsaturated alkyl chains (right).

The TGA/DSC experiment with ASF-1(C3yne) yields implausible TGA/DSC data with a random increase and decrease of the recorded mass (see Figure 10.29). The materials obtained after the experiment appear foam-like and brownisch coloured. It is assumed that the formation of the foam takes place at approximate 250 °C where

a strongly exothermic signal occurs in the DSC curve, which is accompanied by a small increase in mass. This increase in mass can be explained with an experimental error arising from the rapid expansion (powder → foam) in the TGA/DSC set-up which then causes the implausible changes in the TGA curve. Nevertheless, the mass loss allows to clearly determine the decomposition of the material at approximate 250 °C.

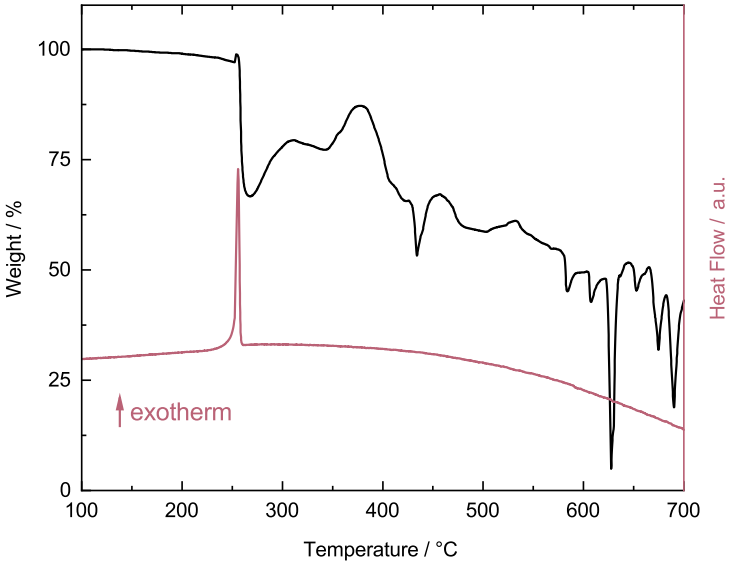

Figure 10.29: TGA/DSC data for ASF1(C3yne).

10.7.2 Mechanical Stability

The mechanical stability was investigated by *in-situ* high-pressure PXRD for ASF-1(CX) (CX = C3, C3ene, C3yne) and ASF-2(C5). For this experiment, the ASF powders were placed into a Kapton™capillary together with silicon oil as a pressure transmitting medium. Hydrostatic mechanical pressure was applied on the capillary in a custom build set-up using water as the pressure medium.[252] The experiments were performed at Dortmunder ELekTronenspeichering-Anlage (DELTA). A detailed description on the experimental set-up and capillary preparation is given in Section 12.1.4. PXRD patterns as a function of mechanical pressure were collected up to a maximum pressure (p_{max}) of 3750 bar (or 4000 bar for ASF-1(C3yne)) with discrete pressure steps (Δp) of 250 bar.

Data Evaluation and Derivation of the Bulk Modulus

The obtained data were evaluated by sequential profile fitting (Pawley method) to extract the evolution of unit cell parameters (i.e. unit cell axis and volume) as a function of pressure (see Figure 10.30 and Figure 10.31). The sequential profile refinements have been performed by manually fitting the first pattern (ASF-1(CX,

CX = C3, C3ene, C3yne) or last pattern (ASF-2(C5)) of each dataset starting with crystallographic parameter from the SCXRD experiments. The determined output parameters were used as start parameters for fitting the data obtained at the next higher (ASF-1(CX), CX = C3, C3ene, C3yne) or lower (ASF-2(C5)) pressure step. Subsequently, this has been done automatically in a batch refinement for all following patterns. The calculated unit cell parameters and goodness values for each refinement are summarized in Section B.1.3.

The pressure-dependent crystallographic data were used to determine the bulk modulus (K) of the ASFs. The bulk modulus K relates the volumetric compression (ΔV) of a solid with respect to uniformly applied pressure (Δp, see Equation 10.1).[253]

$$K = -V\frac{\Delta p}{\Delta V} \tag{10.1}$$

Hence, knowing K_0 (the bulk modulus at ambient pressure) of solid state materials gives insights into its stiffness/flexibility. For comparison, K_0 for sodium chloride (NaCl) amounts to 23.7 GPa[254] whereas the densest and least compressible form of carbon (aggregated diamond nanorods) features a K_0 of 491 GPa[255].

The K_0 values for ASFs were obtained by fitting pressure *vs.* volume ($V(p)$) data with a 2^{nd} order Birch-Murnaghan equation of state (see Equation 10.2; Table 10.11 for determined values and Section B.1.3 for fits).[256]*

$$p = -\frac{2}{3}K_0\left(\left(\frac{V}{V_0}\right)^{-\frac{7}{3}} - \left(\frac{V}{V_0}\right)^{-\frac{5}{3}}\right) \tag{10.2}$$

This procedure for the determination of the bulk modulus has previously been performed for several PFMs (e.g. MOFs).[257–259]

Table 10.11: Summary of the calculated bulk moduli (K_0) for some ASFs with the utilized pressure range.

Compound	Pressure range / bar	Bulk modulus (K_0) / GPa
ASF-1(C3)	10 – 3750	13.5 ± 0.2
ASF-1(C3ene)	10 – 3750	11.4 ± 0.1
ASF-1(C3yne)	1 – 4000	12.9 ± 0.2
ASF-2(C5)	10 – 1000	8.2 ± 0.2

∗ The fitting was performed with the Gnuplot (version 5.2) software package as an error-weighted least square fit.

ASFs' Response to Mechanical Pressure

The ASF-1 materials are stable up to at least 3750 bar (ASF-1(C3) and ASF-1(C3ene)) or 4000 bar (ASF-1(C3)) hydrostatic pressure confirmed by the full reversibility of collected PXRD patterns (see Figure 10.30). All peaks shift to higher 2θ angle at

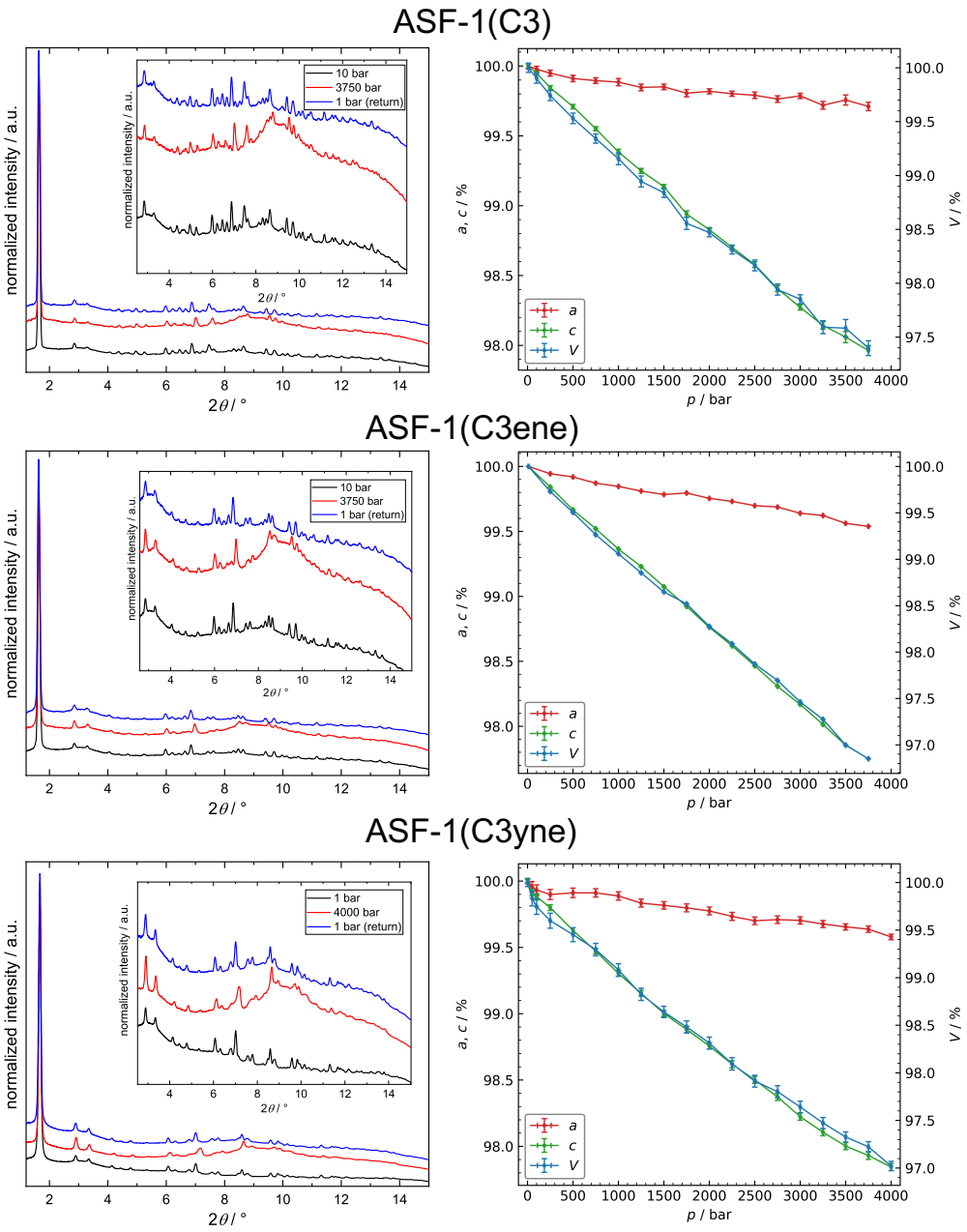

Figure 10.30: Left: Stacked plot of selected PXRD data of ASF-1 materials at the starting pressure (1 or 10 bar), maximum applied pressure (3750 or 4000 bar) and return to starting pressure. The patterns are normalized and vertically offset for clarity. Right: Plots visualizing the progression of the unit cell volume V and cell parameters a and b with increasing mechanical pressure (p) for ASF-1 materials, which have been extracted from the sequential profile refinements (Pawley method).

the maximum applied pressure resulting from the unit cell compression at increased

pressure.* The return patterns show nearly no variation to the starting patterns which represents the reversible cell contraction.

A continuous linear contraction of the unit cell volume ($\approx 3\%$) is found for all ASF-1 materials in the investigated pressure range. The contraction mainly occurs along the crystallographic c axis which equals a compression along the direction of the Na^+ helices (see Figure 10.30). Calculated bulk moduli (K_0) amount to $K_0 =$ 13.5(±0.2) GPa (ASF-1(C3)) > 12.9(±0.2) GPa (ASF-1(C3yne)) > 11.4(±0.1) GPa (ASF-1(C3ene)).

For ASF-2(C5) a decrease of the unit cell volume by about 13% is found over the investigated pressure range, with a drastic decrease of about 10% between 1000 − 2500 bar (see Figure 10.31). Comparison of the PXRD patterns at the starting and

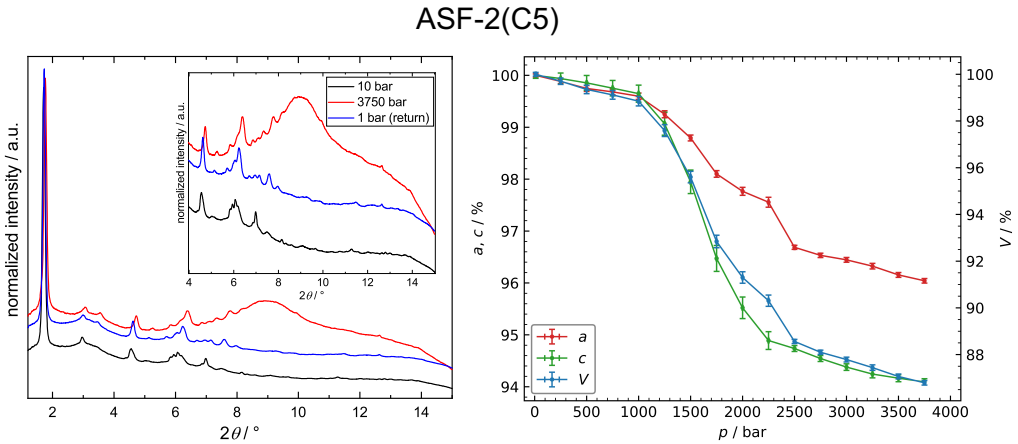

Figure 10.31: Left: Stacked plot of PXRD data of ASF-2(C5) at 10 bar, 3750 bar, and 1 bar (return). The patterns are normalized and vertically offset for clarity. Right: Progression of the unit cell volume V and cell parameters a and b with increasing mechanical pressure p for ASF-2(C5), which have been extracted from the sequential profile refinements (Pawley method).

maximum pressure uncover the appearance and disappearance as well as shifting of individual peaks to higher 2θ angle. This points towards a structural change triggered by the applied mechanical pressure. Unfortunately, the high-pressure PXRD data are insufficient for a structure refinement. However, successful structurless profile fitting suggests a preservation of the symmetry of the structure by contraction of all unit cell axes. It can be postulated that a transition takes place from the ambient pressure ASF-2(C5) phase (present up to 1000 bar) to a denser structural configuration of ASF-2(C5) at high-pressure present from about 2500 bar on. Here, again a continuous volume decrease is found up to 3750 bar. The 1 bar return pattern shows shifting of all peaks present at 3750 bar to lower 2θ and thus the persistence of the high-pressure

* It has to be noted that the increase of background intensity at the maximum pressure point can be explained by the increasing amount of water in the X-ray beam path. See Section 12.1.4 for a description on the utilized set-up.

phase of ASF-2(C5) at ambient pressure. In accordance with this interpretation, the unit cell volume − determined by profile fits, at ambient conditions − is smaller for the high-pressure phase (V = 4622(2) Å^3) than for the ambient pressure phase (V = 4954(4) Å^3).

K_0 has been calculated for the ASF-2(C5) ambient pressure phase and amounts to 8.2(±0.2) GPa. This is about 30% smaller than for the materials with the denser ASF-1 structure type. The higher bulk moduli of the ASF-1 materials indicate a larger stiffness of the ASF-1 structure type. This can be associated with their higher densities but also with the robustness of their inorganic building unit (i.e. [NaO_6] helix decorated with further Na^+ ions) exhibiting a higher connectivity (see Section 10.4.1 and Section 10.6.1).

10.8 Conclusion

It is demonstrated that the self-assembly of specifically designed ABBs with Na^+ ions in aqueous solution leads to 9 different amphiphile salt frameworks (ASFs) in a honeycomb-like packing with cylindrical channels. Depending on the length and flexibility of the chosen pore former (CX), two different honeycomb-like structure types are found − ASF-1(CX) (CX = C3, C3ene, C3yne, C4, C4ene, C4yne) and ASF-2(CX) (CX = C4, C5, C6).

Pore size and functionality of the ASFs can be tuned via choice of the length and degree of saturation of the pore forming alkyl side chain. Gas sorption studies demonstrate permanent porosity towards various gases (N_2, CO_2, *n*-butane, propane and propylene) as well as tuneable gas sorption selectivity regarding the industrially relevant C_3 hydrocarbon separation process − namely propane/propylene separation.

The strong but non-directional ionic bonding between the ABBs and Na^+ ions, results in high thermal and mechanical stability (up to ≈ 400 °C and ≈ 4000 bar), while the kinetic lability of these bonds allows for reversible disassembly (dissolution) and reassembly (recrystallization) of the ASFs in water. The corresponding repeatable liquid phase processing ability of the ASFs from the greenest solvent available (i.e. water) has so far not been demonstrated for any other class of PFMs.[260–262]

Such processing property allows a simple regeneration of the porous materials by dissolving them in water and precipitation of fresh material − overcoming e.g. materials aging issues. On that account, the ASFs can be further directly deposited on surfaces by facile drop casting from an aqueous solution. Remarkably, due to the self-templating of the porous channels by the aggregation of the pore formers, the materials are readily porous directly after crystallization from water and can also be synthesized via mechanochemical synthesis without additional solvent.

Finally, the design concept for ASFs is here demonstrated by choosing 2,5-dialkoxy-1,4-benzenedicarboxylate derivatives as ABBs coordinating to Na^+ ions as nodes. Nevertheless, the outlined requirements on ABBs and nodes is potentially transferable to other building units. It is imaginable that ABBs with an elongated framework connector lead to isoreticular expanded structures, thus providing additional porosity features for ASFs. Further, not only Na^+ ions are possible as nodes. Here, the utilization of other metal ions, such as Li^+ or K^+, should be possible, varying the materials' properties (e.g. thermal/mechanical stability). Consequently, the presented ASFs represent only the beginning for the development of a new class of water-processable porous materials connecting beneficial properties of the emerging porous materials fields of PFMs and PMMs.

11 General Summary and Outlook

The ability of being processable adds an interesting feature to metal-organic frameworks (MOFs), which is especially important towards applications in industry, where materials need to be manufactured in certain forms, such as pellets or thin films. This ability, leading to processable MOFs, was investigated over the course of this thesis, following two different approaches, which were addressed in two parts.

Part I – ZIF Glasses

Representatives of ZIFs, a subfamily of MOFs, were recently reported to melt and to form glasses upon cooling to room temperature. Thus, ZIF glasses offer the option to be processed (e.g. shaped) in their liquid state. In this part, crystalline ZIF glass formers and their corresponding glasses were investigated regarding their (i) porosity and (ii) the fundamentals of their melting behavior.

(i) Porosity in ZIF Glasses

(a) Quantification of Intrinsic Microporosity in ZIF Glasses

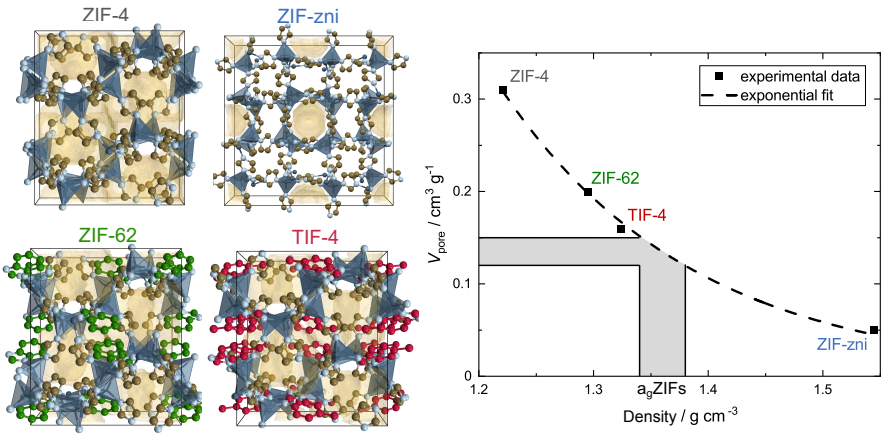

A series of four ZIFs and their corresponding glasses were accessed and their porosity features were compared. The materials differ in their structure (i.e featuring different topologies) and chemical composition (i.e. different types of organic linkers). All of them are found to be porous towards adsorption of several gases.

Based on the obtained data, it is proposed that microporosity is an intrinsic property of ZIF glasses. The intrinsic microporosity in ZIF glasses is a huge benefit compared to conventional porous silica glasses, where microporosity is only obtained by elaborate post-treatment methods, such as acid leaching.[188]

Via quantification of the microporosity in ZIF glasses, the real density (i.e. the density including the intrinsic microporosity) was derived for this class of materials for the first time. The real density is a key materials property, not only important for deeper investigations of the thermodynamics of melting and glass formation, but also as a boundary condition for computational model development of such amorphous materials. Having these values in hand, will lead to more precise and reliable simulation studies in the future.

Moreover, by investigating a series of ZIF glasses, it was uncovered that the porosity features (i.e. pore size and volume) of the glass network are dependent on the type/steric bulk of the linkers. Remarkably, it was found that the incorporation of bulkier linkers in ZIF glasses leads to an increased pore volume and accessibility of the framework for larger gas molecules. This is counterintuitive to the established design principles in crystalline MOFs, where a more bulky linker results in a reduction of the pore volume and size. On that account, it is proposed that design concepts, which have been already developed for porous polymers (i.e inefficient packing of building units leads to an increasing of the pore volume), can be adapted to control the porosity in ZIF glasses.[190–193] Thus, these studies set the stage for the discovery and design of ZIF glasses with porosity features far beyond the state-of-the-art.

(b) Hydrocarbon Separation by ZIF Glasses

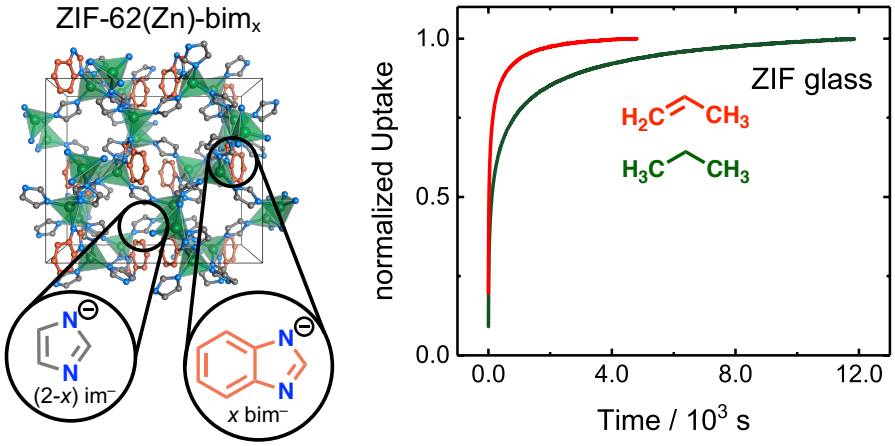

Elaborate gas sorption studies on mixed-linker ZIF-62 glasses (chemical composition $Zn(im)_{2-x}(bim)_x$; $x = 0.35, 0.17, 0.05$; im^- = imidazolate, bim^- = benzimidazolate) demonstrated that they are potential candidates for separation of hydrocarbons, namely propane and propylene. Importantly, diffusion rates into the material can

be even adjusted by different linker ratios in mixed-linker ZIF glasses. The melt-quenched glasses are very interesting membrane materials, as their isotropic nature can help to overcome the issue of permeation flux limiting grain boundaries.[263] After publication of these results, a study on ZIF glass membranes already demonstrated high separation performances for H_2/CH_4, CO_2/N_2 and CO_2/CH_4 mixtures.[137] This study further verifies the proposed benefit of the melt-quenching process to yield isotropic glass membranes.[137,263] Therefore, the conceptual proof for gas separation by ZIF glasses – here presented for the first time – is very encouraging for the future fabrication of high-performance membranes.

(ii) Fundamentals of ZIF Melting

(a) A Cobalt-based ZIF Glass

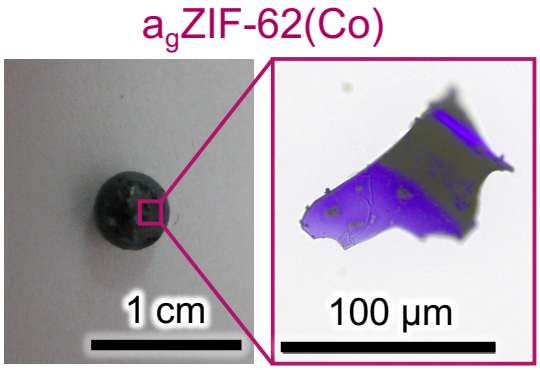

A crystalline ZIF-62 cobalt derivative (chemical composition $Co(im)_{1.70}(bim)_{0.30}$) was synthesized. Thermal analysis revealed that the material melts. Subsequently, the first cobalt-based ZIF glass was prepared. This proves that it is possible to incorporate metal ions other than zinc in ZIF glasses, showing that ZIF glasses with additional metal-centered functionality (e.g. redox activity, magnetism, etc.) can be prepared. Initiated from this study, luminescence was reported for cobalt ion containing ZIF glasses.[129] Just recently, R. Lin et. al demonstrated the accessibility of iron-cobalt bimetallic ZIF glasses, showing promising results in the electrochemical oxygen evolution reaction.[264] Based on the first example synthesized during this work, it turns out that metal-centered functionality presents a powerful tool to extend the scope of applications for ZIF glasses.

(b) Melting Point Engineering by Mixed-Linker ZIFs

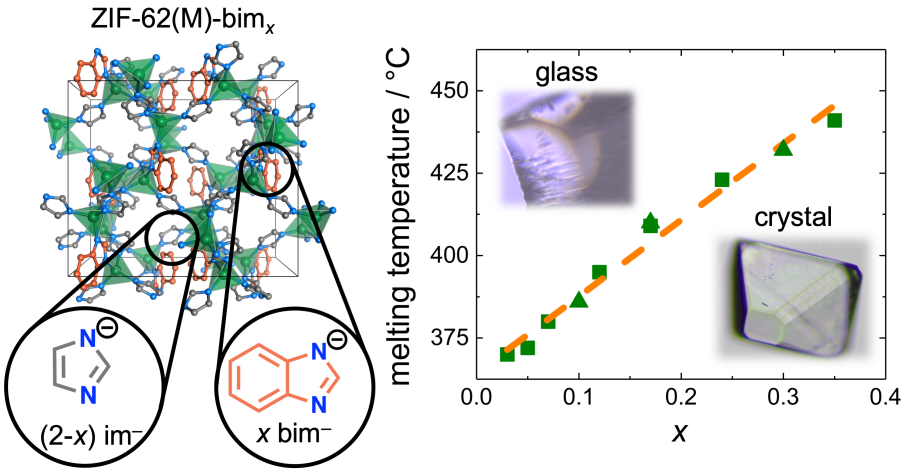

A series of the mixed-linker ZIF system ZIF-62(M)-bim$_x$ (general chemical composition M(im)$_{2-x}$(bim)$_x$ with M = Co^{2+}, Zn^{2+}) with various linker ratios was synthesized. Subsequently, this series was investigated regarding melting and glass formation, which uncovered that their melting temperature is linearly dependent on the bim$^-$ concentration. Thus, the melting point of the ZIF-62(M)-bim$_x$ materials is systematically adjustable from 440 °C (x = 0.35) down to 370 °C (x = 0.03). Additionally, it was found that lower bim$^-$ concentrations ($x \leq 0.03$) lead to a partial recrystallization of the ZIF melt.

First, this demonstrates the huge impact of the bulky bim$^-$ linker on the melting temperature and formation of thermodynamically stable ZIF liquids. From the obtained results, it is hypothesized that a large number of already known ZIFs could also melt – as far as they contain the small im$^-$ linker and another bulkier linker (such as bim$^-$). Consequently, this sets the stage for a systematic search (e.g. implementation of bulky linkers smaller than bim$^-$ in ZIF glass formers to further lower the melting temperature) and the discovery of many more ZIF glasses with various functions far beyond the state-of-the-art.

Additionally, the melting point of 370 °C represents the lowest melting point achieved for a crystalline ZIF, until now. Lower processing temperatures open the door for the preparation of ZIF glass composites incorporating temperature sensitive compounds. Importantly, the here synthesized ZIF-62(Zn)-bim$_{0.05}$ glass former was recently established to fabricate a $CsPbI_3$ perovskite ZIF glass composite. The glass matrix was shown to stabilize non-equilibrium perovskite phases with exceptional optoelectronic properties, which marks a breakthrough for future applications.[265]

All in all, the knowledge gained on (i) the porosity of ZIF glasses and (ii) the fundamentals of ZIF melting has a huge impact on the future development of this

emerging materials class. Some of the results presented here already initiated further research by other groups as outlined above. In addition, this work has also raised new questions which may be the subject of future research projects:

- How exactly can design concepts for porosity in porous polymers be transferred to ZIF glass chemistry?
- Which of the postulated ZIF glass formers really form a ZIF glass?
- Do the postulated requirements for ZIF building units (i.e. secondary bulky linkers smaller then bim^- lead to lower melting points) aid the accessibility of melt-quenched glasses with tailored properties?
- How far can the functionality and chemical diversity of ZIF glass composites be extended?

Part II – A New Class of Water-Processable MOFs

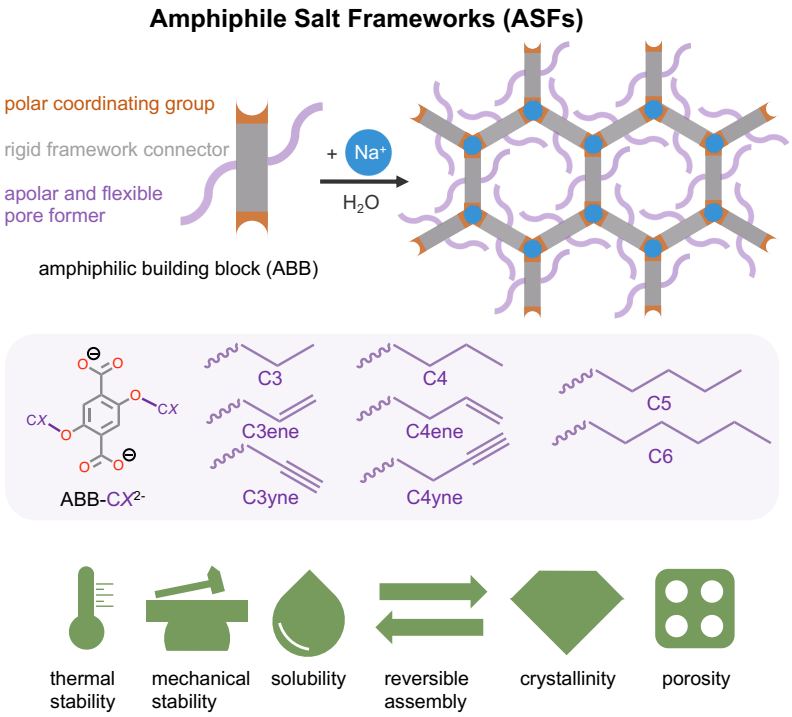

In this part, a design concept for the preparation of water-processable MOFs was developed. The approach is based on a systematic design of amphiphilic organic building units (ABBs) and the selection of kinetically labile inorganic building units (here Na^+ ions). ABBs feature structural directing hydrophobic functionalities (i.e alkyl-chains) which guide the self-assembly of the framework structure. Na^+ ions form strong but kinetically labile bonds to the ABBs hydrophilic part (i.e. carboxylate groups), which help to assemble/disassemmble the framework by hydrolysis.

Based on this design approach, the first examples of a new class of porous and water-processable framework materials, termed amphiphile salt frameworks (ASFs), have been successfully synthesized.

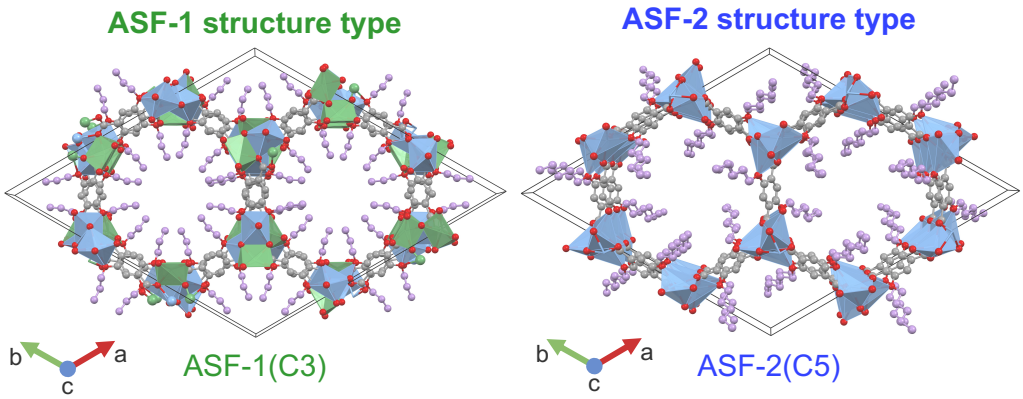

Obtained data on the materials structure and properties show that:

(a) ASFs feature well-defined trigonal microporous structures whose formation is driven by self-templating effects arising from the ABBs. Strikingly, two different ASF structure types (ASF-1 and ASF-2) were obtained. The formation of the respective structure type is dependent on the hydrophobic part of the ABBs (i.e. length of alkyl chain), which emphasizes their structural directionality.

(b) ASFs reversibly assemble from aqueous solution.

(c) ASFs own porosity features, which can be adjusted by the choice of ABB, leading to varying pore volumes and sizes.

(d) ASFs are stable towards high temperature (up to 400 °C) and pressure (up to 4000 bar).

Finally, the ASF materials combine the advantageous properties of porous framework compounds (such as MOFs) with the ability to be processed and recycled from solution.

Future studies will need to show whether the concept is also transferable to other building units and may focus on the following questions.

- Is it possible to change the metrics of the ABBs (e.g. by elongation) in order to derive isoreticular (e.g. expanded) structural motifs further extending the scope of porosity of these materials?
- Is it possible to use other metal ions (e.g. Li^+ or K^+) which could vary the processabilty (e.g. solubility in other solvents) and stability of ASFs?

All in all, investigations towards processable MOFs were addressed by two different approaches – melting and solution-processing. The obtained results aid for a deeper understanding of the fundamentals of MOF melting and the porosity of their derived glasses. Further, a new design approach yields to prototypical solution-processable MOFs (i.e ASFs). Thus, the results obtained in this thesis will help to better understand how the macrostructure of MOFs can be influenced and adjusted in the future.

12 Experimental Section

12.1 X-ray Diffraction Techniques

12.1.1 Single Crystal X-ray Diffraction

Single crystal X-ray diffraction (SCXRD) data were collected on an Oxford Diffraction Xcalibur or a Bruker D8 Venture diffractometer using MoK_α or CuK_α radiation. A N_2 cryostream from Oxford Instruments was used for the sample environment ($T = 100 - 400$ K). Further experimental details for specific data collections and processing can be found in the Appendix.

12.1.2 In-House Powder X-ray Diffraction

Powder X-ray diffraction (PXRD) patterns were recorded at room temperature on a Siemens D5005 diffractometer in Bragg-Brentano geometry. Data were collected with CuK_α radiation in the range from 5 ° to 50 ° 2θ with a step size of 0.02 °. Finely ground samples were deposited on a glass holder or a single crystal zero background sample holder made of silicon (cut along the (610) plane). For phase identification, structureless profile fits (Pawley method)[53] were performed with the TOPAS academic v6 software[56].

12.1.3 Variable-Temperature Powder X-ray Diffraction

Variable-temperature dependent PXRD measurements were performed at Beamline 9, DELTA (Germany) with a monochromatic X-ray beam ($\lambda = 0.6199$ Å) using a MAR345 image plate detector. Finely ground samples were sealed in quartz capillaries, placed on an Anton Paar DHS1100 hot stage and heated under a polyether ether ketone (PEEK) dome. The samples were heated to desired temperatures (e.g. in 25 °C steps). The temperatures were maintained while data collection (isothermal segment). Temperature calibration was performed by reference PXRD measurements of α-quartz. Detector distance calibration was carried out with LaB_6. Data processing was performed with the DAWN software package.[266,267]

12.1.4 High-Pressure Powder X-ray Diffraction

High-pressure powder X-ray diffraction (HP-PXRD) was performed at DELTA (Germany) at Beamline 9. Data of activated ASFs obtained via the solvothermal synthesis route were recorded with a wavelength of 0.4588 Å utilizing a MAR345 image plate detector. Detector distance calibration was carried out with LaB_6. Data processing was performed with the DAWN software package.[266,267]

HP-PXRD Set-Up

A powdered ASF sample was placed in a set-up previously designed for X-ray reflection measurements[252] on liquid samples. The sample carrier was modified to hold a self-made capillary made from Kapton® tubes (outer diameter (OD) = 1.0 mm) which helps to investigate powdered samples (see below). The pressure was applied with water on the capillary. The pressure was controlled with a hydraulic pump from $1 - 4000$ bar with a accuracy of ± 1 bar. Data were collected at various pressure points including a return pattern at ambient pressure after the pressure was released from the sample from the respective maximum applied pressure point. A pressure calibration was performed using potassium bromide (KBr) as a pressure standard.

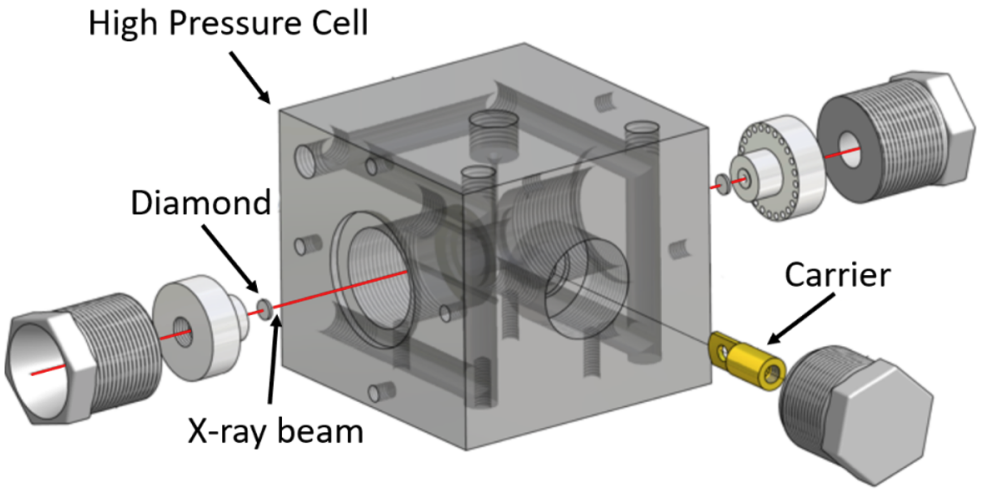

Figure 12.1: Schematic representation of the high-pressure set-up used at DELTA for HP-PXRD diffraction. Material is taken from Reference [252]. Adapted with permission of the International Union of Crystallography

Sample and Capillary Preparation

A sample holding capillary was prepared by first cutting of a $4 - 5$ cm piece of Kapton® tube (OD = 1.0 mm) which was sealed on one end with super glue (UHU

PLUS schnellfest®). A ground samples was filled into the capillary and silicon oil (polymethylphenylsiloxan (CAS: 63148-58-3)) was added on top as a pressure transmitting fluid. The capillary was centrifuged until all remaining air around the powdered solid was displaced by the silicon oil. An additional drop of silicon oil was added on top, and the open side was closed by bending the tube (insuring that no air was trapped in the capillary) and squashing a metal ring around the bended area with a pair of pliers (see Figure 12.2 for illustration).

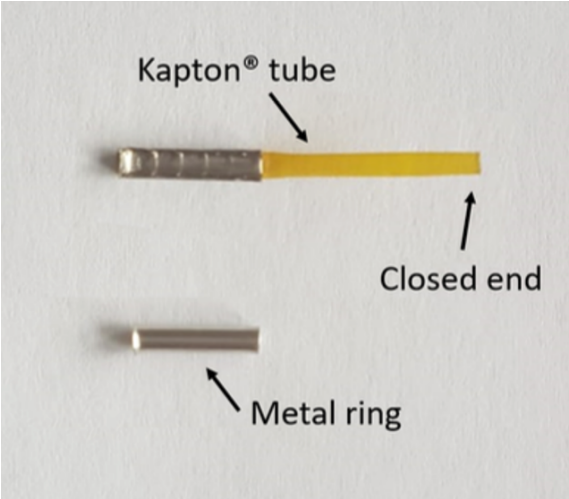

Figure 12.2: Photograph of a representative empty sealed capillary (top) and a metal ring (unsquashed) used for sealing (bottom).

12.1.5 X-ray Total Scattering

X-ray total scattering data for ZIF-4, a_TZIF-4, zni_TZIF-4, a_gZIF-4, ZIF-zni, a_gZIF-zni and a_gZIF-62 (Section 6) as well as ZIF-62(Co) and a_gZIF-62(Co) (Section 7) and ZIF-62(M)-bim$_x$ and a_gZIF-62(M)-bim$_x$ (Section 8) were collected at beamline I15-1 of Diamond Light Source (DLS) using a monochromatic X-ray beam (λ = 0.161669 Å, 76.7 keV). Samples were finely ground before loading into 1.5 mm (OD) borosilicate capillaries. X-ray total scattering data for TIF-4 and a_gTIF-4 (Section 6) were collected at beamline P02.1 at Deutsches Elektronen-Synchrotron (DESY) using a monochromatic X-ray beam (λ = 0.20734 Å, 60 keV). The samples were placed in a 1 mm (OD) quartz glass capillary.

Data integration was performed with the DAWN software package.[266] For all datasets, background subtraction was performed with scattering data collected from an empty capillary. Background subtraction, multiple, container and Compton scattering, as well as for absorption were done with the GudrunX program.[268] The normalized reciprocal space data were Fourier-transformed to yield the X-ray pair distribution functions (XPDFs) in the form of $D(r)$.[60,61]

12.2 Fourier-Transform Infrared Spectroscopy

Fourier-transform infrared (FTIR) spectroscopy was carried out on a Perkin Elmer SpectrumTwo FTIR spectrometer ($\tilde{\nu}$ = 400 cm^{-1} − 4000 cm^{-1}) in reflection mode using a diamond ATR (attenuated total reflectance) unit. Powdered samples were placed on the diamond ATR unit and carefully compressed with a stamp for the measurement.

12.3 Nuclear Magnetic Resonance Spectroscopy

Solution ^{1}H and ^{13}C nuclear magnetic resonance (NMR) spectroscopy was performed with Bruker DPX-300, DPX 500 or Agilent DD2 500 spectrometers.

For crystalline and glassy ZIF samples the solid samples were digested before the measurement using DMSO-d_6 (0.5 mL) and DCl/D_2O (35 wt%, < 0.1 mL) as solvents. Chemical shits were referenced to the residual proton signal of dimethyl sulfoxide (DMSO) and chemical shifts are given relative to tetramethylsilane. The data were processed with the MestReNova (v14.2.0) or ACD/Labs software.

12.4 Thermal Analysis

12.4.1 Simultaneous Thermogravimetric Analysis / Differential Scanning Calorimetry

Simultaneous thermogravimetric analysis / differential scanning calorimetry (TGA/DSC) measurements were conducted on a STA 504 instrument or SDT 650 from TA Instruments under a constant argon flow (4 L h^{-1}) for STA 504 or a nitrogen flow (100 mL min^{-1}) for SDT 650 on powdered samples.

Applied temperature programs are given directly in the main text or next to the plot of the collected data in the Appendix.

12.4.2 Differential Scanning Calorimetry

Differential scanning calorimetry measurements (DSC) were performed on a DSC 25 from TA Instruments under a constant nitrogen flow (50 mL min^{-1}). Before the measurement, the samples were ground and placed in a hermetically sealed aluminum crucible and a hole was pinched into the lid of the sealed crucible. For all DSC measurements a heating rate of +10 °C min^{-1} was applied. Samples of ZIF-4 and ZIF-zni were heated to a maximum temperature of 600 °C. Samples of ZIF-62, TIF-4 and their corresponding glasses were heated to a maximum temperature of

485 °C. Data analysis was performed with the TRIOS (v5.1.0.46403) software from TA Instruments.

12.5 Isothermal Gas Physisorption

Experiments were performed with a Quantachrome iQ MP porosimeter. Prior to the first measurement the ground activated samples were degassed under dynamic vacuum ($p \approx 10^{-5}$ kPa) at 200 °C for 2 h. Gas sorption isotherms were measured with N_2 (77 K), CO_2 (195 K and 273 K) and *n*-butane (273 K), propane and propylene (273 K or 293 K). Between measurements, samples were at least degassed under dynamic vacuum ($p \approx 10^{-5}$ kPa) at ambient temperature for approximately 3 h. After gas adsorption measurement with *n*-butane for ZIF materials, sample were again heated to 200 °C for 30 min under dynamic vacuum ($p \approx 10^{-5}$ kPa). Kinetic gas sorption data were collected for propane and propylene at 293 K by applying a gas pressure of $p \approx 55$ kPa and recording the pressure changes over time.
BET surface areas (S_{BET}) and total pore volume (V_{pore}) analysis were performed with the Quantachrome ASIQwin version 5.2 software. The relative pressure ranges applied and quality factors for the S_{BET} determinations are given in the Appendix.

12.6 Raman Scattering

Raman scattering measurements were performed with a confocal Raman spectrometer (S&I MonoVista Raman Microscope System CRS+ 750/BX51) providing a spatial resolution of about one micrometer. A Helium-Neon laser with 633 nm excitation wavelength (ZIF-62(Zn), ZIF-62(Co), a_gZIF-62(Co)) or the fundamental mode of a Nd:YAG single-frequency laser with 1064 nm wavelength (a_gZIF-62(Zn)) was used in the experiments. The laser power was set through neutral density filters and was carefully chosen in order to avoid a degradation of the sample. For that purpose, after each measurement the surface was visually checked using white light illumination and a video camera installed at the microscope. The laser beam was focused with a 50x microscope objective, properly chosen for the respective excitation wavelength used, on the sample. The laser spot size did not exceed 2 μm. The scattered light was examined using a 0.75m spectrometer (Acton SpectraPro SP2750) with a liquid-nitrogen cooled charge-coupled-device (CCD) camera (Princeton Instruments PyLoN 2KF). For the spectra measured at 633 nm (1064 nm) laser excitation, a Si-based (InGaAs-based) CCD camera was used. Wavelength-adapted edge filters suppressed the laser light, so that scattered light signals with energy shifts of 70 cm^{-1} with respect to the laser line position at zero energy shift could be resolved. The

samples were placed on a microscopy table, whose position could automatically be changed with sub-micrometer spatial scanning resolution.

12.7 Magnetic Measurements

Magnetic measurements as a function of temperature were performed with a Quantum Design MPMS-5S equipped with an AC susceptometry option, while field dependent curves were recorded with the vibrating sample magnetometer (VSM) option of a Quantum Design PPMS DynaCool.

12.8 Scanning Electron Microscopy

Scanning electron microscopy (SEM) imaging was performed with a Hitachi S-4500 instrument. For measurements, samples were placed on a conductive adhesive pad. Imaging was done with 1 kV accelerating voltage on a secondary electron detector. The analysis was done as a service measurement at Fakultät Bio- und Chemieingenieurswesen (Lehrstuhl für Biomaterialien und Polymerwissenschaften) at TU Dortmund by Volker Brandt.

12.9 Synthesis and Characterization

All chemicals were purchased from commercial suppliers (Sigma-Aldrich, abcr, Alfa-Aesar, etc.) and used as received. Yields are given as isolated yields.

12.9.1 Part I

ZIF-4(M)

ZIF-4(M) (M = Zn^{2+} or Co^{2+}) was synthesized adopting protocols already reported in the literature.[143,144] $M(NO_3)_2{\cdot}6H_2O$ (M = Zn^{2+} or Co^{2+}; 4.0 mmol, 1.2 g) and imidazole (Him; 13.2 mmol, 0.9 mg) were dissolved in 90 ml DMF. The clear solution was subsequently stored in an reaction oven for 7 days at 100 °C for the Zn-material or 130 °C for the Co-material. The reaction volume was allowed cooling back to ambient temperature and the formed crystals were filtered off and washed several times with single small portions of overall 20 ml DMF. The materials were obtained as large truncated octahedrally shaped single crystals (colorless for Zn-materials and purple for Co-materials) denoted as as-ZIF-4(M) (as = as-synthesized). After characterization of the as-ZIF-4(M) materials, the crystals were dried at 200 °C und dynamic vacuum ($\approx 10^{-4}$ kPa) for ≈ 20 h yielding the evacuated/activated materials (denoted as ZIF-4(M)).

ZIF-zni(M)

ZIF-zni(Zn) was synthesized after a modified solvothermal synthesis route based on ZIF-4 (see above) by solely replacing the original solvent DMF against ethanol. Sample activation was performed at 200 °C and dynamic vacuum ($p \approx 10^{-4}$ kPa) overnight.

ZIF-zni(Co) was synthesized in analogy to a literature protocol.[195] Imidazole (Him, 10 mmol, 680 mg) was dissolved in 3-methyl-1-butanol (15 mL) and a solution of $Co(OAc)_2 \cdot 4H_2O$ (5.0 mmol, 1.245 g) in quinoline (15 mL) was added. The mixture was stirred at room temperature overnight. Subsequently, the reaction mixture was equally split and transferred into two Teflon-lined autoclaves with a volume of 23 mL each. The autoclaves were sealed and heated to 140 °C for 24 h. After cooling to room temperature, the obtained single crystals were washed with ethanol (3× 15 mL) and dried in air.

ZIF-62(M)/ZIF-62(M)-bim$_x$*

All ZIF-62(M)-bim$_x$ (M = Zn^{2+} or Co^{2+}) were prepared after modified synthesis routes published in the literature.[29,143,144,198,199] $M(NO_3)_2{\cdot}6H_2O$ (M = Zn^{2+} or Co^{2+}; 4.0 mmol, 1.2 g) and varying ratios of imidazole and benzimidazole (total amount 13.2 mmol, molar ratios are given in Table 12.1) were dissolved in 90 ml DMF. The clear solution were divided into ten portions (9 ml each) and filled into ten 12 ml borosilicate reaction vials. The vials were sealed and subsequently stored in an reaction oven for 7 days at 100 °C for the Zn-material or 130 °C for the Co-material. After cooling back to ambient temperature, the reaction volumes were combined and the formed crystals filtered off and washed several times with small portions of overall 20 ml DMF. The as such obtained large truncated octahedrally shaped single crystals (colorless for Zn-materials and purple for Co-materials) are denoted as as-ZIF-62(M)-bim$_x$ (as = as-synthesized). After characterization of the as-ZIF-62(M)-bim$_x$ materials, the crystals were dried at 200 °C und dynamic vacuum ($\approx 10^{-4}$ kPa) for $\approx$ 20 h yielding the evacuated/activated materials (ZIF-62(M)-bim$_x$).

TIF-4

TIF-4 (chemical composition: $(Zn(im)_{1.68}(mbim)_{0.32})$ was synthesized after the same procedure as ZIF-62(Zn)-bim$_{0.35}$ (see above) by replacing the secondary bulky linker benzimidazole (Hbim) by 5-methylbenzimidazole (Hmbim) in the synthesis keeping the same molar ratio. Sample activation was performed at 200 °C and dynamic vacuum ($p \approx 10^{-4}$ kPa) overnight.

* We note that ZIF-62(Zn) equals ZIF-62(Zn)-bim$_{0.35}$ and ZIF-62(Co) equals ZIF-62(Co)-bim$_{0.30}$. The different abbreviations are used in part I of this thesis. In chapter 6 and 7 the shorter abbreviation is used for clarity.

Table 12.1: Applied masses (m) and molar amounts (n) of Him and Hbim in the synthesis mixture of the ZIF-62(M)-bim$_x$ compounds. The x^a values applied in synthesis are given as well as the found values in the corresponding framework – determined by ^{1}H NMR spectroscopy (see Section A.3.6).

Compound	n_{Him}/ mmol	m_{Him}/ mg	n_{Hbim}/ mmol	m_{Hbim}/ mg	x_{applied}	x_{found}
ZIF-62(Zn)-bim$_{0.35}$	11.55	786	1.660	196	0.25	0.35
ZIF-62(Zn)-bim$_{0.24}$	12.32	840	0.880	104	0.13	0.24
ZIF-62(Zn)-bim$_{0.17}$	12.70	865	0.500	60	0.069	0.17
ZIF-62(Zn)-bim$_{0.12}$	12.89	878	0.307	36	0.047	0.12
ZIF-62(Zn)-bim$_{0.07}$	13.04	888	0.155	18	0.024	0.07
ZIF-62(Zn)-bim$_{0.05}$	13.09	891	0.104	12	0.016	0.05
ZIF-62(Zn)-bim$_{0.03}$	13.12	893	0.078	9	0.012	0.03
ZIF-62(Zn)-bim$_{0.02}$	13.14	894	0.063	7	0.009	0.02
ZIF-62(Co)-bim$_{0.30}$	11.55	786	1.660	196	0.25	0.30
ZIF-62(Co)-bim$_{0.10}$	12.89	878	0.307	36	0.047	0.10

a $x = 2\ c_{\mathrm{bim}}\ /\ (\ c_{\mathrm{im}} + c_{\mathrm{bim}})$, c = molar concentration.

12.9.2 Part II

Amphiphilic Building Units

The amphiphilic building blocks (ABBs) can be prepared either from the commercially available diethyl 2,5-dihydroxy-1,4-benzenedicarboxylate or from the precursor dimethyl 2,5-dihydroxy-1,4-benzenedicarboxylate (see below). For the sake of clarity only the protocols for the later procedure are given here. The etherification and saponification reactions can be done analogously by starting with the commercial diethyl 2,5-dihydroxy-1,4-benzenedicarboxylate.

Precursor synthesis

For the synthesis of dimethyl 2,5-dihydroxy-1,4-benzenedicarboxylate, 2,5-dihydroxy-1,4-benzenedicarboxylic acid (5 g, 25.54 mmol) was dissolved in MeOH (250 mL) and sulfuric acid (15 mL) was added. After stirring for 8 h at reflux temperature, MeOH was evaporated and the obtained suspension filtered and washed with distilled water. The yellow solid was dried under dynamic vacuum ($\approx 10^{-4}$ kPa) at 70 °C. Yield: 5.45 g (96%)

^{1}H NMR (500 MHz, DMSO-d_6) δ(ppm) = 3.86 (s, 6H), 7.26 (s, 2H), 9.80 (s, 2H).
^{13}C NMR (126 MHz, DMSO-d_6) δ(ppm) = 53.10, 118.08, 120.44, 150.99, 167.78.

Building block synthesis

Method A – Williamson etherification and hydrolysis. Dimethyl 2,5-dihydroxy-1,4-benzenedicarboxylate (precursor; 1 g, 4.42 mmol, 1 eq.) and potassium carbonate (3.06 g, 22.11 mmol, 5 eq.) was suspended in DMF. The alkyl halide (RX, see Table 12.2, 13.26 mmol, 3 eq.) was added dropwise and the suspension was heated to 80 °C under stirring for 4 h. Afterwards, the solvent was evaporated and aqueous potassium hydroxide solution (30 mL, 10%) was added. The resulting mixture was stirred at reflux temperature for 5 h. Addition of hydrochloric acid (30 mL, 10%) and filtration led to light-yellow solids. The obtained products were dried under dynamic vacuum ($\approx 10^{-4}$ kPa) at 80 °C. The products were characterized via NMR spectroscopy (see below).

Method B – Mitsunobu etherification and hydrolysis. Dimethyl 2,5-dihydroxy-1,4-benzenedicarboxylate (precursor; 1 g, 4.42 mmol, 1 eq.), triphenylphosphine (2.67 g, 10.17 mmol, 2.3 eq.) and diisobutyl azodicarboxylate (2.34 g, 10.17 mmol, 2.3 eq.) were dissolved in THF (8 mL) and a respective alkyl alcohol (ROH, see Table 12.2, 10.17 mmol, 2.3 eq.) – also dissolved in THF (5 mL) – was added

slowly over a period of 30 min while stirring in a sonication bath. Afterwards, the solution was stirred for further 3 h. An aqueous potassium hydroxide solution (30 ml, 10%) was added and the mixture kept in the sonication bath for additional 12 h. The aqueous phase was extracted with ethyl acetate (3x 10 mL), followed by the addition of hydrochloric acid (30 mL, 10%). The light-yellow precipitates were filtered off and dried under dynamic vacuum ($\approx 10^{-3}$ kPa) at 80 °C. The products were characterized via NMR spectroscopy (see below).

Table 12.2: Utilized halides (RX) and alcohols (ROH) to synthesis the amphiphilic build blocks (ABBs; H_2ABB-C*X*) and corresponding yields. Abbreviations: Et = ethyl; Pr = propyl; Bu = butyl; Pen = pentyl; Hex = hexyl; Hept = heptyl.

ABB	RX/ROH	Yield (%)	Method
H_2ABB-C2	Et-OH	94	B
H_2ABB-C3	Pr-Br	88	A
H_2ABB-C3ene	H_2C=CH-CH_2-OH	99	B
H_2ABB-C3yne	HC≡C-CH_2-OH	90	B
H_2ABB-C4	Bu-Br	84	A
H_2ABB-C4ene	H_2C=CH-$(CH_2)_2$-OH	92	B
H_2ABB-C4yne	HC≡C-$(CH_2)_2$-OH	55	B
H_2ABB-C5	Pen-Br	92	A
H_2ABB-C6	Hex-Br	76	A
H_2ABB-C7	Hept-Br	98	A

H_2ABB-C2: ^{1}H NMR (400 MHz, DMSO-d_6) δ(ppm) = 1.29 (t, J=6.9, 6H), 4.04 (q, J=6.9, 4H), 7.26 (s, 2H), 12.89 (s, 2H).
^{13}C NMR (101 MHz, DMSO-d_6) δ(ppm) = 14.69 (s), 64.97 (s), 115.70 (s), 125.59 (s), 150.32 (s), 166.81 (s).

H_2ABB-C3: ^{1}H NMR (500 MHz, DMSO-d_6) δ(ppm) = 0.97 (m, 6H), 1.69 (h, J=7.2), 2H), 3.94 (t, J=6.4, 4H), 7.25 (s, 2H), 13.01 (s, 2H).
^{13}C NMR (126 MHz, DMSO-d_6) δ(ppm) = 10.81 (s), 22.56 (s), 71.08 (s), 115.97 (s), 126.01 (s), 150.88 (s), 167.30 (s).

H_2ABB-C3ene: ^{1}H NMR (500 MHz, DMSO-d_6) δ(ppm) = 4.59 (dt, J=4.8, 1.7, 4H), 5.24 (dq, J=10.7, 1.6, 2H), 5.43 (dq, J=17.3, 1.9, 2H), 6.01 (ddt, J=17.3, 10.6, 4.8, 1H), 7.30 (s, 2H), 12.99 (s, 2H).
^{13}C NMR (126 MHz, DMSO-d_6) δ(ppm) = 69.82 (s), 116.28 (s), 117.41 (s), 125.78 (s), 133.92 (s), 150.51 (s), 167.20 (s).

H_2ABB-C3yne: ^{1}H NMR (500 MHz, DMSO-d_6) δ(ppm) = 3.59 (t, J=2.4, 1H), 4.84 (d, J=2.4, 2H), 7.43 (s, 2H), 13.11 (s, 2H).

^{13}C NMR (126 MHz, DMSO-d_6) δ(ppm) = 57.32 (s), 79.24 (s), 79.47 (s), 117.01 (s), 126.11 (s), 149.95 (s), 166.91 (s).

H_2ABB-C4: ^{1}H NMR (400 MHz, DMSO-d_6) δ(ppm) = 0.91 (t, J=7.4, 6H), 1.43 (m, 4H), 1.65 (m, 4H), 3.98 (t, J=6.3, 4H), 7.25 (s, 2H), 12.90 (s, 2H).
^{13}C NMR (101 MHz, DMSO-d_6) δ(ppm) = 13.69 (s), 18.60 (s), 30.80 (s), 68.84 (s), 115.46 (s), 125.51 (s), 150.41 (s), 166.84 (s).

H_2ABB-C4ene: ^{1}H NMR (700 MHz, DMSO-d_6) δ(ppm) = 2.45 (qt, J=6.6, 1.4, 4H), 4.05 (t, J=6.6, 4H), 5.07 (ddt, J=10.1, 2.1, 1.2, 2H), 5.16 (dq, J=17.2, 1.7, 2H), 5.91 (ddt, J=17.1, 10.3, 6.7, 2H), 7.29 (s, 2H), 12.93 (s, 2H).
^{13}C NMR (101 MHz, DMSO-d_6) δ(ppm) = 33.14 (s), 68.74 (s), 115.92 (s), 117.01 (s), 125.67 (s), 134.78 (s), 150.43 (s), 166.71 (s).

H_2ABB-C4yne: ^{1}H NMR (500 MHz, DMSO-d_6) δ(ppm) = 2.60 (td, J=6.6, 2.7, 4H), 2.87 (t, J=2.6, 2H), 4.09 (t, J=6.7, 4H), 7.32 (s, 2H), 12.97 (s, 2H).
^{1}C NMR (126 MHz, DMSO-d_6) δ(ppm) = 19.41 (s), 68.35 (s), 73.03 (s), 81.55 (s), 116.95 (s), 126.40 (s), 150.80 (s), 167.01 (s).

H_2ABB-C5: ^{1}H NMR (500 MHz, DMSO-d_6) δ(ppm) = 0.89 (t, J=7.2, 6H), 1.36 (m, 8H), 1.68 (m, 4H), 3.97 (t, J=6.4, 4H), 7.26 (s, 2H), 12.93 (s, 2H).
^{13}C NMR (126 MHz, DMSO-d_6) δ(ppm) = 14.38 (s), 22.26 (s), 27.99 (s), 28.83 (s), 69.61 (s), 115.97 (s), 125.96 (s), 150.88 (s),167.29 (s).

H_2ABB-C6: ^{1}H NMR (400 MHz, DMSO-d_6) δ(ppm) = 0.86 (m, 6H), 1.29 (m, 8H), 1.41 (m, 4H), 1.67 (m, 4H), 3.97 (t, J=6.4, 4H), 7.25 (s, 6H), 12.88 (s, 6H).
^{13}C NMR (101 MHz, DMSO-d_6) δ(ppm) = 13.89 (s), 22.06 (s), 24.99 (s), 28.65 (s), 30.90 (s), 69.13 (s), 115.50 (s), 125.46 (s), 150.42 (s), 166.83 (s).

H_2ABB-C7: ^{1}H NMR (600 MHz, DMSO-d_6) δ(ppm) = 12.91 (s, 2H), 7.24 (s, 2H), 3.96 (t, J = 6.4 Hz, 4H), 1.69-1.64 (m, 4H), 1.44-1.38 (m, 4H), 1.33-1.22 (m, 12H), 0.86 (t, J = 6.8 Hz, 6H).
^{13}C NMR (150.94 MHz, DMSO-d_6) δ(ppm) = 166.85, 150.41, 125.54, 115.49, 69.12, 31.24, 28.69, 28.35, 25.28, 22.01, 13.95.

Amphiphile Salt Frameworks

The amphiphile salt frameworks (ASFs) were synthesised after different synthesis routes. The solvothermal synthesis yields to single crystals suitable for SCXRD. The

evaporation synthesis route is easily scalable as desired and yields to polycrystalline powders. Based on the evaporation synthesis approach, ASFs were also deposited on glass plates. Furthermore, a mechanochemical synthesis was conducted.

Solvothermal Synthesis Route

A respective amphiphilic building block (H_2ABB-CX, 0.2 mmol, 1 eq.) was dissolved in a mixture of DMF and EtOH (1:1, $\approx 1 - 2$ mL). Sodium acetate (0.4 mmol, 2 eq.) was dissolved separately in distilled water ($\approx$ 0.2 mL). The solution of sodium acetate in water was filled in a 12 mL borosilicate glass vessel. Pure DMF (4 mL) was carefully added as a second layer and the solution of H_2ABB-CX was added as a third layer. The vessel was sealed with a screw cap and kept in an oven for 24 h at 120 °C. Single crystals for SCXRD analysis were directly selected from the mother liquor. For further analysis (PXRD, IR spectrospcopy, TGA/DSC, gas physisorption) the crystals were filtered and subsequently washed with small amounts of DMF and chloroform. The obtained solids were further dried for approximately 24 h at 100 °C under dynamic vacuum ($\approx 10^{-4}$ kPa).

Evaporation Synthesis Route

A desired amount of an amphiphilic building block (H_2ABB-CX, 1 eq.) was chosen and the appropriate volume of an freshly prepared aqueous sodium hydroxide stock solution (2 M, 2 eq.) was added. The emulsion was kept in a sonication bath and − if necessary − additional small amounts of water were added till a clear solution was obtained. Following, the water was fully evaporated:

1 **evap-a**: at a rotary evaporator at 80 °C and continuous membrane pump vacuum. This process took about $10 - 20$ min.

2 **evap-b** by pouring the solution in a glass vessel and storing the glass vessel in oven at 50 °C without a lid to allow evaporation of the water. The vessel was covered with a beaker to prevent contamination. This process took about $3 - 5$ days.

Deposition on Glass Plate

A clear solution was prepared of the respective ABB and sodium hydroxide as described before (see Evaporation Synthesis Route). A glass plate was preheated in an oven for 10 min which was set to 100 °C. Afterwards, $3 - 5$ drops of the previously prepared solution were casted on the glass plate. The glass plate was stored for further $10 - 30$ min in the oven at 100 °C to yield a film of solids on the glass plate's surface. Shorter reaction times (till all water was evaporated) were found

utilizing H_2ABB-C5 in the reaction, whereas longer reaction times were necessary for H_2ABB-CX (CX = C3, C3ene, C3yne).

Mechanochemical Synthesis

The synthesis was performed in an Achat mortar. Sodium hydroxide (40 mg, 1 mmol) was 'preground' before one of the respective linkers (H_2ABB-C3, H_2ABB-C3ene, H_2ABB-C3yne, H_2ABB-C5; 0.5 mmol) was added to the mortar and ground together for further 10 min. The resulting material was taken out of the mortar without further purification for structural analysis.

Bibliography

[1] S. R. Batten, N. R. Champness, X.-M. Chen, J. Garcia-Martinez, S. Kitagawa, L. Öhrström, M. O'Keeffe, M. Paik Suh, J. Reedijk, *Pure Appl. Chem.* **2013**, *85*, 1715–1724.

[2] J. L. Rowsell, O. M. Yaghi, *Microporous Mesoporous Mater.* **2004**, *73*, 3–14.

[3] J. R. Long, O. M. Yaghi, *Chem. Soc. Rev.* **2009**, *38*, 1213–1214.

[4] S. R. Batten, N. R. Champness, X. M. Chen, J. Garcia-Martinez, S. Kitagawa, L. Öhrström, M. O'Keeffe, M. P. Suh, J. Reedijk, *CrystEngComm* **2012**, *14*, 3001–3004.

[5] B. P. Block, J. Simkin, L. R. Ocone, *J. Am. Chem. Soc.* **1962**, *84*, 1749–1750.

[6] R. West, H. Y. Niu, *J. Am. Chem. Soc.* **1963**, *83*, 2589–2590.

[7] R. Robson, *Dalton Trans.* **2008**, 5113–5131.

[8] R. Robson, *J. Chem. Soc. Dalt. Trans.* **2000**, 3735–3744.

[9] M. Kondo, T. Yoshitomi, H. Matsuzaka, S. Kitagawa, K. Seki, *Angew. Chem. Int. Ed.* **1997**, *36*, 1725–1727.

[10] H. Li, M. Eddaoudi, M. O'Keeffe, O. M. Yaghi, *Nature* **1999**, *402*, 276–279.

[11] X. Zhang, Z. Chen, X. Liu, S. L. Hanna, X. Wang, R. Taheri-Ledari, A. Maleki, P. Li, O. K. Farha, *Chem. Soc. Rev.* **2020**, *49*, 7406–7427.

[12] C. Healy, K. M. Patil, B. H. Wilson, L. Hermanspahn, N. C. Harvey-Reid, B. I. Howard, C. Kleinjan, J. Kolien, F. Payet, S. G. Telfer, P. E. Kruger, T. D. Bennett, *Coord. Chem. Rev.* **2020**, *419*, 213388.

[13] U. Mueller, M. Schubert, F. Teich, H. Puetter, K. Schierle-Arndt, J. Pastré, *J. Mater. Chem.* **2006**, *16*, 626–636.

[14] O. M. Yaghi, M. O' Keeffe, N. W. Ockwig, H. K. Chae, M. Eddaoudi, J. Kim, *Nature* **2003**, *423*, 705–714.

[15] S. Yuan, L. Feng, K. Wang, J. Pang, M. Bosch, C. Lollar, Y. Sun, J. Qin, X. Yang, P. Zhang, Q. Wang, L. Zou, Y. Zhang, L. Zhang, Y. Fang, J. Li, H.-C. Zhou, *Adv. Mater.* **2018**, *30*, 1704303.

[16] M. Eddaoudi, J. Kim, N. Rosi, D. Vodak, J. Wachter, M. O'Keeffe, O. M. Yaghi, *Science* **2002**, *295*, 469–472.

[17] S. L. James, *Chem. Soc. Rev.* **2003**, *32*, 276–288.

[18] D. J. Tranchemontagne, J. L. Mendoza-Cortés, M. O'Keeffe, O. M. Yaghi, *Chem. Soc. Rev.* **2009**, *38*, 1257–1283.

[19] H. Deng, S. Grunder, K. E. Cordova, C. Valente, H. Furukawa, M. Hmadeh, F. Gandara, a. C. Whalley, Z. Liu, S. Asahina, H. Kazumori, M. O'Keeffe, O. Terasaki, J. F. Stoddart, O. M. Yaghi, *Science* **2012**, *336*, 1018–1023.

[20] J. J. Perry IV, J. A. Perman, M. J. Zaworotko, *Chem. Soc. Rev.* **2009**, *38*, 1400.

[21] C. R. Groom, I. J. Bruno, M. P. Lightfoot, S. C. Ward, *Acta Crystallogr. Sect. B* **2016**, *72*, 171–179.

[22] G. Férey, *Chem. Soc. Rev.* **2008**, *37*, 191–214.

[23] R. Freund, S. Canossa, S. M. Cohen, W. Yan, H. Deng, V. Guillerm, M. Eddaoudi, D. G. Madden, D. Fairen-Jimenez, H. Lyu, L. K. Macreadie, Z. Ji, Y. Zhang, B. Wang, F. Haase, C. Wöll, O. Zaremba, J. Andreo, S. Wuttke, C. S. Diercks, *Angew. Chem. Int. Ed.* **2021**, *60*, 23946–23974.

[24] H. Furukawa, K. E. Cordova, M. O'Keeffe, O. M. Yaghi, *Science* **2013**, *341*, 974–986.

[25] M. Pina, R. Mallada, M. Arruebo, M. Urbiztondo, N. Navascués, O. de la Iglesia, J. Santamaria, *Microporous Mesoporous Mater.* **2011**, *144*, 19–27.

[26] R. Ramesh, N. A. Spaldin in *Nanosci. Technol. Vol. 3*, Co-Published with Macmillan Publishers Ltd, UK, **2009**, pp. 20–28.

[27] R. L. Hoffman, B. J. Norris, J. F. Wager, *Appl. Phys. Lett.* **2003**, *82*, 733–735.

[28] C. Martínez, A. Corma in *Compr. Inorg. Chem. II*, *Vol. 5*, Elsevier, **2013**, pp. 103–131.

[29] R. Banerjee, A. Phan, B. Wang, C. Knobler, H. Furukawa, M. O'Keeffe, O. M. Yaghi, *Science* **2008**, *319*, 939–943.

[30] Y. Q. Tian, Y. M. Zhao, Z. X. Chen, G. N. Zhang, L. H. Weng, D. Y. Zhao, *Chem. Eur. J.* **2007**, *13*, 4146–4154.

[31] W. Vermeiren, J. P. Gilson, *Top. Catal.* **2009**, *52*, 1131–1161.

[32] J. Zhang, T. Wu, C. Zhou, S. Chen, P. Feng, X. Bu, *Angew. Chem. Int. Ed.* **2009**, *48*, 2542–2545.

[33] S. Horike, K. Kadota, T. Itakura, M. Inukai, S. Kitagawa, *Dalton Trans.* **2015**, *44*, 15107–15110.

[34] K. Kadota, E. Sivaniah, S. Bureekaew, S. Kitagawa, S. Horike, *Inorg. Chem.* **2017**, *56*, 8744–8747.

[35] J. Sun, L. Semenchenko, W. T. Lim, M. F. Ballesteros Rivas, V. Varela-Guerrero, H. K. Jeong, *Microporous Mesoporous Mater.* **2018**, *264*, 35–42.

[36] J. López-Cabrelles, J. Romero, G. Abellán, M. Giménez-Marqués, M. Palomino, S. Valencia, F. Rey, G. Mínguez Espallargas, *J. Am. Chem. Soc.* **2019**, *141*, 7173–7180.

[37] K. S. Park, Z. Ni, A. P. Cote, J. Y. Choi, H. Huang, F. J. Uribe-Romo, H. K. Chae, M. O'Keeffe, O. M. Yaghi, *PNAS* **2006**, *103*, 10186–10191.

[38] Y. Peng, Y. Li, Y. Ban, H. Jin, W. Jiao, X. Liu, W. Yang, *Science* **2014**, *346*, 1356–1359.

[39] W. Roentgen, *Nature* **1896**, *53*, 274.

[40] M. Laue, W. Friedrich, P. Knipping, *Verl. der Königlich Bayer. Akad. der Wiss.* **1912**, 303.

[41] W. L. Bragg, *Proc. Math. Phys. Series A* **1913**, *89*, 248–277.

[42] W. H. Bragg, W. L. Bragg, *Nature* **1913**, *91*, 557–557.

[43] W. H. Bragg, *Proc. Math. Phys. Series A* **1913**, *89*, 246–248.

[44] W. Massa, *Kristallstrukturbestimmung*, Springer Fachmedien Wiesbaden, **2015**.

[45] *https://www.nobelprize.org/prizes/chemistry/1985/press-release/*, accessed 10.12.2021.

[46] A. L. Patterson, *Phys. Rev.* **1934**, *46*, 372–376.

[47] A. L. Patterson, *Z. Kristallogr. – Cryst. Mater.* **1935**, *90*, 517–542.

[48] O. V. Dolomanov, L. J. Bourhis, R. J. Gildea, J. A. K. Howard, H. Puschmann, *J. Appl. Crystallogr.* **2009**, *42*, 339–341.

[49] J. Brentano, *Proc. Phys. Soc.* **1924**, *37*, 184–193.

[50] T. Runčevski, C. M. Brown, *Cryst. Growth Des.* **2021**, *21*, 4821–4822.

[51] I. C. Madsen, N. V. Y. Scarlett in *Powder Diffraction*, (Eds.: R. E. Dinnebier, S. J. L. Billinge), Royal Society of Chemistry, Cambridge, **2008**, pp. 298–331.

[52] R. B. Von Dreele in *Powder Diffraction*, (Eds.: R. E. Dinnebier, S. J. L. Billinge), Royal Society of Chemistry, Cambridge, **2008**, pp. 266–281.

[53] G. S. Pawley, *J. Appl. Crystallogr.* **1981**, *14*, 357–361.

[54] A. Le Bail, *Powder Diffraction* **2005**, *20*, 316–326.

[55] *Powder Diffraction*, (Eds.: R. E. Dinnebier, S. J. L. Billinge), Royal Society of Chemistry, Cambridge, **2008**.

[56] A. A. Coelho, *J. Appl. Crystallogr.* **2018**, *51*, 210–218.

[57] Y. Liao, *An Online Book* **2006**.

[58] T. Egami, S. J. L. Billinge, *Underneath the Bragg Peaks : Structural Analysis of Complex Materials.* 2nd Ed., Elsevier Science, Burlington, **2012**.

[59] S. Billinge in *Powder Diffraction*, (Eds.: R. E. Dinnebier, S. J. L. Billinge), Royal Society of Chemistry, Cambridge, **2008**, pp. 464–493.

[60] A. K. Soper, E. R. Barney, *J. Appl. Crystallogr.* **2011**, *44*, 714–726.

[61] D. A. Keen, *J. Appl. Crystallogr.* **2001**, *34*, 172–177.

[62] K. S. W. Sing, *Pure Appl. Chem.* **1985**, *57*, 603–619.

[63] Y. L. Zhu, H. Dai, Y. Duan, Q. Chen, M. Zhang, *Cryst. Growth Des.* **2020**, *20*, 2623–2631.

[64] X. Zou, Y. Yang, H. Chen, X.-L. Shi, S. Song, Z.-G. Chen, *Mater. Des.* **2021**, *202*, 109542.

[65] M. Liu, L. Zhang, M. A. Little, V. Kapil, M. Ceriotti, S. Yang, L. Ding, D. L. Holden, R. Balderas-Xicohténcatl, D. He, R. Clowes, S. Y. Chong, G. Schütz, L. Chen, M. Hirscher, A. I. Cooper, *Science* **2019**, *366*, 613–620.

[66] A. K. Sekizkardes, J. T. Culp, T. Islamoglu, A. Marti, D. Hopkinson, C. Myers, H. M. El-Kaderi, H. B. Nulwala, *Chem. Commun.* **2015**, *51*, 13393–13396.

[67] K. S. Sing, R. T. Williams, *Adsorpt. Sci. Technol.* **2004**, *22*, 773–782.

[68] A. Schneemann, V. Bon, I. Schwedler, I. Senkovska, S. Kaskel, R. A. Fischer, *Chem. Soc. Rev.* **2014**, *43*, 6062–6096.

[69] M. Thommes, K. Kaneko, A. V. Neimark, J. P. Olivier, F. Rodriguez-Reinoso, J. Rouquerol, K. S. Sing, *Pure Appl. Chem.* **2015**, *87*, 1051–1069.

[70] D. Ongari, P. G. Boyd, S. Barthel, M. Witman, M. Haranczyk, B. Smit, *Langmuir* **2017**, *33*, 14529–14538.

[71] G. Horvath, K. Kawazoe, *J. Chem. Eng. Japan* **1983**, *16*, 470–475.

[72] P. I. Ravikovitch, G. L. Haller, A. V. Neimark, *Adv. Colloid Interface Sci.* **1998**, *76-77*, 203–226.

[73] R. Evans, U. M. B. Marconi, P. Tarazona, *J. Chem. Soc. Faraday Trans. 2* **1986**, *82*, 1763–1787.

[74] C. Lastoskie, K. E. Gubbins, N. Quirke, *J. Phys. Chem.* **1993**, *97*, 4786–4796.

[75] J. P. Olivier, W. B. Conklin, M. V. Szombathely, *Stud. Surf. Sci. Catal.* **1994**, *87*, 81–89.

[76] A. V. Neimark, *Langmuir* **1955**, *11*, 4183–4184.

[77] J. Landers, G. Y. Gor, A. V. Neimark, *Colloids Surf. A: Physicochem. Eng. Asp.* **2013**, *437*, 3–32.

[78] M. Thommes, K. A. Cychosz, *Adsorption* **2014**, *20*, 233–250.

[79] S. Brunauer, P. H. Emmett, E. Teller, *J. Am. Chem. Soc.* **1938**, *60*, 309–319.

[80] I. Langmuir, *Nobel Lecture* **1932**.

[81] J. Rouquerol, P. Llewellyn, F. Rouquerol in *Stud. Surf. Sci. Catal. Vol. 160*, Elsevier B.V., **2007**, pp. 49–56.

[82] J. J. Beaudoin, J. Marchand in *Handb. Anal. Tech. Concr. Sci. Technol.* Elsevier, **2001**, pp. 528–628.

[83] D. A. Gómez-Gualdrón, P. Z. Moghadam, J. T. Hupp, O. K. Farha, R. Q. Snurr, *J. Am. Chem. Soc.* **2016**, *138*, 215–224.

[84] K. S. Walton, R. Q. Snurr, *J. Am. Chem. Soc.* **2007**, *129*, 8552–8556.

[85] W. G. MacMillian, E. Teller, *J. Phys. Chem.* **1951**, *55*, 17–20.

[86] R. Ozao, T. Okabe, Y. Nishimoto, Y. Cao, N. Whitely, W. P. Pan, *Energy Fuels* **2005**, *19*, 1729–1734.

[87] W. Yang, A. J. Davies, X. Lin, M. Suyetin, R. Matsuda, A. J. Blake, C. Wilson, W. Lewis, J. E. Parker, C. C. Tang, M. W. George, P. Hubberstey, S. Kitagawa, H. Sakamoto, E. Bichoutskaia, N. R. Champness, S. Yang, M. Schröder, *Chem. Sci.* **2012**, *3*, 2993–2999.

[88] E. C. Markham, A. F. Benton, *J. Am. Chem. Soc.* **1931**, *53*, 497–507.

[89] F. C. Tompkins, D. M. Young, *Trans. Faraday Soc.* **1951**, *47*, 88.

[90] O. Talu, *Adv. Colloid Interface Sci.* **1998**, *76-77*, 227–269.

[91] O. Talu, *Chem. Ing. Tech.* **2011**, *83*, 67–82.

[92] A. L. Myers, J. M. Prausnitz, *AIChE J.* **1965**, *11*, 121–127.

[93] C. M. Simon, B. Smit, M. Haranczyk, *Comput. Phys. Commun.* **2016**, *200*, 364–380.

[94] J. Wang, X. Guo, *Chemosphere* **2020**, *258*, 127279.

[95] D. P. Valenzuela, A. L. Myers, O. Talu, I. Zwiebel, *AIChE J.* **1988**, *34*, 397–402.

[96] R. B. Lin, S. Xiang, H. Xing, W. Zhou, B. Chen, *Coord. Chem. Rev.* **2019**, *378*, 87–103.

[97] M. Guo, M. Kanezashi, *Membranes* **2021**, *11*, 310.

[98] L. Li, R.-B. Lin, X. Wang, W. Zhou, L. Jia, J. Li, B. Chen, *Chem. Eng. J.* **2018**, *354*, 977–982.

[99] J. R. Álvarez, E. Sánchez-González, E. Pérez, E. Schneider-Revueltas, A. Martínez, A. Tejeda-Cruz, A. Islas-Jácome, E. González-Zamora, I. A. Ibarra, *Dalton Trans.* **2017**, *46*, 9192–9200.

[100] C. Y. Lee, Y. S. Bae, N. C. Jeong, O. K. Farha, A. A. Sarjeant, C. L. Stern, P. Nickias, R. Q. Snurr, J. T. Hupp, S. T. Nguyen, *J. Am. Chem. Soc.* **2011**, *133*, 5228–5231.

[101] M. Mohamedali, A. Henni, H. Ibrahim, *Adsorption* **2019**, *25*, 675–692.

[102] J. C. Mauro, E. D. Zanotto, *Int. J. Appl. Glass Sci.* **2014**, *5*, 313–327.

[103] B. Cotterell, J. Kamminga, *Mechanics of Pre-industrial Technology: An Introduction to the Mechanics of Ancient and Traditional Material Culture*, Cambridge University Press, **1992**.

[104] B. Schlick-Nolte, *Die Glasgefässe im alten Ägypten*, B. Hessling, Berlin, **1968**.

[105] J. Henderson in *Anc. Glas. An Interdiscip. Explor.* Cambridge University Press, **2013**, pp. 127–157.

[106] O. Schott, PhD thesis, Universität Jena, **2001**.

[107] H. G. Frischat, *Chemie Unserer Zeit* **1977**, *11*, 65–74.

[108] D. L. Morse, J. W. Evenson, *Int. J. Appl. Glass Sci.* **2016**, *7*, 409–412.

[109] E. D. Zanotto, J. C. Mauro, *J. Non-Cryst. Solids* **2017**, *471*, 490–495.

[110] W. Eitel, *Angew. Chem.* **1933**, *46*, 541–541.

[111] R. H. Doremus, *Glass Science*, 2nd Ed., Wiley-Interscience, New York, **1973**.

[112] K. J. Rao, *Structural chemistry of glasses*, 1st Ed., Elsevier, **2002**.

[113] W. H. Zachariasen, *J. Am. Chem. Soc.* **1932**, *54*, 3841–3851.

[114] T. D. Bennett, J.-C. Tan, Y. Yue, E. Baxter, C. Ducati, N. J. Terrill, H. H. .-. Yeung, Z. Zhou, W. Chen, S. Henke, A. K. Cheetham, G. N. Greaves, *Nat. Commun.* **2015**, *6*, 8079.

[115] T. D. Bennett, Y. Yue, P. Li, A. Qiao, H. Tao, N. G. Greaves, T. Richards, G. I. Lampronti, S. A. Redfern, F. Blanc, O. K. Farha, J. T. Hupp, A. K. Cheetham, D. A. Keen, *J. Am. Chem. Soc.* **2016**, *138*, 3484–3492.

[116] R. Gaillac, P. Pullumbi, K. A. Beyer, K. W. Chapman, D. A. Keen, T. D. Bennett, F.-X. Coudert, *Nat. Mater.* **2017**, *16*, 1149–1154.

[117] J. M. Tuffnell, C. W. Ashling, J. Hou, S. Li, L. Longley, M. L. Ríos Gómez, T. D. Bennett, *Chem. Commun.* **2019**, *55*, 8705–8715.

[118] S. Horike, S. S. Nagarkar, T. Ogawa, S. Kitagawa, *Angew. Chem. Int. Ed.* **2020**, *59*, 6652–6664.

[119] S. Li, R. Limbach, L. Longley, A. A. Shirzadi, J. C. Walmsley, D. N. Johnstone, P. A. Midgley, L. Wondraczek, T. D. Bennett, *J. Am. Chem. Soc.* **2019**, *141*, 1027–1034.

[120] M. Stepniewska, M. B. Østergaard, C. Zhou, Y. Yue, *J. Non-Cryst. Solids* **2020**, *530*, 119806.

[121] W. Kauzmann, *Chem. Rev.* **1948**, *43*, 219–256.

[122] A. Qiao, T. D. Bennett, H. Tao, A. Krajnc, G. Mali, C. M. Doherty, A. W. Thornton, J. C. Mauro, G. N. Greaves, Y. Yue, *Sci. Adv.* **2018**, *4*, eaao68279.

[123] H. Tao, T. D. Bennett, Y. Yue, *Adv. Mater.* **2017**, *29*, 1601705.

[124] P. Adhikari, M. Xiong, N. Li, X. Zhao, P. Rulis, W. Y. Ching, *J. Phys. Chem. C* **2016**, *120*, 15362–15368.

[125] Y. Zhao, S. Y. Lee, N. Becknell, O. M. Yaghi, C. A. Angell, *J. Am. Chem. Soc.* **2016**, *138*, 10818–10821.

[126] R. N. Widmer, G. I. Lampronti, B. Kunz, C. Battaglia, J. H. Shepherd, S. A. T. Redfern, T. D. Bennett, *ACS Appl. Nano Mater.* **2018**, *1*, 497–500.

[127] C. Zhou, L. Longley, A. Krajnc, G. J. Smales, A. Qiao, I. Erucar, C. M. Doherty, A. W. Thornton, A. J. Hill, C. W. Ashling, O. T. Qazvini, S. J. Lee, P. A. Chater, N. J. Terrill, A. J. Smith, Y. Yue, G. Mali, D. A. Keen, S. G. Telfer, T. D. Bennett, *Nat. Commun.* **2018**, *9*, 5042.

[128] S. Horike, N. Ma, Z. Fan, S. Kosasang, M. M. Smedskjaer, *Nano Lett.* **2021**, *21*, 6382–6390.

[129] M. A. Ali, J. Ren, T. Zhao, X. Liu, Y. Hua, Y. Yue, J. Qiu, *ACS Omega* **2019**, *4*, 12081–12087.

[130] D. Umeyama, S. Horike, M. Inukai, T. Itakura, S. Kitagawa, *J. Am. Chem. Soc.* **2015**, *137*, 864–870.

[131] S. S. Nagarkar, S. Horike, T. Itakura, B. Le Ouay, A. Demessence, M. Tsujimoto, S. Kitagawa, *Angew. Chem. Int. Ed.* **2017**, *56*, 4976–4981.

[132] Y. Ohara, A. Hinokimoto, W. Chen, T. Kitao, Y. Nishiyama, Y. L. Hong, S. Kitagawa, S. Horike, *Chem. Commun.* **2018**, *54*, 6859–6862.

[133] S. Horike, D. Umeyama, M. Inukai, T. Itakura, S. Kitagawa, *J. Am. Chem. Soc.* **2012**, *134*, 7612–7615.

[134] M. A. Ali, X. Liu, Y. Li, J. Ren, J. Qiu, *Inorg. Chem.* **2020**, *59*, 8380–8386.

[135] G. Jiang, C. Qu, F. Xu, E. Zhang, Q. Lu, X. Cai, S. Hausdorf, H. Wang, S. Kaskel, *Adv. Funct. Mater.* **2021**, 2104300.

[136] K. Tanaka, Y. Tago, M. Kondo, Y. Watanabe, K. Nishio, T. Hitosugi, M. Moriya, *Nano Lett.* **2020**, *20*, 8200–8204.

[137] Y. Wang, H. Jin, Q. Ma, K. Mo, H. Mao, A. Feldhoff, X. Cao, Y. Li, F. Pan, Z. Jiang, *Angew. Chem. Int. Ed.* **2020**, *59*, 4365–4369.

[138] J. Li, J. Wang, Q. Li, M. Zhang, J. Li, C. Sun, S. Yuan, X. Feng, B. Wang, *Angew. Chem. Int. Ed.* **2021**, *60*, 21304–21309.

[139] T. D. Bennett, A. L. Goodwin, M. T. Dove, D. A. Keen, M. G. Tucker, E. R. Barney, A. K. Soper, E. G. Bithell, J. C. Tan, A. K. Cheetham, *Phys. Rev. Lett.* **2010**, *104*, 2–5.

[140] T. D. Bennett, D. A. Keen, J. C. Tan, E. R. Barney, A. L. Goodwin, A. K. Cheetham, *Angew. Chem. Int. Ed.* **2011**, *50*, 3067–3071.

[141] T. D. Bennett, P. Simoncic, S. A. Moggach, F. Gozzo, P. MacChi, D. A. Keen, J. C. Tan, A. K. Cheetham, *Chem. Commun.* **2011**, *47*, 7983–7985.

[142] T. D. Bennett, A. K. Cheetham, *Acc. Chem. Res.* **2014**, *47*, 1555–1562.

[143] M. T. Wharmby, S. Henke, T. D. Bennett, S. R. Bajpe, I. Schwedler, S. P. Thompson, F. Gozzo, P. Simoncic, C. Mellot-Draznieks, H. Tao, Y. Yue, A. K. Cheetham, *Angew. Chem. Int. Ed.* **2015**, *54*, 6447–6451.

[144] S. Henke, M. T. Wharmby, G. Kieslich, I. Hante, A. Schneemann, Y. Wu, D. Daisenberger, T. Cheetham, *Chem. Sci.* **2018**, *9*, 1654–1660.

[145] R. N. Widmer, G. I. Lampronti, S. Chibani, C. W. Wilson, S. Anzellini, S. Farsang, A. K. Kleppe, N. P. Casati, S. G. Macleod, S. A. Redfern, F. X. Coudert, T. D. Bennett, *J. Am. Chem. Soc.* **2019**, *141*, 9330–9337.

[146] K. Li, H. Xiao, J. He, H. Jiang, *Nano* **2018**, *13*, 1850025.

[147] K. Noh, J. Lee, J. Kim, *Isr. J. Chem.* **2018**, *58*, 1075–1088.

[148] M. L. Ríos Gómez, G. I. Lampronti, Y. Yang, J. C. Mauro, T. D. Bennett, *Dalton Trans.* **2020**, *49*, 850–857.

[149] J. Hou, M. L. Ríos Gómez, A. Krajnc, A. McCaul, S. Li, A. M. Bumstead, A. F. Sapnik, Z. Deng, R. Lin, P. A. Chater, D. S. Keeble, D. A. Keen, D. Appadoo, B. Chan, V. Chen, G. Mali, T. D. Bennett, *J. Am. Chem. Soc.* **2020**, *142*, 3880–3890.

[150] C. Zhou, M. Stepniewska, J. M. Sørensen, L. Scarpa, G. Magnacca, V. Boffa, T. D. Bennett, Y. Yue, *Microporous Mesoporous Mater.* **2018**, *265*, 57–62.

[151] L. Longley, S. M. Collins, S. Li, G. J. Smales, I. Erucar, A. Qiao, J. Hou, C. M. Doherty, A. W. Thornton, A. J. Hill, X. Yu, N. J. Terrill, A. J. Smith, S. M. Cohen, P. A. Midgley, D. A. Keen, S. G. Telfer, T. D. Bennett, *Chem. Sci.* **2019**, *10*, 3592–3601.

[152] A. M. Bumstead, M. L. Ríos Gómez, M. F. Thorne, A. F. Sapnik, L. Longley, J. M. Tuffnell, D. S. Keeble, D. A. Keen, T. D. Bennett, *CrystEngComm* **2020**, *22*, 3627–3637.

[153] A. W. Thornton, K. E. Jelfs, K. Konstas, C. M. Doherty, A. J. Hill, A. K. Cheetham, T. D. Bennett, *Chem. Commun.* **2016**, *52*, 3750–3753.

[154] U. Böhme, B. Barth, C. Paula, A. Kuhnt, W. Schwieger, A. Mundstock, J. Caro, M. Hartmann, *Langmuir* **2013**, *29*, 8592–8600.

[155] J. Yang, Y. B. Zhang, Q. Liu, C. A. Trickett, E. Gutiérrez-Puebla, M. Á. Monge, H. Cong, A. Aldossary, H. Deng, O. M. Yaghi, *J. Am. Chem. Soc.* **2017**, *139*, 6448–6455.

[156] K. Li, D. H. Olson, J. Seidel, T. J. Emge, H. Gong, H. Zeng, J. Li, *J. Am. Chem. Soc.* **2009**, *131*, 10368–10369.

[157] M. Hartmann, U. Böhme, M. Hovestadt, C. Paula, *Langmuir* **2015**, *31*, 12382–12389.

[158] R. Gaillac, P. Pullumbi, T. D. Bennett, F. X. Coudert, *Chem. Mater.* **2020**, *32*, 8004–8011.

[159] D. W. Gidley, H. G. Peng, R. S. Vallery, *Annu. Rev. Mater. Res.* **2006**, *36*, 49–79.

[160] K. A. Cychosz, M. Thommes, *Engineering* **2018**, *4*, 559–566.

[161] R. N. Widmer, G. I. Lampronti, S. Anzellini, R. Gaillac, S. Farsang, C. Zhou, A. M. Belenguer, C. W. Wilson, H. Palmer, A. K. Kleppe, M. T. Wharmby, X. Yu, S. M. Cohen, S. G. Telfer, S. A. Redfern, F. X. Coudert, S. G. MacLeod, T. D. Bennett, *Nat. Mater.* **2019**, *18*, 370–376.

[162] P. Stephan, K. Schaber, K. Stephan, F. Mayinger, *Thermodynamik*, Springer Berlin, Heidelberg, **2013**.

[163] G. E. Decker, E. D. Bloch, *ACS Appl. Mater. Interfaces* **2021**, *13*, 51925–51932.

[164] A. Phan, C. J. Doonan, F. J. Uribe-Romo, C. B. Knobler, M. Okeeffe, O. M. Yaghi, *Acc. Chem. Res.* **2010**, *43*, 58–67.

[165] T. Wu, X. Bu, J. Zhang, P. Feng, *Chem. Mater.* **2008**, *20*, 7377–7382.

[166] R. Lehnert, F. Seel, *ZAAC* **1980**, *464*, 187–194.

[167] C. A. Schröder, I. A. Baburin, L. van Wüllen, M. Wiebcke, S. Leoni, *CrystEngComm* **2013**, *15*, 4036–4040.

[168] K. Kihara, G. Donnay, *Canadian Mineralogist* **1985**, *23*, 647–654.

[169] S. R. Elliott, *Nature* **1991**, *354*, 445–452.

[170] S. R. Elliott, *Phys. Rev. Lett.* **1991**, *67*, 711–714.

[171] P. S. Salmon, *Proc. Math. Phys. Series A* **1994**, *445*, 351–365.

[172] N. Ramesh Rao, P. Krishna, S. Basu, B. Dasannacharya, K. Sangunni, E. Gopal, *J. Non-Cryst. Solids* **1998**, *240*, 221–231.

[173] G. Lucovsky, J. C. Phillips, *Phys. Status Solidi B Basic Res.* **2009**, *246*, 1806–1812.

[174] M. Wojdyr, *J. Appl. Crystallogr.* **2010**, *43*, 1126–1128.

[175] T. D. Bennett, S. Cao, J. C. Tan, D. A. Keen, E. G. Bithell, P. J. Beldon, T. Friscic, A. K. Cheetham, *J. Am. Chem. Soc.* **2011**, *133*, 14546–14549.

[176] J. Gandara-Loe, A. Missyul, F. Fauth, L. L. Daemen, Y. Q. Cheng, A. J. Ramirez-Cuesta, P. I. Ravikovitch, J. Silvestre-Albero, *J. Mater. Chem. A* **2019**, *7*, 14552–14558.

[177] D. W. Breck, *Zeolite molecular sieves : structure, chemistry, and use.* Wiley, New York, **1973**.

[178] H. Marsh, B. Brand, *J. Colloid Interface Sci.* **1970**, *33*, 101–116.

[179] D. Klank, C. Blum, D. Schneider, *Chem. Ing. Tech.* **2020**, *92*, 1871–1872.

[180] S. Brunauer, P. H. Emmett, E. Teller, *J. Am. Chem. Soc.* **1938**, *60*, 309–319.

[181] T. F. Willems, C. H. Rycroft, M. Kazi, J. C. Meza, M. Haranczyk, *Microporous Mesoporous Mater.* **2012**, *149*, 134–141.

[182] M. Pinheiro, R. L. Martin, C. H. Rycroft, M. Haranczyk, *CrystEngComm* **2013**, *15*, 7531–7538.

[183] E. S. Kikkinides, P. A. Monson, R. Valiullin, *J. Phys. Chem. C* **2020**, *124*, 21591–21607.

[184] H. G. T. Nguyen, J. C. Horn, M. Bleakney, D. W. Siderius, L. Espinal, *Langmuir* **2019**, *35*, 2115–2122.

[185] *https://gestis.dguv.de/data?name=010030*, accessed 20.12.2021.

[186] *https://gestis.dguv.de/data?name=010020*, accessed 20.12.2021.

[187] *https://gestis.dguv.de/data?name=010100*, accessed 20.12.2021.

[188] D. Enke, F. Janowski, W. Schwieger, *Microporous Mesoporous Mater.* **2003**, *60*, 19–30.

[189] J. Fonseca, T. Gong, L. Jiao, H. L. Jiang, *J. Mater. Chem. A* **2021**, *9*, 10562–10611.

[190] N. B. Mc Keown, P. M. Budd, *Chem. Soc. Rev.* **2006**, *35*, 675–683.

[191] S. Das, P. Heasman, T. Ben, S. Qiu, *Chem. Rev.* **2017**, *117*, 1515–1563.

[192] H. B. Park, C. H. Jung, Y. M. Lee, A. J. Hill, S. J. Pas, S. T. Mudie, E. Van Wagner, B. D. Freeman, D. J. Cookson, *Science* **2007**, *318*, 254–258.

[193] B. J. Butler, D. O. Muhleman, M. A. Slade, M. S. Rice, S. E. Wood, A. R. Vasavada, D. A. Paige, S. E. Wood, D. M. Hunten, K. Lodders, J. Ulrichs, D. E. Shemansky, R. M. Killen, G. J. Taylor, B. G. Bills, D. A. Paige, L. Jorda, J. A. M. Bleeker, J. Geiss, M. Huber, J. Veverka, D. R. Davis, W. K. Hartmann, M. J. Gaffey, R. P. Binzel, T. Gehrels, M. S. Matthews, *Science* **2013**, 303–307.

[194] A. Louis Allred, *J. Inorg. Nucl. Chem.* **1961**, *17*, 215–221.

[195] Y. Q. Tian, C. X. Cai, X. M. Ren, C. Y. Duan, Y. Xu, S. Gao, X. Z. You, *Chem. - A Eur. J.* **2003**, *9*, 5673–5685.

[196] Y. Q. Tian, Z. X. Chen, L. H. Weng, H. B. Guo, S. Gao, D. Y. Zhao, *Inorg. Chem.* **2004**, *43*, 4631–4635.

[197] R. C. Weast, *Handbook of Chemistry and Physics*, 61st Ed., CRC Press, **1981**.

[198] M. Gustafsson, X. Zou, *J. Porous Mater.* **2013**, *20*, 55–63.

[199] M. R. Ryder, B. Civalleri, T. Bennett, S. Henke, S. Rudić, G. Cinque, F. Fernandez-Alonso, J. C. Tan, *Phys. Rev. Lett.* **2014**, *113*, 215502.

[200] H. Walba, R. W. Isensee, *J. Org. Chem.* **1961**, *18*, 2789–2791.

[201] L. Longley, S. M. Collins, C. Zhou, G. J. Smales, S. E. Norman, N. J. Brownbill, C. W. Ashling, P. A. Chater, R. Tovey, C. B. Schönlieb, T. F. Headen, N. J. Terrill, Y. Yue, A. J. Smith, F. Blanc, D. A. Keen, P. A. Midgley, T. D. Bennett, *Nat. Commun.* **2018**, *9*, 2135.

[202] R. D. Shannon, *Acta Crystallogr. Sect. A* **1976**, *32*, 751–767.

[203] Q. S. Mei, K. Lu, *Prog. Mater. Sci.* **2007**, *52*, 1175–1262.

[204] C. J. Martin, D. A. O'Connor, *J. Phys. C Solid State Phys.* **1977**, *10*, 3521–3526.

[205] Y. Du, B. Wooler, M. Nines, P. Kortunov, C. S. Paur, J. Zengel, S. C. Weston, P. I. Ravikovitch, *J. Am. Chem. Soc.* **2015**, *137*, 13603–13611.

[206] J. Yang, Y. B. Zhang, Q. Liu, C. A. Trickett, E. Gutiérrez-Puebla, M. Á. Monge, H. Cong, A. Aldossary, H. Deng, O. M. Yaghi, *J. Am. Chem. Soc.* **2017**, *139*, 6448–6455.

[207] L. Li, R.-B. Lin, X. Wang, W. Zhou, L. Jia, J. Li, B. Chen, *Chem. Eng. J.* **2018**, *354*, 977–982.

[208] J. Peng, H. Wang, D. H. Olson, Z. Li, J. Li, *Chem. Commun.* **2017**, *53*, 9332–9335.

[209] Y. Wang, N.-Y. Huang, X.-W. Zhang, H. He, R.-K. Huang, Z.-M. Ye, Y. Li, D.-D. Zhou, P.-Q. Liao, X.-M. Chen, J.-P. Zhang, *Angew. Chem. Int. Ed.* **2019**, *58*, 7692–7696.

[210] A. Cadiau, K. Adil, P. M. Bhatt, Y. Belmabkhout, M. Eddaoudi, *Science* **2016**, *353*, 137–140.

[211] Z. R. Herm, E. D. Bloch, J. R. Long, *Chem. Mater.* **2014**, *26*, 323–338.

[212] E. D. Bloch, W. L. Queen, R. Krishna, J. M. Zadrozny, C. M. Brown, J. R. Long, *Science* **2012**, *335*, 1606–1610.

[213] C. Martínez, A. Corma, *Coord. Chem. Rev.* **2011**, *255*, 1558–1580.

[214] D. M. D'Alessandro, B. Smit, J. R. Long, *Angew. Chem. Int. Ed.* **2010**, *49*, 6058–6082.

[215] C. Liang, Z. Li, S. Dai, *Angew. Chem. Int. Ed.* **2008**, *47*, 3696–3717.

[216] B. Yilmaz, U. Müller, *Top. Catal.* **2009**, *52*, 888–895.

[217] A. G. Slater, A. I. Cooper, *Science* **2015**, *348*, aaa8075.

[218] B. Li, H.-M. Wen, Y. Cui, W. Zhou, G. Qian, B. Chen, *Adv. Mater.* **2016**, *28*, 8819–8860.

[219] G. Maurin, C. Serre, A. Cooper, G. Férey, *Chem. Soc. Rev.* **2017**, *46*, 3104–3107.

[220] A. E. Baumann, D. A. Burns, B. Liu, V. S. Thoi, *Commun. Chem.* **2019**, *2*, 86.

[221] V. Isaeva, L. Kustov in *Zeolites and Zeolite-Like Materials.* Elsevier, **2016**, pp. 33–109.

[222] B. Yilmaz, N. Trukhan, U. Müller, *Chinese J. Catal.* **2012**, *33*, 3–10.

[223] A. I. Cooper, *Nat. Chem.* **2021**, *13*, 620–621.

[224] M. Simard, D. Su, J. D. Wuest, *J. Am. Chem. Soc.* **1991**, *113*, 4696–4698.

[225] F. A. Almeida Paz, J. Klinowski, S. M. F. Vilela, J. P. C. Tomé, J. A. S. Cavaleiro, J. Rocha, *Chem. Soc. Rev.* **2012**, *41*, 1088–1110.

[226] S. Kitagawa, R. Kitaura, S.-i. Noro, *Angew. Chem. Int. Ed.* **2004**, *43*, 2334–2375.

[227] S. T. Meek, J. A. Greathouse, M. D. Allendorf, *Adv. Mater.* **2011**, *23*, 249–267.

[228] A. P. Côté, A. I. Benin, N. W. Ockwig, M. O'Keeffe, A. J. Matzger, O. M. Yaghi, *Science* **2005**, *310*, 1166–1170.

[229] P. J. Waller, F. Gándara, O. M. Yaghi, *Acc. Chem. Res.* **2015**, *48*, 3053–3063.

[230] S. Kandambeth, K. Dey, R. Banerjee, *J. Am. Chem. Soc.* **2019**, *141*, 1807–1822.

[231] O. M. Yaghi, *J. Am. Chem. Soc.* **2016**, *138*, 15507–15509.

[232] P. M. Budd, B. S. Ghanem, S. Makhseed, N. B. McKeown, K. J. Msayib, C. E. Tattershall, *Chem. Commun.* **2004**, *4*, 230–231.

[233] T. Tozawa, J. T. A. Jones, S. I. Swamy, S. Jiang, D. J. Adams, S. Shakespeare, R. Clowes, D. Bradshaw, T. Hasell, S. Y. Chong, C. Tang, S. Thompson, J. Parker, A. Trewin, J. Bacsa, A. M. Z. Slawin, A. Steiner, A. I. Cooper, *Nat. Mater.* **2009**, *8*, 973–978.

[234] T. Hasell, A. I. Cooper, *Nat. Rev. Mater.* **2016**, *1*, 16053.

[235] S. Pullen, G. H. Clever, *Acc. Chem. Res.* **2018**, *51*, 3052–3064.

[236] A. J. Gosselin, C. A. Rowland, E. D. Bloch, *Chem. Rev.* **2020**, *120*, 8987–9014.

[237] A. I. Cooper, *ACS Cent. Sci.* **2017**, *3*, 544–553.

[238] J. R. Holst, A. Trewin, A. I. Cooper, *Nat. Chem.* **2010**, *2*, 915–920.

[239] Y. Jin, Q. Wang, P. Taynton, W. Zhang, *Acc. Chem. Res.* **2014**, *47*, 1575–1586.

[240] M. A. Little, A. I. Cooper, *Adv. Funct. Mater.* **2020**, *30*, 1909842.

[241] J. C. Tan, A. K. Cheetham, *Chem. Soc. Rev.* **2011**, *40*, 1059–1080.

[242] S. Henke, A. Schneemann, A. Wütscher, R. A. Fischer, *J. Am. Chem. Soc.* **2012**, *134*, 9464–9474.

[243] A. Williamson, *Lond. Edinb. Dublin philos. mag. j. sci.* **1850**, *37*, 350–356.

[244] O. Mitsunobu, M. Yamada, *Bull. Chem. Soc. Jpn.* **1967**, *40*, 2380–2382.

[245] C. A. Hunter, J. K. M. Sanders, *J. Am. Chem. Soc.* **1990**, *112*, 5525–5534.

[246] C. R. Martinez, B. L. Iverson, *Chem. Sci.* **2012**, *3*, 2191.

[247] A. L. Spek, *Acta Crystallogr. Sect. C* **2015**, *71*, 9–18.

[248] B. Chen, X. Zeng, U. Baumeister, G. Ungar, C. Tschierske, *Science* **2005**, *307*, 96–99.

[249] C.-A. Tao, J.-F. Wang, *Crystals* **2020**, *11*, 15.

[250] G. Deacon, *Coord. Chem. Rev.* **1980**, *33*, 227–250.

[251] L. K. Macreadie, O. T. Qazvini, R. Babarao, *ACS Appl. Mater. Interfaces* **2021**, *13*, 30885–30890.

[252] F. J. Wirkert, M. Paulus, J. Nase, J. Möller, S. Kujawski, C. Sternemann, M. Tolan, *J. Synchrotron Radiat.* **2014**, *21*, 76–81.

[253] D. Meschede, *Gerthsen Physik*, 24th ed., Springer, Berlin, Heidelberg, **2010**.

[254] M. Matsui, Y. Higo, Y. Okamoto, T. Irifune, K.-I. Funakoshi, *Am. Mineral.* **2012**, *97*, 1670–1675.

[255] N. Dubrovinskaia, L. Dubrovinsky, W. Crichton, F. Langenhorst, A. Richter, *Appl. Phys. Lett.* **2005**, *87*, 083106.

[256] T. Katsura, Y. Tange, *Minerals* **2019**, *9*, 745.

[257] L. Robison, R. J. Drout, L. R. Redfern, F. A. Son, M. C. Wasson, S. Goswami, Z. Chen, A. Olszewski, K. B. Idrees, T. Islamoglu, O. K. Farha, *Chem. Mater.* **2020**, *32*, 3545–3552.

[258] W. Li, S. Henke, A. K. Cheetham, *APL Mater.* **2014**, *2*, 123902.

[259] S. Dissegna, P. Vervoorts, C. L. Hobday, T. Düren, D. Daisenberger, A. J. Smith, R. A. Fischer, G. Kieslich, *J. Am. Chem. Soc.* **2018**, *140*, 11581–11584.

[260] J. Chu, F.-S. Ke, Y. Wang, X. Feng, W. Chen, X. Ai, H. Yang, Y. Cao, *Commun. Chem.* **2020**, *3*, 5.

[261] A. Knebel, A. Bavykina, S. J. Datta, L. Sundermann, L. Garzon-Tovar, Y. Lebedev, S. Durini, R. Ahmad, S. M. Kozlov, G. Shterk, M. Karunakaran, I. D. Carja, D. Simic, I. Weilert, M. Klüppel, U. Giese, L. Cavallo, M. Rueping, M. Eddaoudi, J. Caro, J. Gascon, *Nat. Mater.* **2020**, *19*, 1346–1353.

[262] H. Yuan, G. Liu, Z. Qiao, N. Li, P. J. S. Buenconsejo, S. Xi, A. Karmakar, M. Li, H. Cai, S. J. Pennycook, D. Zhao, *Adv. Mater.* **2021**, *33*, 2101257.

[263] M. Pera-Titus, *Chem. Rev.* **2014**, *114*, 1413–1492.

[264] R. Lin, X. Li, A. Krajnc, Z. Li, M. Li, W. Wang, L. Zhuang, S. Smart, Z. Zhu, D. Appadoo, J. R. Harmer, Z. Wang, A. G. Buzanich, S. Beyer, L. Wang, G. Mali, T. D. Bennett, V. Chen, J. Hou, *Angew. Chem. Int. Ed.* **2021**, 2–9.

[265] J. Hou, P. Chen, A. Shukla, A. Krajnc, T. Wang, X. Li, R. Doasa, L. H. G. Tizei, B. Chan, D. N. Johnstone, R. Lin, T. U. Schülli, I. Martens, D. Appadoo, M. S. Ari, Z. Wang, T. Wei, S.-c. Lo, M. Lu, S. Li, E. B. Namdas, G. Mali, A. K. Cheetham, S. M. Collins, V. Chen, L. Wang, T. D. Bennett, *Science* **2021**, *374*, 621–625.

[266] M. Basham, J. Filik, M. T. Wharmby, P. C. Y. Chang, B. El Kassaby, M. Gerring, J. Aishima, K. Levik, B. C. A. Pulford, I. Sikharulidze, D. Sneddon, M. Webber, S. S. Dhesi, F. Maccherozzi, O. Svensson, S. Brockhauser, G. Náray, A. W. Ashton, *J. Synchrotron Radiat.* **2015**, *22*, 853–858.

[267] J. Filik, A. W. Ashton, P. C. Y. Chang, P. A. Chater, S. J. Day, M. Drakopoulos, M. W. Gerring, M. L. Hart, O. V. Magdysyuk, S. Michalik, A. Smith, C. C. Tang, N. J. Terrill, M. T. Wharmby, H. Wilhelm, *J. Appl. Crystallogr.* **2017**, *50*, 959–966.

[268] A. K. Soper, *Rutherford Applet. Lab. Tech. Reports* **2011**.

[269] G. M. Sheldrick, *Acta Crystallogr. Sect. C* **2015**, *71*, 3–8.

Appendix

A Appendix to Part I

A.1 Experimental Data to Section 6 – Quantification of Intrinsic Microporosity in ZIF Glasses

A.1.1 In-House Powder X-ray Diffraction

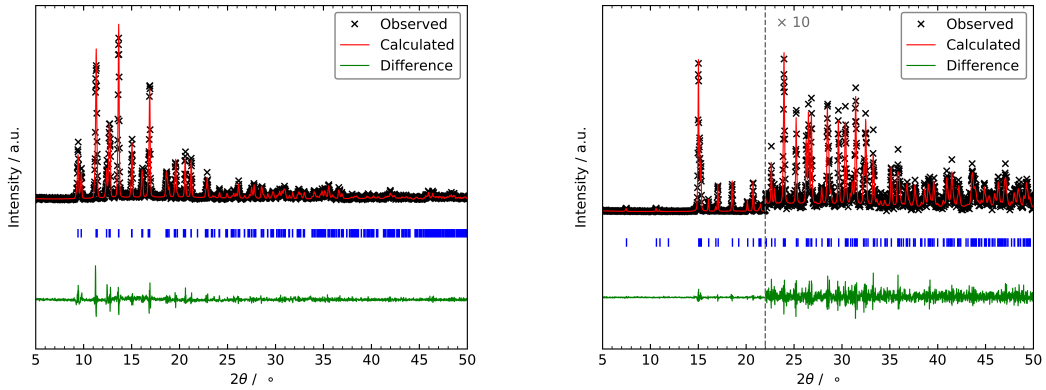

Figure A.1: PXRD pattern with structureless profile fit (Pawley method) of ZIF-4 (left) and zni$_T$ZIF-4.

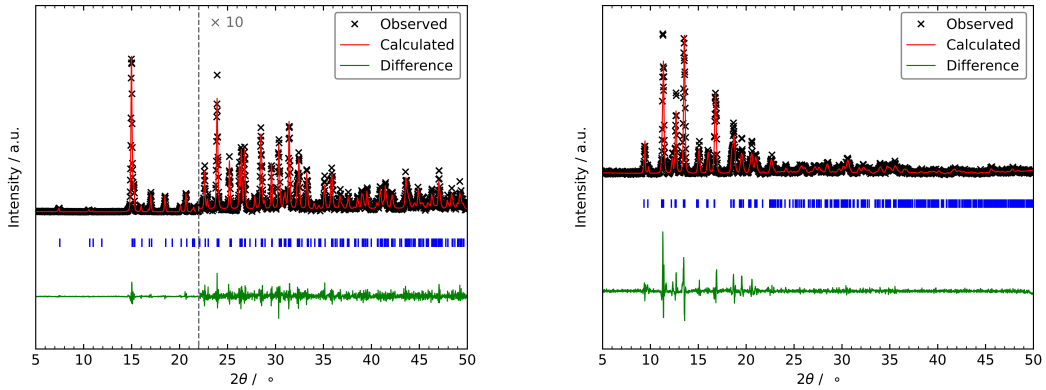

Figure A.2: PXRD pattern with structureless profile fit (Pawley method) of ZIF-zni and ZIF-62.

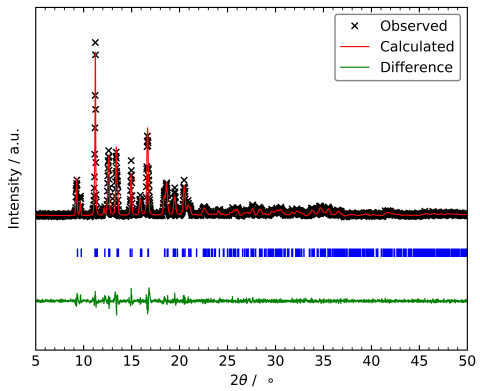

Figure A.3: PXRD pattern with structureless profile fit (Pawley method) of TIF-4.

Table A.1: Unit cell parameters a, b, c and V determined by structureless profile refinements (Pawley method) of the PXRD data of ZIF-4, zni$_T$ZIF-4 and ZIF-zni with corresponding R_{wp}, R_{exp} and χ values.

Compound	ZIF-4	zni$_T$ZIF-4	ZIF-zni
space group	*Pbca*	$I4_1cd$	$I4_1cd$
a / Å	15.488(3)	23.522(2)	23.499(2)
b / Å	15.528(3)	23.522(2)	23.499(2)
c / Å	18.113(4)	12.4512(11)	12.4691(12)
V / Å^3	4356.1(16)	6889.1(14)	6885.6(16)
R_{wp}	20.33	21.98	20.09
R_{exp}	15.72	19.42	16.57
χ	1.29	1.13	1.21

Table A.2: Unit cell parameters a, b, c and V determined by structureless profile refinements (Pawley method) of the PXRD data of ZIF-62 and TIF-4 with corresponding R_{wp}, R_{exp} and χ values.

Compound	ZIF-62	TIF-4
space group	*Pbca*	*Pbca*
a / Å	15.548(10)	15.483(7)
b / Å	15.819(11)	15.789(8)
c / Å	18.164(16)	18.113(10)
V / Å^3	4468(6)	4431(4)
R_{wp}	24.18	21.15
R_{exp}	16.92	16.81
χ	1.43	1.26

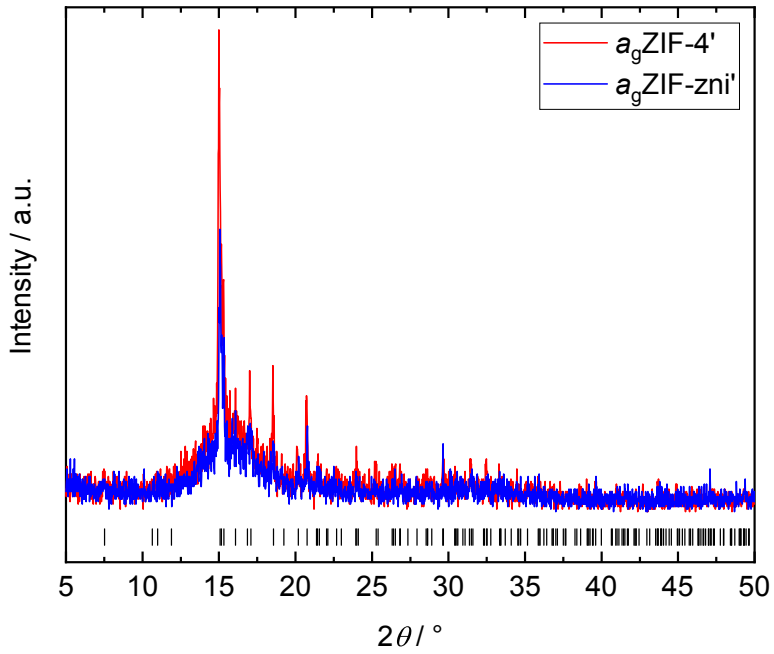

Figure A.4: Overlay of the PXRD patterns of a_gZIF-zni' and a_gZIF-4' which were obtained by attempting to prepare the desired glasses without an isothermal segment in the TGA/DSC program. The black thick marks indicate the allowed Bragg peak positions for ZIF-zni (CCDC code IMIDZB). It becomes clear that residues of the **zni** phase are present in the as such prepared materials.

A.1.2 X-ray Total Scattering

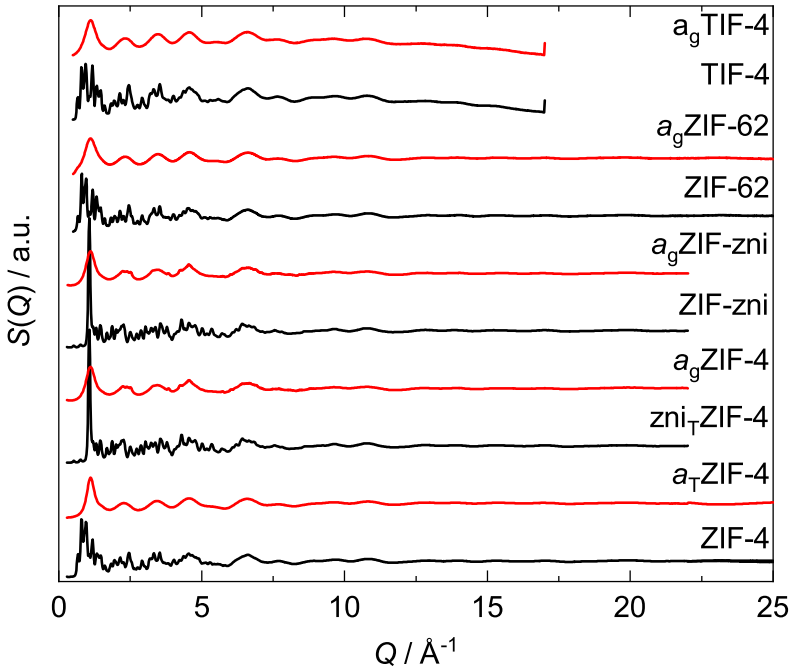

Figure A.5: X-ray total scattering data in the form $S(Q)$ for all investigated materials. Crystalline and amorphous phases are displayed in black or red, respectively.

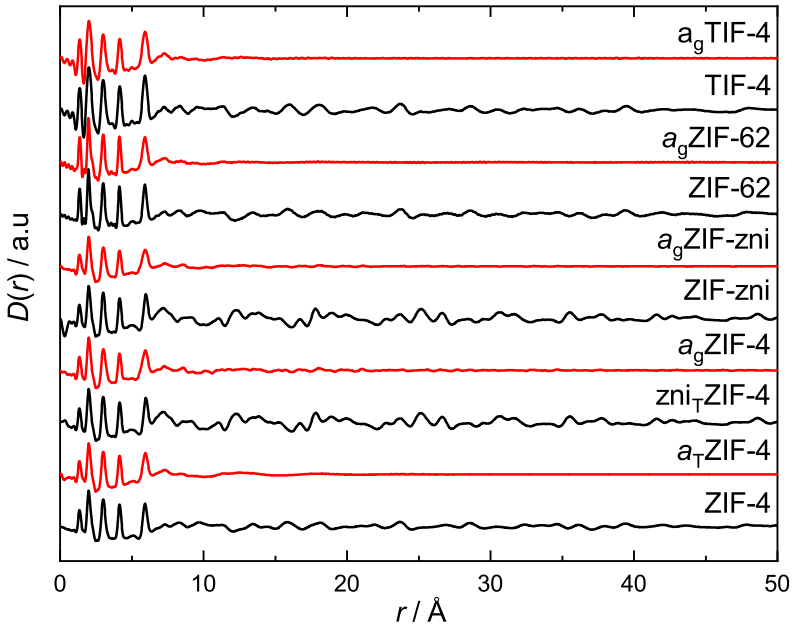

Figure A.6: X-ray total scattering data in the form $D(r)$ for all investigated materials. Crystalline and amorphous phases are displayed in black or red, respectively.

A.1.3 ^{1}H Nuclear Magnetic Resonance Spectroscopy

The spectra were measured in a NMR solvent mixture of DMSO-d_6 and DCl/D_2O to protonate the molecular building units and consequently digest the solid state materials. The particular used NMR solvent mixture contained a small, unidentified contamination which is present in the spectra for zni$_T$ZIF-4, a$_g$ZIF-4 and ZIF-zni (see Figure A.28).

The activation of the materials is verified by the absence of signals ascribed to DMF.

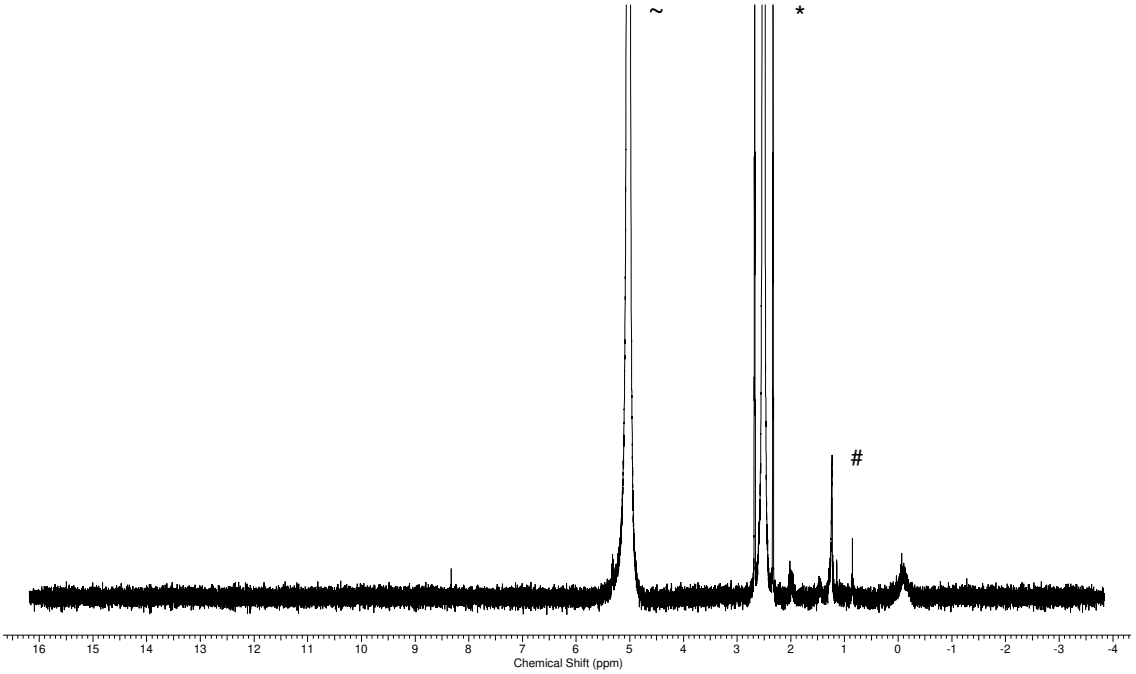

Figure A.7: ^{1}H NMR spectrum of the used DMSO-d_6 solvent with a small amount of DCl/D_2O. It becomes obvious that the used NMR solvent system contains a small, unidentified contamination at 1.25 ppm (marked with #). DMSO is marked with $\star$, D_2O is marked with $\sim$.

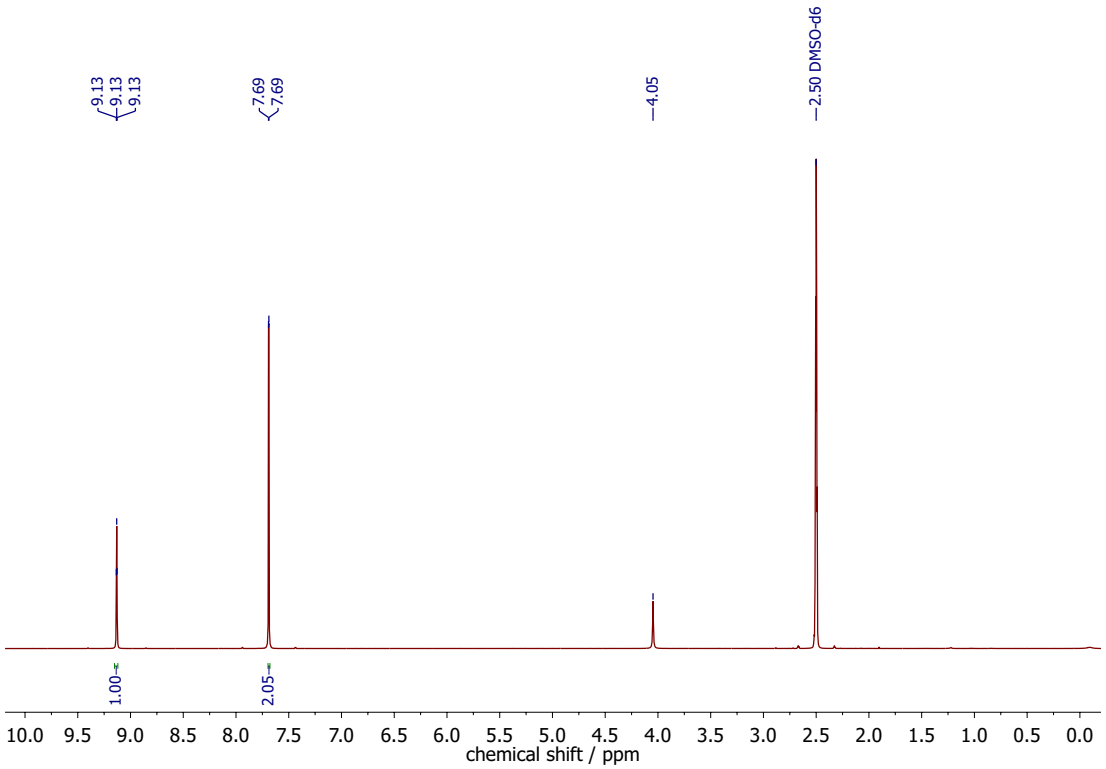

Figure A.8: ^{1}H NMR spectrum of ZIF-4.

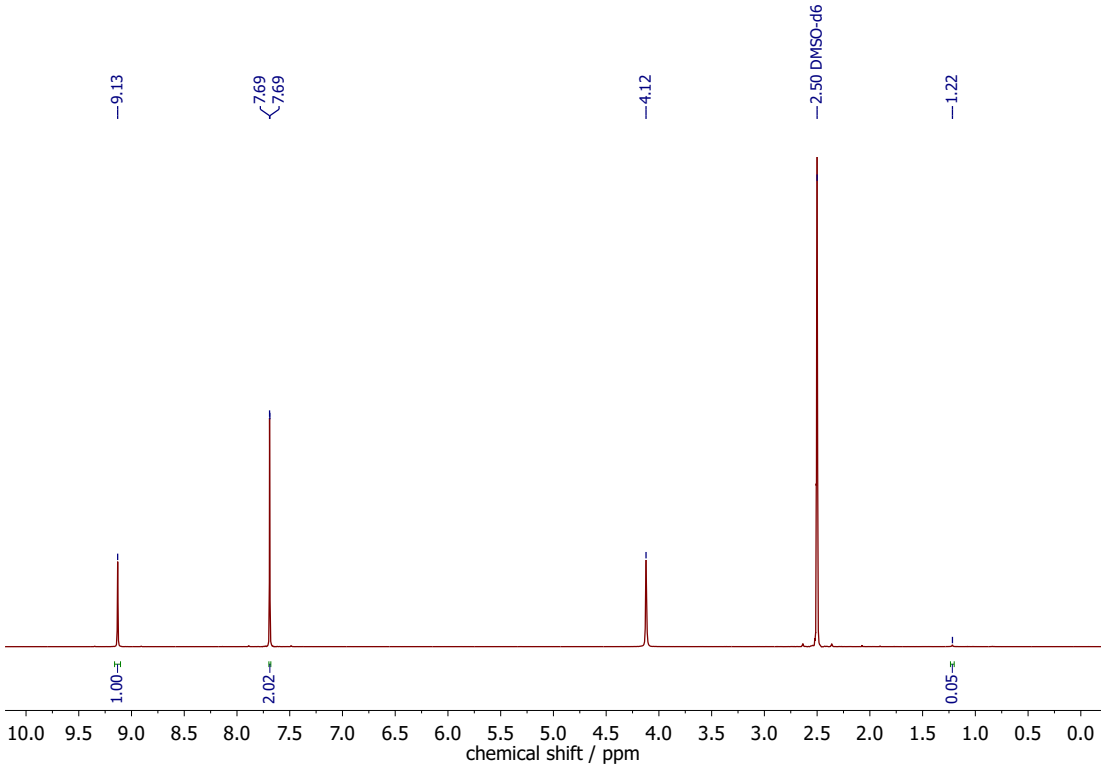

Figure A.9: ^{1}H NMR spectrum of a_TZIF-4.

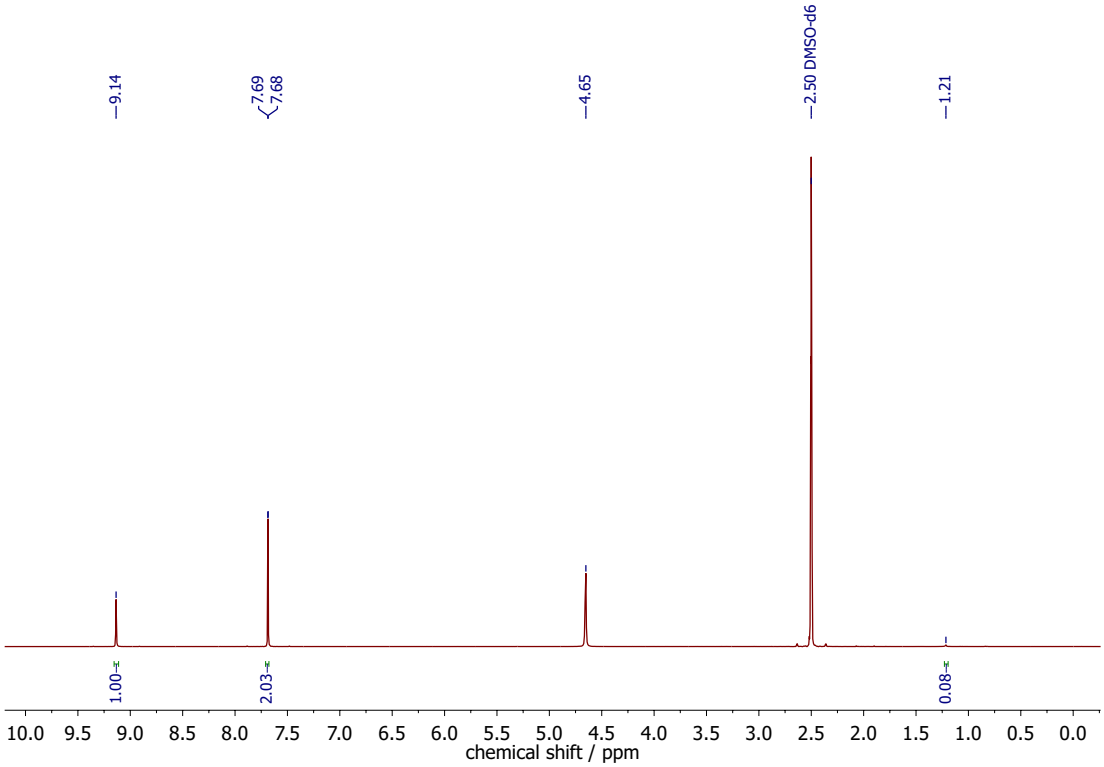

Figure A.10: ^{1}H NMR spectrum of zni$_{\mathrm{T}}$ZIF-4.

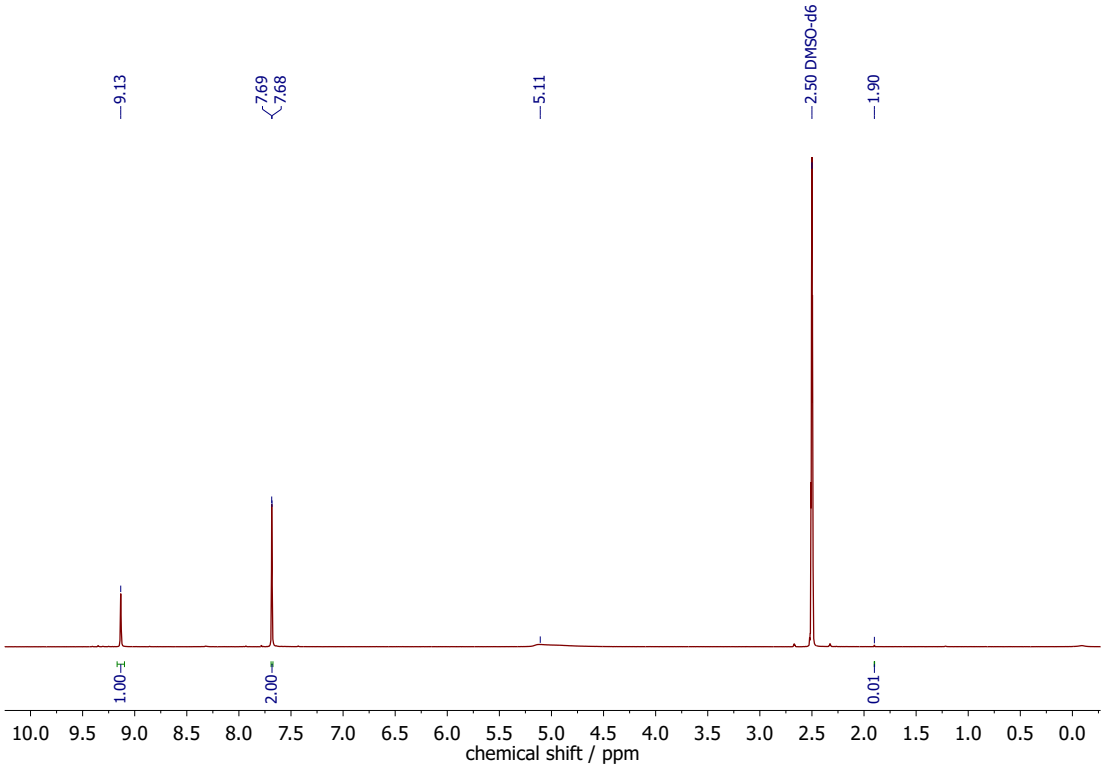

Figure A.11: ^{1}H NMR spectrum of a$_{\mathrm{g}}$ZIF-4.

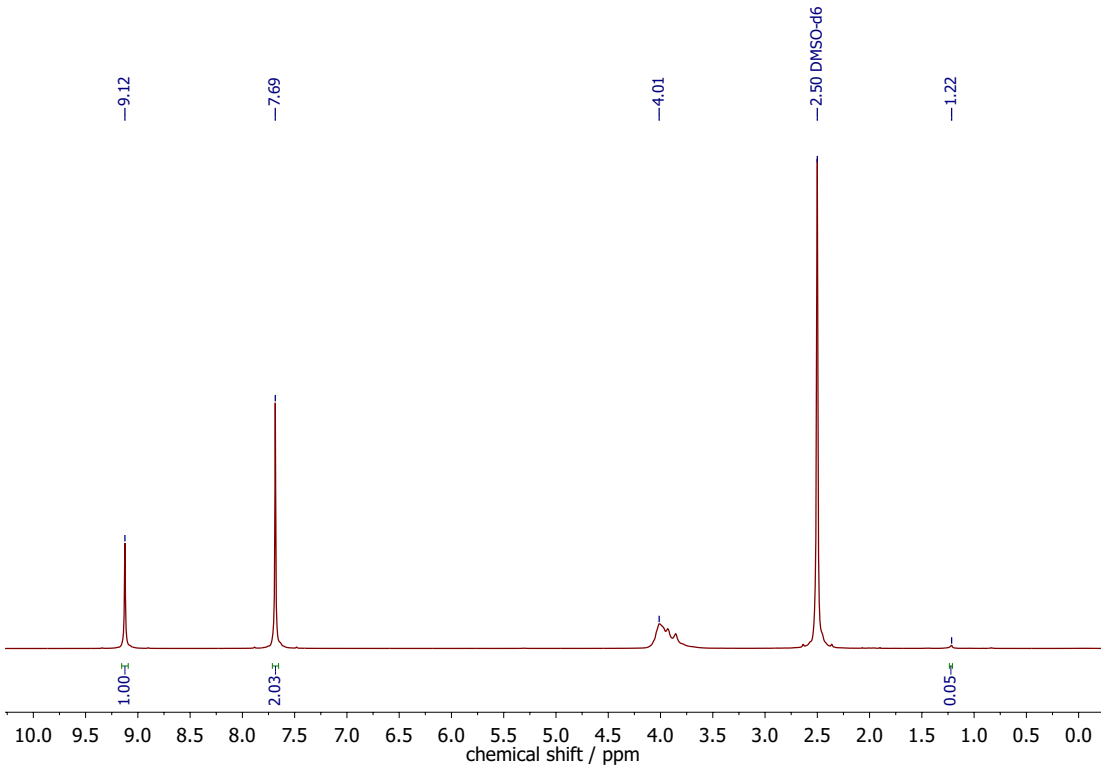

Figure A.12: ^{1}H NMR spectrum of ZIF-zni.

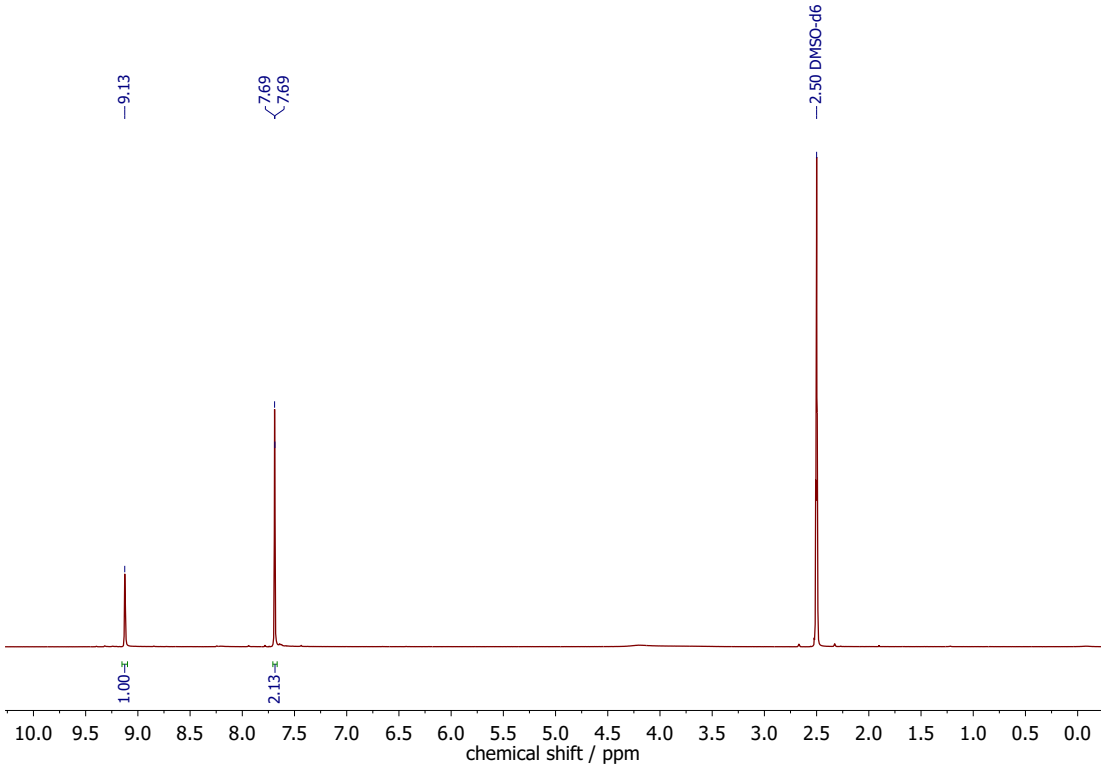

Figure A.13: ^{1}H NMR spectrum of a_gZIF-zni.

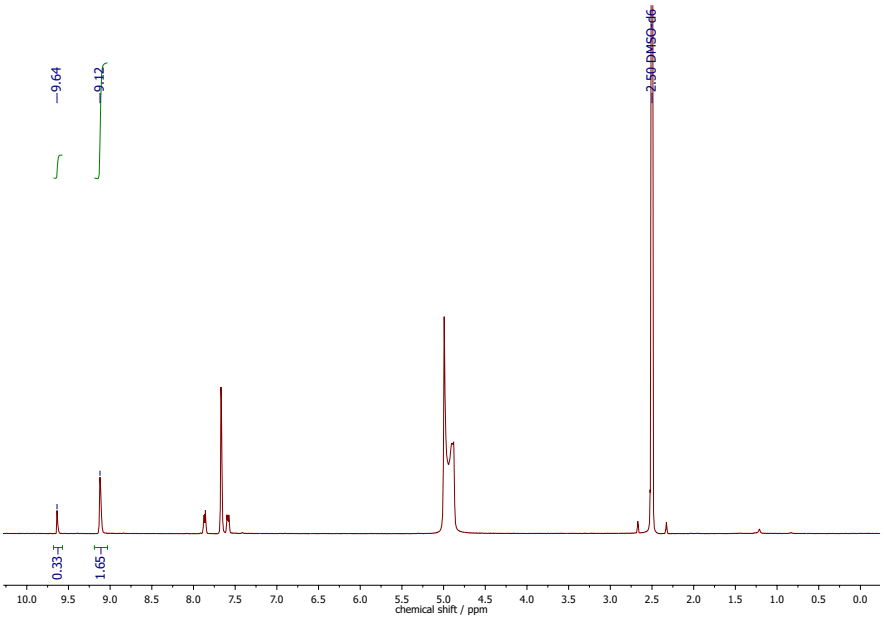

Figure A.14: ^{1}H NMR spectrum of a$_g$ZIF-62. The ratio between the implemented linkers has been determined by the integral corresponding to the proton attached to the carbon atom between the two nitrogen atoms in the imidazolate type linkers. The corresponding signals are integrated. The full integrity of the organic linkers after thermal treatment becomes clear.

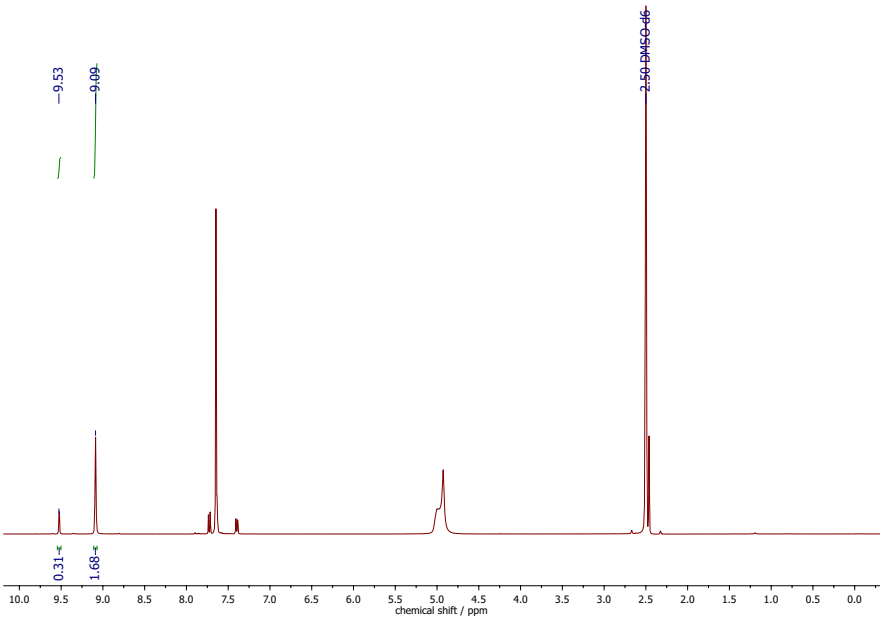

Figure A.15: ^{1}H NMR spectrum of a$_g$TIF-4. The ratio between the implemented linkers has been determined by the integral corresponding to the proton attached to the carbon atom between the two nitrogen atoms in the imidazolate type linkers. The corresponding signals are integrated. The full integrity of the organic linkers after thermal treatment becomes clear.

A.1.4 Simultaneous Thermogravimetric Analysis / Differential Scanning Calorimetry

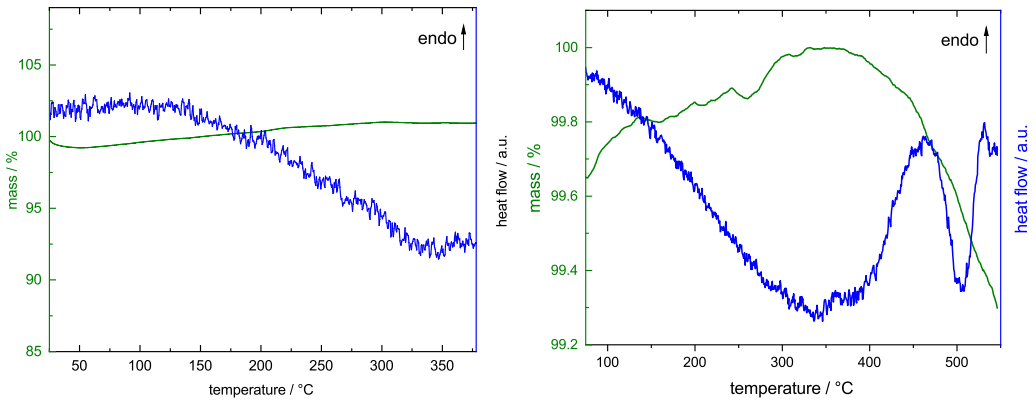

Figure A.16: TGA/DSC data for the preparation of a_TZIF-4 (left) and zni$_T$ZIF-4 (right). The cooling process (rate -10 K min^{-1}) was performed without data collection.

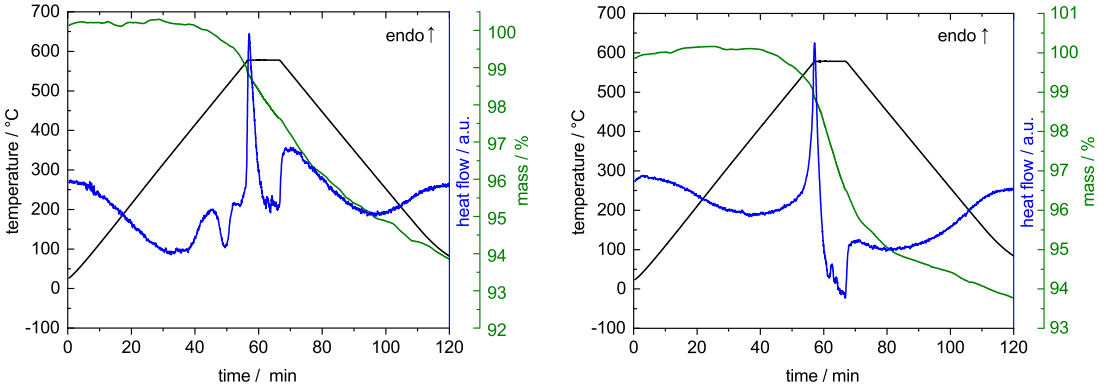

Figure A.17: TGA/DSC data for the preparation of a_gZIF-4 (left) and a_gZIF-zni (right).

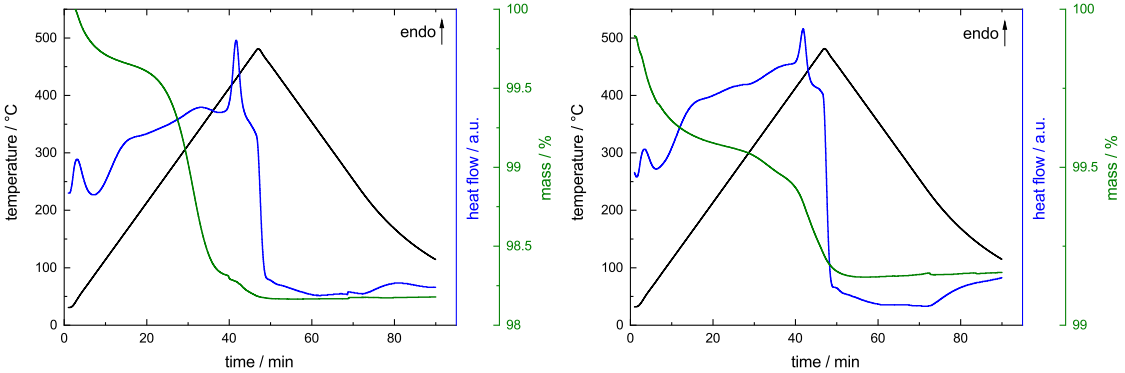

Figure A.18: TGA/DSC data for the preparation of a_gZIF-62 (left) and a_gTIF-4 (right).

A.1.5 Differential Scanning Calorimetry

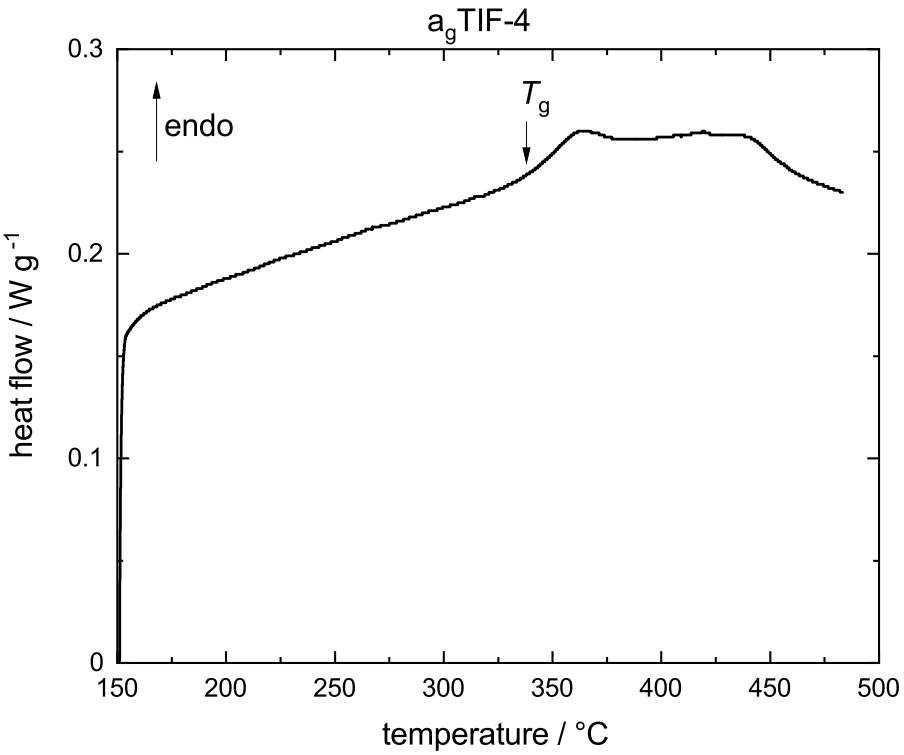

Figure A.19: DSC data for a_gTIF-4 showing a glass transition.

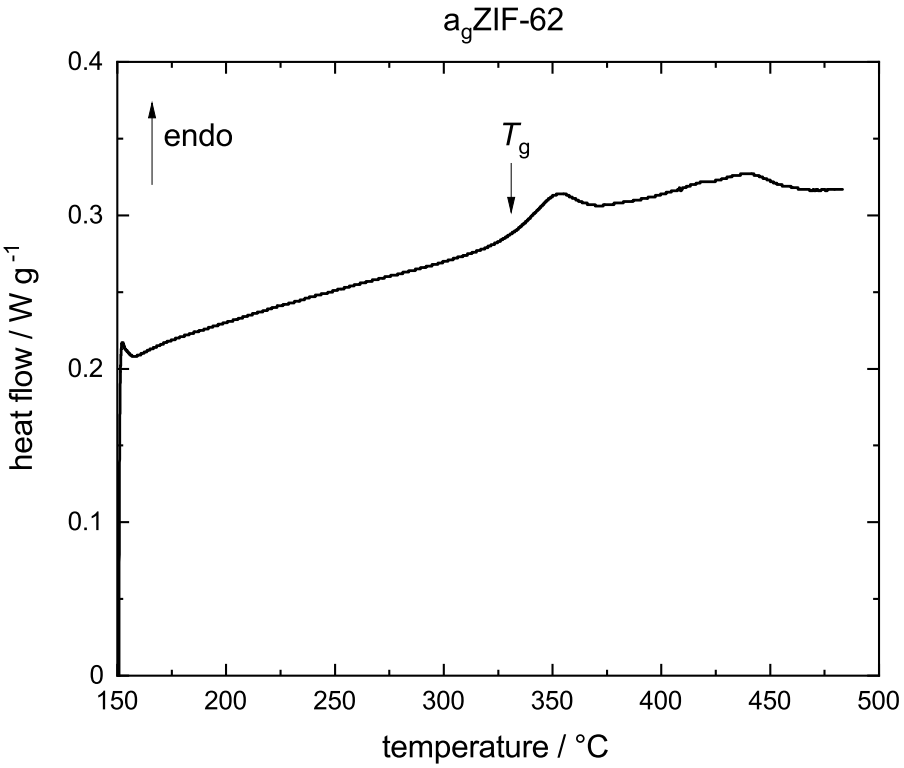

Figure A.20: DSC data for a_gZIF-62 showing a glass transition.

Table A.3: Summary of the phase transition temperature determined from the DSC data.

Material	T_{am}	T_{rc}	$T_{\mathrm{coi\text{-}zni}}$	T_{m}	T_{g}
ZIF-4	336 °C	463 °C	-	579 °C	-
ZIF-zni	-	-	357 °C	585 °C	-
ZIF-62	-	-	-	438 °C	331 °C
TIF-4	-	-	-	436 °C	338 °C

Table A.4: Summary of the phase transition enthalpies determined from the DSC data.

Material	ΔH_{am}	ΔH_{rc}	$\Delta H_{\mathrm{coi\text{-}zni}}$	ΔH_{m}
ZIF-4	-0.28 kJ mol^{-1}	-10.60 kJ mol^{-1}	-	11.46 kJ mol^{-1}
ZIF-zni	-	-	0.08 kJ mol^{-1}	11.88 kJ mol^{-1}
ZIF-62				5.08 kJ mol^{-1}
TIF-4				2.69 kJ mol^{-1}

A.1.6 Gas Physisorption

Additional Gas Physisorption Isotherms

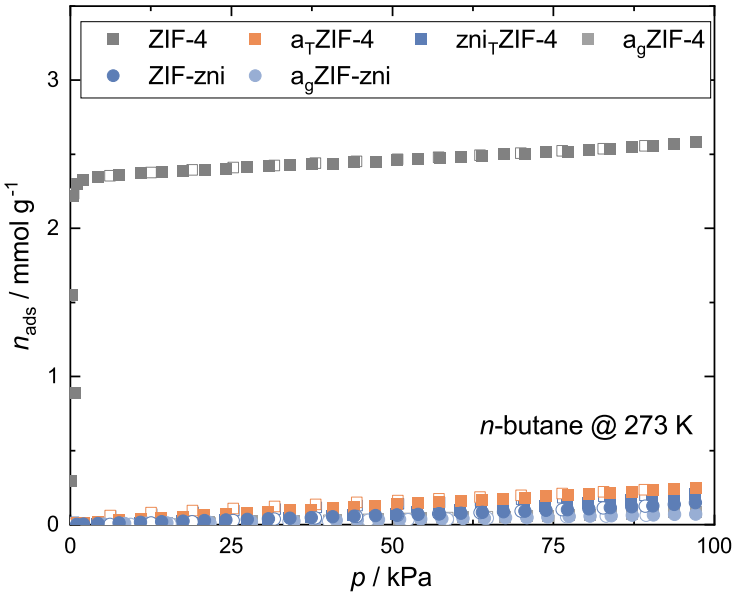

Figure A.21: *n*-butane gas isotherms data at 273 K for ZIF-4 and ZIF-zni and their corresponding investigated thermal products. Adsorption and desorption branches are shown as close and open symbols, respectively.

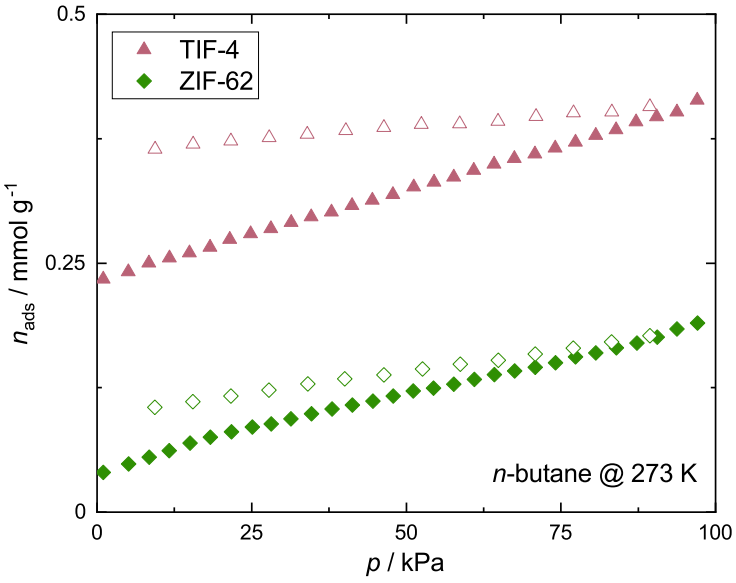

Figure A.22: *n*-butane gas isotherms data at 273 K for ZIF-62 and TIF-4. Adsorption and desorption branches are shown as close and open symbols, respectively.

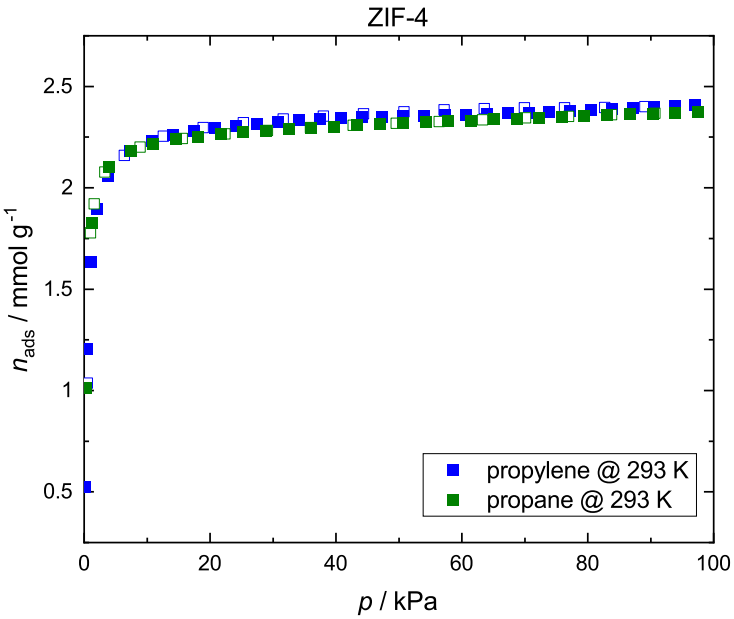

Figure A.23: Propane and Propylene gas physisorption data at 293 K for ZIF-4. Adsorption and desorption branches are shown as close and open symbols, respectively. ZIF-4 shows similar total uptakes for both C3 hydrocarbons with a higher affinity for propane at lower pressures which has been reported in the literature before.[157]

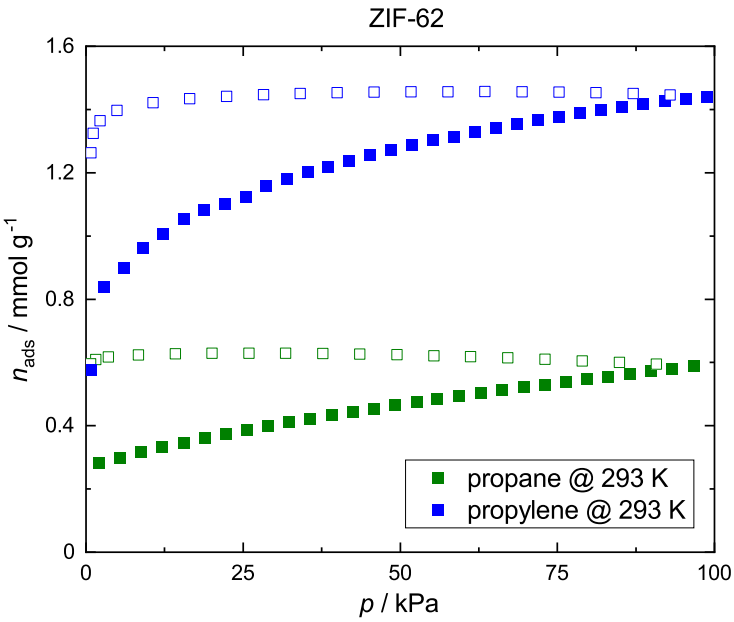

Figure A.24: Propane and Propylene gas physisorption data at 293 K for ZIF-62. Adsorption and desorption branches are shown as close and open symbols, respectively.

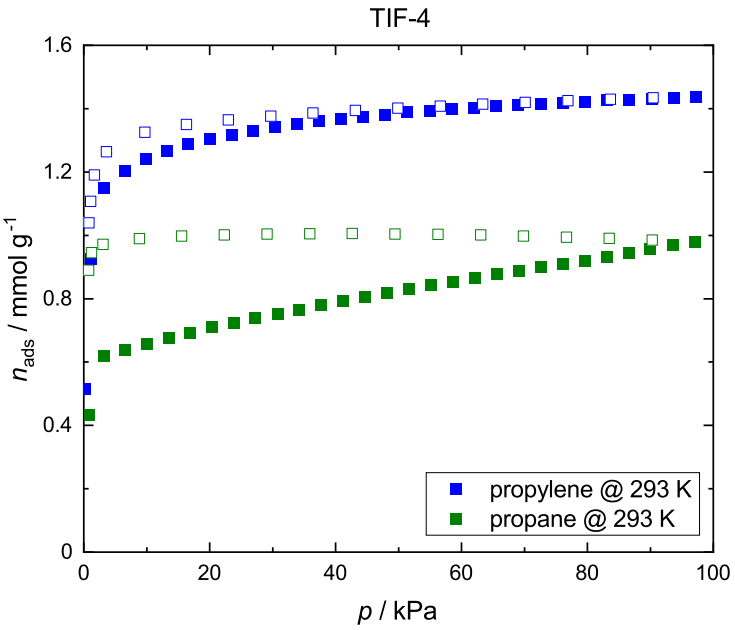

Figure A.25: Propane and Propylene gas physisorption data at 293 K for TIF-4. Adsorption and desorption branches are shown as close and open symbols, respectively.

Table A.5: Summary of maximum gas adsorption capacities of N_2, CO_2 and investigated hydrocarbons at ≈ 95 kPa at different temperatures. Capacities are given in mmol g^{-1}.

temp.	N_2 77 K	*n*-butane 273 K	propane 293 K	propylene 293 K	CO_2 195 K	CO_2 273 K
ZIF-4	8.57	2.59	2.38	2.41	7.22	2.64
a_TZIF-4	0.91	0.25	-	-	2.49	0.89
zni_T-ZIF-4	0.73	0.21	-	-	1.23	1.08
a_gZIF-4	0.72	0.09	0.35	0.70	2.84	1.00
ZIF-zni	0.47	0.15	-	-	1.21	0.97
a_gZIF-zni	0.88	0.07	-	-	3.12	1.21
ZIF-62	0.49	0.19	0.59	1.44	4.70	1.87
a_gZIF-62	0.57	0.44	0.30	0.66	3.34	0.81
TIF-4	0.54	0.41	0.98	1.44	3.76	1.43
a_gTIF-4	0.18	0.52	0.43	0.63	3.40	0.86

Pore Analyis

Table A.6: Pore analysis data for the CO_2 gas physisorption studies at 195 K and 273 K[b]. The total pore volumes (V_{pore})[c] and BET surface areas (S_{BET})[d] are determined.

compound	gas	temperature	BET analysis				V_{pore}
			p/p0 range	C constant	correlation coefficient	S_{BET}	
ZIF-4	CO_2	273 K	0.008-0.027	126.2	0.999	410 m^2 g^{-1}	-
	CO_2	195 K	0.001-0.054	95.1	0.995	473 m^2 g^{-1}	0.31 cm^3 g^{-1}
a_TZIF-4	CO_2	273 K	0.011-0.027	42.0	0.999	199 m^2 g^{-1}	-
	CO_2	195 K	0.001-0.067	148.9	0.995	140 m^2 g^{-1}	0.11 cm^3 g^{-1}
zni$_T$ZIF-4	CO_2	273 K	0.009-0.027	75.6	0.999	193 m^2 g^{-1}	-
	CO_2	195 K	0.001-0.073	1231.5	1	89 m^2 g^{-1}	0.05 cm^3 g^{-1}
a_gZIF-4	CO_2	273 K	0.009-0.027	51.7	0.999	203 m^2 g^{-1}	-
	CO_2	195 K	0.006-0.050	154.8	0.999	186 m^2 g^{-1}	0.12 cm^3 g^{-1}
ZIF-zni	CO_2	273 K	0.006-0.027	84.4	0.999	168 m^2 g^{-1}	-
	CO_2	195 K	0.001-0.048	692.6	0.999	92 m^2 g^{-1}	0.05 cm^3 g^{-1}
a_gZIF-zni	CO_2	273 K	0.005-0.027	52.6	0.998	243 m^2 g^{-1}	-
	CO_2	195 K	0.001-0.056	200.1	0.999	183 m^2 g^{-1}	0.13 cm^3 g^{-1}
ZIF-62	CO_2	273 K	0.006-0.027	193.164	0.999	268 m^2 g^{-1}	-
	CO_2	195 K	0.001-0.051	279.3	0.998	257 m^2 g^{-1}	0.20 cm^3 g^{-1}
a_gZIF-62	CO_2	273 K	0.008-0.027	47.4	0.999	171 m^2 g^{-1}	-
	CO_2	195 K	0.001-0.050	181.5	0.998	194 m^2 g^{-1}	0.14 cm^3 g^{-1}
TIF-4	CO_2	273 K	0.009-0.027	125.7	0.999	224 m^2 g^{-1}	-
	CO_2	195 K	0.001-0.051	222.5	0.998	180 m^2 g^{-1}	0.16 cm^3 g^{-1}
a_gTIF-4	CO_2	273 K	0.002-0.027	52.1	0.998	174 m^2 g^{-1}	-
	CO_2	195 K	0.001-0.050	187.7	0.998	199 m^2 g^{-1}	0.15 cm^3 g^{-1}

b $p_0(CO_2, 273\ K) = 3485$ kPa[162]

c $p/p_0 \approx 0.95$, applied value for the density of pure liquid adsorbate $\rho_{\text{liq}}(CO_2@\ 253\ K) = 1.032\ g\ cm^{-3}$.[87]

d Applied value for cross sectional areas: $\sigma(CO_2\ @\ 273\ K) = 21\ Å^2$/molecule and $\sigma(CO_2\ @195\ K) = 17\ Å^2$/molecule[87].

A.2 Experimental Data to Section 7 – A Cobalt Imidazolate Glass

A.2.1 Single Crystal X-ray Diffraction

Table A.7: Crystallographic data of as-ZIF-62(Co) obtained via SCXRD.

Compound	as-ZIF-62(Co)
CCDC deposition number	1849817
Empirical formula	$C_7H_{6.5}CoN_4$
Formula weight / g mol^{-1}	205.59
Temperature / K	100(2)
Crystal system	orthorhombic
Space group	*Pbca*
a / Å	15.4329(12)
b / Å	15.6983(9)
c / Å	18.1310(12)
α / Å	90
β / Å	90
γ / Å	90
V / Å^3	4392.6(5)
Z	16
ϱ_{calc} / g cm^{-3}	1.244
μ / mm^{-1}	1.520
F(000)	1656.0
Crystal size / mm^3	0.353 × 0.331 × 0.165
Radiation	MoK$_\alpha$ (λ = 0.71073)
2Θ range for data collection / °	5.19 to 59.996
Index ranges	-19 ≤ h ≤ 21, -22 ≤ k ≤ 21, -21 ≤ l ≤ 25
Reflections collected	18464
Independent reflections	6396 [R_{int} = 0.0370, R_{sigma} = 0.0426]
Data/restraints/parameters	6396/31/253
Goodness-of-fit on F^2	1.027
Final R indexes [I ≥ 2σ (I)]	R_1 = 0.0551, wR_2 = 0.1317
Final R indexes [all data]	R_1 = 0.0925, wR_2 = 0.1615
Largest diff. peak/hole / e Å^{-3}	0.63/-0.31

A.2.2 X-ray Total Scattering

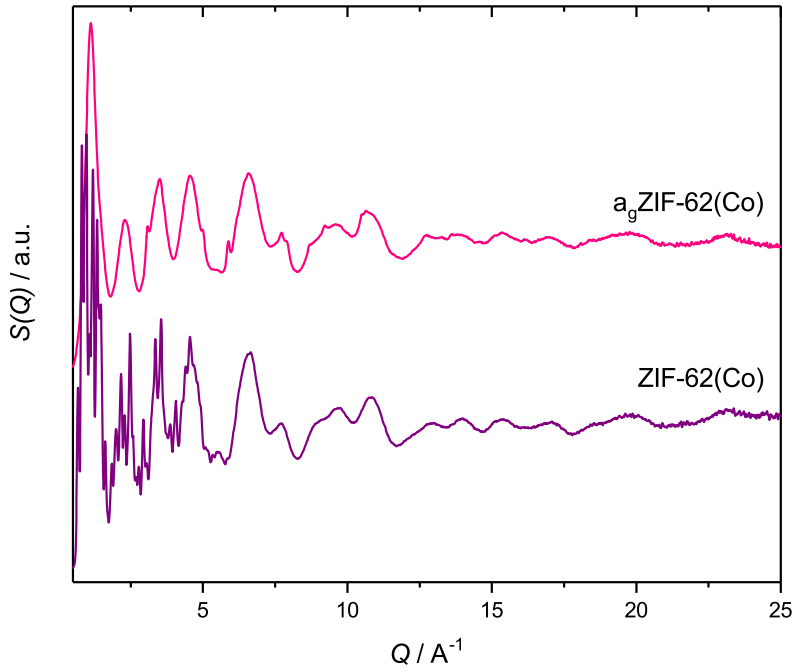

Figure A.26: X-ray total scattering factor as a function of Q for ZIF-62(Co)-bim$_{0.30}$ and a$_g$ZIF-62(Co)-bim$_{0.30}$ derived from collected X-ray total scattering data.

A.2.3 Fourier-Transform Infrared Spectroscopy

These data were collected to verify the activation/desolvation of the material (complete removal of solvents from the pores) which demonstrated with the absence of a vibrational band at 1675 cm^{-1}, ascribed to the carbonyl stretching vibration of DMF.

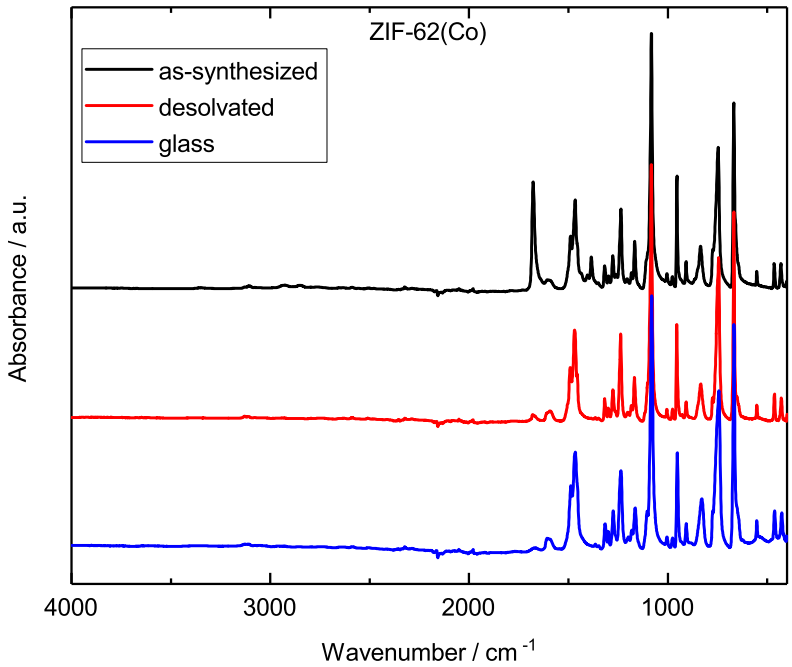

Figure A.27: FTIR spectra of the as-synthesised and desolvated/activated crystalline material as well as of the corresponding glass.

A.2.4 ^{1}H Nuclear Magnetic Resonance Spectroscopy

These data were collected to determine the molar ration of im^- : bim^- in the solid state materials. The derived molar amount of bim^- (x) was determined by the singlet signals of the CH groups at position 2 of the imidazolate ring (**1a** for im^- and **1b** for bim^-, see spectra below). The sum of these two signals was set two 2, matching two protons. Consequently, the integral of the **1b** corresponds to the x value in $Co(im)_{2-x}(bim)_x$. The activation of the materials is further verified by the absence of signals ascribed to DMF.

The spectra were measured in a NMR solvent mixture of DMSO-d_6 and DCl/D_2O to protonate the molecular building units and consequently digest the solid state materials. The particular used NMR solvent mixture contained a small, unidentified contamination which is present in all spectra (see Figure A.28).

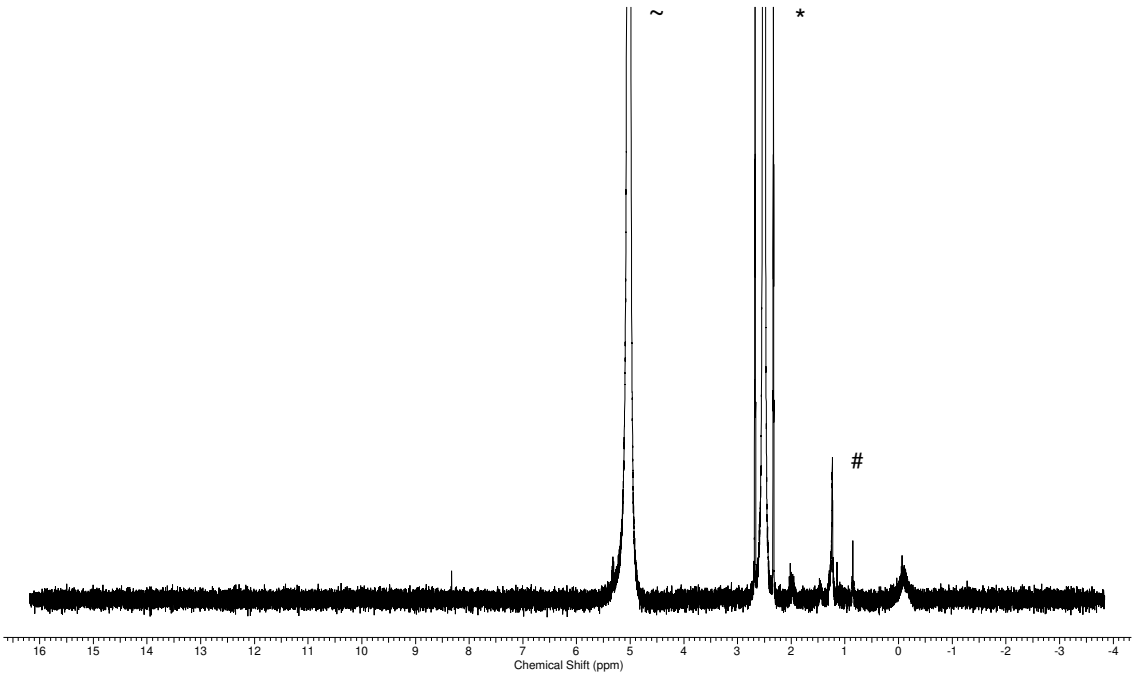

Figure A.28: ^{1}H NMR spectrum of the used DMSO-d_6 solvent with a small amount of DCl/D_2O. It becomes obvious that the used NMR solvent system contains a small, unidentified contamination at 1.25 ppm (marked with #). DMSO is marked with $\star$, D_2O is marked with $\sim$.

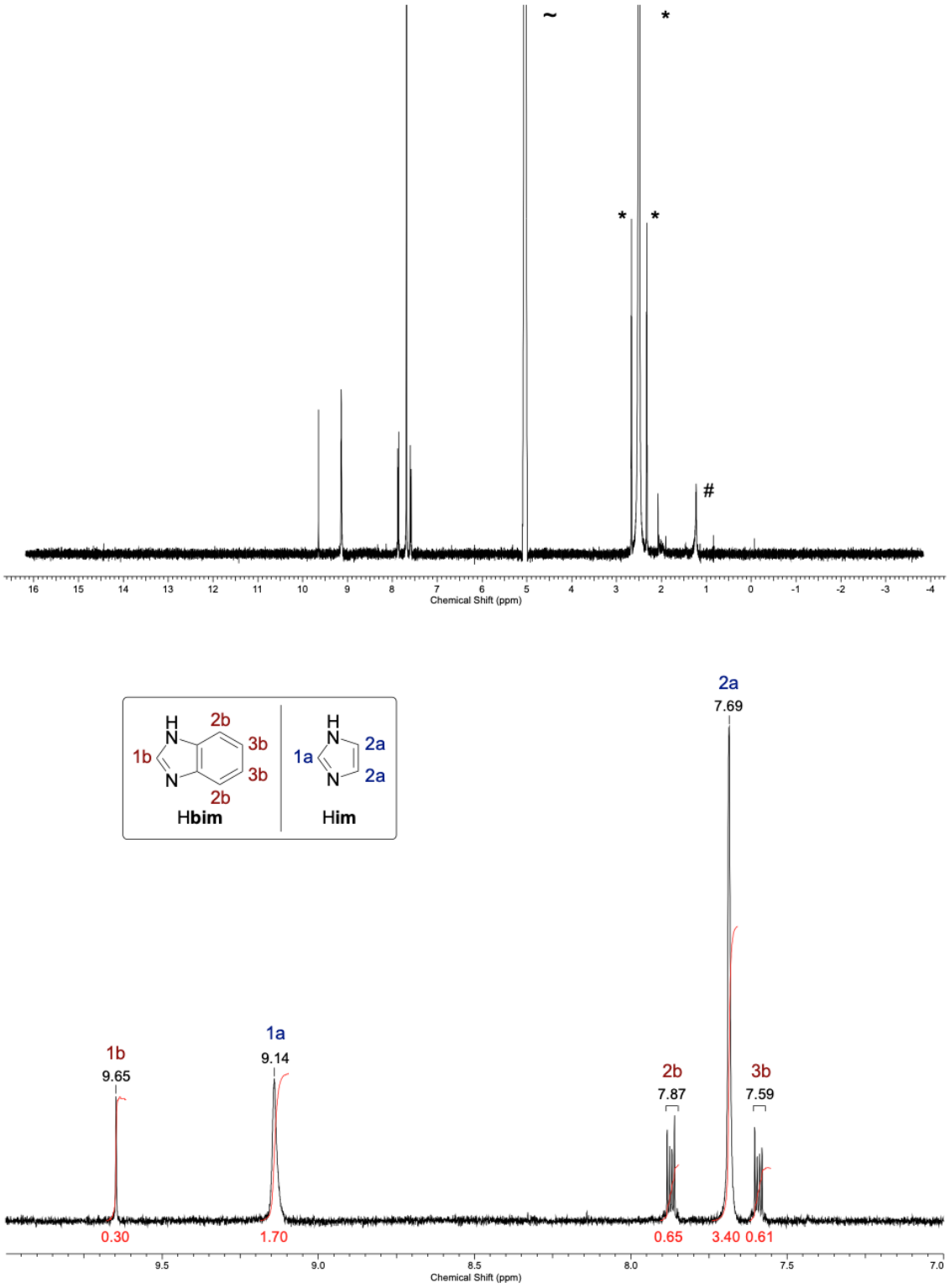

Figure A.29: ^{1}H NMR spectrum of ZIF-62(Co). Top: Full spectrum. Bottom: Zoom into the aromatic region (7.0 ppm to 10.0 ppm). DMSO is marked with $\star$, D_2O is marked with $\sim$ and the small contamination of the DCl/D_2O mixture is marked with #. The ratio between the linkers has been determined by the integral corresponding to the proton attached to the carbon atom between the two nitrogen atoms in the imidazolate type linkers to $Co(im)_{1.70}(bim)_{0.30}$.

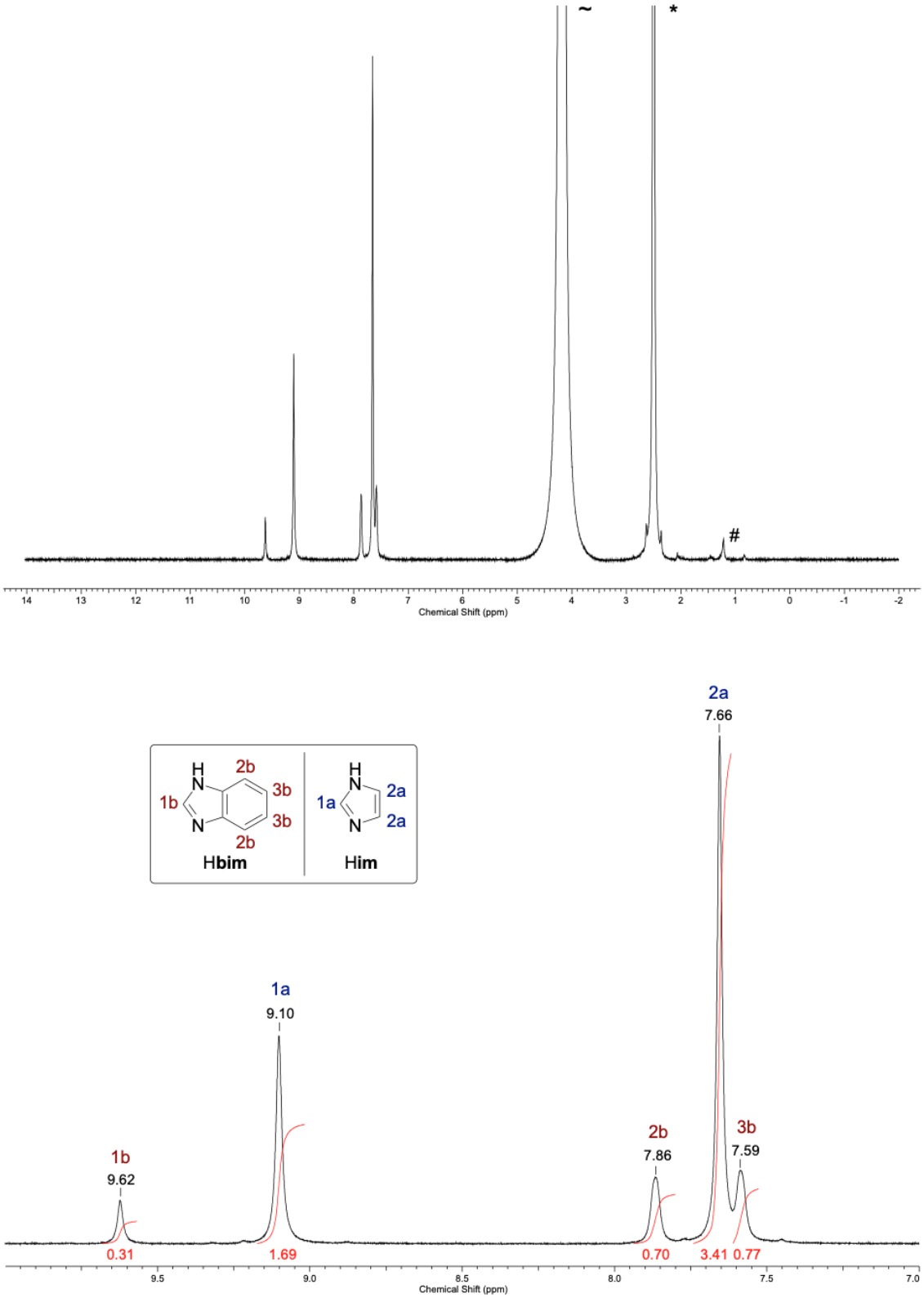

Figure A.30: ^{1}H NMR spectrum of a$_g$ZIF-62(Co). Top: Full spectrum. Bottom: Zoom into the aromatic region (7.0 ppm to 10.0 ppm). DMSO is marked with $\star$, D_2O is marked with $\sim$ and the small contamination of the DCl/D_2O mixture is marked with #. The ratio between the linkers has been determined by the integral corresponding to the proton attached to the carbon atom between the two nitrogen atoms in the imidazolate type linkers to $Co(im)_{1.69}(bim)_{0.31}$

A.3 Experimental Data to Section 8 – Melting Point Engineering by Mixed-Linker ZIFs

A.3.1 Single Crystal X-ray Diffraction

Single crystal X-ray diffraction data (SCXRD) were collected for all eleven as-synthesized (as) ZIFs on an Oxford Diffraction XCalibur diffractometer at 100 K using a liquid nitrogen cryostream of Oxford Instruments for the sample environment (CCDC deposition numbers 1849808-1849812, 1849814-1849818 and 1879396). Additional temperature dependent diffraction experiments were performed on a Bruker D8 Venture diffractometer for ZIF-zni(Co) and the guest-free compounds ZIF-4(Co), ZIF-62(Co)-bim$_{0.30}$ and ZIF-62(Co)-bim$_{0.10}$ (CCDC deposition numbers 1879385-1879395, 1879397, 1898695-1898698). For these materials data were collected at 100, 200, 300 and 400 K also using a liquid nitrogen cryostream of Oxford Instruments for the sample environment. The raw data processing was performed with the APEX3 suite or CrysAlisPro software package. The structure solution and refinement process was conducted with the Olex2[48] interface using SHELXS, SHELXT and SHELXL.[269]

Table A.8: Crystallographic data of as-ZIF-4(Zn) and as-ZIF-62(Zn)-bim$_{0.35}$ obtained via SCXRD.

Compound	as-ZIF-4(Zn)	as-ZIF-62(Zn)-bim$_{0.35}$
CCDC deposition number	1849813	1849816
Empirical formula	$C_{7.5}H_{9.5}N_{4.5}O_{0.5}Zn$	$C_7H_{6.5}N_4Zn$
Formula weight / g mol^{-1}	236.07	212.03
Temperature / K	100(2)	100(2)
Crystal system	orthorhombic	orthorhombic
Space group	*Pbca*	*Pbca*
a / Å	15.6595(5)	15.4567(8)
b / Å	14.6464(4)	15.5793(8)
c / Å	18.3890(7)	18.1340(8)
α / Å	90	90
β / Å	90	90
γ / Å	90	90
V / Å^3	4217.6(2)	4366.7(4)
Z	16	16
ϱ_{calc} / g cm^{-3}	1.487	1.290
μ / mm^{-1}	2.298	2.207
F(000)	1920.0	1704.0
Crystal size / mm^3	0.575 × 0.435 × 0.372	0.351 × 0.291 × 0.173
Radiation	MoK$_\alpha$ (λ = 0.71073)	MoK$_\alpha$ (λ = 0.71073)
2Θ range for data collection / °	5.138 to 64.848	4.338 to 56.992
Index ranges	-23 ≤ h ≤ 22, -8 ≤ k ≤ 20, -27 ≤ l ≤ 23	-20 ≤ h ≤ 19, -20 ≤ k ≤ 17, -24 ≤ l ≤ 12
Reflections collected	17421	13192
Independent reflections	6905 [R_{int} = 0.0215, R_{sigma} = 0.0267]	5327 [R_{int} = 0.0301, R_{sigma} = 0.0439]
Data/restraints/parameters	6905/0/246	5327/39/253
Goodness-of-fit on F^2	1.032	1.020
Final R indexes [I ≥ 2σ (I)]	R_1 = 0.0282, wR_2 = 0.0715	R_1 = 0.0512, wR_2 = 0.1267
Final R indexes [all data]	R_1 = 0.0369, wR_2 = 0.0756	R_1 = 0.0772, wR_2 = 0.1411
Largest diff. peak/hole / e Å^{-3}	0.93/-0.35	0.93/-0.43

Table A.9: Crystallographic data of as-ZIF-62(Zn)-bim$_{0.24}$ and as-ZIF-62(Zn)-bim$_{0.17}$ obtained via SCXRD.

Compound	as-ZIF-62(Zn)-bim$_{0.24}$	as-ZIF-62(Zn)-bim$_{0.17}$
CCDC deposition number	1849812	1849811
Empirical formula	$C_{6.96}H_{6.46}N_4Zn$	$C_{6.68}H_{6.18}N_4Zn$
Formula weight / g mol^{-1}	211.51	207.87
Temperature / K	100(1)	100(1)
Crystal system	orthorhombic	orthorhombic
Space group	*Pbca*	*Pbca*
a / Å	15.4724(7)	15.4399(4)
b / Å	15.5973(11)	15.4843(6)
c / Å	18.1477(8)	18.1529(6)
α / Å	90	90
β / Å	90	90
γ / Å	90	90
V / Å^3	4379.5(4)	4339.9(2)
Z	16	16
ϱ_{calc} / g cm^{-3}	1.283	1.273
μ / mm^{-1}	2.200	2.219
F(000)	1700.0	1668.0
Crystal size / mm^3	0.197 × 0.156 × 0.155	0.408 × 0.327 × 0.245
Radiation	MoK$_\alpha$ (λ = 0.71073)	MoK$_\alpha$ (λ = 0.71073)
2Θ range for data collection / °	4.334 to 56.996	4.488 to 57.996
Index ranges	-13 ≤ h ≤ 20, -15 ≤ k ≤ 20, -24 ≤ l ≤ 21	-21 ≤ h ≤ 21, -21 ≤ k ≤ 21, -24 ≤ l ≤ 24
Reflections collected	13517	41627
Independent reflections	5288 [R_{int} = 0.0280, R_{sigma} = 0.0344]	5767 [R_{int} = 0.0478, R_{sigma} = 0.0255]
Data/restraints/parameters	5288/39/253	5767/63/253
Goodness-of-fit on F^2	1.070	1.110
Final R indexes [I ≥ 2σ (I)]	R_1 = 0.0519, wR_2 = 0.1301	R_1 = 0.0516, wR_2 = 0.1286
Final R indexes [all data]	R_1 = 0.0671, wR_2 = 0.1379	R_1 = 0.0628, wR_2 = 0.1346
Largest diff. peak/hole / e Å^{-3}	1.04/-0.37	1.27/-0.40

Table A.10: Crystallographic data of as-ZIF-62(Zn)-bim$_{0.12}$ and as-ZIF-62(Zn)-bim$_{0.07}$ obtained via SCXRD.

Compound	as-ZIF-62(Zn)-bim$_{0.12}$	as-ZIF-62(Zn)-bim$_{0.07}$
CCDC deposition number	1849810	1849809
Empirical formula	$C_{6.48}H_{5.98}N_4Zn$	$C_{7.78}H_{9.28}N_{4.5}O_{0.5}Zn$
Formula weight / g mol^{-1}	205.26	239.21
Temperature / K	100.0(4)	99.9(3)
Crystal system	orthorhombic	orthorhombic
Space group	*Pbca*	*Pbca*
a / Å	15.3978(4)	15.4686(7)
b / Å	15.3546(5)	15.1468(12)
c / Å	18.1591(5)	18.2938(10)
α / Å	90	90
β / Å	90	90
γ / Å	90	90
V / Å^3	4293.3(2)	4286.2(5)
Z	16	16
ϱ_{calc} / g cm^{-3}	1.270	1.483
μ / mm^{-1}	2.242	2.262
F(000)	1646.0	1943.0
Crystal size / mm^3	0.359 × 0.264 × 0.216	0.561 × 0.357 × 0.262
Radiation	MoK$_\alpha$ (λ = 0.71073)	MoK$_\alpha$ (λ = 0.71073)
2Θ range for data collection / °	4.366 to 57.99	5.174 to 57.996
Index ranges	-20 ≤ h ≤ 21, -20 ≤ k ≤ 20, -24 ≤ l ≤ 24	-20 ≤ h ≤ 17, -20 ≤ k ≤ 7, -24 ≤ l ≤ 19
Reflections collected	34370	13405
Independent reflections	5662 [R_{int} = 0.0253, R_{sigma} = 0.0169]	5513 [R_{int} = 0.0343, R_{sigma} = 0.0453]
Data/restraints/parameters	5662/78/253	5513/122/338
Goodness-of-fit on F^2	1.112	1.049
Final R indexes [I ≥ 2σ (I)]	R_1 = 0.0457, wR_2 = 0.1197	R_1 = 0.0434, wR_2 = 0.1026
Final R indexes [all data]	R_1 = 0.0523, wR_2 = 0.1250	R_1 = 0.0697, wR_2 = 0.1190
Largest diff. peak/hole / e Å^{-3}	1.61/-0.60	0.69/-0.56

Table A.11: Crystallographic data of as-ZIF-62(Zn)-bim$_{0.12}$ and as-ZIF-62(Zn)-bim$_{0.07}$ obtained via SCXRD.

Compound	as-ZIF-62(Zn)-bim$_{0.12}$	as-ZIF-62(Zn)-bim$_{0.07}$
CCDC deposition number	1849810	1849809
Empirical formula	$C_{6.48}H_{5.98}N_4Zn$	$C_{7.78}H_{9.28}N_{4.5}O_{0.5}Zn$
Formula weight / g mol^{-1}	205.26	239.21
Temperature / K	100.0(4)	99.9(3)
Crystal system	orthorhombic	orthorhombic
Space group	*Pbca*	*Pbca*
a / Å	15.3978(4)	15.4686(7)
b / Å	15.3546(5)	15.1468(12)
c / Å	18.1591(5)	18.2938(10)
α / Å	90	90
β / Å	90	90
γ / Å	90	90
V / Å^3	4293.3(2)	4286.2(5)
Z	16	16
ϱ_{calc} / g cm^{-3}	1.270	1.483
μ / mm^{-1}	2.242	2.262
F(000)	1646.0	1943.0
Crystal size / mm^3	0.359 × 0.264 × 0.216	0.561 × 0.357 × 0.262
Radiation	MoK$_\alpha$ (λ = 0.71073)	MoK$_\alpha$ (λ = 0.71073)
2Θ range for data collection / °	4.366 to 57.99	5.174 to 57.996
Index ranges	-20 ≤ h ≤ 21, -20 ≤ k ≤ 20, -24 ≤ l ≤ 24	-20 ≤ h ≤ 17, -20 ≤ k ≤ 7, -24 ≤ l ≤ 19
Reflections collected	34370	13405
Independent reflections	5662 [R_{int} = 0.0253, R_{sigma} = 0.0169]	5513 [R_{int} = 0.0343, R_{sigma} = 0.0453]
Data/restraints/parameters	5662/78/253	5513/122/338
Goodness-of-fit on F^2	1.112	1.049
Final R indexes [I ≥ 2σ (I)]	R_1 = 0.0457, wR_2 = 0.1197	R_1 = 0.0434, wR_2 = 0.1026
Final R indexes [all data]	R_1 = 0.0523, wR_2 = 0.1250	R_1 = 0.0697, wR_2 = 0.1190
Largest diff. peak/hole / e Å^{-3}	1.61/-0.60	0.69/-0.56

Table A.12: Crystallographic data of as-ZIF-62(Zn)-bim$_{0.05}$ and as-ZIF-62(Zn)-bim$_{0.03}$ obtained via SCXRD.

Compound	as-ZIF-62(Zn)-bim$_{0.05}$	as-ZIF-62(Zn)-bim$_{0.03}$
CCDC deposition number	1849808	1849814
Empirical formula	$C_{7.7}H_{5.7}N_{4.5}O_{0.5}Zn$	$C_{7.62}H_{9.12}N_{4.5}O_{0.5}Zn$
Formula weight / g mol^{-1}	234.64	237.12
Temperature / K	100.0(2)	100.0(4)
Crystal system	orthorhombic	orthorhombic
Space group	*Pbca*	*Pbca*
a / Å	15.4872(7)	15.4409(6)
b / Å	15.0774(11)	15.0978(8)
c / Å	18.3105(8)	18.2903(9)
α / Å	90	90
β / Å	90	90
γ / Å	90	90
V / Å^3	4275.6(4)	4263.9(4)
Z	16	16
ϱ_{calc} / g cm^{-3}	1.458	1.478
μ / mm^{-1}	2.266	2.273
F(000)	1878.0	1925.0
Crystal size / mm^3	0.397 × 0.34 × 0.208	0.551 × 0.489 × 0.36
Radiation	MoK$_\alpha$ (λ = 0.71073)	MoK$_\alpha$ (λ = 0.71073)
2Θ range for data collection / °	4.378 to 58	5.176 to 57.998
Index ranges	-17 ≤ h ≤ 20, -20 ≤ k ≤ 19, -24 ≤ l ≤ 23	-21 ≤ h ≤ 17, -20 ≤ k ≤ 11, -16 ≤ l ≤ 24
Reflections collected	20352	14670
Independent reflections	5595 [R_{int} = 0.0343, R_{sigma} = 0.0341]	5660 [R_{int} = 0.0248, R_{sigma} = 0.0286]
Data/restraints/parameters	5595/131/338	5660/115/338
Goodness-of-fit on F^2	1.068	1.119
Final R indexes [I ≥ 2σ (I)]	R_1 = 0.0376, wR_2 = 0.0904	R_1 = 0.0393, wR_2 = 0.0919
Final R indexes [all data]	R_1 = 0.0593, wR_2 = 0.1029	R_1 = 0.0603, wR_2 = 0.1091
Largest diff. peak/hole / e Å^{-3}	0.70/-0.57	0.99/-0.49

Table A.13: Crystallographic data of as-ZIF-62(Zn)-bim$_{0.02}$ obtained via SCXRD.

Compound	as-ZIF-62(Zn)-bim$_{0.02}$
CCDC deposition number	1849815
Empirical formula	$C_{7.58}H_{9.54}N_{4.5}O_{0.62}Zn$
Formula weight / g mol^{-1}	239.07
Temperature / K	100.0(5)
Crystal system	orthorhombic
Space group	*Pbca*
a / Å	15.4061(8)
b / Å	15.2810(11)
c / Å	18.2918(14)
α / Å	90
β / Å	90
γ / Å	90
V / Å^3	4306.2(5)
Z	16
ϱ_{calc} / g cm^{-3}	1.475
μ / mm^{-1}	2.252
F(000)	1944.0
Crystal size / mm^3	0.546 × 0.386 × 0.275
Radiation	MoK$_\alpha$ (λ = 0.71073)
2Θ range for data collection / °	4.454 to 57.994
Index ranges	-18 ≤ h ≤ 21, -20 ≤ k ≤ 18, -24 ≤ l ≤ 12
Reflections collected	15439
Independent reflections	5720 [R_{int} = 0.0363, R_{sigma} = 0.0392]
Data/restraints/parameters	5720/131/327
Goodness-of-fit on F^2	1.042
Final R indexes [I ≥ 2σ (I)]	R_1 = 0.0419, wR_2 = 0.0997
Final R indexes [all data]	R_1 = 0.0655, wR_2 = 0.1149
Largest diff. peak/hole / e Å^{-3}	0.59/-0.47

Table A.14: Crystallographic data of as-ZIF-4(Co) and as-ZIF-62(Co)-bim$_{0.30}$ obtained via SCXRD.

Compound	as-ZIF-4(Co)	as-ZIF-62(Co)-bim$_{0.30}$
CCDC deposition number	1849807	1849817
Empirical formula	$C_{7.5}H_{9.5}CoN_{4.5}O_{0.5}$	$C_7H_{6.5}CoN_4$
Formula weight / g mol^{-1}	229.63	205.59
Temperature / K	103(2)	100(2)
Crystal system	orthorhombic	orthorhombic
Space group	*Pbca*	*Pbca*
a / Å	14.7957(5)	15.4329(12)
b / Å	15.5641(5)	15.6983(9)
c / Å	18.4453(6)	18.1310(12)
α / Å	90	90
β / Å	90	90
γ / Å	90	90
V / Å^3	4247.6(2)	4392.6(5)
Z	16	16
ϱ_{calc} / g cm^{-3}	1.436	1.244
μ / mm^{-1}	1.585	1.520
F(000)	1872.0	1656.0
Crystal size / mm^3	0.819 × 0.576 × 0.34	0.353 × 0.331 × 0.165
Radiation	MoK$_\alpha$ (λ = 0.71073)	MoK$_\alpha$ (λ = 0.71073)
2Θ range for data collection / °	5.204 to 56.96	5.19 to 59.996
Index ranges	-19 ≤ h ≤ 14, -20 ≤ k ≤ 20, -13 ≤ l ≤ 24	-19 ≤ h ≤ 21, -22 ≤ k ≤ 21, -21 ≤ l ≤ 25
Reflections collected	16292	18464
Independent reflections	5088 [R_{int} = 0.0227, R_{sigma} = 0.0239]	6396 [R_{int} = 0.0370, R_{sigma} = 0.0426]
Data/restraints/parameters	5088/12/246	6396/31/253
Goodness-of-fit on F^2	1.044	1.027
Final R indexes [I ≥ 2σ (I)]	R_1 = 0.0415, wR_2 = 0.1105	R_1 = 0.0551, wR_2 = 0.1317
Final R indexes [all data]	R_1 = 0.0532, wR_2 = 0.1220	R_1 = 0.0925, wR_2 = 0.1615
Largest diff. peak/hole / e Å^{-3}	1.22/-1.07	0.63/-0.31

Table A.15: Crystallographic data of as-ZIF-62(Co)-bim$_{0.17}$ and as-ZIF-62(Co)-bim$_{0.10}$ obtained via SCXRD.

Compound	as-ZIF-62(Co)-bim$_{0.17}$	as-ZIF-62(Co)-bim$_{0.10}$
CCDC deposition number	1879396	1849818
Empirical formula	$C_{7.73}H_{8.79}CoN_{4.35}O_{0.35}$	$C_{7.9}H_{9.7}CoN_{4.5}O_{0.5}$
Formula weight / g mol^{-1}	52.29	234.63
Temperature / K	100(2)	100.1(5)
Crystal system	orthorhombic	orthorhombic
Space group	*Pbca*	*Pbca*
a / Å	15.282(2)	15.1566(12)
b / Å	15.664(2)	15.6776(7)
c / Å	18.179(2)	18.2216(15)
α / Å	90	90
β / Å	90	90
γ / Å	90	90
V / Å^3	4351.5(10)	4329.8(5)
Z	16	16
ϱ_{calc} / g cm^{-3}	1.377	1.440
μ / mm^{-1}	1.544	1.556
F(000)	1815.0	1914
Crystal size / mm^3	0.528 × 0.33 × 0.189	0.528 × 0.33 × 0.189
Radiation	MoK$_\alpha$ (λ = 0.71073)	MoK$_\alpha$ (λ = 0.71073)
2Θ range for data collection / °	5.214 to 56.976	5.196 to 56.996
Index ranges	-20 ≤ h ≤ 20, -16 ≤ k ≤ 21, -24 ≤ l ≤ 24	-20 ≤ h ≤ 11, -21 ≤ k ≤ 19, -22 ≤ l ≤ 24
Reflections collected	44785	13241
Independent reflections	5503 [R_{int} = 0.0388, R_{sigma} = 0.0248]	5413 [R_{int} = 0.0360, R_{sigma} = 0.0528]
Data/restraints/parameters	5503/147/337	5413/93/300
Goodness-of-fit on F^2	1.105	1.113
Final R indexes [I ≥ 2σ (I)]	R_1 = 0.0494, wR_2 = 0.1465	R_1 = 0.0687, wR_2 = 0.1648
Final R indexes [all data]	R_1 = 0.0552, wR_2 = 0.1544	R_1 = 0.1087, wR_2 = 0.1920
Largest diff. peak/hole / e Å^{-3}	0.88/-0.44	0.76/-0.77

Table A.16: Crystallographic data of ZIF-4(Co) obtained via SCXRD collected at 100 K or 200 K.

Compound	ZIF-4(Co)	ZIF-4(Co)
CCDC deposition number	1879395	1879394
Empirical formula	$C_6H_6CoN_4$	$C_6H_6CoN_4$
Formula weight / g mol^{-1}	193.08	193.08
Temperature / K	100(2)	200(2)
Crystal system	orthorhombic	orthorhombic
Space group	*Pbca*	*Pbca*
a / Å	15.0835(7)	15.2978(7)
b / Å	15.2881(7)	15.4168(8)
c / Å	18.2031(8)	18.1951(8)
a / Å	90	90
β / Å	90	90
γ / Å	90	90
V / Å^3	4197.6(3)	4291.2(4)
Z	16	16
ϱ_{calc} / g cm^{-3}	1.222	1.195
μ / mm^{-1}	1.586	1.552
F(000)	1552.0	1552.0
Crystal size / mm^3	0.524 × 0.378 × 0.34	0.524 × 0.378 × 0.34
Radiation	MoK$_\alpha$ (λ = 0.71073)	MoK$_\alpha$ (λ = 0.71073)
2Θ range for data collection / °	5.402 to 56	5.326 to 55.996
Index ranges	-19 ≤ h ≤ 19, -19 ≤ k ≤ 20, -21 ≤ l ≤ 24	-17 ≤ h ≤ 20, -20 ≤ k ≤ 20, -24 ≤ l ≤ 23
Reflections collected	32376	33228
Independent reflections	5057 [R_{int} = 0.0362, R_{sigma} = 0.0277]	5174 [R_{int} = 0.0245, R_{sigma} = 0.0164]
Data/restraints/parameters	5057/7/217	5174/7/217
Goodness-of-fit on F^2	1.043	1.079
Final R indexes [I ≥ 2σ (I)]	R_1 = 0.0276, wR_2 = 0.0654	R_1 = 0.0261, wR_2 = 0.0714
Final R indexes [all data]	R_1 = 0.0357, wR_2 = 0.0706	R_1 = 0.0363, wR_2 = 0.0780
Largest diff. peak/hole / e Å^{-3}	0.28/-0.38	0.19/-0.20

Table A.17: Crystallographic data of ZIF-4(Co) obtained via SCXRD collected at 300 K or 400 K.

Compound	ZIF-4(Co)	ZIF-4(Co)
CCDC deposition number	1879392	1879393
Empirical formula	$C_6H_6CoN_4$	$C_6H_6CoN_4$
Formula weight / g mol^{-1}	193.08	193.08
Temperature / K	300(2)	400(2)
Crystal system	orthorhombic	orthorhombic
Space group	*Pbca*	*Pbca*
a / Å	15.487(3)	15.591(5)
b / Å	15.520(2)	15.606(4)
c / Å	18.108(3)	18.103(5)
α / Å	90	90
β / Å	90	90
γ / Å	90	90
V / Å^3	4352.5(12)	4405(2)
Z	16	16
ϱ_{calc} / g cm^{-3}	1.179	1.165
μ / mm^{-1}	1.530	1.512
F(000)	1552.0	1552.0
Crystal size / mm^3	0.524 × 0.378 × 0.34	0.524 × 0.378 × 0.342
Radiation	MoK$_\alpha$ (λ = 0.71073)	MoK$_\alpha$ (λ = 0.71073)
2Θ range for data collection / °	5.712 to 55.988	5.686 to 56
Index ranges	-20 ≤ h ≤ 20, -19 ≤ k ≤ 20, -23 ≤ l ≤ 23	-20 ≤ h ≤ 20, -20 ≤ k ≤ 18, -23 ≤ l ≤ 23
Reflections collected	35183	31691
Independent reflections	5240 [R_{int} = 0.0319, R_{sigma} = 0.0215]	5307 [R_{int} = 0.0425, R_{sigma} = 0.0314]
Data/restraints/parameters	5240/1/217	5307/1/217
Goodness-of-fit on F^2	1.061	1.042
Final R indexes [I ≥ 2σ (I)]	R_1 = 0.0307, wR_2 = 0.0800	R_1 = 0.0372, wR_2 = 0.0993
Final R indexes [all data]	R_1 = 0.0482, wR_2 = 0.0922	R_1 = 0.0710, wR_2 = 0.1228
Largest diff. peak/hole / e Å^{-3}	0.18/-0.19	0.19/-0.21

Table A.18: Crystallographic data of ZIF-62(Co)-bim$_{0.10}$ obtained via SCXRD collected at 100 K or 200 K.

Compound	ZIF-62(Co)bim$_{0.10}$	ZIF-62(Co)bim$_{0.10}$
CCDC deposition number	1879386	1879390
Empirical formula	$C_{6.4}H_{6.2}CoN_4$	$C_{6.4}H_{6.2}CoN_4$
Formula weight / g mol^{-1}	198.08	198.08
Temperature / K	100(2)	200(2)
Crystal system	orthorhombic	orthorhombic
Space group	*Pbca*	*Pbca*
a / Å	15.2069(7)	15.4030(6)
b / Å	15.3558(7)	15.5040(6)
c / Å	18.1389(7)	18.1233(7)
α / Å	90	90
β / Å	90	90
γ / Å	90	90
V / Å^3	4235.7(3)	4328.0(3)
Z	16	16
ϱ_{calc} / g cm^{-3}	1.242	1.216
μ / mm^{-1}	1.574	1.540
F(000)	1594.0	1594.0
Crystal size / mm^3	0.6 × 0.514 × 0.471	0.6 × 0.514 × 0.471
Radiation	MoK$_\alpha$ (λ = 0.71073)	MoK$_\alpha$ (λ = 0.71073)
2Θ range for data collection / °	5.762 to 55.996	5.716 to 55.994
Index ranges	-16 ≤ h ≤ 20, -20 ≤ k ≤ 20, -23 ≤ l ≤ 22	-20 ≤ h ≤ 19, -20 ≤ k ≤ 20, -23 ≤ l ≤ 23
Reflections collected	32985	35350
Independent reflections	5096 [R_{int} = 0.0325, R_{sigma} = 0.0236]	5219 [R_{int} = 0.0283, R_{sigma} = 0.0192]
Data/restraints/parameters	5096/119/325	5219/119/325
Goodness-of-fit on F^2	1.109	1.098
Final R indexes [I ≥ 2σ (I)]	R_1 = 0.0391, wR_2 = 0.0969	R_1 = 0.0323, wR_2 = 0.0823
Final R indexes [all data]	R_1 = 0.0563, wR_2 = 0.1112	R_1 = 0.0492, wR_2 = 0.0945
Largest diff. peak/hole / e Å^{-3}	0.35/-0.40	0.25/-0.25

Table A.19: Crystallographic data of ZIF-62(Co)-bim$_{0.10}$ obtained via SCXRD collected at 300 K or 400 K.

Compound	ZIF-62(Co)bim$_{0.10}$	ZIF-62(Co)bim$_{0.10}$
CCDC deposition number	1879389	1879391
Empirical formula	$C_{6.4}H_{6.2}CoN_4$	$C_{6.4}H_{6.2}CoN_4$
Formula weight / g mol^{-1}	198.08	198.08
Temperature / K	300(2)	400(2)
Crystal system	orthorhombic	orthorhombic
Space group	*Pbca*	*Pbca*
a / Å	15.5088(9)	15.5286(15)
b / Å	15.5888(7)	15.6454(13)
c / Å	18.0871(9)	18.0654(16)
α / Å	90	90
β / Å	90	90
γ / Å	90	90
V / Å^3	4372.8(4)	4389.0(7)
Z	16	16
ϱ_{calc} / g cm^{-3}	1.204	1.199
μ / mm^{-1}	1.524	1.519
F(000)	1594.0	1594.0
Crystal size / mm^3	0.6 × 0.514 × 0.471	0.6 × 0.514 × 0.471
Radiation	MoK$_\alpha$ (λ = 0.71073)	MoK$_\alpha$ (λ = 0.71073)
2Θ range for data collection / °	5.692 to 56	5.676 to 55.988
Index ranges	-19 ≤ h ≤ 20, -20 ≤ k ≤ 20, -23 ≤ l ≤ 23	-20 ≤ h ≤ 20, -20 ≤ k ≤ 20, -23 ≤ l ≤ 23
Reflections collected	33597	43462
Independent reflections	5244 [R_{int} = 0.0335, R_{sigma} = 0.0275]	5271 [R_{int} = 0.0416, R_{sigma} = 0.0268]
Data/restraints/parameters	5244/119/325	5271/119/325
Goodness-of-fit on F^2	1.133	1.094
Final R indexes [I ≥ 2σ (I)]	R_1 = 0.0446, wR_2 = 0.1232	R_1 = 0.0516, wR_2 = 0.1227
Final R indexes [all data]	R_1 = 0.0708, wR_2 = 0.1499	R_1 = 0.0923, wR_2 = 0.1626
Largest diff. peak/hole / e Å^{-3}	0.42/-0.40	0.36/-0.31

Table A.20: Crystallographic data of ZIF-62(Co)-bim$_{0.30}$ obtained via SCXRD collected at 100 K or 200 K.

Compound	ZIF-62(Co)bim$_{0.30}$	ZIF-62(Co)bim$_{0.30}$
CCDC deposition number	1879397	1879385
Empirical formula	$C_{7.2}H_{6.6}CoN_4$	$C_{7.2}H_{6.6}CoN_4$
Formula weight / g mol^{-1}	208.09	208.09
Temperature / K	100(2)	200(2)
Crystal system	orthorhombic	orthorhombic
Space group	*Pbca*	*Pbca*
a / Å	15.3860(7)	15.4766(13)
b / Å	15.6096(7)	15.6759(12)
c / Å	18.0571(7)	18.0353(15)
α / Å	90	90
β / Å	90	90
γ / Å	90	90
V / Å^3	4336.8(3)	4375.5(6)
Z	16	16
ϱ_{calc} / g cm^{-3}	1.275	1.264
μ / mm^{-1}	1.540	1.527
F(000)	1677.0	1677.0
Crystal size / mm^3	0.765 × 0.726 × 0.599	0.765 × 0.726 × 0.599
Radiation	MoK$_\alpha$ (λ = 0.71073)	MoK$_\alpha$ (λ = 0.71073)
2Θ range for data collection / °	5.22 to 55.998	5.198 to 55.992
Index ranges	-20 ≤ h ≤ 19, -20 ≤ k ≤ 20, -23 ≤ l ≤ 23	-19 ≤ h ≤ 20, -18 ≤ k ≤ 20, -23 ≤ l ≤ 23
Reflections collected	44691	31774
Independent reflections	5231 [R_{int} = 0.0340, R_{sigma} = 0.0206]	5276 [R_{int} = 0.0315, R_{sigma} = 0.0243]
Data/restraints/parameters	5231/84/307	5276/84/307
Goodness-of-fit on F^2	1.119	1.093
Final R indexes [I ≥ 2σ (I)]	R_1 = 0.0432, wR_2 = 0.1148	R_1 = 0.0436, wR_2 = 0.1190
Final R indexes [all data]	R_1 = 0.0602, wR_2 = 0.1321	R_1 = 0.0641, wR_2 = 0.1419
Largest diff. peak/hole / e Å^{-3}	0.47/-0.39	0.37/-0.28

Table A.21: Crystallographic data of ZIF-62(Co)-bim$_{0.30}$ obtained via SCXRD collected at 300 K or 400 K.

Compound	ZIF-62(Co)bim$_{0.30}$	ZIF-62(Co)bim$_{0.30}$
CCDC deposition number	1879388	1879387
Empirical formula	$C_{7.2}H_{6.6}CoN_4$	$C_{7.2}H_{6.6}CoN_4$
Formula weight / g mol^{-1}	208.09	208.09
Temperature / K	300(2)	400(2)
Crystal system	orthorhombic	orthorhombic
Space group	*Pbca*	*Pbca*
a / Å	15.5146(11)	15.342(4)
b / Å	15.7585(10)	15.808(3)
c / Å	18.0597(11)	18.030(3)
α / Å	90	90
β / Å	90	90
γ / Å	90	90
V / Å^3	4415.4(5)	4372.5(17)
Z	16	16
ϱ_{calc} / g cm^{-3}	1.252	1.264
μ / mm^{-1}	1.513	1.528
F(000)	1677.0	1677.0
Crystal size / mm^3	0.765 × 0.726 × 0.599	0.765 × 0.726 × 0.599
Radiation	MoK$_\alpha$ (λ = 0.71073)	MoK$_\alpha$ (λ = 0.71073)
2Θ range for data collection / °	5.64 to 56	5.154 to 55.988
Index ranges	-20 ≤ h ≤ 20, -20 ≤ k ≤ 20, -23 ≤ l ≤ 23	-18 ≤ h ≤ 20, -20 ≤ k ≤ 20, -23 ≤ l ≤ 23
Reflections collected	45024	25592
Independent reflections	5319 [R_{int} = 0.0399, R_{sigma} = 0.0256]	5250 [R_{int} = 0.0431, R_{sigma} = 0.0370]
Data/restraints/parameters	5319/84/307	5250/84/307
Goodness-of-fit on F^2	1.098	1.046
Final R indexes [I ≥ 2σ (I)]	R_1 = 0.0466, wR_2 = 0.1388	R_1 = 0.0432, wR_2 = 0.1136
Final R indexes [all data]	R_1 = 0.0750, wR_2 = 0.1740	R_1 = 0.0747, wR_2 = 0.1380
Largest diff. peak/hole / e Å^{-3}	0.43/-0.27	0.36/-0.33

Table A.22: Crystallographic data of ZIF-zni(Co) obtained via SCXRD collected at 100 K or 200 K.

Compound	ZIF-zni(Co)	ZIF-zni(Co)
CCDC deposition number	1898695	1898696
Empirical formula	$C_6H_6CoN_4$	$C_6H_6CoN_4$
Formula weight / g mol^{-1}	193.08	193.08
Temperature / K	100	200
Crystal system	tetragonal	tetragonal
Space group	$I4_1cd$	$I4_1cd$
a / Å	23.3963(6)	23.4363(6)
b / Å	23.3963(6)	23.4363(6)
c / Å	12.4649(3)	12.4615(3)
α / Å	90	90
β / Å	90	90
γ / Å	90	90
V / Å^3	6823.1(4)	6844.6(4)
Z	32	32
ϱ_{calc} / g cm^{-3}	1.504	1.499
μ / mm^{-1}	1.952	1.945
F(000)	3104.0	3104.0
Crystal size / mm^3	0.612 × 0.492 × 0.422	0.612 × 0.492 × 0.422
Radiation	MoK$_\alpha$ (λ = 0.71073)	MoK$_\alpha$ (λ = 0.71073)
2Θ range for data collection / °	5.082 to 72.642	5.078 to 72.624
Index ranges	-38 ≤ h ≤ 38, -38 ≤ k ≤ 38, -20 ≤ l ≤ 20	-39 ≤ h ≤ 39, -38 ≤ k ≤ 39, -20 ≤ l ≤ 20
Reflections collected	45835	76970
Independent reflections	8241 [R_{int} = 0.0289, R_{sigma} = 0.0210]	8287 [R_{int} = 0.1059, R_{sigma} = 0.0419]
Data/restraints/parameters	8241/1/199	8287/1/199
Goodness-of-fit on F^2	1.123	1.028
Final R indexes [I ≥ 2σ (I)]	R_1 = 0.0204, wR_2 = 0.0533	R_1 = 0.0396, wR_2 = 0.1020
Final R indexes [all data]	R_1 = 0.0225, wR_2 = 0.0577	R_1 = 0.0579, wR_2 = 0.1192
Largest diff. peak/hole / e Å^{-3}	0.39/-0.55	0.34/-0.58
Flack parameter	0.003(3)	-0.015(13)

Table A.23: Crystallographic data of ZIF-zni(Co) obtained via SCXRD collected at 300 K or 400 K.

Compound	ZIF-zni(Co)	ZIF-zni(Co)
CCDC deposition number	1898698	1898697
Empirical formula	$C_6H_6CoN_4$	$C_6H_6CoN_4$
Formula weight / g mol^{-1}	193.08	193.08
Temperature / K	300	400
Crystal system	tetragonal	tetragonal
Space group	$I4_1cd$	$I4_1cd$
a / Å	23.4856(11)	23.549(5)
b / Å	23.4856(11)	23.549(5)
c / Å	12.4606(6)	12.446(2)
α / Å	90	90
β / Å	90	90
γ / Å	90	90
V / Å^3	6872.9(7)	6902(3)
Z	32	32
ϱ_{calc} / g cm^{-3}	1.493	1.486
μ / mm^{-1}	1.937	1.929
F(000)	3104.0	3104.0
Crystal size / mm^3	0.612 × 0.492 × 0.422	0.612 × 0.492 × 0.422
Radiation	MoK$_\alpha$ (λ = 0.71073)	MoK$_\alpha$ (λ = 0.71073)
2Θ range for data collection / °	5.072 to 72.624	5.066 to 72.614
Index ranges	-39 ≤ h ≤ 38, -39 ≤ k ≤ 39, -20 ≤ l ≤ 20	-38 ≤ h ≤ 38, -39 ≤ k ≤ 39, -20 ≤ l ≤ 20
Reflections collected	154636	154274
Independent reflections	8311 [R_{int} = 0.1132, R_{sigma} = 0.0319]	8340 [R_{int} = 0.1245, R_{sigma} = 0.0367]
Data/restraints/parameters	8311/1/199	8340/1/199
Goodness-of-fit on F^2	1.046	0.961
Final R indexes [I ≥ 2σ (I)]	R_1 = 0.0425, wR_2 = 0.1102	R_1 = 0.0411, wR_2 = 0.1071
Final R indexes [all data]	R_1 = 0.0698, wR_2 = 0.1347	R_1 = 0.0903, wR_2 = 0.1359
Largest diff. peak/hole / e Å^{-3}	0.31/-0.45	0.21/-0.32
Flack parameter	-0.04(2)	-0.05(3)

A.3.2 In-House Powder X-ray Diffraction

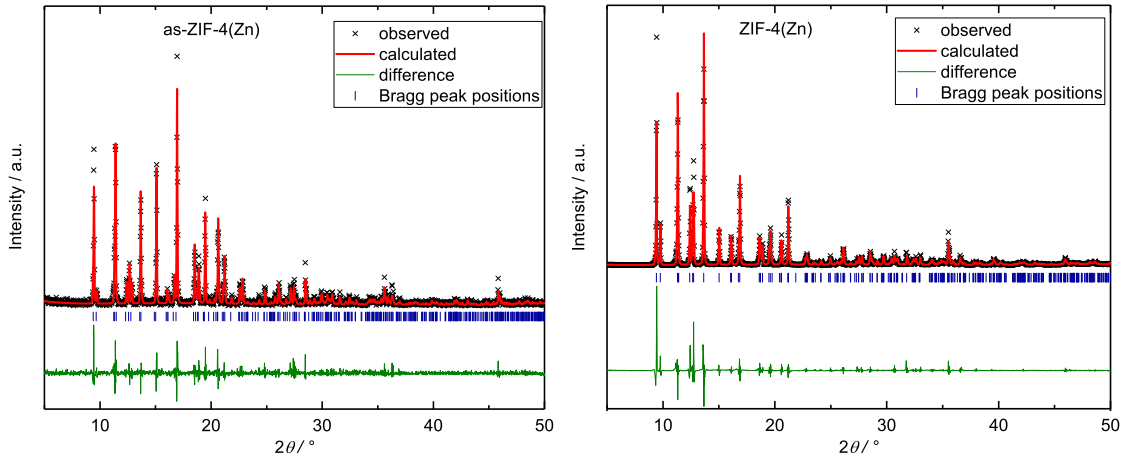

Figure A.31: PXRD pattern with structureless profile fit (Pawley method) of as-ZIF-4(Zn) (left) and ZIF-4(Zn) (right).

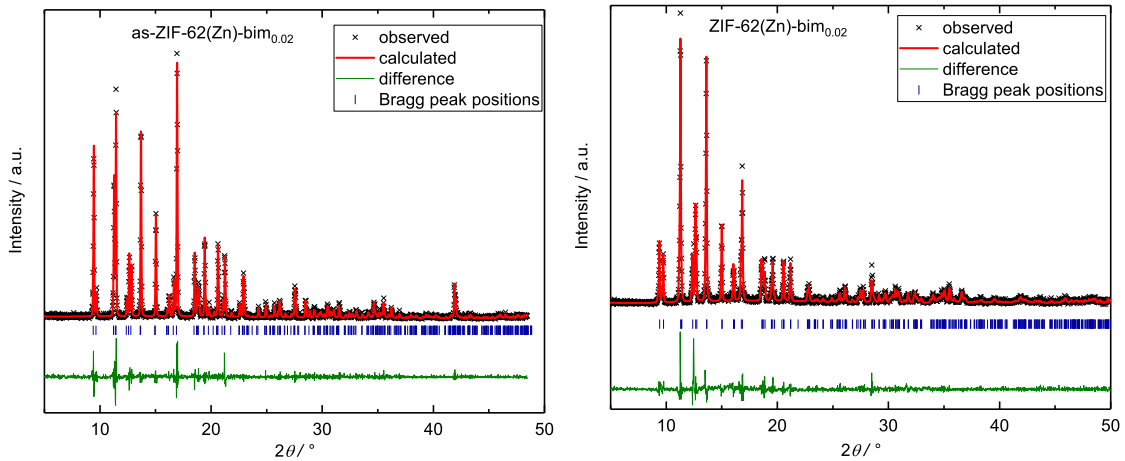

Figure A.32: PXRD pattern with structureless profile fit (Pawley method) of as-ZIF-62(Zn)-bim$_{0.02}$ (left) and ZIF-62(Zn)-bim$_{0.02}$ (right).

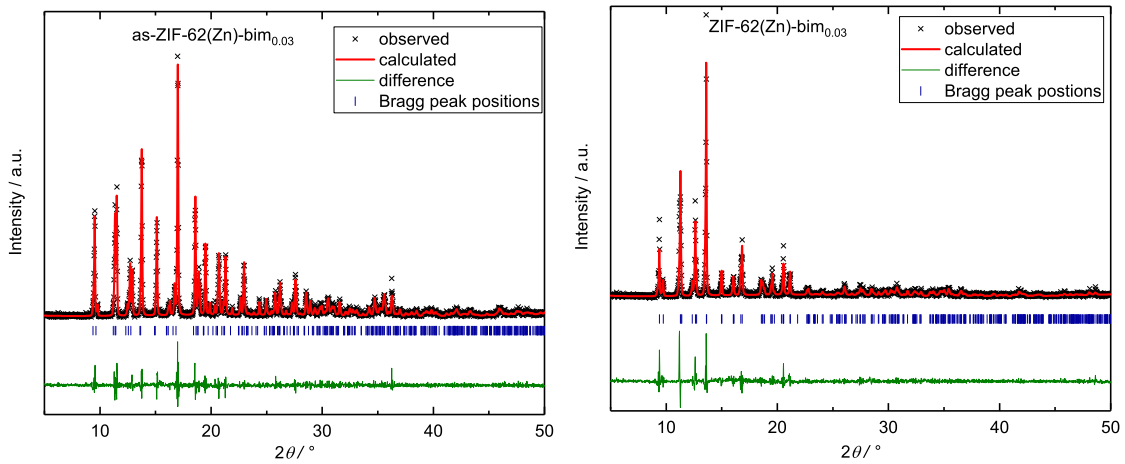

Figure A.33: PXRD pattern with structureless profile fit (Pawley method) of as-ZIF-62(Zn)-bim$_{0.03}$ (left) and ZIF-62(Zn)-bim$_{0.03}$ (right).

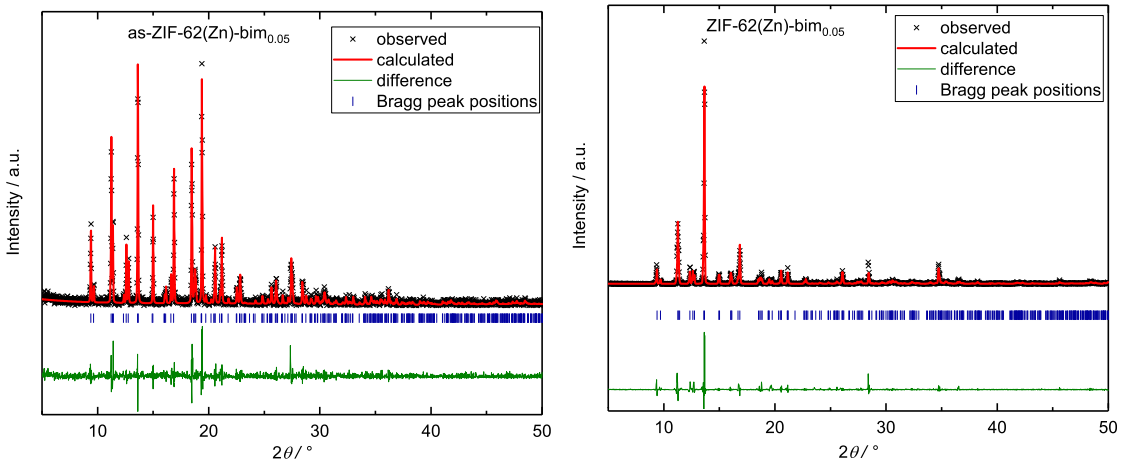

Figure A.34: PXRD pattern with structureless profile fit (Pawley method) of as-ZIF-62(Zn)-bim$_{0.05}$ (left) and ZIF-62(Zn)-bim$_{0.05}$ (right).

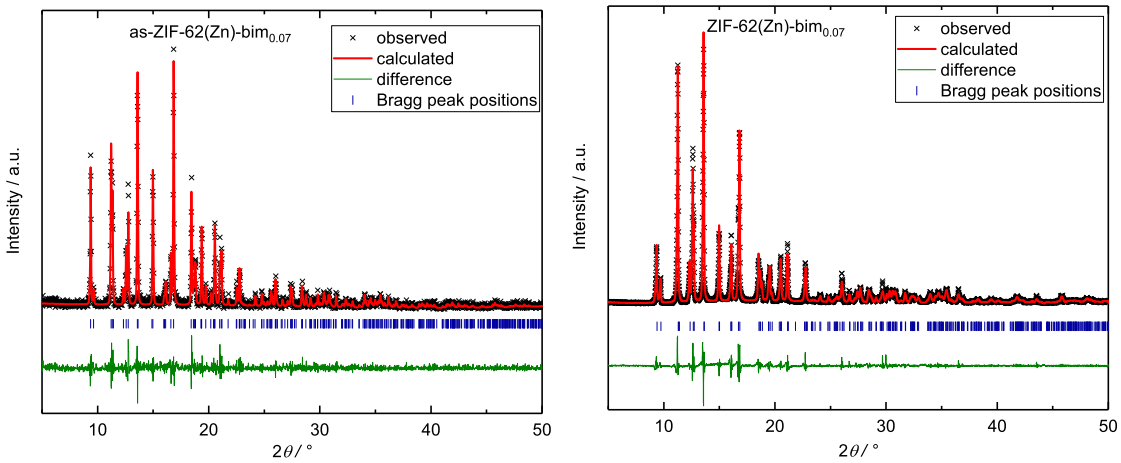

Figure A.35: PXRD pattern with structureless profile fit (Pawley method) of as-ZIF-62(Zn)-bim$_{0.07}$ (left) and ZIF-62(Zn)-bim$_{0.07}$ (right).

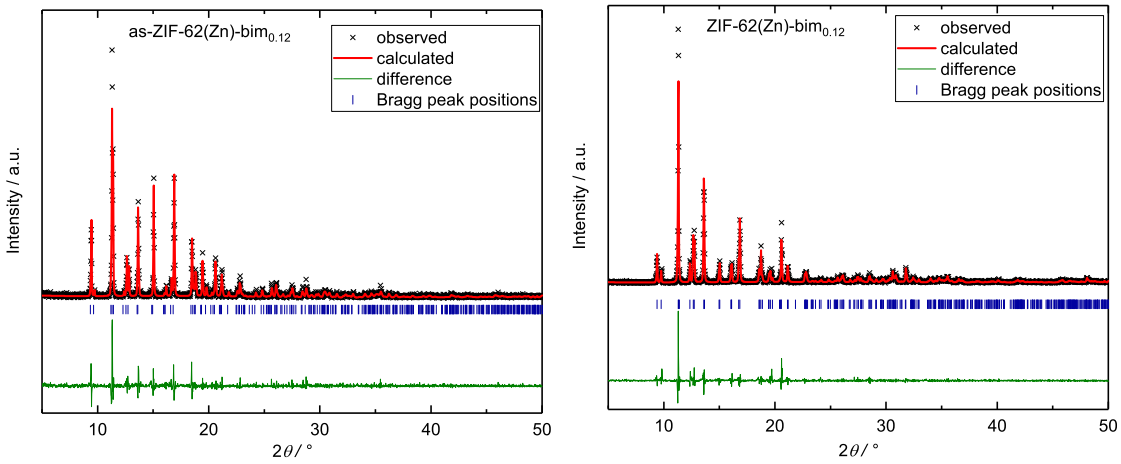

Figure A.36: PXRD pattern with structureless profile fit (Pawley method) of as-ZIF-62(Zn)-bim$_{0.12}$ (left) and ZIF-62(Zn)-bim$_{0.12}$ (right).

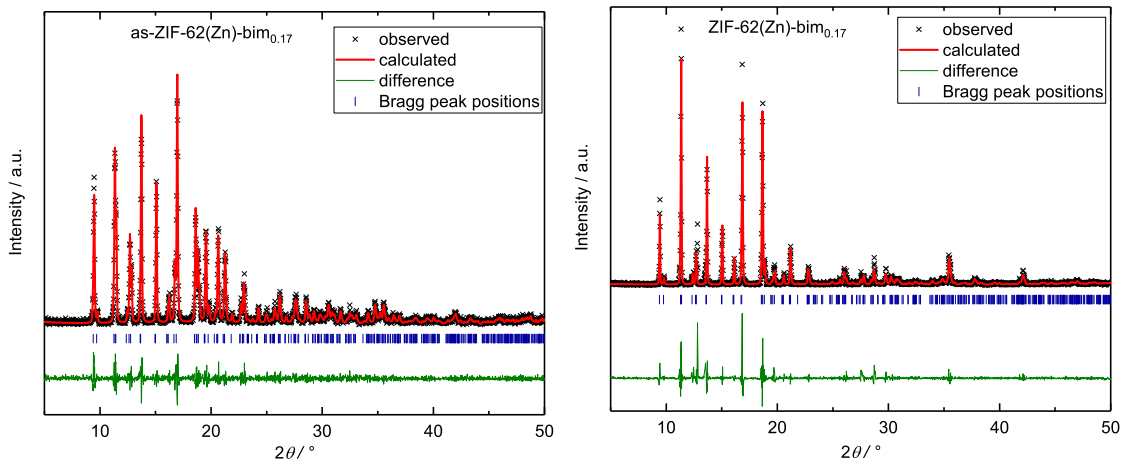

Figure A.37: PXRD pattern with structureless profile fit (Pawley method) of as-ZIF-62(Zn)-bim$_{0.17}$ (left) and ZIF-62(Zn)-bim$_{0.17}$ (right).

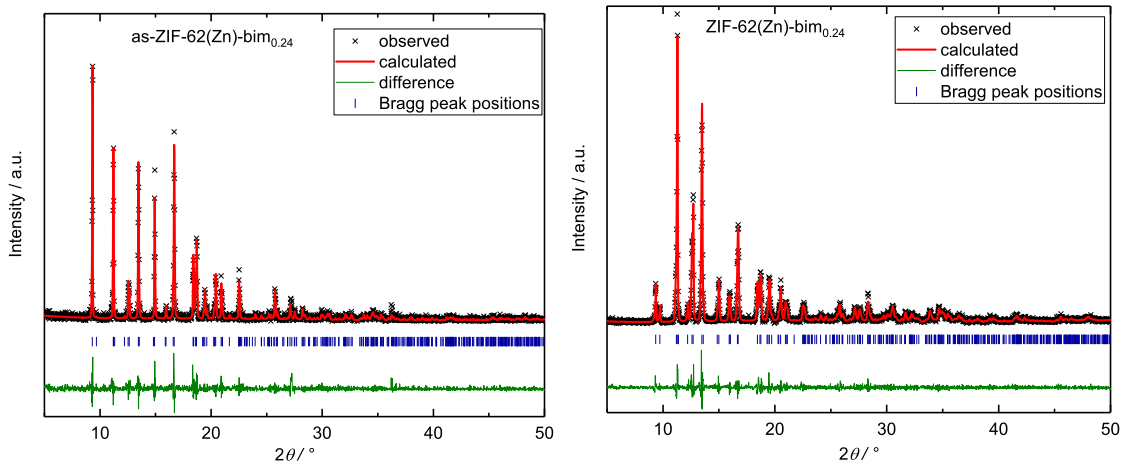

Figure A.38: PXRD pattern with structureless profile fit (Pawley method) of as-ZIF-62(Zn)-bim$_{0.24}$ (left) and ZIF-62(Zn)-bim$_{0.24}$ (right).

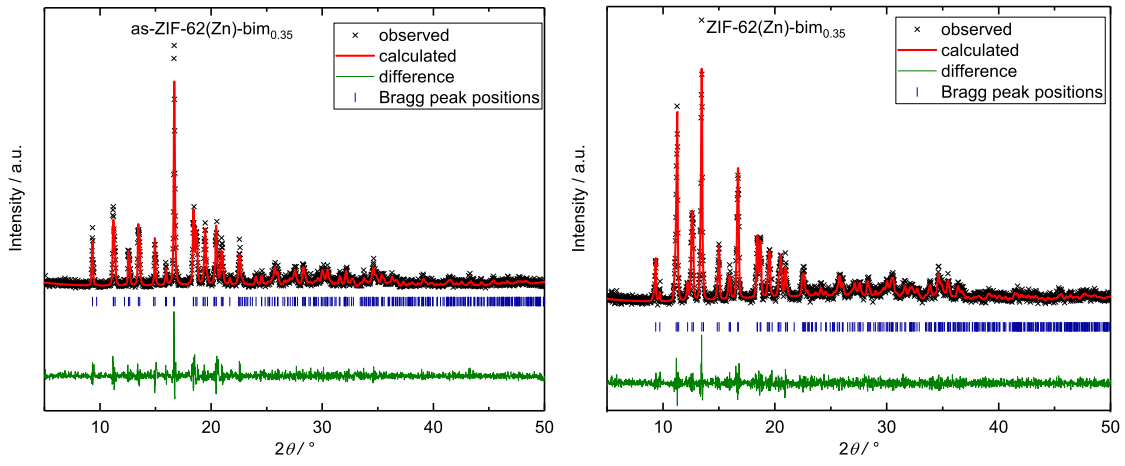

Figure A.39: PXRD pattern with structureless profile fit (Pawley method) of as-ZIF-62(Zn)-bim$_{0.35}$ (left) and ZIF-62(Zn)-bim$_{0.35}$ (right).

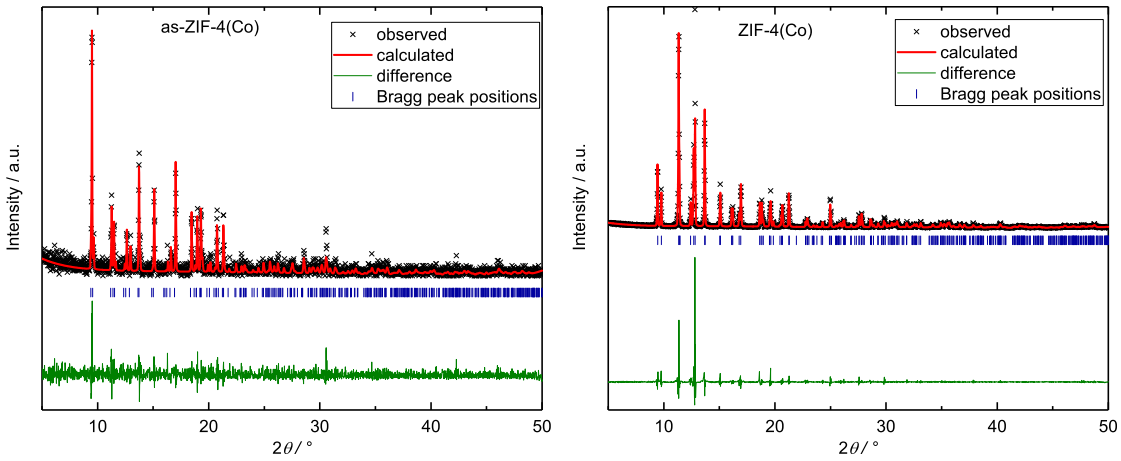

Figure A.40: PXRD pattern with structureless profile fit (Pawley method) of as-ZIF-4(Co) (left) and ZIF-4(Co) (right).

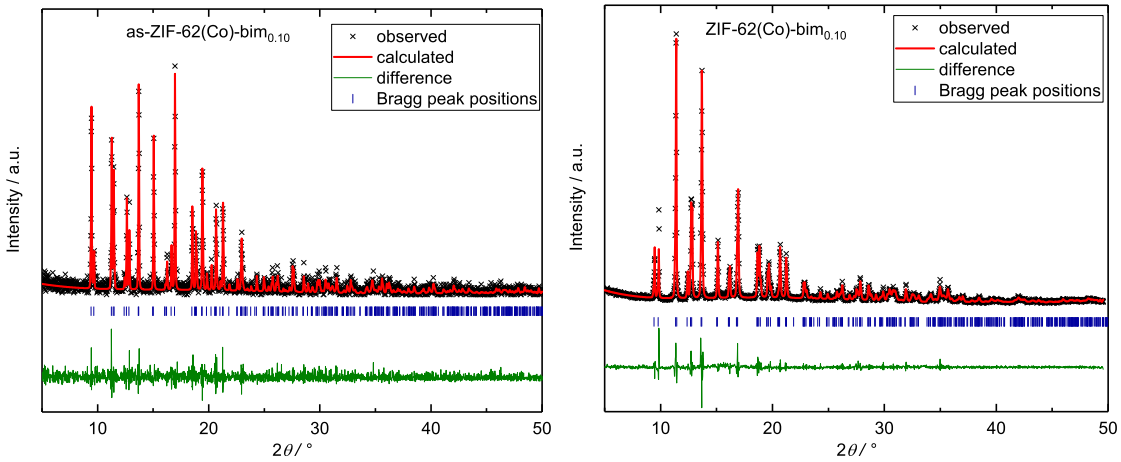

Figure A.41: PXRD pattern with structureless profile fit (Pawley method) of as-ZIF-62(Co)-bim$_{0.10}$ (left) and ZIF-62(Co)-bim$_{0.10}$ (right).

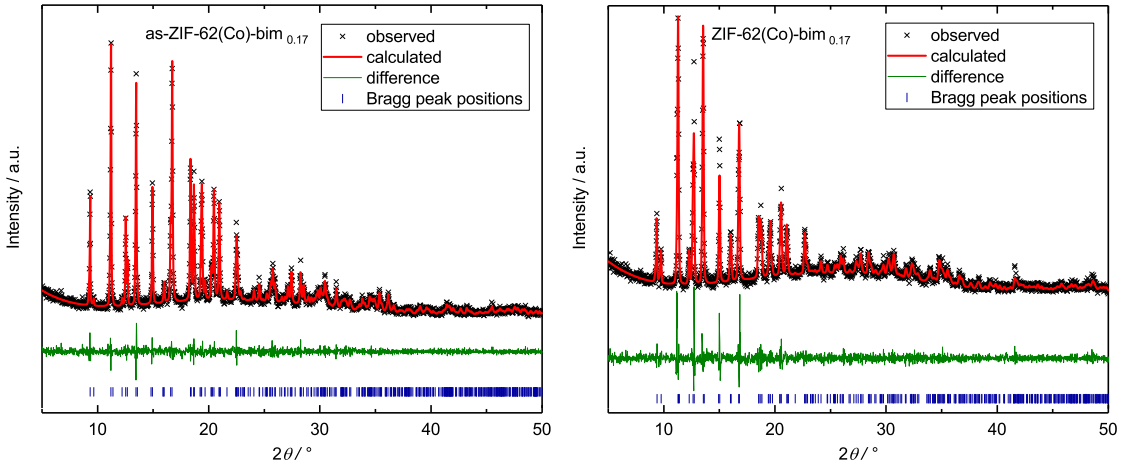

Figure A.42: PXRD pattern with structureless profile fit (Pawley method) of as-ZIF-62(Co)-bim$_{0.17}$ (left) and ZIF-62(Co)-bim$_{0.17}$ (right).

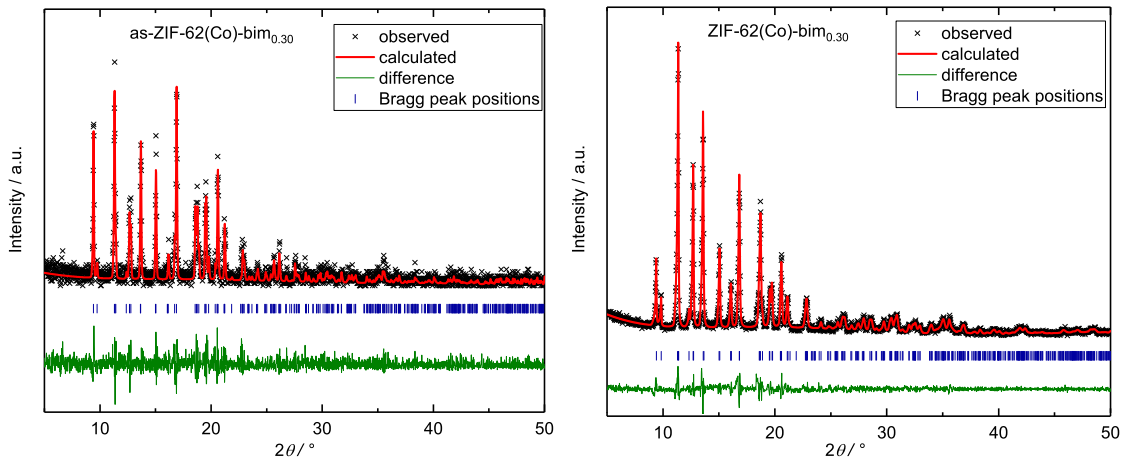

Figure A.43: PXRD pattern with structureless profile fit (Pawley method) of as-ZIF-62(Co)-bim$_{0.30}$ (left) and ZIF-62(Co)-bim$_{0.30}$ (right).

Table A.24: Unit cell parameters a, b, c and V (orthorhombic space group *Pbca*) determined by structureless profile refinements (Pawley method) of the PXRD data of as and desolvated/activated ZIF-4(M) and ZIF-62(M)-bim$_x$ materials with corresponding R_{wp}, R_{exp} and χ values.

Compound	as-ZIF-4(Zn)	ZIF-4(Zn)	as-ZIF-4(Co)	ZIF-4(Co)	as-ZIF-62(Zn)-bim$_{0.35}$	ZIF-62(Zn)-bim$_{0.35}$
a / Å	15.431(2)	15.5205(18)	15.330(5)	15.4180(14)	15.563(7)	15.505(7)
b / Å	15.627(2)	15.5413(18)	15.549(4)	15.5072(10)	15.803(8)	15.809(8)
c / Å	18.312(2)	18.108(2)	18.485(5)	18.0832(16)	18.225(8)	18.172(10)
V / Å^3	4415.9(10)	4367.9(9)	4406(2)	4323.2(6)	4483(3)	4454(4)
R_{wp}	33.71	20.35	46.61	18.06	30.35	22.26
R_{exp}	26.39	3.09	40.21	6.86	24.39	19.56
χ	1.27	6.58	1.16	2.63	1.24	1.14

Compound	as-ZIF-62(Zn)-bim$_{0.27}$	ZIF-62(Zn)-bim$_{0.27}$	as-ZIF-62(Zn)-bim$_{0.17}$	ZIF-62(Zn)-bim$_{0.17}$	as-ZIF-62(Zn)-bim$_{0.12}$	ZIF-62(Zn)-bim$_{0.12}$
a / Å	15.616(2)	15.529(4)	15.4928(3)	15.543(4)	15.491(3)	15.497(2)
b / Å	15.797(2)	15.801(4)	15.554(3)	15.625(4)	15.657(3)	15.609(2)
c / Å	18.264(3)	18.182(5)	18.241(4)	18.111(2)	18.336(4)	18.120(2)
V / Å^3	4505.8(12)	4461(2)	4395.9(16)	4398(2)	4447.5(15)	4383.2(10)
R_{wp}	35.30	20.67	21.73	28.83	33.73	25.08
R_{exp}	29.68	17.12	18.12	17.22	25.92	17.29
χ	1.18	1.21	1.19	1.67	1.30	1.45

Table A.25: Unit cell parameters a, b, c and V (orthorhombic space group *Pbca*) determined by structureless profile refinements (Pawley method) of the PXRD data of as and desolvated/activated ZIF-62(M)-bim$_x$ materials with corresponding R_{wp}, R_{exp} and χ values.

Compound	as-ZIF-62(Zn)-bim$_{0.07}$	ZIF-62(Zn)-bim$_{0.07}$	as-ZIF-62(Zn)-bim$_{0.05}$	ZIF-62(Zn)-bim$_{0.05}$	as-ZIF-62(Zn)-bim$_{0.03}$	ZIF-62(Zn)-bim$_{0.03}$
a / Å	15.475(2)	15.5133(18)	15.475(2)	15.494(3)	15.471(2)	15.517(6)
b / Å	15.608(2)	15.5798(16)	15.584(2)	15.595(3)	15.577(2)	15.578(5)
c / Å	18.329(2)	18.1333(2)	18.328(3)	18.204(4)	18.356(3)	18.149(7)
V / Å^3	4427.6(10)	4382.7(8)	4420(1)	4395.6(15)	4423.9(10)	4387(3)
R_{wp}	29.29	12.36	37.83	30.97	20.75	20.35
R_{exp}	25.35	5.07	31.54	15.55	17.10	19.3
χ	1.15	2.44	1.19	1.99	1.21	1.37

Compound	as-ZIF-62(Zn)-bim$_{0.02}$	ZIF-62(Zn)-bim$_{0.02}$	as-ZIF-62(Co)-bim$_{0.30}$	ZIF-62(Co)-bim$_{0.30}$	as-ZIF-62(Co)-bim$_{0.10}$	ZIF-62(Co)-bim$_{0.10}$
a / Å	15.461(1)	15.506(3)	15.477(4)	15.517(3)	15.409(3)	15.460(2)
b / Å	15.539(1)	15.545(3)	15.551(3)	15.640(2)	15.502(3)	15.579(2)
c / Å	18.330(2)	18.108(4)	18.152(5)	17.967(3)	18.319(4)	18.070(3)
V / Å^3	4404.2(8)	4364.8(16)	4369.0(19)	4360.4(13)	4375.9(14)	4352.1(11)
R_{wp}	24.53	20.35	42.96	11.2	39.38	11.84
R_{exp}	20.23	16.3	38.83	7.2	36.85	7.06
χ	1.21	1.41	1.11	1.56	1.07	1.68

Table A.26: Unit cell parameters a, b, c and V (orthorhombic space group *Pbca*) determined by structureless profile refinements (Pawley method) of the PXRD data of as and desolvated/activated ZIF-62(M)-bim$_x$ materials with corresponding R_{wp}, R_{exp} and χ values.

Compound	as-ZIF-62(Co)-bim$_{0.17}$	ZIF-62(Co)-bim$_{0.17}$
a / Å	15.546(17)	15.498(5)
b / Å	15.7933(19)	15.678(5)
c / Å	18.315(2)	18.106(6)
V / Å^3	4496.7(9)	4399(3)
R_{wp}	7.76	9.69
R_{exp}	6.7	6.83
χ	1.16	1.42

A.3.3 Variable-Temperature X-ray Powder Diffraction

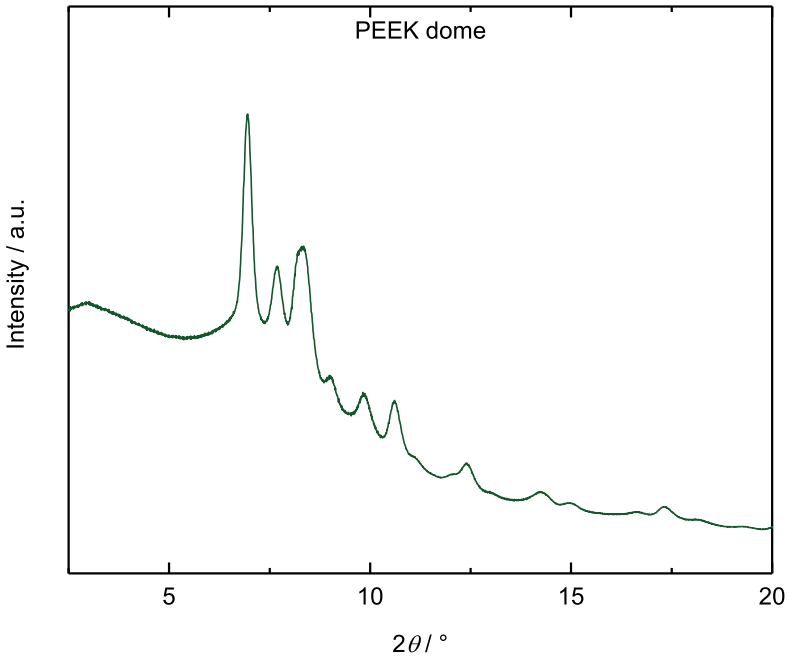

Figure A.44: PXRD pattern of the polyether ether ketone (PEEK) dome without sample. Data were collected at room temperature. The observed peaks are visible in every pattern below.

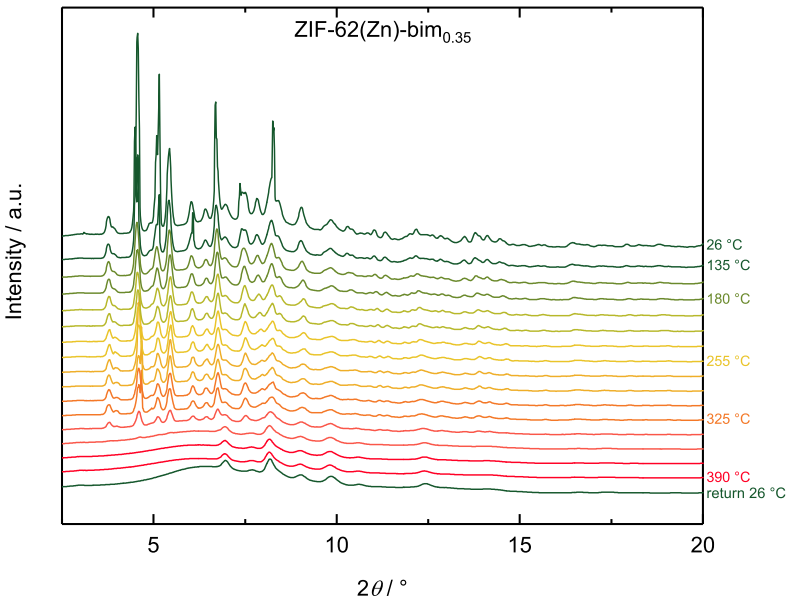

Figure A.45: Stacked plot of the PXRD patterns collected at variable-temperature at DELTA for ZIF-62(Zn)-bim$_{0.35}$. The patterns are vertically offset but not normalized.

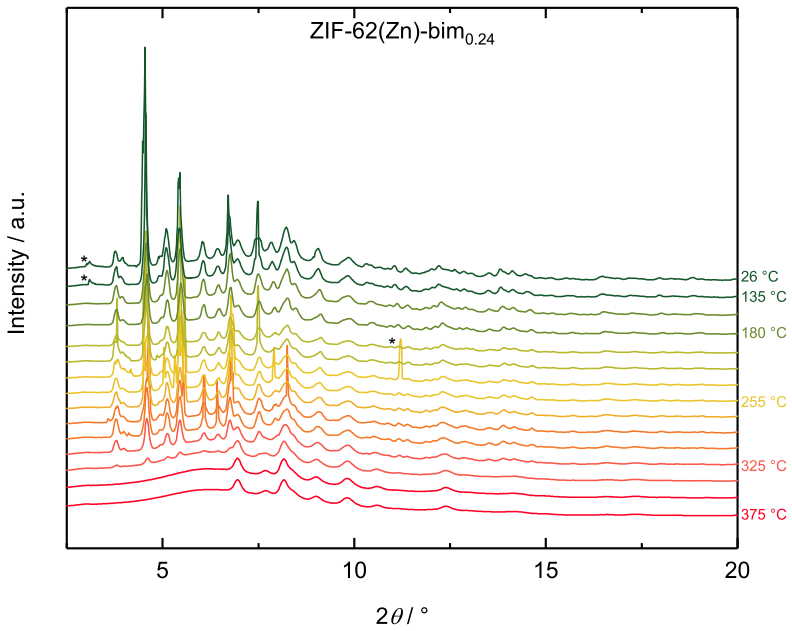

Figure A.46: Stacked plot of the PXRD patterns collected at variable-temperature at DELTA for ZIF-62(Zn)-bim$_{0.24}$. The patterns are vertically offset but not normalized. Small unidentified artifacts are marked with asterisks ($\star$).

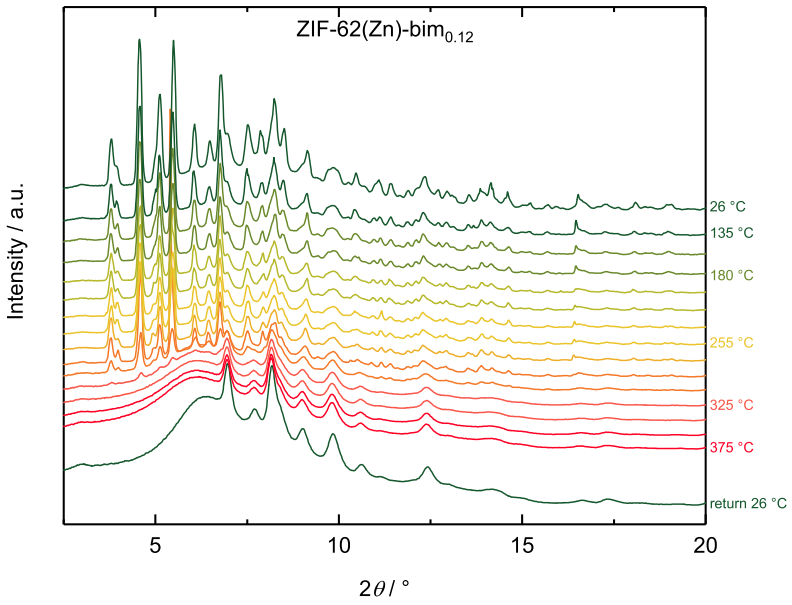

Figure A.47: Stacked plot of the PXRD patterns collected at variable-temperature at DELTA for ZIF-62(Zn)-bim$_{0.12}$. The patterns are vertically offset but not normalized.

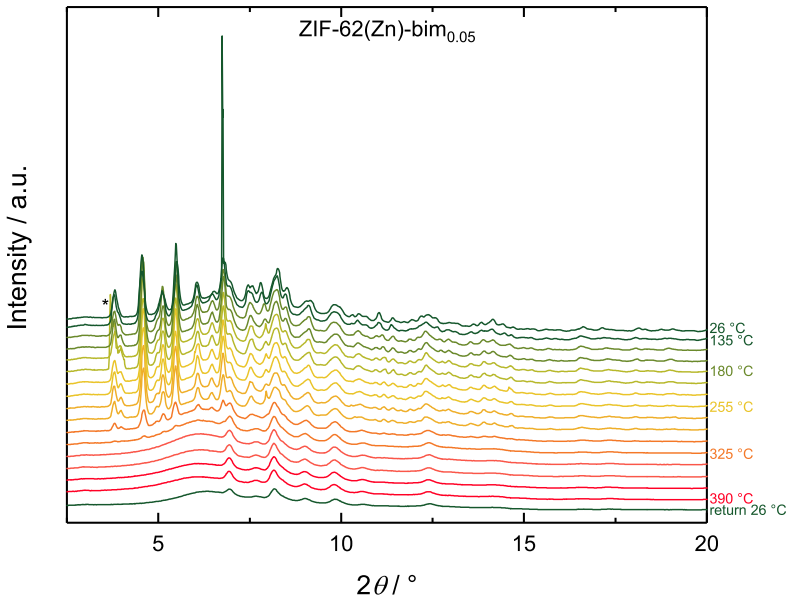

Figure A.48: Stacked plot of the PXRD patterns collected at variable-temperature at DELTA for ZIF-62(Zn)-bim$_{0.05}$. The patterns are vertically offset but not normalized. Small unidentified artifacts are marked with asterisks ($\star$).

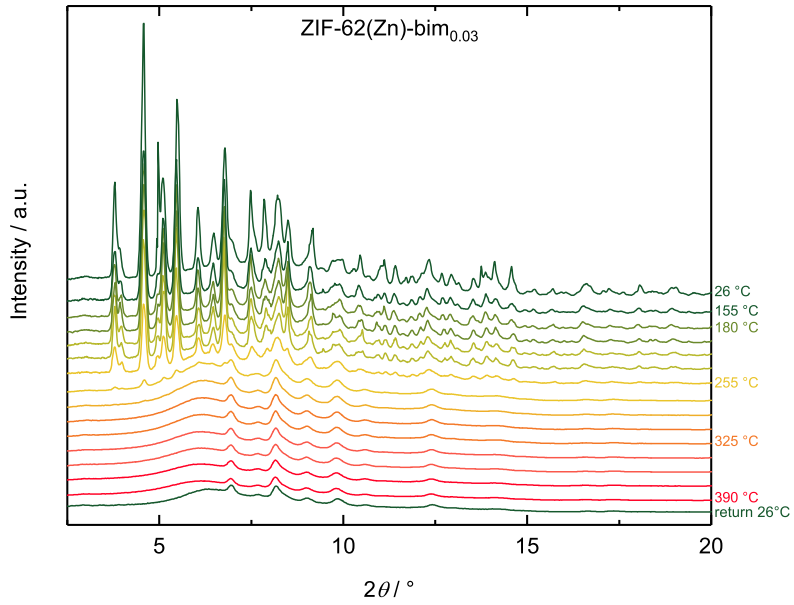

Figure A.49: Stacked plot of the PXRD patterns collected at variable-temperature at DELTA for ZIF-62(Zn)-bim$_{0.03}$. The patterns are vertically offset but not normalized.

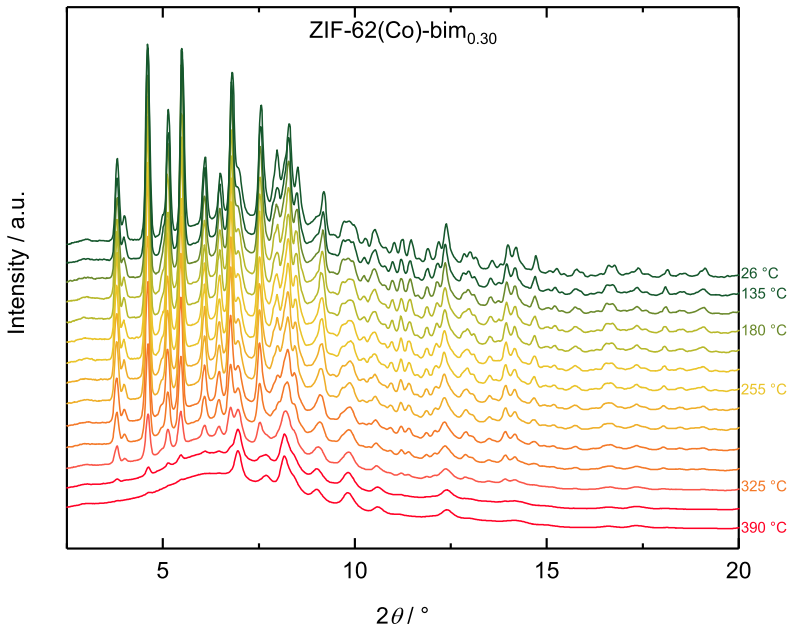

Figure A.50: Stacked plot of the PXRD patterns collected at variable-temperature at DELTA for ZIF-62(Co)-bim$_{0.30}$. The patterns are vertically offset but not normalized.

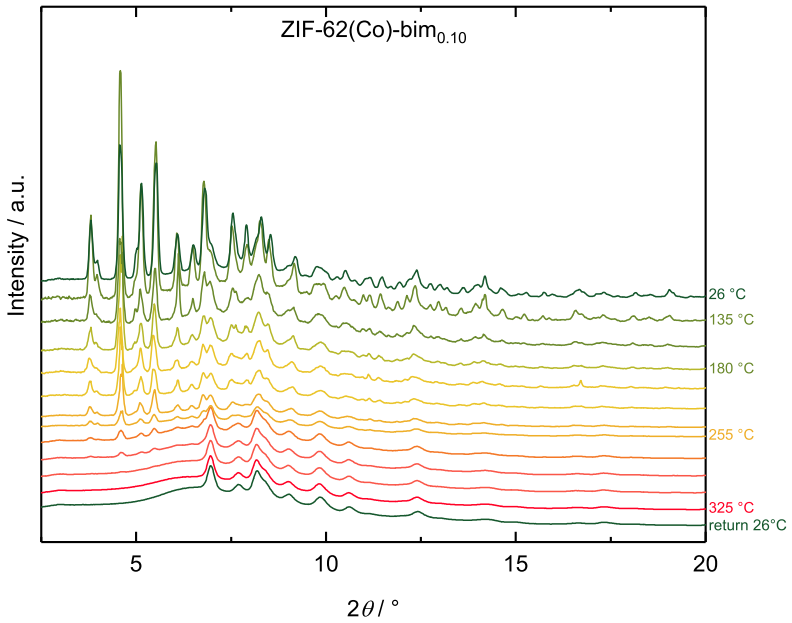

Figure A.51: Stacked plot of the PXRD patterns collected at variable-temperature at DELTA for ZIF-62(Co)-bim$_{0.10}$. The patterns are vertically offset but not normalized.

A.3.4 X-ray Total Scattering

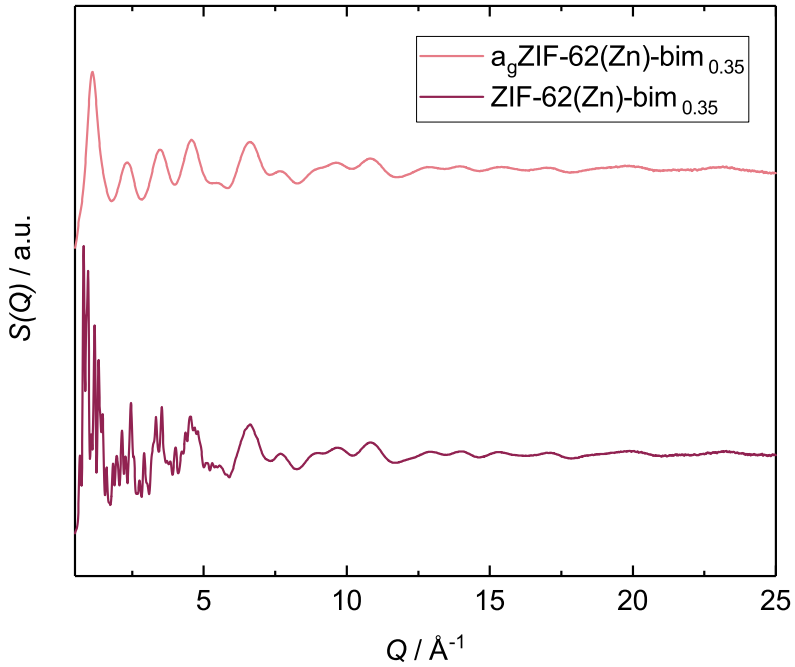

Figure A.52: X-ray total scattering factor as a function of Q for ZIF-62(Zn)-bim$_{0.35}$ and a$_g$ZIF-62(Zn)-bim$_{0.35}$ derived from collected X-ray total scattering data.

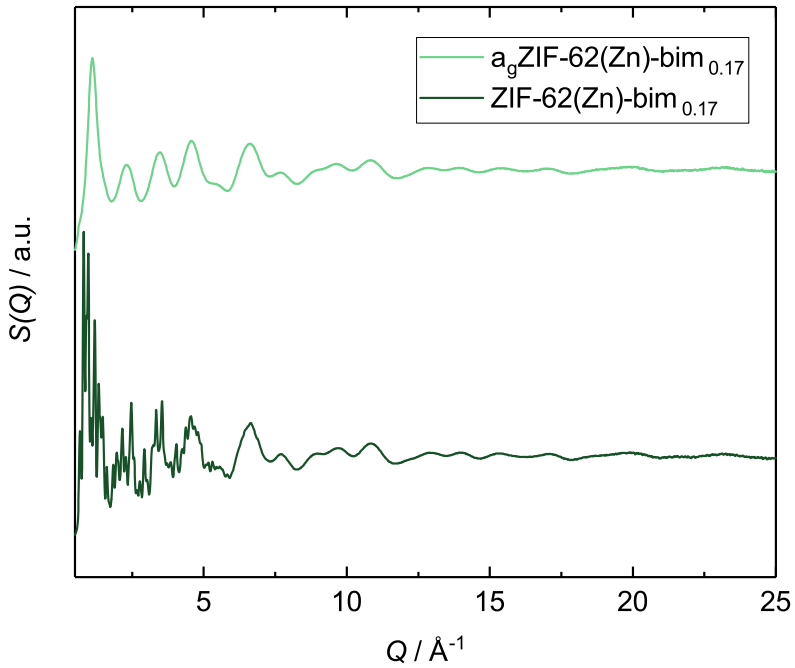

Figure A.53: X-ray total scattering factor as a function of Q for ZIF-62(Zn)-bim$_{0.17}$ and a$_g$ZIF-62(Zn)-bim$_{0.17}$ derived from collected X-ray total scattering data.

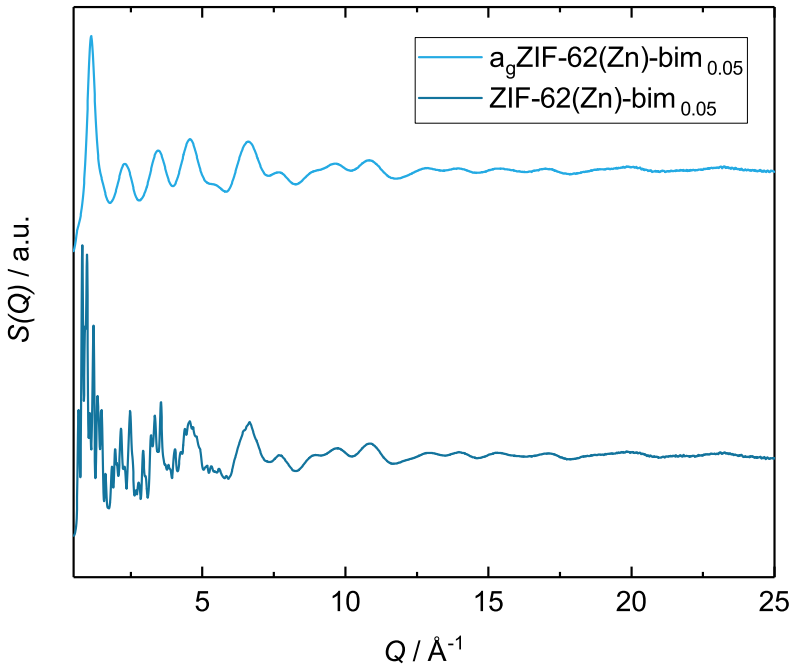

Figure A.54: X-ray total scattering factor as a function of Q for ZIF-62(Zn)-bim$_{0.05}$ and a$_g$ZIF-62(Zn)-bim$_{0.05}$ derived from collected X-ray total scattering data.

A.3.5 Fourier-Transform Infrared Spectroscopy

These data were collected to verify the activation/desolvation of the material (complete removal of solvents from the pores) which demonstrated with the absence of a vibrational band at 1675 cm^{-1}, ascribed to the carbonyl stretching vibration of DMF.

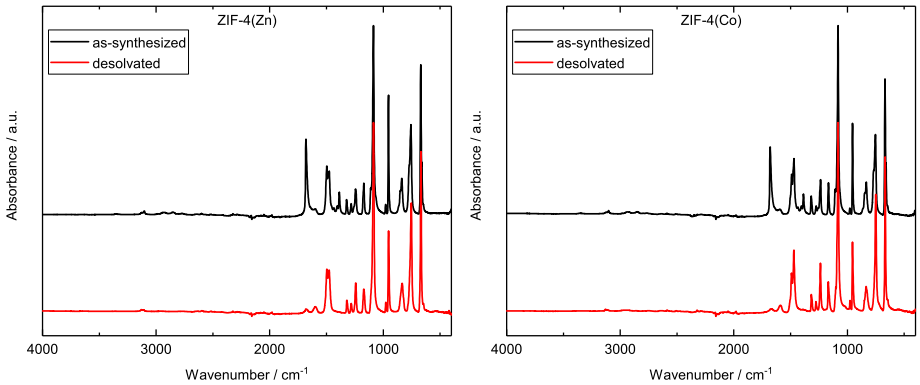

Figure A.55: FTIR spectroscopy data of the as and desolvated/activated materials of ZIF-4(M).

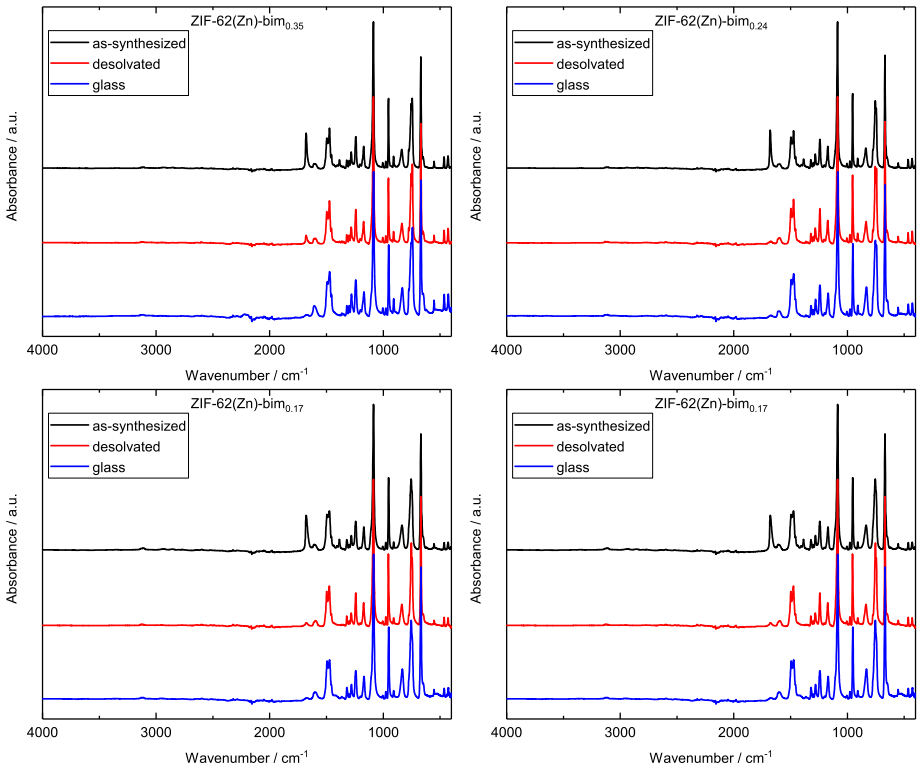

Figure A.56: FTIR spectroscopy data of the as and desolvated/activated crystalline materials as well as their corresponding glasses of ZIF-62(Zn)-bim$_x$ (x = 0.35, 0.24, 0.17 and 0.12).

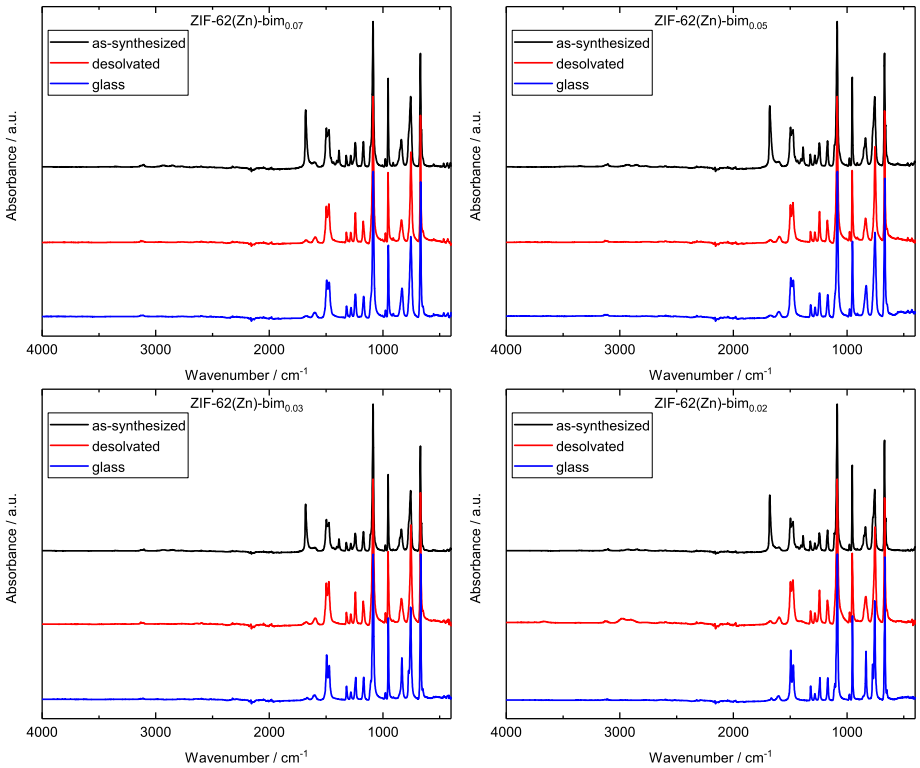

Figure A.57: FTIR spectroscopy data of the as and desolvated/activated crystalline materials as well as their corresponding glasses of ZIF-62(Zn)-bim$_x$ (x = 0.07, 0.05, 0.03 and 0.02).

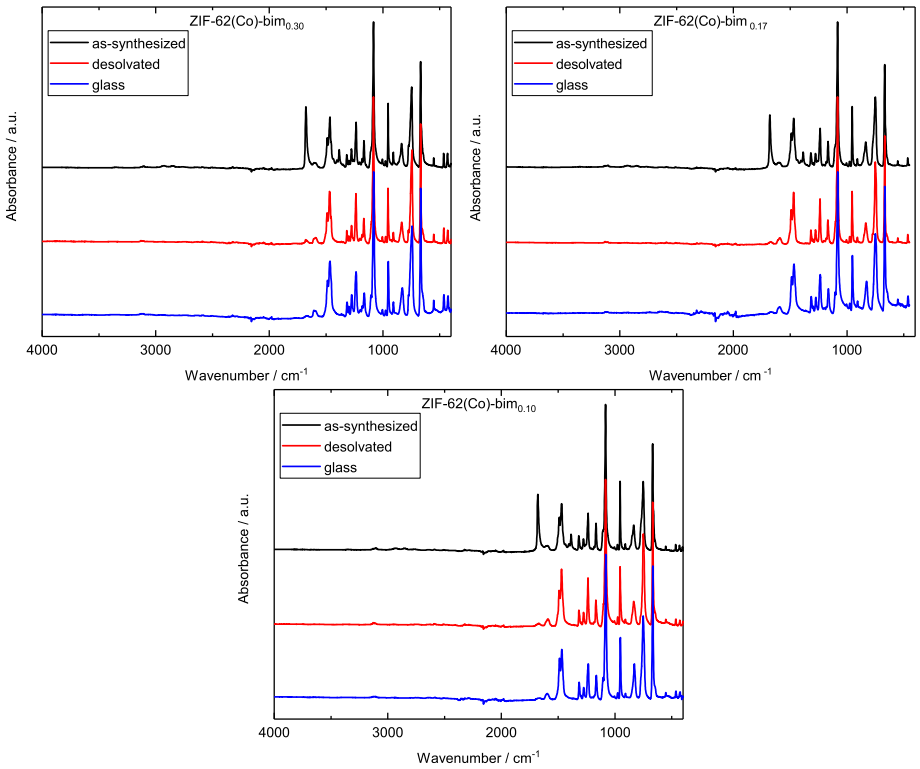

Figure A.58: FTIR spectroscopy data of the as and desolvated/activated crystalline materials as well as their corresponding glasses of ZIF-62(Co)-bim$_x$ (x = 0.30, 0.17 and 0.10).

A.3.6 ^{1}H Nuclear Magnetic Resonance Spectroscopy

Data for ZIF-4(M) and ZIF-62(M)-bim$_x$ as well as their corresponding glasses a_gZIF-62(M)-bim$_x$

These data were collected to determine the molar ration of im$^-$: bim$^-$ in the solid state materials. The derived molar amount of bim$^-$ (x) was determined by the singlet signals of the CH groups at position 2 of the imidazolate ring (**1a** for im$^-$ and **1b** for bim$^-$, see spectra below). The sum of these two signals was set two 2, matching two protons. Consequently, the integral of the **1b** corresponds to the x value in the abbreviation ZIF-62(M)-bim$_x$ (M = Zn^{2+}, Co^{2+}). The activation of the materials is verified by the absence of signals ascribed to DMF.

The spectra were measured in a NMR solvent mixture of DMSO-d$_6$ and DCl/D$_2$O to protonate the molecular building units and consequently digest the solid state materials. The particular used NMR solvent mixture contained a small, unidentified contamination which is present in all spectra (see Figure A.59).

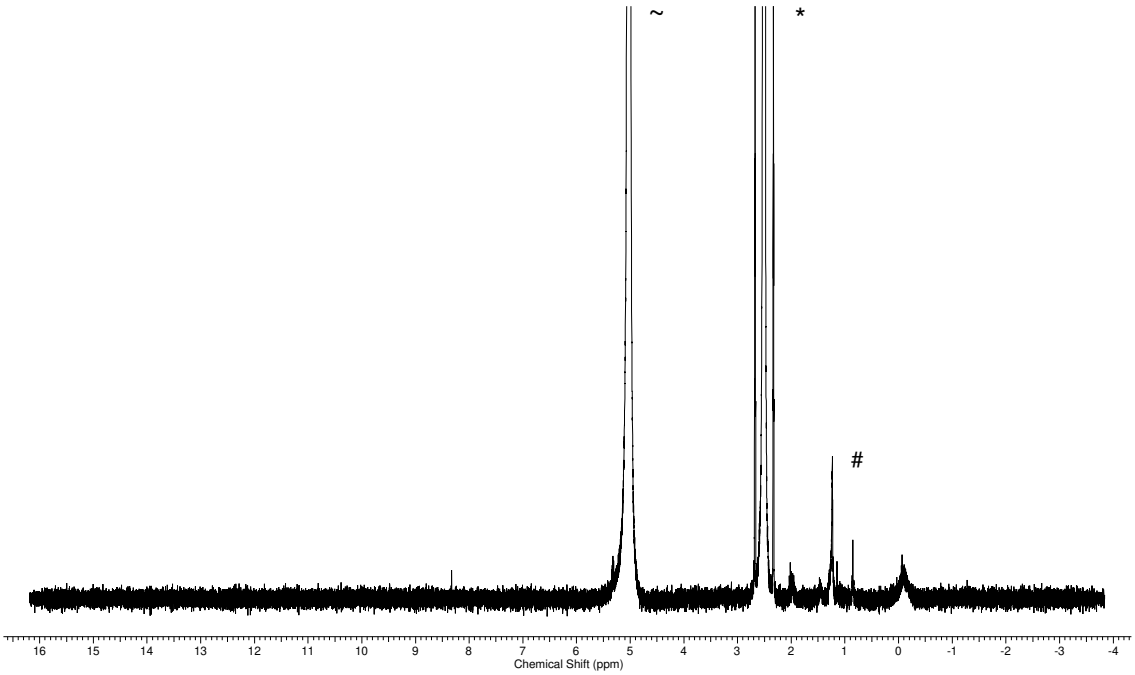

Figure A.59: ^{1}H NMR spectrum of the used DMSO-d$_6$ solvent with a small amount of DCl/D$_2$O. It becomes obvious that the used NMR solvent system contains a small, unidentified contamination at 1.25 ppm (marked with #). DMSO is marked with $\star$, D$_2$O is marked with $\sim$.

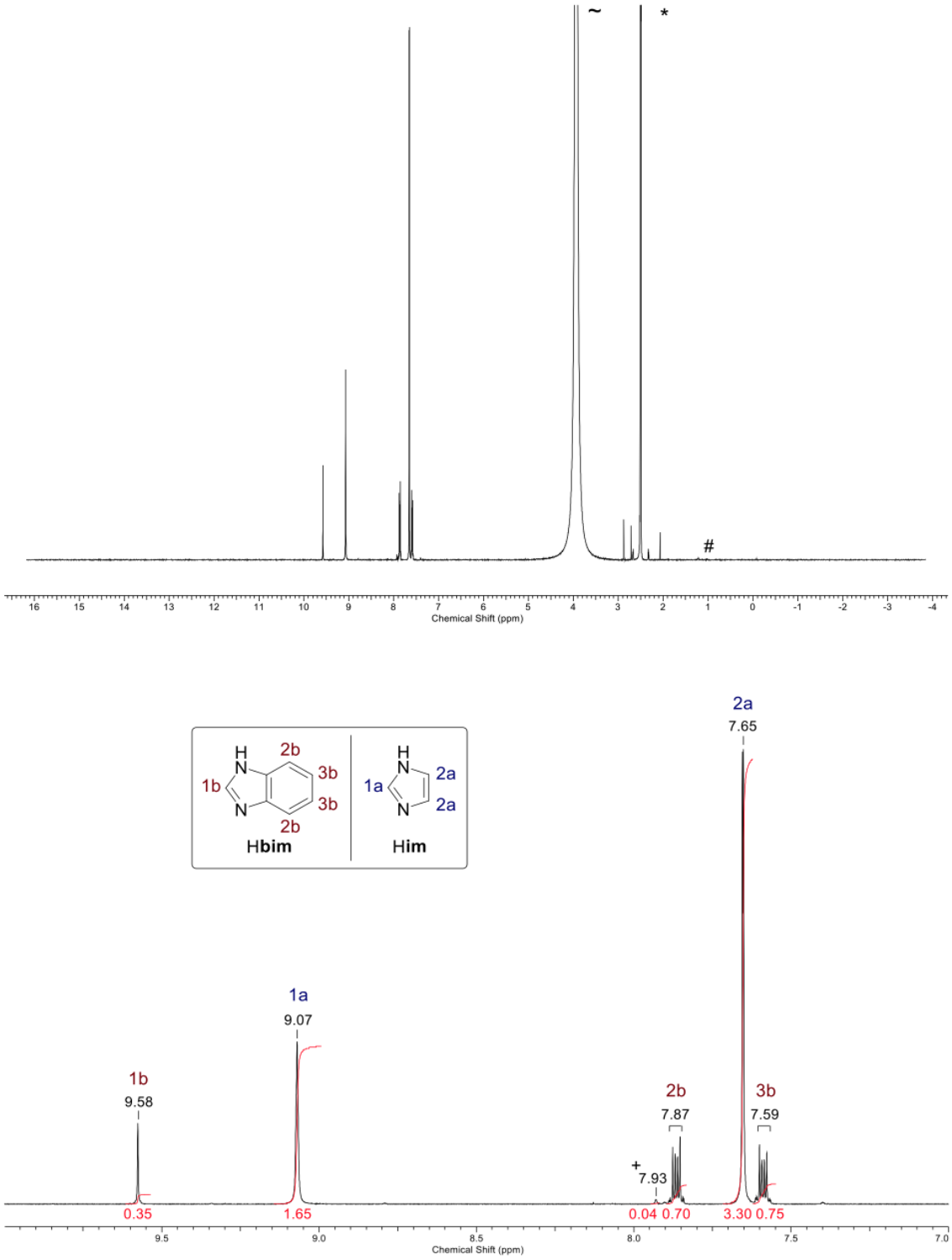

Figure A.60: ^{1}H NMR spectrum of ZIF-62(Zn)-bim$_{0.35}$. Top: Full spectrum. Bottom: Zoom into the aromatic region (7.0 ppm to 10.0 ppm). A very small residue of DMF ($\sim$ 0.04 molecules per formula unit) is detected after the activation (formyl proton at 7.93 ppm, marked with +). This very small amount is not effecting the following investigation on this material. DMSO is marked with $\star$, D_2O is marked with $\sim$ and the small contamination of the mixture is marked with #.

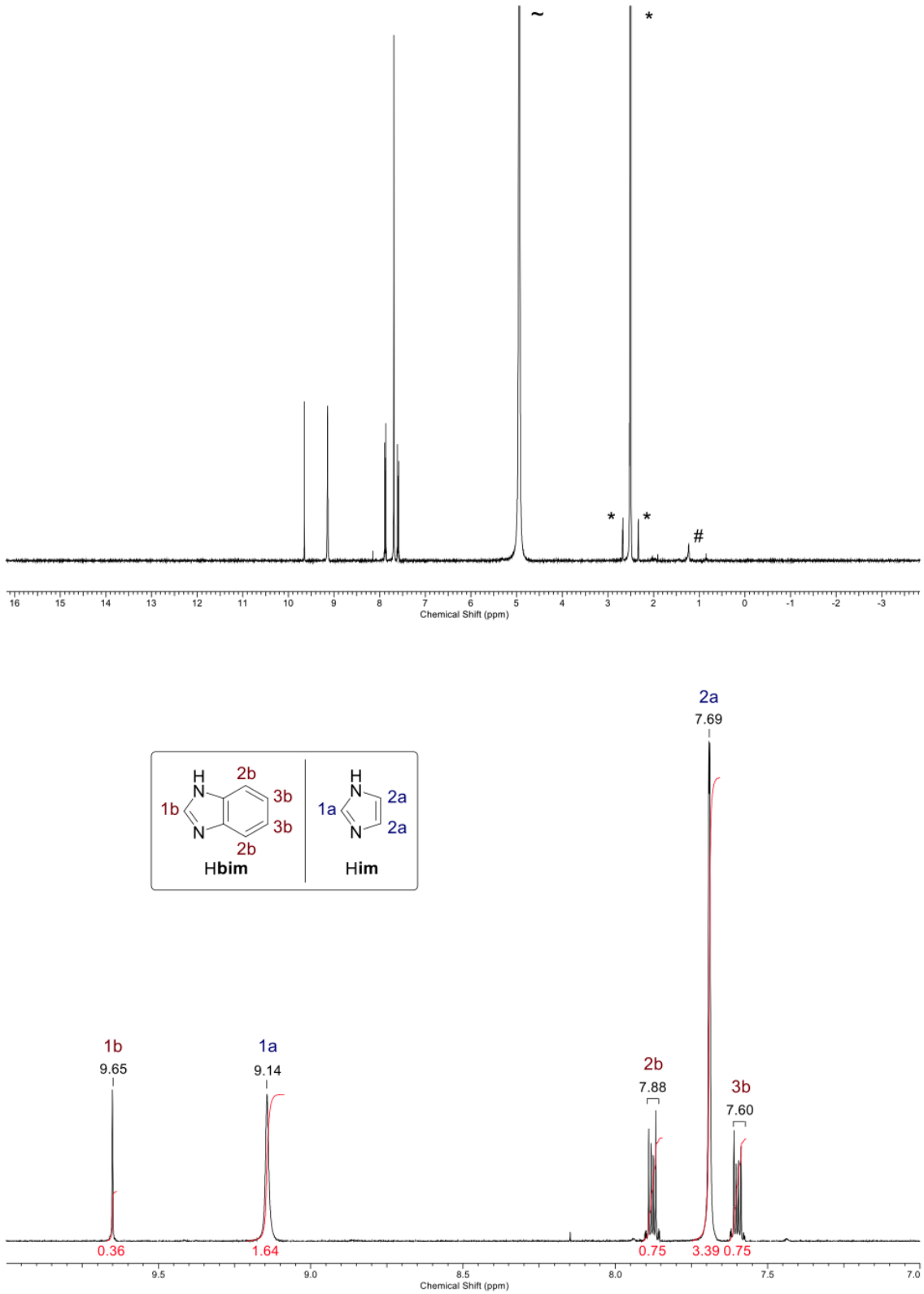

Figure A.61: ^{1}H NMR spectrum of a_gZIF-62(Zn)-bim$_{0.35}$. Top: Full spectrum. Bottom: Zoom into the aromatic region (7.0 ppm to 10.0 ppm). DMSO is marked with $\star$, D_2O is marked with $\sim$ and the small contamination of the DCl/D_2O mixture is marked with #.

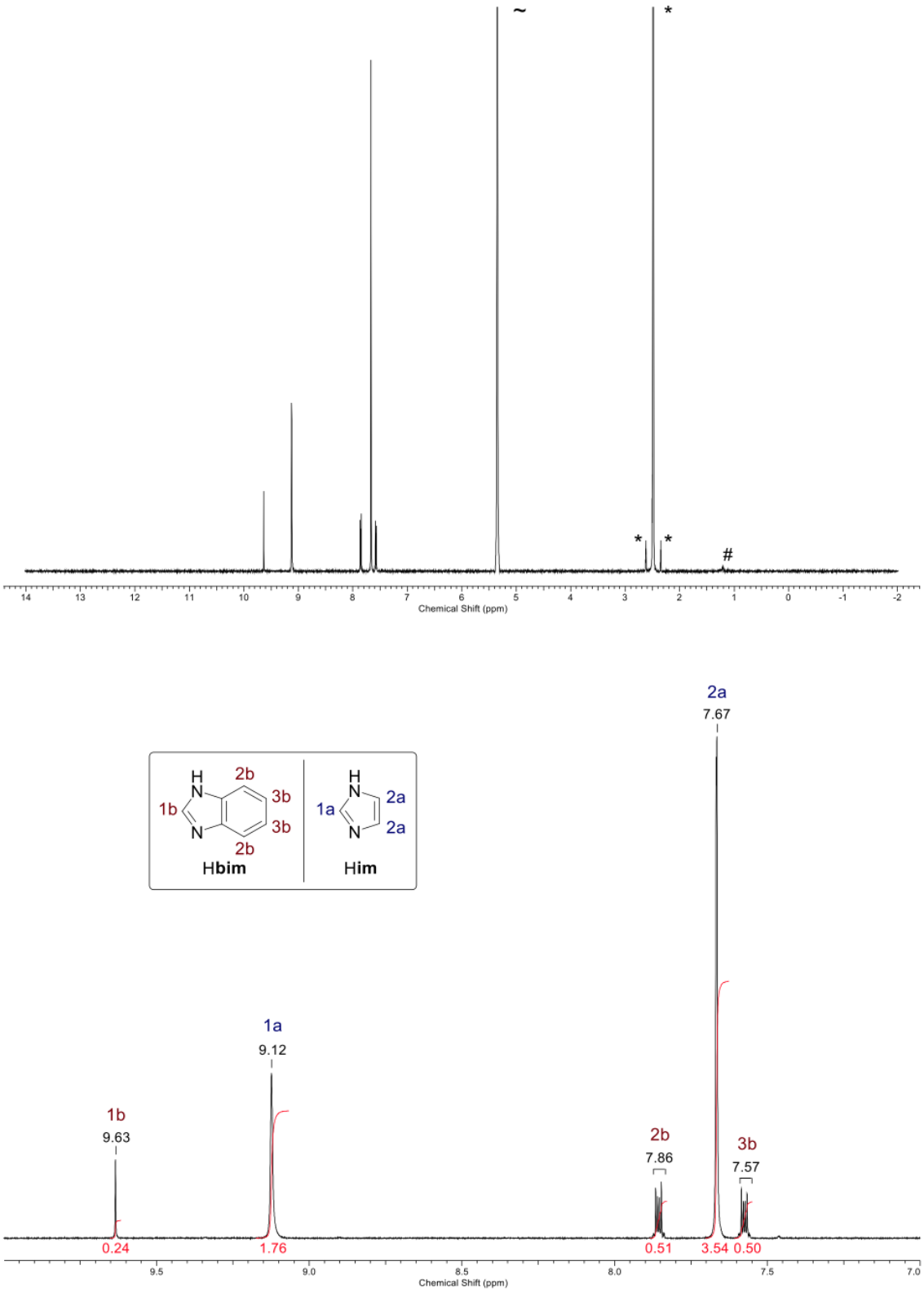

Figure A.62: ^{1}H NMR spectrum of ZIF-62(Zn)-bim$_{0.24}$. Top: Full spectrum. Bottom: Zoom into the aromatic region (7.0 ppm to 10.0 ppm). DMSO is marked with $\star$, D_2O is marked with $\sim$ and the small contamination of the DCl/D_2O mixture is marked with #.

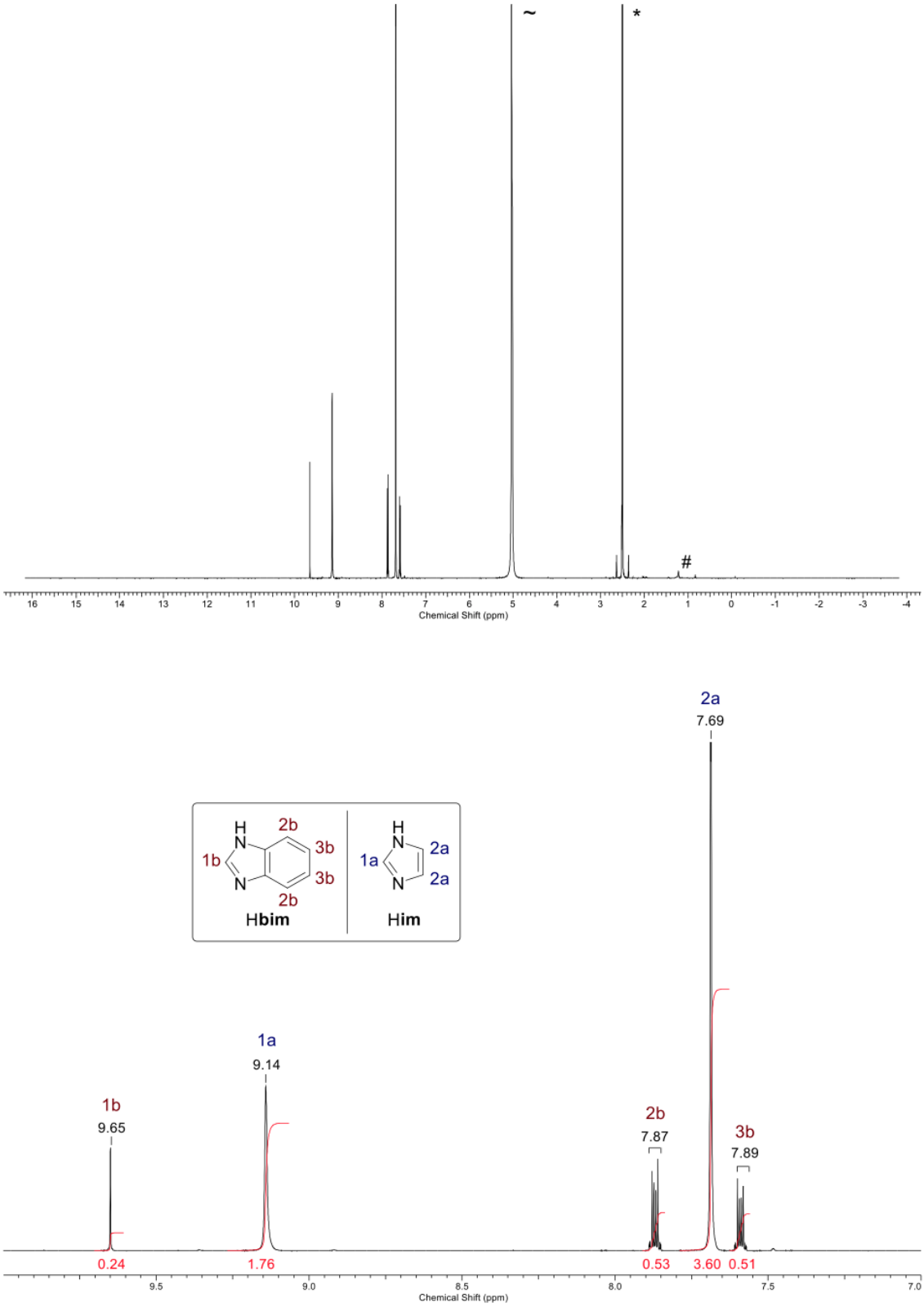

Figure A.63: ^{1}H NMR spectrum of a_gZIF-62(Zn)-bim$_{0.24}$. Top: Full spectrum. Bottom: Zoom into the aromatic region (7.0 ppm to 10.0 ppm). DMSO is marked with $\star$, D_2O is marked with $\sim$ and the small contamination of the DCl/D_2O mixture is marked with #.

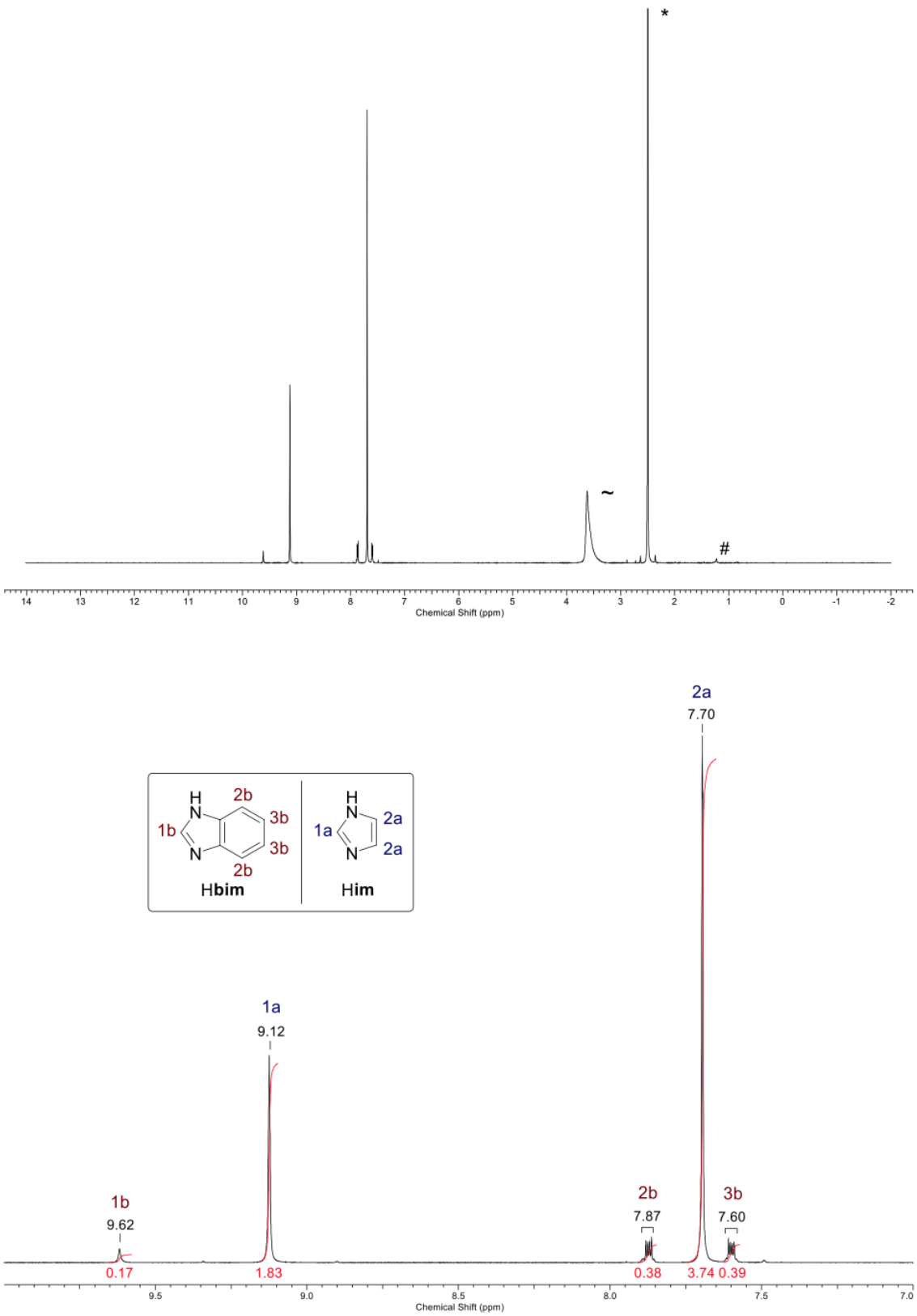

Figure A.64: ^{1}H NMR spectrum of ZIF-62(Zn)-bim$_{0.17}$. Top: Full spectrum. Bottom: Zoom into the aromatic region (7.0 ppm to 10.0 ppm). DMSO is marked with $\star$, D_2O is marked with $\sim$ and the small contamination of the DCl/D_2O mixture is marked with #.

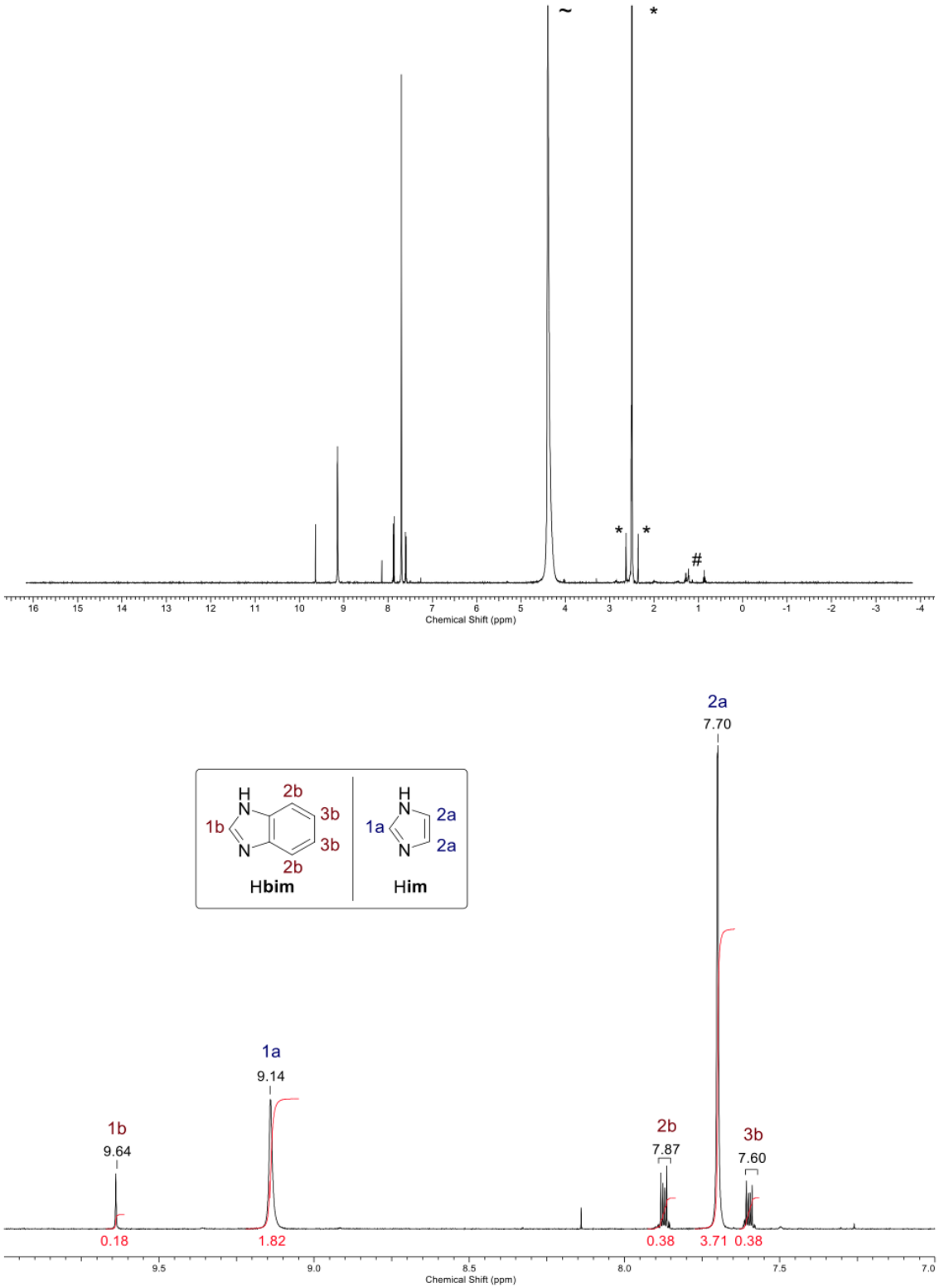

Figure A.65: ^{1}H NMR spectrum of a_gZIF-62(Zn)-bim$_{0.17}$. Top: Full spectrum. Bottom: Zoom into the aromatic region (7.0 ppm to 10.0 ppm). DMSO is marked with $\star$, D_2O is marked with $\sim$ and the small contamination of the DCl/D_2O mixture is marked with #.

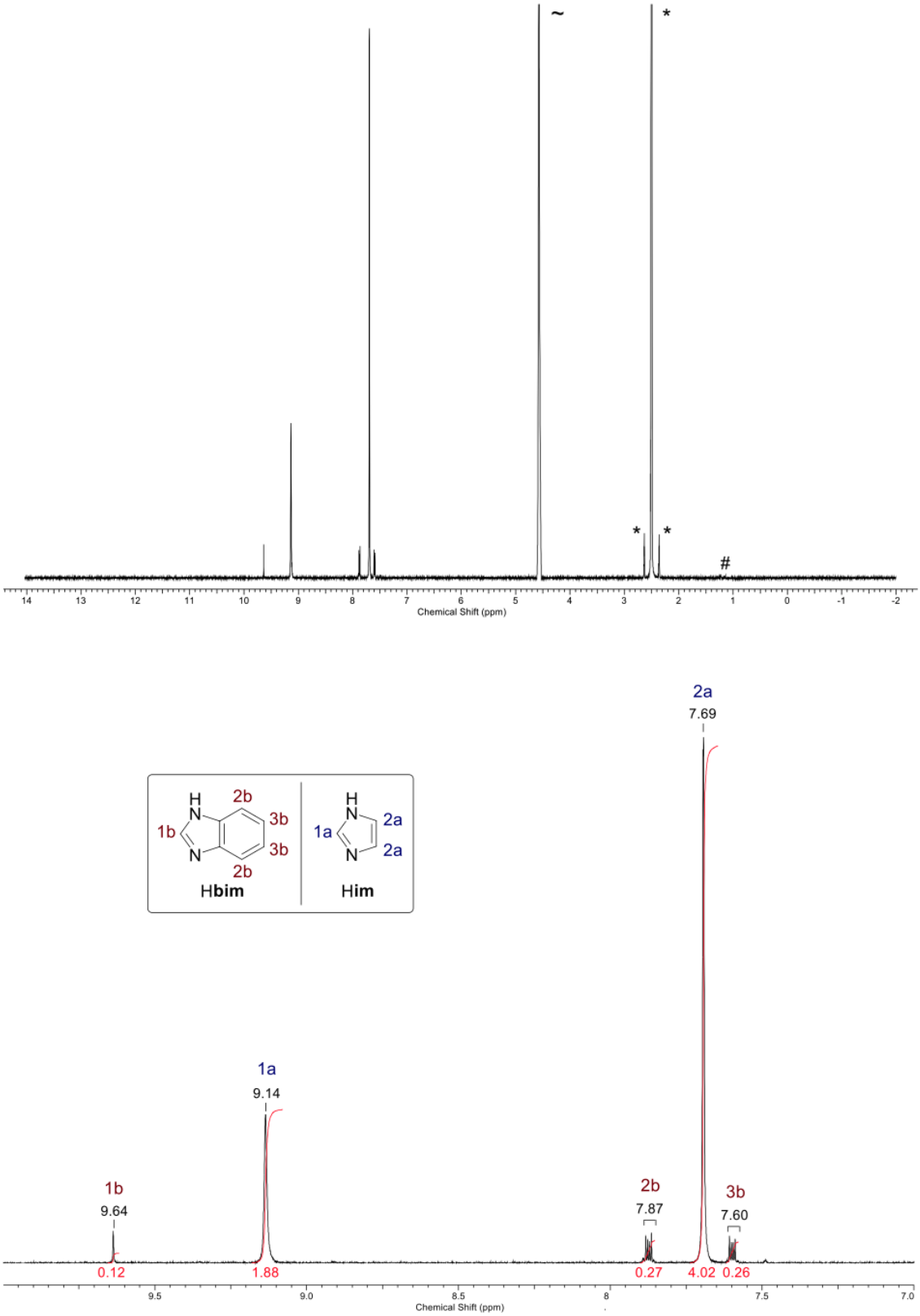

Figure A.66: ^{1}H NMR spectrum of ZIF-62(Zn)-bim$_{0.12}$. Top: Full spectrum. Bottom: Zoom into the aromatic region (7.0 ppm to 10.0 ppm). DMSO is marked with $\star$, D_2O is marked with $\sim$ and the small contamination of the DCl/D_2O mixture is marked with #.

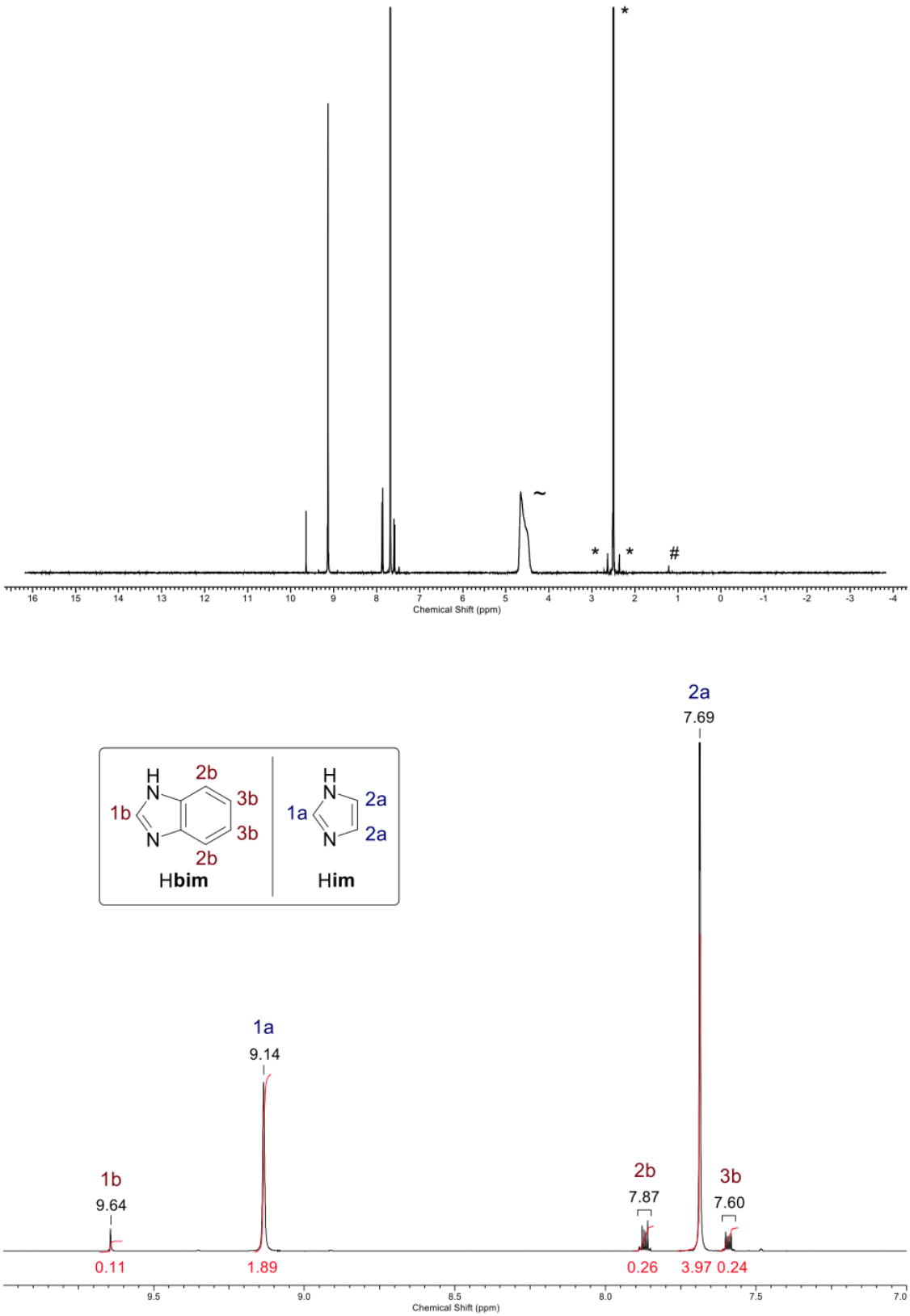

Figure A.67: ^{1}H NMR spectrum of a_gZIF-62(Zn)-bim$_{0.12}$. Top: Full spectrum. Bottom: Zoom into the aromatic region (7.0 ppm to 10.0 ppm). DMSO is marked with $\star$, D_2O is marked with $\sim$ and the small contamination of the DCl/D_2O mixture is marked with #.

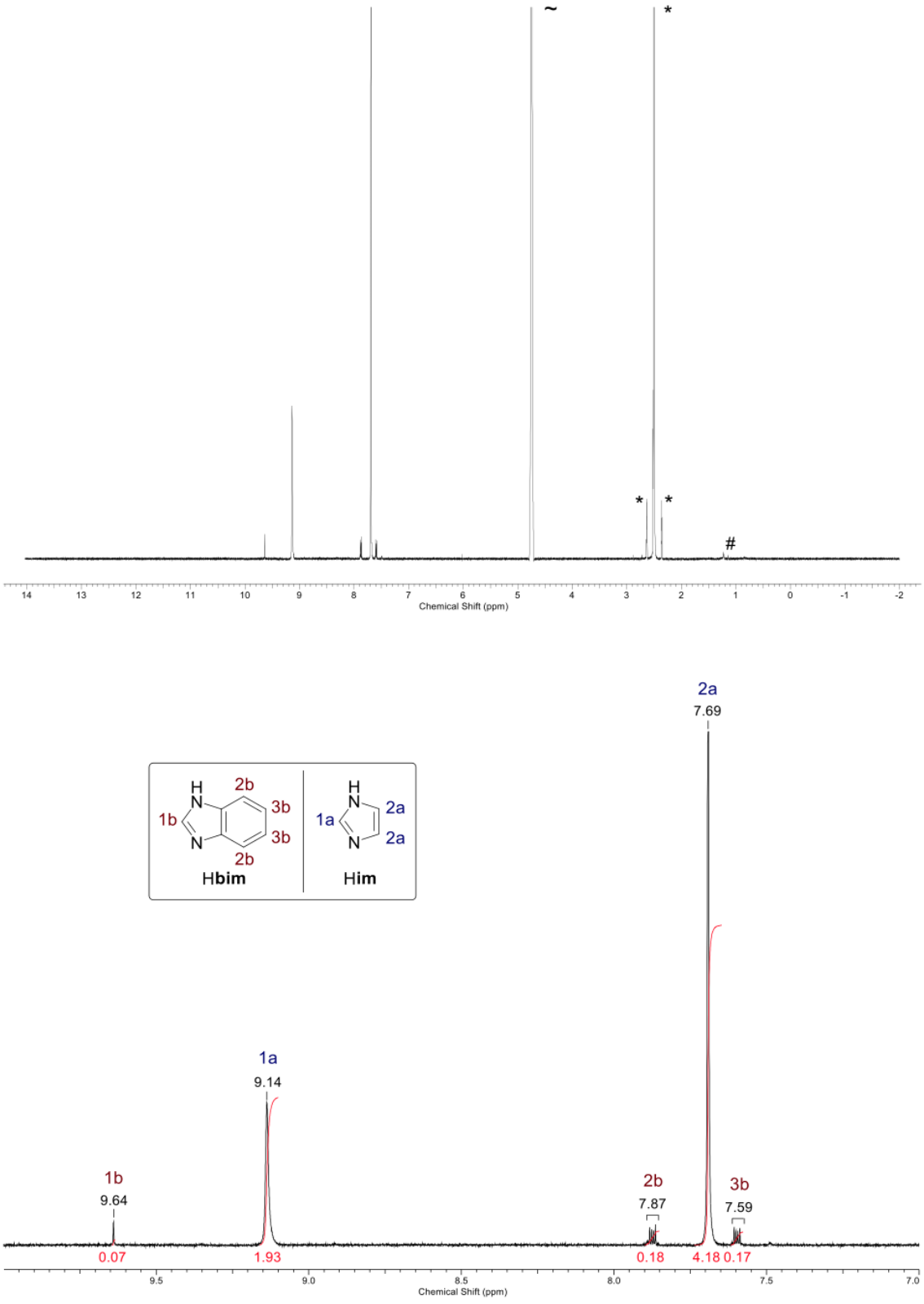

Figure A.68: ^{1}H NMR spectrum of ZIF-62(Zn)-bim$_{0.07}$. Top: Full spectrum. Bottom: Zoom into the aromatic region (7.0 ppm to 10.0 ppm). DMSO is marked with $\star$, D_2O is marked with $\sim$ and the small contamination of the DCl/D_2O mixture is marked with #.

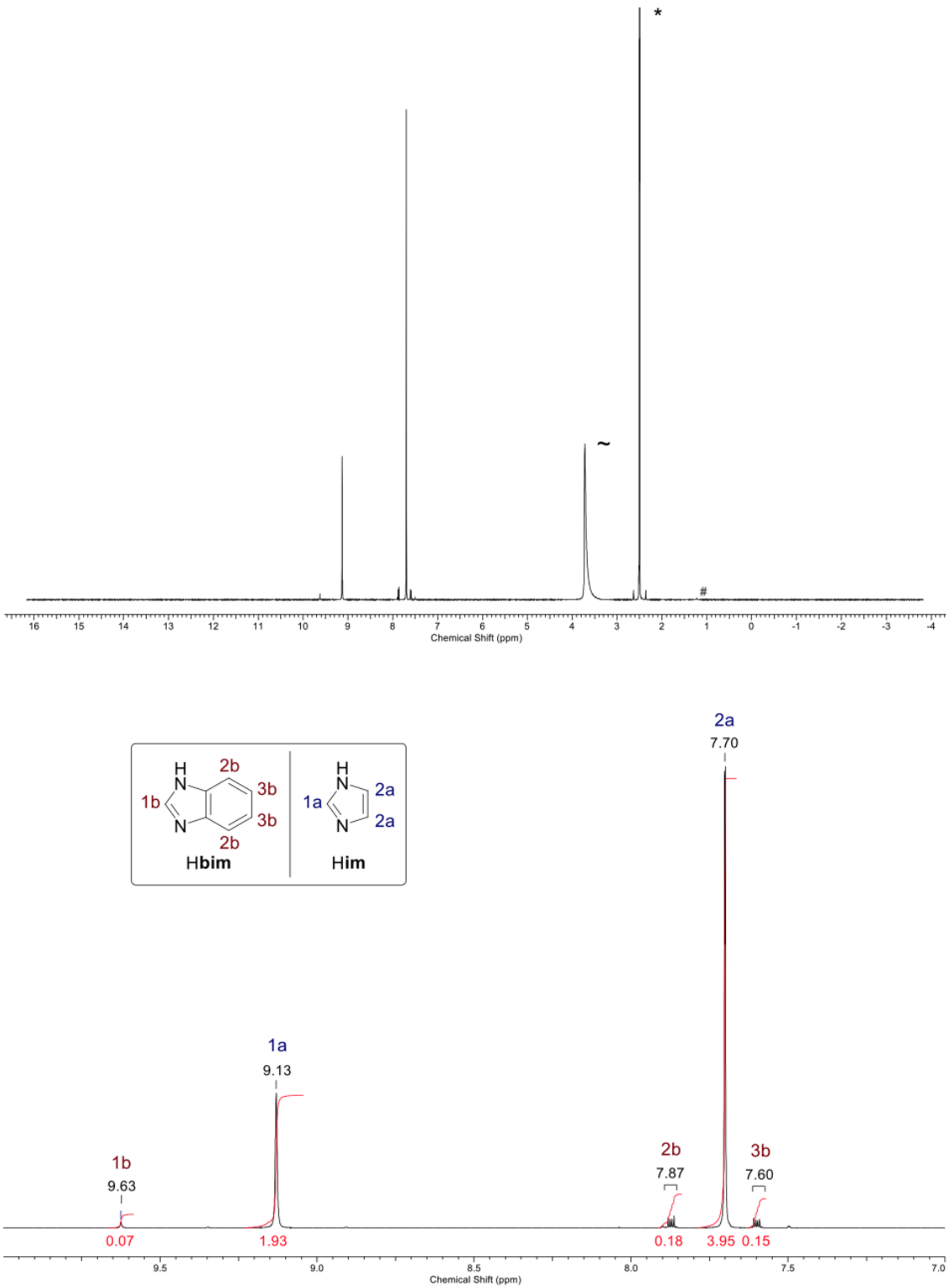

Figure A.69: ^{1}H NMR spectrum of a_gZIF-62(Zn)-bim$_{0.07}$. Top: Full spectrum. Bottom: Zoom into the aromatic region (7.0 ppm to 10.0 ppm). DMSO is marked with $\star$, D_2O is marked with $\sim$ and the small contamination of the DCl/D_2O mixture is marked with #.

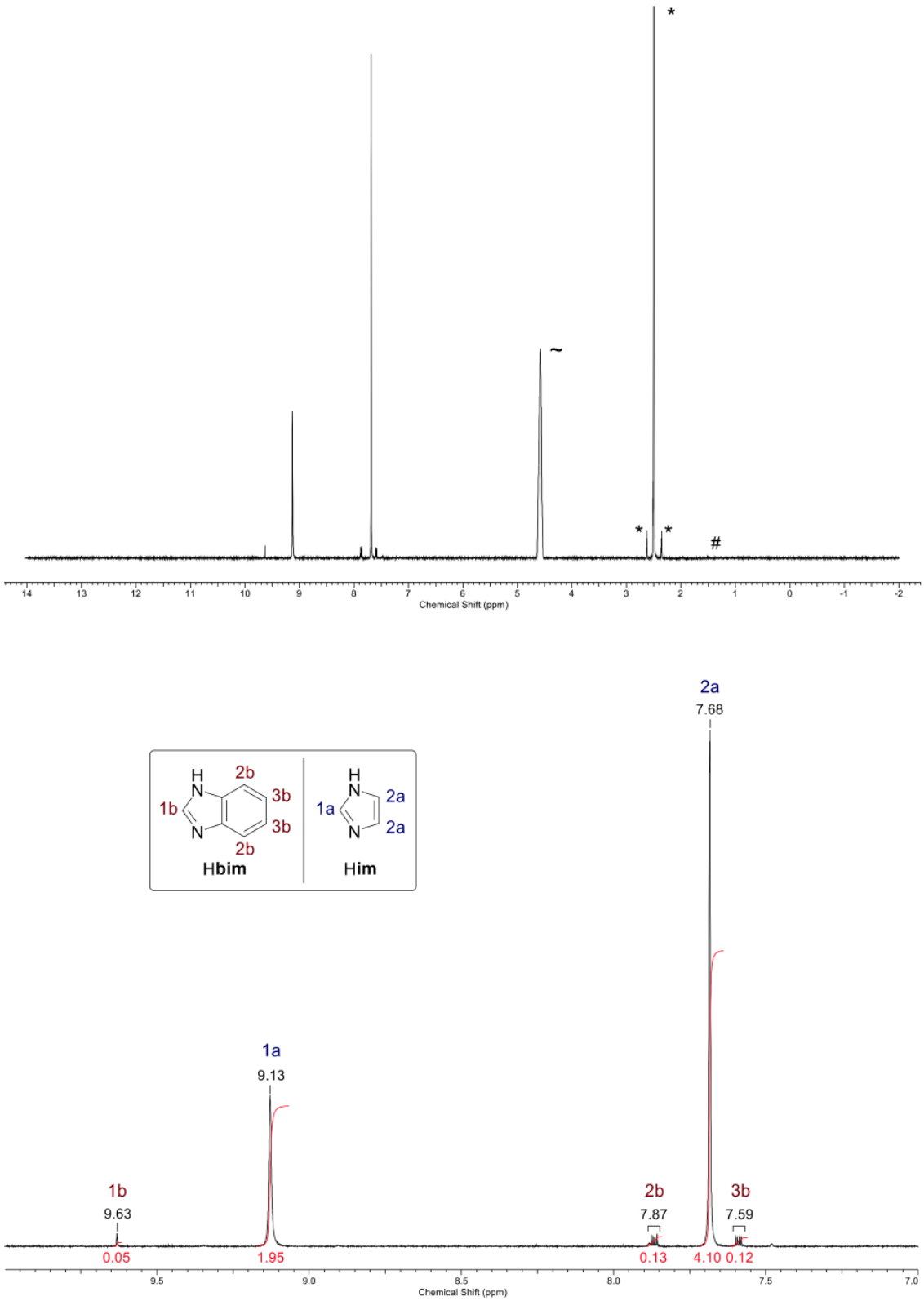

Figure A.70: ^{1}H NMR spectrum of ZIF-62(Zn)-bim$_{0.05}$. Top: Full spectrum. Bottom: Zoom into the aromatic region (7.0 ppm to 10.0 ppm). DMSO is marked with $\star$, D_2O is marked with $\sim$ and the small contamination of the DCl/D_2O mixture is marked with #.

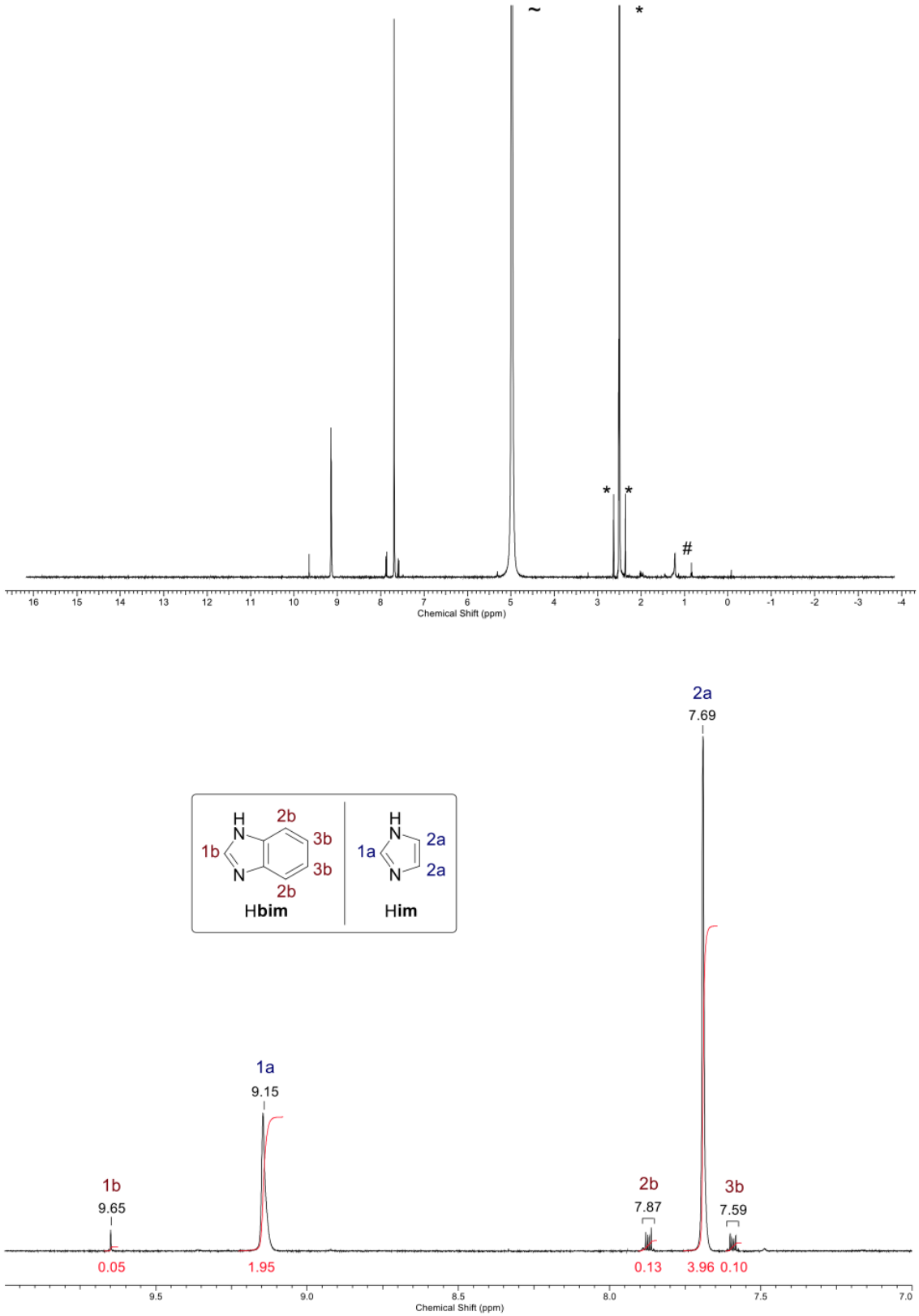

Figure A.71: ^{1}H NMR spectrum of a_gZIF-62(Zn)-bim$_{0.05}$. Top: Full spectrum. Bottom: Zoom into the aromatic region (7.0 ppm to 10.0 ppm). DMSO is marked with $\star$, D_2O is marked with $\sim$ and the small contamination of the DCl/D_2O mixture is marked with #.

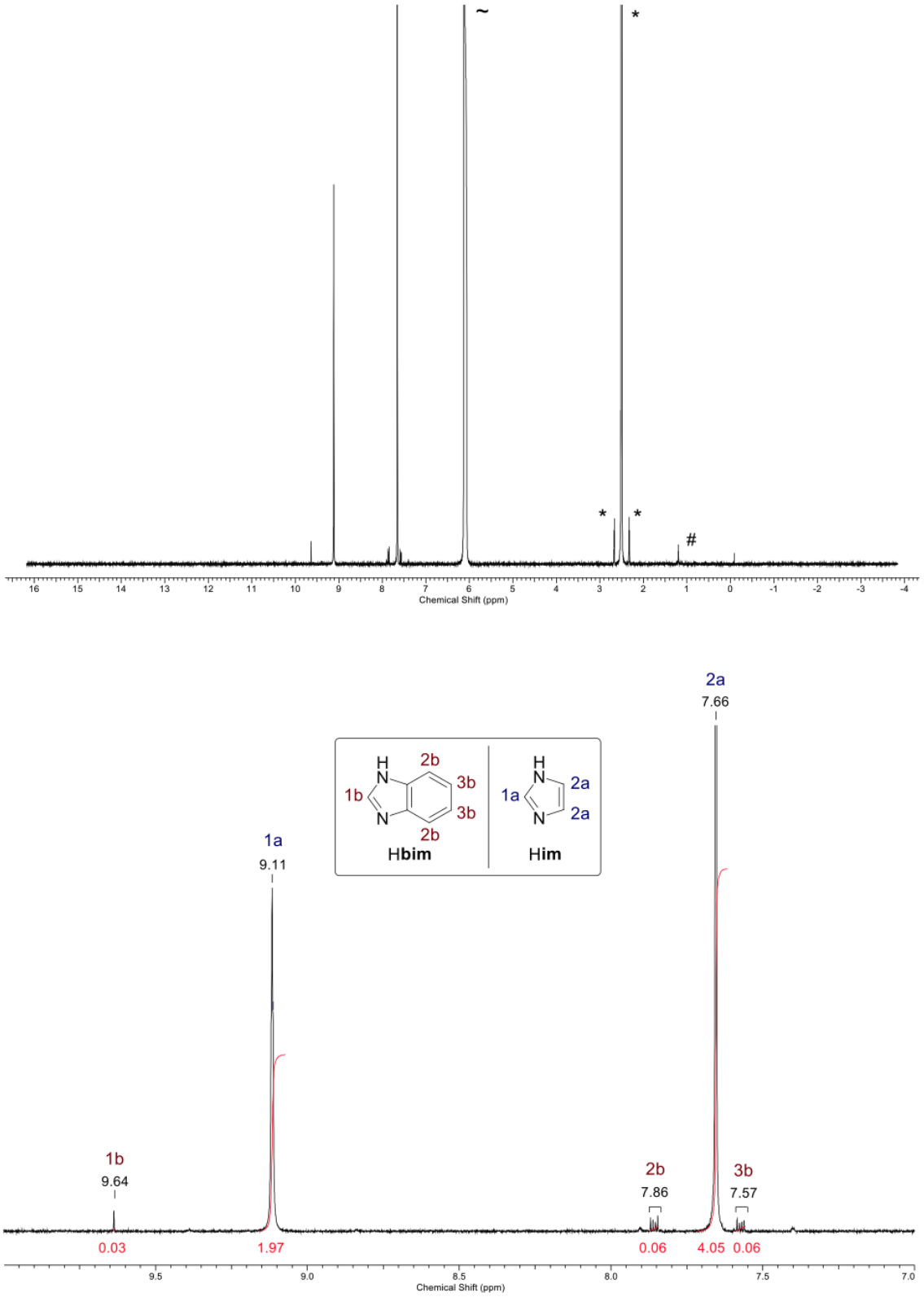

Figure A.72: ^{1}H NMR spectrum of ZIF-62(Zn)-bim$_{0.03}$. Top: Full spectrum. Bottom: Zoom into the aromatic region (7.0 ppm to 10.0 ppm). DMSO is marked with $\star$, D_2O is marked with $\sim$ and the small contamination of the DCl/D_2O mixture is marked with #.

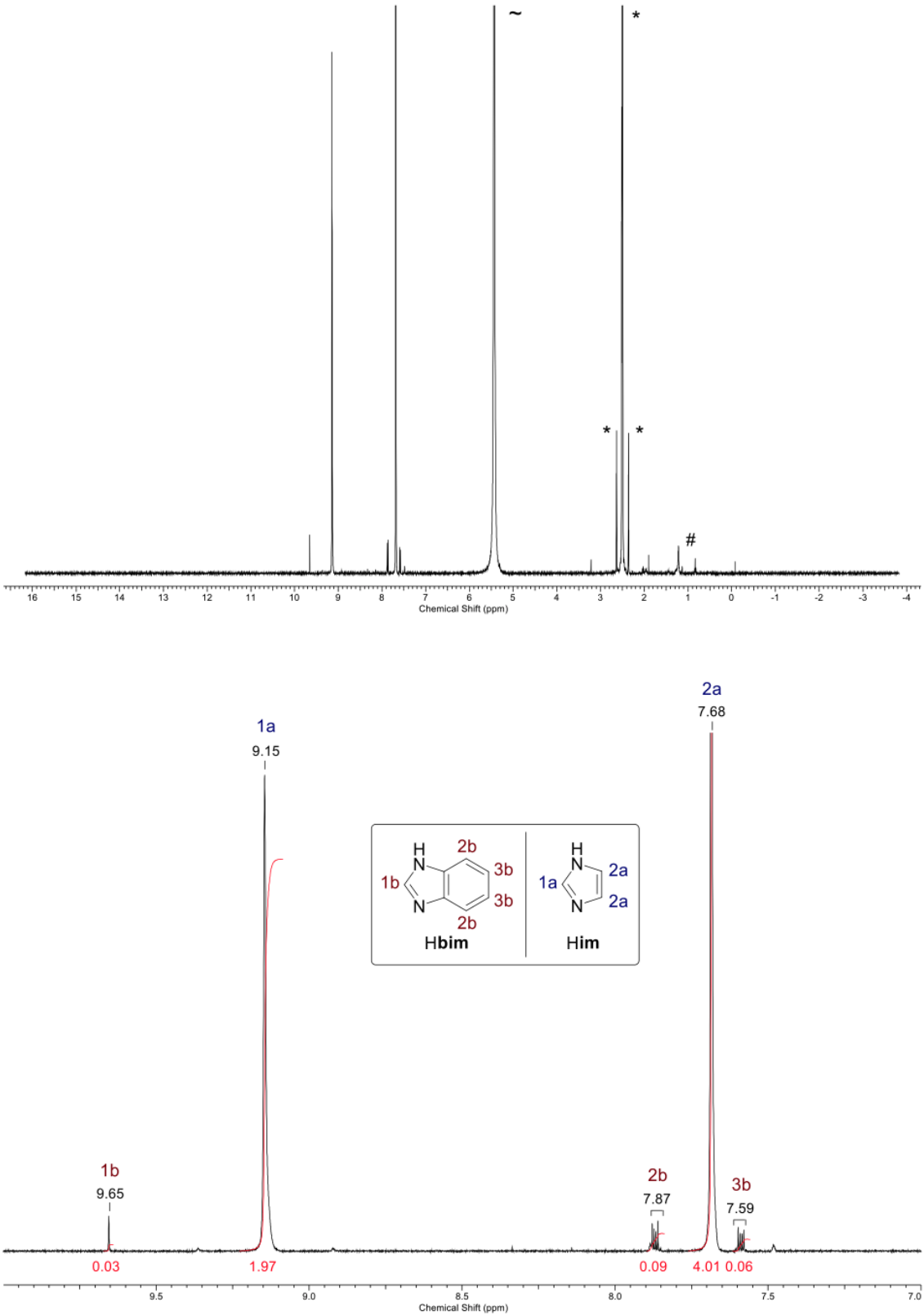

Figure A.73: ^{1}H NMR spectrum of a_gZIF-62(Zn)-bim$_{0.03}$. Top: Full spectrum. Bottom: Zoom into the aromatic region (7.0 ppm to 10.0 ppm). DMSO is marked with $\star$, D_2O is marked with $\sim$ and the small contamination of the DCl/D_2O mixture is marked with #.

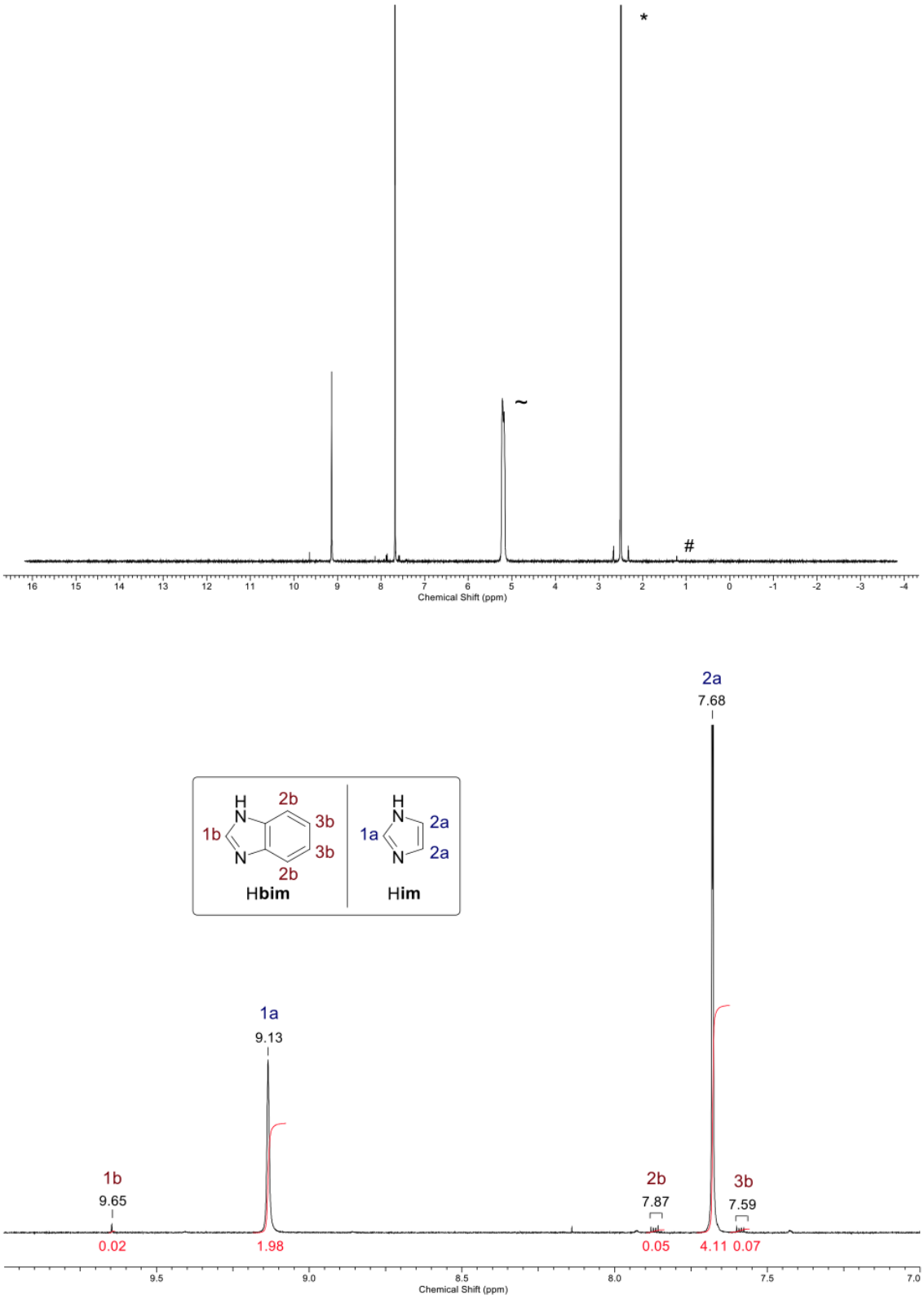

Figure A.74: ^{1}H NMR spectrum of ZIF-62(Zn)-bim$_{0.02}$. Top: Full spectrum. Bottom: Zoom into the aromatic region (7.0 ppm to 10.0 ppm). DMSO is marked with $\star$, D_2O is marked with $\sim$ and the small contamination of the DCl/D_2O mixture is marked with #.

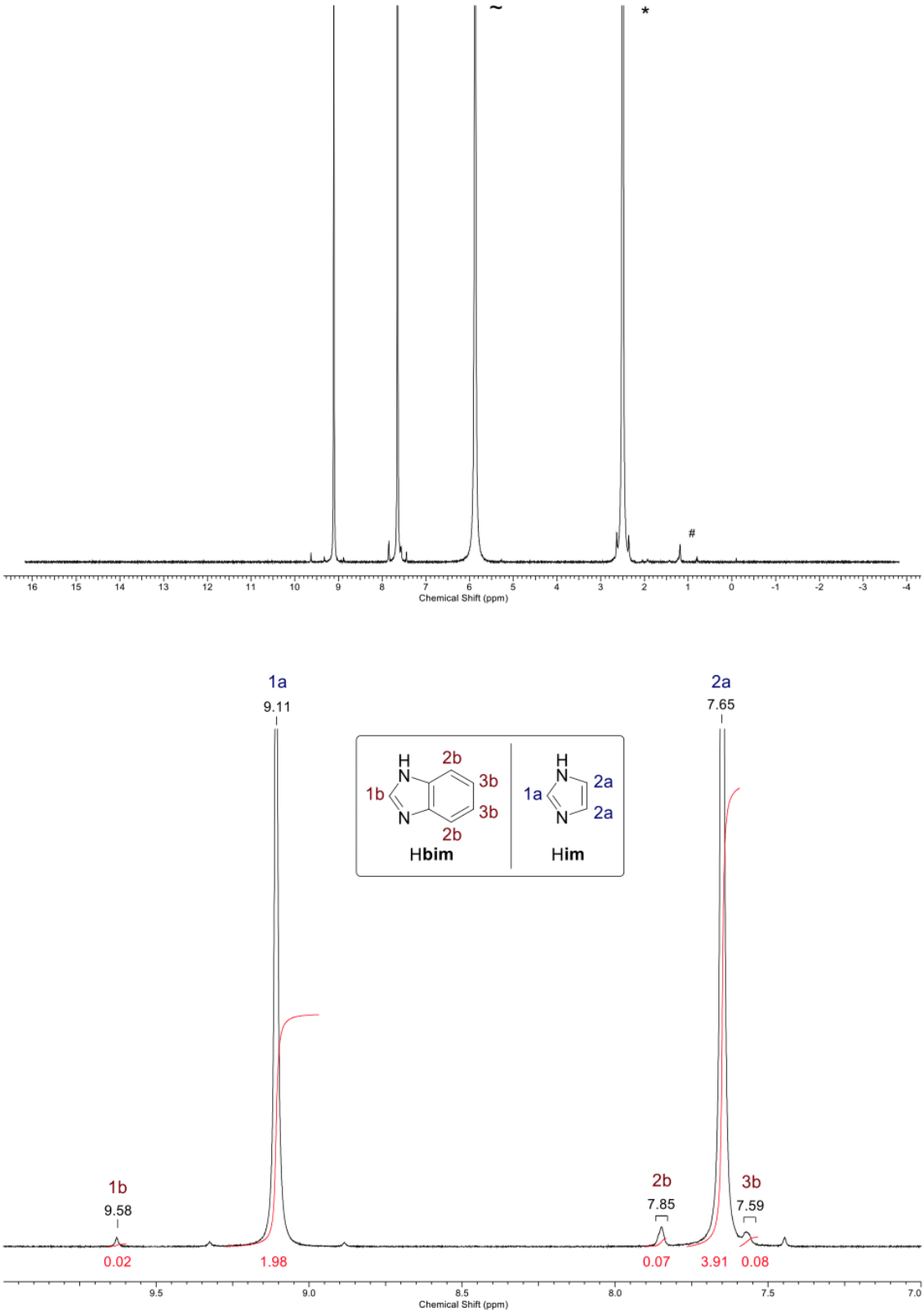

Figure A.75: ^{1}H NMR spectrum of a_gZIF-62(Zn)-bim$_{0.02}$. Top: Full spectrum. Bottom: Zoom into the aromatic region (7.0 ppm to 10.0 ppm). DMSO is marked with $\star$, D_2O is marked with $\sim$ and the small contamination of the DCl/D_2O mixture is marked with #.

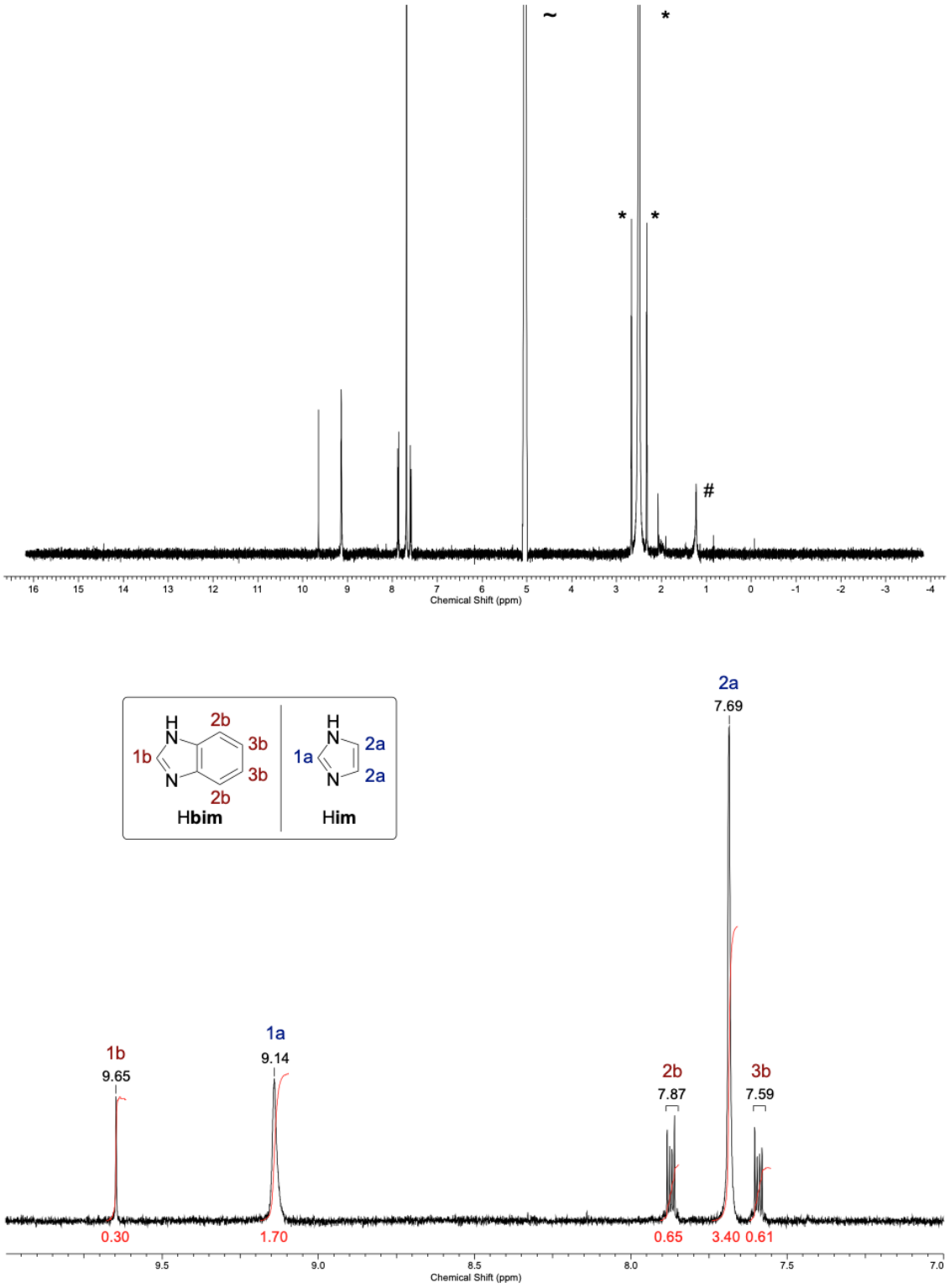

Figure A.76: ^{1}H NMR spectrum of ZIF-62(Co)-bim$_{0.30}$. Top: Full spectrum. Bottom: Zoom into the aromatic region (7.0 ppm to 10.0 ppm). DMSO is marked with $\star$, D_2O is marked with $\sim$ and the small contamination of the DCl/D_2O mixture is marked with #.

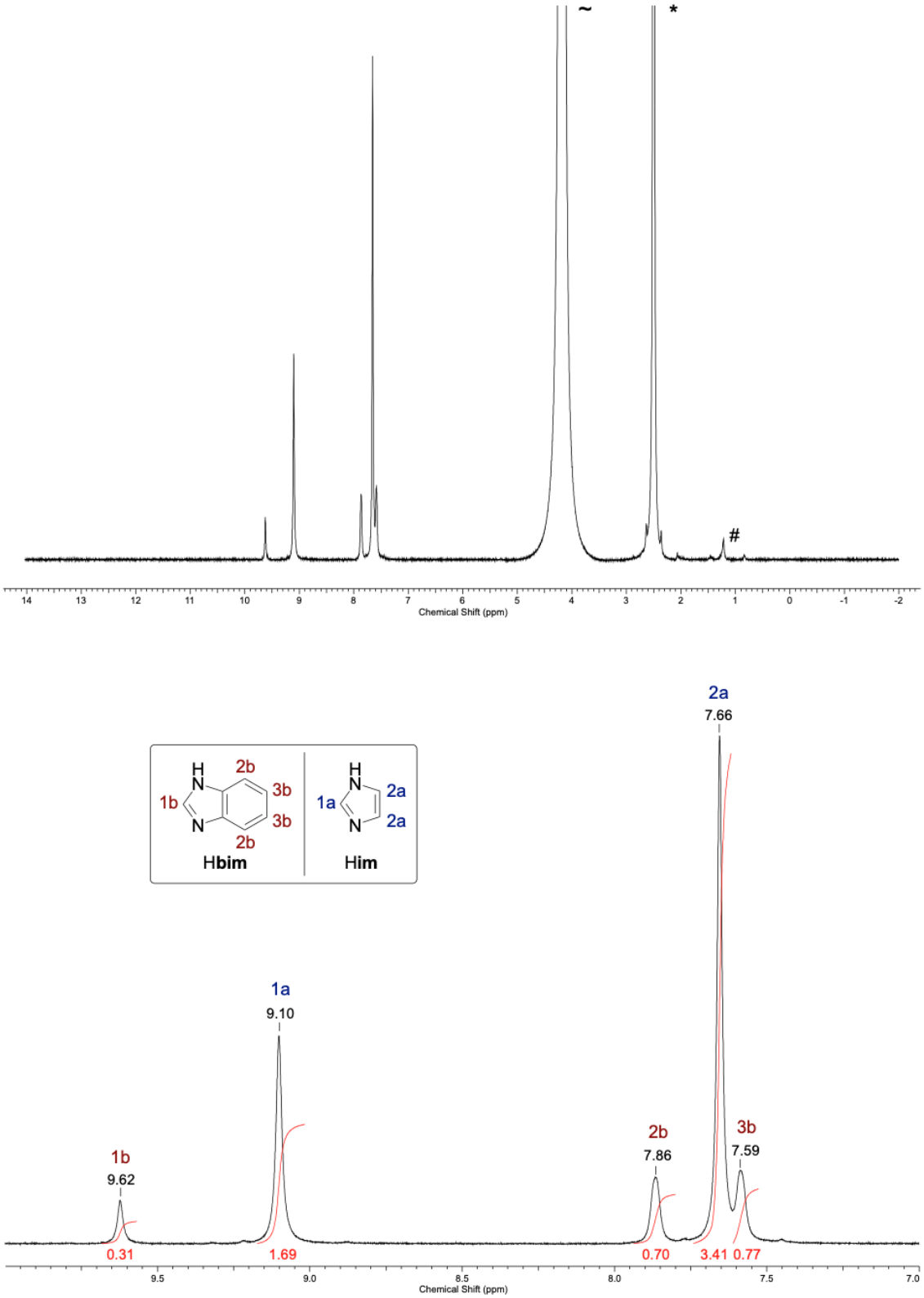

Figure A.77: ^{1}H NMR spectrum of a_gZIF-62(Co)-bim$_{0.30}$. Top: Full spectrum. Bottom: Zoom into the aromatic region (7.0 ppm to 10.0 ppm). DMSO is marked with $\star$, D_2O is marked with $\sim$ and the small contamination of the DCl/D_2O mixture is marked with #.

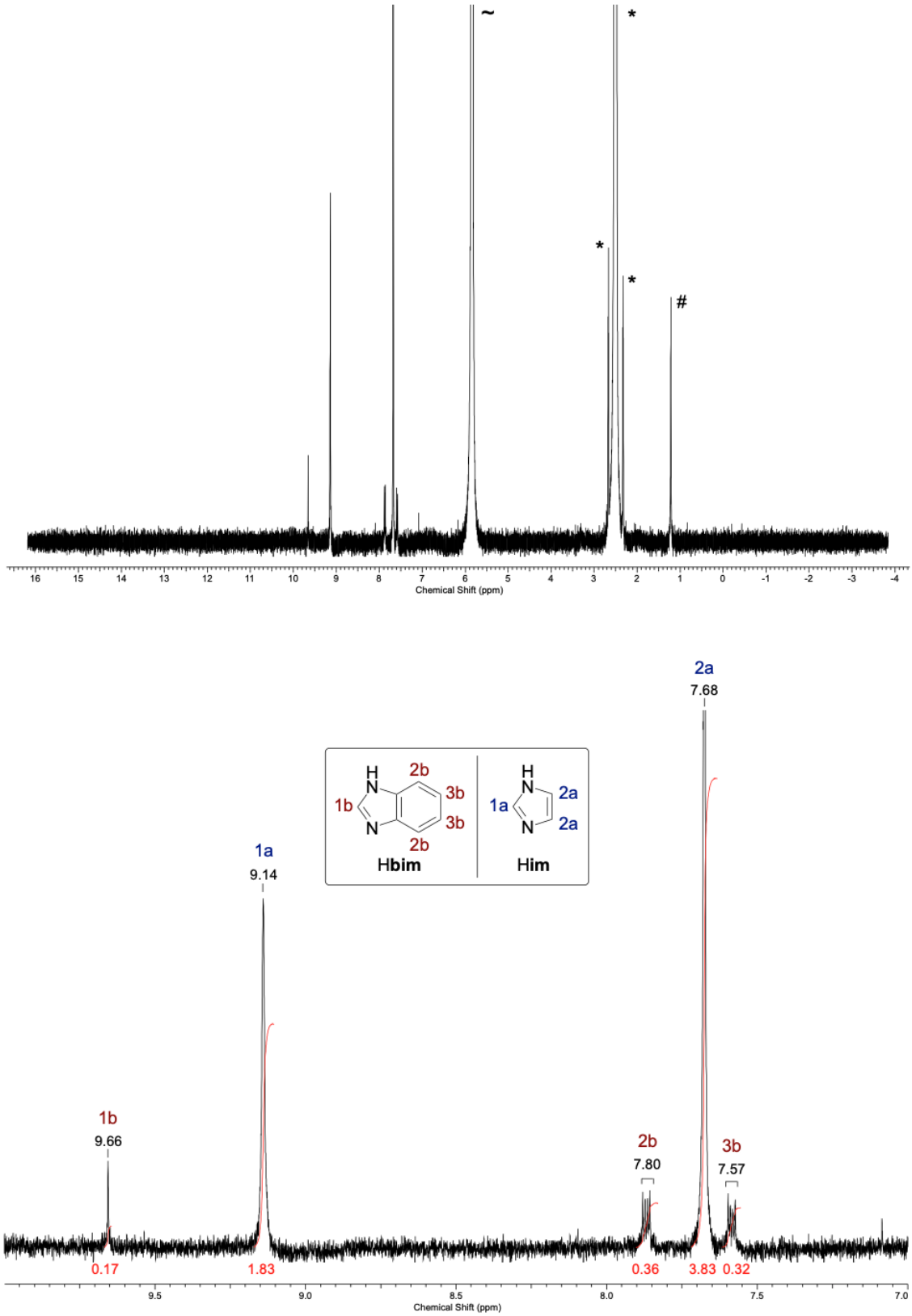

Figure A.78: ^{1}H NMR spectrum of ZIF-62(Co)-bim$_{0.17}$. Top: Full spectrum. Bottom: Zoom into the aromatic region (7.0 ppm to 10.0 ppm). DMSO is marked with $\star$, D_2O is marked with $\sim$ and the small contamination of the DCl/D_2O mixture is marked with #.

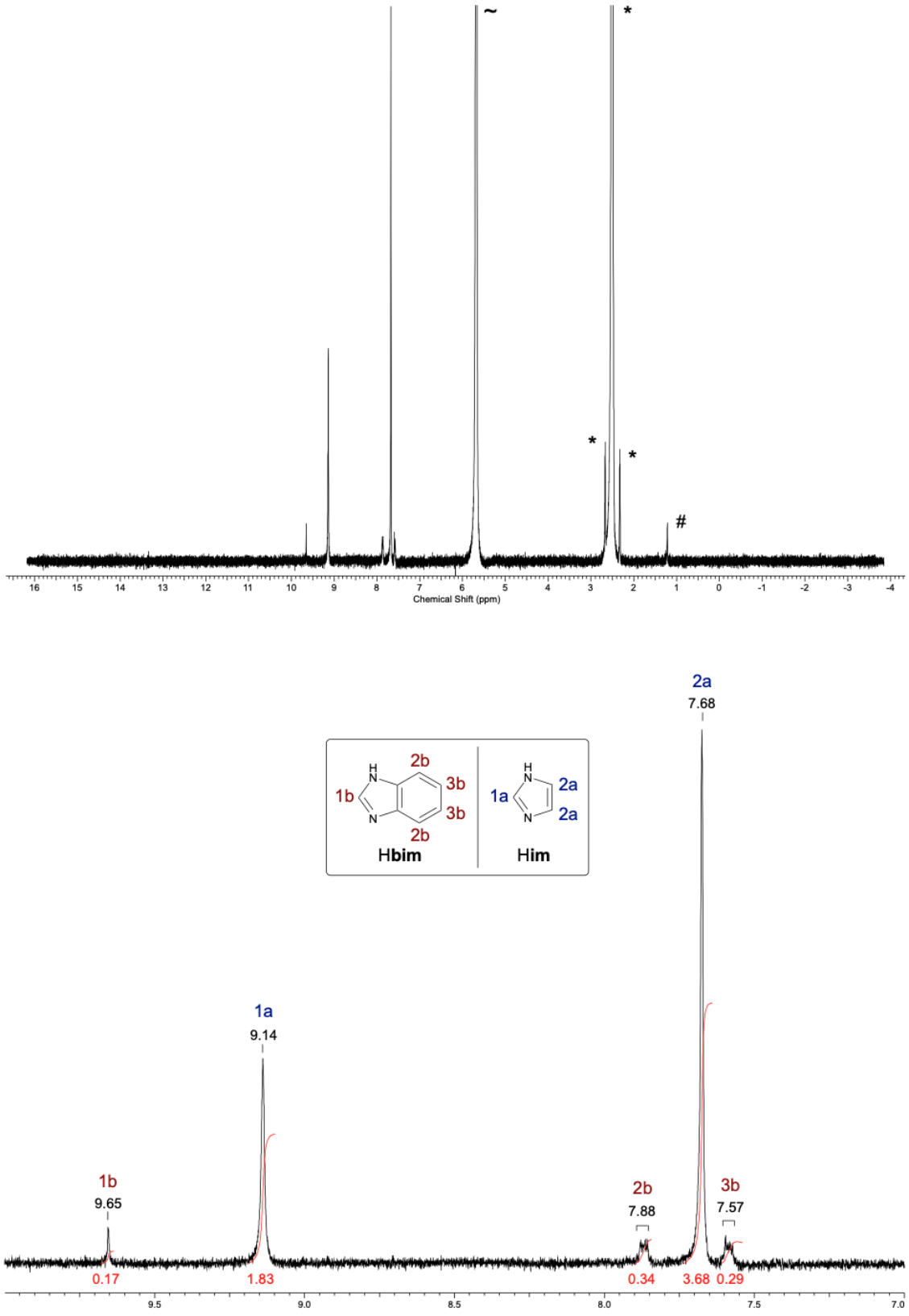

Figure A.79: ^{1}H NMR spectrum of a_gZIF-62(Co)-bim$_{0.17}$. Top: Full spectrum. Bottom: Zoom into the aromatic region (7.0 ppm to 10.0 ppm). DMSO is marked with $\star$, D_2O is marked with $\sim$ and the small contamination of the DCl/D_2O mixture is marked with #.

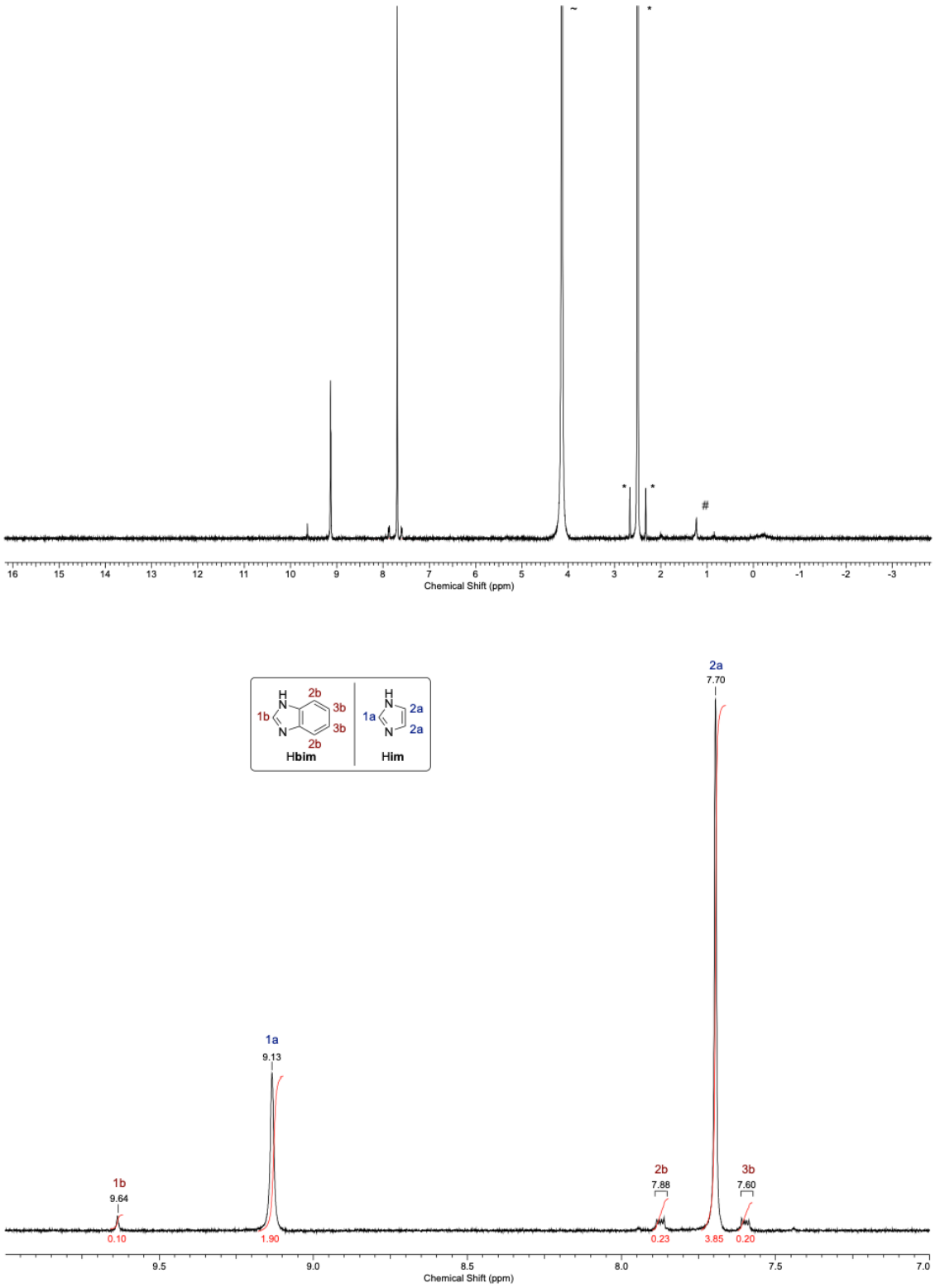

Figure A.80: ^{1}H NMR spectrum of ZIF-62(Co)-bim$_{0.10}$. Top: Full spectrum. Bottom: Zoom into the aromatic region (7.0 ppm to 10.0 ppm). DMSO is marked with $\star$, D_2O is marked with $\sim$ and the small contamination of the DCl/D_2O mixture is marked with #.

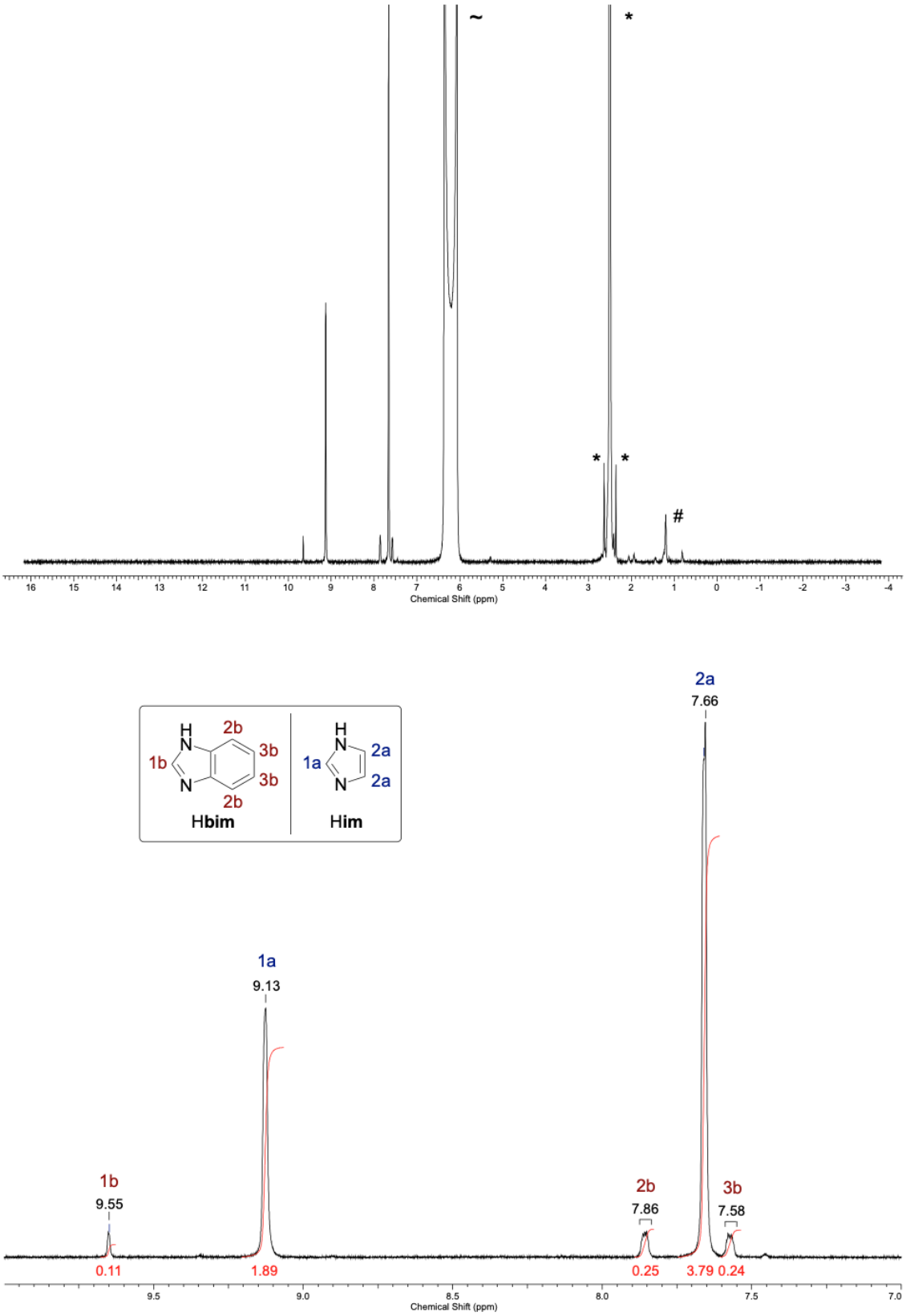

Figure A.81: ^{1}H NMR spectrum of a_gZIF-62(Co)-bim$_{0.10}$. Top: Full spectrum. Bottom: Zoom into the aromatic region (7.0 ppm to 10.0 ppm). DMSO is marked with $\star$, D_2O is marked with $\sim$ and the small contamination of the DCl/D_2O mixture is marked with #.

Data for as-ZIF-4(M) and as-ZIF-62(M)-bim$_x$

These data have been used to determine the amount of DMF in the pores of the as-ZIF-62(Zn)-bim$_x$ materials (see Table 8.3). In all spectra, the signal ascribed to the formyl proton of DMF is labeled with 'DMF'. The sum of the integrals of the **1a** and **1b** protons of the Him and Hbim linkers, respectively, is set to ≈2. Consequently, the integral of DMF corresponds approximately to the number of DMF molecules per formula unit of the ZIF.

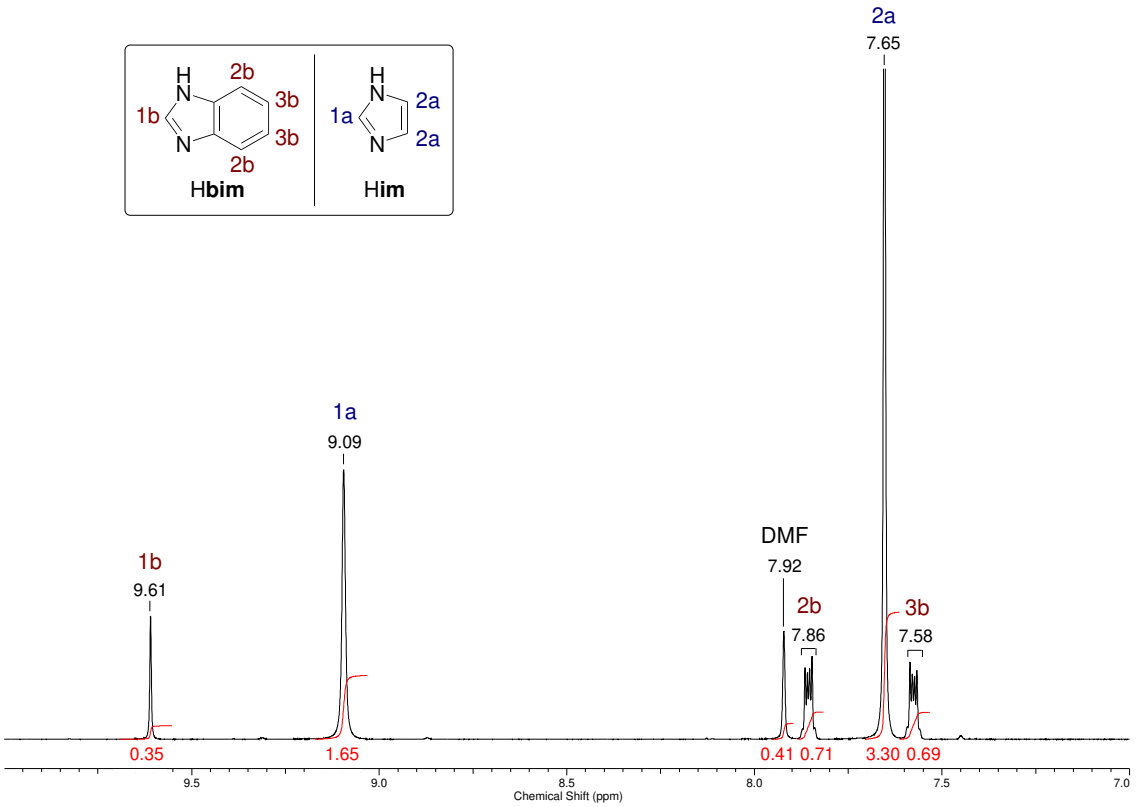

Figure A.82: ^{1}H NMR spectrum of as-ZIF-62(Zn)-bim$_{0.35}$. Zoom into the aromatic region (7.0 ppm to 10.0 ppm).

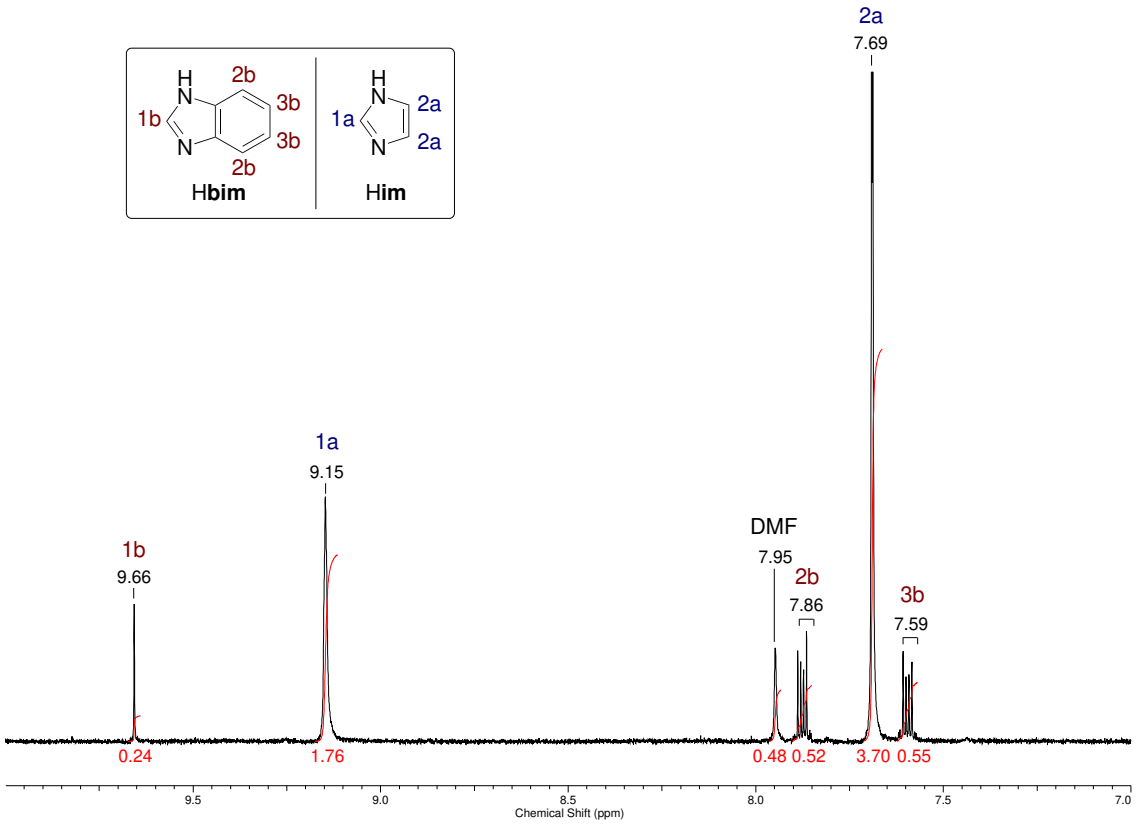

Figure A.83: ^{1}H NMR spectrum of as-ZIF-62(Zn)-bim$_{0.24}$. Zoom into the aromatic region (7.0 ppm to 10.0 ppm).

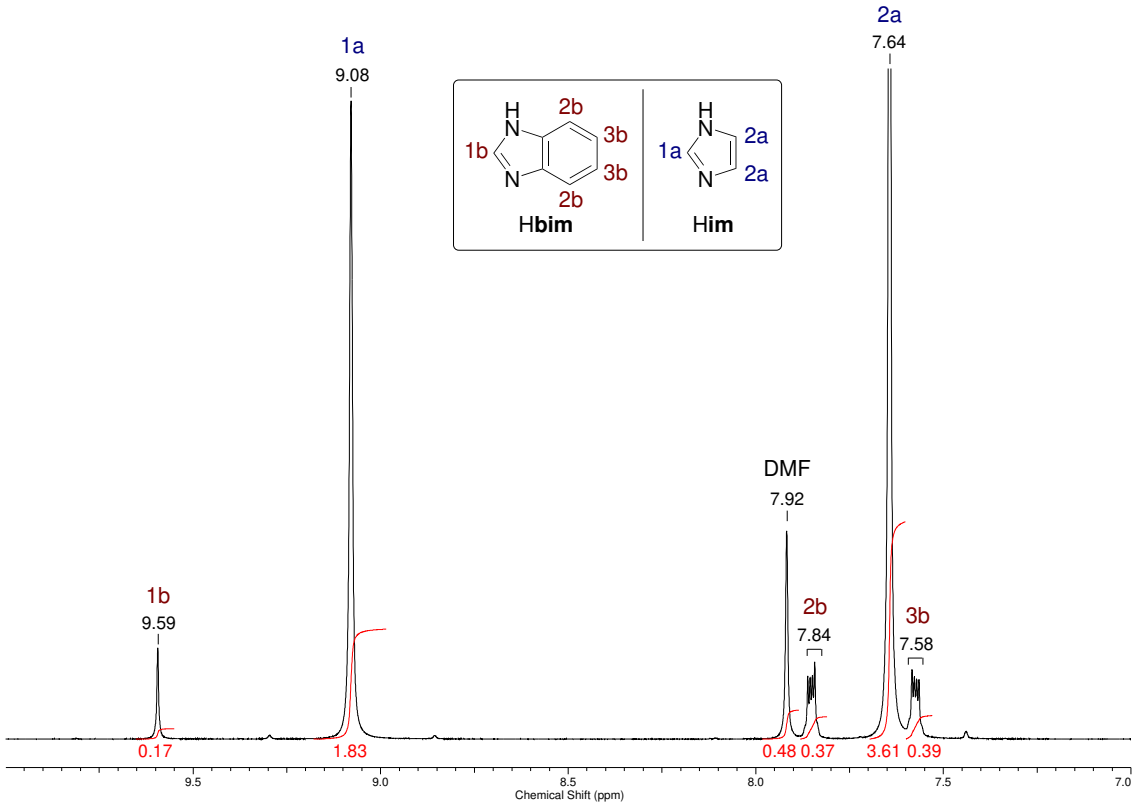

Figure A.84: ^{1}H NMR spectrum of as-ZIF-62(Zn)-bim$_{0.17}$. Zoom into the aromatic region (7.0 ppm to 10.0 ppm).

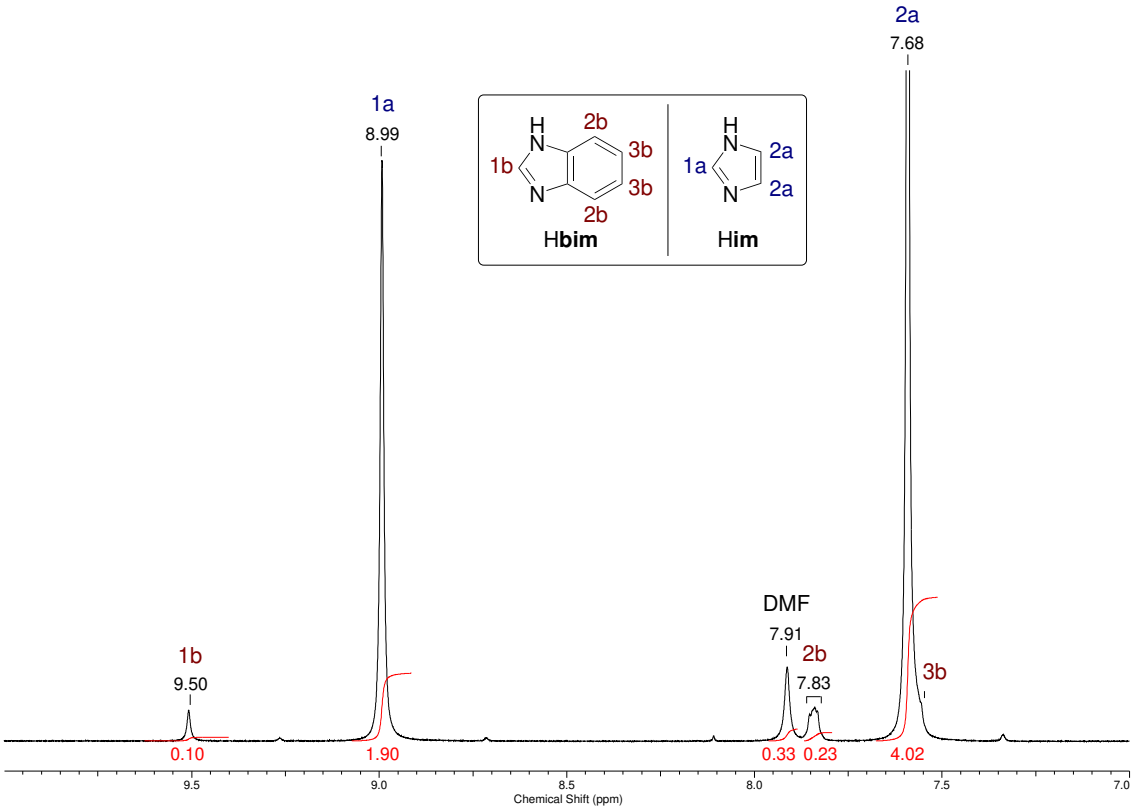

Figure A.85: ^{1}H NMR spectrum of as-ZIF-62(Zn)-bim$_{0.12}$. Zoom into the aromatic region (7.0 ppm to 10.0 ppm).

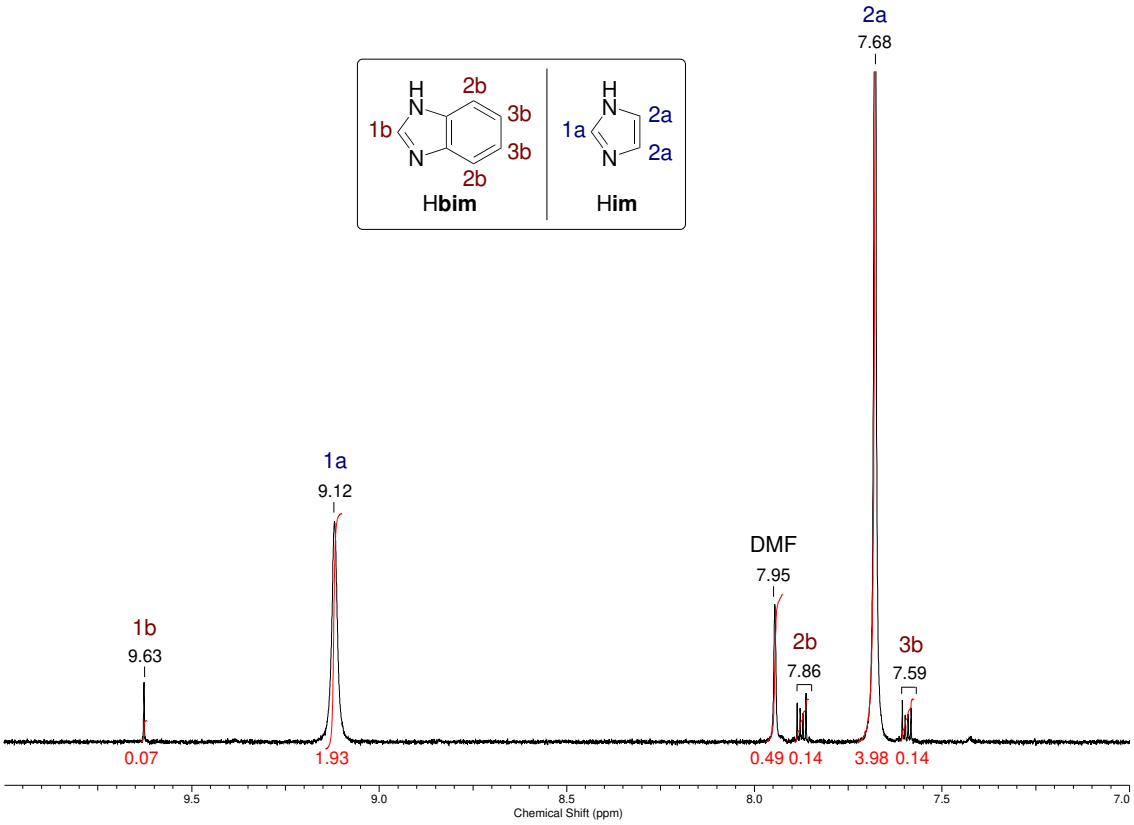

Figure A.86: ^{1}H NMR spectrum of as-ZIF-62(Zn)-bim$_{0.07}$. Zoom into the aromatic region (7.0 ppm to 10.0 ppm).

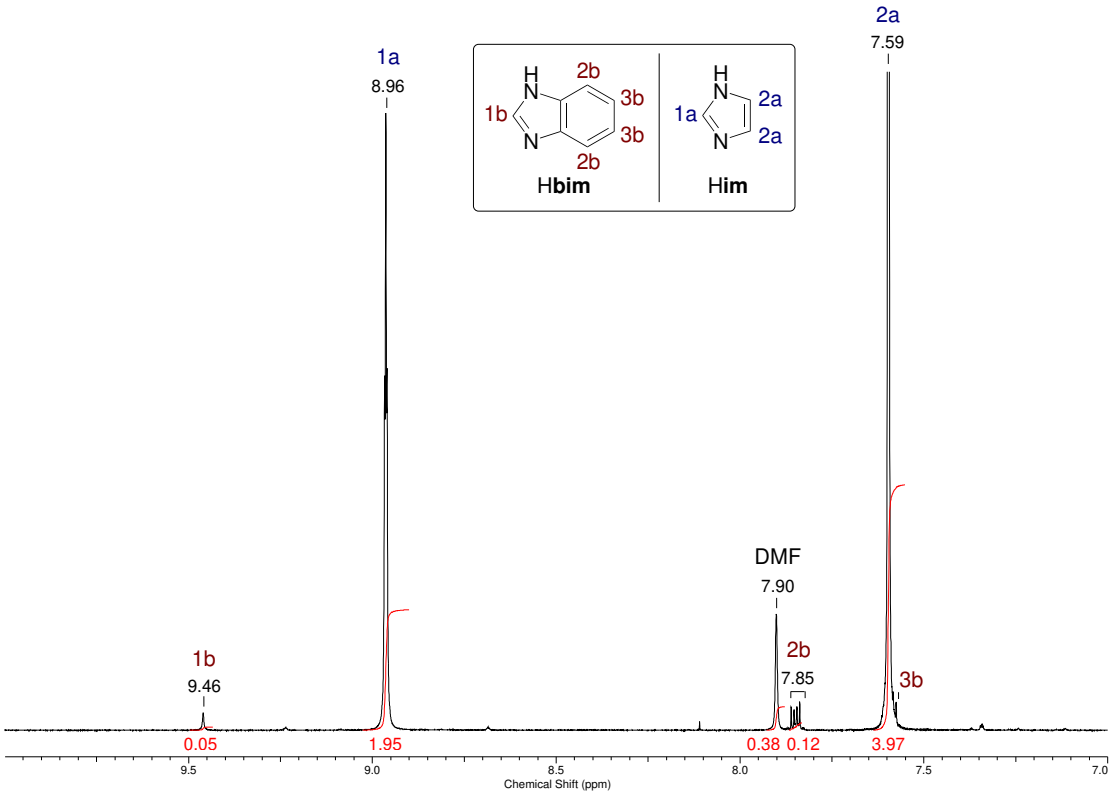

Figure A.87: ^{1}H NMR spectrum of as-ZIF-62(Zn)-bim$_{0.05}$. Zoom into the aromatic region (7.0 ppm to 10.0 ppm).

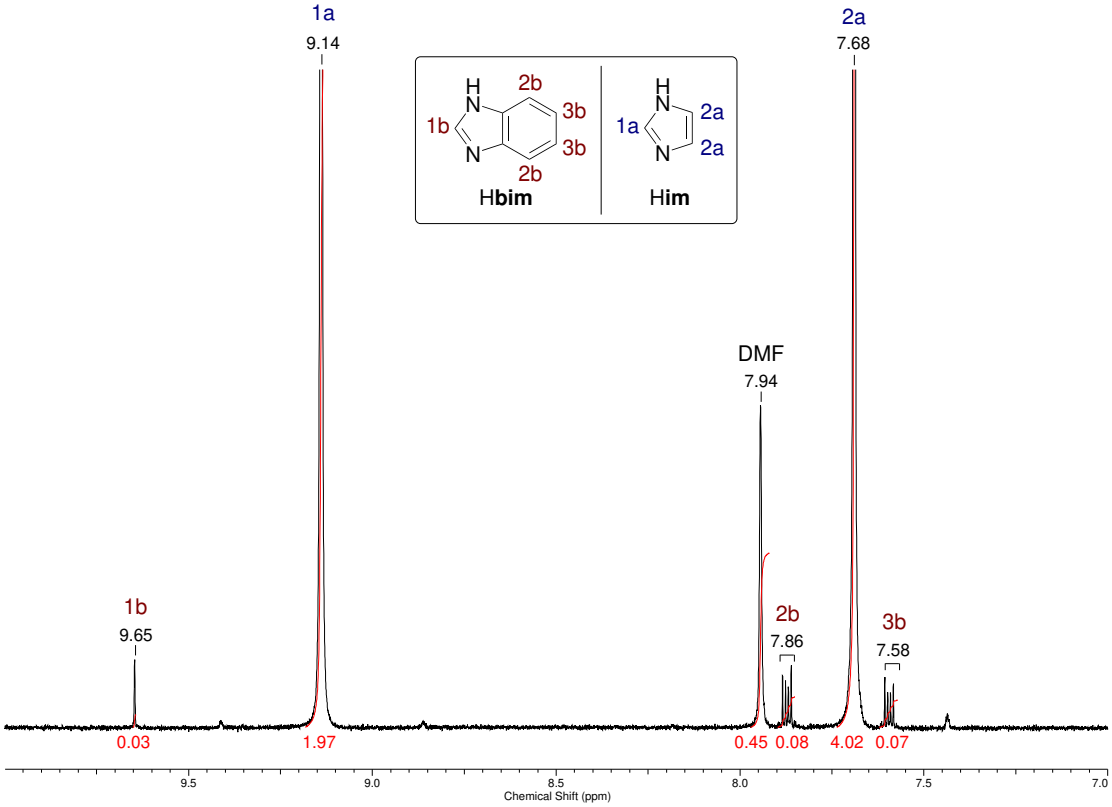

Figure A.88: ^{1}H NMR spectrum of as-ZIF-62(Zn)-bim$_{0.03}$. Zoom into the aromatic region (7.0 ppm to 10.0 ppm).

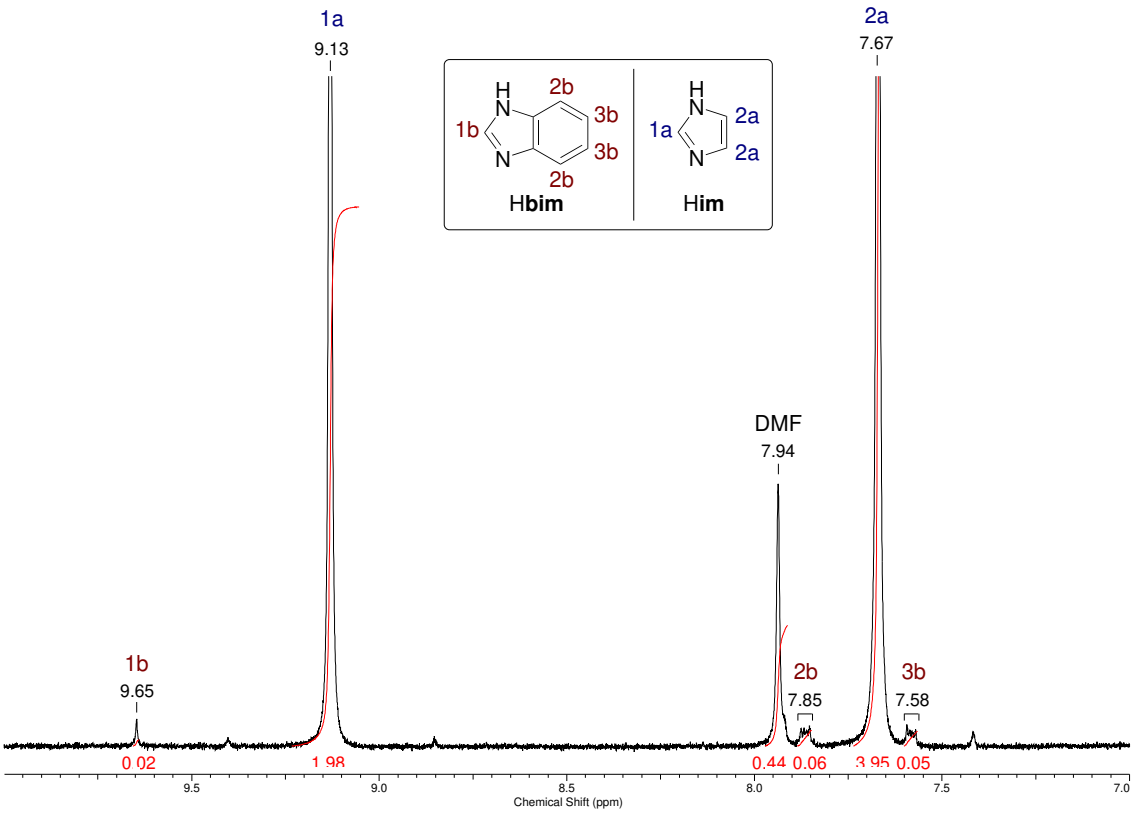

Figure A.89: ^{1}H NMR spectrum of as-ZIF-62(Zn)-bim$_{0.02}$. Zoom into the aromatic region (7.0 ppm to 10.0 ppm).

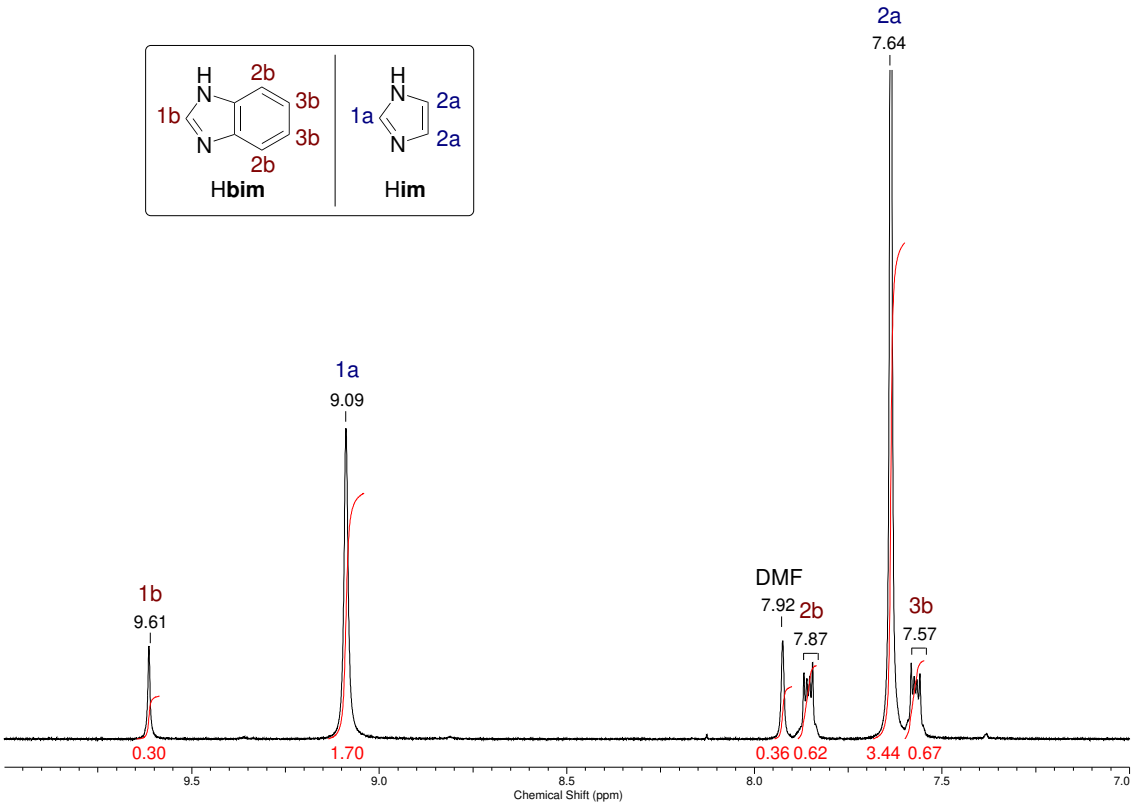

Figure A.90: ^{1}H NMR spectrum of as-ZIF-62(Co)-bim$_{0.30}$. Zoom into the aromatic region (7.0 ppm to 10.0 ppm).

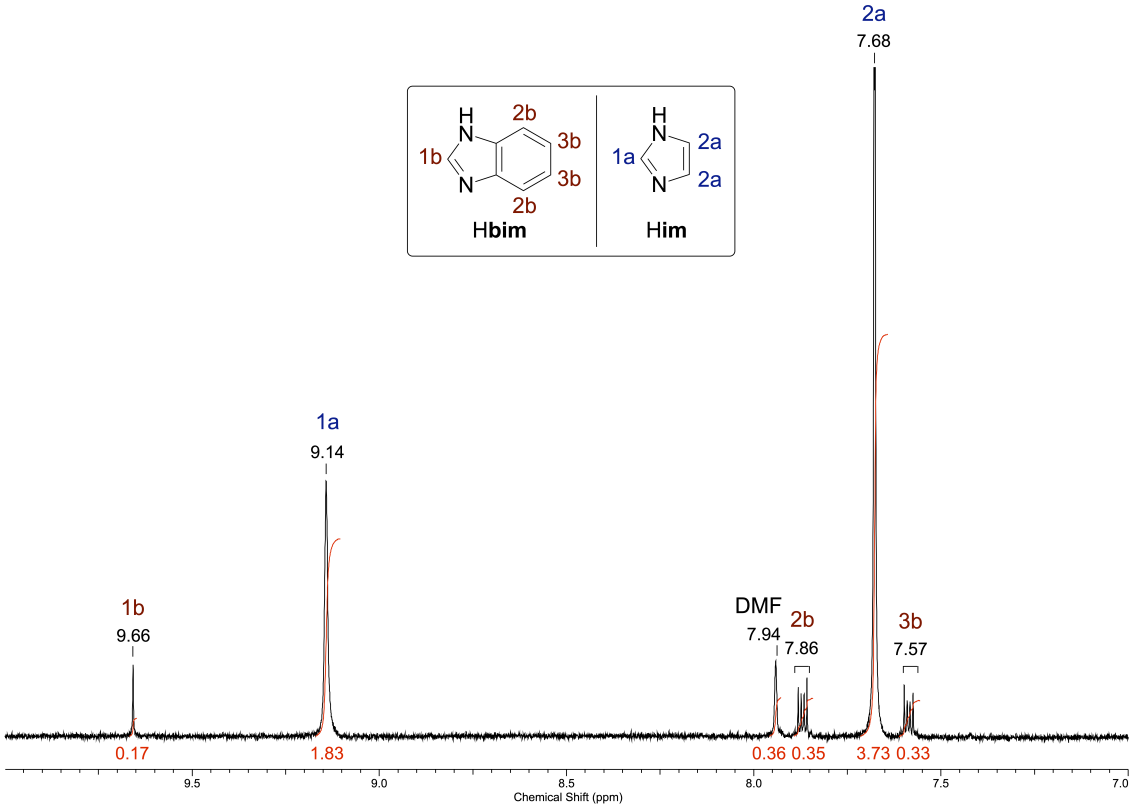

Figure A.91: ^{1}H NMR spectrum of as-ZIF-62(Co)-bim$_{0.17}$. Zoom into the aromatic region (7.0 ppm to 10.0 ppm).

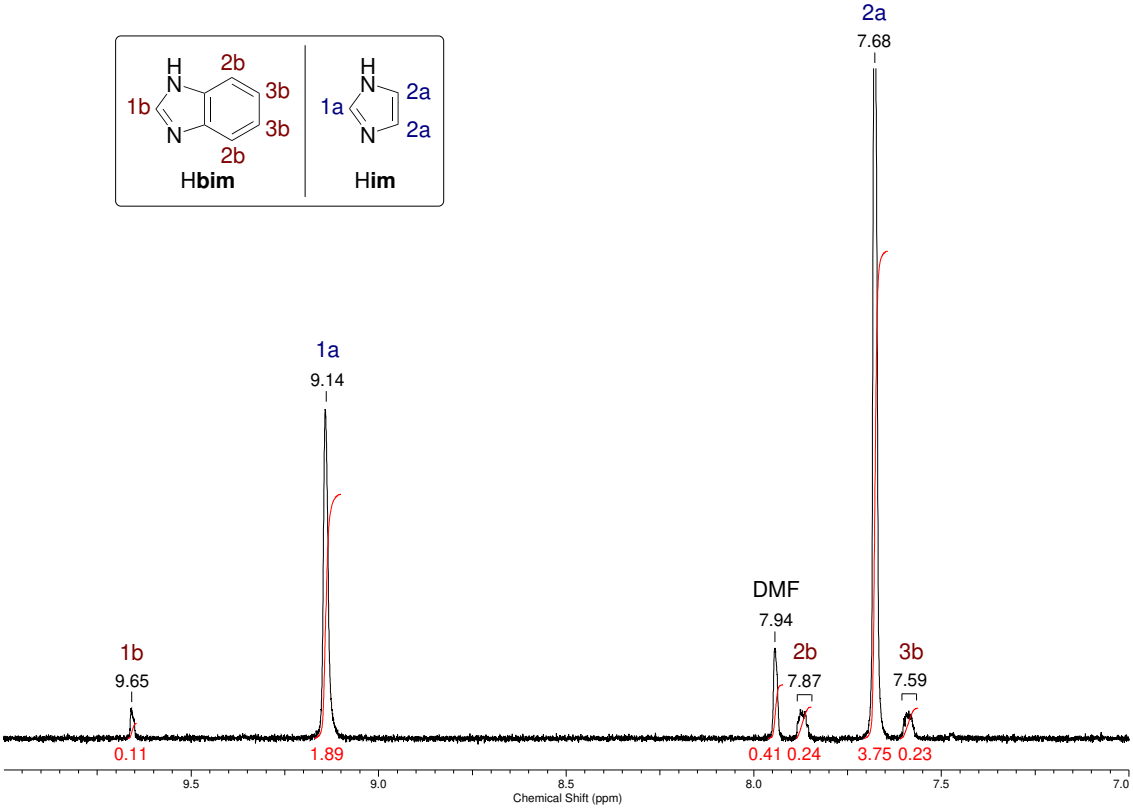

Figure A.92: ^{1}H NMR spectrum of as-ZIF-62(Co)-bim$_{0.10}$. Zoom into the aromatic region (7.0 ppm to 10.0 ppm).

A.3.7 Simultaneous Thermogravimetric Analysis / Differential Scanning Calorimetry

Three different temperature programs were used for TGA/DSC data collection. The respective performed program is given in the captions for the collected data set. The programs are described in detail below. All temperature programs were conducted with a heating/cooling rate of 10 °C min^{-1} for all upscans and downscans.

program 1 (one upscan):
$T = 25\,°C \rightarrow 750\,°C$

program 2 (three upscan, two downscans):
$T = 25\,°C \rightarrow 475\,°C \rightarrow 50\,°C \rightarrow 475\,°C \rightarrow 50\,°C \rightarrow 475\,°C$

program 3 (three upscan, two downscans):
$T = 25\,°C \rightarrow 510\,°C \rightarrow 50\,°C \rightarrow 510\,°C \rightarrow 50\,°C \rightarrow 510\,°C$

TGA/DSC Experiments – One Upscan

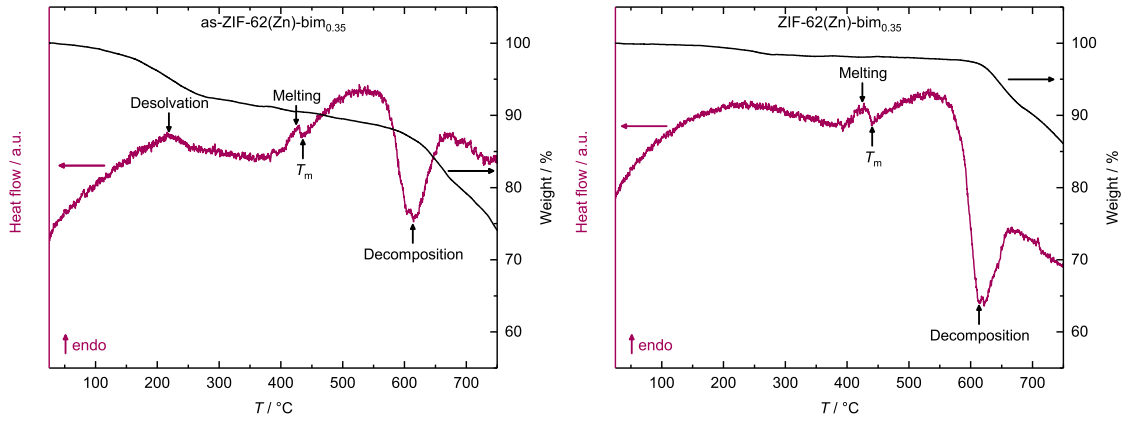

Figure A.93: TGA/DSC data of as-ZIF-62(Zn)-$bim_{0.35}$ (left) and ZIF-62(Zn)-$bim_{0.35}$ (right). Data were collected conducting temperature program 1.

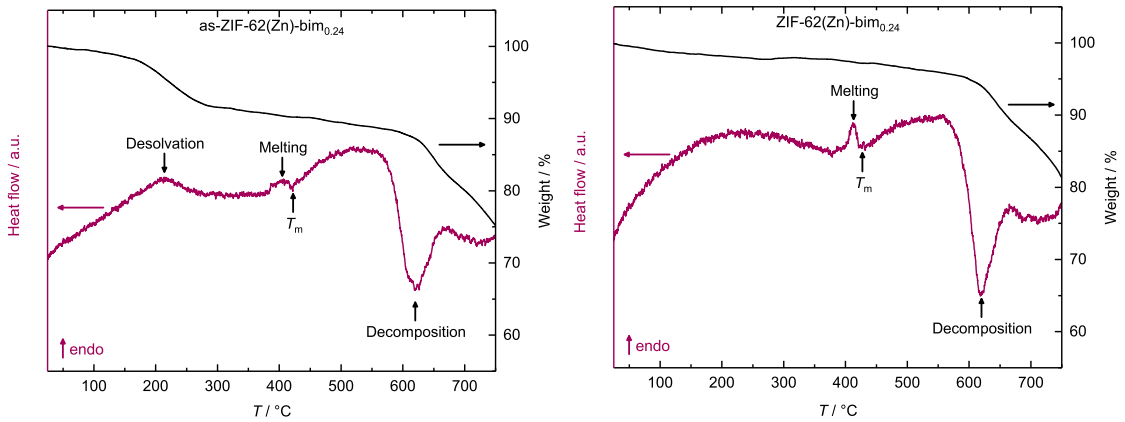

Figure A.94: TGA/DSC data of as-ZIF-62(Zn)-bim$_{0.24}$ (left) and ZIF-62(Zn)-bim$_{0.24}$ (right). Data were collected conducting temperature program 1.

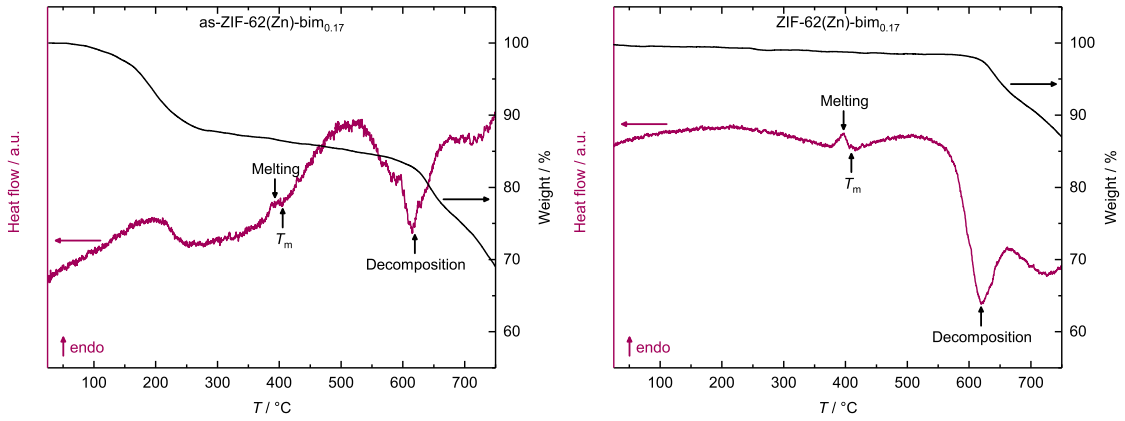

Figure A.95: TGA/DSC data of as-ZIF-62(Zn)-bim$_{0.17}$ (left) and ZIF-62(Zn)-bim$_{0.17}$ (right). Data were collected conducting temperature program 1.

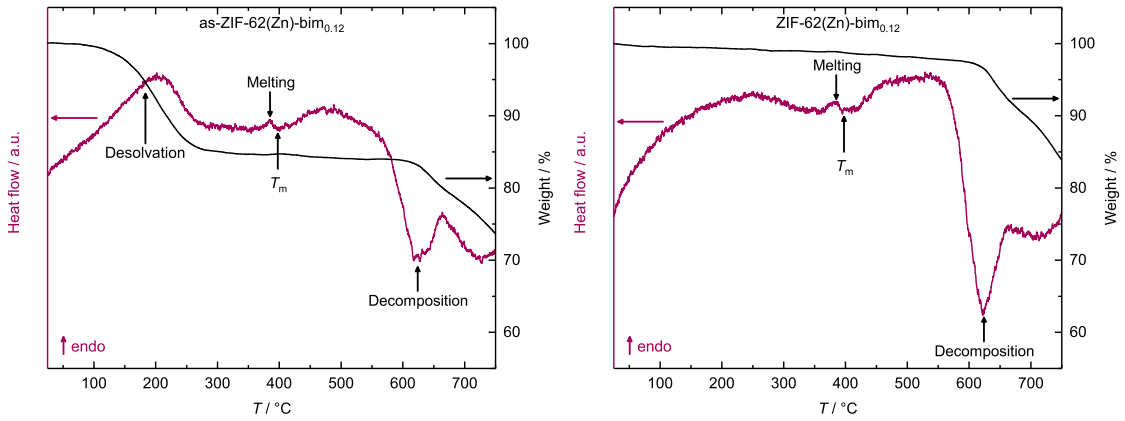

Figure A.96: TGA/DSC data of as-ZIF-62(Zn)-bim$_{0.12}$ (left) and ZIF-62(Zn)-bim$_{0.12}$ (right). Data were collected conducting temperature program 1.

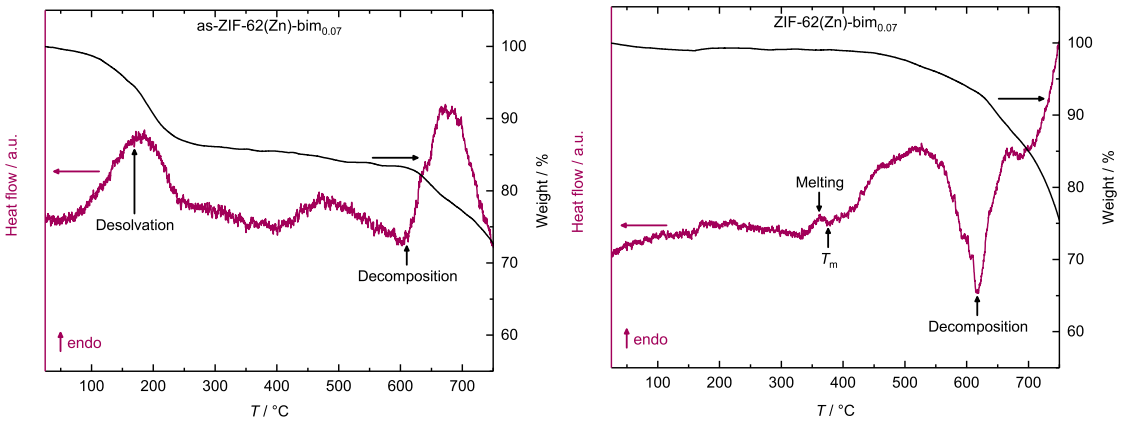

Figure A.97: TGA/DSC data of as-ZIF-62(Zn)-bim$_{0.07}$ (left) and ZIF-62(Zn)-bim$_{0.07}$ (right). Data were collected conducting temperature program 1.

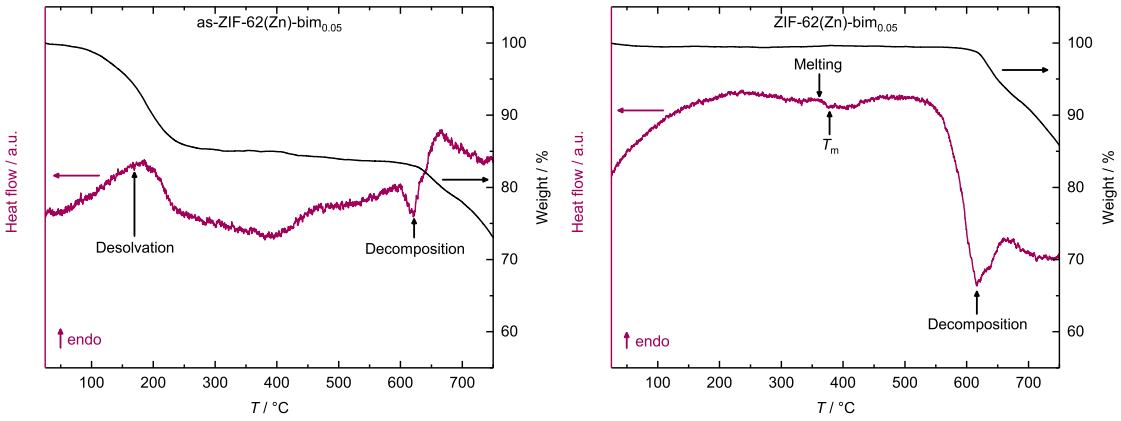

Figure A.98: TGA/DSC data of as-ZIF-62(Zn)-bim$_{0.05}$ (left) and ZIF-62(Zn)-bim$_{0.05}$ (right). Data were collected conducting temperature program 1.

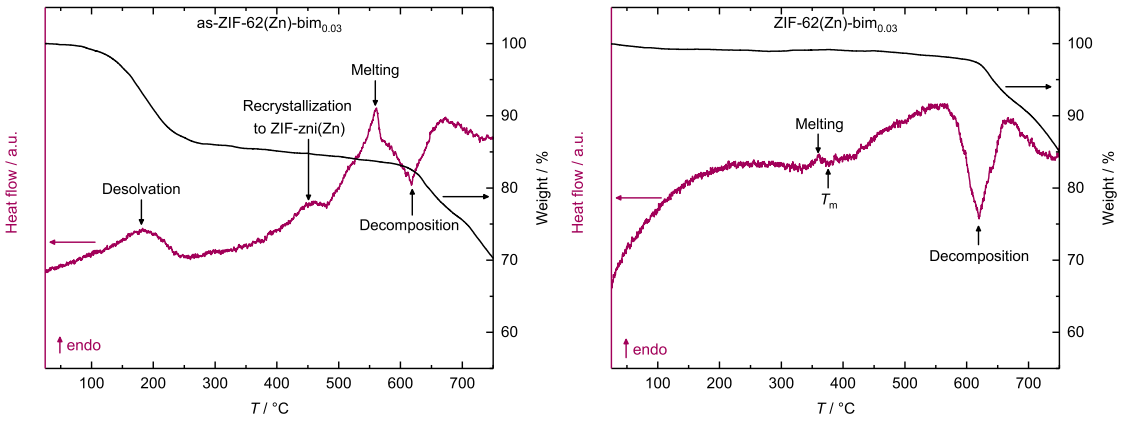

Figure A.99: TGA/DSC data of as-ZIF-62(Zn)-bim$_{0.03}$ (left) and ZIF-62(Zn)-bim$_{0.03}$ (right). Data were collected conducting temperature program 1.

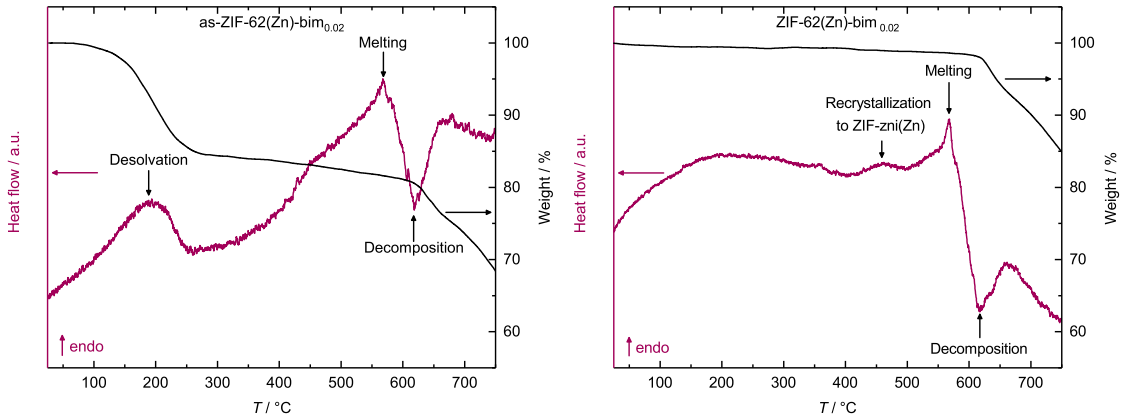

Figure A.100: TGA/DSC data of as-ZIF-62(Zn)-bim$_{0.02}$ (left) and ZIF-62(Zn)-bim$_{0.02}$ (right). Data were collected conducting temperature program 1.

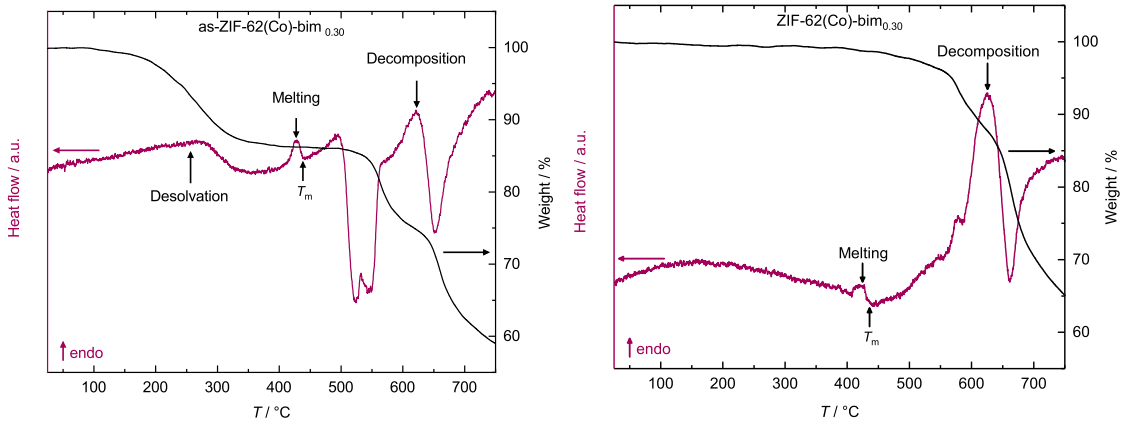

Figure A.101: TGA/DSC data of as-ZIF-62(Co)-bim$_{0.30}$ (left) and ZIF-62(Co)-bim$_{0.30}$ (right). Data were collected conducting temperature program 1.

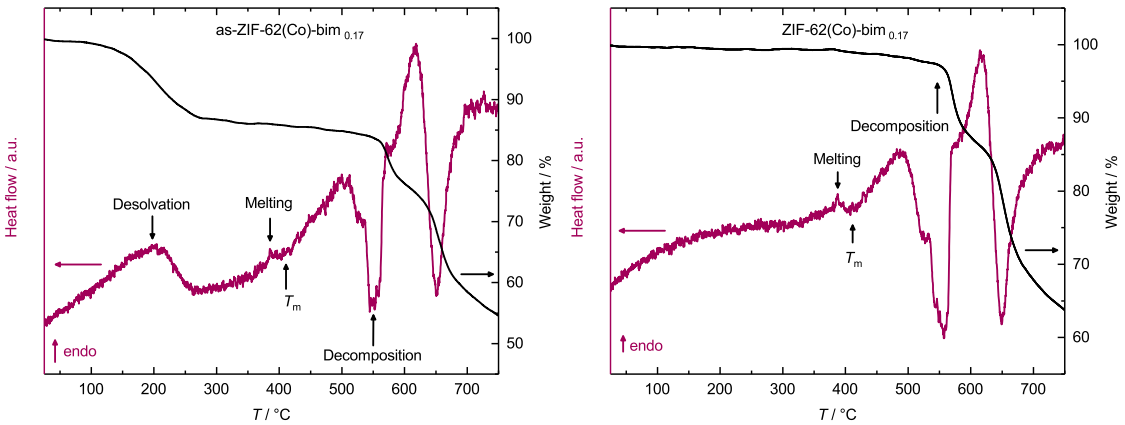

Figure A.102: TGA/DSC data of as-ZIF-62(Co)-bim$_{0.17}$ (left) and ZIF-62(Co)-bim$_{0.17}$ (right). Data were collected conducting temperature program 1.

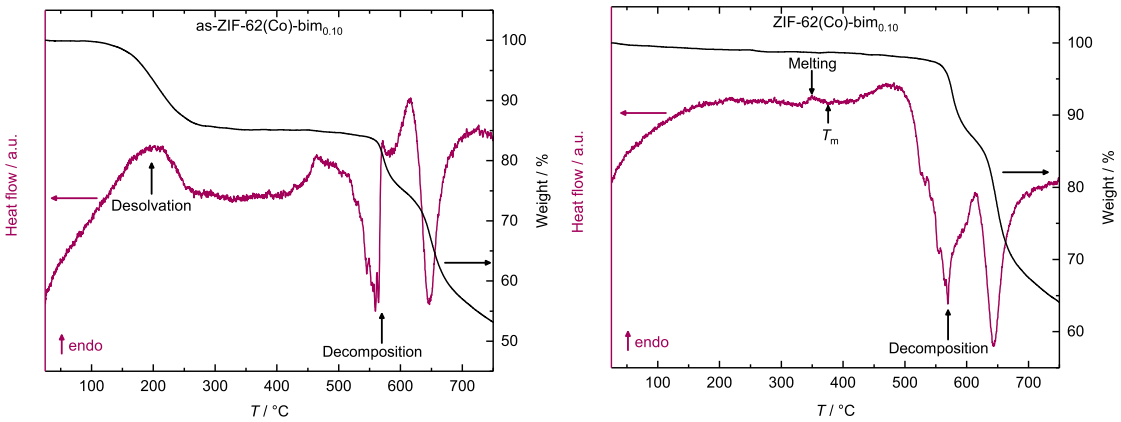

Figure A.103: TGA/DSC data of as-ZIF-62(Co)-bim$_{0.10}$ (left) and ZIF-62(Co)-bim$_{0.10}$ (right). Data were collected conducting temperature program 1.

DSC Traces of Cyclic TGA/DSC Experiments – Three Upscans

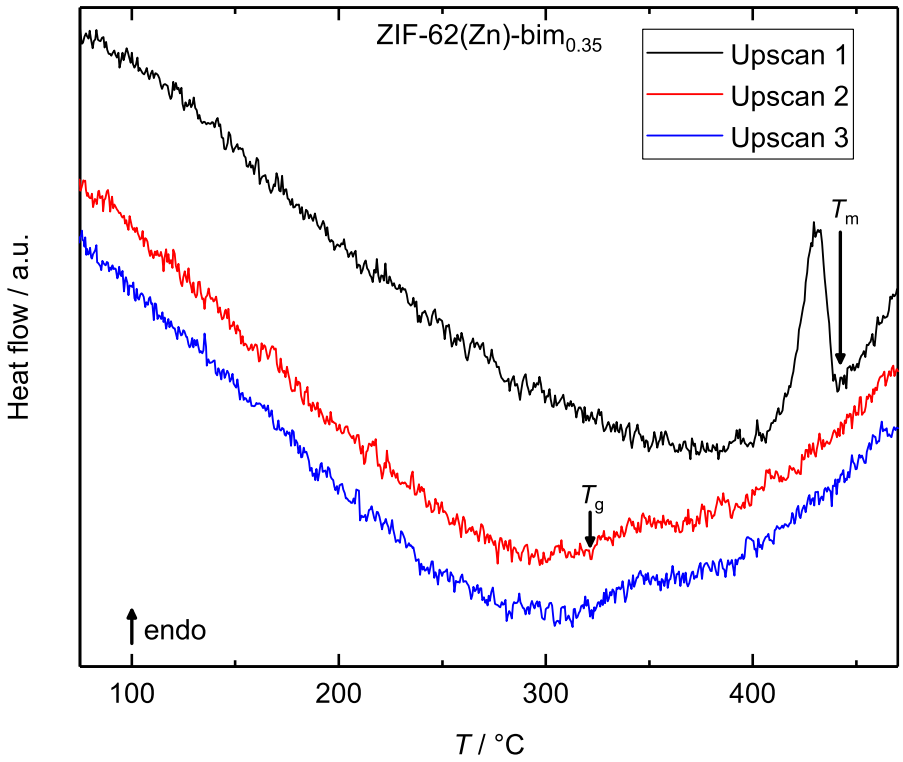

Figure A.104: DSC traces of the upscans of the TGA/DSC experiment for ZIF-62(Zn)-bim$_{0.35}$ conducting temperature program 2.

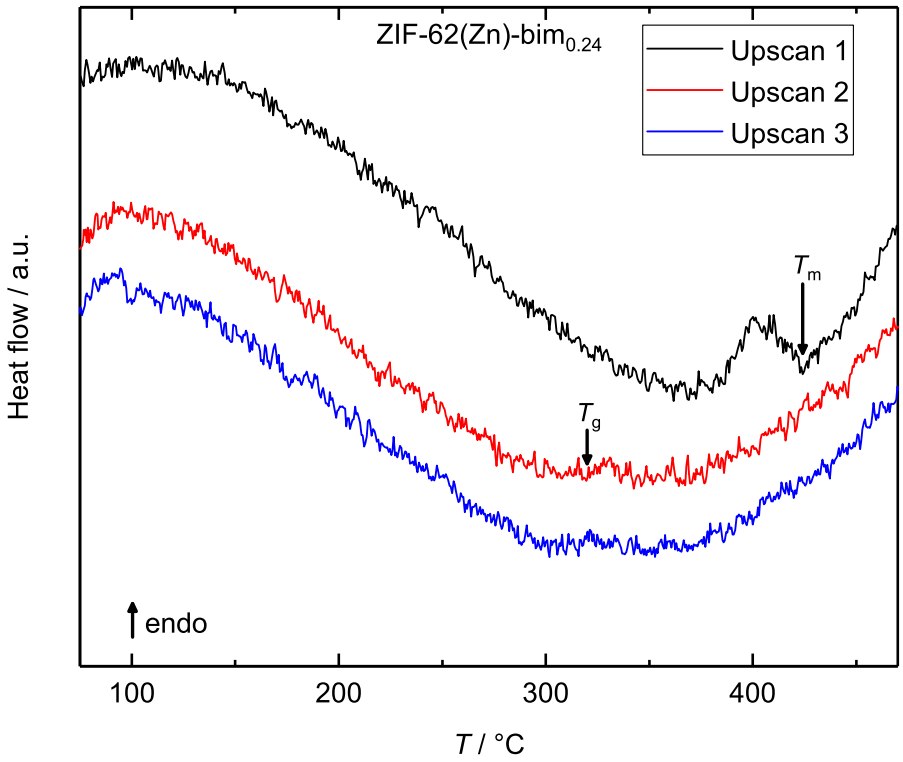

Figure A.105: DSC traces of the upscans of the TGA/DSC experiment for for ZIF-62(Zn)-bim$_{0.24}$ conducting temperature program 2.

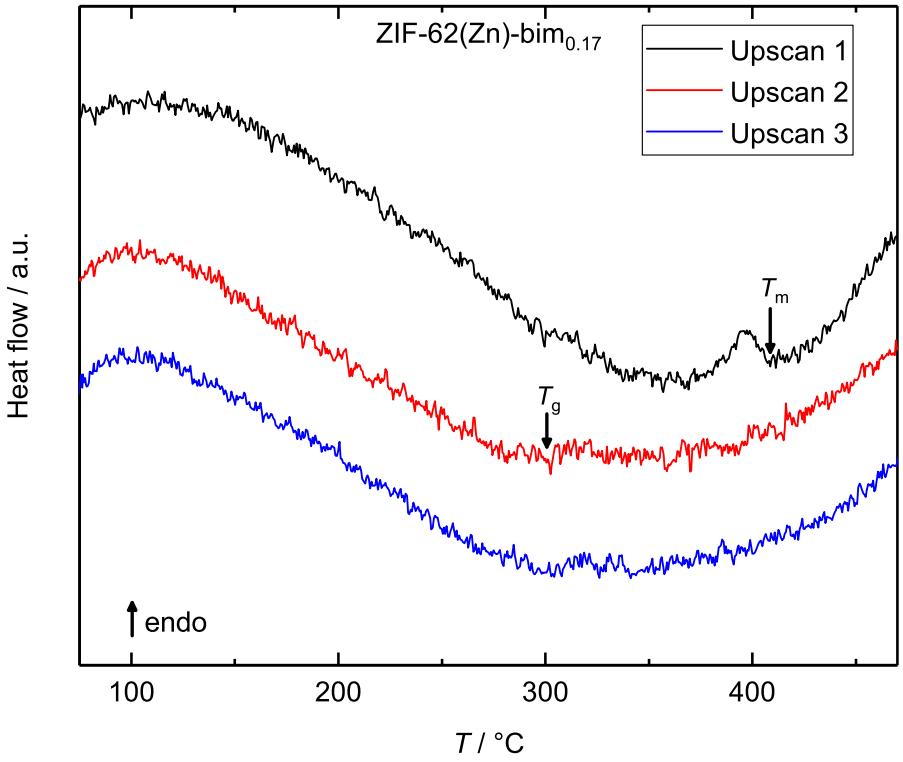

Figure A.106: DSC traces of the upscans of the TGA/DSC experiment for ZIF-62(Zn)-bim$_{0.17}$ conducting temperature program 2.

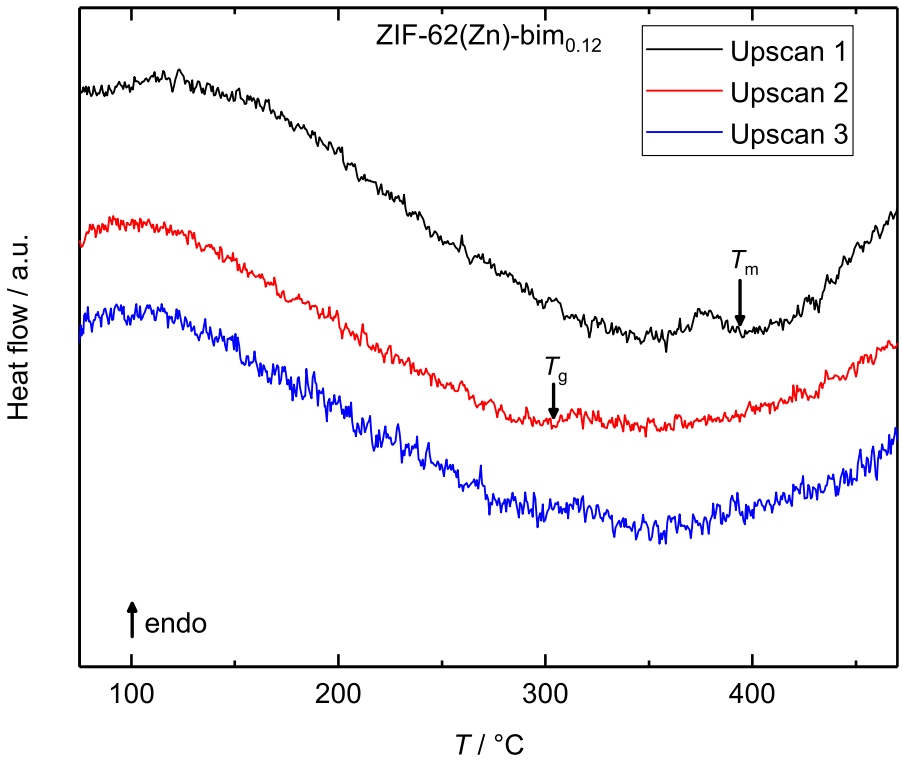

Figure A.107: DSC traces of the upscans of the TGA/DSC experiment for for ZIF-62(Zn)-bim$_{0.12}$ conducting temperature program 2.

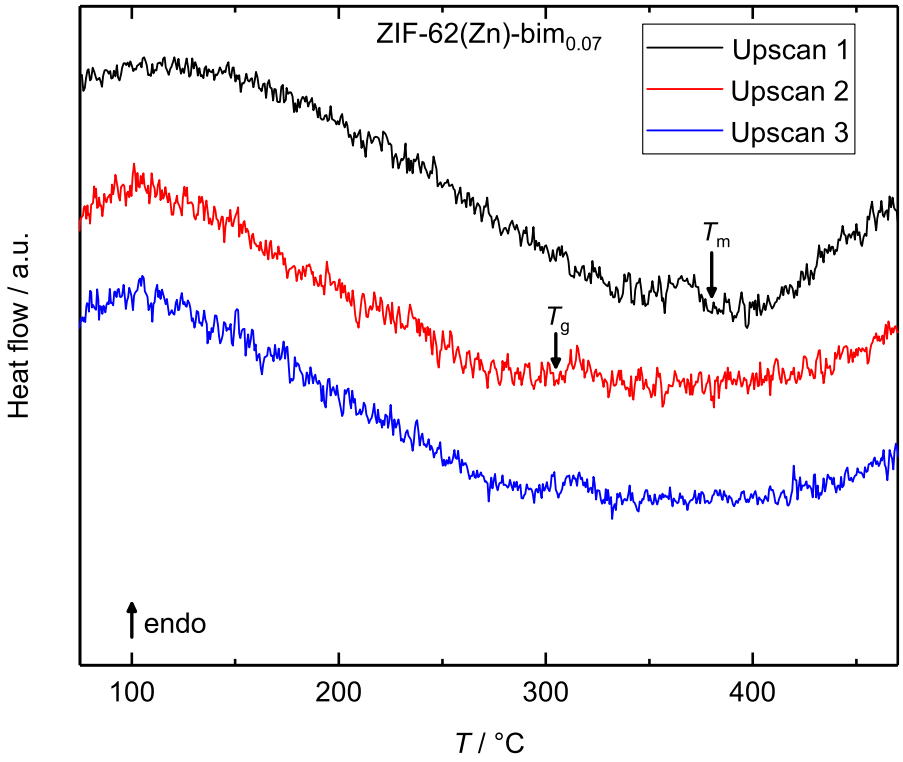

Figure A.108: DSC traces of the upscans of the TGA/DSC experiment for for ZIF-62(Zn)-bim$_{0.07}$ conducting temperature program 2.

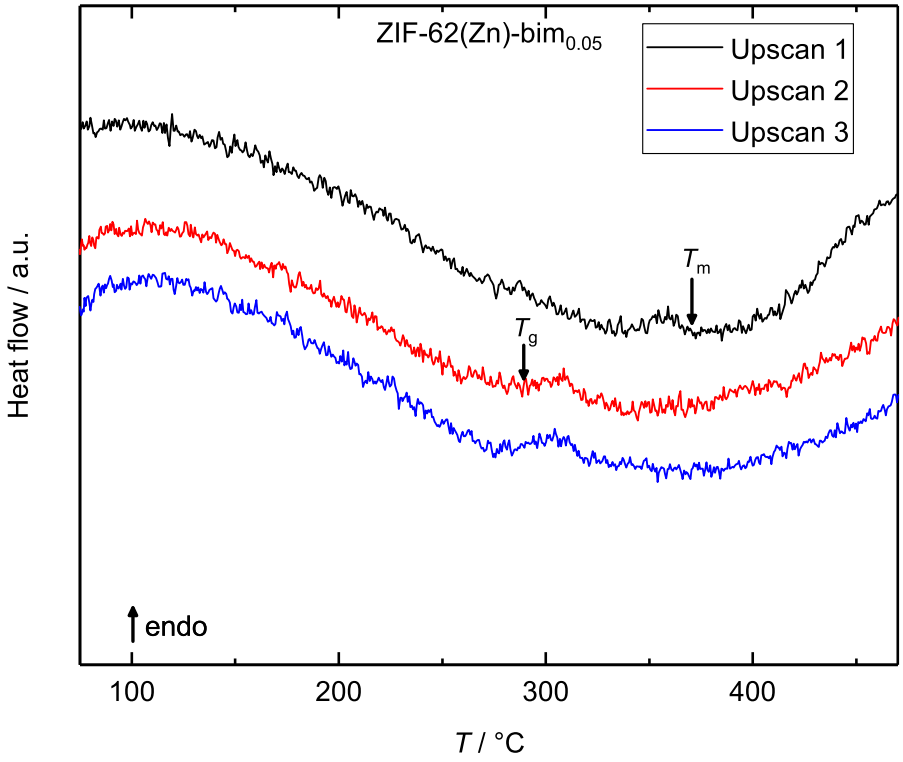

Figure A.109: DSC traces of the upscans of the TGA/DSC experiment for for ZIF-62(Zn)-bim$_{0.05}$ conducting temperature program 2.

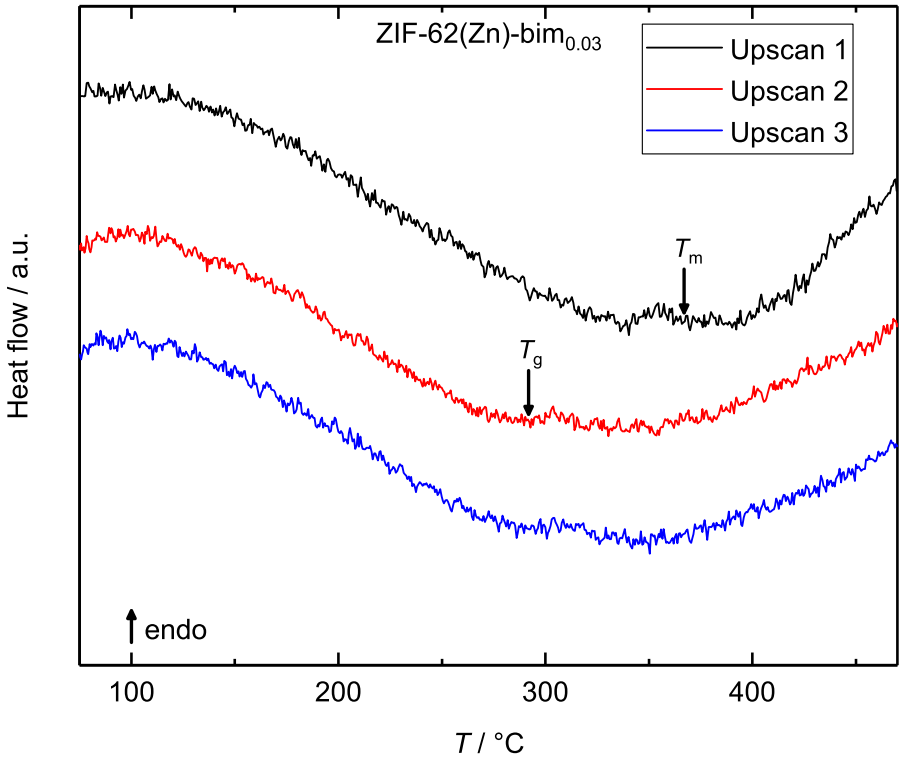

Figure A.110: DSC traces of the upscans of the TGA/DSC experiment for for ZIF-62(Zn)-bim$_{0.03}$ conducting temperature program 2.

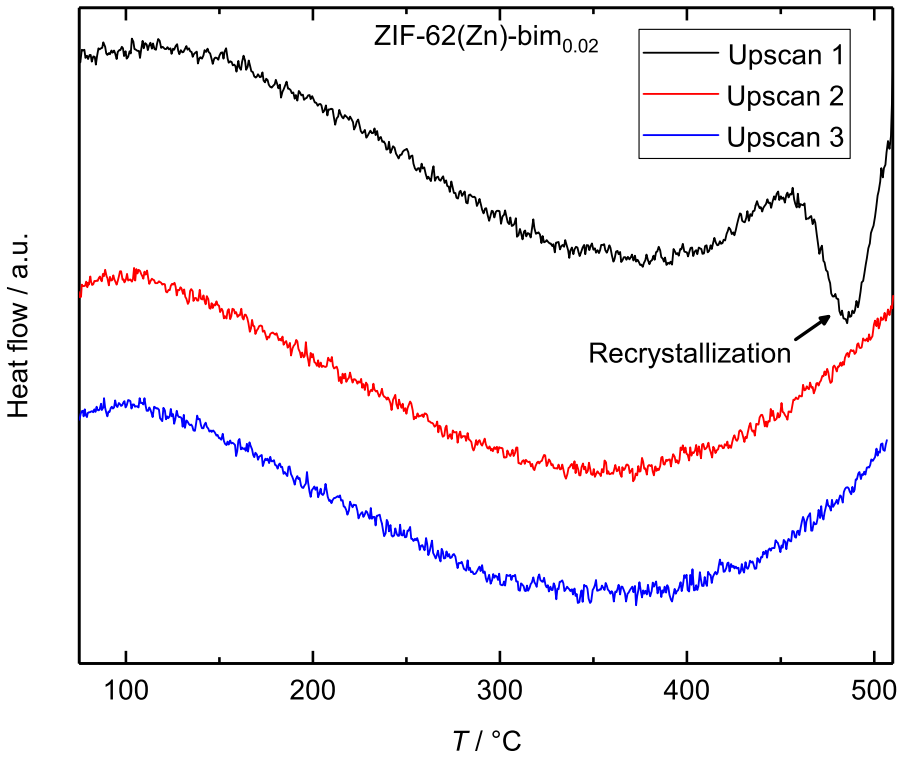

Figure A.111: DSC traces of the upscans of the TGA/DSC experiment for for ZIF-62(Zn)-bim$_{0.02}$ conducting temperature program 3.

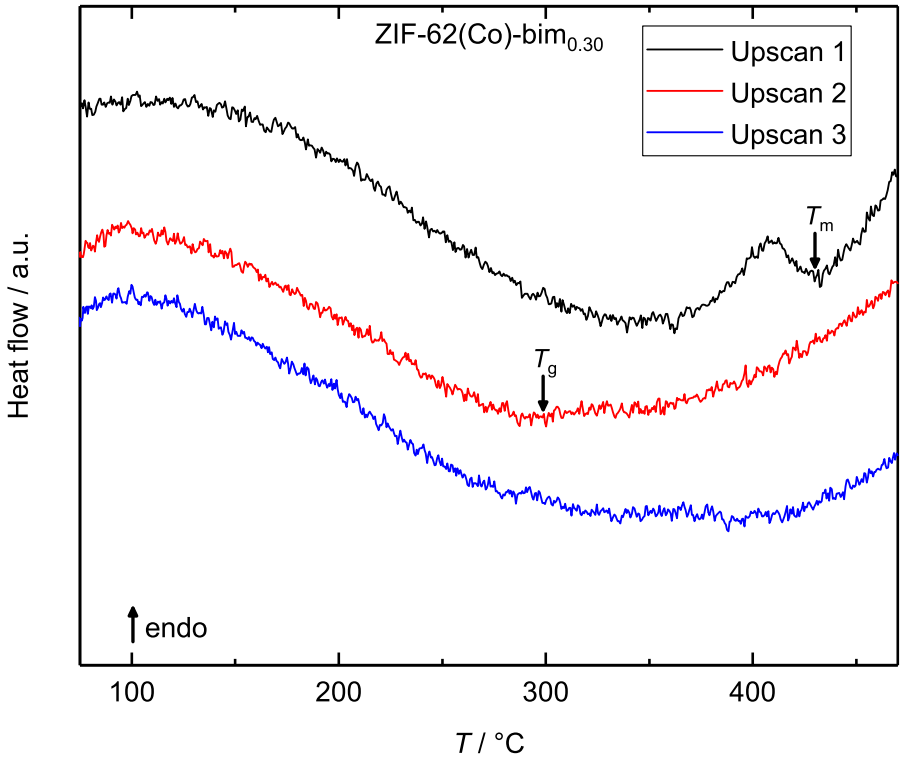

Figure A.112: DSC traces of the upscans of the TGA/DSC experiment for for ZIF-62(Co)-bim$_{0.30}$ conducting temperature program 2.

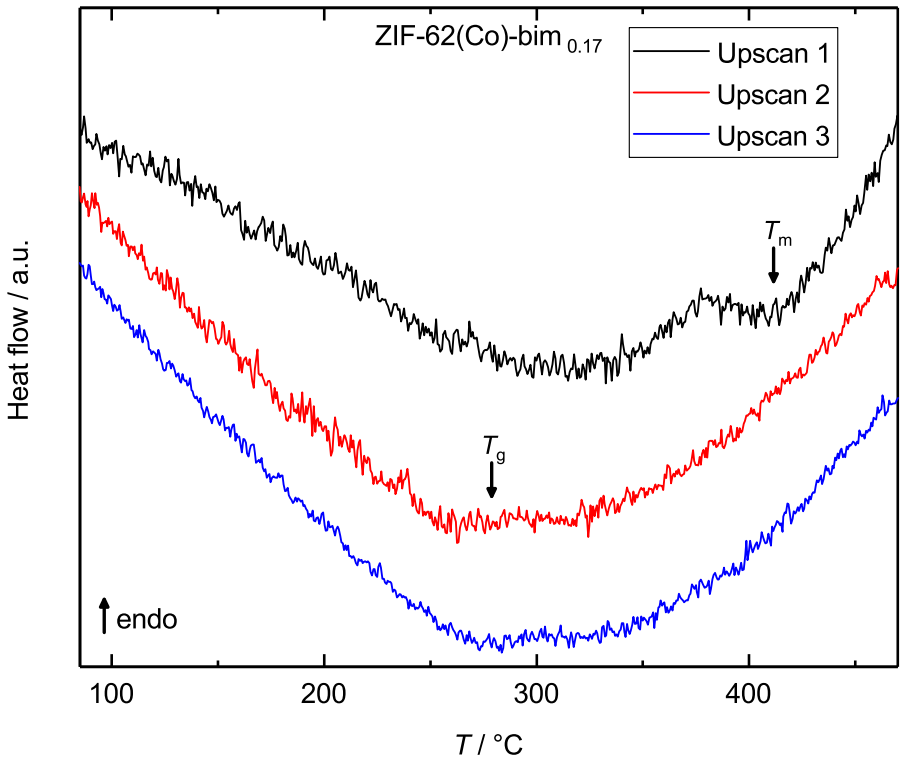

Figure A.113: DSC traces of the upscans of the TGA/DSC experiment for for ZIF-62(Co)-bim$_{0.17}$ conducting temperature program 2.

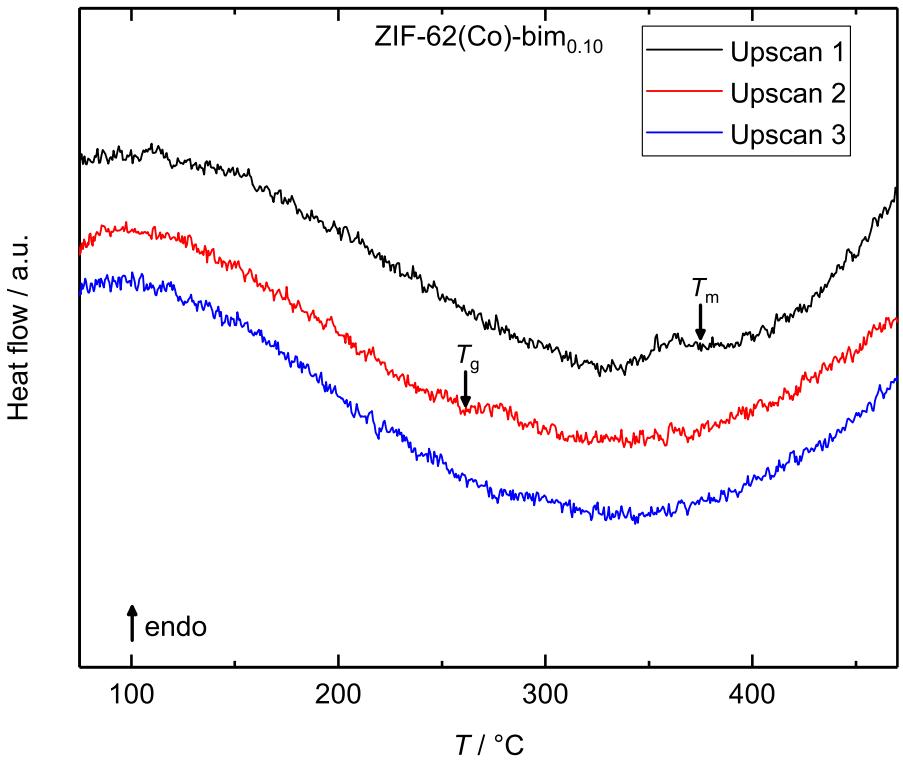

Figure A.114: DSC traces of the upscans of the TGA/DSC experiment for for ZIF-62(Co)-bim$_{0.10}$ conducting temperature program 2.

Table A.27: Thermodynamic values for the various ZIF-62(M)-bim$_x$ compounds calculated from the TGA/DSC experiments conducting program 2. Only for ZIF-62(Zn)-bim$_{0.02}$ program 3 was used showing solely the partial recrystallisation to ZIF-zni(Zn).

Compound	T_m / °C	ΔH_m / kJ mol^{-1}	ΔS_m / J mol^{-1} K^{-1}	T_g / °C	$T_g\ T_m^{-1}$ [a]
ZIF-62(Zn)-bim$_{0.35}$	441	2.46	3.45	320	0.83
ZIF-62(Zn)-bim$_{0.24}$	423	1.79	2.57	305	0.83
ZIF-62(Zn)-bim$_{0.17}$	409	1.08	1.58	303	0.85
ZIF-62(Zn)-bim$_{0.12}$	395	0.70	1.06	303	0.86
ZIF-62(Zn)-bim$_{0.07}$	380	0.49	0.75	298	0.87
ZIF-62(Zn)-bim$_{0.05}$	372	0.45	0.70	298	0.87
ZIF-62(Zn)-bim$_{0.03}$	370	0.44	0.68	292	0.88
ZIF-62(Zn)-bim$_{0.02}$	no melting but partial recrystallization to ZIF-zni(Zn)				
ZIF-62(Co)-bim$_{0.30}$	432	2.65	3.75	290	0.80
ZIF-62(Co)-bim$_{0.17}$	410	1.15	1.69	278	0.81
ZIF-62(Co)-bim$_{0.10}$	386	0.82	1.24	260	0.81

a Calculations were performed using temperature values in K.

A.3.8 Photographs

Figure A.115: Photographs of ZIF-62(M)-bim$_x$ materials after conducting temperature program 2 or 3. It becomes evident that all materials show signs of macroscopic flow and are molten to a monolith. This is even true for the partial recrystallized samples of ZIF-62(Zn)-bim$_{0.03}$ and ZIF-62(Zn)-bim$_{0.02}$.

B Appendix to Part II

B.1 Experimental Data to Section 10 – Amphiphile Salt Frameworks

B.1.1 Single Crystal X-ray Diffraction

Single crystal diffraction data were collected on an Oxford Diffraction Xcalibur, Agilent SuperNova or Bruker D8 Venture diffractometer utilizing MoK_α or CuK_α radiation. Raw data processing was performed with the APEX3 suite or CrysalisPro software package. Structure solution and refinement was conducting with the Olex2[48] graphical interface using SHELXS, SHELXT and SHELXL.[269] Twinned crystals were found for the data collections yielding the crystal structures for ASF-2(C5) and ASF-2(C6). In both cases the twin law [-1 0 0; 0 -1 0; 0 0 1] was determined with Olex2 and the respective two reflection sets were merged. If appropriate, a squeezing procedure[247] was applied on the datasets while data refinement with the implementation in Olex2[48] or for the twinned ASF-2(C5) dataset using the PLATON software package (see Table 10.1). The *.cifs are on the enclosed CD. All single crystals were selected directly after the synthesis from the mother liquor of the reaction mixture.

Crystal Structure of Na_2(ABB-C3yne)$(H_2O)_6$

In the crystal structure of Na_2(ABB-C3yne)$(H_2O)_6$ the Na^+ ions are not coordinating to O atoms of the ABB-3yne^{2-}. As a consequence, coordination occurs solely between water molecules and Na^+ ions (see Figure B.1). Five water molecules coordinate to one Na^+ ion and the coordination sphere is saturated by weak interaction of the side chains of the linker molecules resulting in a distorted square planar pyramidal coordination environment for $Na_2(H_2O)_5$ polyhedra. These polyhedra are connected by edge and corner sharing forming two dimensional layers. Between two adjacent layers, the deprotonated linker molecules are stacked, interacting by hydrogen bonding via their carboxylate oxygen atoms to these layers.

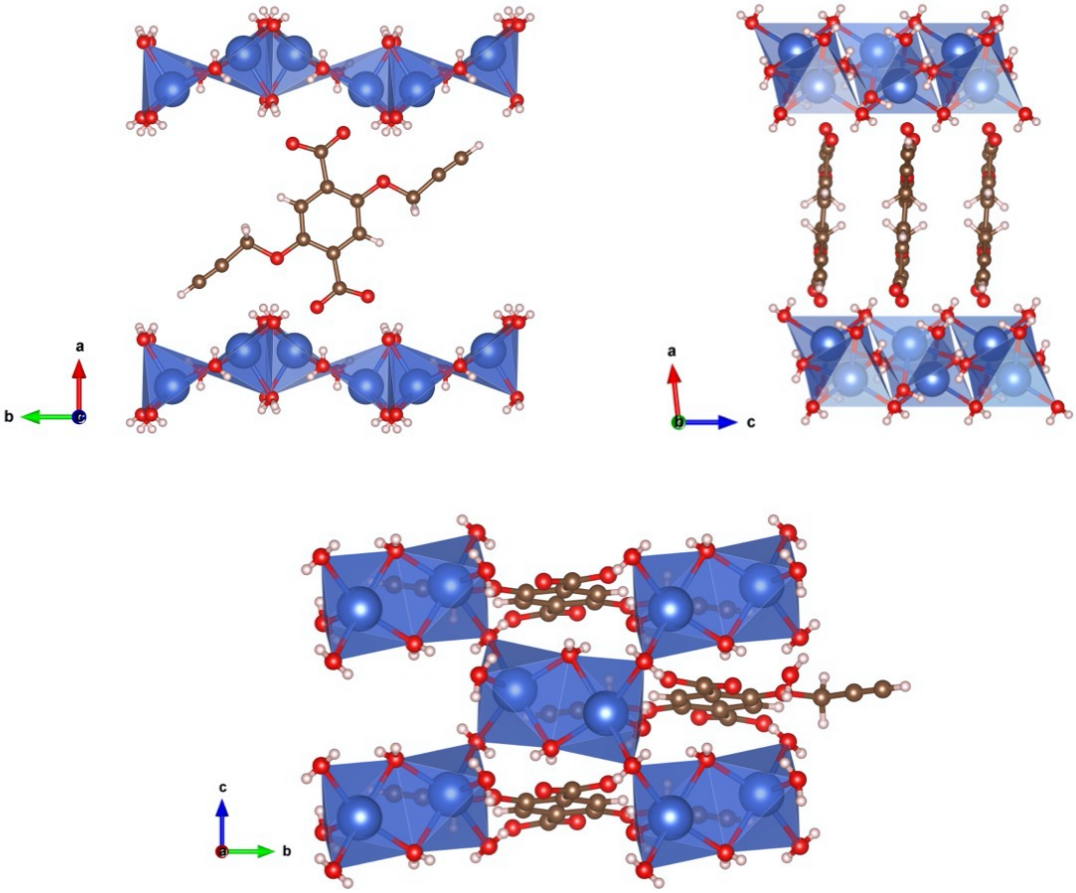

Figure B.1: Representation of the crystal structure of Na_2(ABB-C3yne)$(H_2O)_6$. Top-left: Packing of ABBs between Na^+ water layers, viewing along the crystallographic *c* axis. Top-right: Packing of ABBs between Na^+ water layers, viewing along the crystallographic *b* axis. Bottom: Top view on the two dimensional layered structure, the edge and corner sharing between $Na_2(H_2O)_5$ polyhedra becomes evident. Coordination environments of Na^+ are displayed as blue polyhedra. Color code: Na (blue); O (red); C (brown); H (white).

Table B.1: Crystallographic data for $Na_2(ABB\text{-}C3yne)(H_2O)_6$ obtained via SCXRD.

Compound	$Na_2(ABB\text{-}C3yne)(H_2O)_6$
Empirical formula	$C_{14}H_{20}O_{12}Na_2$
Formula weight / g mol^{-1}	426.29
Temperature / K	121(2)
Crystal system	monoclinic
Space group	$P2_1/c$
a / Å	12.6804(4)
b / Å	10.4191(3)
c / Å	7.0182(2)
α / Å	90
β / Å	96.281(3)
γ / Å	90
V / Å^3	921.67(5)
Z	2
ϱ_{calc} / g cm^{-3}	1.5359
μ / mm^{-1}	1.562
F(000)	446.3
Crystal size / mm^3	0.2542 × 0.1319 × 0.0976
Radiation	CuK_α (λ = 1.54184)
2Θ range for data collection / °	7.02 to 152.4
Index ranges	-15 ≤ h ≤ 15, -12 ≤ k ≤ 12, -8 ≤ l ≤ 8
Reflections collected	8653
Independent reflections	1903 [R_{int} = 0.0257, R_{sigma} = 0.0180]
Data/restraints/parameters	1903/0/143
Goodness-of-fit on F^2	1.057
Final R indexes [$I \geq 2\sigma$ (I)]	R_1 = 0.0531, wR_2 = 0.1633
Final R indexes [all data]	R_1 = 0.0567, wR_2 = 0.1676
Largest diff. peak/hole / e Å^{-3}	0.41/-0.35

B.1.2 In-House Powder X-ray Diffraction

PXRD data are sorted after the different performed synthesis routes.

Solvothermal Synthesis Route

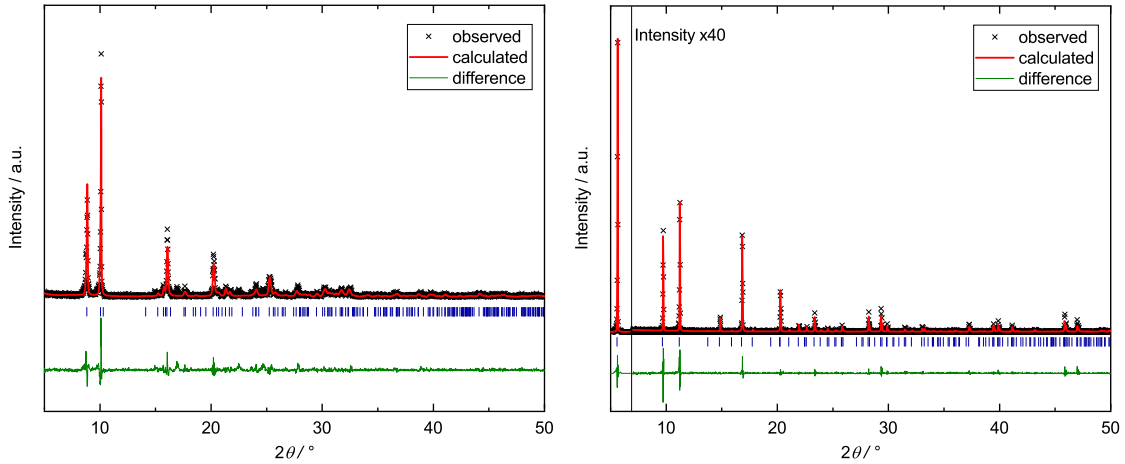

Figure B.2: PXRD pattern with structureless profile fit (Pawley method) of ASF-3(C2) (left) and ASF-1(C3) (right). Blue tick marks indicate the allowed Bragg peak positions.

Table B.2: Unit cell parameters determined by the above displayed structureless profile fits (Pawley method) of the obtained PXRD patterns and corresponding R_{wp}, R_{exp} and χ values.

Pawley fit Compound	Figure B.2 left ASF-3(C2)	Figure B.2 right ASF-1(C3)
crystal system	triclinic	trigonal
space group	$P\bar{1}$	$R\bar{3}c$
a / Å	6.486(2)	31.6644(16)
b / Å	9.901(6)	31.6644(16)
c / Å	11.235(7)	8.2074(11)
α / °	63.99(4)	90
β / °	78.09(6)	90
γ / °	76.89(6)	120
V / Å^3	626.8(6)	7126.5(12)
R_{wp} / %	37.27	26.57
R_{exp} / %	26.06	12.26
χ	1.43	2.17

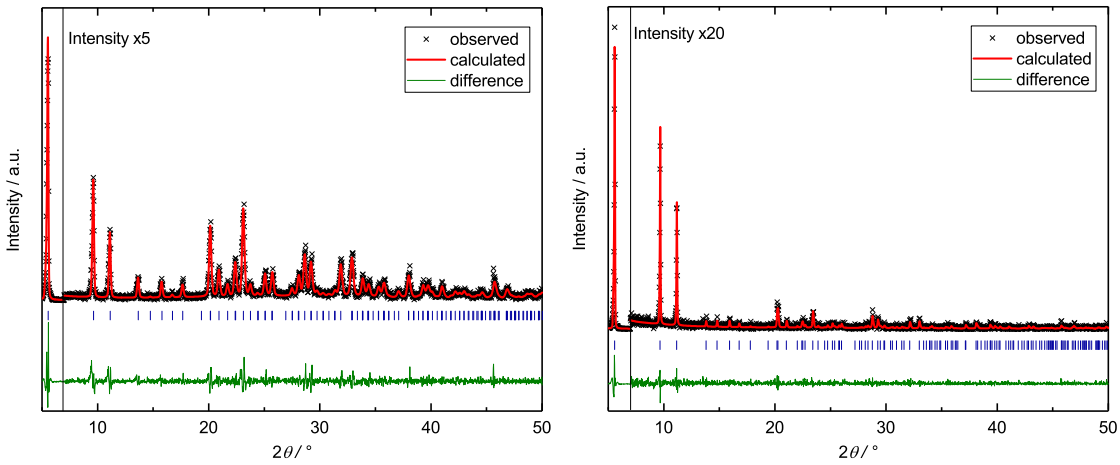

Figure B.3: PXRD pattern with structureless profile fit (Pawley method) of ASF-1(C3ene) (left) and ASF-1(C3yne) (right). Blue tick marks indicate the allowed Bragg peak positions.

Table B.3: Unit cell parameters determined by the above displayed structureless profile fits (Pawley method) of the obtained PXRD patterns and corresponding R_{wp}, R_{exp} and χ values.

Pawley fit Compound	Figure B.3 left ASF-1(C3ene)	Figure B.3 right ASF-1(C3yne)
crystal system	trigonal	trigonal
space group	$R\bar{3}c$	$R\bar{3}c$
a / Å	31.764(6)	31.694(4)
b / Å	31.764(6)	31.694(4)
c / Å	8.2749(13)	8.162(2)
α / °	90	90
β / °	90	90
γ / °	120	120
V / Å^3	7231(3)	7100(3)
R_{wp} / %	21.22	25.23
R_{exp} / %	14.69	18.69
χ	1.44	1.35

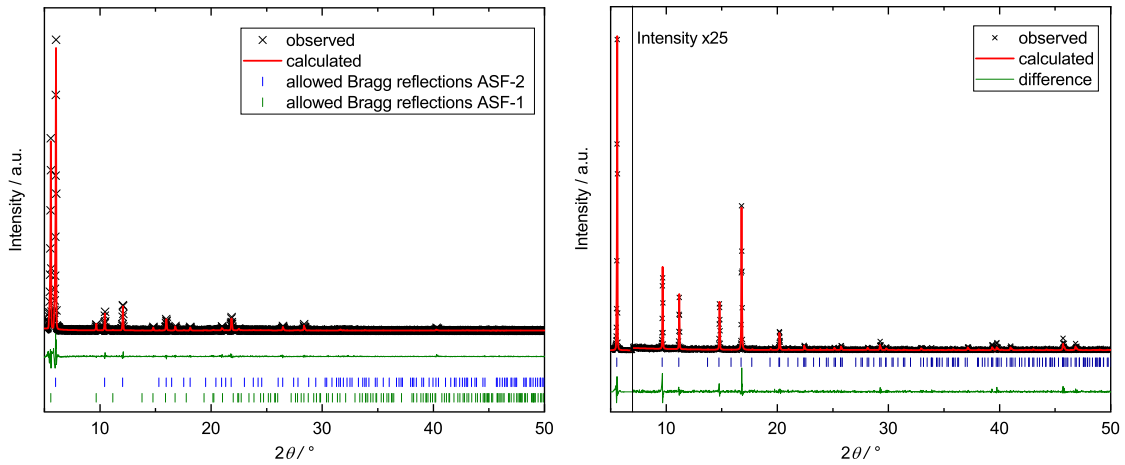

Figure B.4: Left: PXRD pattern obtained after the solvothermal synthesis with H_2ABB-C4. The dual phase Pawley fit verifies the formation of ASF-1(C4) and ASF-2(C4). Green tick marks indicate the allowed Bragg peak positions for the ASF-1 structure type. Blue tick marks indicate the allowed Bragg peak positions for the ASF-2 structure type. Right: PXRD pattern with structureless profile fit (Pawley method) of ASF-1(C4ene). Blue tick marks indicate the allowed Bragg peak positions.

Table B.4: Unit cell parameters determined by the above displayed structureless profile fits (Pawley method) of the obtained PXRD patterns and corresponding R_{wp}, R_{exp} and χ values.

Pawley fit	Figure B.4 left		Figure B.4 right
Compound	ASF-1(C4)	ASF-2(C4)	ASF-1(C4ene)
crystal system	trigonal	trigonal	trigonal
space group	$R\bar{3}c$	$R\bar{3}$	$R\bar{3}c$
a / Å	31.721(5)	29.371(3)	31.753(2)
b / Å	31.721(5)	29.371(3)	31.753(2)
c / Å	8.1633(19)	5.943(2)	8.220(6)
α / °	90	90	90
β / °	90	90	90
γ / °	120	120	120
V / Å^3	7114(3)	4440.2(17)	7178(5)
R_{wp} / %	32.96		24.25
R_{exp} / %	26.59		14.79
χ	1.24		1.64

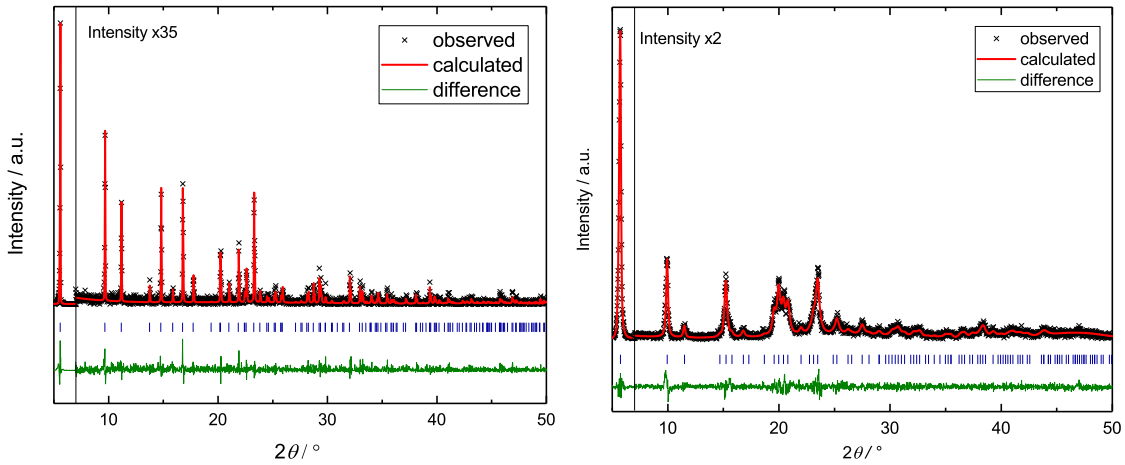

Figure B.5: PXRD pattern with structureless profile fit (Pawley method) of ASF-1(C4yne) (left) and ASF-2(C5) (right). Blue tick marks indicate the allowed Bragg peak positions.

Table B.5: Unit cell parameters determined by the above displayed structureless profile fits (Pawley method) of the obtained PXRD patterns and corresponding R_{wp}, R_{exp} and χ values.

Pawley fit Compound	Figure B.5 left ASF-1(C4yne)	Figure B.5 right ASF-2(C5)
crystal system	trigonal	trigonal
space group	$R\bar{3}c$	$R\bar{3}$
a / Å	31.719(2)	30.757(8)
b / Å	31.719(2)	30.757(8)
c / Å	8.2174(6)	6.190(3)
α / °	90	90
β / °	90	90
γ / °	120	120
V / Å^3	7160.1(10)	5072(4)
R_{wp} / %	31.20	18.77
R_{exp} / %	23.15	15.56
χ	1.35	1.21

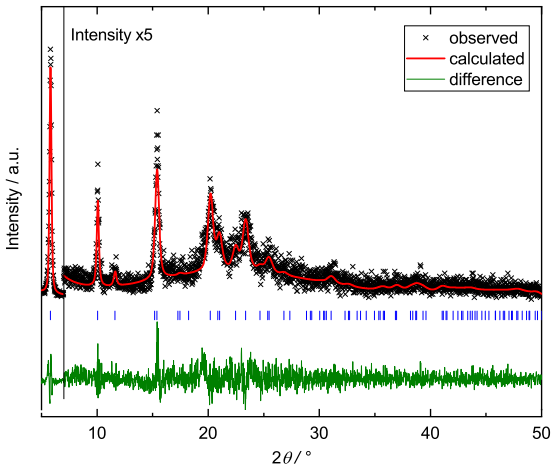

Figure B.6: PXRD pattern with structureless profile fit (Pawley method) of ASF-2(C6). Blue tick marks indicate the allowed Bragg peak positions.

Table B.6: Unit cell parameters determined by the above displayed structureless profile fits (Pawley method) of the obtained PXRD patterns and corresponding R_{wp}, R_{exp} and χ values.

Pawley fit Compound	Figure B.6 ASF-1(C4yne)
crystal system	trigonal
space group	$P3_1$
a / Å	17.57(3)
b / Å	17.57(3)
c / Å	6.31(3)
α / °	90
β / °	90
γ / °	120
V / Å^3	1689(11)
R_{wp} / %	25.97
R_{exp} / %	21.61
χ	1.20

Evaporation Synthesis Route (evap-a)

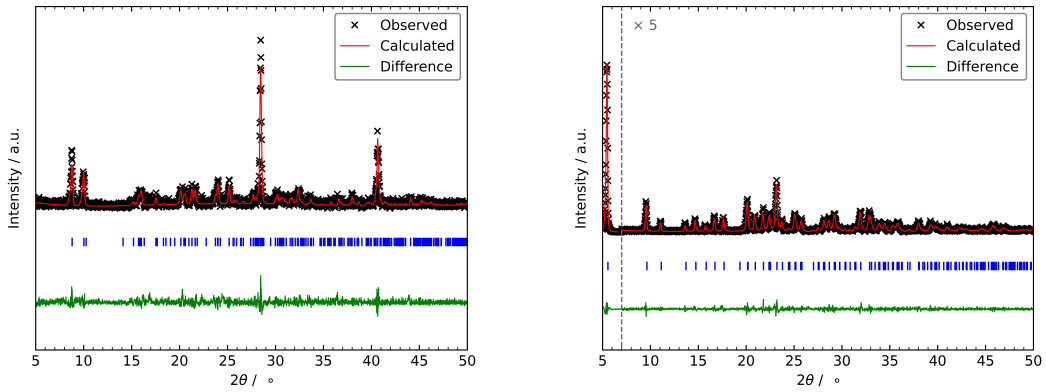

Figure B.7: PXRD pattern with structureless profile fit (Pawley method) of ASF-3(C2) (left) and ASF-1(C3) (right). Blue tick marks indicate the allowed Bragg peak positions.

Table B.7: Unit cell parameters determined by the above displayed structureless profile fits (Pawley method) of the obtained PXRD patterns and corresponding R_{wp}, R_{exp} and χ values.

Pawley fit Compound	Figure B.7 left ASF-3(C2)	Figure B.7 right ASF-1(C3)
crystal system	triclinic	trigonal
space group	$P\bar{1}$	$R\bar{3}c$
a / Å	6.4821(18)	31.744(5)
b / Å	9.934(2)	31.744(5)
c / Å	11.248(3)	8.2340(9)
α / °	63.923(18)	90
β / °	78.18(3)	90
γ / °	76.95(3)	120
V / Å^3	629.1(3)	7185(2)
R_{wp} / %	33.36	18.32
R_{exp} / %	27.11	15.18
χ	1.23	1.21

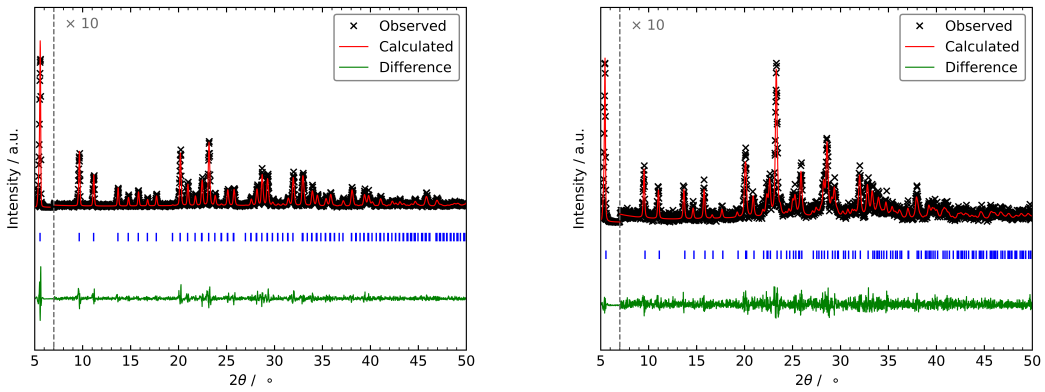

Figure B.8: PXRD pattern with structureless profile fit (Pawley method) of ASF-1(C3ene) (left) and ASF-1(C3yne) (right). Blue tick marks indicate the allowed Bragg peak positions.

Table B.8: Unit cell parameters determined by the above displayed structureless profile fits (Pawley method) of the obtained PXRD patterns and corresponding R_{wp}, R_{exp} and χ values.

Pawley fit Compound	Figure B.8 left ASF-1(C3ene)	Figure B.8 right ASF-1(C3yne)
crystal system	trigonal	trigonal
space group	$R\bar{3}c$	$R\bar{3}c$
a / Å	31.725(5)	31.794(5)
b / Å	31.725(5)	31.794(5)
c / Å	8.2650(11	8.1638(10)
α / °	90	90
β / °	90	90
γ / °	120	120
V / Å^3	7204(2)	7147(3)
R_{wp} / %	22.44	21.02
R_{exp} / %	13.71	18.55
χ	1.64	1.13

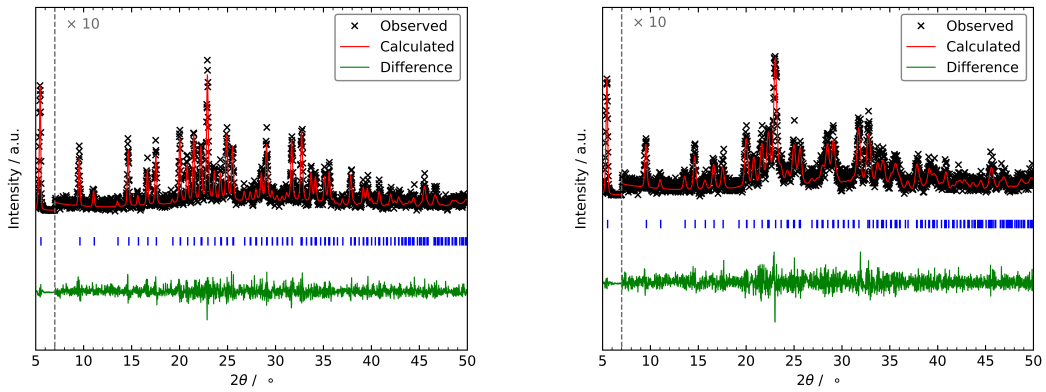

Figure B.9: PXRD pattern with structureless profile fit (Pawley method) of ASF-1(C4ene) (left) and ASF-1(C4yne) (right). Blue tick marks indicate the allowed Bragg peak positions.

Table B.9: Unit cell parameters determined by the above displayed structureless profile fits (Pawley method) of the obtained PXRD patterns and corresponding R_{wp}, R_{exp} and χ values.

Pawley fit Compound	Figure B.9 left ASF-1(C4ene)	Figure B.9 right ASF-1(C4yne)
crystal system	trigonal	trigonal
space group	$R\bar{3}c$	$R\bar{3}c$
a / Å	31.821(6)	31.914(12)
b / Å	31.821(6)	31.914(12)
c / Å	8.3381(12)	8.284(2)
α / °	90	90
β / °	90	90
γ / °	120	120
V / Å^3	7312(3)	7307(6)
R_{wp} / %	22.56	23.25
R_{exp} / %	19.63	20.97
χ	1.15	1.11

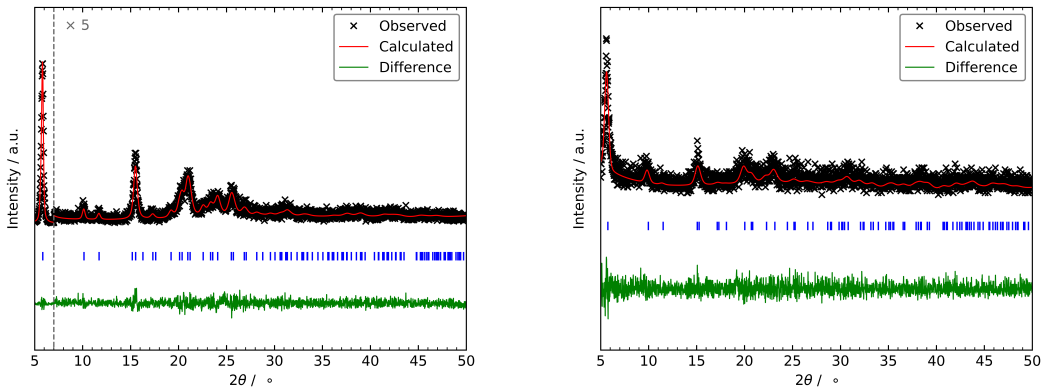

Figure B.10: PXRD pattern with structureless profile fit (Pawley method) of ASF-2(C5) (left) and ASF-2(C6) (right). Blue tick marks indicate the allowed Bragg peak positions.

Table B.10: Unit cell parameters determined by the above displayed structureless profile fits (Pawley method) of the obtained PXRD patterns and corresponding R_{wp}, R_{exp} and χ values.

Pawley fit Compound	Figure B.10 left ASF-2(C5)	Figure B.10 right ASF-2(C6)
crystal system	trigonal	trigonal
space group	$R\bar{3}$	$P3_1$
a / Å	30.18(3)	17.72(14)
b / Å	30.18(3)	17.72(14)
c / Å	5.980(10)	6.35(9)
α / °	90	90
β / °	90	90
γ / °	120	120
V / Å^3	4716(12)	1728(37)
R_{wp} / %	21.56	36.22
R_{exp} / %	19.03	32.20
χ	1.13	1.12

Evaporation Synthesis Route (evap-b)

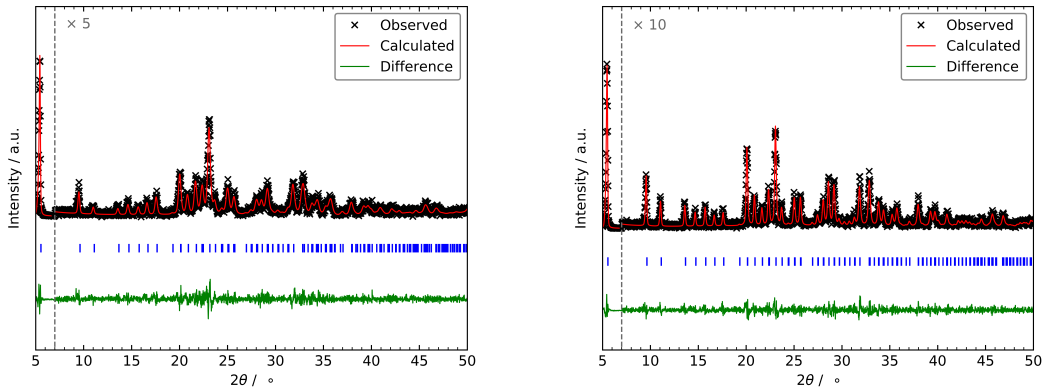

Figure B.11: PXRD pattern with structureless profile fit (Pawley method) of ASF-1(C3) (left) and ASF-1(C3ene) (right). Blue tick marks indicate the allowed Bragg peak positions.

Table B.11: Unit cell parameters determined by the above displayed structureless profile fits (Pawley method) of the obtained PXRD patterns and corresponding R_{wp}, R_{exp} and χ values.

Pawley fit Compound	Figure B.11 left ASF-1(C3)	Figure B.11 right ASF-1(C3ene)
crystal system	trigonal	trigonal
space group	$R\bar{3}c$	$R\bar{3}c$
a / Å	31.798(11)	31.761(5)
b / Å	31.798(11)	31.761(5)
c / Å	8.2532(15)	8.2728(10)
α / °	90	90
β / °	90	90
γ / °	120	120
V / Å^3	7227(5)	7227(2)
R_{wp} / %	23.79	19.80
R_{exp} / %	20.32	16.39
χ	1.17	1.21

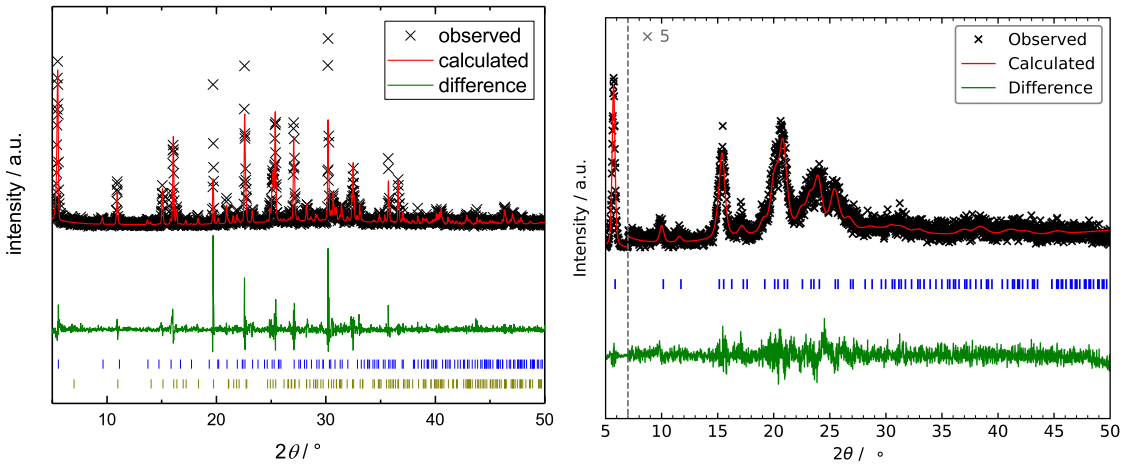

Figure B.12: Left: PXRD pattern obtained after the evaporation synthesis (evap-b) with H_2ABB-C3yne. The dual phase Pawley fit verifies the formation of Na_2(ABB-C3yne)$(H_2O)_6$ and ASF-1(C3ene). Yellow tick marks indicate the allowed Bragg peak positions for the Na_2(ABB-C3yne)$(H_2O)_6$ structure type. Blue tick marks indicate the allowed Bragg peak positions for the ASF-1 structure type. Right: PXRD pattern with structureless profile fit (Pawley method) of ASF-2(C5). Blue tick marks indicate the allowed Bragg peak positions.

Table B.12: Unit cell parameters determined by the above displayed structureless profile fits (Pawley method) of the obtained PXRD patterns and corresponding R_{wp}, R_{exp} and χ values.

Pawley fit	Figure B.12 left		Figure B.12 right
Compound	Na_2(ABB-C3yne)$(H_2O)_6$	ASF-1(C3yne)	ASF-2(C5)
crystal system	moniclinic	trigonal	trigonal
space group	$P2_1/c$	$R\bar{3}c$	$R\bar{3}$
a / Å	12.695(2)	31.781(5)	30.15(18)
b / Å	10.450(2)	31.781(5)	30.15(18)
c / Å	7.1105(7)	8.1998(12)	5.99(3)
α / °	90	90	90
β / °	96.087(8)	90	90
γ / °	90	120	120
V / Å^3	938.0(3)	7173(2)	4719(60)
R_{wp} / %	29.25		22.33
R_{exp} / %	21.03		18.52
χ	1.39		1.21

B.1.3 High-Pressure Powder X-ray Diffraction

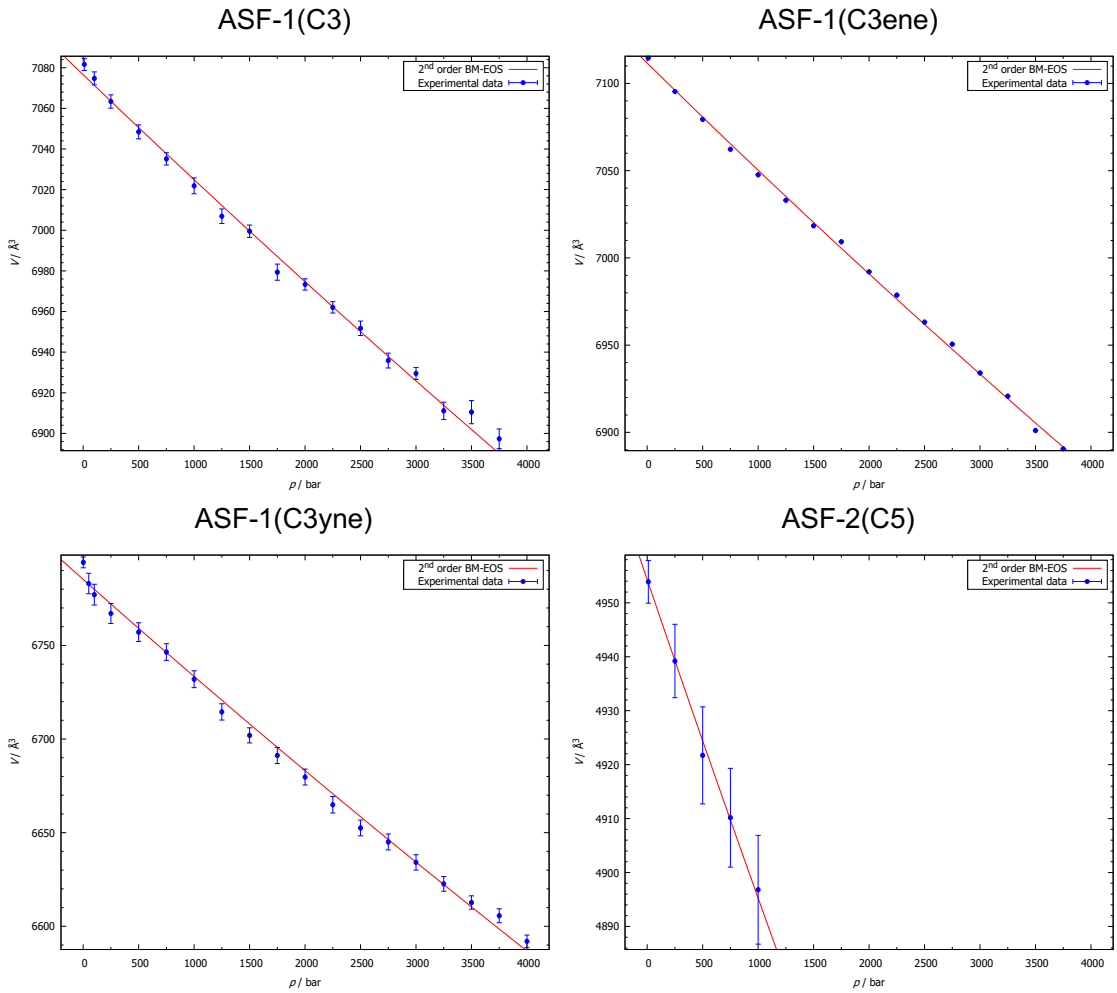

Figure B.13: Plots of fits of the 2nd order Burch-Murnaghan equation of state on the pressure dependent volume data ($V(p)$) obtained from sequential profile fitting (Pawley method) of HP-PXRD data for ASFs.

HP-PXRD Data for ASF-1(C3)

Table B.13: Unit cell parameters and goodness values obtained from the sequential profile fits (Pawley method) of the HP-PXRD data for ASF-1(C3).

pressure / bar	10	100	250	500
crystal system	trigonal	trigonal	trigonal	trigonal
space group	$R\bar{3}c$	$R\bar{3}c$	$R\bar{3}c$	$R\bar{3}c$
a / Å	31.596(6)	31.589(7)	31.580(7)	31.568(7)
b / Å	31.596(6)	31.589(7)	31.580(7)	31.568(7)
c / Å	8.1908(12)	8.1866(12)	8.1781(13)	8.1670(13)
α / °	90	90	90	90
β / °	90	90	90	90
γ / °	120	120	120	120
V / Å^3	7082(3)	7075(3)	7063(3)	7048(3)
R_{wp} / %	2.50	2.53	2.52	2.41
R_{exp} / %	4.35	4.68	5.02	5.35
χ	0.58	0.54	0.50	0.45

Table B.14: Unit cell parameters and goodness values obtained from the sequential profile fits (Pawley method) of the HP-PXRD data for ASF-1(C3).

pressure / bar	750	1000	1250	1500
crystal system	trigonal	trigonal	trigonal	trigonal
space group	$R\bar{3}c$	$R\bar{3}c$	$R\bar{3}c$	$R\bar{3}c$
a / Å	31.563(6)	31.560(8)	31.548(8)	31.549(6)
b / Å	31.563(6)	31.560(8)	31.548(8)	31.549(6)
c / Å	8.1541(12)	8.1405(16)	8.1293(15)	8.1201(14)
α / °	90	90	90	90
β / °	90	90	90	90
γ / °	120	120	120	120
V / Å^3	7035(3)	7022(4)	7007(4)	7000(3)
R_{wp} / %	2.05	2.41	2.19	1.80
R_{exp} / %	5.73	6.09	6.43	6.76
χ	0.36	0.40	0.34	0.27

Table B.15: Unit cell parameters and goodness values obtained from the sequential profile fits (Pawley method) of the HP-PXRD data for ASF-1(C3).

pressure / bar	1750	2000	2250	2500
crystal system	trigonal	trigonal	trigonal	trigonal
space group	$R\bar{3}c$	$R\bar{3}c$	$R\bar{3}c$	$R\bar{3}c$
a / Å	31.535(8)	31.539(6)	31.534(6)	31.530(7)
b / Å	31.535(8)	31.539(6)	31.534(6)	31.530(7)
c / Å	8.1040(19)	8.0949(13)	8.0845(13)	8.0744(17)
α / °	90	90	90	90
β / °	90	90	90	90
γ / °	120	120	120	120
V / Å^3	6979(4)	6973(3)	6962(3)	6952(4)
R_{wp} / %	2.20	2.24	2.04	2.44
R_{exp} / %	7.23	5.10	5.39	5.45
χ	0.30	0.44	0.38	0.45

Table B.16: Unit cell parameters and goodness values obtained from the sequential profile fits (Pawley method) of the HP-PXRD data for ASF-1(C3).

pressure / bar	2750	3000	3250	3500
crystal system	trigonal	trigonal	trigonal	trigonal
space group	$R\bar{3}c$	$R\bar{3}c$	$R\bar{3}c$	$R\bar{3}c$
a / Å	31.522(8)	31.529(6)	31.508(9)	31.520(11)
b / Å	31.522(8)	31.529(6)	31.508(9)	31.520(11)
c / Å	8.0603(18)	8.0493(16)	8.039(2)	8.032(3)
α / °	90	90	90	90
β / °	90	90	90	90
γ / °	120	120	120	120
V / Å^3	6936(4)	6930(3)	6911(4)	6910(6)
R_{wp} / %	2.08	1.93	2.29	2.86
R_{exp} / %	5.85	5.55	5.91	6.31
χ	0.35	0.35	0.39	0.45

Table B.17: Unit cell parameters and goodness values obtained from the sequential profile fits (Pawley method) of the HP-PXRD data for ASF-1(C3).

pressure / bar	3750
crystal system	trigonal
space group	$R\bar{3}c$
a / Å	31.505(9)
b / Å	31.505(9)
c / Å	8.024(3)
α / °	90
β / °	90
γ / °	120
V / Å^3	6897(5)
R_{wp} / %	2.28
R_{exp} / %	6.73
χ	0.34

Table B.18: Unit cell parameters and goodness values obtained from the sequential profile fits (Pawley method) of the HP-PXRD data for ASF-1(C3).

pressure / bar	1 (return)
crystal system	trigonal
space group	$R\bar{3}c$
a / Å	31.593(7)
b / Å	31.593(7)
c / Å	8.1879(14)
α / °	90
β / °	90
γ / °	120
V / Å^3	7078(4)
R_{wp} / %	2.52
R_{exp} / %	7.26
χ	0.35

HP-PXRD Data for ASF-1(C3ene)

Table B.19: Unit cell parameters and goodness values obtained from the sequential profile fits (Pawley method) of the HP-PXRD data for ASF-1(C3ene).

pressure / bar	10	250	500	750
crystal system	trigonal	trigonal	trigonal	trigonal
space group	$R\bar{3}c$	$R\bar{3}c$	$R\bar{3}c$	$R\bar{3}c$
a / Å	31.587(4)	31.569(5)	31.562(4)	31.546(4)
b / Å	31.587(4)	31.569(5)	31.562(4)	31.546(4)
c / Å	8.2338(6)	8.2208(7)	8.2063(6)	8.1944(6)
α / °	90	90	90	90
β / °	90	90	90	90
γ / °	120	120	120	120
V / Å^3	7115(2)	7095(2)	7079.4(20)	7062.3(20)
R_{wp} / %	1.28	1.30	1.25	1.24
R_{exp} / %	4.98	5.12	5.28	5.46
χ	0.26	0.25	0.24	0.23

Table B.20: Unit cell parameters and goodness values obtained from the sequential profile fits (Pawley method) of the HP-PXRD data for ASF-1(C3ene).

pressure / bar	1000	1250	1500	1750
crystal system	trigonal	trigonal	trigonal	trigonal
space group	$R\bar{3}c$	$R\bar{3}c$	$R\bar{3}c$	$R\bar{3}c$
a / Å	31.539(4)	31.527(4)	31.519(4)	31.523(4)
b / Å	31.539(4)	31.527(4)	31.519(4)	31.523(4)
c / Å	8.1814(6)	8.1704(6)	8.1576(6)	8.1451(6)
α / °	90	90	90	90
β / °	90	90	90	90
γ / °	120	120	120	120
V / Å^3	7047.6(18)	7033.0(19)	7018.4(18)	7009(2)
R_{wp} / %	1.15	1.18	1.13	1.24
R_{exp} / %	5.58	5.70	5.81	4.36
χ	0.21	0.21	0.19	0.28

Table B.21: Unit cell parameters and goodness values obtained from the sequential profile fits (Pawley method) of the HP-PXRD data for ASF-1(C3ene).

pressure / bar	2000	2250	2500	2750
crystal system	trigonal	trigonal	trigonal	trigonal
space group	$R\bar{3}c$	$R\bar{3}c$	$R\bar{3}c$	$R\bar{3}c$
a / Å	31.509(4)	31.502(4)	31.490(3)	31.488(4)
b / Å	31.509(4)	31.502(4)	31.490(3)	31.488(4)
c / Å	8.1319(6)	8.1201(6)	8.1073(5)	8.0945(6)
α / °	90	90	90	90
β / °	90	90	90	90
γ / °	120	120	120	120
V / Å^3	6991.6(19)	6978.5(19)	6962.5(16)	6950.3(17)
R_{wp} / %	1.12	1.08	0.95	0.92
R_{exp} / %	4.73	5.01	5.27	5.52
χ	0.24	0.22	0.18	0.17

Table B.22: Unit cell parameters and goodness values obtained from the sequential profile fits (Pawley method) of the HP-PXRD data for ASF-1(C3ene).

pressure / bar	3000	3250	3500	3750
crystal system	trigonal	trigonal	trigonal	trigonal
space group	$R\bar{3}c$	$R\bar{3}c$	$R\bar{3}c$	$R\bar{3}c$
a / Å	31.472(4)	31.468(4)	31.450(4)	31.441(4)
b / Å	31.472(4)	31.468(4)	31.450(4)	31.441(4)
c / Å	8.0829(6)	8.0703(6)	8.0569(6)	8.0484(7)
α / °	90	90	90	90
β / °	90	90	90	90
γ / °	120	120	120	120
V / Å^3	6933.6(17)	6920.8(18)	6901.2(17)	6890.2(19)
R_{wp} / %	0.88	0.79	0.76	0.83
R_{exp} / %	5.79	6.18	6.43	6.63
χ	0.15	0.13	0.12	0.13

Table B.23: Unit cell parameters and goodness values obtained from the sequential profile fits (Pawley method) of the HP-PXRD data for ASF-1(C3ene).

pressure / bar	1 (return)
crystal system	trigonal
space group	$R\bar{3}c$
a / Å	31.577(5)
b / Å	31.577(5)
c / Å	8.2307(7)
α / °	90
β / °	90
γ / °	120
V / Å^3	7108(2)
R_{wp} / %	1.02
R_{exp} / %	7.02
χ	0.14

HP-PXRD Data for ASF-1(C3yne)

Table B.24: Unit cell parameters and goodness values obtained from the sequential profile fits (Pawley method) of the HP-PXRD data for ASF-1(C3yne).

pressure / bar	1	50	100	250
crystal system	trigonal	trigonal	trigonal	trigonal
space group	$R\bar{3}c$	$R\bar{3}c$	$R\bar{3}c$	$R\bar{3}c$
a / Å	31.231(6)	31.218(12)	31.210(11)	31.199(12)
b / Å	31.231(6)	31.218(12)	31.210(11)	31.199(12)
c / Å	8.0437(11)	8.037(2)	8.0340(20)	8.0276(18)
α / °	90	90	90	90
β / °	90	90	90	90
γ / °	120	120	120	120
V / Å^3	6794(3)	6783(5)	6777(5)	6767(6)
R_{wp} / %	1.46	1.90	1.75	1.58
R_{exp} / %	2.45	2.52	2.60	2.89
χ	0.60	0.76	0.67	0.55

Table B.25: Unit cell parameters and goodness values obtained from the sequential profile fits (Pawley method) of the HP-PXRD data for ASF-1(C3yne).

pressure / bar	500	750	1000	1250
crystal system	trigonal	trigonal	trigonal	trigonal
space group	$R\bar{3}c$	$R\bar{3}c$	$R\bar{3}c$	$R\bar{3}c$
a / Å	31.203(11)	31.202(9)	31.195(9)	31.179(9)
b / Å	31.203(11)	31.202(9)	31.195(9)	31.179(9)
c / Å	8.0138(17)	8.0011(16)	7.9876(17)	7.9757(16)
α / °	90	90	90	90
β / °	90	90	90	90
γ / °	120	120	120	120
V / Å^3	6757(5)	6746(4)	6732(4)	6715(4)
R_{wp} / %	1.46	1.33	1.31	1.26
R_{exp} / %	3.19	3.51	3.78	4.09
χ	0.46	0.38	0.35	0.31

Table B.26: Unit cell parameters and goodness values obtained from the sequential profile fits (Pawley method) of the HP-PXRD data for ASF-1(C3yne).

pressure / bar	1500	1750	2000	2250
crystal system	trigonal	trigonal	trigonal	trigonal
space group	$R\bar{3}c$	$R\bar{3}c$	$R\bar{3}c$	$R\bar{3}c$
a / Å	31.172(9)	31.166(9)	31.160(9)	31.149(9)
b / Å	31.172(9)	31.166(9)	31.160(9)	31.149(9)
c / Å	7.9633(17)	7.9537(18)	7.9436(19)	7.932(2)
α / °	90	90	90	90
β / °	90	90	90	90
γ / °	120	120	120	120
V / Å^3	6701(4)	6691(4)	6679(4)	6665(4)
R_{wp} / %	1.35	1.41	1.40	1.44
R_{exp} / %	3.51	2.87	2.94	2.88
χ	0.38	0.49	0.48	0.50

Table B.27: Unit cell parameters and goodness values obtained from the sequential profile fits (Pawley method) of the HP-PXRD data for ASF-1(C3yne).

pressure / bar	2500	2750	3000	3250
crystal system	trigonal	trigonal	trigonal	trigonal
space group	$R\bar{3}c$	$R\bar{3}c$	$R\bar{3}c$	$R\bar{3}c$
a / Å	31.139(9)	31.139(9)	31.137(9)	31.129(8)
b / Å	31.139(9)	31.139(9)	31.137(9)	31.129(8)
c / Å	7.923(2)	7.913(2)	7.901(2)	7.892(2)
α / °	90	90	90	90
β / °	90	90	90	90
γ / °	120	120	120	120
V / Å^3	6653(4)	6645(4)	6634(4)	6622(4)
R_{wp} / %	1.35	1.27	1.21	1.17
R_{exp} / %	2.92	2.95	2.98	3.00
χ	0.46	0.43	0.41	0.39

Table B.28: Unit cell parameters and goodness values obtained from the sequential profile fits (Pawley method) of the HP-PXRD data for ASF-1(C3yne).

pressure / bar	3500	3750	4000
crystal system	trigonal	trigonal	trigonal
space group	$R\bar{3}c$	$R\bar{3}c$	$R\bar{3}c$
a / Å	31.121(7)	31.116(8)	31.101(7)
b / Å	31.121(7)	31.116(8)	31.101(7)
c / Å	7.883(2)	7.877(2)	7.870(2)
α / °	90	90	90
β / °	90	90	90
γ / °	120	120	120
V / Å^3	6612(4)	6605(4)	6593(3)
R_{wp} / %	1.06	1.09	1.00
R_{exp} / %	3.03	3.04	3.05
χ	0.35	0.36	0.33

Table B.29: Unit cell parameters and goodness values obtained from the sequential profile fits (Pawley method) of the HP-PXRD data for ASF-1(C3yne).

pressure / bar	1 (return)
crystal system	trigonal
space group	$R\bar{3}c$
a / Å	31.234(5)
b / Å	31.234(5)
c / Å	8.0459(14)
α / °	90
β / °	90
γ / °	120
V / Å^3	6798(4)
R_{wp} / %	1.31
R_{exp} / %	3.12
χ	0.42

HP-PXRD Data for ASF-2(C5)

Table B.30: Unit cell parameters and goodness values obtained from the sequential profile fits (Pawley method) of the HP-PXRD data for ASF-2(C5).

pressure / bar	10	250	500	750
crystal system	trigonal	trigonal	trigonal	trigonal
space group	$R\bar{3}$	$R\bar{3}$	$R\bar{3}$	$R\bar{3}$
a / Å	30.462(9)	30.426(13)	30.385(17)	30.365(17)
b / Å	30.462(9)	30.426(13)	30.385(17)	30.365(17)
c / Å	6.165(4)	6.161(7)	6.156(9)	6.149(9)
α / °	90	90	90	90
β / °	90	90	90	90
γ / °	120	120	120	120
V / Å^3	4954(4)	4939(7)	4922(9)	4910(9)
R_{wp} / %	1.17	0.99	1.08	1.01
R_{exp} / %	2.64	2.38	2.47	2.56
χ	0.44	0.42	0.44	0.39

Table B.31: Unit cell parameters and goodness values obtained from the sequential profile fits (Pawley method) of the HP-PXRD data for ASF-2(C5).

pressure / bar	1000	1250	1500	1750
crystal system	trigonal	trigonal	trigonal	trigonal
space group	$R\bar{3}$	$R\bar{3}$	$R\bar{3}$	$R\bar{3}$
a / Å	30.339(19)	30.23(2)	30.094(17)	29.88(2)
b / Å	30.339(19)	30.23(2)	30.094(17)	29.88(2)
c / Å	6.143(10)	6.107(14)	6.038(14)	5.947(15)
α / °	90	90	90	90
β / °	90	90	90	90
γ / °	120	120	120	120
V / Å^3	4897(10)	4834(13)	4736(12)	4599(13)
R_{wp} / %	0.96	0.98	0.79	0.68
R_{exp} / %	2.54	2.67	2.80	2.93
χ	0.38	0.37	0.28	0.23

Table B.32: Unit cell parameters and goodness values obtained from the sequential profile fits (Pawley method) of the HP-PXRD data for ASF-2(C5).

pressure / bar	2000	2250	2500	2750
crystal system	trigonal	trigonal	trigonal	trigonal
space group	$R\bar{3}$	$R\bar{3}$	$R\bar{3}$	$R\bar{3}$
a / Å	29.78(2)	29.72(3)	29.452(12)	29.405(13)
b / Å	29.78(2)	29.72(3)	29.452(12)	29.405(13)
c / Å	5.889(13)	5.850(11)	5.840(4)	5.828(4)
α / °	90	90	90	90
β / °	90	90	90	90
γ / °	120	120	120	120
V / Å^3	4523(12)	4474(12)	4387(4)	4364(5)
R_{wp} / %	0.68	0.71	0.80	0.81
R_{exp} / %	3.05	2.97	2.88	2.78
χ	0.22	0.24	0.28	0.29

Table B.33: Unit cell parameters and goodness values obtained from the sequential profile fits (Pawley method) of the HP-PXRD data for ASF-2(C5).

pressure / bar	3000	3250	3500	3750
crystal system	trigonal	trigonal	trigonal	trigonal
space group	$R\bar{3}$	$R\bar{3}$	$R\bar{3}$	$R\bar{3}$
a / Å	29.379(14)	29.342(16)	29.290(14)	29.256(13)
b / Å	29.379(14)	29.342(16)	29.290(14)	29.256(13)
c / Å	5.818(4)	5.810(4)	5.805(4)	5.800(4)
α / °	90	90	90	90
β / °	90	90	90	90
γ / °	120	120	120	120
V / Å^3	4349(5)	4332(6)	4313(5)	4300(5)
R_{wp} / %	0.80	0.82	0.84	0.88
R_{exp} / %	2.71	2.71	2.81	2.83
χ	0.30	0.30	0.30	0.31

Table B.34: Unit cell parameters and goodness values obtained from the sequential profile fits (Pawley method) of the HP-PXRD data for ASF-2(C5).

pressure / bar	1 (return)
crystal system	trigonal
space group	$R\bar{3}$
a / Å	29.966(6)
b / Å	29.966(6)
c / Å	5.943(2)
α / °	90
β / °	90
γ / °	120
V / Å^3	4622(2)
R_{wp} / %	0.87
R_{exp} / %	3.03
χ	0.29

B.1.4 Fourier-Transform Infrared Spectroscopy

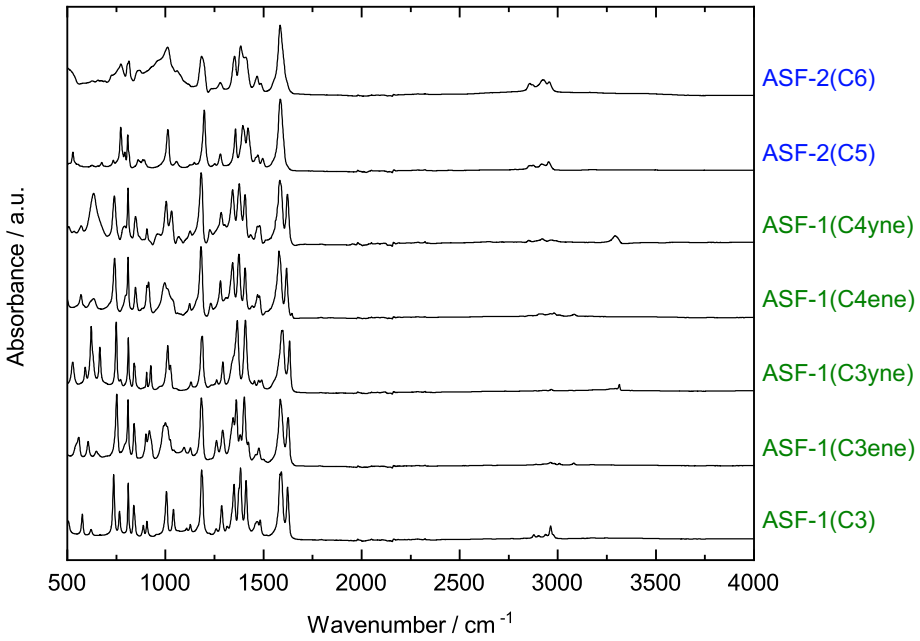

Figure B.14: FTIR spectroscopy data of ASFs obtained after the evaporation synthesis route at 80 °C in a rotary evaporator (evap-a).

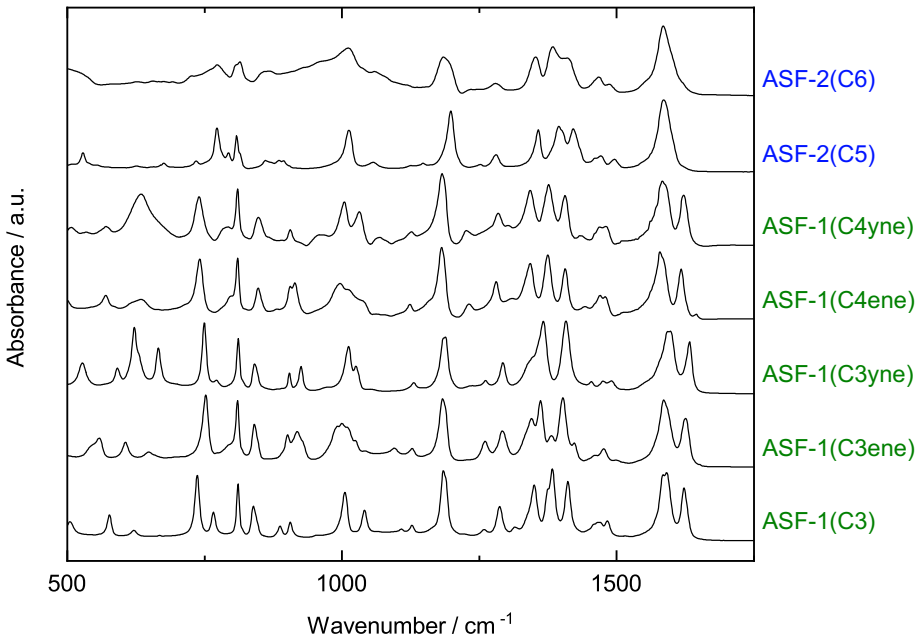

Figure B.15: FTIR spectroscopy data of ASFs obtained after the evaporation synthesis route at 80 °C in a rotary evaporator (evap-a). Zoom into the region 500-1750 cm^{-1}.

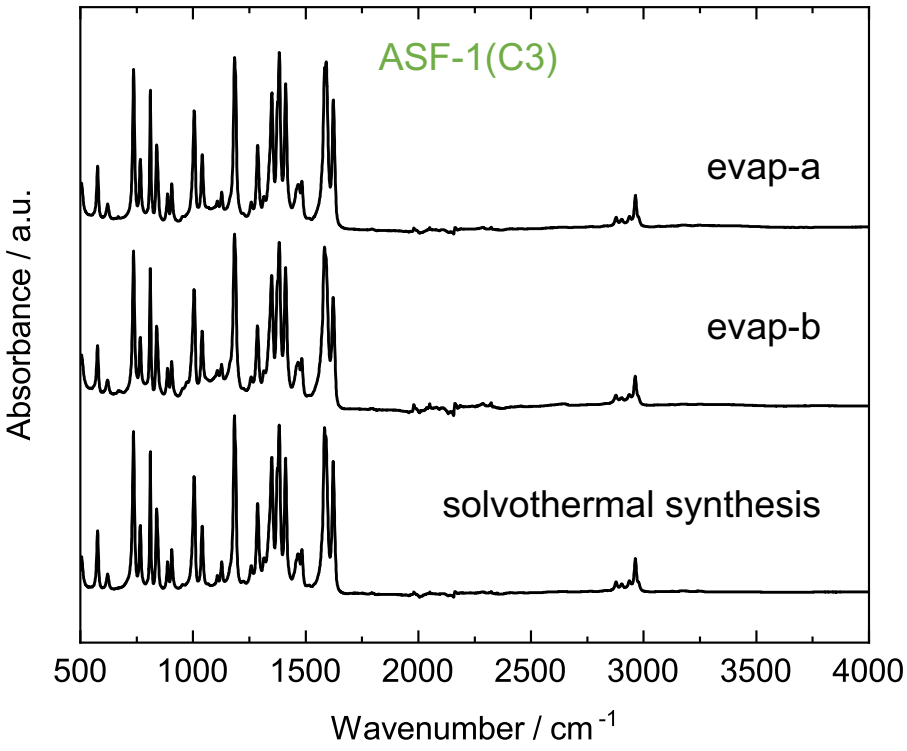

Figure B.16: Stacked Plot of FTIR spectroscopy data for ASF-1(C3) obtained after the three different synthesis routes.

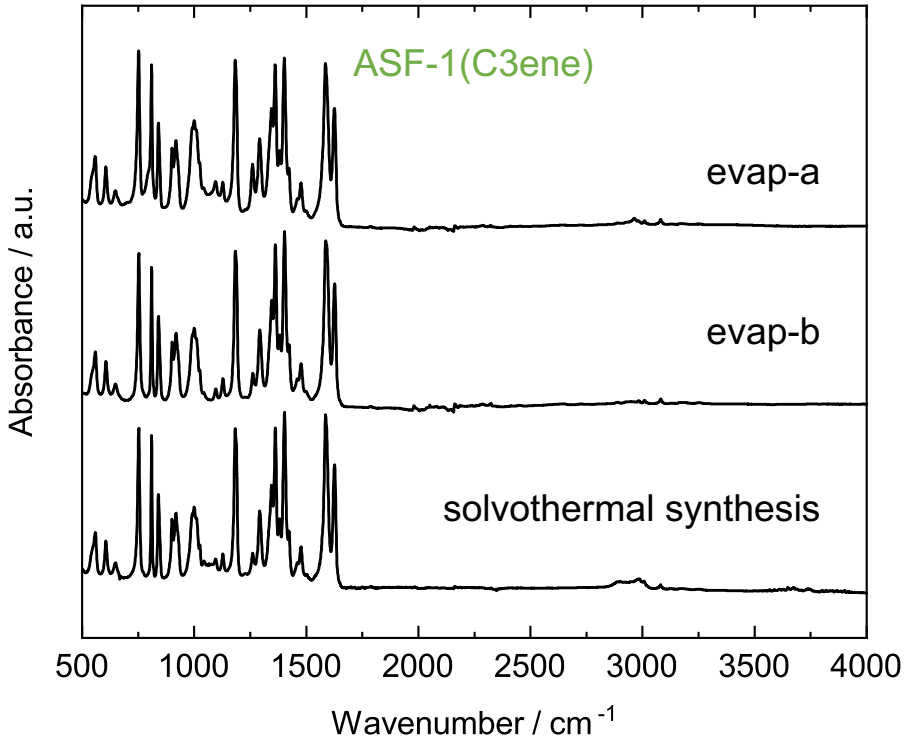

Figure B.17: Stacked Plot of FTIR spectroscopy data for ASF-1(C3ene) obtained after the three different synthesis routes.

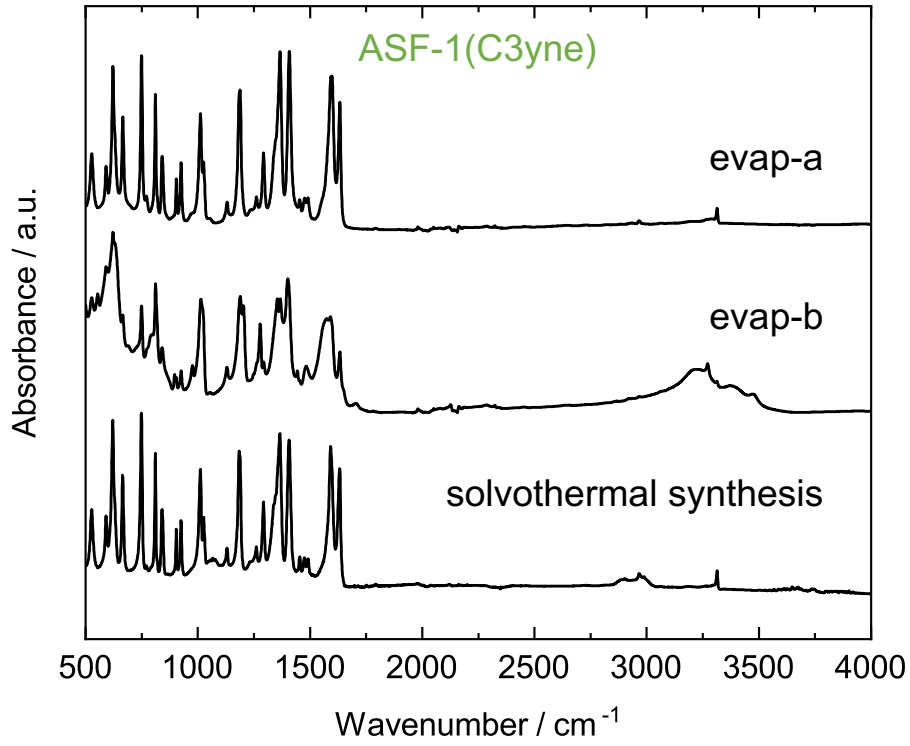

Figure B.18: Stacked Plot of FTIR spectroscopy data for ASF-1(C3yne) obtained after the three different synthesis routes. It has to be noted that method evap-b yields a phase mixture of ASF-1(C3yne) and a hydrate phase as found by PXRD data (see Section B.1.1 for a crystal structure description and Section B.1.2 for a profile fit to PXRD data verifying the formation of two phases).

B.1.5 Gas Physisorption

Additional Gas Physisorption Isotherms

Table B.35: Maximum gas adsorption capacities at ≈ 95 kPa of ASFs obtained after the solvothermal synthesis route.

Gas	N_2	CO_2	*n*-butane	propane	propylene
Temperature	77 K	195 K	273 K	273 K	273 K
ASF-2(C5)	3.23	2.08	1.10	1.00	1.08
ASF-1(C3)	2.32	1.20	0.85	0.70	0.72
ASF-1(C3ene)	4.26	2.72	1.14	0.95	0.99
ASF-1(C3yne)	0.73	4.09	0.80	0.79	0.94

Table B.36: Maximum gas adsorption capacities at ≈ 95 kPa[b] of ASFs obtained after an evaporation synthesis route – method evap-a.

Gas	CO_2	*n*-butane	propane	propylene
Temperature	195 K	273 K	273 K	273 K
ASF-2(C5)	1.10	0.81	0.52	0.80
ASF-1(C3)	1.15	0.86	0.74	0.76
ASF-1(C3ene)	2.21	0.73	0.62	0.76
ASF-1(C3yne)	3.22	0.81	0.75	0.87

b Notice, to determine the maximum gas adsorption capacities for *n*-butane of ASF-1(C3) and ASF-1(C3yne) a pressure of ≈ 75 kPa was used. This was neccessary due to starting of gas condensation on presumably particle surfaces at higher pressures (steep rise of isotherm).

Table B.37: Maximum gas adsorption capacities at ≈ 95 kPa[a] of ASFs obtained after an evaporation synthesis route − method evap-b.

Gas	CO_2	*n*-butane	propane	propylene
Temperature	195 K	273 K	273 K	273 K
ASF-2(C5)	1.35	1.04	0.85	0.84
ASF-1(C3)	-	-	-	-
ASF-1(C3ene)	2.40	0.88	0.82	0.87
ASF-1(C3yne)	-	-	-	-

a Notice, to determine the maximum gas adsorption capacities for *n*-butane of ASF-1(C3ene) and ASF-2(C5) a pressure of ≈ 85 kPa was used. This was neccessary due to starting of gas condensation on presumably particle surfaces at higher pressures (steep rise of isotherm).

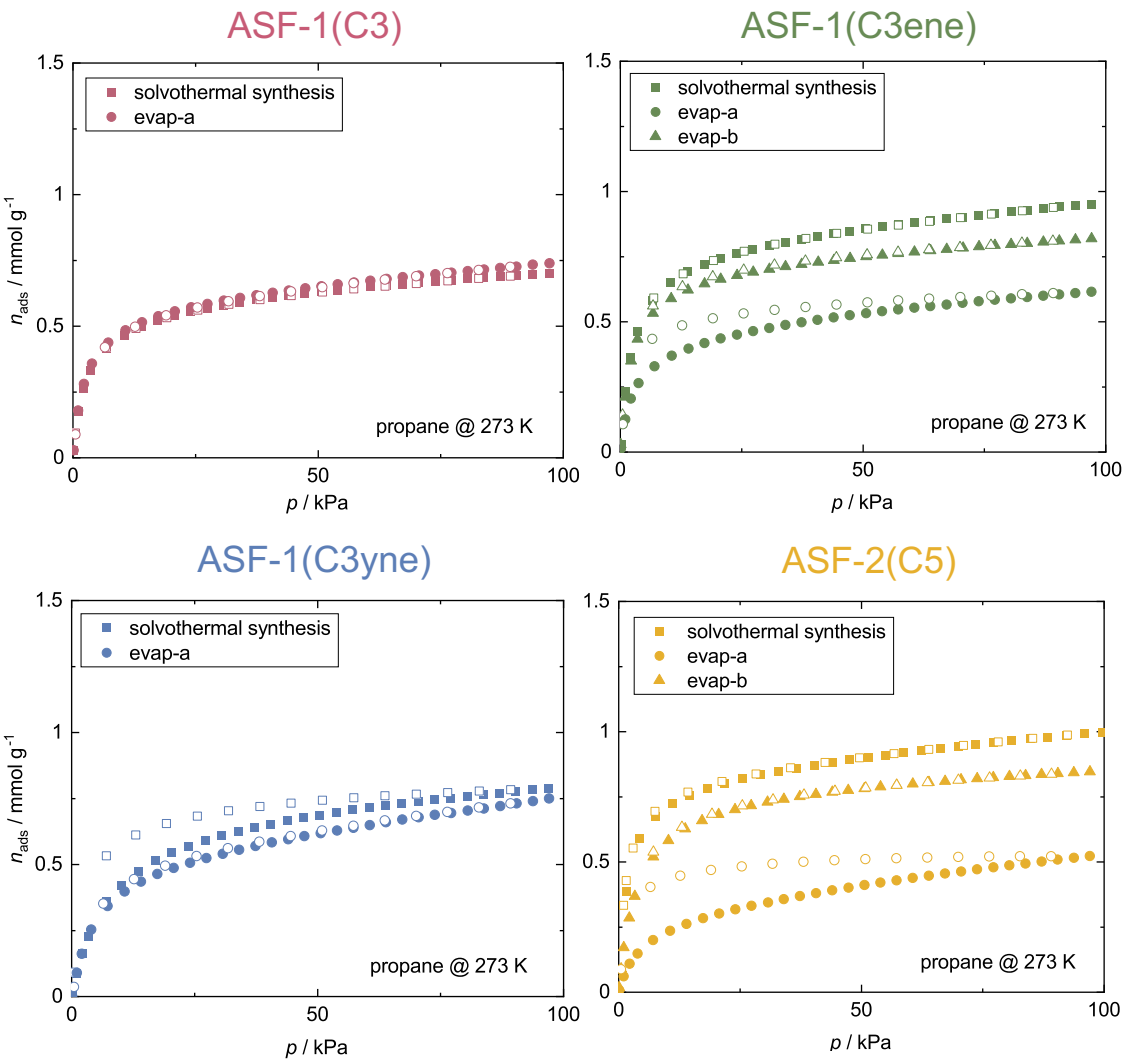

Figure B.19: Physisorption gas isotherms for propane collected at 273 K compared regarding different synthesis routes. Adsorption and desorption branches are shown as closed and open symbols, respectively.

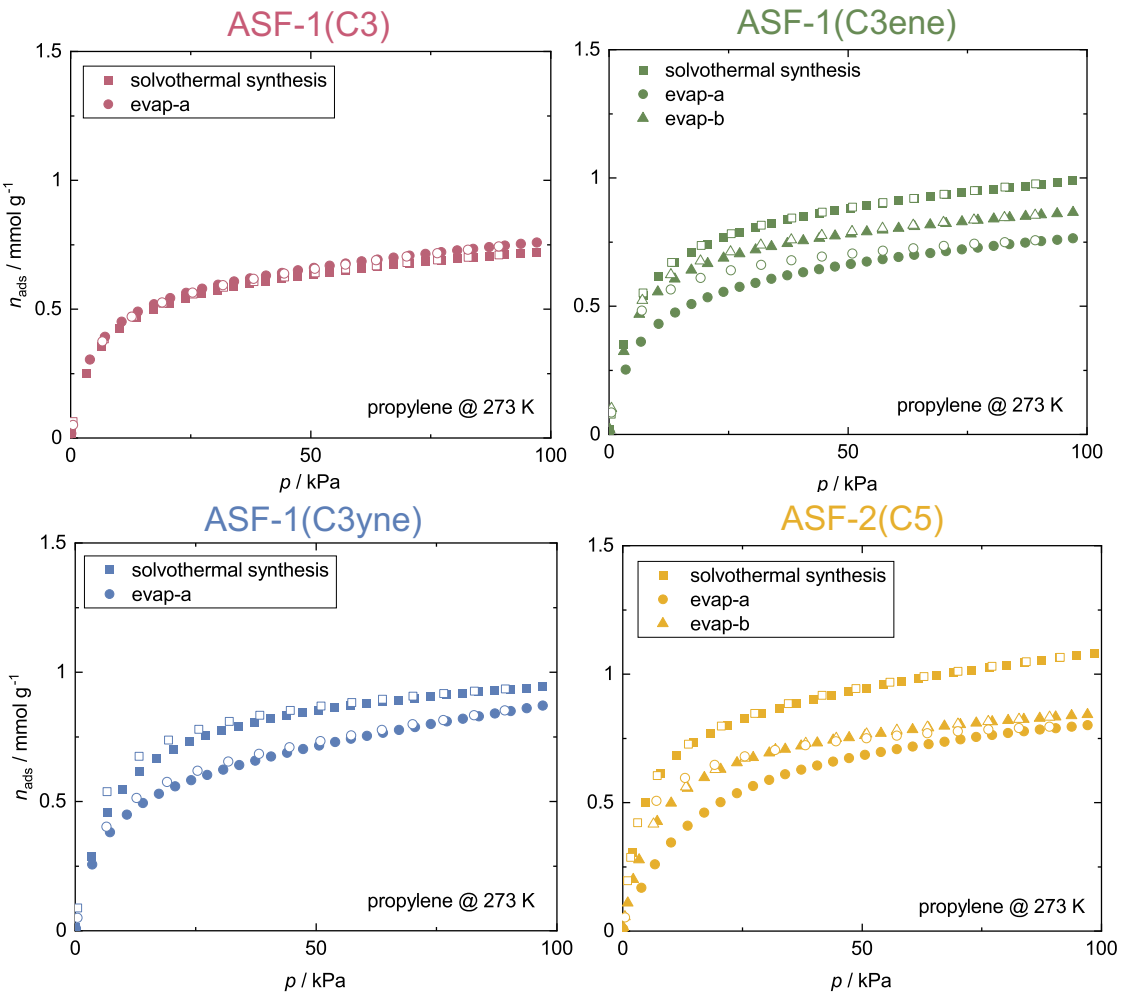

Figure B.20: Physisorption gas isotherms for propylene collected at 273 K compared regarding different synthesis routes. Adsorption and desorption branches are shown as closed and open symbols, respectively.

Pore Analysis

Table B.38: Summary of specific surface areas (S_{BET}) determined from N_2 @ 77 K and CO_2 @ 195 K isotherms for selected ASF materials.[a]

N_2 @ 77 K				
Compound	Specific surface area (BET) / $m^2\,g^{-1}$	R^2	C	p/p_0 range
ASF-1(C3)	115	0.999	5123	0.005-0.01
ASF-1(C3ene)	294	0.999	998	0.005-0.01
ASF-1(C3yne)	34	0.999	447	0.005-0.01
ASF-2(C5)	209	0.994	302	0.001-0.01
CO_2 @ 195 K				
Compound	Specific surface area (BET) / $m^2\,g^{-1}$	R^2	C	p/p_0 range
ASF-1(C3)	85	0.996	18	0.05-0.24
ASF-1(C3ene)	193	0.994	6	0.14-0.24
ASF-1(C3yne)	309	0.996	14	0.05-0.26
ASF-2(C5)	142	0.999	8	0.06-0.23

a Applied value for cross sectional areas: $\sigma(N_2$ @ 77 K) = 16.4 Å^2/molecule and $\sigma(CO_2$ @ 195 K) = 17 Å^2/molecule[87].

List of Publications

1. L. Frentzel-Beyme, P. Kolodzeiski, J.-B. Weiß, S. Henke. Quantification of gas-accesible microporosity in metal-organic framework glasses. DOI:10.26434/chemrxiv-2021-lq308.
2. R. Pallach, J. Keupp, K. Terlinden, L. Frentzel-Beyme, M. Kloß, A. Machalica, J. Kotschy, S. K. Vasa, P. A. Chater, C. Sternemann, M. T. Wharmby, R. Linser, R. Schmid, S. Henke, Frustrated flexibility in metal-organic frameworks. *Nat. Commun.*, **2021**, *12*, 1–12.
3. L. Frentzel-Beyme, M. Kloss, P. Kolodzeiski, R. Pallach, S. Henke, Meltable Mixed-Linker Zeolitic Imidazolate Frameworks and Their Microporous Glasses - From Melting Point Engineering to Selective Hydrocarbon Sorption. *J. Am. Chem. Soc.* **2019**, *141*, 12362–12371.
4. L. Frentzel-Beyme, M. Kloss, R. Pallach, S. Salamon, H. Moldenhauer, J. Landers, H. Wende, J. Debus, S. Henke, Porous purple glass – A cobalt imidazolate glass with accessible porosity from a meltable cobalt imidazolate framework. *J. Mater. Chem. A* **2019**, *7*, 985–990.
5. L. C. Wilkins, J. L. Howard, S. Burger, L. Frentzel-Beyme, D. L. Browne, R. L. Melen, Exploring Multistep Continuous-Flow Hydrosilylation Reactions Catalyzed by Tris(pentafluorophenyl)borane. *Adv. Synth. Catal.* **2017**, *359*, 2580–2584.

Immer beide Hände hoch!

Eidesstattliche Versicherung (Affidavit)

Frentzel-Beyme, Louis — 208039

Name, Vorname
(Surname, first name)

Matrikel-Nr.
(Enrolment number)

Belehrung:

Wer vorsätzlich gegen eine die Täuschung über Prüfungsleistungen betreffende Regelung einer Hochschulprüfungsordnung verstößt, handelt ordnungswidrig. Die Ordnungswidrigkeit kann mit einer Geldbuße von bis zu 50.000,00 € geahndet werden. Zuständige Verwaltungsbehörde für die Verfolgung und Ahndung von Ordnungswidrigkeiten ist der Kanzler/die Kanzlerin der Technischen Universität Dortmund. Im Falle eines mehrfachen oder sonstigen schwerwiegenden Täuschungsversuches kann der Prüfling zudem exmatrikuliert werden, § 63 Abs. 5 Hochschulgesetz NRW.

Die Abgabe einer falschen Versicherung an Eides statt ist strafbar.

Wer vorsätzlich eine falsche Versicherung an Eides statt abgibt, kann mit einer Freiheitsstrafe bis zu drei Jahren oder mit Geldstrafe bestraft werden, § 156 StGB. Die fahrlässige Abgabe einer falschen Versicherung an Eides statt kann mit einer Freiheitsstrafe bis zu einem Jahr oder Geldstrafe bestraft werden, § 161 StGB.

Die oben stehende Belehrung habe ich zur Kenntnis genommen:

Official notification:

Any person who intentionally breaches any regulation of university examination regulations relating to deception in examination performance is acting improperly. This offence can be punished with a fine of up to EUR 50,000.00. The competent administrative authority for the pursuit and prosecution of offences of this type is the chancellor of the TU Dortmund University. In the case of multiple or other serious attempts at deception, the candidate can also be unenrolled, Section 63, paragraph 5 of the Universities Act of North Rhine-Westphalia.

The submission of a false affidavit is punishable.

Any person who intentionally submits a false affidavit can be punished with a prison sentence of up to three years or a fine, Section 156 of the Criminal Code. The negligent submission of a false affidavit can be punished with a prison sentence of up to one year or a fine, Section 161 of the Criminal Code.

I have taken note of the above official notification.

Dortmund, 22.12.2021

Ort, Datum
(Place, date)

Unterschrift
(Signature)

Titel der Dissertation:
(Title of the thesis):

Towards Processable Metal-Organic Frameworks – Porous Glasses and Water-Processable Materials

Ich versichere hiermit an Eides statt, dass ich die vorliegende Dissertation mit dem Titel selbstständig und ohne unzulässige fremde Hilfe angefertigt habe. Ich habe keine anderen als die angegebenen Quellen und Hilfsmittel benutzt sowie wörtliche und sinngemäße Zitate kenntlich gemacht.
Die Arbeit hat in gegenwärtiger oder in einer anderen Fassung weder der TU Dortmund noch einer anderen Hochschule im Zusammenhang mit einer staatlichen oder akademischen Prüfung vorgelegen.

I hereby swear that I have completed the present dissertation independently and without inadmissible external support. I have not used any sources or tools other than those indicated and have identified literal and analogous quotations.

The thesis in its current version or another version has not been presented to the TU Dortmund University or another university in connection with a state or academic examination.*

*Please be aware that solely the German version of the affidavit ("Eidesstattliche Versicherung") for the PhD thesis is the official and legally binding version.

Dortmund, 22.12.2021

Ort, Datum
(Place, date)

Unterschrift
(Signature)